New bifunctional chelators for main group and transition metals: from molecules to materials and their biomedical applications

Lledos, Marina

Award date:
2018

Awarding institution:
University of Bath

New bifunctional chelators for main group and transition metals: from molecules to materials and their biomedical applications

Marina Lledos

A thesis submitted for the degree of Doctor of Philosophy

University of Bath

Department of Chemistry

March 2018

COPYRIGHT

Table of Contents

Acknowledgements

First of all I would like to thank my supervisor, Sofia Pascu, for giving me the opportunity to work on this project. It was not easy when I started, coming from a different field, and I have encountered many obstacles in the way (as you well know), but after three and a half years I can say that I have really enjoyed working in this field of chemistry and I have learnt so much! Thanks for supporting me to attend conferences and courses, and for encouraging me to gain expertise in many different techniques. It has been a pleasure to be part of the SIP group. I would also like to thank my second supervisor, Ian Eggleston, whose help has been of great value for all the aspects relative to peptide chemistry. Every time I have needed your help you have been there willing to offer support and advise me.

To my colleagues and friends in the Pascu group, in particular those with whom I have spent most of my time: Sophia, Federico, Fernando, Vincenzo, Haobo, Sam and Giuseppe. It has been great working with all of you and learning from each other. I could not have been in a better group with better people! I have really enjoyed your company during these almost four years and the long days in the lab have been fun with all of you. I would like to thank Sophia for being a great support in everything, ever since we started our PhDs together, which seems a long time ago now. I am very grateful to Fernando as well for being such a good friend, and for reading the different chapters of my thesis and providing useful suggestions. Also special thanks to Federico for the nice times spent together, especially in the last months, and for coping with my mood changes in the most stressful moments. Simone has been a good friend in the department who has joined us in many events, and I want to thank him for lending us stuff every time we ran out of something in the lab. Thanks to all of you for all the good and fun things that we have lived together. Our Friday evenings at the pub were definitely the best way to end the week, and I hope to keep this tradition wherever I go.

Thanks to Andrea, with whom I have become friends just in this last period of my PhD, for being an excellent friend and partner in crime, and for living by the “un jager tonto” motto together with Fernando.

I have also had the chance to meet some Spanish people who are amazing women and great chemists: Maia, Lucia, Sara and Eva, we have had so many laughs together. Our cigarette breaks were such a good way to unwind for a few minutes and talk about things that were non-science related (*e. g.*, caramelitos). I also enjoyed our lunch breaks discussing about our soap opera lives. You have been great friends ever since I met you, and we have had some crazy

experiences together. Thanks for your help and support, for cheering the fun times and for listening to me when I felt down.

I feel very lucky to have been able to meet such amazing people in Bath who have contributed to making my time here some of the best years of my life. I love all of you and I am sure that our friendship doesn't end with this PhD. I would also like to extend this to the countless other people I have met while studying at the University of Bath who have made it such a pleasant place to work.

I am grateful to David, once part of the SIP group, for teaching me so much about materials chemistry and for being always willing to help even after he moved back to Spain.

Thanks to Andy for making me see the bright side of organic chemistry and teaching me so many things about it. Discussions with him were indeed useful towards the success of some reactions in this thesis.

Craig John was a great support when I first moved to Bath and during the first part of my PhD, and I have good memories of the time we cheered, setting up in this city and exploring it together.

At this point of my career I am grateful to everyone who has contributed somehow to my chemistry education, including my secondary school science teachers and all the lecturers I had while studying for my degree at the Universitat de Barcelona, whom I really appreciate and of whom I keep great memories. You have all contributed to my passion for chemistry.

My friends in Barcelona, especially Maria del Mar and Júlia, made me have a very enjoyable time every time I was back on holiday, making me feel as if time had not passed and I had never left that city. It was great to look for fun activities to do together, and the Barcelona experience was always fun and real with you. Also thanks for listening to eternal voice messages about life and the ins and outs of my PhD.

Finally, I want to thank my family, and especially my parents the most: Agustí and Chus. Gràcies per donar-me suport sempre en tot el que he volgut fer a la vida, i per ensenyar-me tantes coses. Sou un pilar fonamental a la meva vida i sense vosaltres no seria qui sóc ni on sóc avui. Gràcies per les visites i per totes les hores parlant per Skype, i per mimar-me tant cada cop que vinc a veure-us a Barcelona. Espero que estigueu tan orgullosos de mi com jo ho estic de vosaltres. Miquel, també va per tu. Us estimo moltíssim!

Abstract

This work describes investigations into the synthesis of new potential multimodal agents for medical imaging of cancer cells. For this purpose, two approaches were used: (i) based on novel fluorescent nanohybrids based on iron oxide nanoparticles, and (ii) based on a symmetric tripodal core that can be functionalised, giving rise to bifunctional chelating molecular and nanocomposite agents. Each Chapter of this thesis describes the synthesis and characterisation of the different components of the desired probes. The cellular viability of the as-prepared imaging agents was evaluated using different cell lines (*e. g.*, PC-3, EMT6 and FEK-4) and assays, such as MTT and crystal violet. Laser scanning confocal microscopy investigations were carried out on the new fluorescent conjugates synthesised hereby to study their localisation within cancer cells.

Chapter 1 describes the context of this work, starting with a background of cancer and tumour hypoxia, and including overviews of different imaging modalities particularly applied to diagnosis, staging and follow-up of prostate cancer (PET, SPECT, MRI, confocal and epi-fluorescence microscopy, FLIM and TCSPC). The synthesis and development of some radioisotopes for use in PET/SPECT imaging is detailed. The use of imaging probes based on thiosemicarbazide derivatives is described together with their advantages, due to the importance of this type of compounds in tumour hypoxia detection and multimodality imaging potential. Moreover, the use of iron oxide nanoparticles as scaffolds for biomedical and nanomedicine applications, with special importance for magnetic resonance imaging, is reviewed. Finally, the use of bombesin, a GRP-targeting peptide, as a vector for the recognition of cancer cells and its incorporation into imaging probes is discussed.

Chapter 2 describes synthetic approaches towards the functionalisation of a tripodal symmetric organic core containing $–CH_2Br$ units used as starting material. Novel fluorophores based on BODIPY were synthesised and characterised hereby, together with other compounds including different linkers. The most promising fluorescent molecules synthesised and characterised hereby were tested in PC-3 cells using single and two-photon laser scanning confocal microscopy, and their cell viability was evaluated by means of MTT assays. Furthermore, two deferoxamine-based molecules were synthesised and radiolabelled with zirconium-89.

Chapter 3 describes the synthesis of a peptide sequence (the [7-13] bombesin fragment, of interest for cancer cells targeting) using solid-phase peptide synthesis, and the attempts to incorporate this into the fluorescent tripodal molecule synthesised in the previous chapter.

Moreover, the synthesis of a deferoxamine-bombesin conjugate as a new chelator for main group and transition metals is reported herein.

Chapter 4 describes the synthesis of novel thiosemicarbazide-based ligands, some structural investigations using NMR spectroscopy and the single crystal X-ray diffraction data collected to fully characterise the main new molecules emerging from this study. The complexation tests to incorporate several metals from main group and transition metals (*e. g.*, Zr(IV), Ga(III) and Cu(II)) and the results obtained are reported. The behaviour of the ligands in three different cell lines was assessed via crystal violet assays, and their IC_{50} values calculated after 24, 48 and 72 hours of incubation in cells.

Chapter 5 describes the synthesis and characterisation of novel imaging probes based on benign iron oxide nanoparticles coated with a silica shell. These were functionalised with two types of fluorophores: quantum dots ($Cd_{0.1}Zn_{0.9}Se$) and a potential hypoxia targeting unit, and three radiolabelling methods using gallium-68 were developed. An alternative system based on citric acid-coated iron oxide nanoparticles and functionalised with a BODIPY derivative was synthesised. The most promising nanocomposites in terms of kinetic stability were tested in PC-3 cells, using single and two-photon laser scanning confocal microscopy to study their fluorescent properties. Their cell viability was tested in PC-3 cells using MTT assays over a range of conditions and timescales.

Chapter 6 constitutes a summary of the work carried out and results found during this thesis and includes some proposals for future work based on the research findings described here.

Chapter 7 contains all the experimental details and characterisation data for the compounds described in this thesis.

The *Appendices* provide supporting spectroscopic evidence and X-ray diffraction data for the new compounds synthesised in this work.

List of abbreviations

AcCN	Acetonitrile
APCI	Atmospheric-pressure chemical ionisation
ASAP	Atmospheric solids analysis probe
ATSM	Diacetyl-bis(N-4-methylthiosemicarbazone)
BAM	Biologically active molecule
BBN	Bombesin
BET	Brunauer, Emmet and Teller
BJH	Barrett-Joyner-Halenda
BODIPY	4,4-difluoro-4-bora-3a,4a-diaza-s-indacene
CD	Circular dichroism
CLF	Central Laser Facilities
COSY	Correlation spectroscopy
CT	Computed tomography
DBCO	Dibenzocyclooctyne
DCM	Dichloromethane
DDQ	2,3- dichloro-5,6-dicyano-1,4-benzoquinone
DF	Desferal
DFO	Deferoxamine
DIPEA	N,N'-diisopropylethylamine
DLS	Dynamic light scattering
DMF	N,N'-dimethylformamide
DMSO	Dimethyl sulfoxide
DNA	Deoxyribonucleic acid
DOSY	^{1}H diffusion-ordered spectroscopy
DOTA	1,4,7,10-tetraazacyclododecane-1,4,7,10-tetraacetic acid
DTPA	Diethylenetriaminepentaacetic acid
E.A.	Elemental analysis
EDC	N-(3-dimethylaminopropyl)-N'-ethylcarbodiimide
EDTA	Ethylenediaminetetraacetic acid
EDX	Energy dispersive X-ray spectroscopy
EI	Electron ionisation
EMEM	Eagle's Minimum Essential Medium
EMT6	Mice breast cancer cells
ER	Endoplasmic reticulum
ESI	Electrospray ionisation
EtOH	Ethanol
fcc	Face-centered cubic
FCS	Activated foetal calf serum

FEK-4	Epithelial fibroblast cells
FLIM	Fluorescence lifetime imaging
FLT	Fluorescence lifetime
Fmoc	9-fluorenylmethyloxycarbonyl
FP	Focal point
FT-IR	Fourier transform infrared spectroscopy
F-5-TSC	Fluorescein-5-thiosemicarbazide
GRP	Gastrin-releasing peptide
GRPr	Gastrin-releasing peptide receptor
HATU	1-[bis(dimethylamino)methylene]-1H-1,2,3-triazolo[4,5-b]pyridinium-3-oxide
HBTU	*N,N,N′,N′*-tetramethyl-*O*-(1*H*-benzotriazol-1-yl)uronium hexafluorophosphate
HIF-1	Hypoxia-inducible factor-1
HOBt	1-hydroxybenzotriazole
HPLC	High performance liquid chromatography
HSQC	Heteronuclear single quantum coherence spectroscopy
IGEPAL	Polyoxyethylene(5)isooctylphenyl ether
IgG	Immunoglobulin G
IONPs	Iron oxide nanoparticles
m/z	Mass to charge ratio
mAb	Monoclonal antibody
MALDI	Matrix-assisted laser desorption/ionisation
MeOH	Methanol
MRI	Magnetic resonance imaging
MS	Mass spectrometry
MTT	3-(4,5-dimetrhylthiazol-2-yl)-2,5-diphenyltetrazolium bromide
nESI	Nanoelectrospray ionisation
NHS	N-hydroxysuccinimide
NMB	Neuromedin B
NMR	Nuclear magnetic resonance
NMSF	National Mass Spectrometry Facility
NPs	Nanoparticles
NODASA	1,4,7-triazacyclononane-1-succinic acid-4,7-diacetic acid
NOESY	^{1}H-^{1}H nuclear Overhauser enhancement spectroscopy
NOTA	1,4,7-triazacyclononane-N,N',N''-triacetic acid
ODA	Octadecanamine
ORTEP	Oak ridge thermal-ellipsoid plot program
o/n	Overnight
PBS	Phosphate buffered saline
PC-3	Prostate cancer cells
PEG	Polyethylene glycol
PET	Positron emission tomography

PETIC	Positron Emission Tomography Imaging Centre
PyBOP	(benzotriazol-1-yloxy)tripyrrolidinophosphonium hexafluorophosphate
QDs	Quantum dots
QY	Quantum yield
SPECT	Single-photon emission tomography
RAL	Rutherford Appleton Laboratory
RCY	Radiochemical yield
RNA	Ribonucleic acid
Rf	Retention factor
ROESY	^{1}H-^{1}H rotating frame Overhauser enhancement spectroscopy
RPMI	Roswell Park Memorial Institute
RT	Room temperature
Rt	Retention time
SPAAC	Strain-promoted alkyne–azide cycloaddition
SPIONs	Superparamagnetic iron oxide nanoparticles
SPPS	Solid-phase peptide synthesis
st	Stretching
STEM	Scanning transmission electron microscopy
STS	Solid target system
$t_{1/2}$	Half-life
TCSPC	Time-correlated single photon counting
TEM	Transmission electron microscopy
TEOS	Tetraethylorthosilicate
TFA	Trifluoroacetic acid
TGA	Thermogravimetric analysis
THF	Tetrahydrofuran
TIPS	Triisopropylsilane
TLC	Thin layer chromatography
TMS	Tetramethylsilane
TOP	Trioctylphosphine
TOPO	Trioctylphosphine oxide
WHO	World Health Organisation
wt	Percentage by weight
W/O	Water-in-oil
XRD	X-ray diffraction
β^{+}	Positron
δ	Chemical shift in ppm (NMR)

List of compounds (* indicates that the compound is novel)

Chapter 2

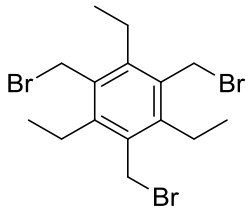

(1)

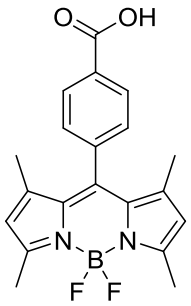

(2)

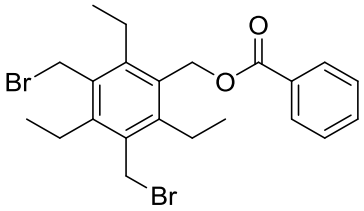

(3) *

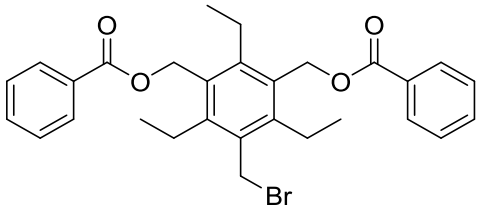

(4) *

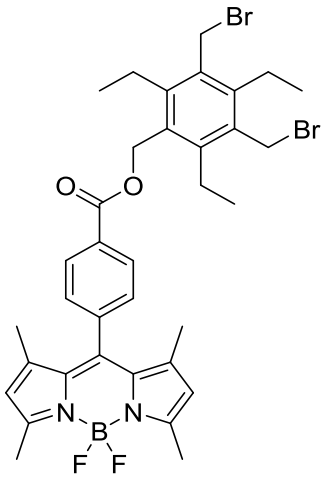

(5) *

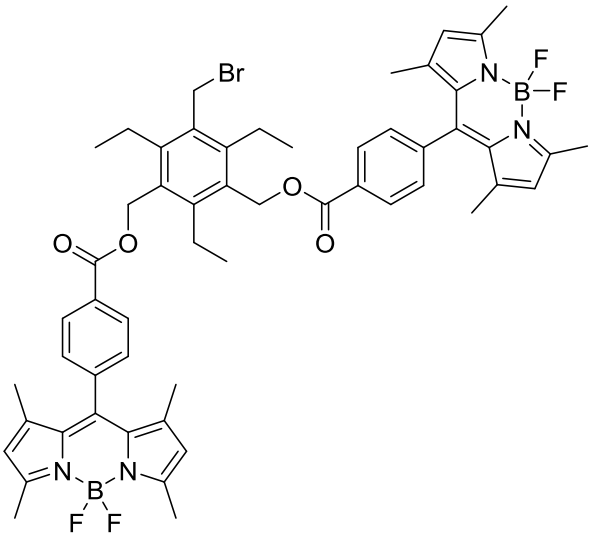

(6) *

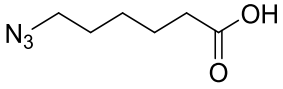

(7)

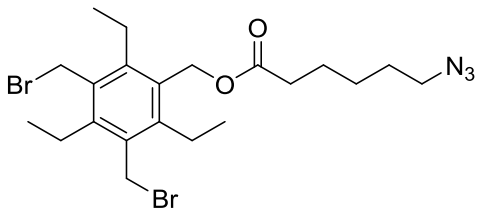

(8) *

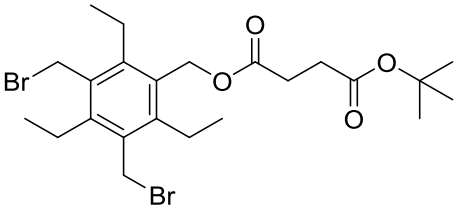

(9) *

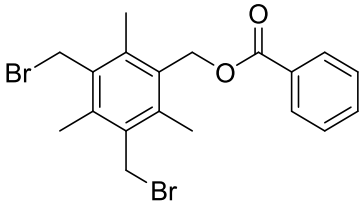

(10) *

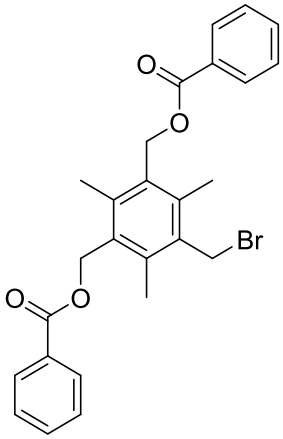

(11) *

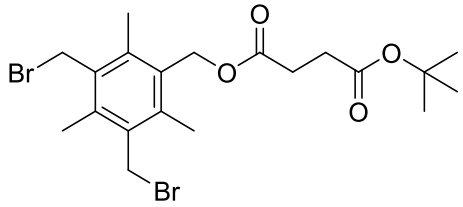

(12) *

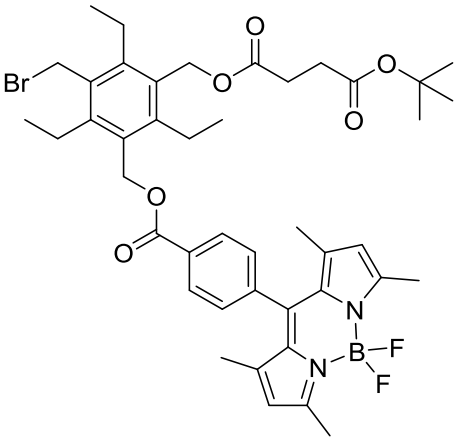

(13) *

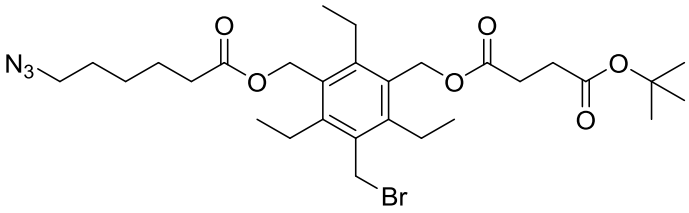

(14) *

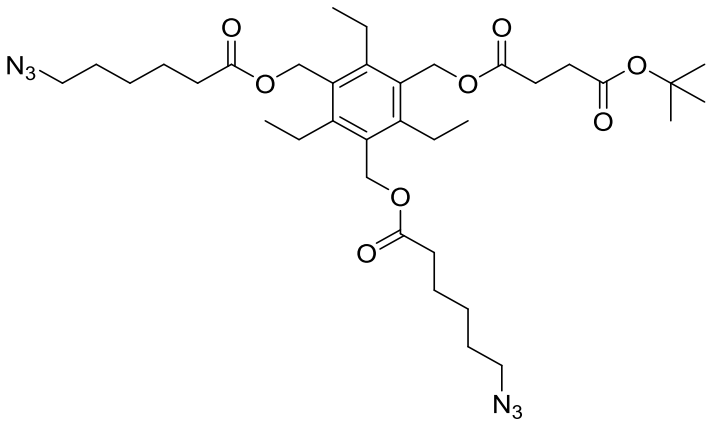

(15) *

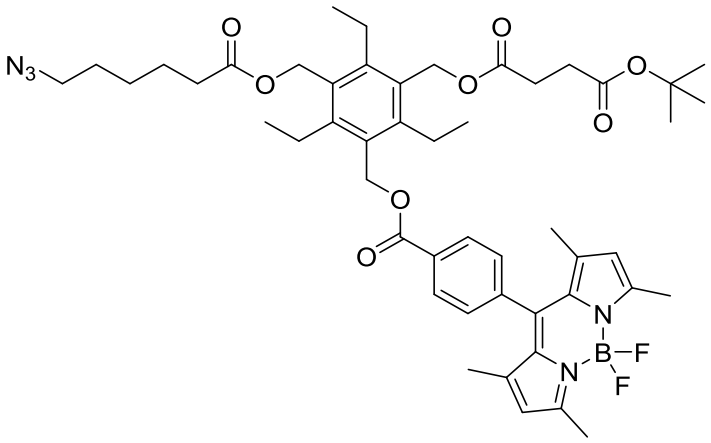

(16) *

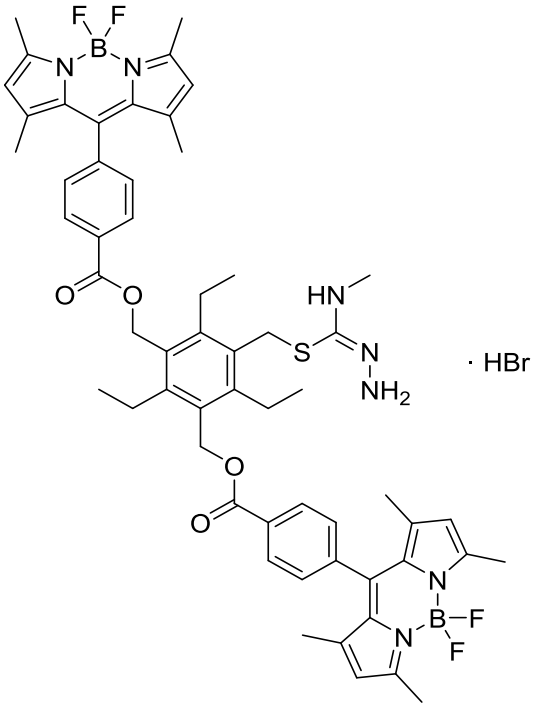

(17) *

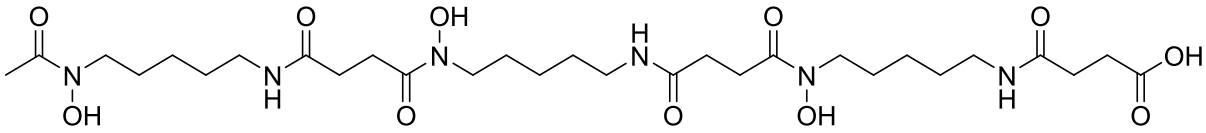

(18)

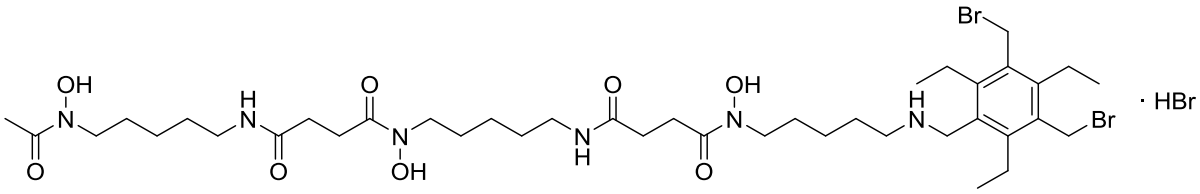

(19) *

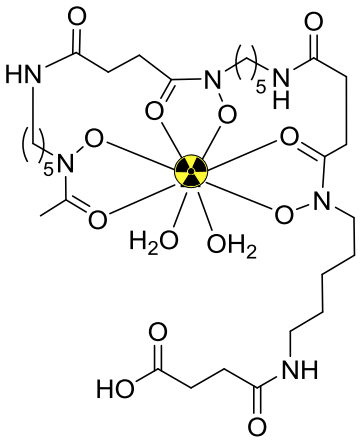

(20)

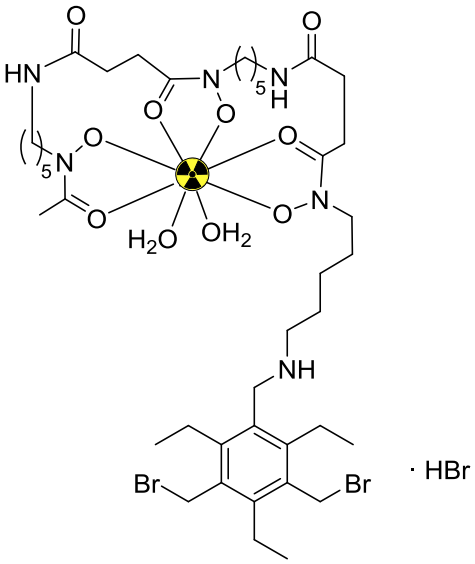

(21) *

Chapter 3

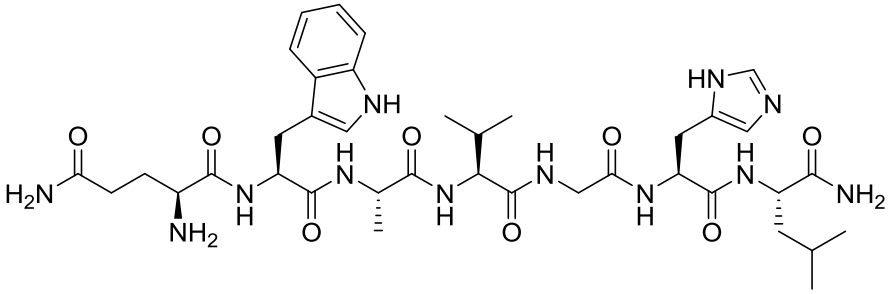

(22)

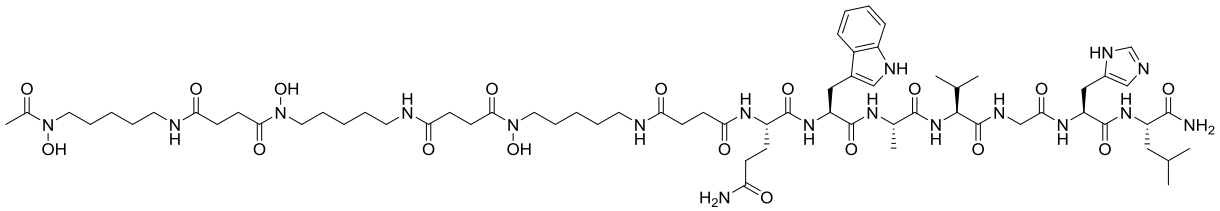

(23) *

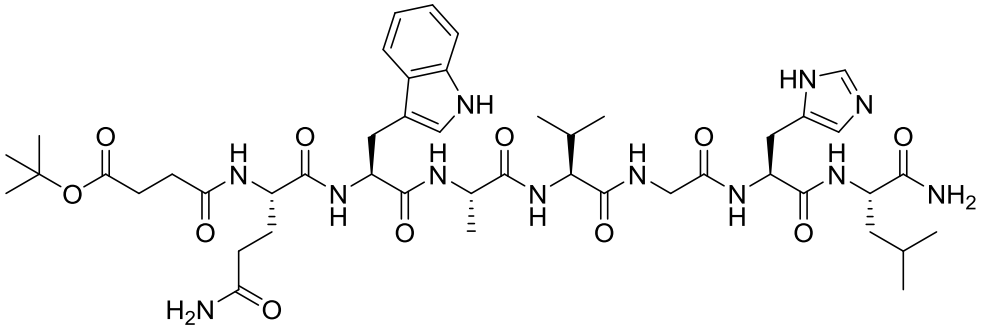

(24) *

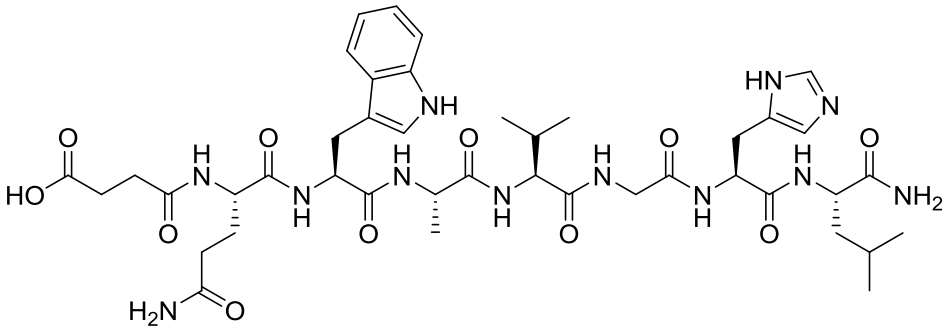

(25) *

Chapter 4

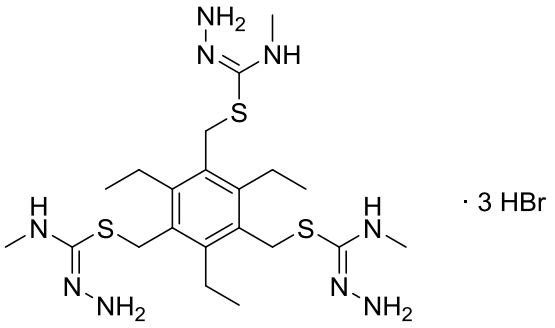

· 3 HBr

(26) *

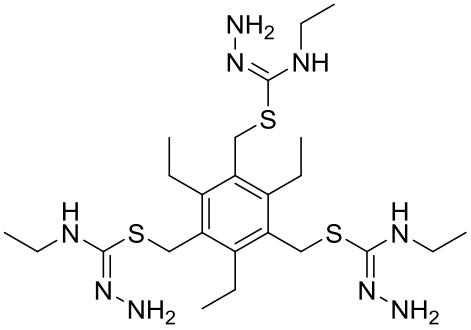

· 3 HBr

(27) *

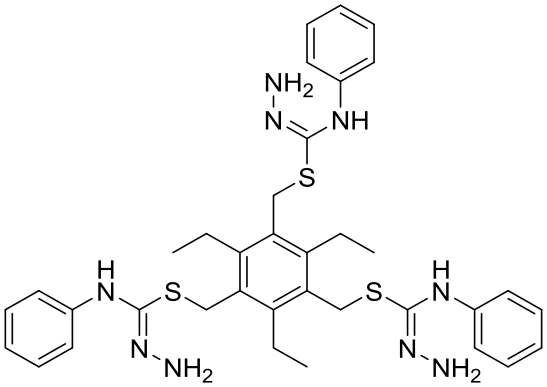

· 3 HBr

(28) *

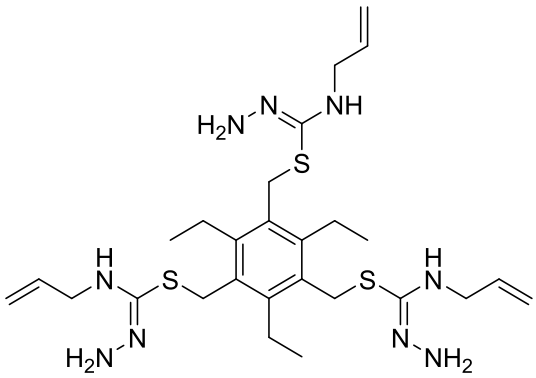

· 3 HBr

(29) *

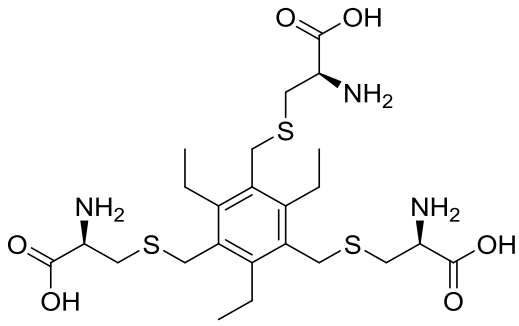

· 3 HBr

(30) *

Chapter 5

Fe_3O_4

(31)

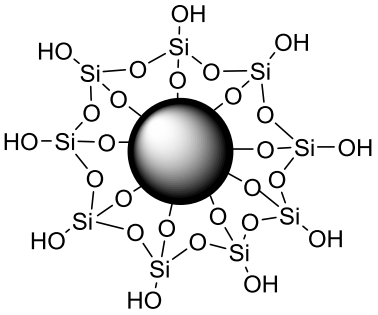

(32)

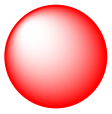

$Cd_{0.1}Zn_{0.9}Se$

(33)

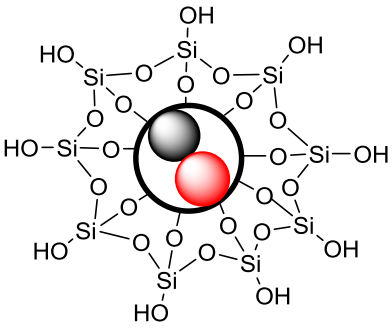

(34) *

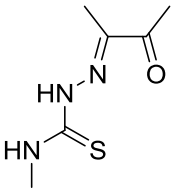

(35a)

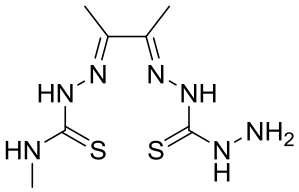

(35b)

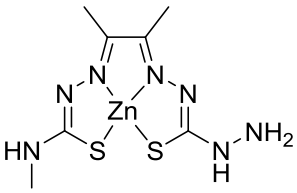

(35c)

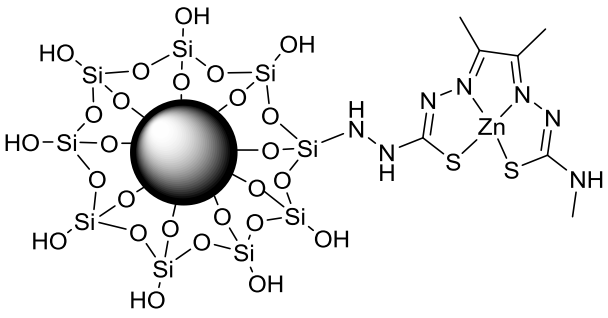

(36) *

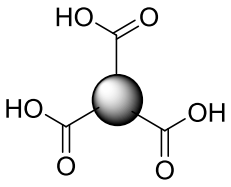

(37)

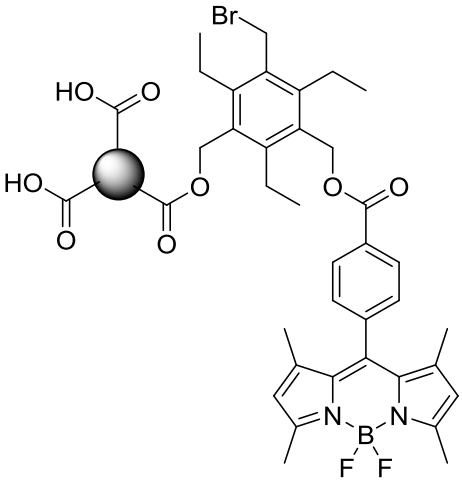

(38) *

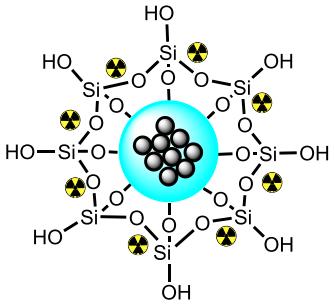

(39) *

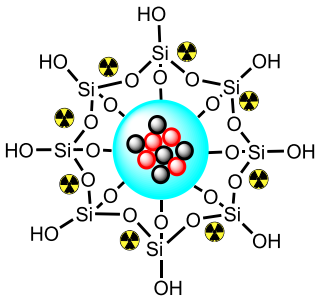

(40) *

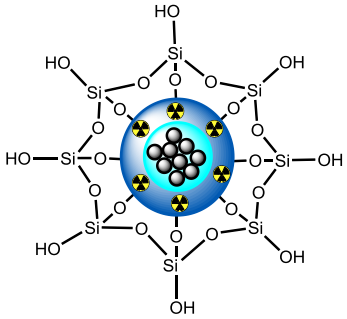

(41) *

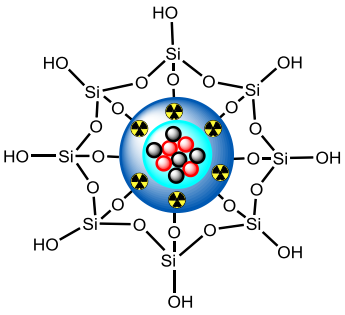

(42) *

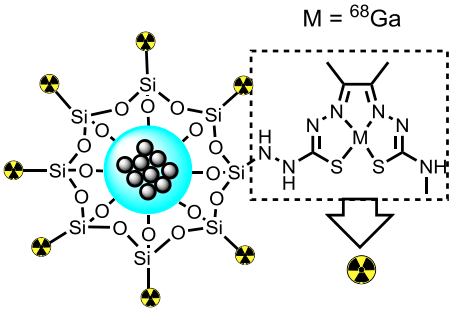

(43) *

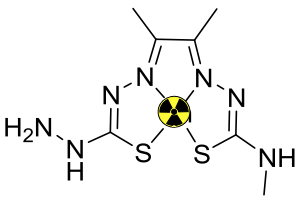

(44)

Chapter 1. Introduction

1.1. Background

Cancer is one of the top ten causes of death in the world in the 21st century. According to a cancer statistics report from the World Health Organization (WHO), in the year 2012, 14.1 million adults were diagnosed with cancer, and from these, 8.2 million (58.2%) died from cancer worlwide.[1] Hence, the importance for increased research in drug discovery in order to diagnose and treat cancer is clear.[2-4]

It has been proven that the earlier the stage at which the tumour is diagnosed, the higher the patient's survival rate will be. This is clearly illustrated in *Chart 1.1*, which shows prostate cancer diagnosis and the 5-year survival rate by stage from a study carried out in men between 2006 and 2012 in the United States.

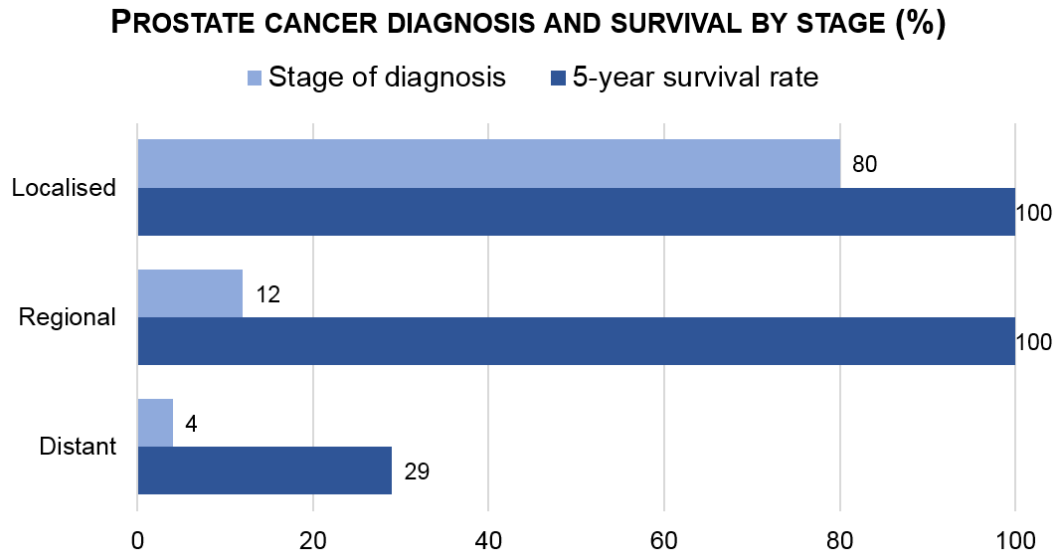

Chart 1.1. Prostate cancer diagnosis and 5-year survival rate by stage, 2006 – 2012. Data obtained from reference [5].

As seen from *Chart 1.1*, until recently around 80% of prostate cancers were diagnosed at the localised stage, allowing 100% of those patients to survive in a 5-year term. Around 12% of cases were localised at the regional stage, with the tumour at a spreading stage (adjacent), and then the survival rate in a 5-year term was still 100%. Finally, only 4% of patients were diagnosed at a late stage, from which only 29% survived five years post-diagnosis. Consequently, it is easily seen that an early cancer diagnosis is equally important as the treatment for this, since an early diagnosis can improve the patients' survival rate.

Currently, four methods are being used in clinical practise to diagnose cancer:[6-12]

- Blood or other sample testing techniques by targeting overexpressed molecules, such as sugars, fats, proteins, ribonucleic acid (RNA) and deoxyribonucleic acid (DNA). However, there is a lack of sensitivity and selectivity in the current testing reagents.[13]
- Biopsy is the most common way to diagnose cancer, consisting in the collection of a tissue sample from the site of interest for a subsequent examination of the morphology and gene status.
- Medical imaging (or molecular imaging) is useful in the cases when the location of a tumour in a specific site is difficult. Molecular imaging has the capacity to speed up the diagnosis process, and combined with blood sample testing it enables the location of a tumour and an early cancer detection.[14]
- Endoscopy is generally applied at the middle or late stages of cancer diagnosis in combination with other imaging tools to confirm a cancer diagnosis, or with biopsy to collect a tissue sample for further investigations.[14]

From all the above mentioned cancer diagnostic techniques, medical imaging is the one that is concentrating an important part of the research in this field. Medical imaging techniques commonly used in cancer diagnosis include X-ray computed tomography (CT scans), X-ray imaging, magnetic resonance imaging (MRI) and positron emission tomography (PET).[15-17] Similar to PET, single-photon emission computed tomography (SPECT) can also be used to detect pathologies, although its sensitivity is much lower than that of PET. All these techniques are based in the use of a source of energy (X-ray, magnetism, gamma or positron decay) to create a detailed view of the body in order to locate a tumour mass, and they can be used to detect all types of cancer.

Many medical imaging methods are based on the use of radioisotopes (mainly positron and gamma emitters) as contrast agents. For example, PET uses positron-emitting radioisotopes such as ^{68}Ga ($t_{1/2}$ = 68.3 min), a popular radioisotope in clinical research. When ^{68}Ga is anchored onto an adequate *in vivo* delivery vehicle in precancerous stages, it selectively concentrates around infected sites and areas of inflammation, and it can report on areas of rapid cell division. However, there are longer lived metallic isotopes which will most probably become more promising in future diagnostic imaging applications, since their longer circulation *in vivo* enhances the tumour/background ratio.[18] One of these promising radioisotopes is ^{89}Zr ($t_{1/2}$ = 78.4 h), as will be described in the next sections.[6]

As such, there is a need to develop new imaging contrast molecules which can selectively concentrate around the affected sites.

1.2. Cancer and tumour hypoxia

Hypoxia appears as a result of a disequilibrium between the supply and the consumption of oxygen in a number of different diseased tissues, including tumours. Areas with O_2 tensions (pO_2 values) ≤ 2.5 mmHg are considered hypoxic tissue areas. These areas can be found in a broad variety of human malignancies (*e.g.*, breast, uterine, cervix, vulva, head and neck, prostate, rectum and lung cancer, brain tumours and malignant melanomas).[19-28] Hypoxia starts at a very early stage during tumour development from a tumour diameter of just a few millimetres,[29-32] and it is a characteristic feature of the environment found in advanced solid tumours. It has been proven that this can promote tumour progression and resistance to therapy. As such, tissue hypoxia is seen as a central factor for tumour aggressiveness and metastasis, independent of aspects such as tumour stage and nodal status.[19, 29]

Hypoxia occurs in tissues as a consequence of inadequate blood supply, affecting tumour cell biology.[29] In normal (healthy) tissues or organs, the O_2 supply matches the metabolic requirements, while in locally advanced solid tumours, the O_2 consumption rate of some cells can outweigh a restricted oxygen supply and result in the development of tissue areas with very low O_2 levels.[19] It has been found that 50-60% of locally advanced solid tumours may suffer from some hypoxic and/or anoxic tissue areas that are heterogeneously distributed within the tumour mass.[19]

Non-invasive assessment of hypoxia is possible via imaging techniques such as PET or SPECT by detection of radiolabelled tracers or with MRI techniques. However, clinical experience using these methods in patients is so far very limited.[19]

As mentioned before, cells in hypoxic regions are resistant to both radiotherapy and chemotherapy, so that hypoxia is a serious concern that moreover contributes to tumour progression.[29, 30] This is thought to be caused by an absence of oxygen-based free radical processes that otherwise make cells sensitive to ionising radiation. Many studies have been carried out to stablish the relationship between tumour size and therapeutic sensitivity, and a size-dependent variation in hypoxic fractions was found. Studies on lung nodules of three different sizes showed that, while there was no evidence of necrosis on 0-5 mm^3 nodules, both 6 mm^3 and 20 mm^3 nodules contained substantial areas of dead cells, implying hypoxia. Consequently, hypoxia would be expected to scale with tumour size.[33] *Figure 1.1* shows a schematic description of hypoxic regions in malignant solid tumours.

Even though nowadays there is much research invested in hypoxia and despite all the information collected in the past few decades, there are still many important questions to answer in order to develop the long-standing goal of exploiting tumour hypoxia as the best validated target in oncology.[34]

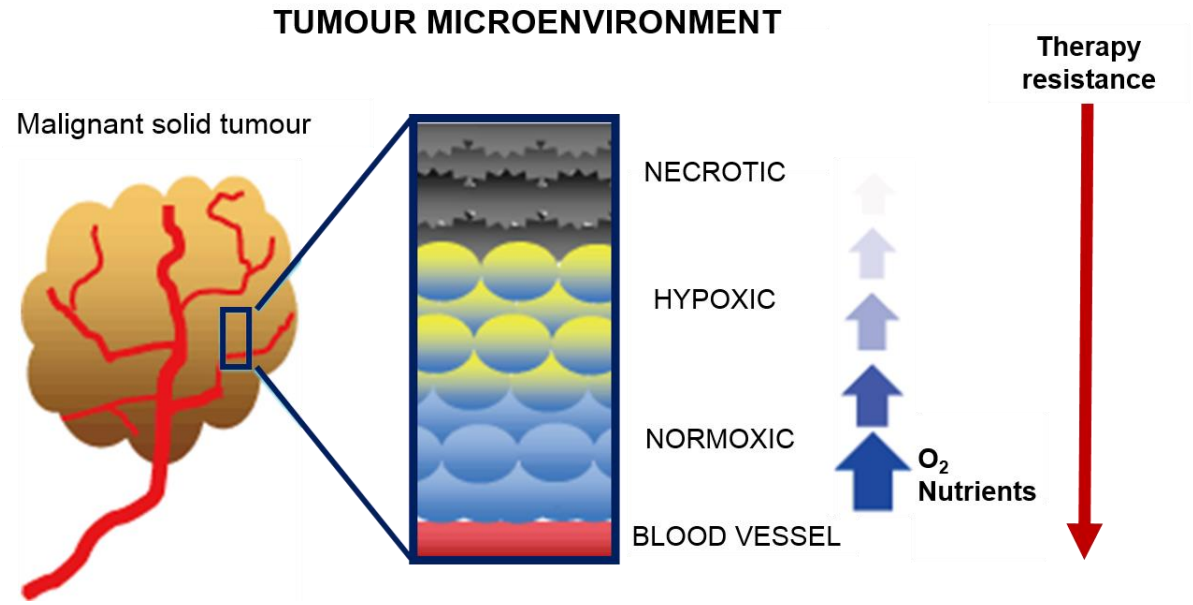

Figure 1.1. Representation of a malignant solid tumour with its three differenced areas. The tissue area next to the blood vessel is normoxic as the supply and consumption of O_2 is "normal", as it should be in most healthy cells. The next area is hypoxic, having a deficit of O_2. Finally, the last area is necrotic, which corresponds to dead cells. As seen in the arrows next to the different areas, therapy resistance is greater at necrotic and hypoxic areas, and O_2 and nutrients arrive less effectively at these areas. Adapted from reference [35].

1.3. Medical and optical imaging and its underlying basic physicochemical concepts

1.3.1. Positron emission tomography (PET)

Positron emission tomography is a relevant technique among the ones commonly used in medical imaging for cancer diagnosis. PET is an imaging modality frequently used for screening, diagnosing and staging body tissues to identify or follow certain chronic conditions such as cancer and/or neurodegenerative diseases. Thanks to PET, it is possible to understand the fundamentals of the underlying biology of these diseases and to improve and discover new treatments.[36-41] It has emerged as an imaging modality with excellent sensitivity for *in vivo* studies in the field of molecular imaging.[42, 43]

This technique can be thought of as a small camera that can take photos of a subject of interest with an exposure time that goes from a few seconds to several minutes. This imaginary camera does not image visible light, instead it images high-energy gamma-rays that are emitted from the radioisotope present inside the subject. In this regard, it is possible to label biological molecules with a radioactive isotope: an isotope able to ultimately produce two gamma-rays by emitting a positron from its nucleus. This positron (the antimatter counterpart of an electron) eventually collides with a nearby electron and they annihilate each other in order to produce energy in the form of two very energetic gamma-rays (511 keV), which are emitted in opposite directions and placed at 180 degrees with respect to each other (*Figure 1.2*).[44]

As such, every PET scan requires a positron-emitting radioisotope to be inserted into the body. The two main challenges in the synthesis of positron-emitting labelled compounds are: (i) the short half-lives of most of the common cyclotron-generated PET radioisotopes (*Table 1.1*), and (ii) the extremely low radioisotopic concentrations that are used (pM-nM).[36, 45, 46]

Because of the extremely short half-lives of some of the positron-emitting isotopes used in PET, the chemistry that leads to the incorporation of the isotope into the parent molecule, and its subsequent introduction into the subject's body needs to be as rapid as possible.[44]

There is a wide variety of radioisotopes that can be employed for PET. Some of them are more commonly used: ^{15}O, ^{13}N, ^{11}C and ^{18}F; and others are less common: ^{14}O, ^{64}Cu, ^{62}Cu, ^{124}I, ^{76}Br, ^{82}Rb and ^{68}Ga. Most of these isotopes need to be produced in a cyclotron, but some of them – such as ^{68}Ga and ^{82}Rb – can be produced using a generator. Once labelled tracers are

introduced into the subject, their distribution and concentration can be followed by PET imaging.[44, 47]

Table 1.1. Half-lives of the most commonly used positron emitters.[36]

Isotope	Half-life
^{15}O	2.04 min
^{13}N	9.96 min
^{11}C	68 min
^{18}F	110 min
^{68}Ga	68.3 min
^{64}Cu	12.7 h
^{89}Zr	78.4 h

Among the isotopes listed in *Table 1.1*, ^{11}C and ^{18}F are the most commonly used due to their relatively longer half-lives. The half-lives of ^{13}N and ^{15}O are too short to carry out complex radiochemical syntheses of more than one reaction step. An example of the use of ^{15}O is the radiolabelling of water, butanol and gases (CO, CO_2) for inhalation studies.[48] Regarding ^{13}N, this radioisotope is incorporated into nitrite/nitrate and ammonia, and these labelled compounds can be used as starting materials to prepare other more complex labelled products (*e.g.*, amino acids).[49-51]

There are several criteria that tracers need to fulfil to be successfully used as imaging probes for PET. The most important one is that the positron-emitting isotope must be chemically linked to the molecule of interest and not easily dissociate. If it does dissociate, the radioisotope will be the one followed by PET imaging instead of the tracer. Consequently, it is important to choose a radiotracer with a high specificity for the target molecule since interaction of the radiotracer with other molecules could interfere with the aiming radioactive signal that is detected by the PET camera. It is also desirable to choose a radiotracer that has a high affinity for its target in order to obtain high-contrast PET images. Moreover, another important criterion is that the label must not significantly modify the biological properties of the parent molecule. Finally, the distribution of the radiopharmaceutical in the body should be related to the physiological response to measure functionality of the biochemical process under research.[44, 49, 52-54]

Nowadays, PET is being used in conjunction with other diagnostic techniques such as computed tomography (CT) in order to provide more detailed information about malignant (cancerous) tumours and other lesions. The combination of these two techniques is promising in the diagnosis and treatment of several types of cancer.

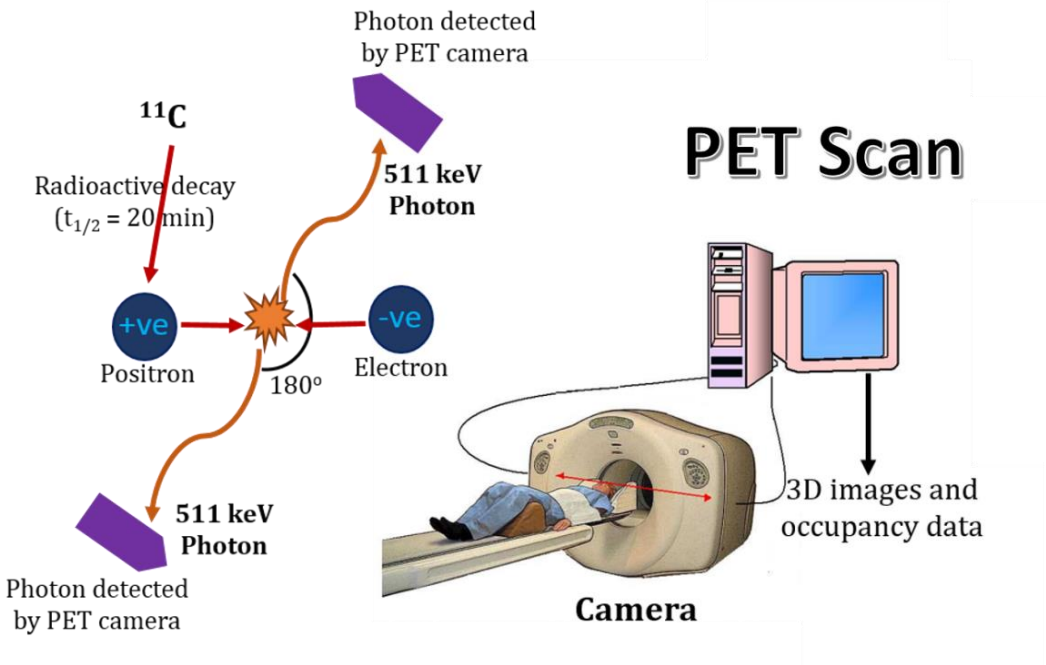

Figure 1.2. Principle of positron annihilation. PET cameras can detect paired gamma rays (511 keV each), produced by the positron annihilations, that travel in opposite directions at 180° to each other. Hence, positron decay can be localised without collimation by using the principles of coincidence detection. Since PET cameras do not require collimators, they have a much higher count rate than SPECT systems. Adapted from reference [55].

1.3.2. Single-photon emission computed tomography (SPECT)

As well as positron emitters, there are isotopes that are beta-emitters (such as ^{3}H and ^{14}C). Beta-particles (electrons) do not travel significant distances in tissue and hence do not produce annihilation events, as positrons do. For this reason, beta-emitter isotopes are not of use for non-invasive imaging of living subjects. However, these kind of isotopes can also be used with tracers for imaging living subjects with a different type of camera ("gamma-cameras"), which do not require the production of two coincident gamma-rays. These type of cameras are employed in a process known as single-photon emission computed tomography, in which they are rotated around the subject to produce tomographic images.

In comparison to SPECT, PET is at least ten times more sensitive, and positron-emitting isotopes produce less perturbation to the biochemical behaviour of the radiolabelled parent molecules because these can readily be substituted for naturally occurring atoms. SPECT systems have improved spatial resolution, although they lose in sensitivity. In conclusion, PET is a more powerful technique for imaging most molecular events (*Table 1.2*). *Figure 1.3* shows brain images taken with PET and SPECT, respectively.

Other beta-emitter isotopes are ^{99m}Tc, ^{111}In and ^{123}I. One advantage of SPECT when compared to PET is that in SPECT it is possible to use several different radiolabelled tracers at the same time because this technique can distinguish gamma-rays of different energies. Contrary to this, a PET camera takes images that reflect gamma-ray events with the same energy (in colour, whose scale reflects the concentration of the isotope).[44, 56]

Table 1.2. Comparison of some aspects of PET and SPECT.

	SPECT	**PET**
Used radioisotope	Photon emitter	Positron emitter
Average half-life of isotopes	Hours to days	Seconds to minutes
Examples of isotopes	^{99m}Tc, ^{201}Tl, ^{131}I, ^{111}In, ^{123}I, ^{133}Xe	^{18}F, ^{11}C, ^{13}N, ^{15}O, ^{68}Ga
Spatial resolution	x	3x
Contrast resolution	x	2x
Signal noise:ratio	x	2x
Variety of ligands	Poor	Higher
Availability	Available	Rare
Cost	Affordable	Expensive
Sensitivity	High	Very high

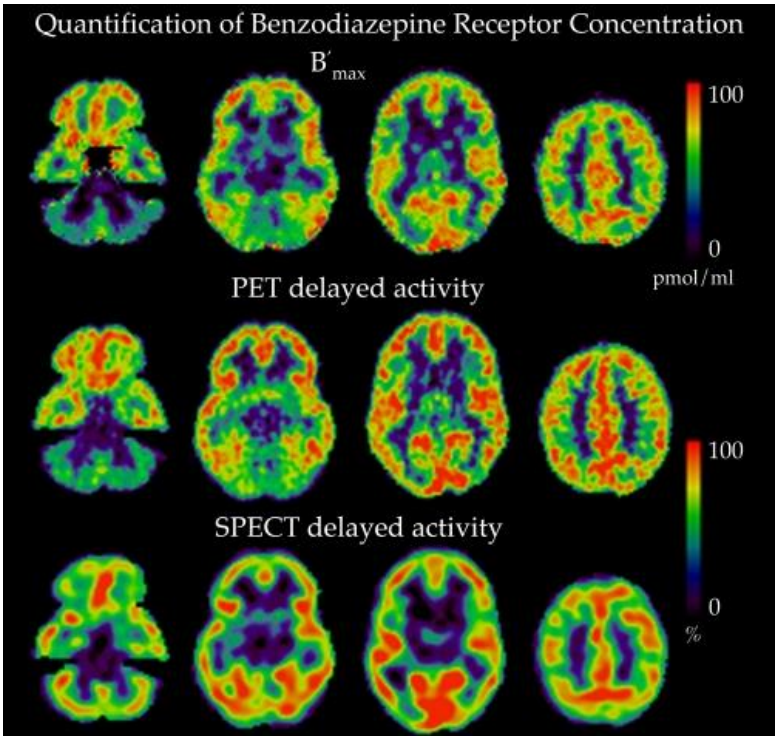

Figure 1.3. Benzodiazepine receptor concentration shown in images, obtained using PET (middle) and SPECT (bottom). Adapted from reference [57].

1.3.3. Magnetic resonance imaging (MRI)

Magnetic resonance imaging is an imaging technique that relies on the naturally occurring magnetic properties of the abundant ^{1}H nuclei in the water and fatty molecules in body tissues to produce detailed images of any part of the body. The hydrogen nuclei behave like a small magnetic bar, and under normal circumstances without the action of an external magnetic field, hydrogen atoms spin in the body in random directions with their axes randomly aligned. There are two energy values in the magnetic field for the ^{1}H nucleus, corresponding to m = +1/2 and m = -1/2. The first energy state is described by the spin function α, and the second one is described by the spin function β. There is an energy gap between these two energy levels, with β being the one with a higher energy in the presence of a magnetic field.

In order to produce images using MRI, a strong magnetic field is applied (using an MRI scanner), and this makes the protons' axes align in the magnetic field direction, either in the α or β energy states. This uniform alignment creates a magnetic vector oriented along the axis of the MRI scanner. When additional energy in the form of a radiofrequency is applied, some protons that are in the lower energy state have enough energy to transition to the higher energy state. Finally, when the radiofrequency source is turned off, the protons that have moved to the higher energy β position return to their original state (α), and this causes a signal (and a radio wave) to be emitted. This emitted energy sends a signal to a computer, which uses mathematical formulae to convert the signal into an image of anatomical details with high tissue contrast and high spatial resolution. It can provide information about the exact location of the protons in the body, and also distinguish between different types of tissues, due to the protons in different tissues realigning at different speeds and producing distinct signals. These steps are schematically shown in *Figure 1.4*.[58, 59]

Compared to X-ray and computed tomography, MRI uses radiation in the radiofrequency range which does not cause any known biological damage when it passes through the tissues.[59, 60]

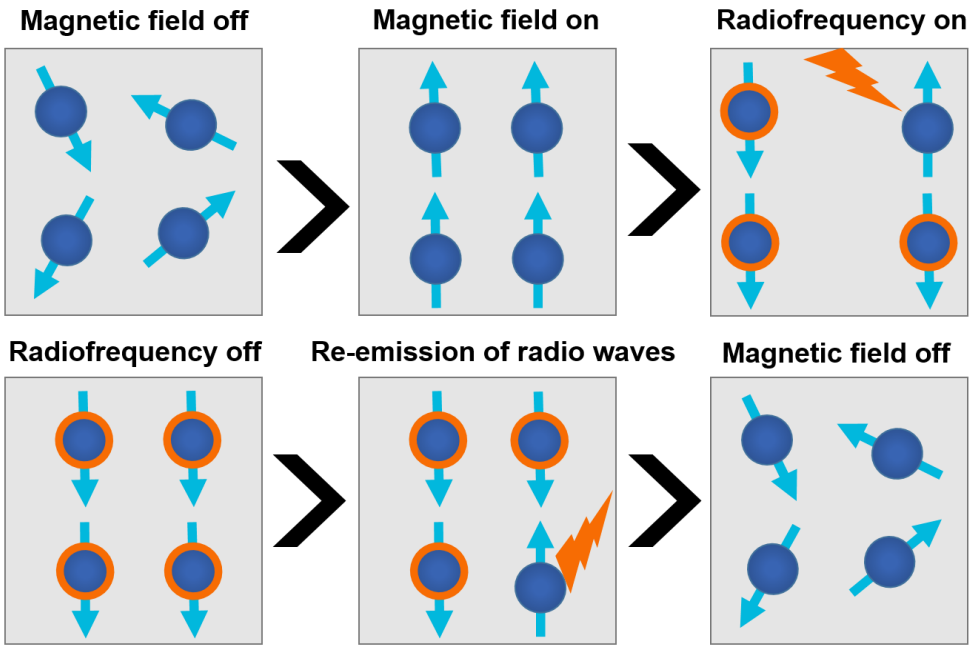

Figure 1.4. Schematic representation of the different steps that occur to the hydrogen nuclei to create signals in MRI.

1.3.4. Confocal and epi-fluorescence microscopy

The invention of confocal microscopy is attributed to Marvin Minsky, who produced a microscope in 1955.[61] The development of confocal microscopy was mostly driven by the aim of imaging biological events as they occur in living tissue (*in vivo*), and Minsky had the goal of imaging neural networks in unstained preparations of living brains. The principle of confocal microscopy discovered by Minsky, and patented in 1957, is used in all the modern confocal microscopes. *Figure 1.5* illustrates this principle, which is the same as the one applied in epi-fluorescence microscopy, and which is still the basic configuration of most modern confocal systems used for fluorescence imaging. Minsky's original configuration used a pinhole placed in front of a zirconium arc source as the point source of light.[62]

Confocal microscopy presents many advantages when compared to conventional optical microscopy, such as the controllable depth of field, the elimination of image degrading out-of-focus information, and the ability to collect serial optical sections from thick specimens. Confocal microscopy has become very popular in the past few years, due in part to the possibility of obtaining high-quality images from samples prepared for conventional optical microscopy. One of its major applications in the biomedical sciences involves imaging either fixed or living cells and tissues that have been labelled with a fluorescent probe.[62, 63]

The major advantage of the confocal approach is that it uses spatial filtering in order to eliminate out-of-focus light or flare in specimens that are thicker than the plane of focus. Confocal microscopy uses point illumination where only a part or a point of the sample is excited at any one time. It uses a pinhole in an optically conjugate plane in front of the detector to eliminate out-of-focus information and produce better quality images compared with wide-field images. In theory, only light from the focused focal plane reaches the detector. This is due to the attenuation of the light intensity, which rapidly falls off above and below the plane of focus as the beam converges and diverges. This reduces the excitation of molecules that are out of the focal plane, hence eliminating a lot of unwanted background signals. Any out-of-focus light that enters the photo-detector normally has an intensity that is too weak to be detected. Moreover, any point of light that is in the focal plane but not at the focal point will be blocked by the pinhole screen.[62, 64, 65]

Three-dimensional images can be made from scanning many thin sections through the sample to create numerous optical sections that can be stacked together to produce an image. Generally, in order to obtain higher resolution images, a laser is used as the excitation source because it provides discrete wavelengths with very high intensities as well as a point light source of illumination. Depending on the laser system used, the desired wavelength can be selected, enabling a wider range of fluorophore probes/labels to be utilised.[62, 66, 67]

Figure 1.5 shows the basic configuration of a confocal microscope. As it can be seen, a laser is used to provide the excitation light. The laser light (blue) first reflects off a dichroic mirror, followed by two other mirrors, which scan the laser across the sample. Next, the dye in the specimen is excited by the laser light. It fluoresces, and the fluorescent emitted light (green) is descanned by the same mirrors that are also used to scan the excitation light (blue) coming from the laser. The emitted light then passes through the dichroic mirror and is focused onto the pinhole. The light that passes through the pinhole is measured by a detector (*e.g.*, a photomultiplier tube). At a given instant, only one point of the sample is observed, so that there can never be a complete image of the sample. The detector of the microscope is attached to a computer, which builds up the image.[62]

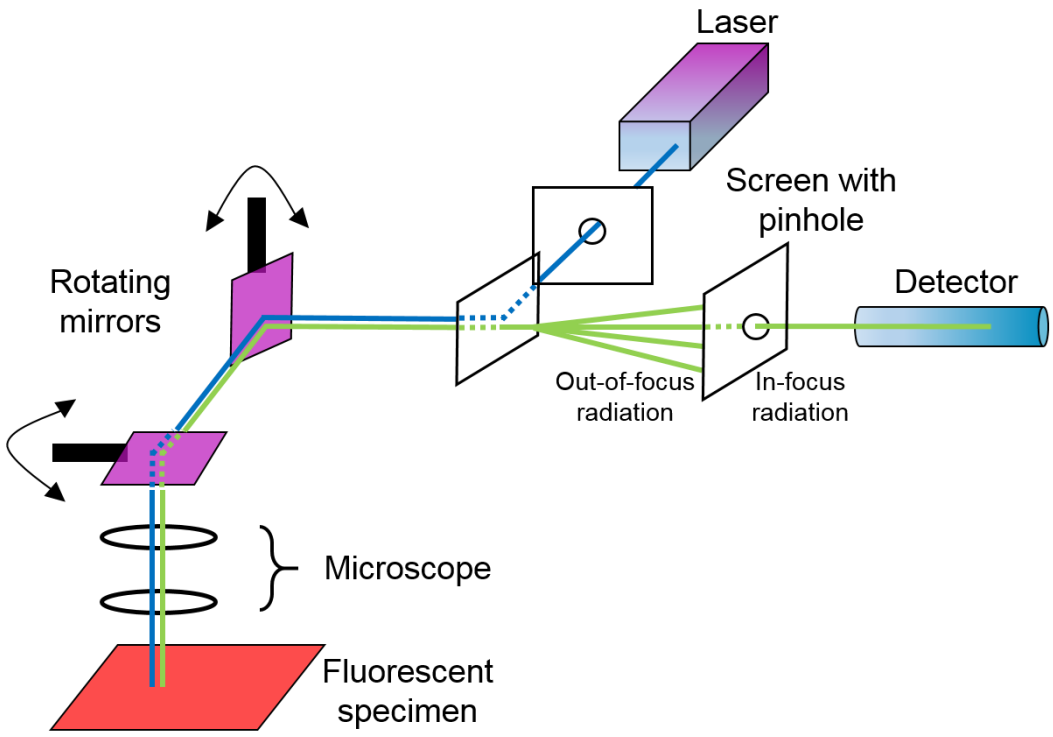

Figure 1.5. Schematic representation of the basic set-up of a confocal microscope. The light coming from the laser is scanned across the specimen by the scanning mirrors. Optical sectioning occurs as the light passes through a pinhole on its way to the detector.

1.3.5. Two-photon fluorescence lifetime imaging microscopy (FLIM) and time-correlated single-photon counting (TCSPC)

Two-photon fluorescence microscopy has found applications in many fields of tissue research thanks to its deep tissue penetration and its limited photochemical damage.

Figure 1.6 schematically shows the differences between one-photon (left) and two-photon (right) excitation techniques. In one-photon excitation, one photon from the light with the appropriate energy can excite the targeted molecule and raise its energy state from the ground energy state to an excited level. Once in the excited state, the molecule can relax to the lowest vibrational level in this state, and from there it can return to the ground state while emitting a photon. In contrast to this, the principle of a two-photon microscope is that, during the excitation process, two photons that have twice the wavelength and half the energy of one photon are absorbed simultaneously to excite the molecule and reach the same excited energy level. Another difference between these two modalities is that in a one-photon microscope, all the dye molecules along the beam-path outside the focal point (FP) are also excited and, for this reason, out-of-focus light needs to be eliminated using a pinhole. In a two-photon microscope, only the dye molecules that are within the FP are excited, while the fluorophores outside of the

focal plane are not excited because the simultaneous two-photon absorption is only possible at the focal plane. For this reason, the pinhole that is used in laser scanning confocal microscopy is not required to obtain a sharp image from one plane in a tissue volume.[68] Three-dimensional analysis of deeper tissue with minimal loss of fluorescence and reduced phototoxicity is possible thanks to the properties of two-photon microscopy.[69, 70]

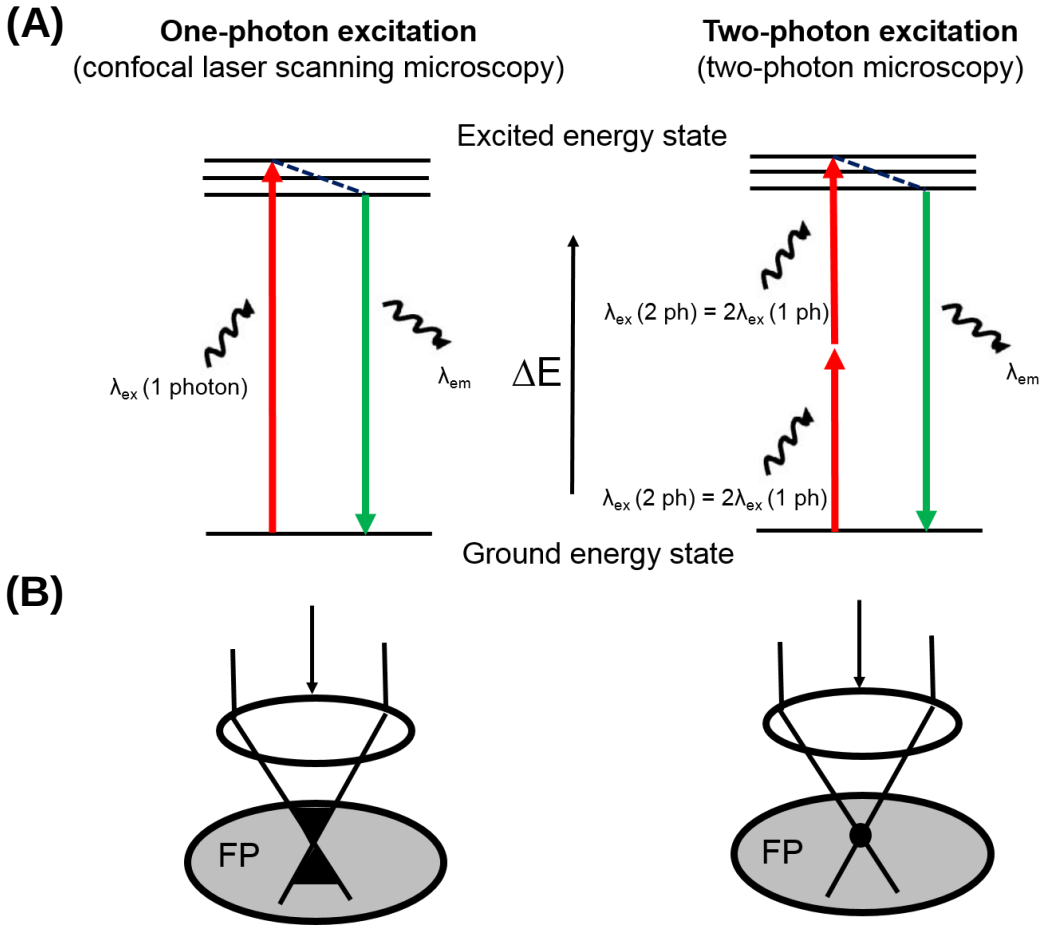

Figure 1.6. Scheme representing the differences between one-photon excitation and two-photon excitation. **(A)** Jablonski diagrams, and **(B)** excitation of the specimen through a beam-path (FP: focal point). Adapted from reference [68].

The fluorescence lifetime (FLT) is defined as the average time that a molecule remains in an excited state before returning to the ground state by emitting a photon, and is characteristic of each fluorophore. It is determined as the time when the intensity of the fluorophore decreases by 1/*e*, which is approximately 36%, from the initial excited energy value. FLT is an intrinsic characteristic of each fluorescent molecule and is independent of the fluorescence intensity and concentration. When the biological environment of a fluorescent molecule is changed (*e.g.*, temperature, redox state, pH, or protein-binding state) this changes the FLT of that fluorophore. For this reason, fluorescence lifetime imaging (FLIM) is an imaging technique in

which the contrast is based on the lifetime of the individual fluorophore rather than its emission spectrum.[71]

FLIM techniques can be classified in two types: time-domain, by multidimensional time-correlated single-photon counting (TCSPC), and frequency-domain. In TCSPC, the time between sample excitation by a pulsed laser and the arrival of the emitted photon at the detector is measured. TCSPC records the photon density over time, so that it is a one-dimensional technique. Specifically, TCSPC uses a multidimensional time-correlated single-photon counting process. The focused beam of a high frequency pulsed laser is used to scan the sample. Data recording is based on detecting single photons and determining the arrival times of the photons with respect to the laser pulses as well as the beam in the moment of photon detection. As a result, a three-dimensional data array representing the pixels of the two-dimensional scan is obtained, with each pixel containing photons in many time channels for consecutive times after the excitation pulses.[71, 72]

The basic set-up of a FLIM instrument is shown in *Figure 1.7*, and it includes a pulsed laser source, a detector, a dichroic mirror to separate fluorescence signal from excitation light, a TCSPC unit to measure the time between excitation and fluorescence emission, and an objective to focus the excitation light into the sample and collect the fluorescence signal.[68]

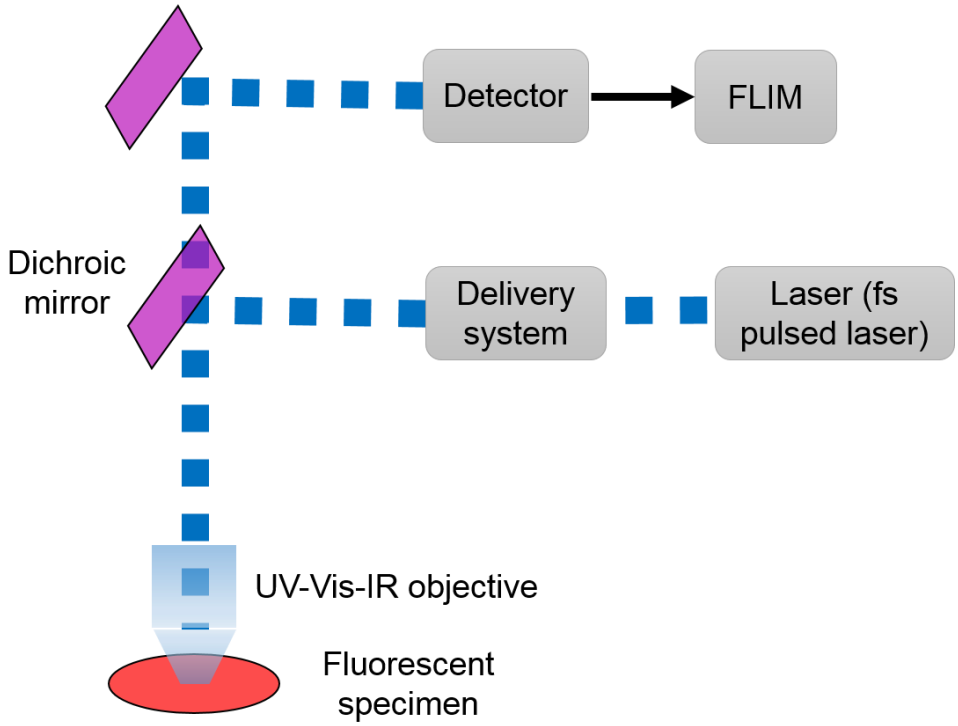

Figure 1.7. Schematic representation of the basic set-up of a two-photon microscope and fluorescence lifetime imaging. This is a simplified overview of this type of microscope. Adapted from reference [68].

1.4. Radioisotopes and their aqueous chemistry

1.4.1. Zirconium-89

Zirconium-89 is a very promising radioisotope for PET imaging thanks to its unique properties, which will be described in this section, and this will also touch upon current methods applied in the production of this isotope using a cyclotron.

(A) Zirconium and its properties

Klaproth discovered zirconium (Zr) in 1789 as "zircon" in the form of orthosilicate $ZrSiO_4$. The first time zirconium was isolated as a metal was in 1824 by Berzelius. For many years, Zr was used in industrial applications such as the fabrication of fake diamonds, but at that time the medical community had not yet paid much attention to this element and it was only used in its impure form, zircon. However, during the atomic testing period of the 1950s and 1960s, two isotopes of zirconium, ^{93}Zr and ^{95}Zr, appeared as relevant fission products. This led to the first studies of the radiochemistry of Zr, which were published in a National Academy of Sciences (NAS) report in 1960.[73]

From having a relevant paper in fission/fall-out, scientists started investigating the biological distribution of ^{93}Zr ($t_{1/2}$ = 1.53 million years) and ^{95}Zr ($t_{1/2}$ = 65 days) radioisotopes in animals. These studies comprised parameters of relevance such as the biodistribution and toxicity of ^{95}Zr in rats or mice, and some interesting results came out, such as the observed high affinity of Zr to the bones by autoradiography and its low toxicity in rats. Due to these favourable properties, in the past few years zirconium has reached a relevant role as a potential positron emission tomography isotope for the labelling of monoclonal antibodies (mAbs) for *in vivo* cancer imaging.[73-80] Some of the successful applications of ^{89}Zr found in the last decades include the assessing of target expression, *in vivo* biodistribution and pharmacokinetics of antibodies in applications of cancer diagnosis, treatment planning and monitoring, and dosimetry.[81-84]

Despite the successful *in vivo* results described above, the nuclear medicine community has taken a long time to embrace the potential of zirconium-89 due to the lack of efficient methods of separation from the ^{89}Y target material and because of the difficult aqueous chelation chemistry.[85]

(B) Properties of zirconium-89

Zirconium-89 has a half-life of 78.4 h, the longest among all the β^+ emitting radiometals currently available on the market, and allows imaging up to a week after the injection of a ^{89}Zr-

based probe.[81, 86] Moreover, it is compatible with the relatively slow blood clearance of most immunoglobulin G (IgG) antibodies used in radioimmunodiagnosis ($t_{1/2}$ = 1-2 days).[73] Other properties, such as its β^+ decay ratio of 22.3% and its maximum energy of 897 keV, make it an ideal candidate for PET imaging (*Figure 1.8*). One disadvantage that should be taken into consideration is that its intense gamma emission (100% yield), with energy of 909 keV, dictates very careful calibration and set-up of the imaging equipment in order to obtain a good image quality.[87]

Zirconium's oxidation state is +4 and its preferred coordination number is 8, which makes hydrolysis likely to happen in aqueous solution.[85] The hexa-aqua ion $Zr(H_2O)_6^{4+}$ can only exist at very low Zr concentrations, and in highly acidic aqueous solutions. In neutral solutions and in the absence of complexing agents, Zr species can be mostly found as a polynuclear and polymeric form.[73, 88, 89]

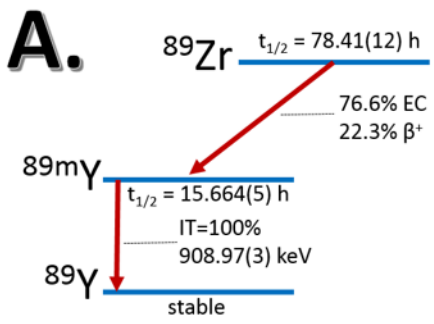

B.

Half-life	78.4(12) h
Decay Mode	ε = 76.6% β^+ = 22.3%
$E(\beta^+)$	395.5(11) keV
β^+ end-point energy (keV)	902(3) keV
Abundance, $I_{\beta+}$ (%)	22.74(24)
E_γ (keV) (intensity, I_γ (%))	511.0 (45.5%) 909.2 (99.0%)

Figure 1.8. (A) Decay scheme of ^{89}Zr, and **(B)** some decay characteristics of ^{89}Zr. Adapted from reference [90].

(C) Radiosynthesis of zirconium-89

It is possible to produce some isotopes of zirconium using a cyclotron as shown in the *Table 1.3* below.

Table 1.3. Properties of some zirconium isotopes.[91] $t_{1/2}$ is the half-life of the radioisotopes; I_γ and E_γ refer to the intensity and energy of the γ emission, respectively; I_{EC} denotes the intensity of the electron capture decay; $I_{\beta+}$ is the intensity of the positron emission decay, and $E_{max(\beta+)}$ and $E_{ave(\beta+)}$ designate the maximum and average energies of the decay by positron emission, respectively.

Isotope	$t_{1/2}$	I_γ	E_γ	I_{EC}	$I_{\beta+}$	$E_{max(\beta+)}$	$E_{ave(\beta+)}$
^{86}Zr	16.5 h	100%	241 keV				
^{88}Zr	83.4 d	100%	390 keV				
^{89}Zr	78.4 h	100%	909 keV	76.6%	22.3%	897 keV	397 keV

These three isotopes can be produced using different nuclear reactions with particle energies between 5 and 85 MeV. Among the three of them, zirconium-89 is the most promising one for investigating new immunoPET agents to use in *in vivo* imaging of cancerous tumours, and to guide and plan radioimmunotherapy.[91-93]

As shown in *Figure 1.9*, three principal routes can be used to produce ^{89}Zr at accelerators, which are:

1. The bombardment of ^{89}Y with protons or deuterons, termed as ^{89}Y(p,n)^{89}Zr or ^{89}Y(d,2n)^{89}Zr reactions.
2. Alpha-induced nuclear reactions on Sr, resumed as ^{nat}Sr(α,xn)^{89}Zr process.
3. Neutron activation via ^{90}Zr(n,2n)^{89}Zr reaction.[87, 91]

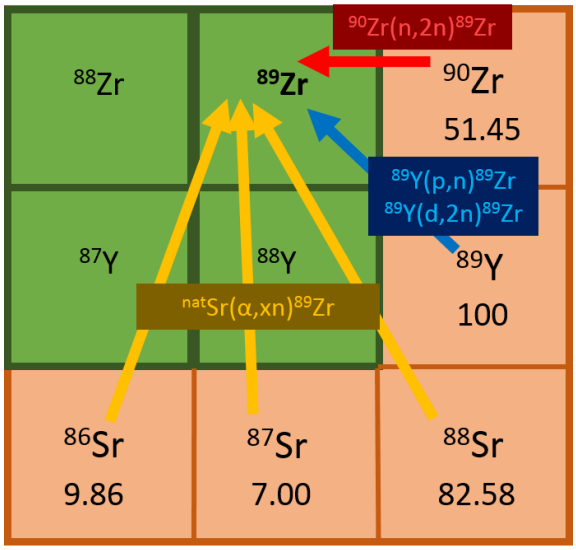

Figure 1.9. Scheme of the three paths that can be followed for the production of ^{89}Zr. Adapted from reference [91].

Among these three main production paths, (**1**) is the most popular due to yttrium being monoisotopic (isotopic abundance = 100%). This means that natural yttrium is comprised of only yttrium-89 and hence it does not require enrichment, which makes it a favourable target material and adds an extra advantage to the production of ^{89}Zr with a proton biomedical cyclotron: the target does not require a costly, enriched target material.[87, 91, 94]

New methods are being investigated to find more efficient ways to produce the new promising immunoPET target, ^{89}Zr. Walther *et al.* have examined the production, separation and characterisation of this isotope, including supplementation of a commercial Cyclone 18/9 with a self-made solid target system (STS).[95] Holland *et al.* have reported standardised methods for the routine production and isolation of high-purity and high-specific activity ^{89}Zr using a small cyclotron with optimised conditions and a solid, commercially available ^{89}Y-foil target.[85] Infantino *et al.* have optimised the widely used Monte Carlo simulation code FLUKA to

prototype a solid target for the production of ^{89}Zr by irradiation of a metallic ^{89}Y target foil in a proton biomedical cyclotron through the reaction (**1**) described above.[87] Moreover, the group of Marshall at the Positron Emission Tomography Imaging Centre (PETIC) in Cardiff has also worked on the optimisation of this process using an *in silico* model to reduce the amount of generated by-products such as ^{88}Zr.[96] Finally, in an example published by Safeghi *et al.*, the production of ^{89}Zr in an accelerator is reported via proton bombardment on sedimented $^{89}Y_2O_3$ as a target.[91]

(D) Ligands of relevance to ^{89}Zr stabilisation

Any biomolecular PET tracer needs to be able to form a stable radiometal chelate. Up to now, several efforts have been attempted to complex zirconium with many different aqueous chelators, of which deferoxamine B (DFO) has become the most successful and commonly used.[97] *Figure 1.10* shows three different chelators and the complexes formed with Zr^{4+}. Although there are some differences between the three chelators, each structure shows a coordination number of eight.[90]

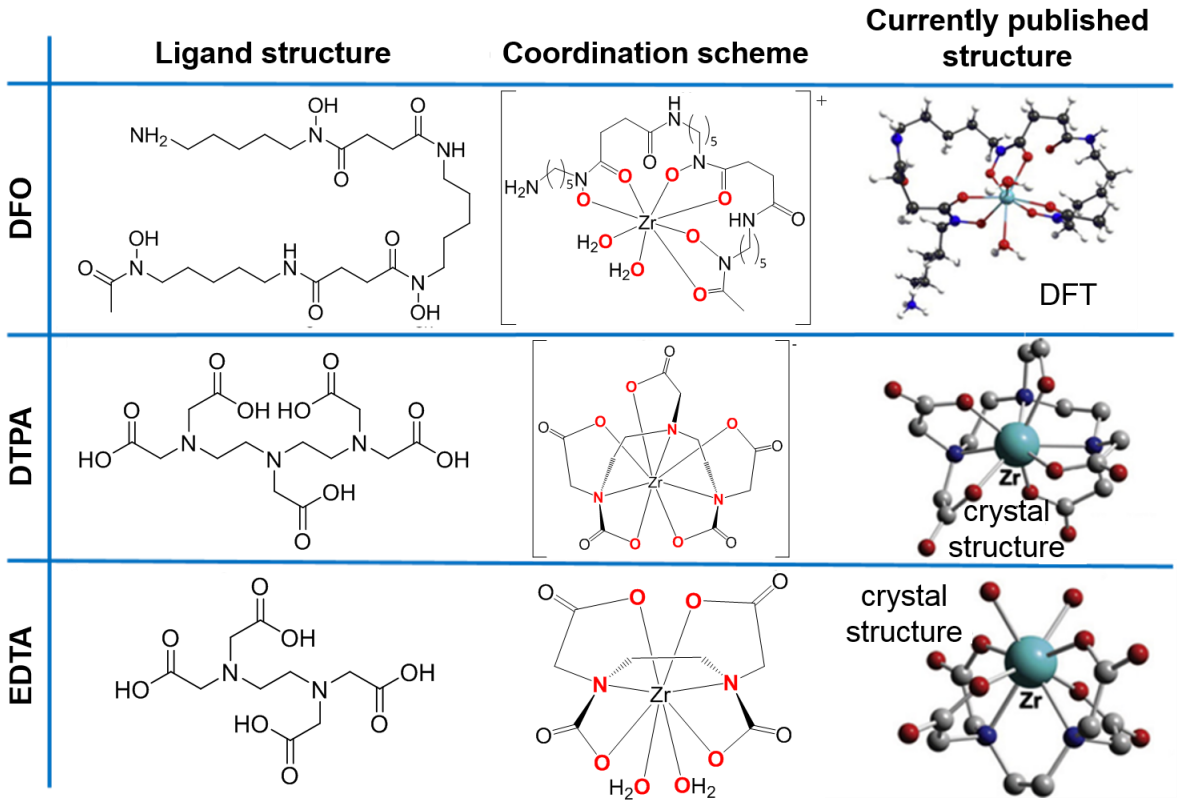

Figure 1.10. Ligand structure, coordination scheme and currently published structure of some common chelators for Zr^{4+} and their complexes with the metal: DFT structure (Zr-DFO[98]), and crystal structures (Zr-DTPA[99] and Zr-EDTA[100]). Adapted from reference [90].

The reason of the success of deferoxamine as the most prominent Zr^{4+} chelator employed is that it is a hexadentate, bifunctional siderophore with three hydroxamate groups for chelating metals and a primary amine tail that can be modified by different reaction paths for conjugation to a biomolecule.[101] Deferoxamine B is commercially available in the form of the iron chelator Desferal (DF), and it is a natural product; a microorganism-produced siderophore with 3 hydroxamate groups.[90, 102]

It is known that the presence of the three hydroxamate groups in DFO makes this molecule a suitable and effective chelator for Zr^{4+}, and it is proven that the success of many of the ^{89}Zr-based PET imaging is thanks to the value of DFO as a chelator for this ion.[90, 94, 103] Even though there is not a crystal structure of Zr-DFO, DFT-modelling of the metal complex suggests that it has a coordination number of eight, with two coordination sites on the zirconium ion occupied by H_2O molecules, as can be seen in *Figure 1.11*.[104]

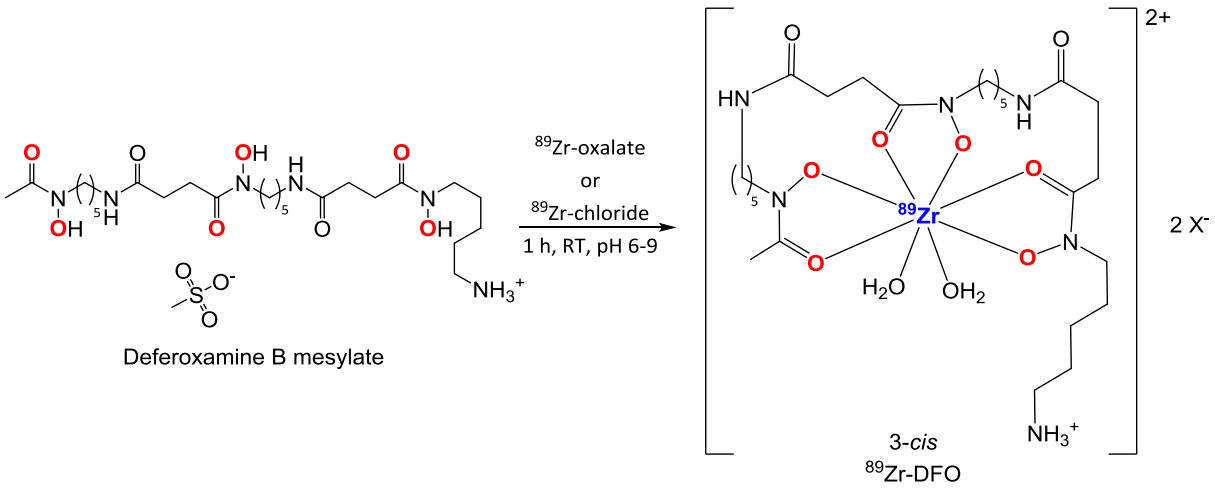

Figure 1.11. Complexation reaction between $[^{89}Zr(C_2O_4)_4]^{4-}$ and DFO. Adapted from reference [77].

Although DFO is the best known chelator for ^{89}Zr, there is a growing need for the search of new and better ligands in order to form stable radiometal chelates with tuneable properties. It is believed that a better ligand than DFO can be found.[105] The ideal chelator for this ion to allow stable Zr^{4+} chelation would be a ligand that satisfies two conditions: it should be octadentate and be oxygen-rich.[90] A ligand satisfying these conditions would create a more stable, robust system for chelating Zr, and would help to minimise the problems found in PET imaging involving the complex ^{89}Zr-DFO, namely the release of free $^{89}Zr^{4+}$ *in vivo* and uptake by bones and other non-targeted organs of the body.[90] This uptake is directly related to chelate instability, which releases ^{89}Zr during the long circulation time of monoclonal antibodies.[106, 107] In order to solve these issues of non-specific accumulation in tissues and organs, some recent

studies have investigated the modification of the conjugation chemistry used to link DFO to antibodies and the synthesis of more effective chelators.[98, 104, 105, 108]

Once the ^{89}Zr tracer is attached to a deferoxamine moiety, this ligand is conjugated to the antibody.[109] Regarding this conjugation, two main methods are commonly used at the moment. One involves a succinic acid linker between the amino function of the DFO and an amino function on the antibody, and the other deals with a p-isothiocyanatobenzyl-deferoxamine derivative.[73] *Figure 1.12* shows a schematic view of the complex ^{89}Zr-DFO attached to an antibody.

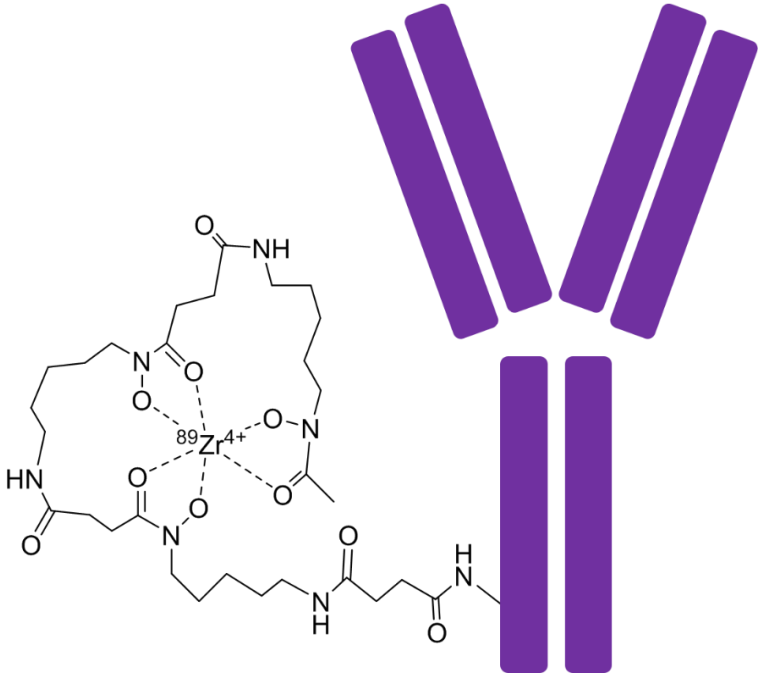

Figure 1.12. Schematic overview of a ^{89}Zr-labelled antibody using DFO as chelator. Adapted from reference [110].

1.4.2. Gallium-68

Gallium-68 as a positron emitter nuclide, recently available from generators, is of great interest in current medical imaging at a preclinical level due to some important advantages that will be explained in the next sections.

(A) Gallium and its relevant properties for radioactive synthesis in water

The radioisotope gallium-68 has a half-life of 67.7 min, which is compatible with the pharmacokinetics of most radiopharmaceuticals of low molecular weight such as antibody fragments, peptides and oligonucleotides. ^{68}Ga decays to 89% under β^+ decay into stable zinc-68, and to 11% via electron capture. Its average positron energy, $E_{\beta+}$, per disintegration of 740 keV is ideal for PET imaging, providing a high spatial resolution.[111-113]

The only stable oxidation state of gallium in aqueous solution is +3, being the three hydrated Ga^{3+} ion stable only under acidic conditions. Due to the almost exclusive formation of $[Ga(OH)_4]^-$ ions, the solubility of this ion is high at physiological pH. However, hydrolysis to the insoluble compound $Ga(OH)_3$ when its concentration exceeds the nanomolar level makes it less soluble in the pH range of 3-7.[114-116]

Ga^{3+} complexes have a preferred coordination number of six, although some chelates can be four- or five-coordinated. The Ga^{3+} ion is a hard Lewis acid, and thus it forms thermodynamically stable complexes with ligands that are hard Lewis bases. These are ligands containing oxygen, nitrogen and sulphur donor atoms, but also softer functional groups have been found to be suitable for Ga^{3+}, such as phenolate and thiol groups.[114, 116, 117]

(B) Radiosynthesis of gallium-68

In contrast to zirconium-89, gallium-68 is a generator-produced nuclide. Generators present some advantages like allowing clinical studies without an on-site cyclotron, or if cyclotron beam time is not available, and they can generate radionuclides and radioactive probes at any time on demand.[111, 114]

Gallium-68 can be produced from a generator system that consists of an inorganic or organic matrix that immobilises the parent radionuclide, ^{68}Ge. The pair $^{68}Ge/^{68}Ga$ is ideal for a generator strategy, due to the combination of the half-lives of these ions ($t_{1/2}$ = 270.9 d and $t_{1/2}$ = 67.7 min for ^{68}Ge and ^{68}Ga, respectively), suitable for radiopharmaceutical synthesis. The preferred production path of ^{68}Ge is via the (p,2n) reaction on gallium targets (*Figure 1.13*). In order to avoid break-through, a good separation system of the stationary mother (^{68}Ge) from the soluble daughter (^{68}Ga) is mandatory. Since the chemical properties of the two generated ions, Ge^{4+} and Ga^{3+} are sufficiently different, there are several different methods that allow efficient separation, the most commonly used being ion exchange chromatography.[111, 114]

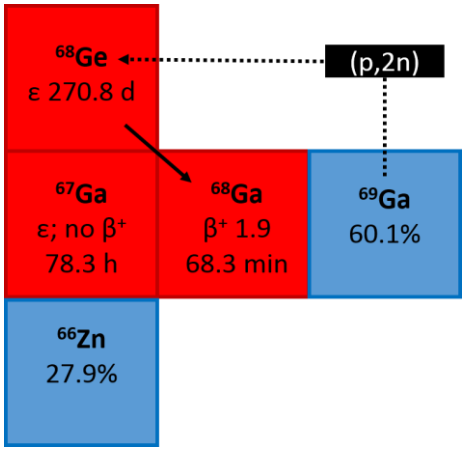

Figure 1.13. Production of ^{68}Ge by the (p,2n) reaction of ^{69}Ga. Adapted from reference [114].

(C) Ligands of relevance to the radiochemistry of gallium

As mentioned before, the majority of chelators designed for Ga^{3+} are hexadentate, although several chelates that are reported to be stable *in vivo* have coordination numbers of four or five. Gallium forms complexes with bifunctional chelators, that is, ligands that have functionalities that allow covalent coupling to a targeting vector – such as peptides and antibodies – as well as binding of the metal cation.

Deferoxamine B, the most commonly used chelator to form stable complexes with ^{89}Zr, was one of the first molecules used in the radiolabelling of $^{68}Ga^{3+}$, due to the resulting high radiochemical yield. However, whilst high radiolabelling yields occur at concentrations > 5 μM, at a nanomolar level (< 50 nM) DFO is not a good chelating agent for gallium.[114, 118, 119]

1,4,7,10-Tetraazacyclododecane-1,4,7,10-tetraacetic acid (DOTA) is one of the best known chelators used for radiometals in an oxidation state of +3. $Ga(DOTA)^-$ is stable enough to be used in clinical practice. However, there is still another chelator for Ga^{3+} with a higher thermodynamical stability constant, 1,4,7-triazacyclononane-N,N',N''-triacetic acid (NOTA). The high thermodynamic stability of the Ga^{3+} chelates with NOTA is due to the fact that the small cation perfectly fits in the cyclic cavity of the nine-membered triazamacrocyclic ligand, such that the chelator can encapsulate the metal ion with high efficiency. *Figure 1.14* shows the structure of the ligands DOTA and NOTA.[114]

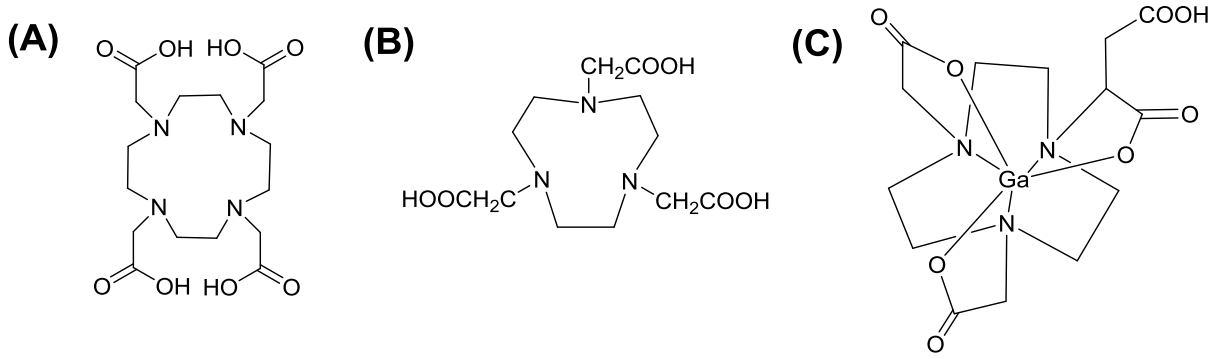

Figure 1.14. Structural formula of common chelators for metallic radioisotopes: **(A)** DOTA, and **(B)** NOTA. **(C)** Structural formula of Ga(NODASA). Adapted from reference [114].

Another very stable gallium chelator is 1,4,7-triazacyclononane-1-succinic acid-4,7-diacetic acid (NODASA), forming the complex Ga(NODASA), which also has the potential for biomolecule coupling using the prelabelling approach thanks to the free carboxylate group available, the other three carboxylates being protected by the metal ion (*Figure 1.14*).[114, 120]

1.5. Thiosemicarbazide-based complexes in hypoxia targeting

Interest in the past decades has grown in the study of thiosemicarbazides (*Figure 1.15*), the simple hydrazine derivatives of thiocarbamic acid, and the compounds that they can produce.[121, 122] Thiosemicarbazones are Schiff base ligands that have S and N as donor atoms. These compounds have found applications in many fields and their coordination chemistry is also being investigated. Their applications are mainly in the field of pharmacology due to their biological activity, and include: (i) anti-bacterial activity, (ii) anti-fungal activity, (iii) anti-malarial activity, and (iv) anti-tumour activity.[123]

The ability of thiosemicarbazones to chelate metal ions plays a key role in their biological activity and many of their applications. The biological activity of this class of compounds is usually enhanced on complexation of the metal, showing evidence of inhibitory behaviour against cancer.[124, 125] Thanks to their thione-thiol equilibrium, they are highly versatile reagents and can act as monodentate or bidentate ligands when coordinated to a metal.[126] Coordination to metal ions gives these compounds different geometries, enabling the synthesis and characterisation of compounds with unique stereochemistry when compared to pure organic ligands. One of their main disadvantages is the poor solubility of thiosemicarbazones and their metal complexes in aqueous solutions, making them less promising for *in vivo* applications. However, more studies are needed.[124]

One of the most promising areas in which thiosemicarbazone derivatives are being investigated is their use against cancer.[127]

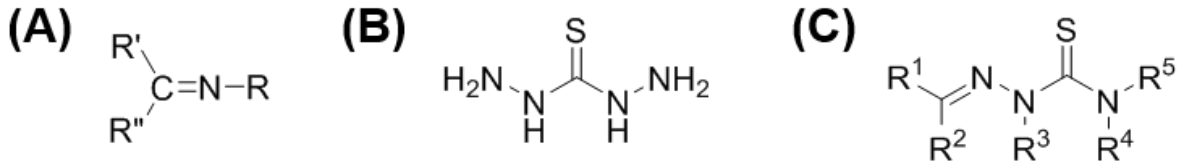

Figure 1.15. (A) General structure of a Schiff base, **(B)** thiosemicarbazide, and **(C)** general structure of thiosemicarbazones.

1.5.1. ^{64}Cu(ATSM): copper(II)-diacetyl-bis(N-4-methylthiosemicarbazone)

For successful imaging and therapy, the choice of radioisotope and bifunctional chelator is of great importance: chelators need to be easily attached to a biomolecule and radiolabelling conditions need to be biocompatible. There are previous reports of the use of some ^{64}Cu-labelled macrocyclic chelators for the labelling of biomolecules. However, most of them require the use of high temperatures over long periods of time for efficient labelling, which is not compatible with sensitive biological systems, since these cannot usually stand elevated

temperatures and extreme pH ranges. Therefore, what researchers aim to find is a chelating system with relatively fast labelling kinetics at room temperature, at near neutral pH and giving high yields.[128]

One such system, of great interest at the moment in the PET imaging field, is the complex ^{64}copper(II)-diacetyl-bis(N-4-methylthiosemicarbazone), ^{64}Cu(ATSM). The N_2S_2-type bis(thiosemicarbazone) ligands form stable neutral and planar complexes with Cu(II) ions. When using Cu(ATSM), radiolabelling takes places easily at room temperature and near physiological pH.[128-130] *Figure 1.16* shows a radioactive ^{64}Cu(ATSM) complex, linked to a biologically active molecule.

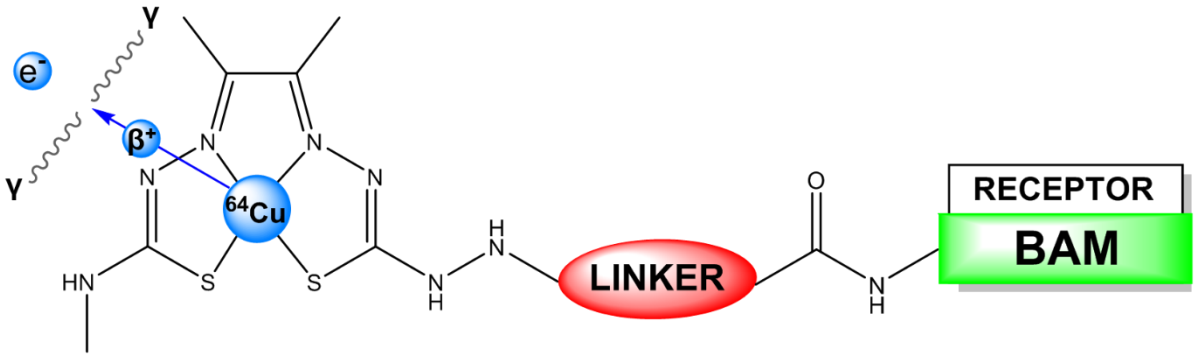

Figure 1.16. Schematic diagram of a functionalised bis(thiosemicarbazone) complex based on a Cu(ATSM/A) core, conjugated to a biologically active molecule (BAM) for receptor targeted imaging, via an organic linker. Adapted from reference [128].

It is known that dithiosemicarbazones possess anti-tumour properties, and when complexed with Cu(II), their anti-tumour activity is enhanced even more. This, together with other factors already mentioned such as the simplicity of the chemistry and the availability of copper radioisotopes, turned this class of ligands into promising radiopharmaceuticals.[131-133]

Using copper radionuclides presents many advantages. In the first place, copper has mainly only two oxidation states (I and II) and has a relatively simple coordination and redox chemistry. In an aqueous environment, only Cu(II) is stable enough. In the second place, the high natural abundance of copper makes it easy to understand its biochemistry and metabolism in humans. Moreover, copper has several positron-emitting isotopes, which are quite versatile thanks to their broad range of decay schemes [^{60}Cu ($t_{1/2}$ = 0.40 h, β^+ = 93%, EC = 7%); ^{61}Cu ($t_{1/2}$ = 3.32 h, β^+ = 62%, EC = 38%); ^{62}Cu ($t_{1/2}$ = 0.16 h, β^+ = 98%, EC = 2%); and ^{64}Cu ($t_{1/2}$ = 12.7 h, β^+ = 17%, EC = 43%)].[131, 134, 135] All these features make positron-emitting isotopes of copper very attractive options on which to base new positron-emitting radiopharmaceuticals. Among all these radioisotopes, copper-64 is the most commonly used due to its half-life of 12.7 h, which

is ideally suited for PET studies conducted over a 48 hour period. Another advantage of copper-64 is that, apart from decaying by positron emission (17%), it also decays by β^- emission (43%), allowing it to be used as both a diagnostic (imaging) and therapeutic (radiotherapy) radionuclide.[128, 131, 134] Thanks to having a β^+ maximum energy of 0.66 MeV, PET images taken by using ^{64}Cu are of very high quality.[131]

Radioactive ^{64}Cu isotope can decay by three processes: positron emission, electron capture, and beta decay. This property makes it an unusual isotope and allows it to be produced by using either a cyclotron or a generator. The most common production method for ^{64}Cu uses the ^{64}Ni(p,n)^{64}Cu reaction on a cyclotron. The target to produce ^{64}Cu is enriched ^{64}Ni (99.6%), which is bombarded on the cyclotron. After the bombardment, ^{64}Cu is separated from the target nickel via a one-step procedure using an ion exchange column. Once they are separated, the enriched ^{64}Ni can be recovered to 85 - 95%, and reused for future bombardments. This makes this radiosynthesis of ^{64}Cu highly cost-efficient.[136, 137]

In order to obtain the copper-64 complex to be used in PET imaging, a transmetallation reaction takes place starting from the corresponding Zn(ATSM) complex. Due to the fact that the structures of the zinc complex and those of the copper analogue are very similar, the characterisation and the uptake mechanisms of the complexes may be quite similar and can be studied with the Zn complexes. This allows two advantages: firstly, zinc (II) is diamagnetic, which facilitates the characterisation of new ligand systems and complexes by using NMR. Secondly, the zinc(II) complexes are weakly fluorescent, which allows fluorescence microscopy to be used to track the uptake and intracellular distribution of the zinc(II) bis(thiosemicarbazonato) complexes in cancer cells.[133]

When labelled with a positron-emitting isotope of copper, Cu(ATSM) has been shown, *in vivo* and *in vitro*, to be selective for hypoxic tissue. Moreover, clinical studies with this complex have produced non-invasive imaging data that is predictive of cancer patients' response to conventional therapy.[131] As seen in the schematic representation in *Figure 1.17*, the redox activity of Cu(II) allows the trapping of ^{64}Cu in hypoxic cells via a bioreductive mechanism. However, this mechanism is not totally well understood and it is not clear if it is just the action of copper that makes the complex hypoxia selective.[131]

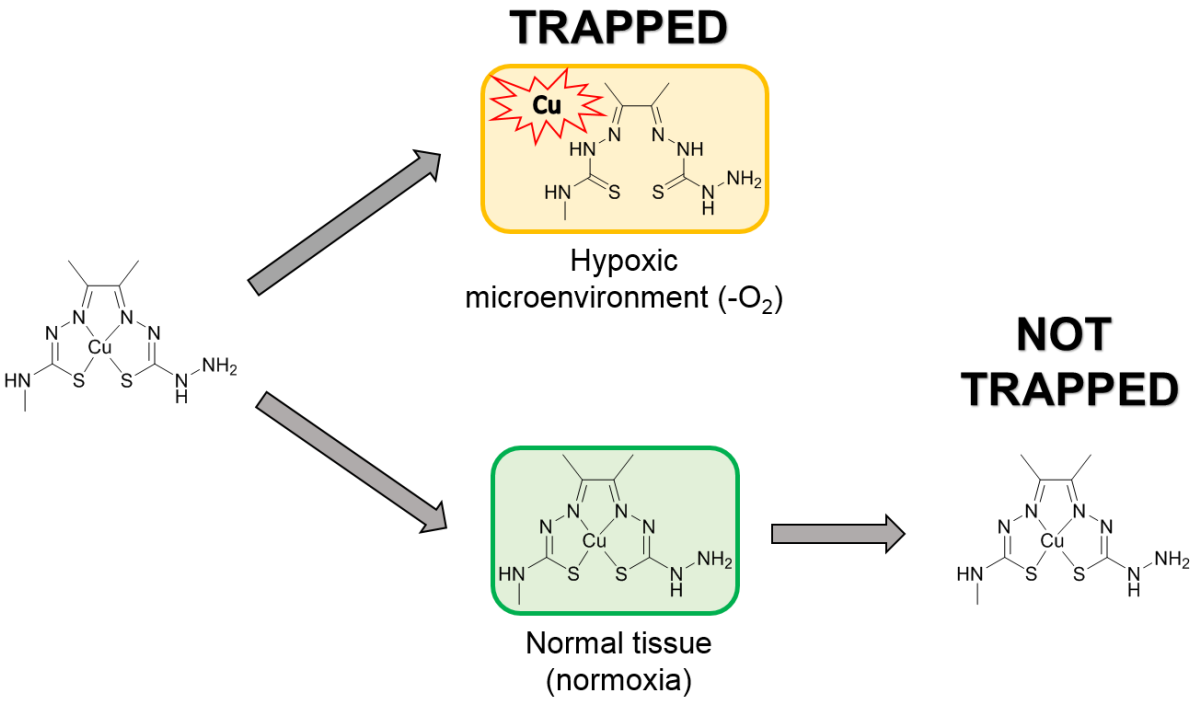

Figure 1.17. Diagram showing schematically that, whilst ^{64}Cu is trapped in hypoxic cells via a bioreductive mechanism due to the lack of O_2, it is not trapped in normal (healthy) cells, where there is a normal level of O_2. Adapted from reference [131].

In this context, the ability of some radiolabelled molecules such as Cu(ATSM) to undergo chemical changes in the presence or absence of oxygen, in conjunction with the use of PET, makes them promising agents for bioimaging and therapeutic techniques.[131]

1.6. Nanomaterials for medicinal applications: nanomedicines design

Nanomedicine is based on the application of nanotechnology to the area of medicine. Materials that have at least one of their dimensions within the nano scale are known as nanomaterials. Their use has led to the development of novel devices to detect malignant tumours at an early stage, in diagnostic applications, and also to important improvements in efficient drug delivery systems for therapy.[138] Nanobiotechnology has helped to develop a personalised medicine adapted to a specific patient.[139]

When applied to therapy, nanoparticles can be used as platforms or carriers for insoluble or poorly soluble drugs. Moreover, hydrophilic molecules or polymers can be added to a nanoparticle surface to improve its solubility and biocompatibility.[140]

As it has been already mentioned in this chapter, cancer causes a large number of deaths and an early diagnosis of this is extremely important for a patient's survival. For this reason, there is a need to invest in research towards the discovery of new tools to allow detection of a tumour at a very initial stage.[6, 141] For imaging applications, nanomaterials can be used to target tumour biomarkers such as cell membrane proteins. It is also possible to target intracellular proteins, although the relatively large size of nanoparticles makes it difficult for them to cross the cell's membrane barrier.[139, 142]

1.6.1. Iron oxide nanoparticles as synthetic scaffolds for MRI contrast agents

Different types of iron oxides are known, among which there is hematite (α-Fe_2O_3), maghemite (γ-Fe_2O_3) and magnetite (Fe_3O_4). In this section, attention is focused on magnetite due to its magnetic properties that allow it to be used as an MRI contrast agent.[143, 144]

As shown in *Figure 1.18*, Fe_3O_4 has the structure of a face-centered spinel, that is based on 32 O^{2-} ions and close-packed along the (111) direction. This type of iron oxide contains divalent and trivalent iron. The arrangement is a cubic spinel structure consisting of a cubic close-packed array of oxide ions, in which all the Fe^{2+} ions occupy half of the octahedral places and the Fe^{3+} are split evenly across the remaining octahedral and tetrahedral sites. In stoichiometric magnetite where Fe^{II}/Fe^{III} = 1/2, the divalent iron ions can be partly or totally replaced by other divalent ions (*e.g.*, Co, Zn…), and for this reason Fe_3O_4 can be considered both an *n*- and *p*-type semiconductor. Due to it having a very small bandgap (0.1 eV), Fe_3O_4 is the iron oxide with the lowest resistivity.[143, 145]

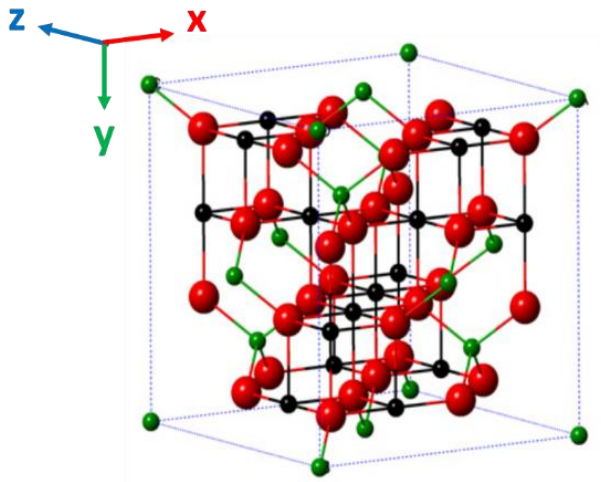

Figure 1.18. Crystal structure and crystallographic data of magnetite. The black ball is Fe^{2+}, the green ball is Fe^{3+}, and the red ball is O^{2-}. Adapted from reference [143].

Magnetite iron oxide nanoparticles with the appropriate properties can be used for several biomedical applications, such as MRI contrast agents.[146, 147] The requirement is that the particles have high magnetisation values, a narrow particle size distribution and sizes of less than 100 nm.[148, 149] The surface coating needs to be non-toxic and biocompatible and it is desirable to allow for a targetable delivery in a specific area.[150] Accordingly, superparamagnetic iron oxide nanoparticles are used as contrast agents for MRI, one of the main applications being for early detection of cancer.[151, 152] These nanoparticles enhance the signal-to-noise ratio thanks to their unique nanoscale superparamagnetism; that is, high magnetism in an external magnetic field, but no residual magnetism when the external magnetic field is removed.[153, 154]

Currently, many of the MRI contrast agents available on the market are gadolinium chelate-based positive contrast agents. One advantage of the iron oxide nanoparticles when compared to the gadolinium chelates is that they have better biocompatibility.[155]

MRI contrast agents can be positive contrast agents (T_1-weighted contrast agents) and negative contrast agents (T_2-weighted contrast agents), depending on whether they shorten the T_1 or the T_2 relaxation times of water protons inside organs, and both types lead to contrast in the magnetic resonance images.[156, 157] For magnetic iron oxide nanoparticles, it is their size that determines if they can be used as negative or positive contrast agents. Consequently, nanoparticles larger than 10 nm are negative contrast agents, while when they are smaller than 5 nm as the recently discovered extremely small iron oxide nanoparticles, they can be potential positive contrast agents.[158, 159]

1.6.2. Quantum dots for optical imaging

Quantum dots (QDs) are a type of nanoparticles composed of semiconductor materials that emit light. Their size is within the nanoscale range and, thanks to this property, they have discrete electronic energy states and this gives them some unique optical and electrical properties which are different from discrete molecules or bulk materials.[139, 160] These unique properties of QDs make them very promising and versatile luminophores, and when compared to traditional fluorescent probes, QDs have advantages such as size-tuneable light emission, narrow and symmetric emission spectra, and broad absorption spectra.[146, 161] Moreover, when they are coupled to biomolecular affinity ligands (*e.g.*, antibodies, peptides or small molecules), QDs can be used for highly sensitive and specific detection of molecular biomarkers or tumour cells.[162, 163]

The size of a quantum dot determines the wavelength of its emission. Usually, the smaller the size of a quantum dot, the closer its emission light is to the blue end of the spectrum; and the larger its size, the closer the emission light is to the red end. Quantum dots are usually within the visible light spectrum, but they can also be tuned beyond that, into the infrared or ultraviolet.[139] *Figure 1.19* shows different vials containing QDs of increasing size and the change in their colours when this happens. Probes with emissions that cover the whole visible to near infrared wavelength range can be synthesised thanks to the size-dependent properties of this type of nanomaterials.[161]

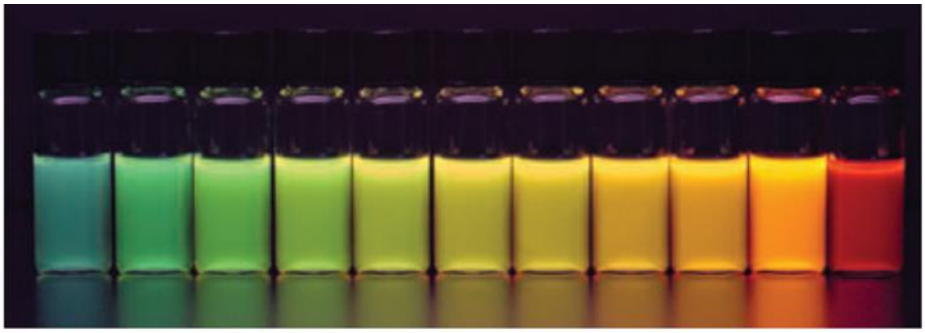

Figure 1.19. Vials containing QDs of increasing size from left to right and their fluorescence emission. Reproduced from reference [161].

Usually, quantum dots are made of hundreds to thousands of atoms of elements from group II and VI; III and V; I, III and VI_2 or IV. One of the main problems of QDs when they are used for biomedical applications is their toxicity, which is a major concern for *in vivo* imaging. However, their toxicity is not a concern when analyses of cells and tissues are carried out on *in vitro* or *ex vivo* clinical patient samples, and such uses of this kind of fluorophore are the most important and clinically relevant applications of them, as they are ultrasensitive probes for *in*

vitro biodiagnostics.[164-167] For this purpose, a new range of novel heavy metal-free quantum dots are being investigated from different semiconductor materials.[160] Another problem of QDs that emerges when used for biomedical applications is the size of the bioconjugated nanocrystals, as this produces steric hindrance and nonspecific protein adsorption.[161]

A very common type of quantum dot nanocrystals are those with a core made of CdSe, and they allow the wavelength of fluorescence emission to be tuned between approximately 500 and 650 nm by modifying the core size.[161, 168, 169] The formation of ternary alloys using CdSe has also been investigated, leading to nanocrystals made of three elements such as $CdSe_xS_{1-x}$, $CdTe_xSe_{1-x}$, or $Hg_xCd_{1-x}Te$, to name some examples. In these nanocrystals, the core size remains constant, whilst the fluorescence wavelength changes due to the modifications in the chemical composition.[161, 170, 171] *Figure 1.20* shows how CdTe QDs can be doped with Hg^{2+} in exchange of the Cd^{2+} cation, leading to $Hg_xCd_{1-x}Te$ alloyed nanocrystals.[172]

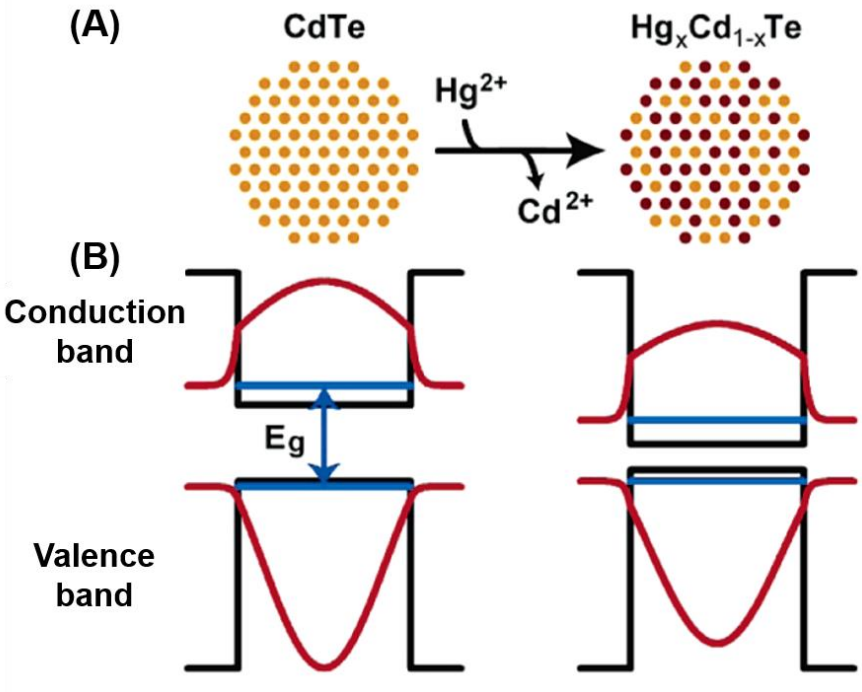

Figure 1.20. (A) CdTe QDs where Cd^{2+} is replaced by Hg^{2+}, forming $Hg_xCd_{1-x}Te$ QDs, and **(B)** potential energy wells (black lines), quantum-confined kinetic energy levels (blue lines), and wave functions (red lines) of electrons and holes in CdTe (left) and $Hg_xCd_{1-x}Te$ (right) QDs, calculated using the effective mass approximation. Reproduced from reference [172].

1.7. Functionalised peptides as targeting molecules

Peptides are molecules containing different amino acids that are linked together by peptide bonds, -C(=O)NH-. The number of amino acids in peptides can differ, going from two to approximately 50. The main difference between proteins and peptides is that the latter do not have a properly defined 3D structure as proteins do (tertiary structure).[173]

When some types of tumours are developed, certain peptide receptors may be overexpressed. Based on this concept, receptors can be targeted so that peptides can be used as targeting molecules for molecular imaging.[173] Monoclonal antibodies started to be widely used as potential targeting molecules about 30 years ago. However, when trying to use this principle in reality, the main issue was the very high molecular mass of antibodies (around 150 kDa).[174, 175] It is only recently that some drugs based on antibodies or fragments of these have become commercially available for diagnosis or therapy of cancer. Around 25 years ago, an alternative to radiolabelled antibodies was discovered: a radiolabelled peptide, of much smaller molecular mass (around 1.5 kDa), which was a somatostatin analogue.[173, 176] It was found that most human endocrine tumours express a high density of somatostatin receptors, and thanks to this a method could be developed in order to localise these tumours and their metastases *in vivo* after injecting a radiolabelled somatostatin analogue.[177] Using γ-cameras, the tumours could be identified after the radioligand bound to their receptors and these were internalised.[173, 178] This approach has been studied with different peptides and radioligands and due to its success, the targeting of overexpressed peptide receptors in tumours using small peptides has gained great interest in nuclear medicine.[175]

The basic principle of *in vivo* peptide receptor targeting of cancer is schematically shown in *Figure 1.21*. The radiolabelled peptide (P) is injected into the patient and distributed in the whole body. If the patient has a tumour with cancer cells expressing the corresponding peptide receptor (P-R), the radiopeptide will bind to it and internalise with the receptor into the cell, as expressed with arrows, where the radioactivity will accumulate. γ-Cameras can scan the whole body and detect the radioactivity accumulated in the tumour. The remaining radioactivity in the body will rapidly be cleared through the kidneys.[173]

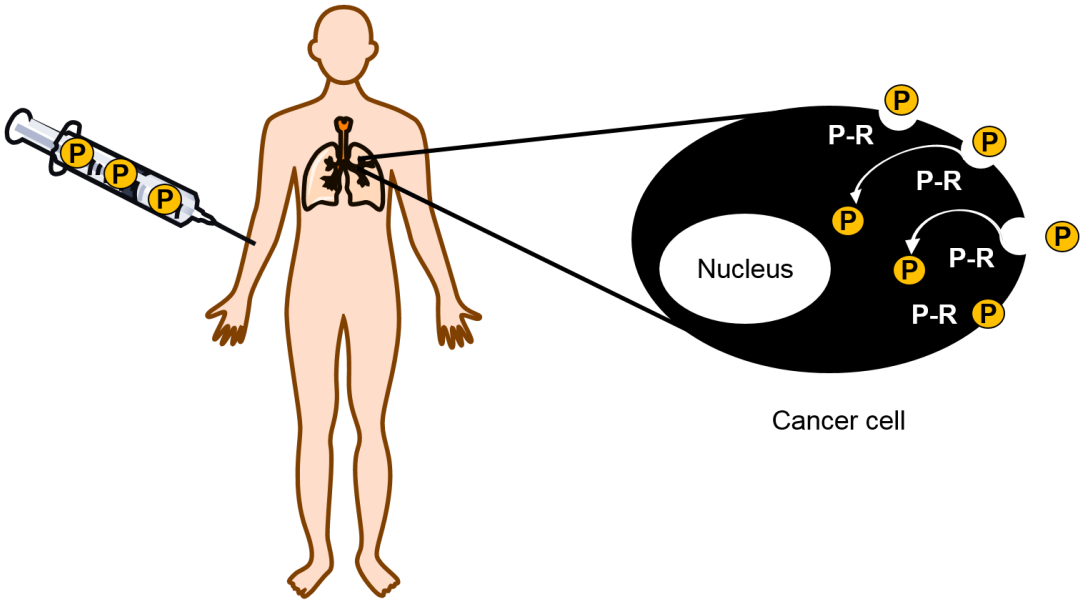

Figure 1.21. Scheme of the *in vivo* peptide receptor targeting of cancer. Adapted from reference [173].

1.7.1. Bombesin and its derivatives

The family of bombesin (BBN) peptides owes its name from the original terminology that V. Erspamer and his co-workers used to name the first natural ligand described, bombesin, a peptide of 14 amino acids that was isolated from the skin of the European frog *Bombina bombina*.[179-181]

Bombesin has a C-terminal region and ends in Gly-His-Leu-Met-NH_2. This makes this peptide similar to two bombesin-related peptides present in mammals: gastrin-releasing peptide (GRP) and neuromedin B (NMB). The first one, GRP, contains 27 amino acids and was first isolated from porcine stomach. The same C-terminal amino acids are shared with bombesin, giving them similar biological activities. NMB is a peptide containing 10 amino acids that was originally isolated from porcine spinal cord, and has a COOH terminus ending in Gly-His-Phe-Met-NH_2. The genes encoding for these peptides in humans are on chromosome 18q21 for GRP, and 15q11 for NMB, and they encode for 148 and 117 amino acid precursors, respectively.[182]

The structure of bombesin is shown in *Figure 1.22*, showing the L- configuration as it is made of naturally occurring L-amino acids.

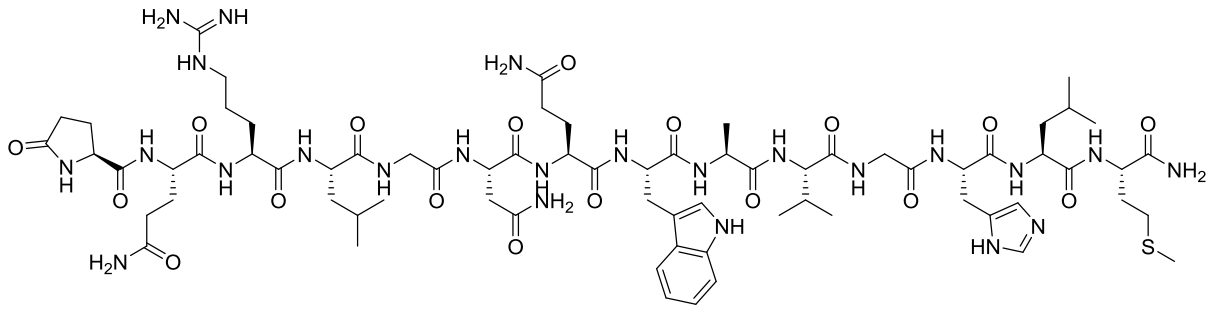

Figure 1.22. Structure of natural L-bombesin:
Pyr-Gln-Arg-Leu-Gly-Asn-Gln-Trp-Ala-Val-Gly-His-Leu-Met-NH_2.

The mammalian bombesin family of receptors contains three classes of similar receptors: (i) BB_1-receptor or NMBR: a 390 amino acid NMB-selective receptor, (ii) BB_2-receptor or GRPR: a 348 amino acid GRP-selective receptor, and (iii) BB_3-receptor: a 399 amino acid receptor that does not have a preference for either peptide.[182] These receptors are all G protein-coupled receptors, and they signal primarily through phospholipase C-mediated cascades. They also stimulate tyrosine phosphorylation of a number of signalling proteins, but in most tissues they do not activate adenylate cyclase.[182]

All these receptors are overexpressed in a broad range of tumours, including breast, pancreatic and prostate cancers. The overexpression of these receptors by various tumours plays a crucial role in many aspects of their treatment and management, such as providing targets to deliver cytotoxic treatment or image the tumours. Accordingly, some bombesin-receptor ligands have been used to couple to other compounds for tumour imaging. Examples of these are: coupling to fluorescent probes to be used for optical imaging,[183-185] conjugation to superparamagnetic iron oxide nanoparticles to enhance detection by MRI,[186, 187] and coupling to gold nanorods coated with PEG that can be used for photoacoustical imaging, especially in breast cancer identification, among many others.[188, 189]

1.8. Aim and objectives

This project involves the design, synthesis and characterisation of novel multimodal systems suitable for optical imaging as well as PET/SPECT and MRI. Such systems are of relevance to early diagnosis and progression monitoring of degenerative diseases including tumour targeting, using optical imaging and positron emission tomography. By following a rational design process, we aim to construct highly kinetically stable systems, which may be anchored onto targeting biomolecules such as peptides, to be further functionalised. These systems will improve the efficacy of binding to cells and the effectiveness of bioimaging techniques.

To sum up, this project aims to build multimodal imaging systems following two approaches, one based on a tripodal organic core that can be trifunctionalised using the right conditions with three different labels, including a fluorescent molecule (*Figure 1.23(A)*). The second approach is based on magnetic iron oxide nanoparticles suitable for magnetic resonance imaging, a fluorescent probe and a coordinated radioisotope that will allow PET or SPECT imaging (*Figure 1.23(B)*). These systems will need to be biocompatible and suitable for a cellular environment in order to be used as radiolabelling agents.

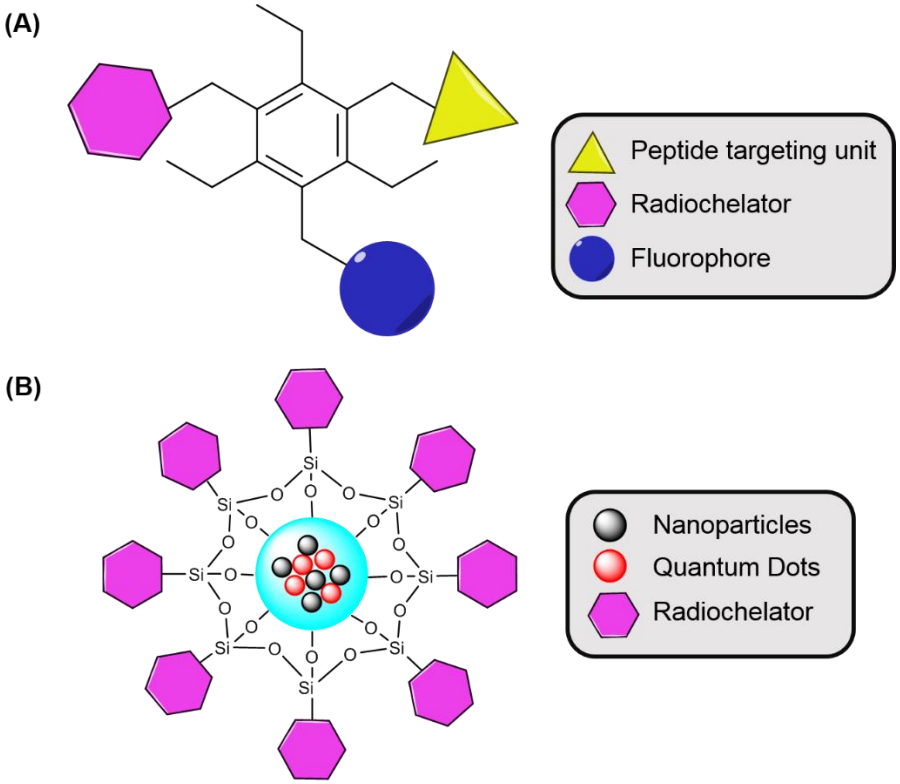

Figure 1.23. (A) Scheme of a tripodal organic core trifunctionalised with three different labels, and **(B)** scheme of silica-coated nanoparticles functionalised with fluorescent quantum dots and a chelator.

The specific objectives are:

- The design and synthesis of a new scaffold based on the trifunctionalisation with three different labels of a symmetric tripodal organic core. Such labels include a fluorophore, and BODIPY derivatives will be especially considered due to their low cytotoxicity and high fluorescent properties.
- The synthesis of a fragment of a bombesin peptide and the coupling of this to one of the arms of the tripodal ligand to act as a targeting molecule for prostate cancer cells.
- The synthesis of tripodal ligands based on different thiosemicarbazides which can coordinate to metals, due to their multimodal properties and potential hypoxia selectivity.
- The synthesis of iron oxide nanoparticles and functionalisation of these with quantum dots and metal-ligand complexes.
- The *in vitro* evaluation of the most promising compounds in different cell lines, focusing strongly on prostate cancer cells, and cytotoxicity studies.
- The radiolabelling of the most promising bifunctional chelators and scaffolds with ^{68}Ga(III) and/or ^{89}Zr(IV) ions in water.

1.9. References for Chapter 1

1. F. Bray, J. S. Ren, E. Masuyer and J. Ferlay, *Int. J. Cancer*, 2013, **132**, 1133-1145.
2. C. H. Leung, H. J. Zhong, H. Yang, Z. Cheng, D. S. H. Chan, V. P.-Y. Ma, R. Abagyan, C.-Y. Wong and D. L. Ma, *Angew. Chem. Int. Ed.*, 2012, **51**, 9010-9014.
3. C. H. Leung, H. J. Zhong, D. S. H. Chan and D. L. Ma, *Coord. Chem. Rev.*, 2013, **257**, 1764-1776.
4. D. L. Ma, D. S. H. Chan and C. H. Leung, *Chem. Sci.*, 2011, **2**, 1656-1665.
5. R. L. Siegel, K. D. Miller and A. Jemal, *CA Cancer J. Clin.*, 2017, **67**, 7-30.
6. V. Mirabello, D. G. Calatayud, R. L. Arrowsmith, H. Ge and S. I. Pascu, *J. Mater. Chem. B*, 2015, **3**, 5657-5672.
7. V. Wagner, A. Dullaart, A.-K. Bock and A. Zweck, *Nat. Biotechnol.*, 2006, **24**, 1211-1217.
8. P. B. Bach, J. N. Mirkin, T. K. Oliver, C. G. Azzoli, D. Berry, O. W. Brawley, T. Byers, G. A. Colditz, M. K. Gould, J. R. Jett, A. L. Sabichi, R. Smith-Bindman and D. E. Wood, *JAMA*, 2012, **307**, 2418-2429.
9. A. S. Ross, *Gastrointest. Endosc.*, **74**, 571-572.
10. E. Sausville and D. Longo, 2005, **16**, 464.
11. R. A. Smith, D. Manassaram-Baptiste, D. Brooks, V. Cokkinides, M. Doroshenk, D. Saslow, R. C. Wender and O. W. Brawley, *CA Cancer J. Clin.*, 2014, **64**, 30-51.
12. R. Dennis, S. Tou and R. Miller, *Medicine*, 2011, **39**, 243-249.
13. C. L. Sawyers, *Nature*, 2008, **452**, 548-552.
14. H. Ono, *Eur. J. Gastroenterol. Hepatol.*, 2006, **18**, 863-866.
15. H. Zhu, M. Wang, D. Feng, Y. Feng, Y. Ren, J. Chen, Y. He and J. Yuan, *Oncol. Lett.*, 2014, **7.1**, 195-198.
16. M. Pilewskie and T. A. King, *Cancer*, 2014, **120**, 2080-2089.
17. D. W. Townsend, J. P. J. Carney, J. T. Yap and N. C. Hall, *J. Nucl. Med.*, 2004, **45**, 4S-14S.
18. S. Pascu, P. A. Waghorn, T. Conry, B. Lin, C. James and J. M. Zayed, *Adv. Inorg. Chem.*, 2009, **61**, 131-178.
19. P. Vaupel and A. Mayer, *Cancer Metastasis Rev.*, 2007, **26**, 225-239.
20. P. Vaupel, O. Thews and M. Hoeckel, *Med. Oncol.*, 2001, **18**, 243-259.
21. P. Vaupel and M. Höckel, in *Recombinant Human Erythropoietin (rhEPO) in Clinical Oncology*, Springer Vienna, Vienna, Editon edn., 2002, pp. 127-146.
22. P. Vaupel, A. Mayer and M. Höckel, in *Methods in Enzymology*, Academic Press, New York, Editon edn., 2004, vol. 381, pp. 335-354.
23. P. Vaupel and M. Höckel, in *Recombinant Human Erythropoietin (rhEPO) in Clinical Oncology: Scientific and Clinical Aspects of Anemia in Cancer*, Springer Vienna, Vienna, Editon edn., 2008, pp. 283-305.
24. P. Vaupel, A. Mayer, S. Briest and M. Höckel, in *Oxygen Transport to Tissue XXVI*, Springer US, Boston, Editon edn., 2005, pp. 333-342.
25. P. Vaupel, *Oncologist*, 2008, **13**, 21-26.
26. P. Vaupel, M. Höckel and A. Mayer, *Antioxid. Redox Signal.*, 2007, **9**, 1221-1236.
27. P. Vaupel and L. Harrison, *Oncologist*, 2004, **9**, 4-9.
28. J. M. Brown and W. R. Wilson, *Nat. Rev. Cancer*, 2004, **4**, 437-447.
29. M. Kunz and S. M. Ibrahim, *Mol. Cancer*, 2003, **2**, 23-23.
30. J. Folkman, *J. Natl. Cancer Inst.*, 1990, **82**, 4-6.
31. J. Folkman and Y. Shing, *J. Biol. Chem.*, 1992, **267**, 10931-10934.
32. G. Helmlinger, F. Yuan, M. Dellian and R. K. Jain, *Nat. Med.*, 1997, **3**, 177-182.
33. J. A. Stanley, W. U. Shipley and G. G. Steel, *Br. J. Cancer*, 1977, **36**, 105-113.
34. W. R. Wilson and M. P. Hay, *Nat. Rev. Cancer*, 2011, **11**, 393-410.
35. *Institute of Microbial Chemistry (IMC)*, http://www.bikaken.or.jp/english/, (accessed October 2017).

36. P. W. Miller, H. Audrain, D. Bender, A. J. deMello, A. D. Gee, N. J. Long and R. Vilar, *Chem. Eur. J.*, 2011, **17**, 460-463.
37. E. M. Rohren, T. G. Turkington and R. E. Coleman, *Radiology*, 2004, **231**, 305-332.
38. W. A. Weber, *J. Clin. Oncol.*, 2006, **24**, 3282-3292.
39. Y. F. Tai and P. Piccini, in *Positron Emission Tomography: Clinical Practice*, Springer London, London, Editon edn., 2006, pp. 453-461.
40. M. E. Phelps, *Proc. Natl. Acad. Sci.*, 2000, **97**, 9226-9233.
41. J. S. Fowler, N. D. Volkow, G.-J. Wang, Y.-S. Ding and S. L. Dewey, *J. Nucl. Med.*, 1999, **40**, 1154-1163.
42. S. Maschauer, J. Einsiedel, R. Haubner, C. Hocke, M. Ocker, H. Hübner, T. Kuwert, P. Gmeiner and O. Prante, *Angew. Chem. Int. Ed.*, 2010, **49**, 976-979.
43. S. M. Ametamey, M. Honer and P. A. Schubiger, *Chem. Rev.*, 2008, **108**, 1501-1516.
44. S. S. Gambhir, *Nat. Rev. Cancer*, 2002, **2**, 683-693.
45. J. S. Fowler and A. P. Wolf, *Acc. Chem. Res.*, 1997, **30**, 181-188.
46. P. W. Miller, N. J. Long, R. Vilar and A. D. Gee, *Angew. Chem. Int. Ed.*, 2008, **47**, 8998-9033.
47. K. Strijckmans, *Comput. Med. Imaging Graph.*, 2001, **25**, 69-78.
48. M. Ito, A. A. Lammertsma, R. J. S. Wise, S. Bernardi, R. S. J. Frackowiak, J. D. Heather, C. G. McKenzie, D. G. T. Thomas and T. Jones, *Neuroradiology*, 1982, **23**, 63-74.
49. P. H. Elsinga, *Methods*, 2002, **27**, 208-217.
50. M. G. Stabin, M. Tagesson, S. R. Thomas, M. Ljungberg and S. E. Strand, *Appl. Radiat. Isot.*, 1999, **50**, 73-87.
51. J. Krivokapich, J. R. Barrio, S.-C. Huang and H. R. Schelbert, *J. Am. Coll. Cardiol.*, 1990, **16**, 1158-1167.
52. W. C. Eckelman, *Nucl. Med. Biol.*, 1994, **21**, 759-769.
53. A. van Waarde, P. H. Elsinga, R. L. Anthonio, T. J. Visser, P. K. Blanksma, G. M. Visser, A. M. J. Paans and W. Vaalburg, in *Cardiac Positron Emission Tomography: Viability, Perfusion, Receptors and Cardiomyopathy*, Springer Netherlands, Dordrecht, Editon edn., 1995, pp. 171-182.
54. W. C. Eckelman, *Nucl. Med. Biol.*, 1998, **25**, 169-173.
55. E. V. Garcia, *J. Nucl. Cardiol.*, 2015, **22**, 1316-1316.
56. M. S. Rosenthal, J. Cullom, W. Hawkins, S. C. Moore, B. M. Tsui and M. Yester, *J. Nucl. Med.*, 1995, **36**, 1489-1513.
57. *Universite de Geneve, Neuroscience center*, http://neurocenter.unige.ch, (accessed October 2017).
58. R. W. Brown, Y.-C. N. Cheng, E. M. Haacke, M. R. Thompson and R. Venkatesan, in *MRI*, John Wiley & Sons Ltd, New York, Editon edn., 2014, pp. 1-17.
59. A. Berger, *BMJ*, 2002, **324**, 35.
60. E. M. Haacke, N. Y. C. Cheng, M. J. House, Q. Liu, J. Neelavalli, R. J. Ogg, A. Khan, M. Ayaz, W. Kirsch and A. Obenaus, *MRI*, 2005, **23**, 1-25.
61. M. Minsky, *Scanning*, 1988, **10**, 128-138.
62. I. Santos, *Angew. Chem. Int. Ed.*, 2016, **55**, 35-35.
63. X. Li, Y. He, S. S. Talukdar and M. T. Swihart, *Langmuir*, 2003, **19**, 8490-8496.
64. Z. M. Markovic, L. M. Harhaji-Trajkovic, B. M. Todorovic-Markovic, D. P. Kepić, K. M. Arsikin, S. P. Jovanović, A. C. Pantovic, M. D. Dramićanin and V. S. Trajkovic, *Biomaterials*, 2011, **32**, 1121-1129.
65. H. Sun, L. Cao and L. Lu, *Nano Res.*, 2011, **4**, 550-562.
66. F. Erogbogbo, K.-T. Yong, R. Hu, W.-C. Law, H. Ding, C.-W. Chang, P. N. Prasad and M. T. Swihart, *ACS Nano*, 2010, **4**, 5131-5138.
67. K. Yang, L. Hu, X. Ma, S. Ye, L. Cheng, X. Shi, C. Li, Y. Li and Z. Liu, *Adv. Mater.*, 2012, **24**, 1868-1872.
68. Y. Miura, G. Huettmann, R. Orzekowsky-Schroeder, P. Steven, M. Szaszák, N. Koop and R. Brinkmann, *Invest. Ophthalmol. Vis. Sci.*, 2013, **54**, 3366-3377.
69. W. Denk, J. H. Strickler and W. W. Webb, *Science*, 1990, **248**, 73.
70. D. Brinks, A. J. Klein and A. E. Cohen, *Biophys. J.*, 2015, **109**, 914-921.

71. W. Becker, *J. Microsc.*, 2012, **247**, 119-136.
72. R. R. Duncan, A. Bergmann, M. A. Cousin, D. K. Apps and M. J. Shipston, *J. Microsc.*, 2004, **215**, 1-12.
73. D. S. Abou, T. Ku and P. M. Smith-Jones, *Nucl. Med. Biol.*, 2011, **38**, 675-681.
74. L. T. McClinton and J. Schubert, *J. Pharmacol. Exp. Ther.*, 1948, **94**, 1-6.
75. B. V. Rama Sastry, L. K. Owens and C. O. T. Ball, *Nature*, 1964, **201**, 410-411.
76. W. E. Meijs, H. J. Haisma, R. P. Klok, F. B. van Gog, E. Kievit, H. M. Pinedo and J. D. M. Herscheid, *J. Nucl. Med.*, 1997, **38**, 112-118.
77. J. P. Holland, V. Divilov, N. H. Bander, P. M. Smith-Jones, S. M. Larson and J. S. Lewis, *J. Nucl. Med.*, 2010, **51**, 1293-1300.
78. J. P. Holland, E. Caldas-Lopes, V. Divilov, V. A. Longo, T. Taldone, D. Zatorska, G. Chiosis and J. S. Lewis, *PLoS ONE*, 2010, **5**, e8859.
79. A. Ruggiero, J. P. Holland, J. S. Lewis and J. Grimm, *J. Nucl. Med.*, 2010, **51**, 1123-1130.
80. J. C. Haygarth and R. A. Graham, in *Review of Extraction, Processing, Properties & Applications of Reactive Metals*, John Wiley & Sons, Inc., New York, Editon edn., 1999, pp. 1-71.
81. Y. Zhou, K. E. Baidoo and M. W. Brechbiel, *Adv. Drug Deliv. Rev.*, 2013, **65**, 1098-1111.
82. M. J. W. D. Vosjan, L. R. Perk, G. W. M. Visser, M. Budde, P. Jurek, G. E. Kiefer and G. A. M. S. van Dongen, *Nat. Protoc.*, 2010, **5**, 739-743.
83. E. C. F. Dijkers, J. G. W. Kosterink, A. P. Rademaker, L. R. Perk, G. A. M. S. van Dongen, J. Bart, J. R. de Jong, E. G. E. de Vries and M. N. Lub-de Hooge, *J. Nucl. Med.*, 2009, **50**, 974-981.
84. L. R. Perk, G. W. M. Visser, M. J. W. D. Vosjan, M. Stigter-van Walsum, B. M. Tijink, C. R. Leemans and G. A. M. S. van Dongen, *J. Nucl. Med.*, 2005, **46**, 1898-1906.
85. J. P. Holland, Y. Sheh and J. S. Lewis, *Nucl. Med. Biol.*, 2009, **36**, 729-739.
86. Y. Zhang, H. Hong and W. Cai, *Curr. Radiopharm.*, 2011, **4**, 131-139.
87. A. Infantino, G. Cicoria, D. Pancaldi, A. Ciarmatori, S. Boschi, S. Fanti, M. Marengo and D. Mostacci, *Appl. Radiat. Isot.*, 2011, **69**, 1134-1137.
88. B. M. Zeglis and J. S. Lewis, *J. Vis. Exp.*, 2015, 52521.
89. T. Sasaki, T. Kobayashi, I. Takagi and H. Moriyama, *J. Nucl. Sci. Technol.*, 2008, **45**, 735-739.
90. M. A. Deri, B. M. Zeglis, L. C. Francesconi and J. S. Lewis, *Nucl. Med. Biol.*, 2013, **40**, 3-14.
91. J. M. Link, K. A. Krohn and M. J. O'Hara, *Appl. Radiat. Isot.*, 2017, **122**, 211-214.
92. T. J. Wadas, E. H. Wong, G. R. Weisman and C. J. Anderson, *Chem. Rev.*, 2010, **110**, 2858-2902.
93. T. K. Nayak and M. W. Brechbiel, *Bioconjugate Chem.*, 2009, **20**, 825-841.
94. I. Verel, G. W. M. Visser, R. Boellaard, M. Stigter-van Walsum, G. B. Snow and G. A. M. S. van Dongen, *J. Nucl. Med.*, 2003, **44**, 1271-1281.
95. M. Walther, P. Gebhardt, P. Grosse-Gehling, L. Würbach, I. Irmler, S. Preusche, M. Khalid, T. Opfermann, T. Kamradt, J. Steinbach and H.-P. Saluz, *Appl. Radiat. Isot.*, 2011, **69**, 852-857.
96. A. M. Dabkowski, S. J. Paisey, E. Spezi, J. Chester and C. Marshall, *AIP Conf. Proc.*, 2017, **1845**, 020005.
97. N. Bhatt, D. Pandya and T. Wadas, *Molecules*, 2018, **23**, 638.
98. M. Patra, A. Bauman, C. Mari, C. A. Fischer, O. Blacque, D. Haussinger, G. Gasser and T. L. Mindt, *Chem. Commun.*, 2014, **50**, 11523-11525.
99. A. B. Ilyukhin, R. L. Davidovich, I. N. Samsonova and L. V. Teplukhina, *Crystallogr. Rep.*, 2000, **45**, 39-43.
100. A. I. Pozhidaev, M. A. Porai-Koshits and T. N. Polynova, *J. Struct. Chem.*, 1974, **15**, 548-553.
101. C. J. Adams, J. J. Wilson and E. Boros, *Mol. Pharm.*, 2017, **14**, 2831-2842.
102. J. R. Dilworth and S. I. Pascu, *Chem. Soc. Rev.*, 2018.

103. M. J. Morris, N. Pandit-Taskar, C. R. Divgi, S. Bender, J. A. O'Donoghue, A. Nacca, P. Smith-Jones, L. Schwartz, S. Slovin, R. Finn, S. Larson and H. I. Scher, *Clin. Cancer Res.*, 2007, **13**, 2707-2713.
104. D. N. Pandya, S. Pailloux, D. Tatum, D. Magda and T. J. Wadas, *Chem. Commun.*, 2015, **51**, 2301-2303.
105. M. A. Deri, S. Ponnala, B. M. Zeglis, G. Pohl, J. J. Dannenberg, J. S. Lewis and L. C. Francesconi, *J. Med. Chem.*, 2014, **57**, 4849-4860.
106. G. W. Severin, J. T. Jørgensen, S. Wiehr, A.-M. Rolle, A. E. Hansen, A. Maurer, M. Hasenberg, B. Pichler, A. Kjær and A. I. Jensen, *Nucl. Med. Biol.*, 2015, **42**, 360-368.
107. M. T. Ma, L. K. Meszaros, B. M. Paterson, D. J. Berry, M. S. Cooper, Y. Ma, R. C. Hider and P. J. Blower, *Dalton Trans.*, 2015, **44**, 4884-4900.
108. F. Guerard, Y.-S. Lee, R. Tripier, L. P. Szajek, J. R. Deschamps and M. W. Brechbiel, *Chem. Commun.*, 2013, **49**, 1002-1004.
109. L. G. Meimetis, E. Boros, J. C. Carlson, C. Ran, P. Caravan and R. Weissleder, *Bioconjugate Chem.*, 2016, **27**, 257-263.
110. F. C. J. van de Watering, M. Rijpkema, L. Perk, U. Brinkmann, W. J. G. Oyen and O. C. Boerman, *Biomed. Res. Int.*, 2014, **2014**, 13.
111. K. Stockhofe, J. Postema, H. Schieferstein and T. Ross, *Pharmaceuticals*, 2014, **7**, 392.
112. F. Roesch, *Curr. Radiopharm.*, 2012, **5**, 202-211.
113. R. Weissleder and M. J. Pittet, *Nature*, 2008, **452**, 580-589.
114. M. Fani, J. P. André and H. R. Maecke, *Contrast Media Mol. Imaging*, 2008, **3**, 53-63.
115. M. A. Green, in *New Trends in Radiopharmaceutical Synthesis, Quality Assurance, and Regulatory Control*, Springer US, New York, Editon edn., 1991, pp. 119-127.
116. S. M. Moerlein and M. J. Welch, *Int. J. Nucl. Med. Biol.*, 1981, **8**, 277-287.
117. A. Al-Nahhas, Z. Win, T. Szyszko, A. Singh, C. Nanni, S. Fanti and D. Rubello, *Anticancer Res.*, 2007, **27**, 4087-4094.
118. A. Yokoyama, Y. Ohmomo, K. Horiuchi, H. Saji, H. Tanaka, K. Yamamoto, Y. Ishil and K. Torizuka, *J. Nucl. Med.*, 1982, **23**, 909-914.
119. C. Caraco, L. Aloj and W. C. Eckelman, *Appl. Radiat. Isot.*, 1998, **49**, 1477-1479.
120. J. P. Andre, H. R. Maecke, J. P. Andre, M. Zehnder, L. Macko and K. G. Akyel, *Chem. Commun.*, 1998, 1301-1302.
121. C. M. Reis, D. S. Pereira, R. O. Paiva, L. F. Kneipp and A. Echevarria, *Molecules*, 2011, **16**, 10668.
122. T. Plech, M. Wujec, A. Siwek, U. Kosikowska and A. Malm, *Eur. J. Med. Chem.*, 2011, **46**, 241-248.
123. M. Kalhor, M. Shabani, I. Nikokar and S. Reyhaneh Banisaeed, *Iran J. Pharm. Res.*, 2015, **14**, 67-75.
124. S. A. Khan, A. M. Asiri, K. Al-Amry and M. A. Malik, *Sci. World J.*, 2014, **2014**, 9.
125. M. Khandani, T. Sedaghat, N. Erfani, M. R. Haghshenas and H. R. Khavasi, *J. Mol. Struct.*, 2013, **1037**, 136-143.
126. E. Pahonțu, C. Paraschivescu, D.-C. Ilieș, D. Poirier, C. Oprean, V. Păunescu, A. Gulea, T. Roșu and O. Bratu, *Molecules*, 2016, **21**, 674.
127. Z. Afrasiabi, E. Sinn, S. Padhye, S. Dutta, S. Padhye, C. Newton, C. E. Anson and A. K. Powell, *J. Inorg. Biochem.*, 2003, **95**, 306-314.
128. R. Hueting, M. Christlieb, J. R. Dilworth, E. G. Garayoa, V. Gouverneur, M. W. Jones, V. Maes, R. Schibli, X. Sun and D. A. Tourwe, *Dalton Trans.*, 2010, **39**, 3620-3632.
129. S. R. Bayly, R. C. King, D. J. Honess, P. J. Barnard, H. M. Betts, J. P. Holland, R. Hueting, P. D. Bonnitcha, J. R. Dilworth, F. I. Aigbirhio and M. Christlieb, *J. Nucl. Med.*, 2008, **49**, 1862-1868.
130. J. P. Holland, F. I. Aigbirhio, H. M. Betts, P. D. Bonnitcha, P. Burke, M. Christlieb, G. C. Churchill, A. R. Cowley, J. R. Dilworth, P. S. Donnelly, J. C. Green, J. M. Peach, S. R. Vasudevan and J. E. Warren, *Inorg. Chem.*, 2007, **46**, 465-485.
131. A. L. Vavere and J. S. Lewis, *Dalton Trans.*, 2007, **35**, 4893-4902.
132. D. H. Petering, *Bioinorg. Chem.*, 1972, **1**, 255-271.

133. H. G. Petering, H. H. Buskirk and G. E. Underwood, *Cancer Res.*, 1964, **24**, 367-372.
134. P. J. Blower, J. S. Lewis and J. Zweit, *Nucl. Med. Biol.*, 1996, **23**, 957-980.
135. P. McQuade, D. J. Rowland, J. S. Lewis and M. J. Welch, *Curr. Med. Chem.*, 2005, **12**, 807-818.
136. A. Niccoli Asabella, G. L. Cascini, C. Altini, D. Paparella, A. Notaristefano and G. Rubini, *Biomed. Res. Int.*, 2014, **2014**, 786463.
137. O. Jacobson, I. D. Weiss, L. Szajek, J. M. Farber and D. O. Kiesewetter, *Bioorg. Med. Chem.*, 2009, **17**, 1486-1493.
138. W. Lu, H. Hong and W. Cai, *Eur. J. Nanomed.*, 2016, **8**, 151-170.
139. F. Mensah, H. Seyoum and P. Misra, in *Applied Spectroscopy and the Science of Nanomaterials*, Springer Singapore, Singapore, Editon edn., 2015, vol. 2, pp. 253-277.
140. J. M. Harris and R. B. Chess, *Nat. Rev. Drug. Discov.*, 2003, **2**, 214-221.
141. D. S. Abou, D. L. J. Thorek, N. N. Ramos, M. W. H. Pinkse, H. T. Wolterbeek, S. D. Carlin, B. J. Beattie and J. S. Lewis, *Pharm. Res.*, 2013, **30**, 878-888.
142. C. Kaittanis, T. M. Shaffer, D. L. J. Thorek and J. Grimm, *Crit. Rev. Oncog.*, 2014, **19**, 143-176.
143. W. Wu, Z. Wu, T. Yu, C. Jiang and W.-S. Kim, *Sci. Technol. Adv. Mater.*, 2015, **16**, 023501.
144. D. L. J. Thorek, J. Czupryna, A. K. Chen and A. Tsourkas, in *Cancer Imaging*, Academic Press, Amsterdam, Editon edn., 2008, pp. 85-95.
145. D. S. Abou, J. E. Pickett and D. L. J. Thorek, *Br. J. Radiol.*, 2015, **88**, 20150185.
146. B. A. Kairdolf, X. Qian and S. Nie, *Anal. Chem.*, 2017, **89**, 1015-1031.
147. J. Shi, P. W. Kantoff, R. Wooster and O. C. Farokhzad, *Nat. Rev. Cancer*, 2017, **17**, 20-37.
148. S. Laurent, D. Forge, M. Port, A. Roch, C. Robic, L. Vander Elst and R. N. Muller, *Chem. Rev.*, 2008, **108**, 2064-2110.
149. D. L. J. Thorek, E. R. Elias and A. Tsourkas, *Mol. Imaging*, 2009, **8**, 221-220.
150. Q. Zhou and Y. Wei, *Chem. Res. Toxicol.*, 2017, **30**, 73-80.
151. O. L. Gobbo, K. Sjaastad, M. W. Radomski, Y. Volkov and A. Prina-Mello, *Theranostics*, 2015, **5**, 1249-1263.
152. E. Boros, A. M. Bowen, L. Josephson, N. Vasdev and J. P. Holland, *Chem. Sci.*, 2015, **6**, 225-236.
153. P. Padwal, R. Bandyopadhyaya and S. Mehra, *J. Chem. Technol. Biotechnol.*, 2015, **90**, 1773-1781.
154. D. Thorek, D. Ulmert, N.-F. Diop, D. Abou, M. Doran, R. Huang and J. Grimm, *J. Nucl. Med.*, 2013, **54**, 6.
155. Z. R. Stephen, F. M. Kievit and M. Zhang, *Mater. Today*, 2011, **14**, 330-338.
156. Z. Shen, A. Wu and X. Chen, *Mol. Pharm.*, 2017, **14**, 1352-1364.
157. N. A. Keasberry, M. Banobre-Lopez, C. Wood, G. J. Stasiuk, J. Gallo and N. J. Long, *Nanoscale*, 2015, **7**, 16119-16128.
158. H. Wei, O. T. Bruns, M. G. Kaul, E. C. Hansen, M. Barch, A. Wiśniowska, O. Chen, Y. Chen, N. Li, S. Okada, J. M. Cordero, M. Heine, C. T. Farrar, D. M. Montana, G. Adam, H. Ittrich, A. Jasanoff, P. Nielsen and M. G. Bawendi, *Proc. Natl. Acad. Sci. USA*, 2017, **114**, 2325-2330.
159. D. L. J. Thorek, A. K. Chen, J. Czupryna and A. Tsourkas, *Ann. Biomed. Eng.*, 2006, **34**, 23-38.
160. I. V. Martynenko, A. P. Litvin, F. Purcell-Milton, A. V. Baranov, A. V. Fedorov and Y. K. Gun'ko, *J. Mater. Chem. B*, 2017, **5**, 6701-6727.
161. B. A. Kairdolf, A. M. Smith, T. H. Stokes, M. D. Wang, A. N. Young and S. Nie, *Annu. Rev. Anal. Chem.*, 2013, **6**, 143-162.
162. E. S. Lee, K. Na and Y. H. Bae, *J. Controlled Release*, 2003, **91**, 103-113.
163. R. Weissleder, K. Kelly, E. Y. Sun, T. Shtatland and L. Josephson, *Nat. Biotechnol.*, 2005, **23**, 1418-1423.

164. Y. Xing, Q. Chaudry, C. Shen, K. Y. Kong, H. E. Zhau, L. W. Chung, J. A. Petros, R. M. O'Regan, M. V. Yezhelyev, J. W. Simons, M. D. Wang and S. Nie, *Nat. Protoc.*, 2007, **2**, 1152-1165.
165. X. Wu, H. Liu, J. Liu, K. N. Haley, J. A. Treadway, J. P. Larson, N. Ge, F. Peale and M. P. Bruchez, *Nat. Biotechnol.*, 2003, **21**, 41-46.
166. S. Kim, Y. T. Lim, E. G. Soltesz, A. M. De Grand, J. Lee, A. Nakayama, J. A. Parker, T. Mihaljevic, R. G. Laurence, D. M. Dor, L. H. Cohn, M. G. Bawendi and J. V. Frangioni, *Nat. Biotechnol.*, 2004, **22**, 93-97.
167. J. Liu, S. K. Lau, V. A. Varma, R. A. Moffitt, M. Caldwell, T. Liu, A. N. Young, J. A. Petros, A. O. Osunkoya, T. Krogstad, B. Leyland-Jones, M. D. Wang and S. Nie, *ACS Nano*, 2010, **4**, 2755-2765.
168. P. Alivisatos, *Nat. Biotechnol.*, 2004, **22**, 47-52.
169. A. M. Smith and S. Nie, *Acc. Chem. Res.*, 2010, **43**, 190-200.
170. M. D. Regulacio and M.-Y. Han, *Acc. Chem. Res.*, 2010, **43**, 621-630.
171. R. E. Bailey and S. Nie, *J. Am. Chem. Soc.*, 2003, **125**, 7100-7106.
172. A. M. Smith and S. Nie, *J. Am. Chem. Soc.*, 2011, **133**, 24-26.
173. J. C. Reubi, *Endocr. Rev.*, 2003, **24**, 389-427.
174. D. M. Goldenberg, F. DeLand, E. Kim, S. Bennett, F. J. Primus, J. R. J. van Nagell, N. Estes, P. DeSimone and P. Rayburn, *N. Engl. J. Med.*, 1978, **298**, 1384-1388.
175. T. M. Behr, S. Memtsoudis, R. M. Sharkey, R. D. Blumenthal, R. M. Dunn, S. Gratz, E. Wieland, K. Nebendahl, H. Schmidberger, D. M. Goldenberg and W. Becker, *Int. J. Cancer*, 1998, **77**, 787-795.
176. A. N. Serafini, *J. Nucl. Med.*, 1993, **34**, 533-536.
177. J. C. Reubi, *J. Nucl. Med.*, 1995, **36**, 1825-1835.
178. E. P. Krenning, W. A. P. Breeman, P. P. M. Kooij, J. S. Lameris, W. H. Bakker, J. W. Koper, L. Ausema, J. C. Reubi and S. W. J. Lamberts, *Lancet*, 1989, **333**, 242-244.
179. R. T. Jensen, J. F. Battey, E. R. Spindel and R. V. Benya, *Pharmacol. Rev.*, 2008, **60**, 1-42.
180. V. Erspamer, G. F. Erspamer and M. Inselvini, *J. Pharm. Pharmacol.*, 1970, **22**, 875-876.
181. A. Anastasi, V. Erspamer and M. Bucci, *Experientia*, 1971, **27**, 166-167.
182. N. Gonzalez, T. W. Moody, H. Igarashi, T. Ito and R. T. Jensen, *Curr. Opin. Endocrinol. Diabetes Obes.*, 2008, **15**, 58-64.
183. L. Ma, P. Yu, B. Veerendra, T. L. Rold, L. Retzloff, A. Prasanphanich, G. Sieckman, T. J. Hoffman, W. A. Volkert and C. J. Smith, *Mol. Imaging*, 2007, **6**, 171-180.
184. Q.-Y. Cai, P. Yu, C. Besch-Williford, C. J. Smith, G. L. Sieckman, T. J. Hoffman and L. Ma, *Prostate*, 2013, **73**, 842-854.
185. H. Chen, S. Wan, F. Zhu, C. Wang, S. Cui, C. Du, Y. Ma and Y. Gu, *Contrast Media Mol. Imaging*, 2014, **9**, 122-134.
186. J. Atefeh, S. Mojtaba, S. Saber Farjami, H. Zahra, R. Ahmad Bitarafan, B. Komail and N. Ali, *Nanotechnology*, 2015, **26**, 075101.
187. A. L. Martin, J. L. Hickey, A. L. Ablack, J. D. Lewis, L. G. Luyt and E. R. Gillies, *J. Nanopart. Res.*, 2009, **12**, 1599-1608.
188. P. Moreno, I. Ramos-Álvarez, T. W. Moody and R. T. Jensen, *Expert Opin. Ther. Targets*, 2016, **20**, 1055-1073.
189. Z. Heidari, R. Sariri and M. Salouti, *J. Photochem. Photobiol. B*, 2014, **130**, 40-46.

Chapter 2. Synthesis and characterisation of systems based on a symmetric tripodal organic core

2.1. Overview of Chapter 2

This Chapter describes the synthesis and characterisation of new symmetric tripodal derivatives having a fully-substituted benzene core (compound **1**) and featuring a range of functionalities. In order to substitute this molecule with three different labels several reactions have been carried out, and are described hereby (*Figure 2.1*). A pathway to multifunctional structures involves the careful design and synthesis, often multi-stage, of an organic ligand with precisely spaced functional groups. As seen in natural systems, there is a close relationship between the structure of a compound and its functionality.[1] In this chapter, the construction of a multi-membered, complex chemical entity using self-assembly driven processes where building blocks are held together by dynamic covalent bonds has been investigated and is reported.[2]

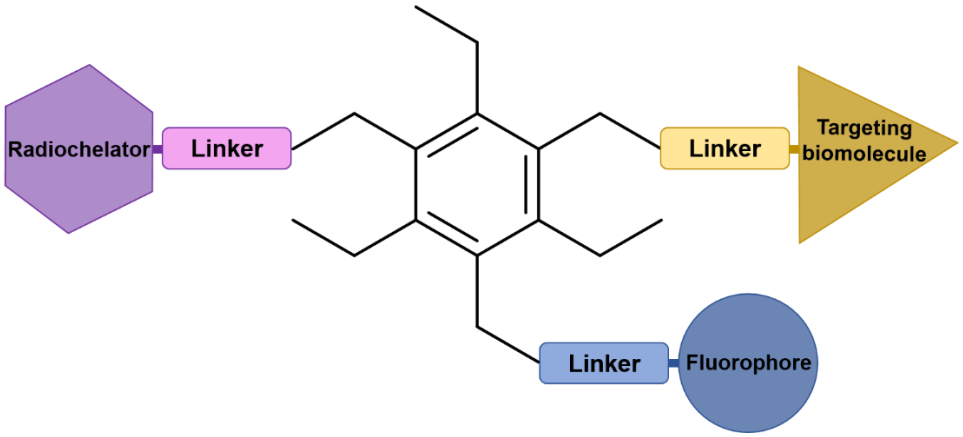

Figure 2.1. Aimed tripodal ligand with three different labels attached.

After exploring a variety of conditions, the reaction between a tripodal core precursor and several carboxylic acid derivatives was achieved, and this yielded a mixture of products that were purified by silica gel column chromatography (*Scheme 2.1*). Several new mono- and disubstituted products were isolated and characterised spectroscopically after purification of the crude mixture.

The optimum reaction conditions were found using simple starting materials such as benzoic acid, and a 4,4-difluoro-4-bora-3a,4a-diaza-s-indacene (BODIPY) derivative was synthesised and attached to the tripodal core, obtaining the mono- and disubstituted BODIPY derivatives. Furthermore, two different linkers were incorporated into the system and one of these will be

used to couple to a peptide (the [7-13] bombesin fragment). An alternative other linker, which contains an azido functional group, was incorporated with the aim of carrying out “click” chemistry with an alkyne derivative via a strain-promoted alkyne-azide cycloaddition (SPAAC) (copper-free) reaction using a dibenzocyclooctyne acid derivative.[3] Moreover, a screening of the reaction conditions including temperature, stoichiometry of the starting materials and time was carried out in order to make the reaction more accessible for biomolecules. This was necessary as it has been shown that peptide-based building blocks usually need to be treated at lower temperatures and for shorter periods of time as they are sensitive to heat due to supramolecular arrangements.

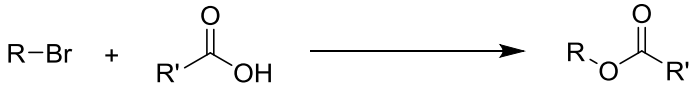

Scheme 2.1. General scheme for the reaction of bromide derivatives and carboxylic acid groups to form an ester derivative.

The cytotoxicity of the most promising compounds emerging hereby, which incorporated a BODIPY derivative, was tested for their activity in prostate cancer cells (PC-3 cell line) using MTT assays. Colocalisation studies by confocal fluorescence imaging using LysoTracker Red and ER-Tracker Red co-staining assays, which localise within the lysosomes and the endoplasmic reticulum, respectively, were carried out. The living cells were imaged with a laser scanning confocal microscope and using associated techniques, mainly at the Rutherford Appleton Laboratory (RAL).

2.2. Synthesis and characterisation of the tripodal organic core

The precursor 1,3,5-tris(bromomethyl)-2,4,6-triethylbenzene was chosen as the starting material in order to attach up to three different labels and create a potential multimodal system.

The tripodal core derivative (compound **1**) was synthesised following a previously described procedure.[4] In order to obtain this compound, zinc powder was first dissolved in acetic acid and mixed with HBr, triethylbenzene and paraformaldehyde. The mixture was heated to 90 ^{o}C under reflux and stirred for 48 hours (*Scheme 2.2*). The precipitate was then isolated, and the filtrate (a red-brown liquid) was heated up again and stirred for 24 more hours to increase the yield of the reaction (see experimental details). Finally, a substantial amount of a white powder was obtained, and TLC was performed in order to check its purity, using a 1:9 ratio of acetone:hexane. The TLC showed a single spot, indicating that the compound isolated was pure. After this, the product was characterised and used without further purification.

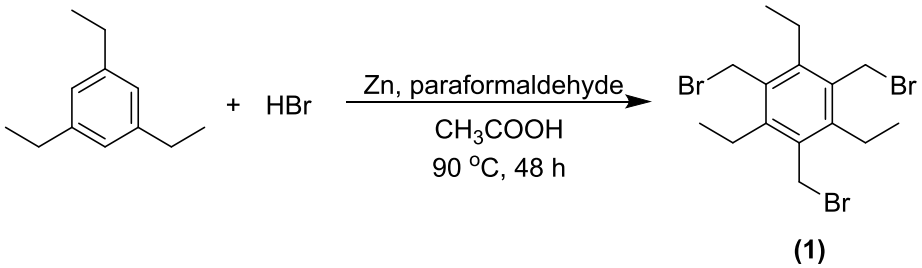

Scheme 2.2. Reaction to obtain compound **1**.

HPLC analysis was performed to check more accurately the purity of this product as it is important for it to be completely pure in order to be used in the next steps that will be described in this chapter. The HPLC chromatogram in the 280 nm channel shows a single peak at 12.4 minutes (*Appendix A*), indicating that the compound was pure and there were no traces of starting materials or by-products.

This product was then characterised via NMR spectroscopy. Resonances in the ^{1}H NMR spectrum matched with the resonances expected for this structure (*Figure 2.2*). The singlet with an integral related to 6 H atoms at 4.57 ppm is due to the protons from the bromomethyl groups, H^{1}. The quartet at 2.92 ppm integrates for 6 H and corresponds to the three CH_2 groups of the ethyl arms, H^{2}; while the triplet at 1.33 ppm refers to the three CH_3 resonances from the same ethyl groups, H^{3}. The peak at approximately 2.20 ppm is due to acetic acid traces still present in the sample.

In order to confirm the molecular structure, mass spectrometry was performed. The spectrum obtained using nanoelectrospray ionisation in the positive mode shows a highly intense peak at m/z = 457.9507, which corresponds to the $[M+NH_4]^+$ ion (*Appendix A*), as it can be seen from the amplification of the obtained and expected isotopic patterns. The effect of the two bromine isotopes, ^{79}Br and ^{81}Br, can be observed in this mass spectrum. These two isotopes exist in an approximately 1:1 ratio (50.5:49.5, exactly). This means that a compound containing one bromine atom will have two peaks similar in height in the molecular ion region, depending on which bromine isotope the molecular ion contains. In the spectrum for compound **1**, peaks of similar intensity with a gap of two m/z units can be observed, evidencing the presence of bromine atoms in the molecule.

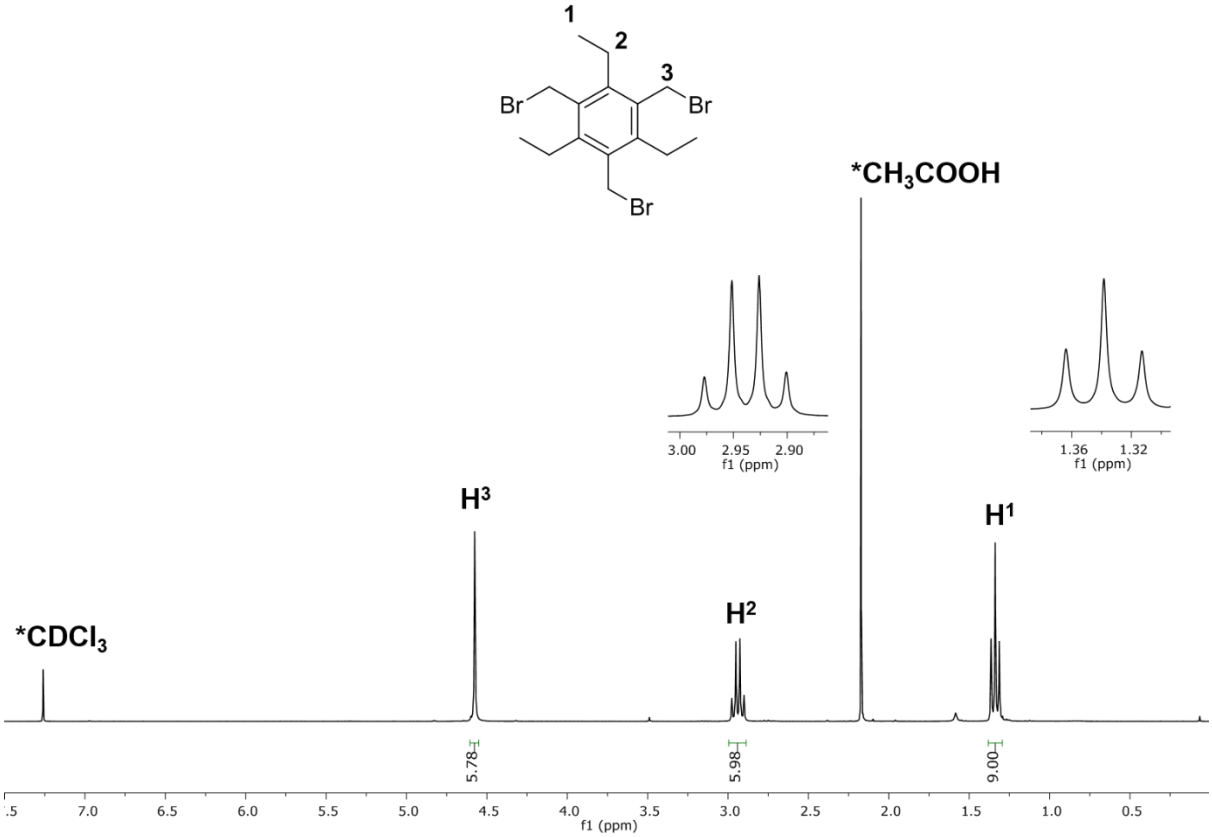

Figure 2.2. ^1H NMR (300 MHz, $CDCl_3$, 298 K) spectrum of compound **1**.

Finally, the compound was analysed by FT-IR spectroscopy. The obtained spectrum confirmed that the expected functional groups can be found in the product (*Appendix A*).

2.3. Synthesis and characterisation of a BODIPY (boron-dipyrromethene) derivative

Compounds incorporating BODIPY are a class of fluorescent dyes based on a dipyrromethene system complexed with a tetrasubstituted boron atom, commonly a BF_2 unit. BODIPY derivatives have become widely popular as imaging dyes due to the numerous advantages that they present: BODIPY probes are highly stable, have large extinction coefficients, intense absorption, high quantum yields and are stable in physiological environments.[5-7] For this reason, BODIPY-based dyes have been used as scaffolds for the construction of multifunctional fluorescent probes.[8]

In this chapter, a BODIPY derivative with a carboxylic acid substituent was synthesised and characterised to be used as a fluorophore in the aimed tripodal multimodal system. The synthesis consisted of the reaction between 2,4-dimethylpyrrole and 4-formylbenzoic acid in dichloromethane at room temperature with a couple of drops of trifluoroacetic acid, adding 2,3-dichloro-5,6-dicyano-1,4-benzoquinone (DDQ), triethylamine and boron trifluoride diethyl etherate (*Scheme 2.3*). A purple slurry crude was obtained, which was purified by silica gel column chromatography, and the fraction of interest was further purified by recrystallisation from THF/hexane, to finally yield a red solid (compound **2**). This synthesis was challenging due to the fact that many by-products are obtained from the polymerisation of pyrrole, which are difficult to separate from the desired compound. Moreover, as previously reported, the yield for this reaction was rather low (20-30%), but consistent with literature data, and much higher than those of porphyrins, which are typically less than 20%.[9-11]

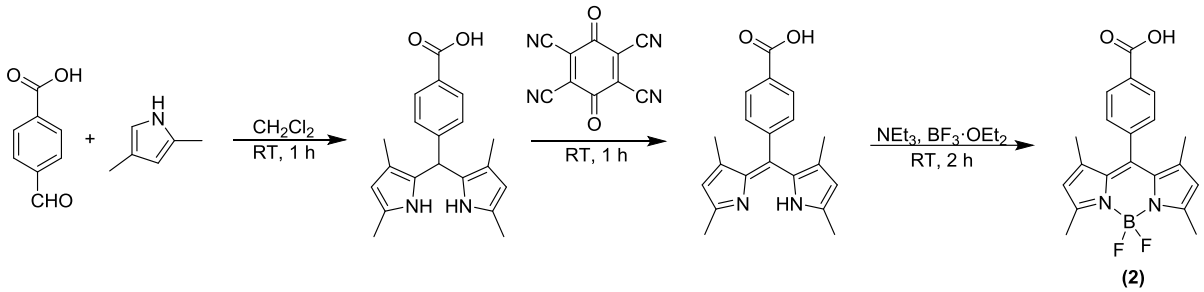

Scheme 2.3. Reaction to obtain compound **2**.

The purity of the BODIPY derivative (compound **2**) was tested by HPLC (*Appendix A*). A high intensity peak at 9.2 minutes was shown using the 500 nm channel, corresponding to the compound of interest. Other minor peaks can be seen, which can be assigned to impurities but due to their much lower intensity they can be ignored.

NMR spectroscopy was carried out to confirm the structure of this molecule. The ^{1}H NMR spectrum shows two doublets that integrate for 2 H each, at 8.11 and 7.52 ppm, and these are the protons in the benzene core H^1 and H^2, respectively (*Figure 2.3*). A singlet at 6.19 ppm integrating for two protons corresponds to the 2 H from the substituted pyrrole rings, H^4. In the upfield region of the spectrum, two singlets can be found at 2.45 and 1.32 ppm and correspond to the methyl groups attached to the pyrrole rings, H^5 and H^3, respectively, and integrate for 6 H resonances each.

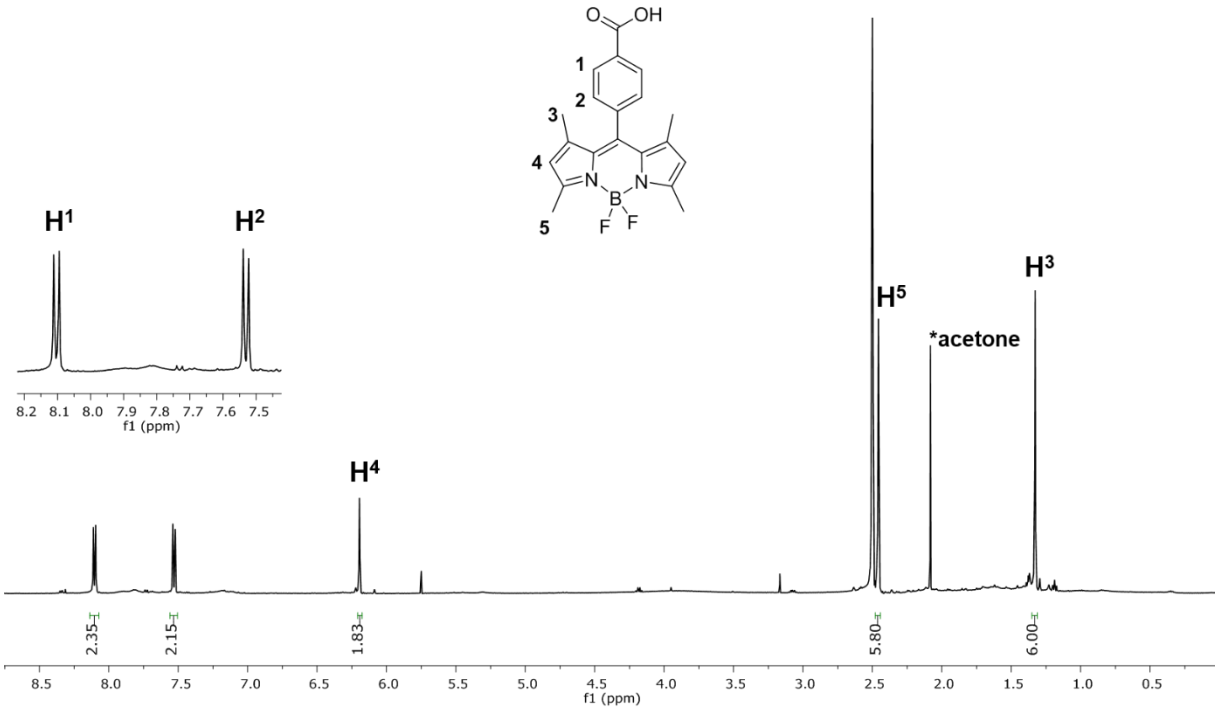

Figure 2.3. ^{1}H NMR (500 MHz, DMSO-d_6, 298 K) spectrum of compound **2**.

Further characterisation of this compound includes mass spectrometry, which was carried out using electrospray ionisation in negative mode, and the spectrum revealed a peak at m/z = 367.1455, which corresponds to the $[M-H]^-$ ion (*Appendix A*).

2.4. Monofunctionalisation strategies of the tripodal core

After several different functionalisation attempts aiming to derivatise the tripodal core (compound **1**) and attach different moieties, it was found that the reaction between this product and different carboxylic acids was successful. The mechanism for this reaction is a nucleophilic substitution catalysed by a base, in which the carboxylic group attacks the carbon adjacent to the bromide that acts as the leaving group.[12]

In this context, a first reaction was carried out using benzoic acid as a test as this is an inexpensive and common reagent. 1,3,5-tris(bromomethyl)-2,4,6-triethylbenzene (compound **1**) and benzoic acid were mixed in acetonitrile in a 1:1 ratio, together with 1.5 equivalents of potassium carbonate as the base, and the mixture was stirred under reflux overnight (*Scheme 2.4*). The reaction was followed by TLC at different times and three spots could be clearly identified, one due to the starting material (compound **1**) and two additional ones. After this time, the solvent was evaporated and the crude solid dissolved in chloroform and extracted three times with an aqueous solution of sodium hydroxide to remove any possible remaining traces of acid. The organic layers were concentrated under vacuum and the obtained solid was purified by silica gel column chromatography to yield three different compounds: the mono- and disubstituted tripodal molecules (compounds **3** and **4**, respectively), and some unreacted starting material (compound **1**). The proportions found in the final mixture were 51% (monosubstituted, **3**), 31% (disubstituted, **4**) and 18% (starting material, **1**).

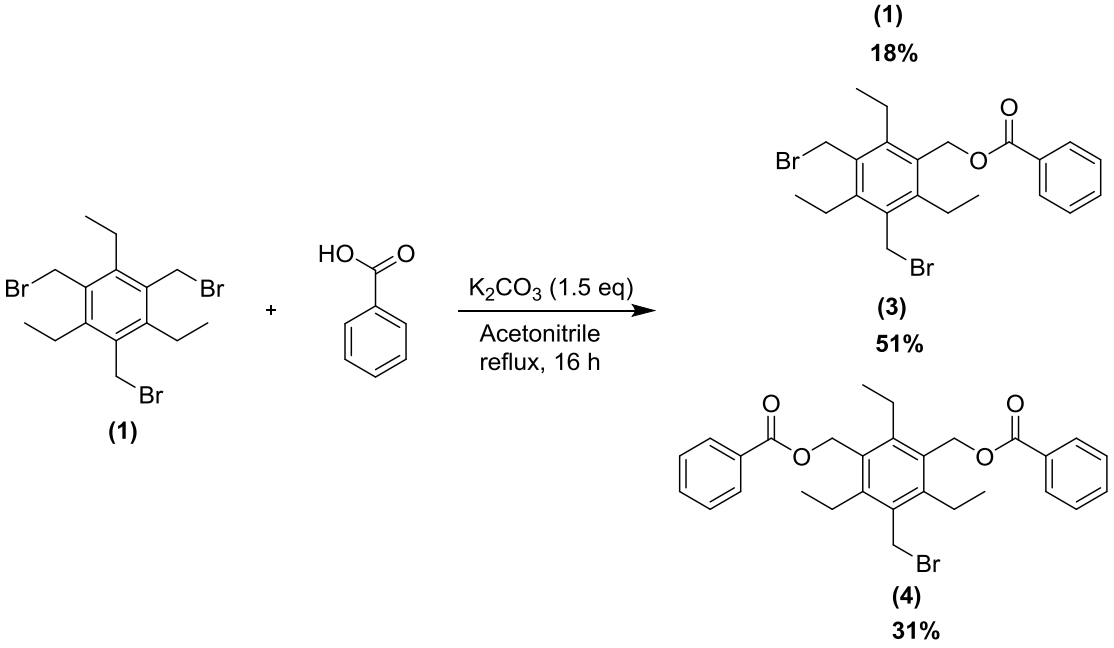

Scheme 2.4. Reaction between compound **1** and benzoic acid yielding two new products (compounds **3** and **4**) and excess of the starting material.

The two new products were characterised by NMR spectroscopy. The ^{1}H NMR spectra for the new synthesised compounds **3** and **4** have resonances with coupling patterns and associated coupling constants that match with the expected ones for these molecules (*Figure 2.4*), thus confirming the molecular structures in solution proposed.

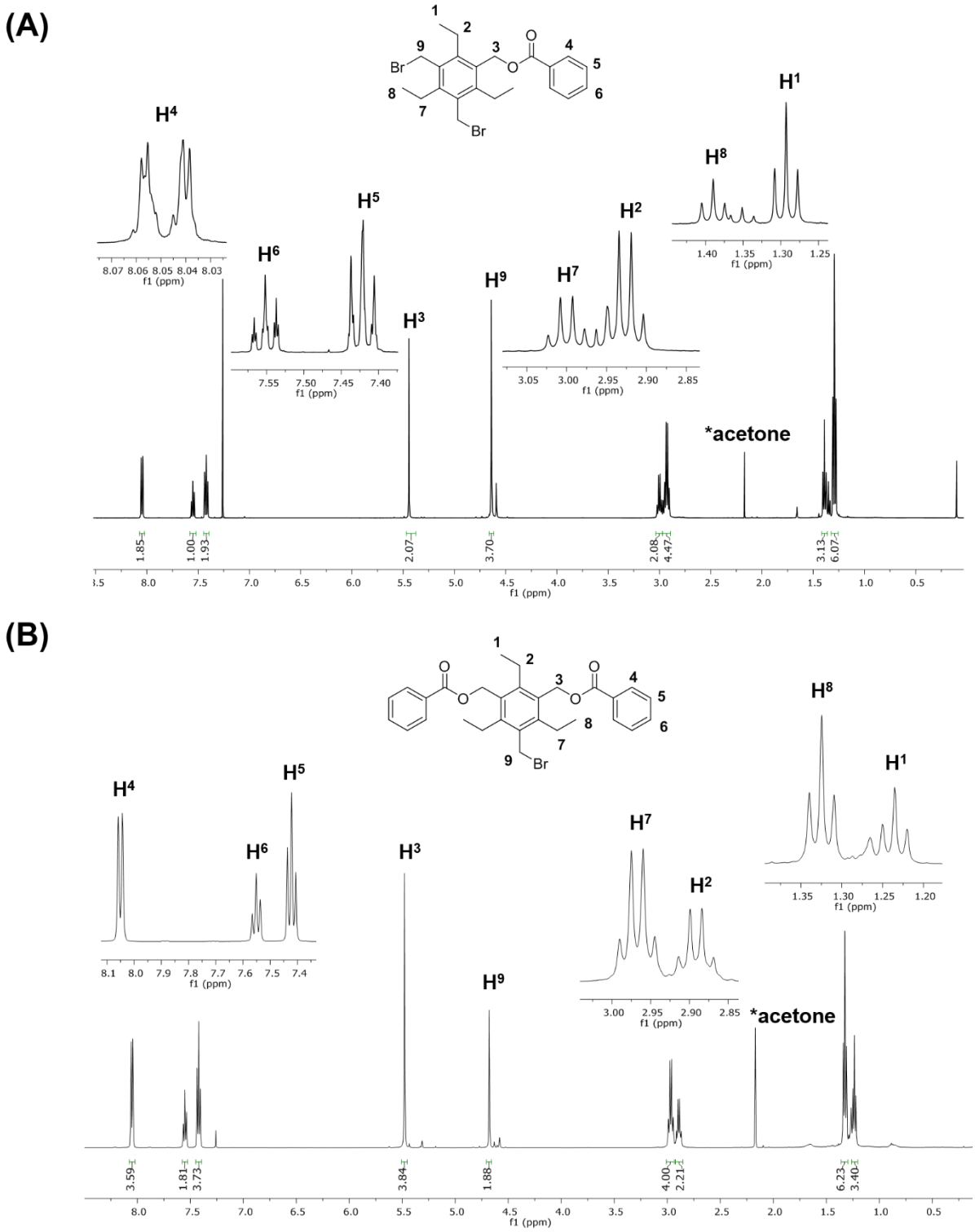

Figure 2.4. ^{1}H NMR (500 MHz, $CDCl_3$, 298 K) spectra of compounds **3 (A)**, and **4 (B)**.

The two spectra have nine different peaks each, corresponding to the nine different groups of equivalent protons in each molecule. The resonances occurred at same or similar chemical shift in both cases, but integrate for different number of protons depending on the substitution of each molecule, and they also show different multiplicity. In this context, there are peaks at 8.05, 7.55 and 7.42 ppm that in the case of compound **3** are multiplets and for compound **4** are a doublet and two triplets, and they correspond to H^4, H^6 and H^5, respectively. For compound **3**, they integrate for 2 H, 1 H and 2 H, respectively, and for compound **4** they integrate double, due to the double substitution of this molecule, which contains two units of the benzoic acid derivative. The different multiplicity for these peaks is mainly due to the fact that the rotation of compound **4** is hindered due to the existence of two bulky groups, while compound **3** has only one. In the upfield region of the spectra there are two singlets, the more deshielded one corresponds to H^3, and integrates for 2 H in the case of compound **3** (5.44 ppm) and for 4 H in the case of compound **4** (5.48 ppm). The less deshielded singlet (4.64 ppm for compound **3** and 4.68 ppm for compound **4**) corresponds to the protons in the CH_2Br groups, and integrates for 4 H and 2 H for the mono- and disubstituted products, respectively. The ethyl groups attached to the benzene core appear as two different groups of resonances, as there are two ethyl groups equivalent between them and another one inequivalent. Accordingly, quartets at 3.00 and 2.93 ppm in the spectrum of compound **3** correspond to H^7 (J = 7.6 Hz) and H^2 (J = 7.6 Hz), and they are two quartets integrating for 2 and 4 H, respectively. For this same molecule, the two triplets at 1.39 and 1.29 ppm correspond to H^8 (J = 7.6 Hz) and H^1 (J = 7.6 Hz) and integrate for 3 and 6 H, respectively. In the case of compound **4**, the two quartets at 2.97 and 2.89 ppm correspond to H^7 (J = 7.6 Hz) and H^2 (J = 7.5 Hz) and integrate for 4 and 2 H, respectively. Finally, the two quartets at 1.32 and 1.24 ppm for this compound correspond to H^8 (J = 7.6 Hz) and H^1 (J = 7.5 Hz) and integrate for 6 and 3 H, respectively.

The ^1H resonances of all the products were assigned with the help of a two dimensional ^1H-^1H COSY spectrum. The COSY NMR spectrum of compound **4** shows the coupling resonances between protons in the ethyl groups H^1-H^2, H^7-H^8, and the aromatic protons, H^4-H^5 and H^5-H^6 (*Figure 2.5*).

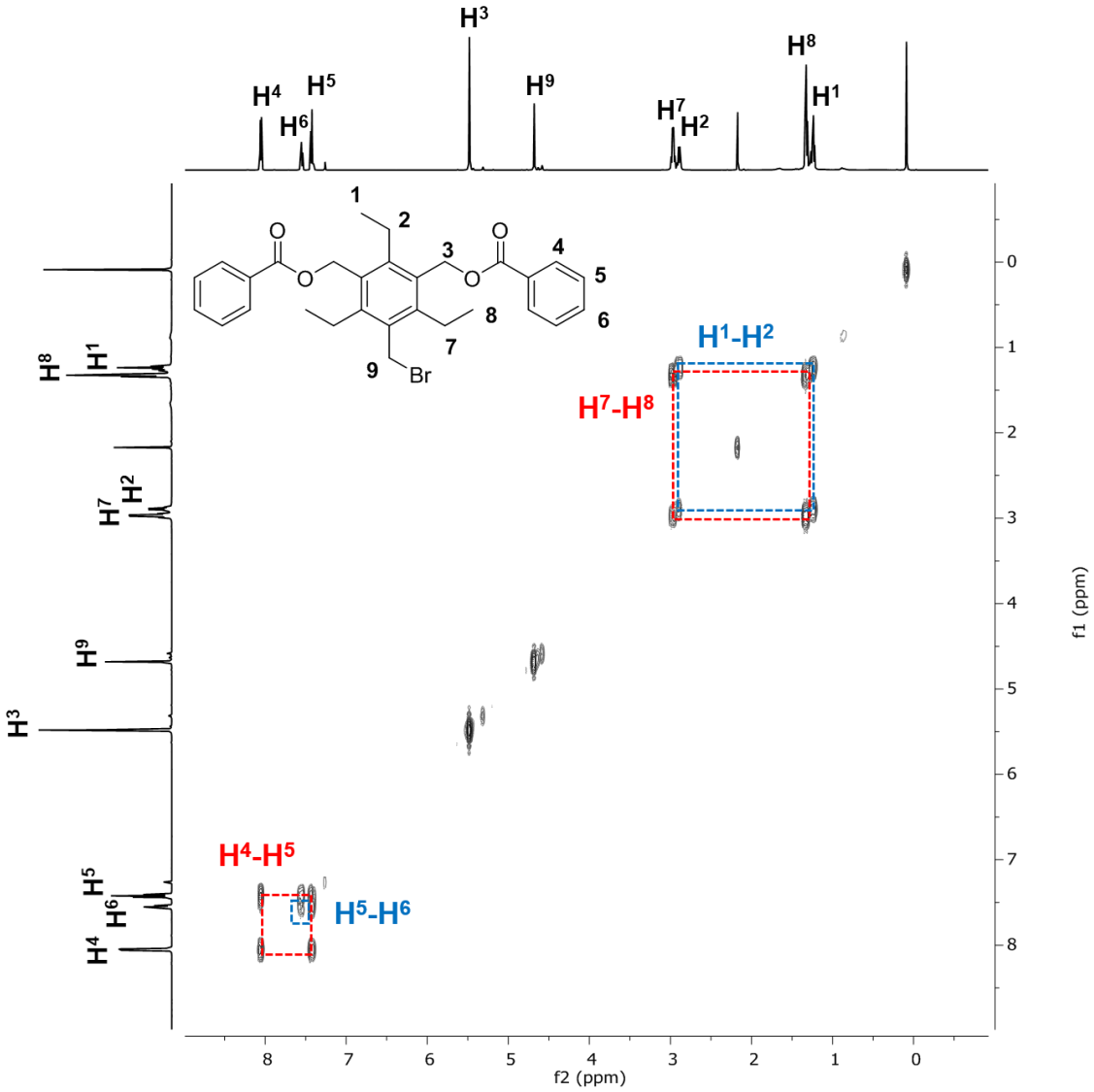

Figure 2.5. ^{1}H-^{1}H COSY NMR (500 MHz, $CDCl_3$, 298 K) spectrum of compound **4**.

After the successful synthesis of compounds **3** and **4**, the same conditions were adapted and applied to attach the previously synthesised BODIPY derivative (compound **2**) to the tripodal precursor unit (compound **1**). This time, the mono- and disubstituted products (compounds **5** and **6**, respectively) were obtained in proportions of 34% and 32% in the final mixture, respectively, and the remaining 34% of the mixture corresponded to unreacted tripodal ligand used as starting material (compound **1**) (*Scheme 2.5*). This is almost a 1:1:1 ratio of starting material, mono- and disubstituted products, which differs from the ratio obtained in the previous reaction, which was of almost 1:3:2, with a much bigger proportion of monosubstituted product formed in the mixture.

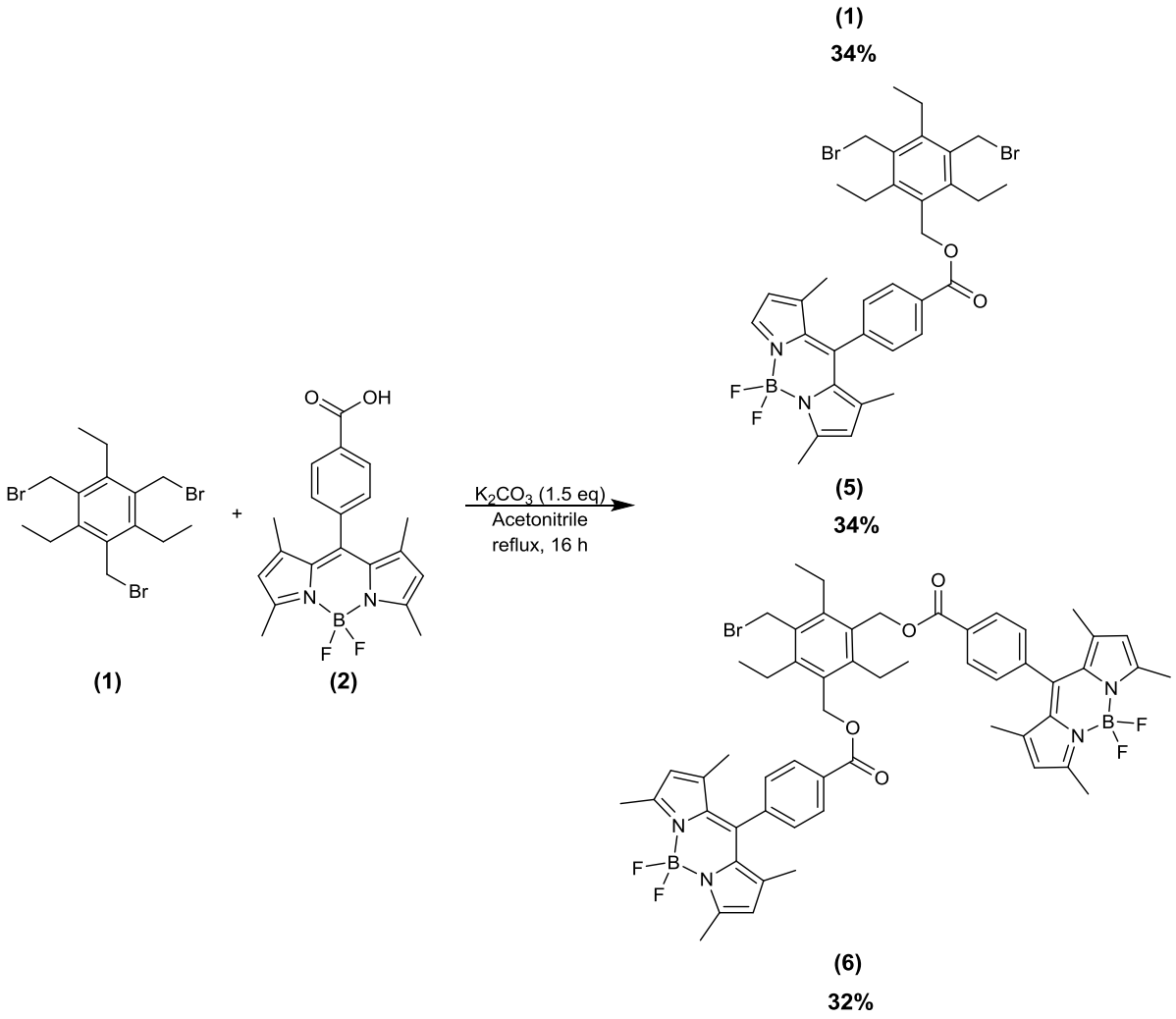

Scheme 2.5. Reaction between compound **1** and compound **2** yielding two new products (compounds **5** and **6**) and excess of the starting material.

The two new BODIPY derivatives reported hereby are promising as cellular imaging probes due to their high fluorescence and contain one and two free bromomethyl arms that can be further functionalised with different labels.[13] These two new products were characterised by NMR spectroscopy and mass spectrometry using nanoelectrospray ionisation in the positive mode. From the spectrum for the monosubstituted BODIPY derivative (compound **5**), a peak at m/z = 729.1490 can be seen, which corresponds to the protonated $[M+H]^+$ ion (*Figure 2.6*). For the disubstituted derivative (compound **6**), the peak at m/z = 1016.3777 can be assigned to the $[M+H]^+$ ion (*Appendix A*).

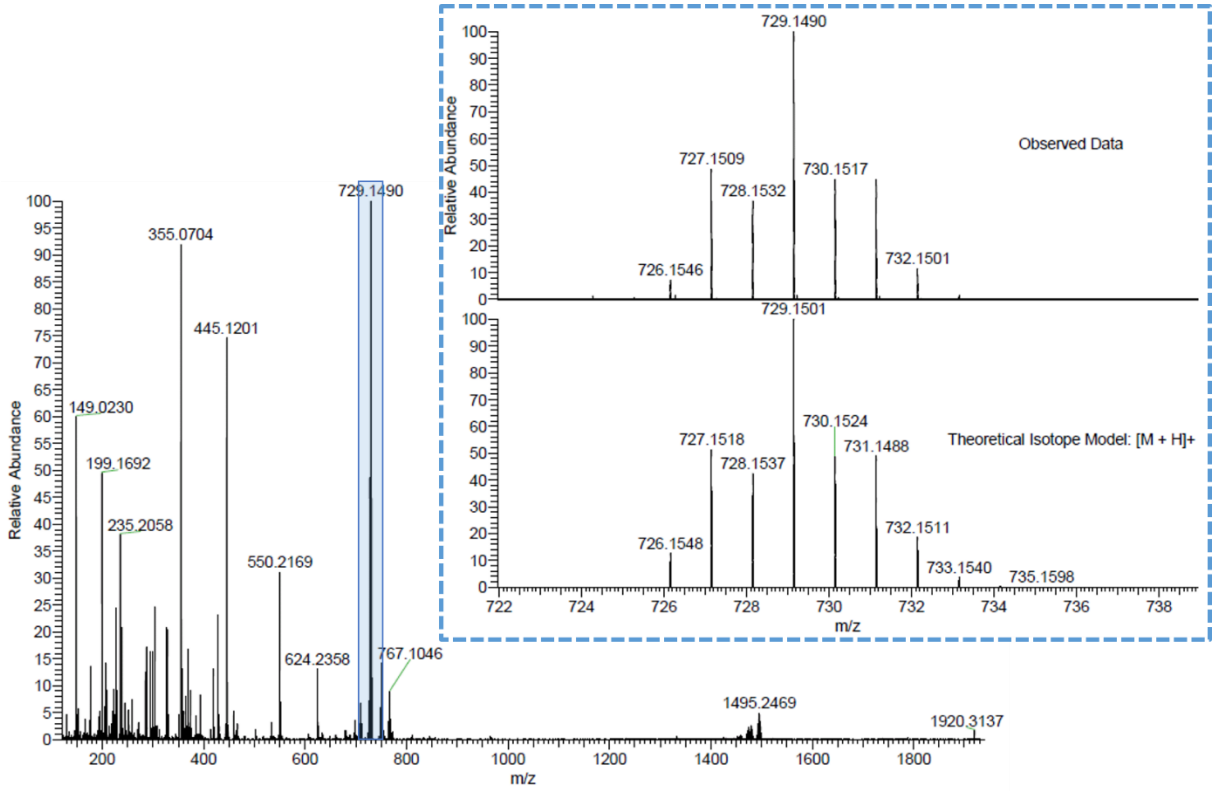

Figure 2.6. Mass spectrum of compound **5** using nESI+, and amplification of the isotopic pattern.

^{1}H NMR spectroscopy was used to compare the spectra of the new products with those of the two starting materials (compounds **1** and **2**). For the monosubstituted product (compound **5**) (*Figure 2.7*), two doublets at 8.16 and 7.38 ppm that integrate for 2 H each correspond to the four protons of the benzene ring in the BODIPY molecule, H^5 and H^6, respectively. The singlets at 5.98 and 5.48 ppm, which integrate for 2 H each, correspond to H^8 and H^4, respectively, and the next singlet at 4.63 ppm that integrates for 4 H is due to H^1. In the upfield region of the spectrum, two quartets at 2.99 and 2.94 ppm that slightly overlap correspond to H^{10} (J = 7.6 Hz) and H^2 (J = 7.7 Hz), respectively, which are the CH_2 groups of protons from the ethyl substituents of the tripodal ligand. The six methyl groups from the BODIPY molecule that are attached to the two pyrrole rings appear as two singlets that integrate for 6 H each at 2.54 and 1.35 ppm, for H^9 and H^7, respectively. Finally, the two CH_3 groups from the ethyl substituents appear as two triplets at 1.38 and 1.30 ppm, again in a slightly overlapped region, and correspond to H^{11} (J = 7.6 Hz) and H^3 (J = 7.5 Hz), respectively.

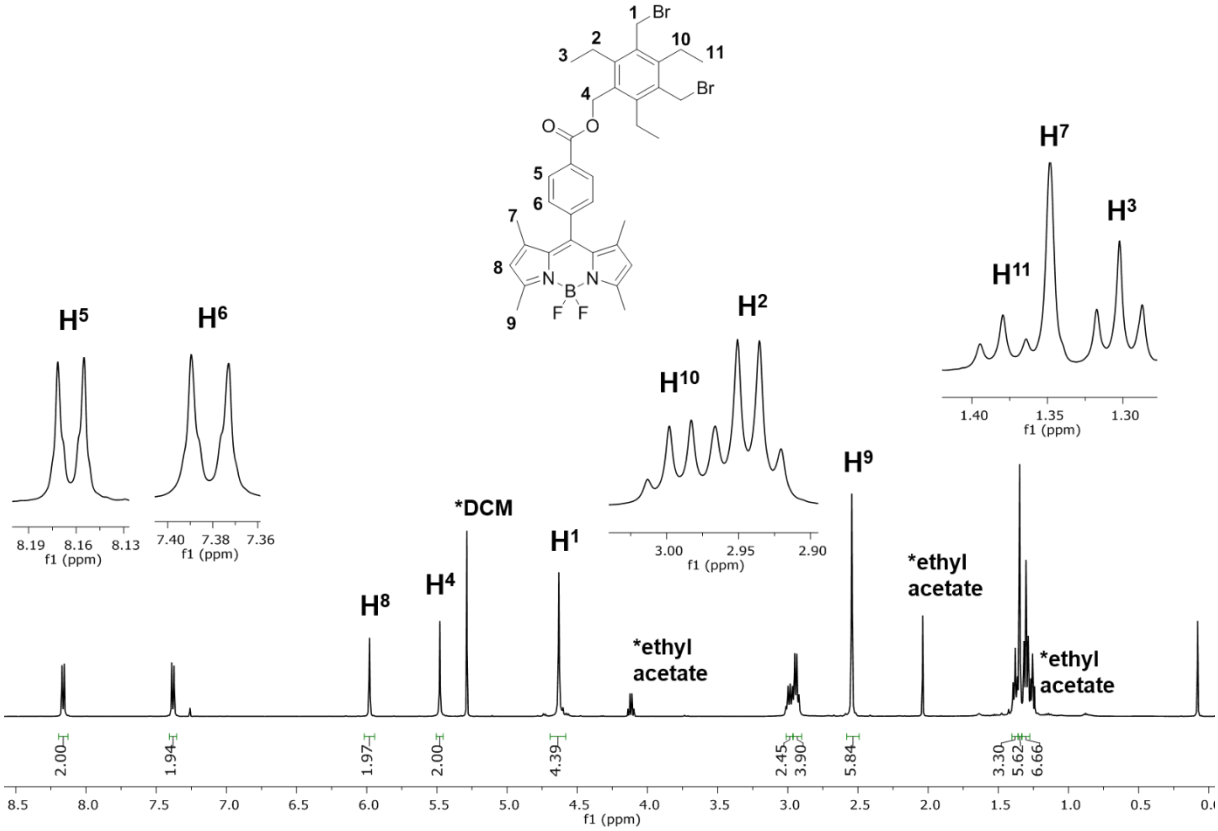

Figure 2.7. ^{1}H NMR (500 MHz, $CDCl_3$, 298 K) spectrum of compound **5**.

Comparing the spectrum of compound **5** to the one of compound **6** (*Figure 2.8*), a similar distribution of peaks can be observed. The main difference is that in the ^{1}H NMR spectrum of compound **6**, all the resonances corresponding to the BODIPY substituent integrate for two times the number of protons, due to the disubstitution of this molecule. Moreover, the resonances due to the ethyl groups that are attached to the benzene core of the tripodal ligand and the CH_2 groups next to the ester and the bromo units keep their multiplicity but their integration changes.

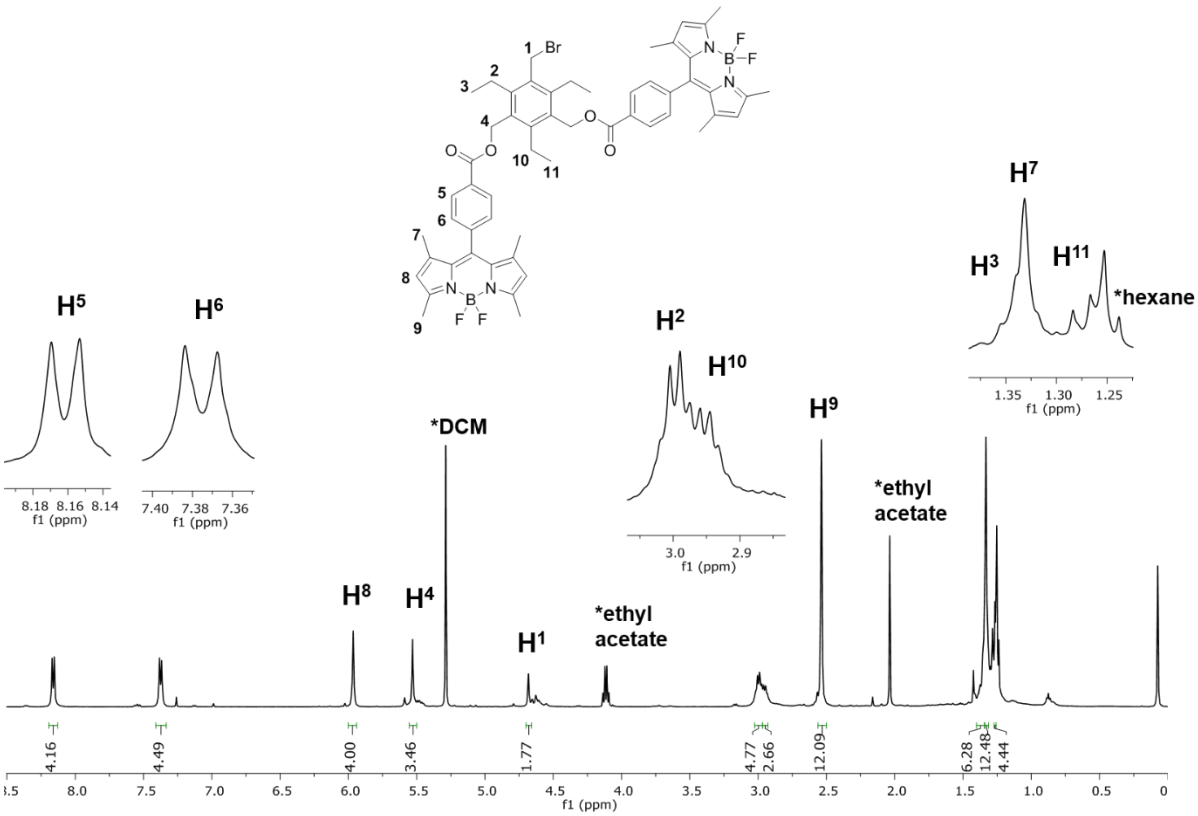

Figure 2.8. ^{1}H NMR (500 MHz, $CDCl_3$, 298 K) spectrum of compound **6**.

^{19}F NMR spectrum was recorded on all the BODIPY derivatives, as it can be seen for compound **5** (*Figure 2.9*). A quartet at -146.2 ppm was observed, due to the coupling between the two fluorine nuclei (which are equivalent) with the boron nucleus. ^{11}B has a spin quantum number of 3/2, which is the reason why a quartet is seen from the coupling with only one atom. Due to ^{10}B, that exists in an abundance of almost 20% and has a spin quantum number of 3, yielding broader peaks than ^{11}B, the quartet is not symmetrical. The coupling constant for this resonance was found to be 32.1 Hz.

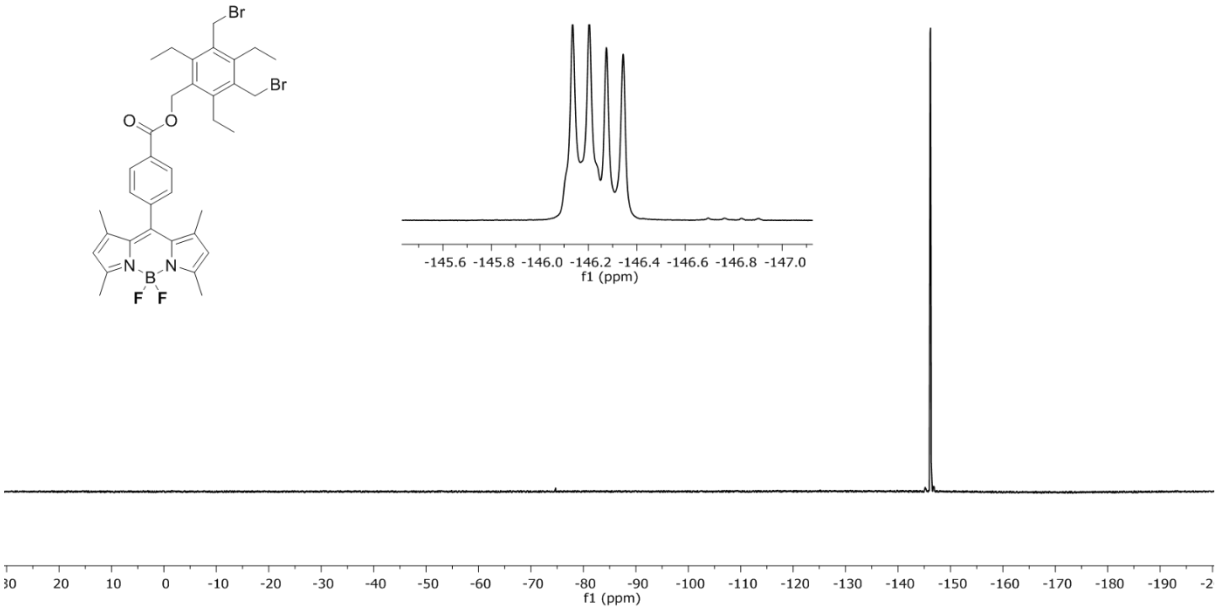

Figure 2.9. ^{19}F NMR (470 MHz, $CDCl_3$, 298 K) spectrum of compound **5**.

^{11}B NMR experiments were also carried out, as shown for compound **5** (*Figure 2.10*). In this case, a triplet at 0.7 ppm with a coupling constant of 32.8 Hz can be seen, due to the coupling between the boron nucleus and the two fluorine nuclei, which are equivalent.

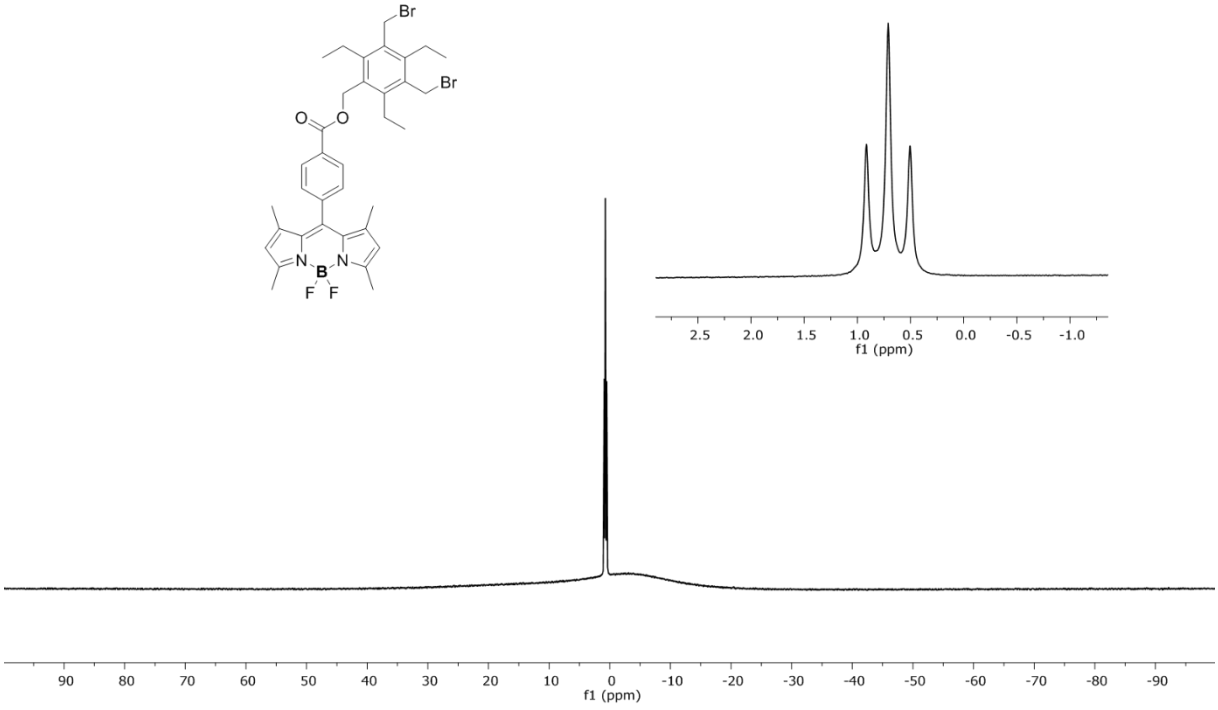

Figure 2.10. ^{11}B NMR (160 MHz, $CDCl_3$, 298 K) spectrum of compound **5**.

Next, a linker with a terminal carboxylic acid group and a tert-butoxide group was attached to the tripodal ligand (compound **1**) using the reaction conditions already described and purified by silica gel column chromatography (*Scheme 2.6*). The carboxylic acid group protected with

a tert-butoxide group can be later used to attach a peptide with previous deprotection. Compound **9** was obtained.

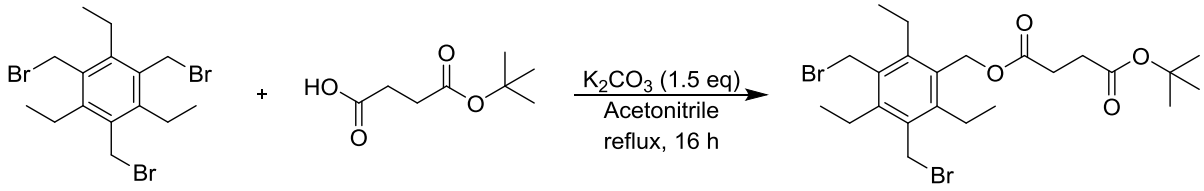

Scheme 2.6. Reaction between compound **1** and 4-(tert-butoxy)-4-oxobutanoic acid to produce the monosubstituted derivative (compound **9**).

The purity of this product after column chromatography was tested by HPLC, and a peak at 12.3 minutes was observed in the chromatogram in the 280 nm channel (*Figure 2.11*).

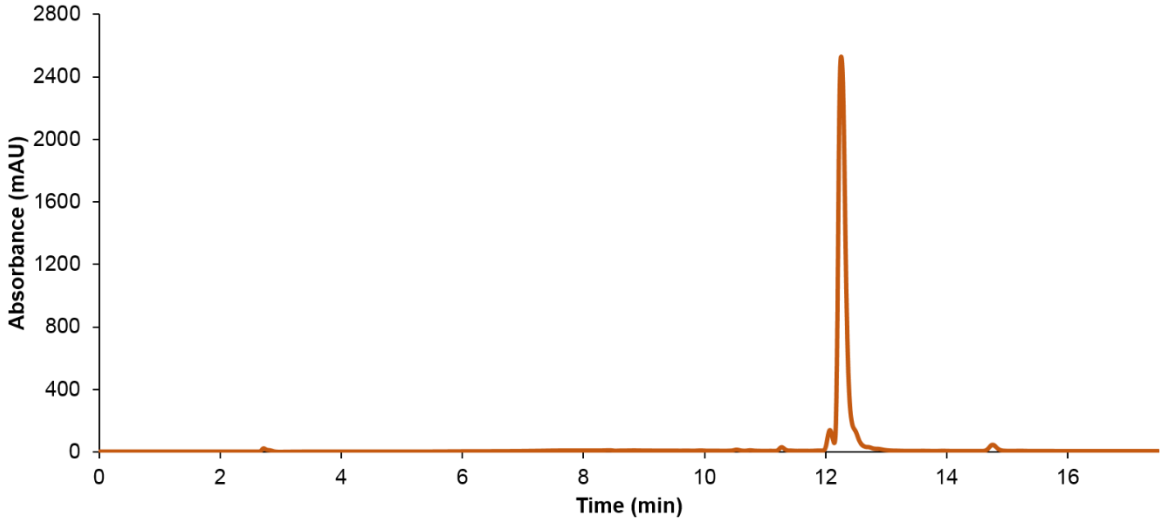

Figure 2.11. HPLC chromatogram of compound **9** in the 280 nm channel.

The new monosubstituted product was also characterised by mass spectrometry. The mass spectrum recorded using nanoelectrospray ionisation in positive mode revealed a peak at m/z = 552.1132, corresponding to the $[M+NH_4]^+$ ion (*Appendix A*).

NMR spectroscopy was used to characterise this new molecule (*Figure 2.12*). The ^1H NMR spectrum shows two singlets at 5.20 and 4.59 ppm, due to H^3 and H^7, respectively, and corresponding to 2 and 4 H. In the upfield region of the spectrum, there are two quartets that integrate for 2 and 4 H at 2.95 and 2.84 ppm, and correspond to H^8 (J = 7.7 Hz) and H^2 (J = 7.6 Hz) respectively. Between 2.63 and 2.53 ppm there is a multiplet corresponding to the protons of the two CH_2 groups of the succinate linker attached to the molecule, H^4 and H^5. The 9 protons from the tert-butoxide group, H^6, appear as a singlet at 1.42 ppm. Finally, at 1.35

and 1.25 ppm there are two triplets that integrate for 3 and 6 H, respectively, and correspond to H^9 (J = 7.6 Hz) and H^1 (J = 7.6 Hz). In this spectrum, a second order pattern can be observed in the case of the resonances corresponding to H^4 and H^5. These protons are chemically equivalent but magnetically inequivalent. Therefore, instead of seeing two triplets, a second order coupling system is observed. The magnetical inequivalence is due to the orientation of the ethyl and bromomethyl arms with respect to the plane of the phenyl ring.

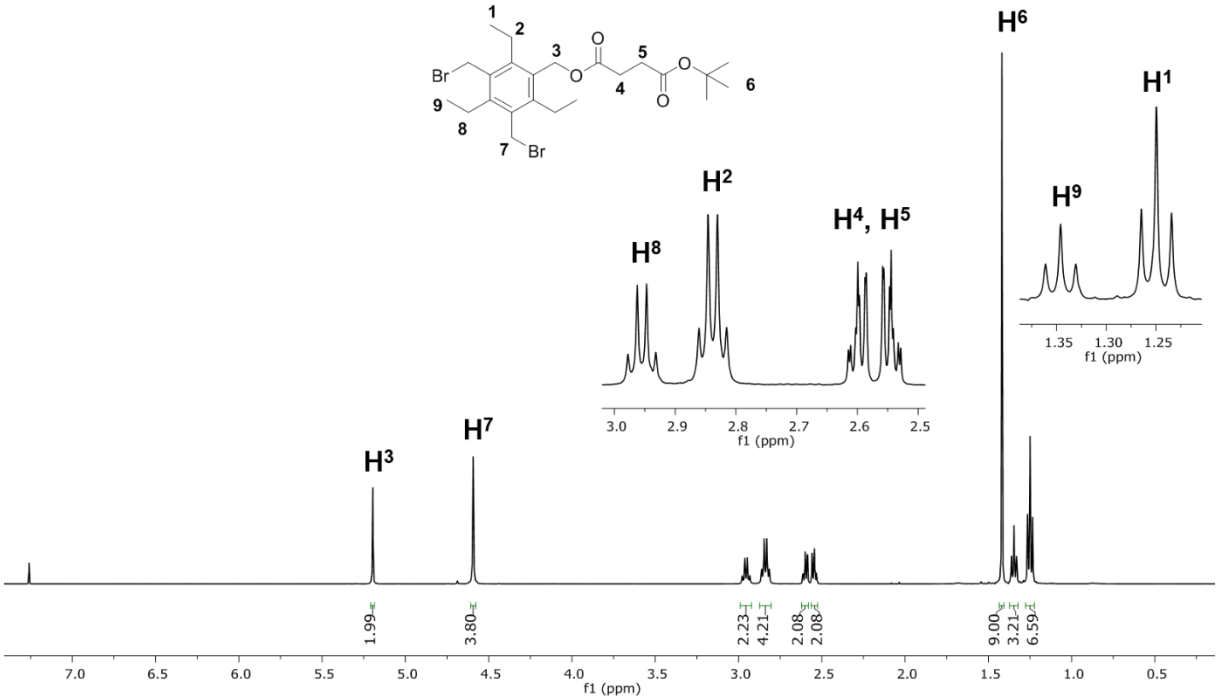

Figure 2.12. ^{1}H NMR (500 MHz, $CDCl_3$, 298 K) spectrum of compound **9**.

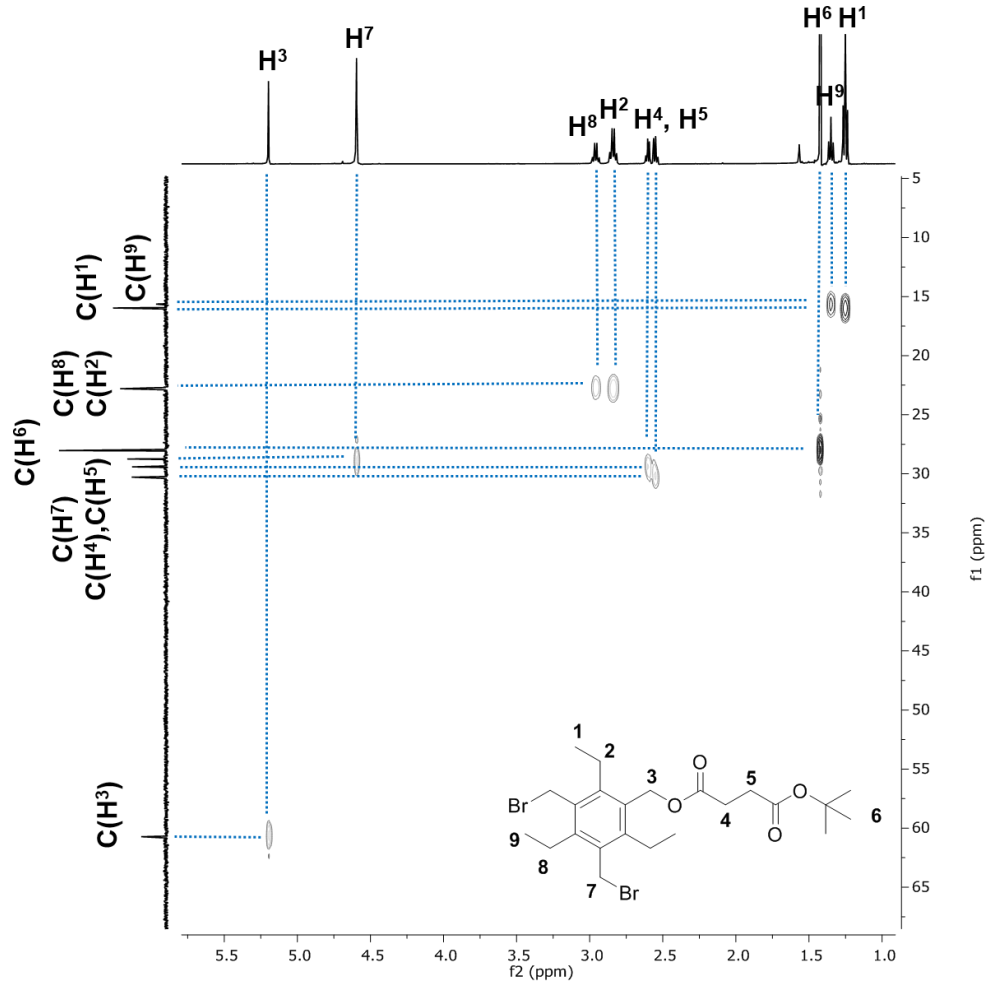

Figure 2.13. ^{1}H-^{13}C HSQC NMR (500 MHz, $CDCl_3$, 298 K) spectrum of compound **9**.

^{1}H-^{13}C HSQC and ^{1}H-^{13}C HMBC NMR experiments were carried out to assign the different resonances in the $^{13}C\{^{1}H\}$ spectrum to each different carbon atom in the molecule. Accordingly, ^{1}H-^{13}C HSQC was recorded in deuterated chloroform and the carbon atoms directly bound to one or more protons could be identified (*Figure 2.13*). To assign the carbon resonances due to C atoms that are not directly linked to protons, such as the carbons that form the phenyl ring or the two carbonyl groups, the ^{1}H-^{13}C HMBC spectrum was used (*Figure 2.14*). This way, the aromatic carbons and the carbons from the two carbonyl groups could be assigned to resonances between 130 and 150 ppm, and at approximately 175 ppm, respectively.

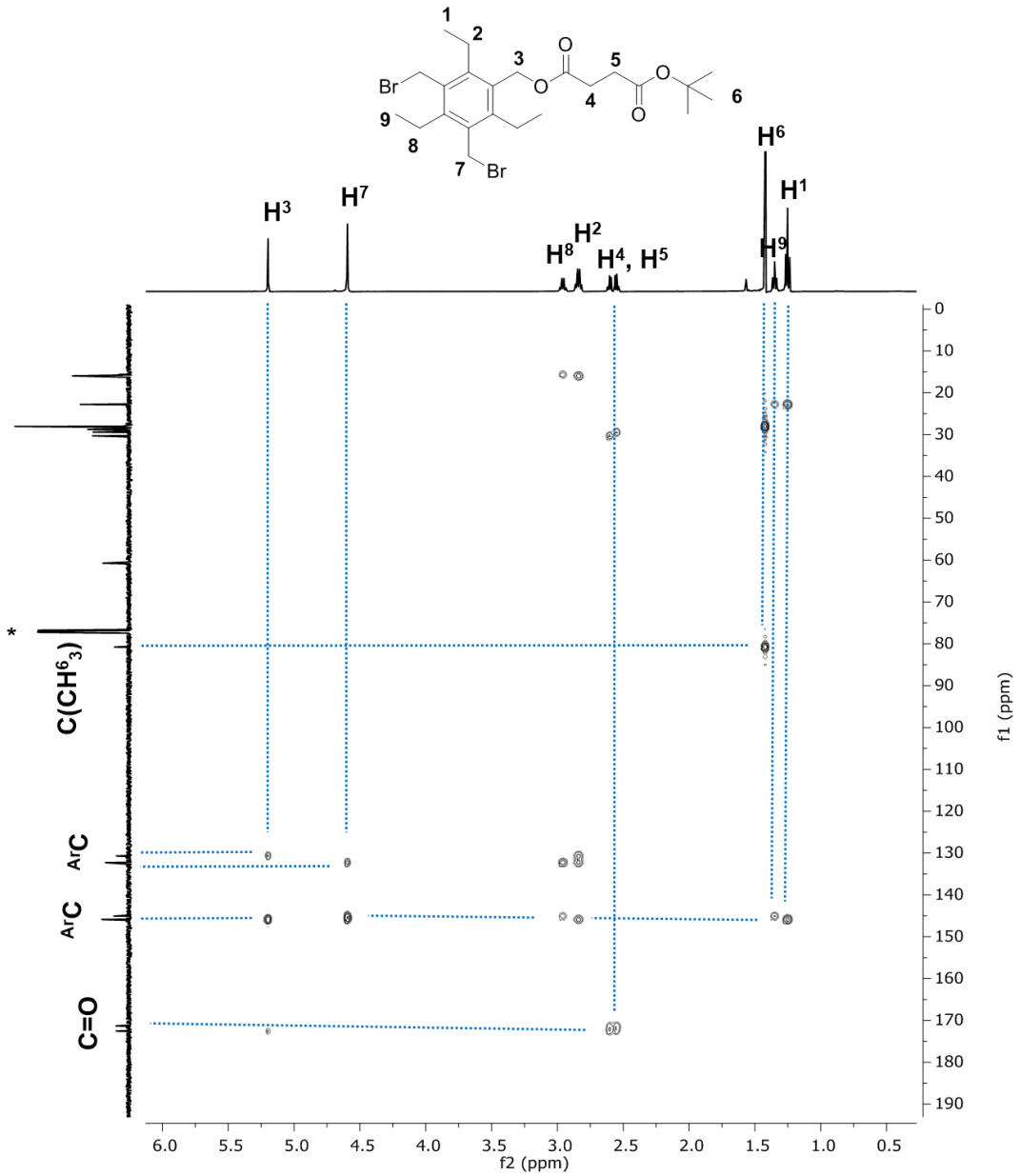

Figure 2.14. ^{1}H-^{13}C HMBC NMR (500 MHz, $CDCl_3$, 298 K) spectrum of compound **9**.

Finally, all the carbon atoms in compound **9** could be assigned to their resonances in the $^{13}C\{^{1}H\}$ NMR spectrum (*Figure 2.15*).

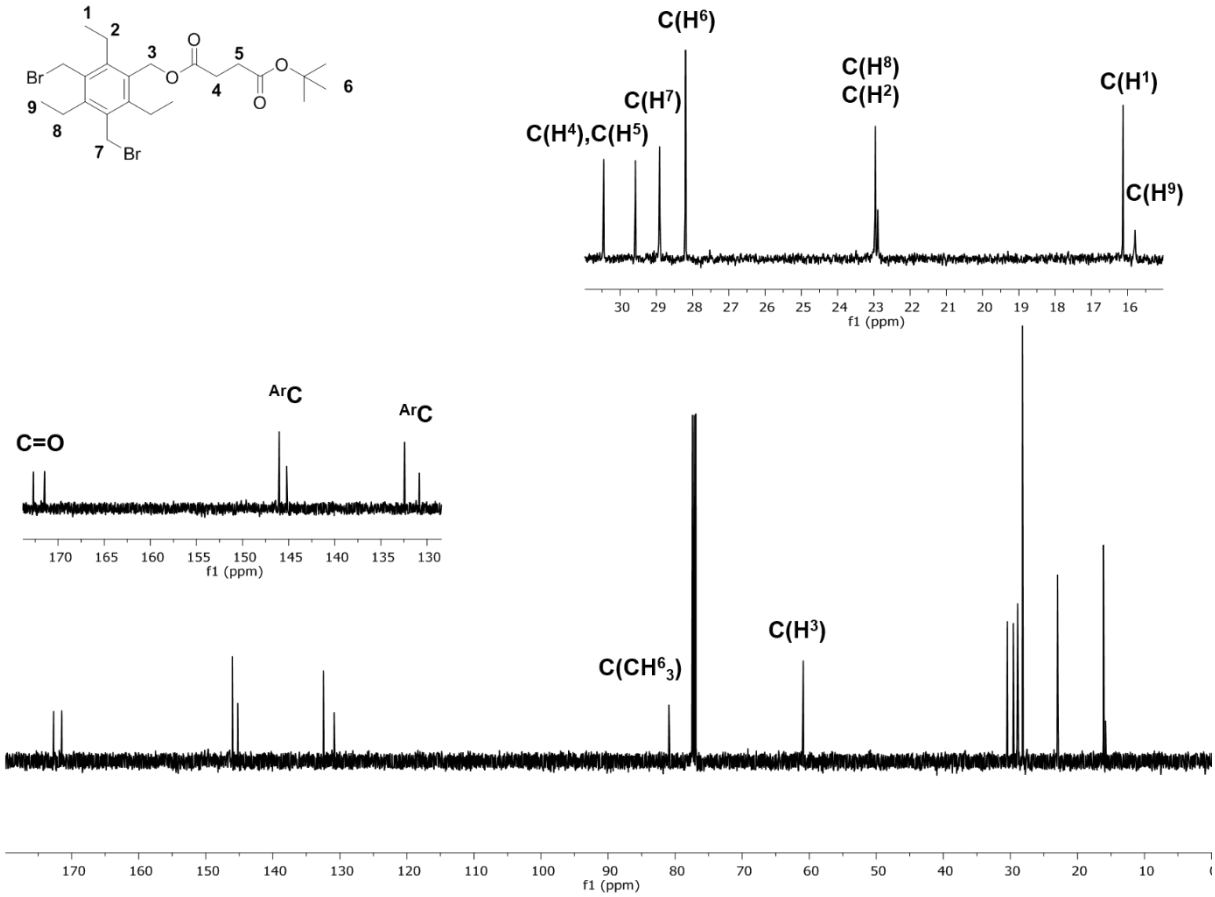

Figure 2.15. $^{13}C\{^{1}H\}$ NMR (126 MHz, $CDCl_3$, 298 K) spectrum of compound **9**.

Another linker containing a carboxylic acid group at one end and an azido functional group at the other was synthesised in order to attach it to the tripodal ligand (compound **1**) and use it to perform click chemistry with a compound containing an alkyl group. In this context, 6-azidohexanoic acid (compound **7**) was synthesised from bromohexanoic acid using sodium azide by performing a reaction at room temperature for 16 hours. The new compound could be isolated as a yellow oil and was fully characterised. The ^{1}H NMR spectrum confirmed that the desired product was obtained (*Appendix A*). The acidic proton can be observed as a broad singlet at 10.62 ppm. The rest of protons of this molecule appear in the upfield region of the spectrum as two triplets that integrate for 2 H each and correspond to H^1 (3.24 ppm) and H^5 (2.33 ppm), respectively. An overlapped doublet of quintuplets appears between 1.65 and 1.54 ppm corresponding to 4 H, H^2 and H^4. Finally, H^3 appears as a multiplet at 1.40 ppm and integrates for two protons.

Next, 6-azidohexanoic acid (compound **7**) was incorporated into the tripodal ligand (compound **1**) following the same reaction conditions previously described with potassium carbonate and

acetonitrile as a solvent (*Scheme 2.7*). Compound **8** was isolated after silica gel column chromatography, and was characterised spectroscopically.

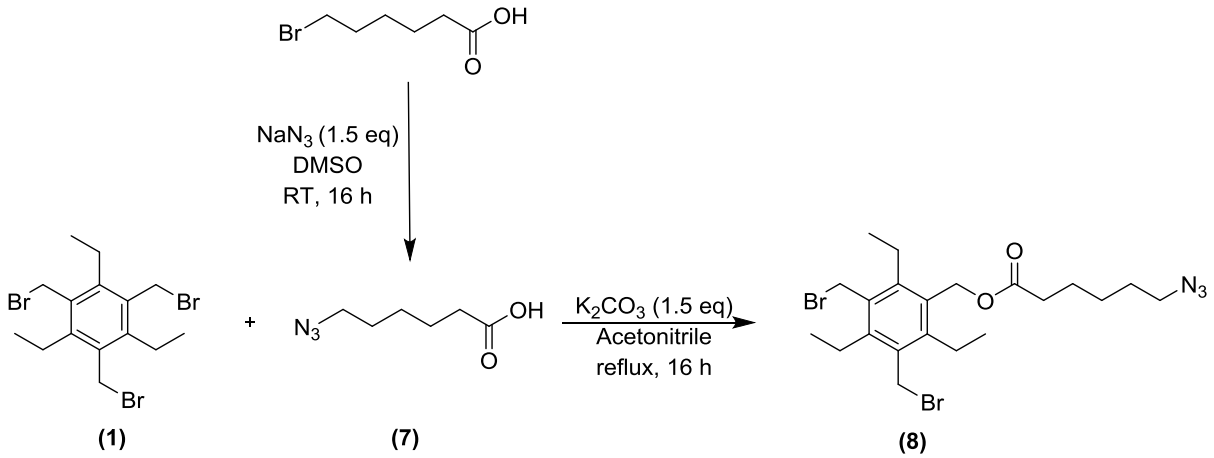

Scheme 2.7. Reaction between compound **1** and 6-azidohexanoic acid (compound **7**) to produce the monosubstituted derivative (compound **8**).

The new monosubstituted product was characterised by MS and NMR spectroscopy. The ^{1}H NMR spectrum of compound **8** shows the same peaks as for compound **7**, plus the peaks due to the ethyl groups from the tripodal core (H^{1}, H^{2}, H^{11} and H^{10} at 1.25, 2.84, 1.35 and 2.96 ppm, respectively), the methyl groups next to the bromide atoms (H^{9} at 4.60 ppm) and the protons next to the new ester bond (H^{3} at 5.18 ppm) (*Figure 2.16*). The coupling constants for the two triplets that are due to H^{8} and H^{4} are 6.9 and 7.5 Hz, respectively; and those for the two quartets that correspond to H^{10} and H^{2} are 7.6 and 7.6 Hz, respectively.

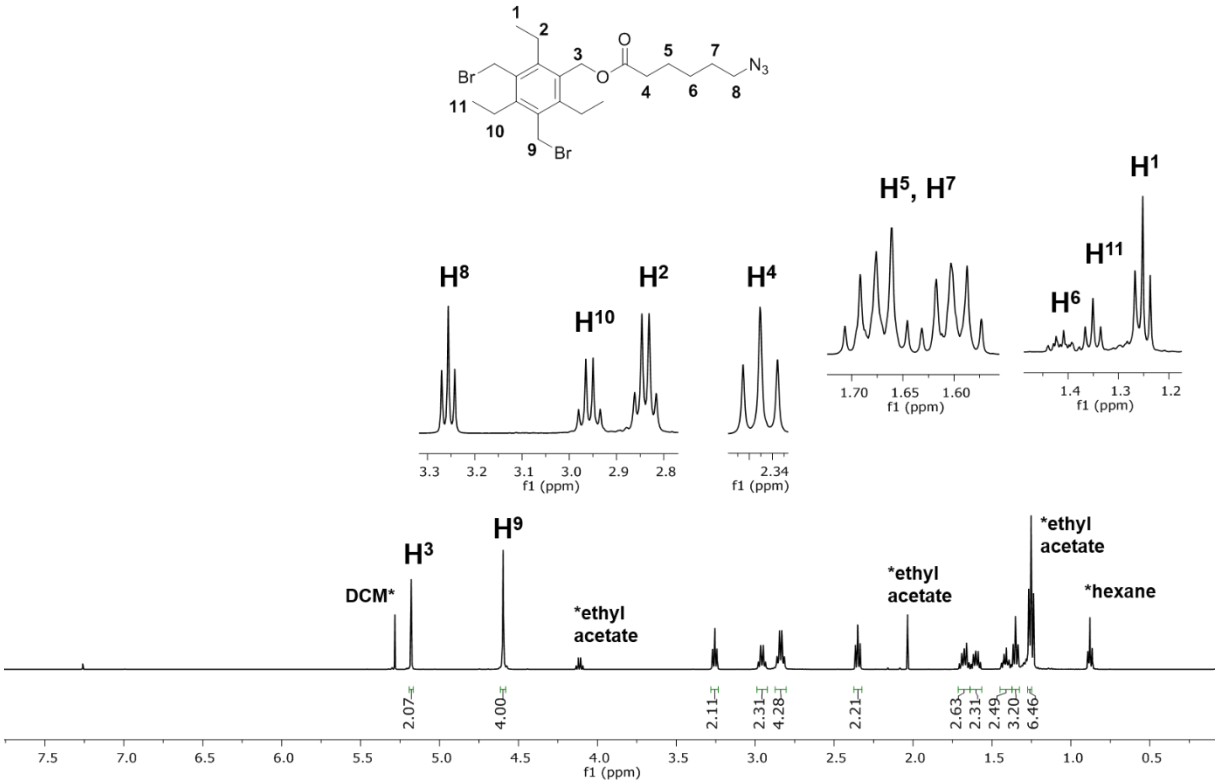

Figure 2.16. ^{1}H NMR (500 MHz, $CDCl_3$, 298 K) spectrum of compound **8**.

Compound **8** was synthesised aiming towards its future use in performing “click” chemistry, and subsequently attaching a radiochelator, such as deferoxamine (DFO), for potential applications in PET and SPECT imaging.[14] Following this approach, a cyclooctyne derivative functionalised with a carboxylic acid group was used to couple to DFO. This cyclooctyne derivative was chosen because it can be used in strain-promoted copper-free azide-alkyne “click” chemistry reactions, and it can react with compounds containing an azido group without the need of a Cu(I) catalyst to form a stable triazole linkage. The reaction between dibenzocyclooctyne (DBCO) acid and DFO takes place in three steps. Firstly, the activation of the carboxylic acid group in order for it to react with an amine is necessary, and this was carried out using benzotriazol-1-yl-oxytripyrrolidinophosphonium hexafluorophosphate (PyBOP) as activating reagent. Then, the deferoxamine mesylate salt was deprotonated using triethylamine to obtain a neutral terminal amino group. The final step involves the addition of this neutral DFO compound to the activated carboxylic acid to force the coupling of these two products (*Scheme 2.8*).

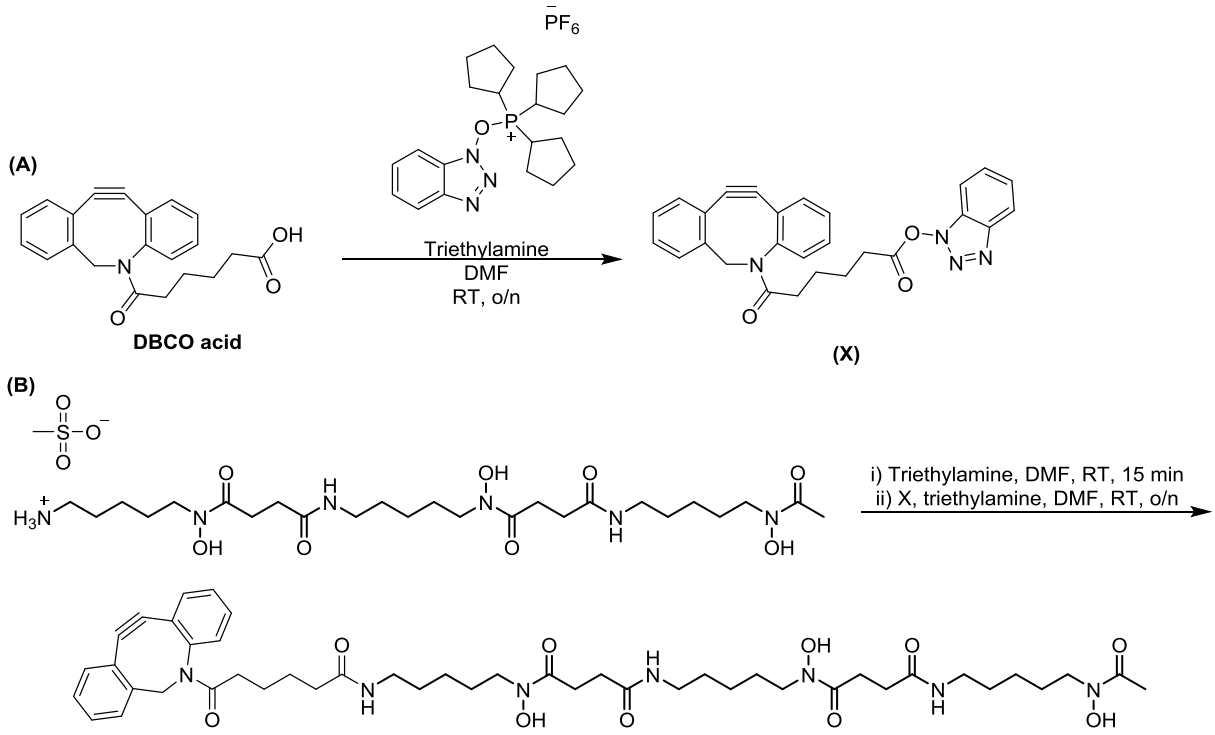

Scheme 2.8. Reaction between dibenzocyclooctyne (DBCO) acid and deferoxamine (DFO). This coupling reaction takes place in three steps: **(A)** activation of the carboxylic acid group of DBCO with PyBOP (1), followed by **(B)** deprotonation of the terminal amine of DFO which is initially a salt (2), and coupling of the activated DBCO acid with the neutral DFO (3).

The above reaction was followed by HPLC at different stages, taking aliquots from the reaction flask at different times (*Figure 2.17*). After 48 hours, the solvent was removed under reduced pressure and the yellow solid that emerged was purified by silica gel column chromatography using a solvent system of methanol in dichloromethane. One fraction was isolated and dried under vacuum, and mass spectrometry was performed to identify significant fragments of the product. This was not possible and conclusive results could not be deducted. Due to time restrains and cost of the dibenzocyclooctyne acid derivative this reaction could not be repeated.

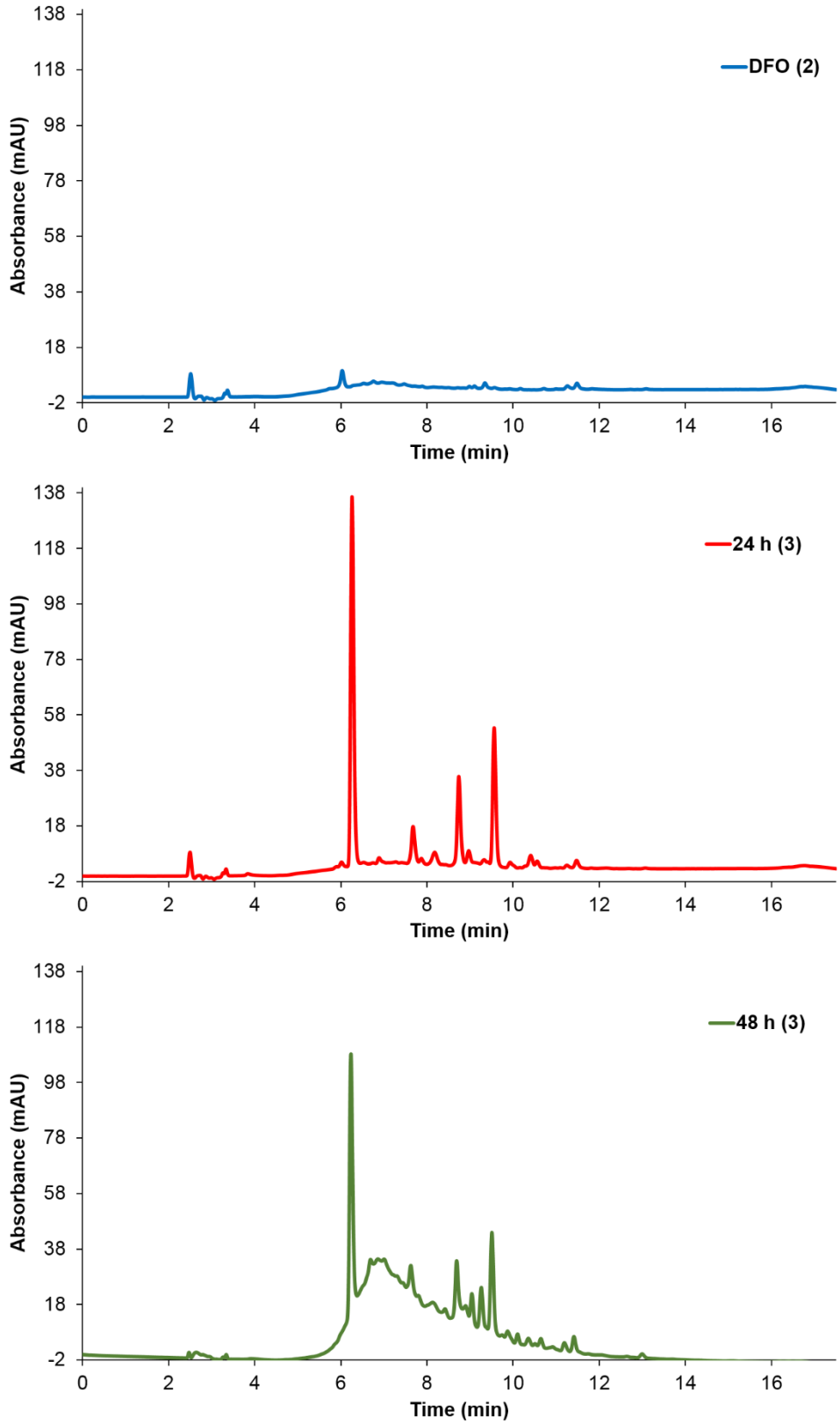

Figure 2.17. HPLC chromatograms in the 280 nm channel of the reaction described in *Scheme 2.8* at different times. DFO (2) (blue line) refers to deferoxamine after it has been free-based; 24 h (3) (red line) refers to the step 3 of the reaction after 24 hours, and 48 h (3) (green line) refers to the same step of the reaction after 48 hours.

2.5. Difunctionalisation strategies of the tripodal core

Orthogonal coupling of several different functionalities has been a very important area of research in drug discovery and molecular imaging design.[15]

In order to include two different substituents in the tripodal molecule, compound **9** was reacted with 6-azidohexanoic acid (compound **7**) using the same conditions previously described for this type of reactions (*Scheme 2.9*). From this reaction, the disubstituted (compound **14**) and trisubstituted (compound **15**) products could be isolated and fully characterised, together with some remaining monosubstituted starting material (compound **9**). The final mixture contained three different products in percentages of 40% (di-, **14**), 52% (trisubstituted, **15**) and 8% (unreacted starting material, **9**). These were separated by silica gel column chromatography using a solvent system of ethyl acetate in hexane.

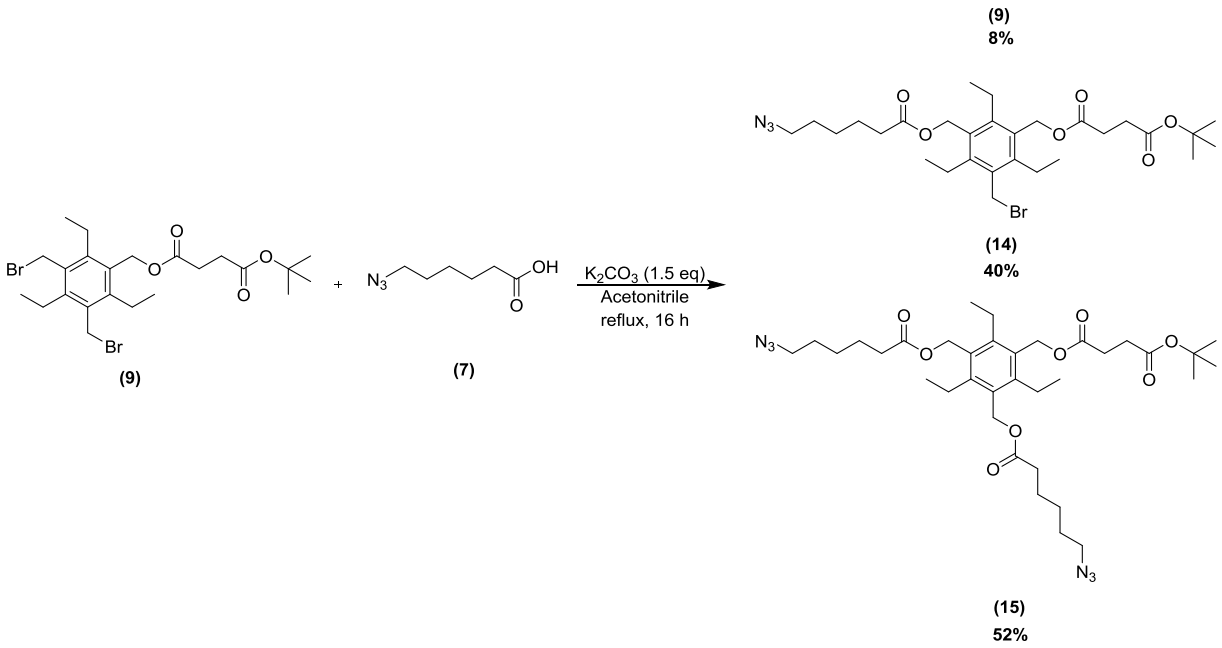

Scheme 2.9. Reaction between compound **9** and compound **7** yielding two new products (compounds **14** and **15**) and excess of unreacted starting material.

The new products were characterised by HPLC (*Figure 2.18*), and they all showed to be pure with a peak around 12.3 minutes. The very similar retention times of these two new compounds and the monosubstituted starting material is due to the similarity of their structures, which differ in the number of linkers that they are functionalised with, but at the same time these two types of linkers have similar structures and functional groups.

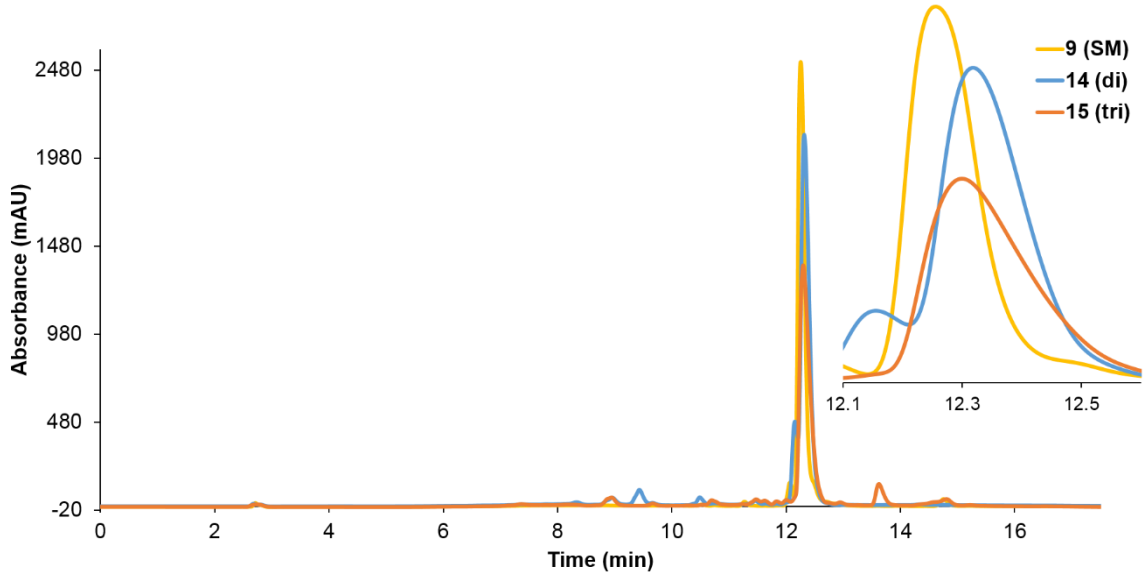

Figure 2.18. HPLC chromatogram in the 280 nm channel of compounds **9** (yellow line), **14** (blue line), and **15** (orange line), and amplification of the area with the maximum intensity peaks.

The new molecules were also characterised by mass spectrometry and NMR spectroscopy. The mass spectrum of compound **14** using nanoelectrospray ionisation in positive mode shows a peak at m/z = 627.2740, which corresponds to the $[M+NH_4]^+$ ion. The mass spectrum of compound **15** using atmospheric pressure chemical ionisation in positive mode, shows peaks at m/z = 704.4345 and 709.3901, which correspond to the $[M+NH_4]^+$ and $[M+Na]^+$ ions, respectively (*Appendix A*).

The ^{1}H NMR spectrum of compound **14** (*Figure 2.19*) showed a multiplet at around 5.19 ppm which corresponds to H^3 and H^{12}, and integrates for 4 H in total. Next, a singlet at 4.61 ppm that corresponds to the sole CH_2Br group integrates for 2 protons, H^9. In the upfield region of the spectrum, the two protons next to the azido functional group, H^{17}, appear as a triplet at 3.25 ppm with a coupling constant of 6.9 Hz. A multiplet between approximately 2.85 and 2.73 ppm that integrates for 6 H corresponds to the protons in the three ethyl groups, H^2, H^7 and H^{10}. The two adjacent CH_2 groups of the succinate linker (H^4 and H^5) can be found as multiplets at 2.58 and 2.54 ppm, and these peaks integrate for 4 H in total. A triplet at 2.34 ppm with a coupling constant of 7.5 Hz is due to H^{13}, the two proton resonances next to the carbonyl group of one of the two ester linkages. The 4 H corresponding to H^{14} and H^{16} appear as two quintuplets at 1.67 and 1.59 ppm (J = 7.5 and 7.1 Hz, respectively). Next, the 9 H from the tert-butoxide group appear as a singlet at 1.41 ppm, and this is overlapped with a multiplet corresponding to 2 H from one of the linkers, H^{15}. A multiplet with a shape similar to a triplet integrating for 6 H at 1.25 ppm corresponds to H^8 and H^{11}, which appear together due to the

similarity between the two linkers that makes the molecule almost symmetric. Finally, the remaining proton resonances from the CH_3 group, H^1, appear as a triplet at 1.16 ppm (J = 7.5 Hz).

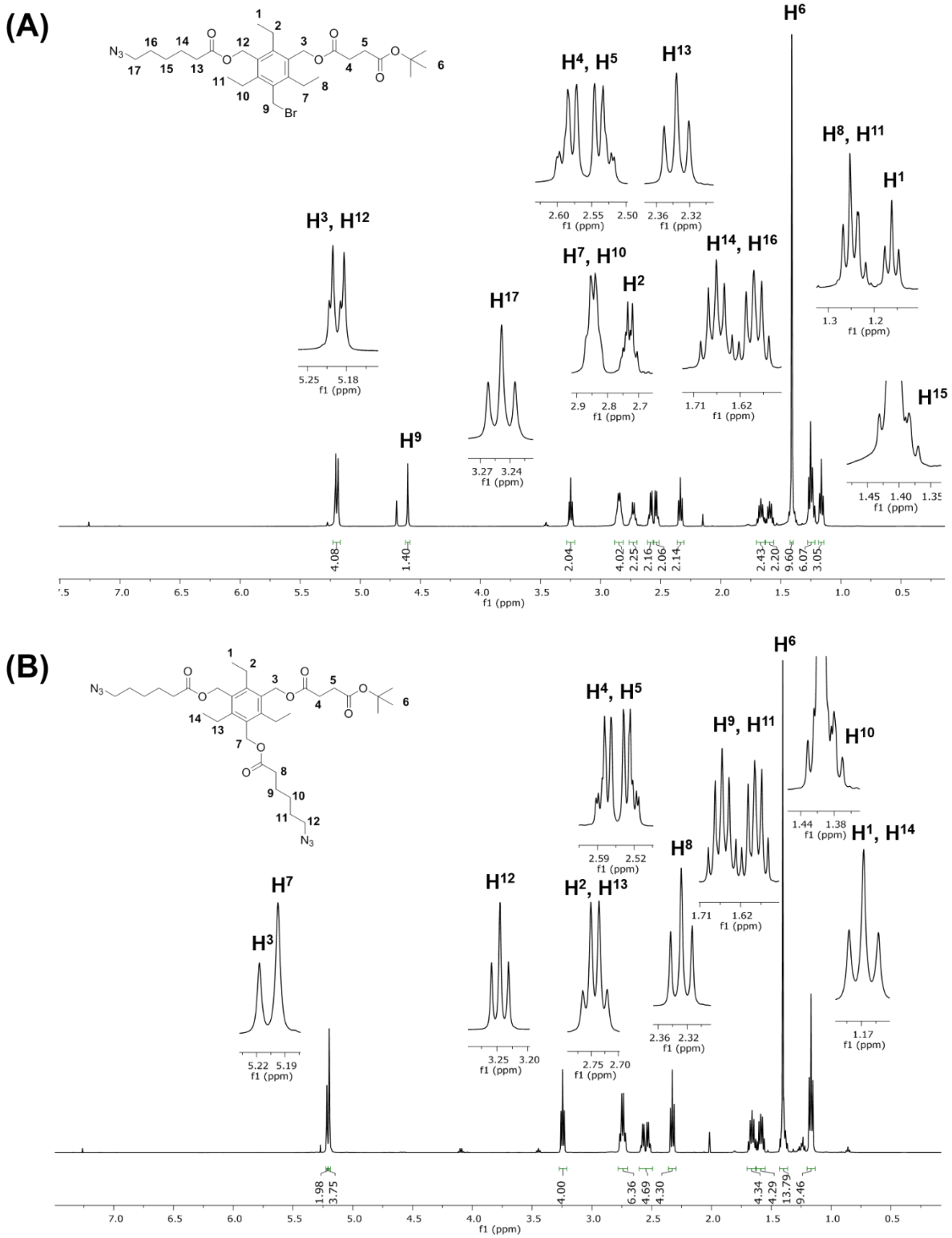

Figure 2.19. ^{1}H NMR (500 MHz, $CDCl_3$, 298 K) spectra of compounds **14 (A)**, and **15 (B)**.

Compound **15** consists of a trisubstituted tripodal core with two azido terminal linkers and a succinate derivative, which make the molecule completely symmetric. In this context, the two CH_2 groups next to the two different ester bonds appear as two singlets at 5.22 and 5.20 ppm for H^3 and H^7, respectively, which correspond to 2 and 4 H. A triplet at 3.24 ppm corresponds to H^{12} and integrates for 4 H, with a coupling constant of 6.9 Hz. At 2.74 ppm there is a quadruplet integrating for 6 H and corresponds to the CH_2 protons from the ethyl groups, H^2 and H^{13} (J = 7.5 Hz). There is a multiplet between 2.59 and 2.51 ppm that corresponds to the protons of the two CH_2 groups from the succinate linker, H^4 and H^5. Next, a triplet at 2.33 ppm with a coupling constant of 7.5 Hz that integrates for 4 H corresponds to H^8. Two quintuplets at 1.66 and 1.59 ppm are due to H^9 and H^{11} (J = 7.6 and 7.6 Hz, respectively), some of the methylene groups from the azido terminal linker. The 9 H from the tert-butoxide group appear at 1.40 ppm as a singlet, overlapped with the H^{10} protons. Finally, there is a triplet at 1.17 ppm that corresponds to 9 H, which was assigned to H^1 and H^{14} (J = 7.5 Hz).

FT-IR spectroscopy was carried out to characterise the newly synthesised compounds, **14** and **15**, and compare them to the starting materials (compounds **7** and **9**) (*Figure 2.20*). In the four spectra, a band at approximately 1700 cm^{-1} due to the carbonyl functional group stretching can be identified. Moreover, in compounds **7**, **14**, and **15**, the stretching due to the azido functional group can be seen as a band at around 2000 cm^{-1}. For compounds **14** and **15**, a band at around 1150 cm^{-1} corresponding to the ester C-O-C stretching can be observed (*Table 2.1*).

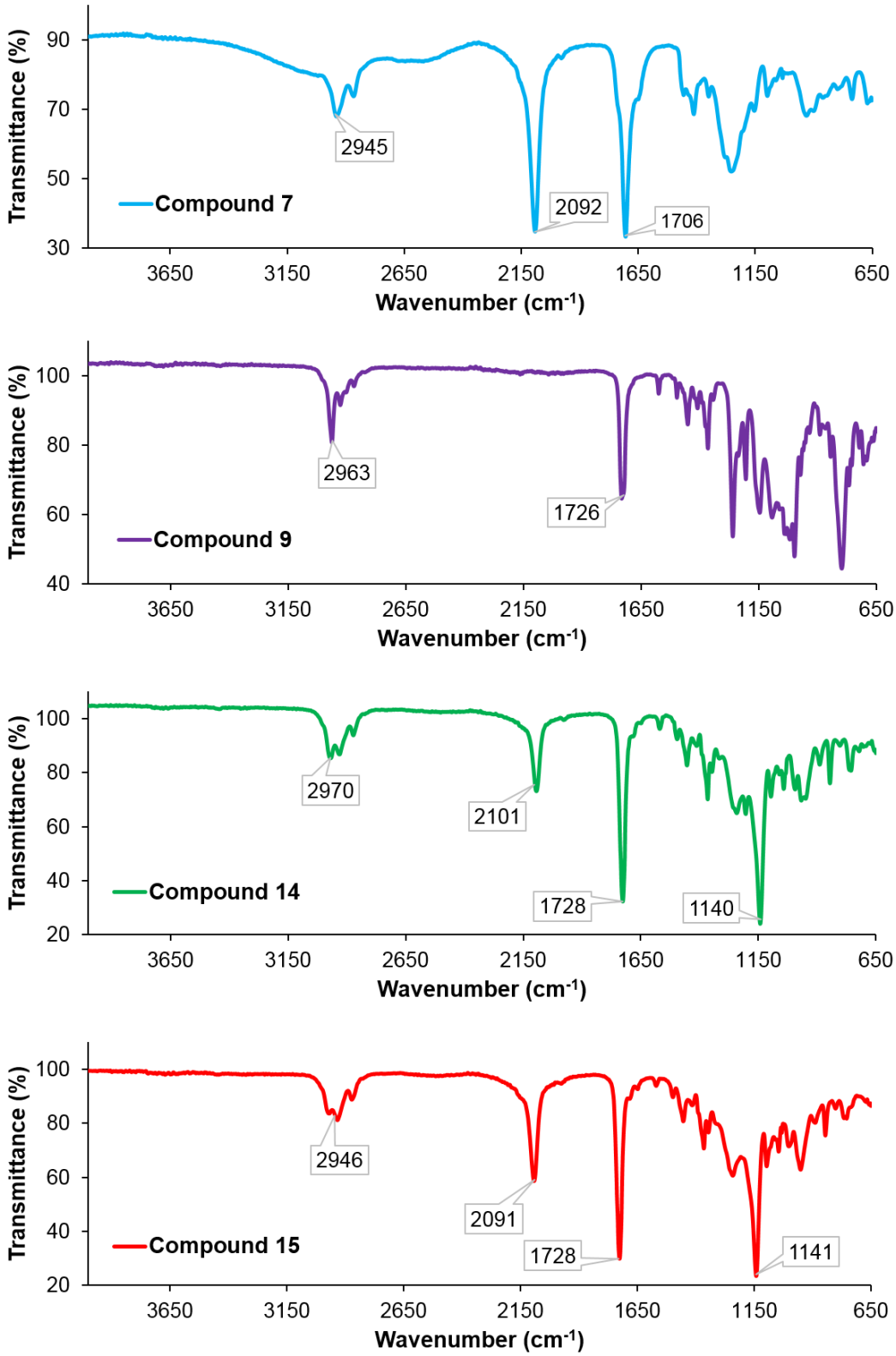

Figure 2.20. FT-IR spectra of compounds **7** (blue), **9** (purple), **14** (green) and **15** (red).

Table 2.1. Band assignment for the FT-IR spectra of compounds **7**, **9**, **14** and **15** (*Figure 2.20*).

Compound	Wavenumber / cm^{-1}	Vibrational mode
7	2945	C-H st
	2092	$-N_3$ st
	1706	C=O st
9	2963	C-H st
	1726	C=O st
14	2970	C-H st
	2101	N_3 st
	1728	C=O st
	1140	C-O-C st
15	2946	C-H st
	2091	$-N_3$ st
	1728	C=O st
	1141	C-O-C st

Another difunctionalisation reaction that was carried out was that between the monosubstituted BODIPY derivative (compound **5**) and 4-(tert-butoxy)-4-oxobutanoic acid, a succinate derivative linker, to produce the disubstituted product (compound **13**) (*Scheme 2.10*). The reaction mechanism, as previously, is a nucleophilic substitution where a new ester linkage is formed, with the bromide atom acting as the leaving group.

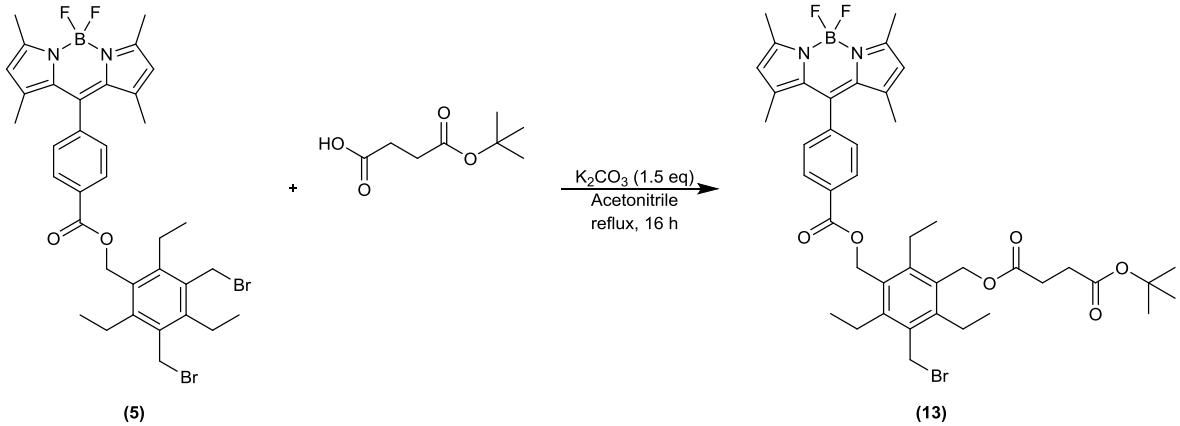

(5) (13)

Scheme 2.10. Reaction between compound **5** and 4-(tert-butoxy)-4-oxobutanoic acid yielding the disubstituted product (compound **13**).

Compound **13** was analysed by mass spectrometry using electron (impact) ionisation in positive mode, and from the spectrum a peak can be seen at m/z = 822.4, corresponding to the molecular ion, $[M]^{+\cdot}$ (*Appendix A*). In this case, no other side-products could be isolated.

The ^{1}H NMR spectrum of compound **13** shows different peaks corresponding to the different groups of equivalent protons present in the molecule (*Figure 2.21*). In this context, there is a doublet at 8.16 ppm that corresponds to the two protons named as H^{14}. There is another doublet at 7.39 ppm that corresponds to the other group of two protons from the benzene core of the BODIPY molecule, H^{13}. Two singlets at 5.98 and 5.49 ppm correspond to H^{16} and H^{12}, the two protons attached to the pyrrole ring and the two protons next to one of the ester linkages, respectively. A singlet at 4.64 ppm corresponds to H^{3}. Slightly more upfield, there is a multiplet between 2.97 and 2.81 ppm that integrates for 6 H and corresponds to H^{2}, H^{7} and H^{10}, the CH_2 protons from the ethyl groups attached to the tripodal core. Another multiplet between 2.61 and 2.56 ppm that is slightly overlapped with a singlet at 2.55 ppm corresponds to H^{4} and H^{5}, the 4 H from the succinate linker. The above mentioned singlet integrates for 6 H and corresponds to H^{17}, assigned to the two methyl groups from the BODIPY molecule. Another singlet at 2.04 ppm corresponds to H^{9}, the two protons from the CH_2Br group. Between 1.5 and 1.0 ppm there are peaks that are due to the remaining protons: a singlet at 1.42 ppm corresponds to the 9 H from the tert-butoxide group of the molecule, H^{6}; another singlet at 1.34 ppm corresponds to H^{15}, the other two CH_3 groups from the BODIPY molecule. Finally, there is a multiplet between 1.24 and 1.18 ppm that corresponds to H^{1}, H^{8} and H^{11}, the CH_3 protons from the three ethyl groups of the tripodal core.

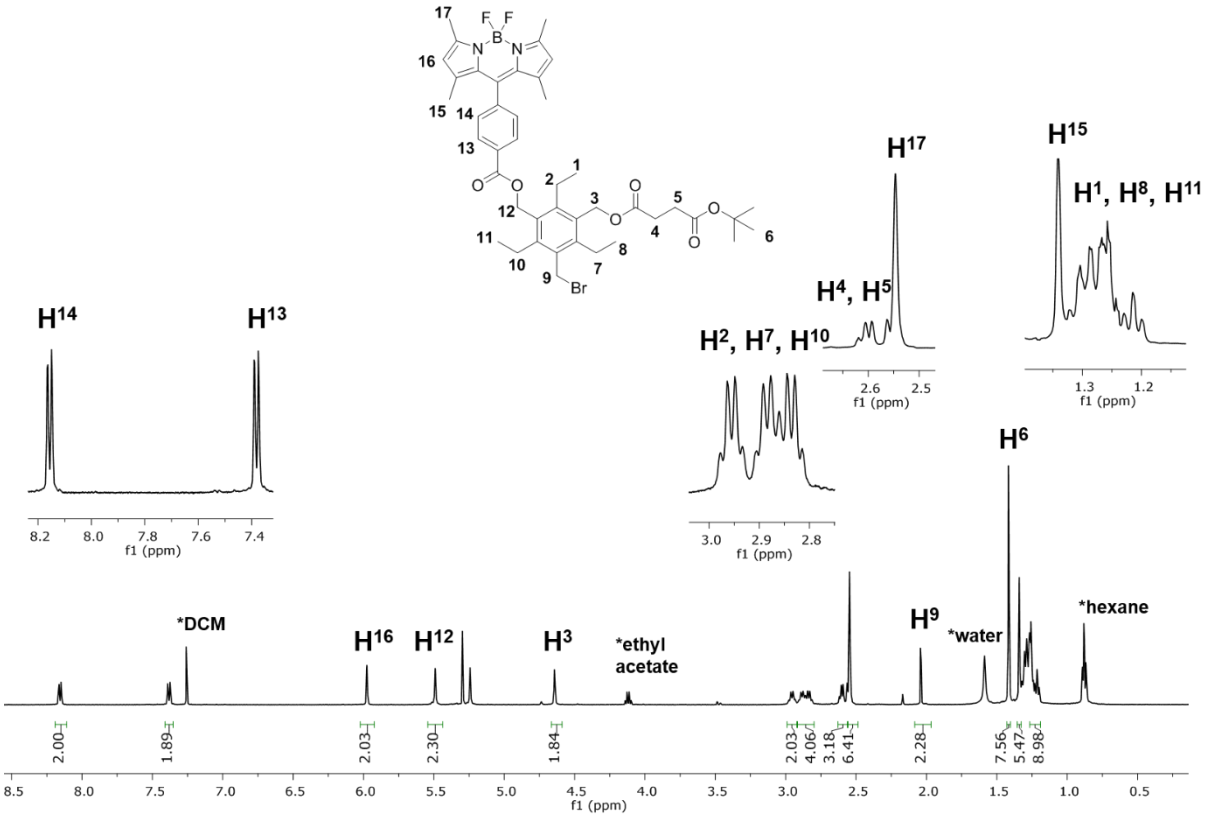

Figure 2.21. ^{1}H NMR (500 MHz, $CDCl_3$, 298 K) spectrum of compound **13**.

2.6. Trifunctionalisation strategies of the tripodal core

The disubstituted product containing two different linkers (compound **14**) was used to attach the synthesised BODIPY derivative (compound **2**) to the third arm, in order to make it fluorescent and obtain compound **16** (*Scheme 2.11*).

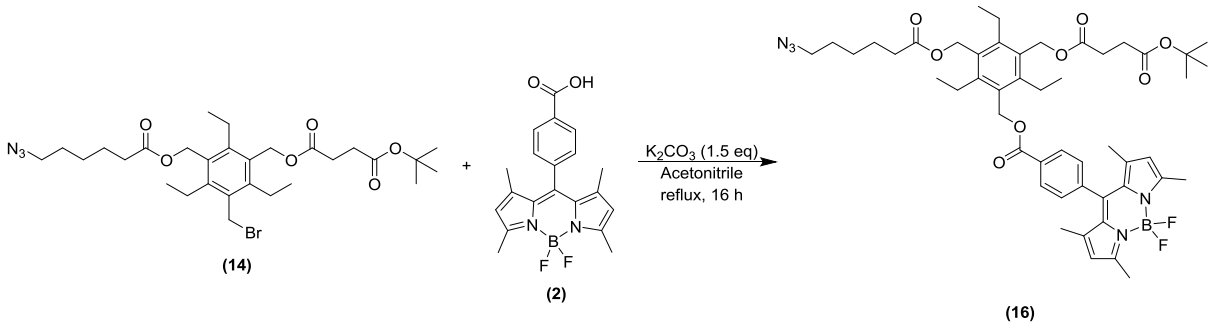

Scheme 2.11. Reaction between the disubstituted tripodal derivative (compound **14**) and compound **2** yielding a trisubstituted molecule (compound **16**).

In order to achieve the desired trifunctionalisation of the core, the conditions used involved a 1:1 ratio of reagents and 1.5 equivalents of potassium carbonate in acetonitrile stirring overnight under reflux. The same work-up described in *Section 2.4* was followed. The final desired product was purified by silica gel column chromatography with a solvent system of ethyl acetate in hexane, and an orange solid was obtained. The purity of this product was tested by HPLC, and the chromatogram showed a single peak at 14.6 minutes in the 500 nm channel, confirming the purity of this compound (*Figure 2.22*).

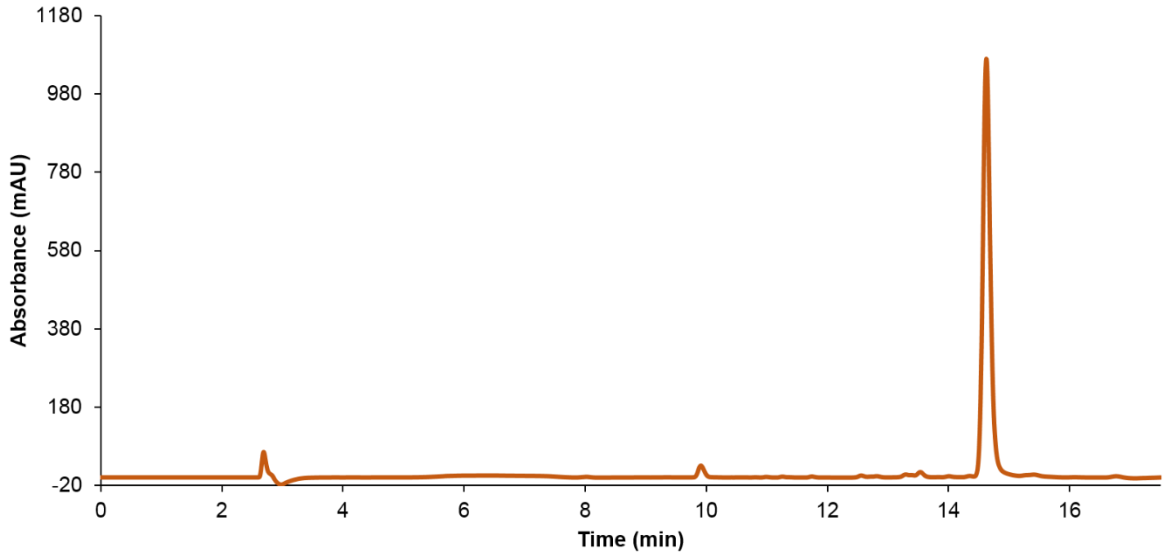

Figure 2.22. HPLC chromatogram of compound **16** in the 500 nm channel.

Compound **6** was used as starting material to create a new trisubstituted molecule with two BODIPY derivatives and one 4-methyl-3-thiosemicarbazide arm. In this context, compound **6** was dissolved in acetonitrile together with 4-methyl-3-thiosemicarbazide in a 1:1 ratio and they were stirred overnight under reflux (*Scheme 2.12*). The brown solid obtained from this reaction (compound **17**) was analysed by mass spectrometry using electrospray ionisation in positive mode, and it showed a peak at m/z = 1040.4874, which corresponds to the $[M+H]^+$ ion (*Appendix A*).

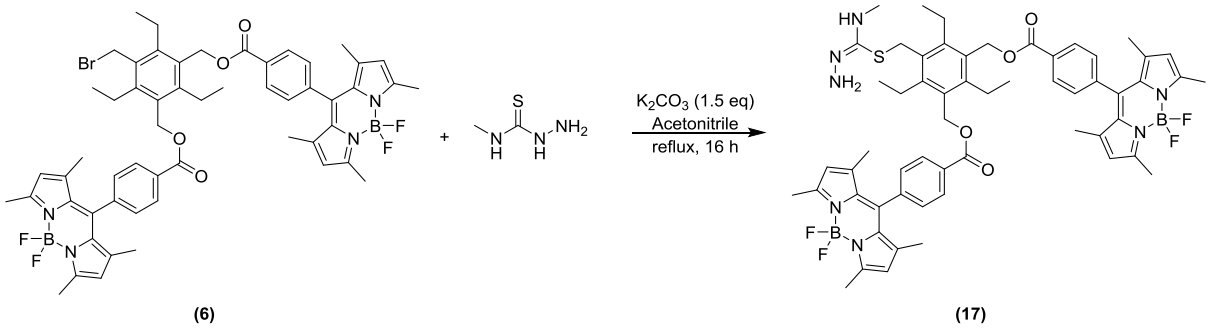

Scheme 2.12. Reaction between the disubstituted tripodal derivative (compound **6**) and 4-methyl-3-thuiosemicarbazide yielding a trisubstituted molecule (compound **17**).

Compound **17** was synthesised with the idea of using it to coordinate to a metal, potentially on the arm substituted with a thiosemicarbazide derivative (*Figure 2.23*). In this context, zinc(II) acetate was used since it was anticipated that a diamagnetic complex would be obtained, meaning that the NMR spectrum of the resulting complex can be easily interpreted. The reaction was carried out using one equivalent of the substituted product (compound **17**) and one equivalent of the metal salt (zinc acetate); they were mixed in methanol and stirred under reflux for 16 hours. The resulting orange-brown solution was dried under vacuum, and the resulting solid was dissolved in dichloromethane and washed with water several times. The two different phases were treated independently but only a brown solid was obtained from the organic phase, which was analysed. NMR spectroscopy was carried out and the resulting spectrum was different from the starting material (compound **17**). However, mass spectrometry using both positive mode nanoelectrospray ionisation and matrix-assisted laser desorption/ionisation (MALDI) did not show the expected ions, though highly complex and multiply charged ions were observed at higher m/z showing no incorporation of zinc. The possible formation of complex polymeric structures, or supramolecular units connected by hydrogen bonds, would hinder the characterisation of the final product.[16]

(A)

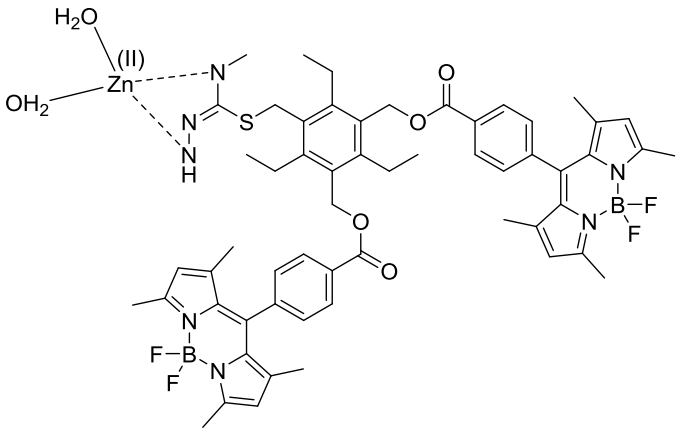

(B)

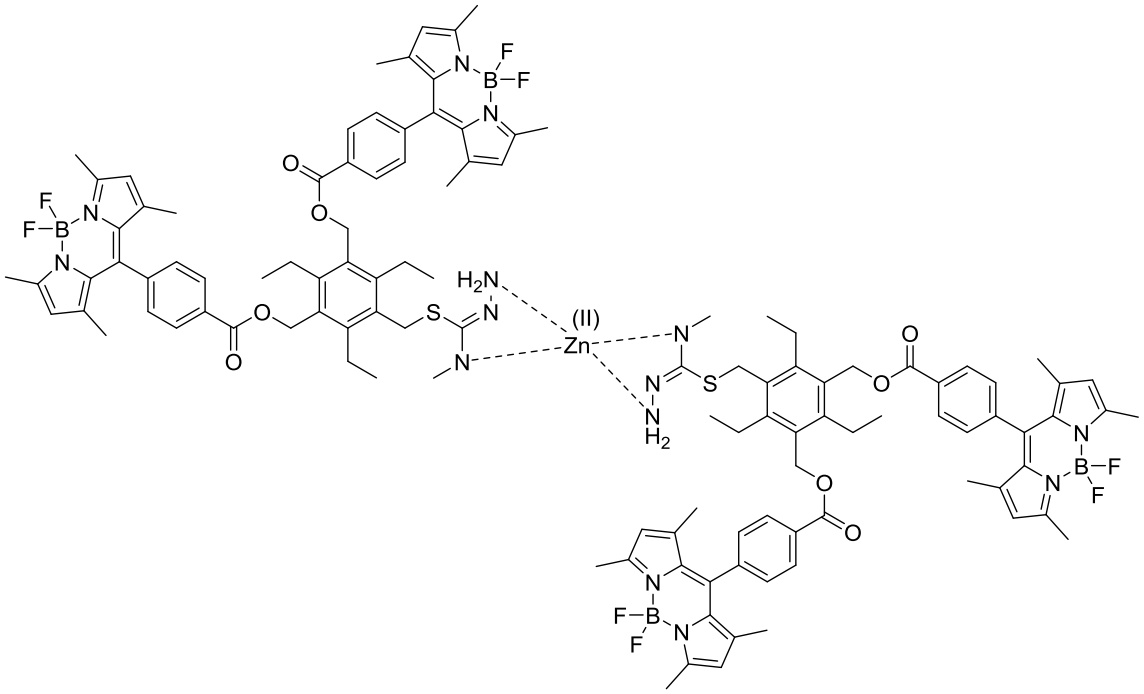

Figure 2.23. Proposed structures of the synthesised compound **17** coordinated to zinc(II); **(A)** with one molecule of the ligand and two remaining water molecules coordinated to the metal ion, and **(B)** with two molecules of the ligand.

2.7. Optimisation of the reaction conditions for the functionalisation of the tripodal core

In order to make the substitution reaction of compound **1** more accessible for the conjugation of biomolecules or peptides, an optimisation of the reaction conditions was carried out studying the reaction crude at different times, and also using different temperatures and various equivalents of the tripodal ligand (starting material). For this purpose, two slightly different tripodal molecules and benzoic acid were used for all the optimisation studies. Other parameters, such as the base (K_2CO_3) or the solvent (acetonitrile), were not modified as these do not play a key role in the stoichiometry of the reaction.

In the case of the reaction time study, benzoic acid and compound **1** were used as starting materials at a 1:1 ratio together with 1.5 equivalents of potassium carbonate. The reaction mixture was dissolved in acetonitrile and stirred under reflux at 100 ^{o}C. Aliquots of this suspension were taken at different times, starting at time = 0 when the temperature reached 100 ^{o}C. Each aliquot was filtered through cotton wool to remove the potassium carbonate and dried under a nitrogen flow. The resulting white solid was dissolved in deuterated chloroform and analysed by ^{1}H NMR spectroscopy (*Figure 2.24*). Resonances at 4.58, 4.62 and 4.67 ppm corresponding to the starting material (compound **1**), the mono- (compound **3**), and the disubstituted (compound **4**) products, respectively, were used to determine the proportion of each compound present. This procedure was repeated several times, at the beginning every hour until 4 hours had passed from the start of the reaction, and then every 2 hours until 8 hours had passed. The next aliquot was collected 24 hours after the start, and finally the last one was taken 2 hours after that, after 26 hours in total from the start of the reaction.

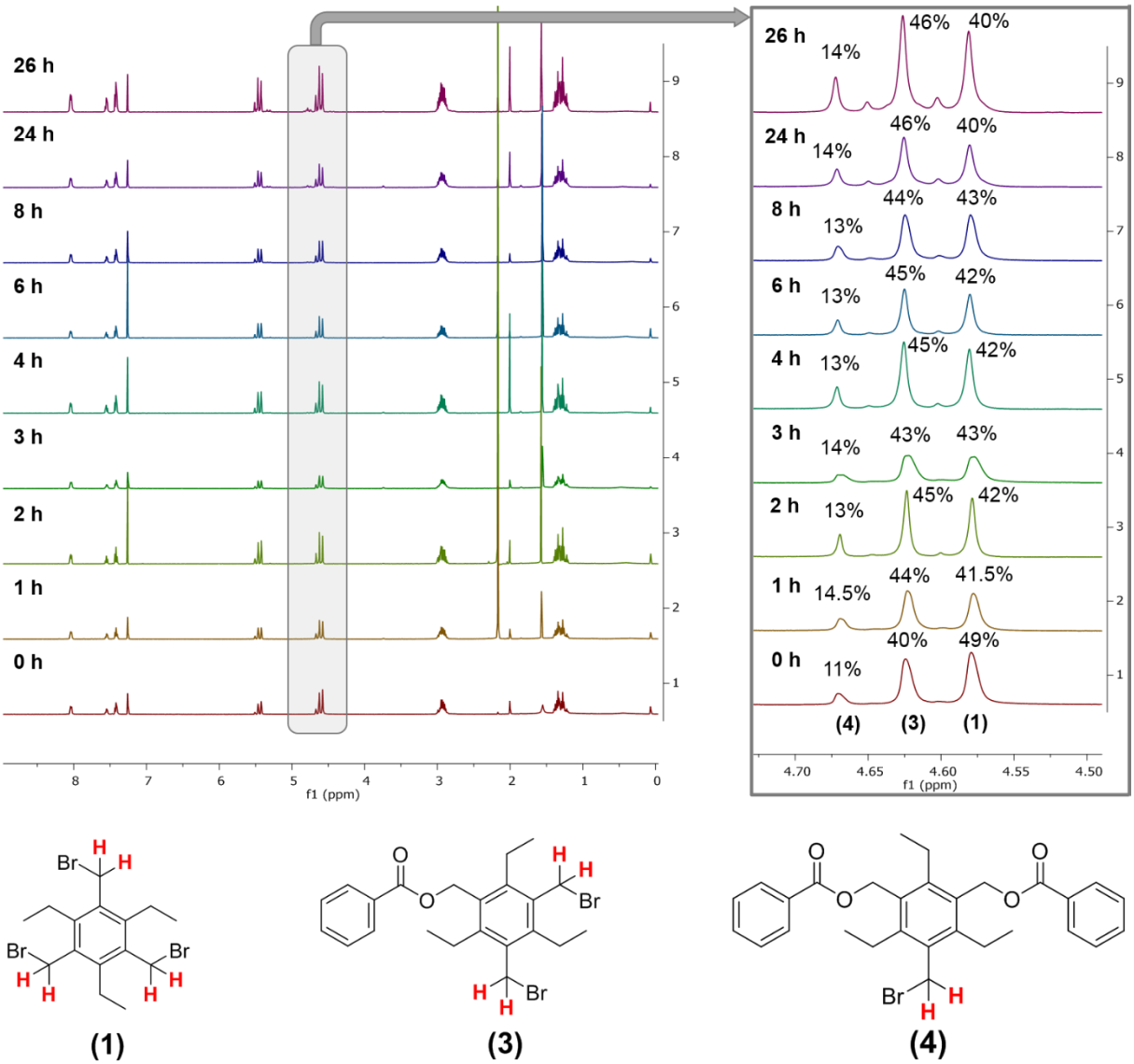

(1) (3) (4)

Figure 2.24. ^{1}H NMR (500 MHz, $CDCl_3$, 298 K) spectra of the crude mixture at different times, specified in every spectrum. Percentages over the peaks indicate the proportion of each compound (**1**, **3** and **4**) present at the mixture at each time.

It can be seen that at the start of the process, when t = 0 hours (at 100 ^{o}C), the percentage of starting material (compound **1**) is the highest (49%), and a very small amount of disubstituted product has been formed (11%). However, after one hour has passed, the amounts do not vary significantly, and after 24 hours the distribution of the products in the mixture does not change anymore, obtaining a 46% of the monosubstituted compound, a 14% of the disubstituted derivative, and still containing a 40% of unreacted starting material (compound **1**).

The temperature and stoichiometry studies were carried out with benzoic acid and a variety of compound **1**, a tripodal core substituted with methyl instead of ethyl groups (*Scheme 2.13*), and modifying the chosen factor in each case.

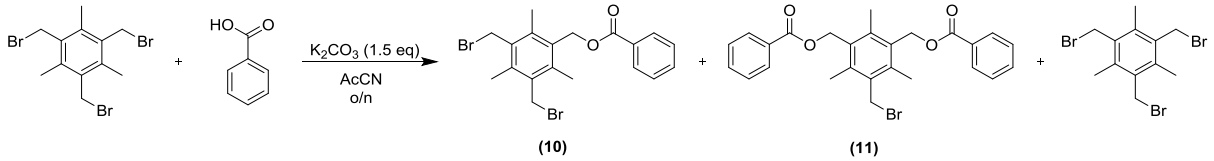

Scheme 2.13. Reaction between 1,3,5-tris(bromomethyl)-2,4,6-trimethylbenzene and benzoic acid to form a mixture of unreacted tripodal ligand and mono- and disubstituted products (compounds **10** and **11**, respectively).

Upon completion of the temperature screening, 1,3,5-tris(bromomethyl)-2,4,6-trimethylbenzene was deemed suitable to be used as a tripodal starting material and the same conditions described above were used. Three parallel reactions were set up at three different temperatures: 25 ^{o}C (room temperature), 40 ^{o}C and 60 ^{o}C. All the reactions took place overnight and, after this time, the solvent was removed under reduced pressure, and the white solid was dissolved in dichloromethane and washed with an aqueous solution of sodium hydroxide. The organic layers were collected and the solvent was removed under reduced pressure. The crude product was purified by silica gel column chromatography using a solvent system of ethyl acetate in hexane. When a lower temperature is used there is a lower percentage of unreacted starting material in the final mixture, and a higher percentage of monosubstituted product is formed. The amount of disubstituted product formed does not change significantly using the three different temperatures. However, there is a change in the amount of the monosubstituted product formed (increases) and the unreacted starting material (decreases) when the temperature is lower (*Table 2.2*). This is likely due to the fact that at a higher temperature the nucleophilic substitution occurs faster and the disubstituted product is formed more quickly than at lower temperatures, exhausting all the available acid derivative earlier and leaving more unreacted starting material.[17]

Table 2.2. Different temperatures used for the functionalisation reaction of the tripodal core and percentages of each compound found in the final mixture.

Temperature (^{o}C)	Starting material (%)	Monosubstituted product (%)	Disubstituted product (%)
RT (25)	12	60	28
40	27	42	31
60	42	26	32

The same general procedure for the reaction and purification of the final mixture was used when the stoichiometry of the reaction was the parameter studied. In this case, it was the number of equivalents of the tripodal ligand used as starting material, 1,3,5-tris(bromomethyl)-2,4,6-trimethylbenzene, that were modified. It was thought that if there were more molecules of the tripodal compound, there would be less chances to obtain the disubstituted product, as this would push the reaction towards the formation of the monosubstituted derivative. With this approach in mind, two and five equivalents of 1,3,5-tris(bromomethyl)-2,4,6-trimethylbenzene were used against one equivalent of benzoic acid. The number of equivalents of base (potassium carbonate) used remained unchanged in both cases (*i. e.,* 1.5 eq). It was noticed that, when the number of equivalents of the tripodal starting material was increased, a higher percentage of monosubstituted product was formed, and a lower amount of the disubstituted product was produced. When five equivalents of tripodal starting material were used, no disubstituted product could be isolated, although the purification of the final reaction mixture became more difficult due to the close retention factors of the two compounds seen in the TLC plate (*Table 2.3*).

Table 2.3. Different number of equivalents of tripodal ligand used for the functionalisation reaction of the tripodal core and percentages of each compound found in the final mixture.

Starting material equivalents	Starting material (%)	Monosubstituted product (%)	Disubstituted product (%)
2	9	77	14
5	34	66	-

In summary, it was seen from this study of the reaction conditions using benzoic acid that a lower temperature and the use of a higher number of equivalents of the tripodal ligand (used as starting material) favour the formation of the monosubstituted product, which can be obtained in a somewhat higher percentage from the final mixture. This finding is important for the investigation into the step-wise synthetic functionalisation of the tripodal ligand, and it can help towards the trifunctionalisation of the molecule.[18]

2.8. Attempted functionalisation reactions of the tripodal core

The functionalisation of the tripodal organic core (compound **1**) with 1, 2, and 3 deferoxamine (DFO) units, respectively, was attempted, applying the previously reported method where amines have been shown to act as nucleophiles.[19] Accordingly, a commercial deferoxamine mesylate salt was used together with the tripodal ligand and a base to react under different conditions and achieve the desired products (*Scheme 2.14*).

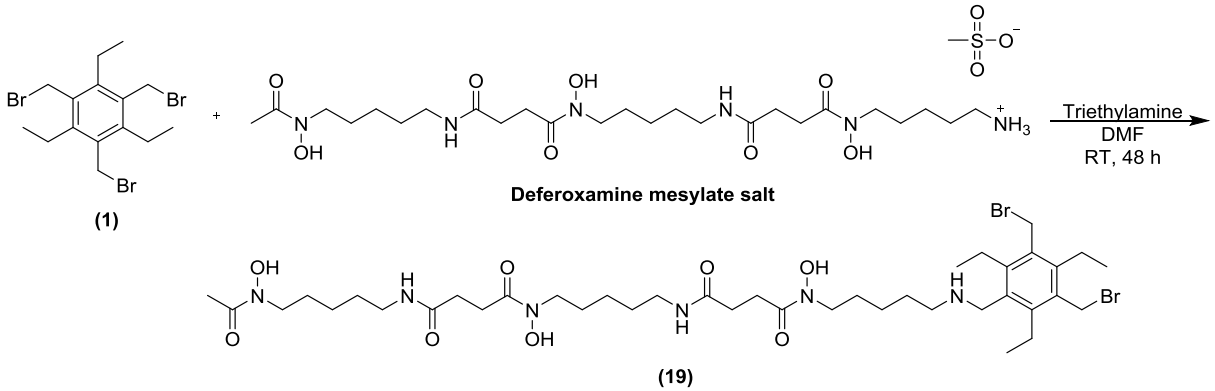

Scheme 2.14. General reaction between compound **1** and deferoxamine mesylate salt to produce compound **19**.

In order to obtain this desired product (compound **19**), different reaction conditions were first attempted (*Table 2.4*). All of these reactions were carried out under nitrogen atmosphere and using dry solvents. They all involved as work-up the removal of the solvent under reduced pressure and, in some cases, extractions with water and organic solvents to remove the base and obtain the desired product in the organic phase, which was dried under vacuum. Yellowish oils were obtained in most cases, which were characterised by mass spectrometry and other techniques such as NMR spectroscopy. No conclusive results regarding the identity of the final products due to the complexity of the spectra, where a full assignment could not be achieved.

Table 2.4. Different conditions used to carry out the reaction between compound **1** and deferoxamine (DFO) mesylate salt.

Comp. 1 / eq	DFO salt / eq	Base / eq	Solvent	T / ºC	Time / h
1	1	K_2CO_3 / excess	DMF	60	24
1	2	K_2CO_3 / excess	DMF	60	24
1	4	K_2CO_3 / excess	DMF	60	24
3	1	K_2CO_3 / excess	DMF	60	24
1	1	DIPEA / 2	DMF	90	1
1	1.4	K_2CO_3 / 1.03	DMF	80	48
1	1	NaOH / 1	MeOH	55	4
2	1	NaOH / 1	MeOH	55	4
1	1	NEt_3 / 3	H_2O/AcCN	20	1.5
1	1	K_2CO_3 / 1.5	DMF	150 (reflux)	24
1.2	1	NEt_3 / 1	DMF	25	48

When this reaction was carried out following the last set of conditions specified in *Table 2.4*, an oil could be isolated that, when was characterised by HPLC (*Appendix A*) and mass spectrometry, showed to contain the desired product (compound **19**). Taken together, these two analyses support the hypothesis that a desired compound of an acceptable purity for further investigations was achieved. The mass spectrum recorded using electrospray ionisation in negative mode shows a peak at m/z = 919.3429, that corresponds to the $[M-H]^-$ ion, as well as a good isotopic pattern match (*Figure 2.25*).

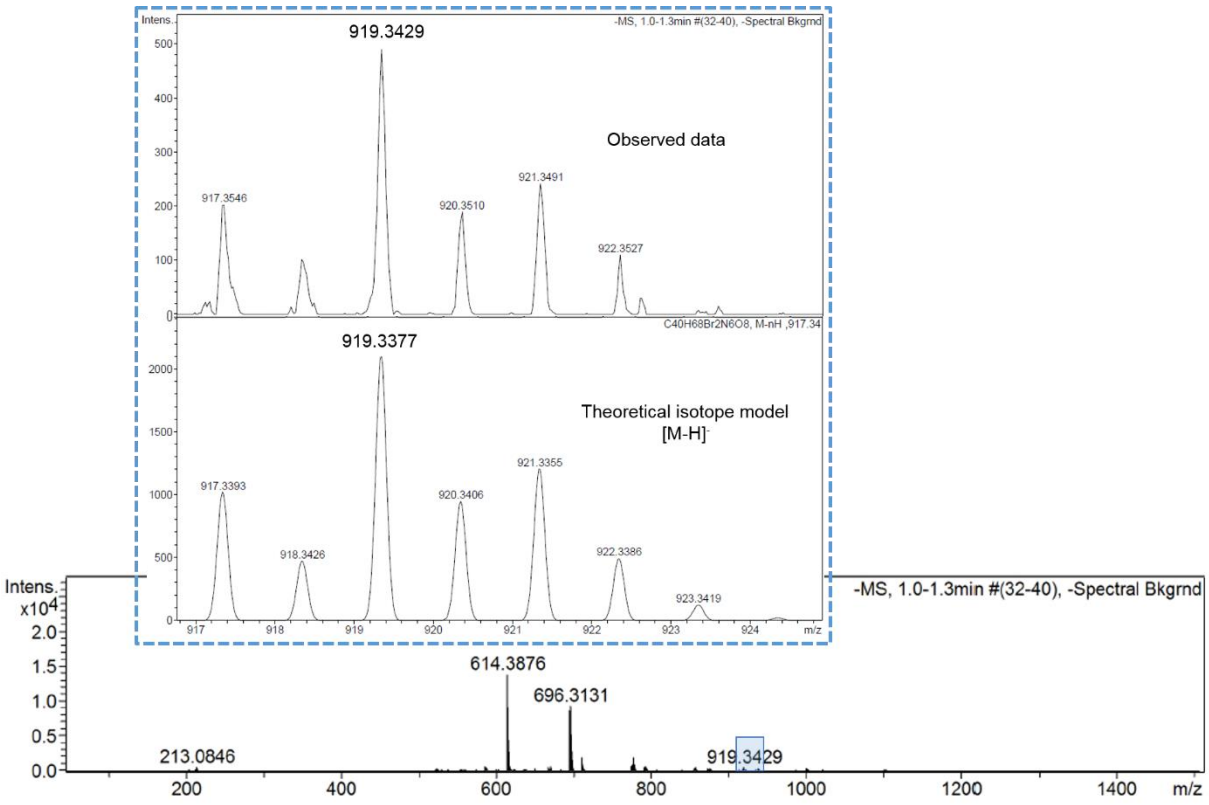

Figure 2.25. Mass spectrum of compound **19** using ESI-, and amplification of the isotopic pattern.

Regarding the HPLC chromatogram, a major peak can be seen at 7.4 minutes in the 280 nm channel, and peaks of lower intensity can be observed before and after this main one (*Appendix A*). The compound obtained via this synthesis was later used for radiolabelling experiments with the positron-emitting isotope zirconium-89 (*Section 2.9*).

Since it was found that the optimisation of the previously described reaction does not lead to promising results, the coupling of deferoxamine to a succinic anhydride tail tag was pursued instead, in order to change the terminal free amino group of the molecule for a carboxylic acid group, with different reactivity and potentially more readily functionalisable (*Scheme 2.15*).

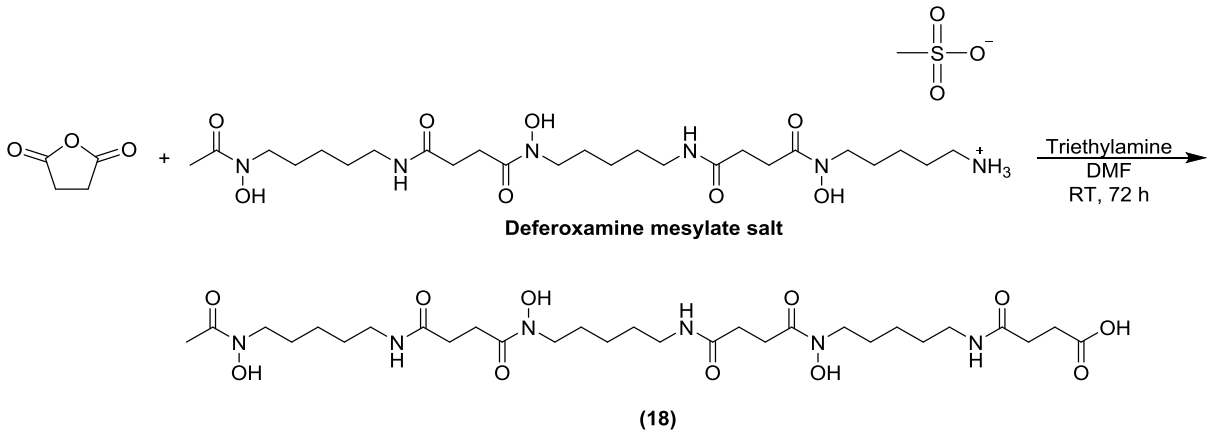

Scheme 2.15. Reaction between deferoxamine mesylate salt and succinic anhydride to achieve the coupling of these two reagents using triethylamine as a base, and form compound **18**.

In order to achieve a terminal carboxylic acid group, different conditions were tried varying the number of equivalents of deferoxamine mesylate salt and succinic anhydride, all of them using N,N'-dimethylformamide as a solvent, and at different temperatures and reaction times (*Table 2.5*).[20] However, it was not until a base was added that the desired product could be identified. In this context, the optimal conditions found for this reaction were DFO salt:succinic anhydride:triethylamine in a 1:1.2:1 ratio, stirring at room temperature for 72 hours. The work-up in all the cases involved the removal of the solvent under reduced pressure to yield a yellow oil.

Table 2.5. Different conditions used to carry out the reaction between deferoxamine (DFO) mesylate salt and succinic anhydride.

Succinic / eq	DFO salt / eq	Base / eq	Solvent	T / ºC	Time / h
1.2	1	-	DMF	0, then RT	17
1.2	1	-	DMF	30	24
1	1	-	DMF	RT	24
2	1	-	DMF	RT	24
1.2	1	NEt_3 / 2	DMF	RT	72

When the reaction was carried out following the last conditions specified in the above table with a base, an oil could be isolated and characterised by mass spectrometry using electrospray ionisation in negative mode. The spectrum showed a peak at m/z = 659.3631, which corresponds to the $[M-H]^-$ ion for the expected molecule (compound **18**) (*Figure 2.26*), and a good isotopic pattern match. The use of triethylamine facilitated the completion of the

reaction by deprotonating the ammonium group of the DFO salt, and making it more readily available to attack the succinic anhydride group.

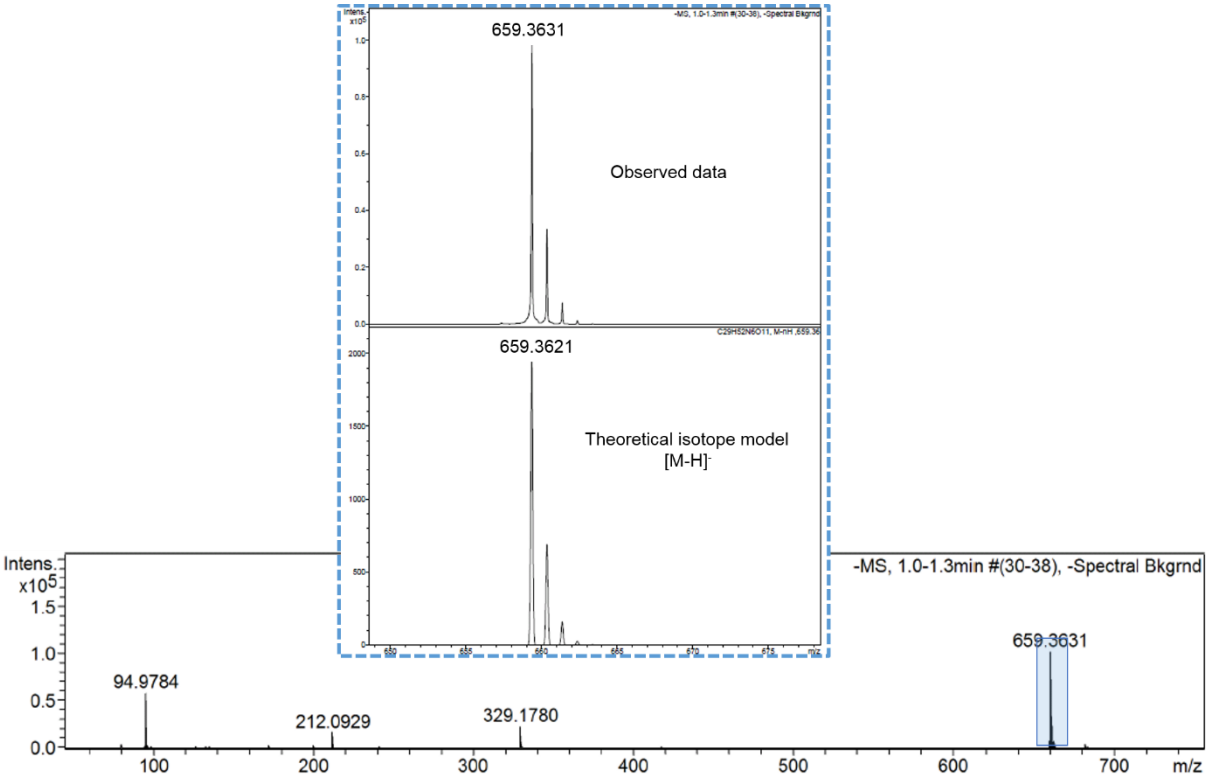

Figure 2.26. Mass spectrum of compound **18** using ESI-, and amplification of the isotopic pattern.

The purity of this compound was checked by HPLC using a solvent system of water and acetonitrile both containing 0.1% of trifluoroacetic acid. The chromatogram showed a peak at approximately 6.9 minutes in the 280 nm channel (*Figure 2.27*). Protonation on the column is likely to account for broadening of this trace (0.1% TFA).[21]

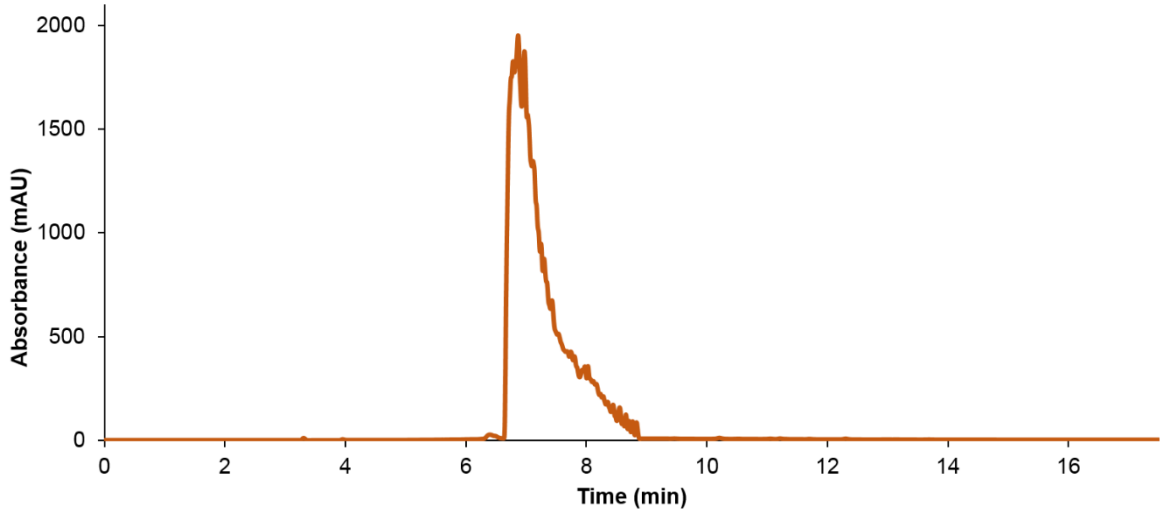

Figure 2.27. HPLC chromatogram of compound **18** in the 280 nm channel.

Since the reaction between the tripodal ligand (compound **1**) and carboxylic acid derivatives was previously successfully employed to form ester products, compound **1** was reacted with compound **18** to produce the corresponding ester (*Figure 2.28*). The reaction was performed under two different conditions: (i) using the DFO derivative:tripodal ligand in a 1:1.2 ratio and adding 1 equivalent of triethylamine, using DMF as a solvent and mixing the reagents at 25 ^{o}C for 48 hours, and (ii) using the reagents in a 1:1 ratio with 2 equivalents of K_2CO_3, using DMF as a solvent and mixing the reagents under reflux at 150 ^{o}C for 24 hours. In both cases the solvent was removed under reduced pressure when the reaction time was finished. When using the conditions specified in (ii), extractions were carried out with dichloromethane and water, and finally the organic layers were removed under vacuum. Using the procedure (ii), a dark brown solid was obtained, which was characterised by ^{1}H NMR spectroscopy.

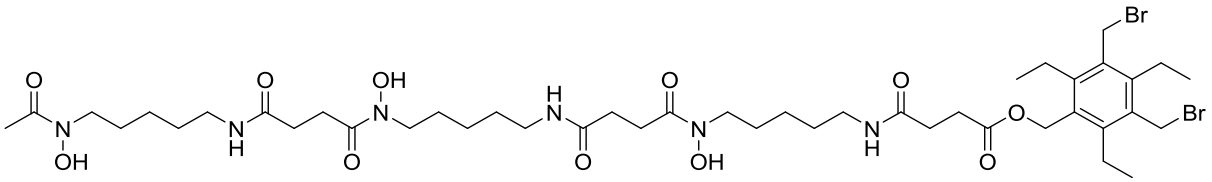

Figure 2.28. Desired product obtained from the reaction between compounds **1** and **18**.

The ^{1}H NMR spectrum of compound **19** was compared to that of DFO (*Figure 2.29*) and at the same time also to the one of compound **18** (*Figure 2.30*).

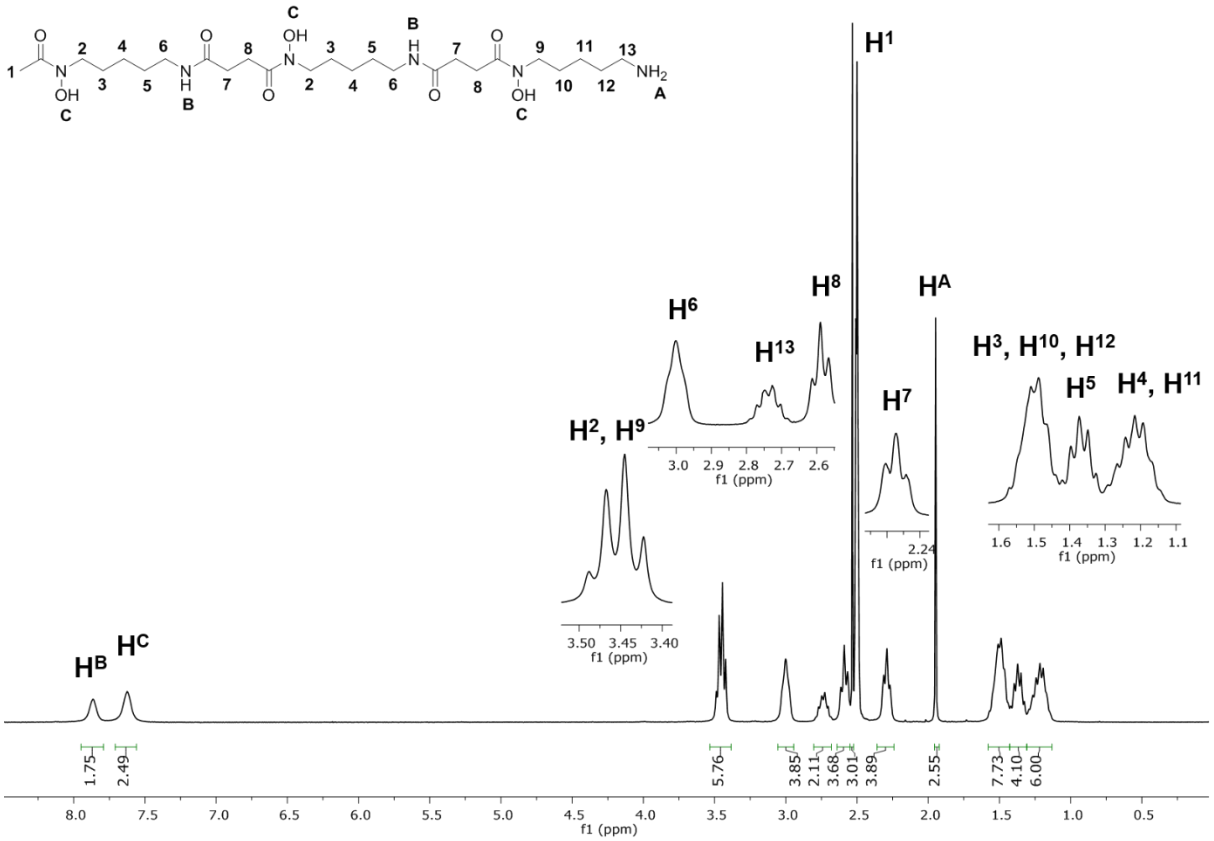

Figure 2.29. ^{1}H NMR (500 MHz, DMSO-d_6, 298 K) spectrum of deferoxamine (DFO).

In the ^{1}H NMR spectrum of deferoxamine, a singlet at 2.53 ppm that corresponds to 3 H is assignable to the protons of the terminal methyl group, H^{1}. The two protons of the terminal primary amine group appear as another singlet at 1.94 ppm. The rest of aliphatic protons resonances can be found between approximately 3.60 and 1.00 ppm. The resonances for the protons from the secondary amines appear as a broad singlet at 7.86 ppm, and the ones for the protons from the OH groups appear as another broad singlet at 7.62 ppm.

Due to the complexity of the molecule most of the peaks could not be assigned fully, however it can be seen that the spectra of compounds **18** and **19** are different to the one of the pure DFO, with different peaks and multiplicity.

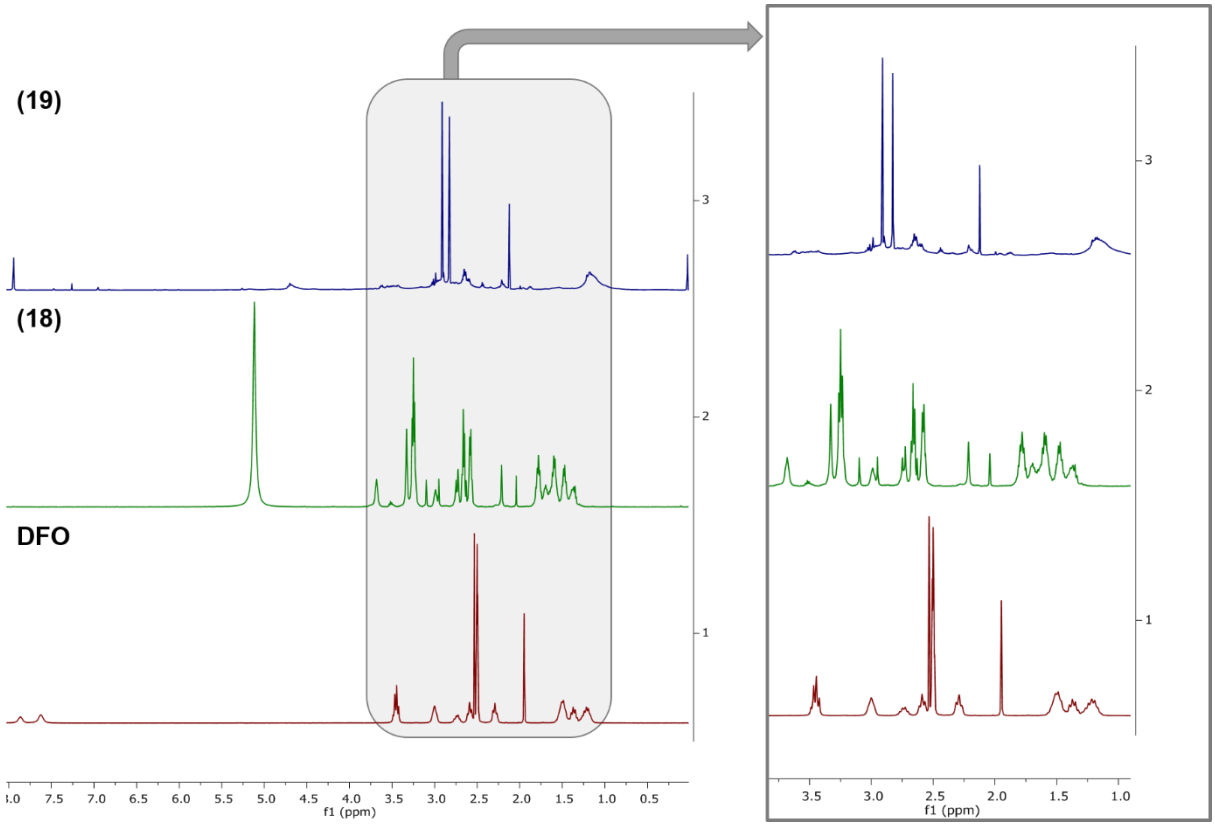

Figure 2.30. ^{1}H NMR (500 MHz, 298 K) spectra of DFO (DMSO-d_6), and compounds **18** (CD_3OD) and **19** ($CDCl_3$).

Taking advantage of the fact that an amine is a nucleophile and it can undergo substitution reactions by displacing the bromide group of the arms of the tripodal ligand, the reaction between compound **1** and Zn(ATSM/A) (compound **35c**) was attempted (*Scheme 2.16*).

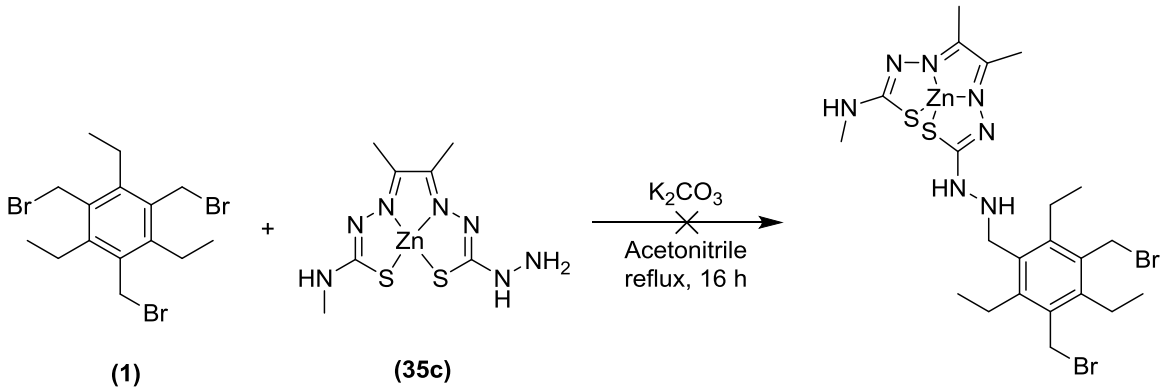

(1) **(35c)**

Scheme 2.16. Attempted reaction between compound **1** and Zn(ATSM/A) (compound **35c**).

This reaction was carried out under the same conditions that proved to be successful for the functionalisation of the tripodal core (compound **1**), using a 1:1 ratio of reagents with 1.5 equivalents of K_2CO_3, acetonitrile as a solvent, and stirring the mixture under reflux overnight. An orange suspension was obtained, which was analysed by TLC at different times but the

reaction mixture did not reveal any clear spots. Acetonitrile was removed under reduced pressure and the crude solid was dissolved in dichloromethane to carry out aqueous extractions. The organic phase was dried under vacuum and an orange solid was obtained, which was analysed by mass spectrometry and NMR spectroscopy but this did not yield conclusive results. The obtained product appeared to be rather insoluble and this hindered its characterisation.

In order to introduce a fluorescent tag, fluorescein-5-thiosemicarbazide was used. This molecule is a derivative of fluorescein, a non-toxic, commercial, organic fluorescent dye typically used for imaging applications, very common in confocal laser scanning microscopy due to its ability to produce good contrast and quality images, and also due to being excited by the ordinarily used 488 nm wavelength of an Ar^+ laser.[1, 22] Moreover, fluorescein tags have advantages such as low toxicity to cells, high quantum yields (0.85 – 0.97), water solubility, large extinction coefficients (90000 $M^{-1}cm^{-1}$), high photostability and being biologically tolerable.[23, 24] On the down side, fluorescein derivatives present many different isomers and tautomers, their equilibria in solution are pH dependent, and this makes it difficult for them to be characterised (*Scheme 2.17*).[25, 26]

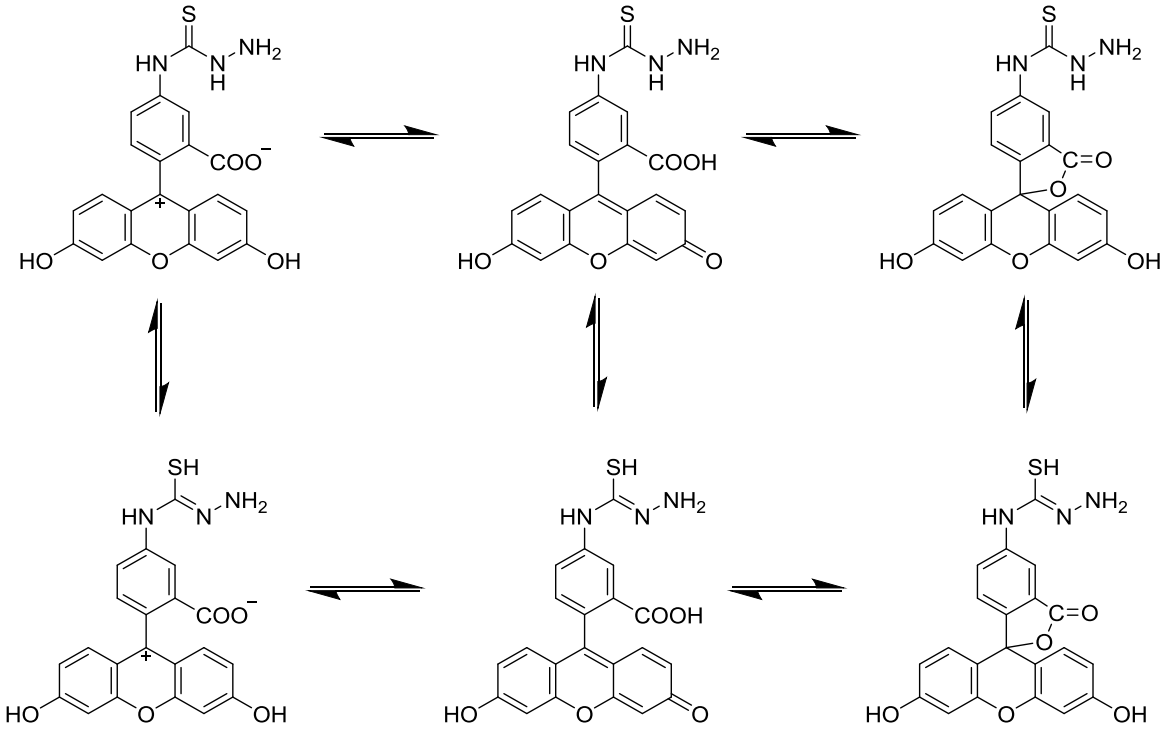

Scheme 2.17. Tautomerism of fluorescein-5-thiosemicarbazide.[25]

Accordingly, the coupling of fluorescein-5-thiosemicarbazide to the tripodal ligand (compound **1**) was attempted in order to create a fluorescent molecule able to be further functionalised.

Several conditions were used with the aim of optimising this reaction (*Scheme 2.18*). The solvent used in all the cases was acetonitrile as this can easily dissolve the two products, and all the reactions took place overnight and at different temperatures, since these conditions have been proven to work with compounds of similar reactivity (*Table 2.6*).

Table 2.6. Conditions used for the reaction between fluorescein-5-thiosemicarbazide (F-5-TSC) and compound **1**.

Entry	Comp. 1 / eq	F-5-TSC / eq	Base / eq	Solvent	T / ºC	Time / h
1	1	1	-	AcCN/DMF	66	16
2	1	1	-	AcCN	80, reflux	16
3	1	1	-	AcCN	90, reflux	16
4	1	1	K_2CO_3 / 1.5	AcCN	100, reflux	16

In all the cases, filtrations or extractions were carried out once the reaction time was finished and in some the crude was purified by silica gel column chromatography, yielding a mixture of products difficult to characterise. When conditions shown in the entries 2 and 3 of the above table were used, a solid precipitated. It was filtered, and the filtrate was dried under vacuum to yield another solid.

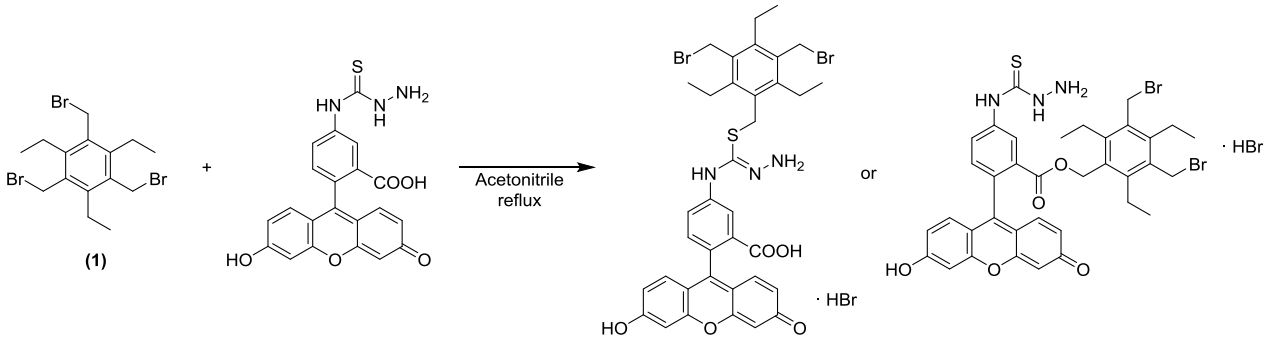

Scheme 2.18. Reaction between compound **1** and fluorescein-5-thiosemicarbazide to obtain the conjugate as an HBr salt.

The solid materials were analysed by mass spectrometry using electrospray ionisation in negative mode, and in the case of the solid coming from the filtrate, a peak corresponding to the expected molecule could be observed at m/z = 780.0656, with other peaks in the isotopic pattern due to minor impurities (*Figure 2.31*). The overall structure of the obtained molecule is unclear based on information from solution spectroscopies alone, as the tripodal core and the fluorescein unit can be attached either by a sulphur atom or by an ester linkage (as described in *Chapter 4* for thiosemicarbazide derivatives).

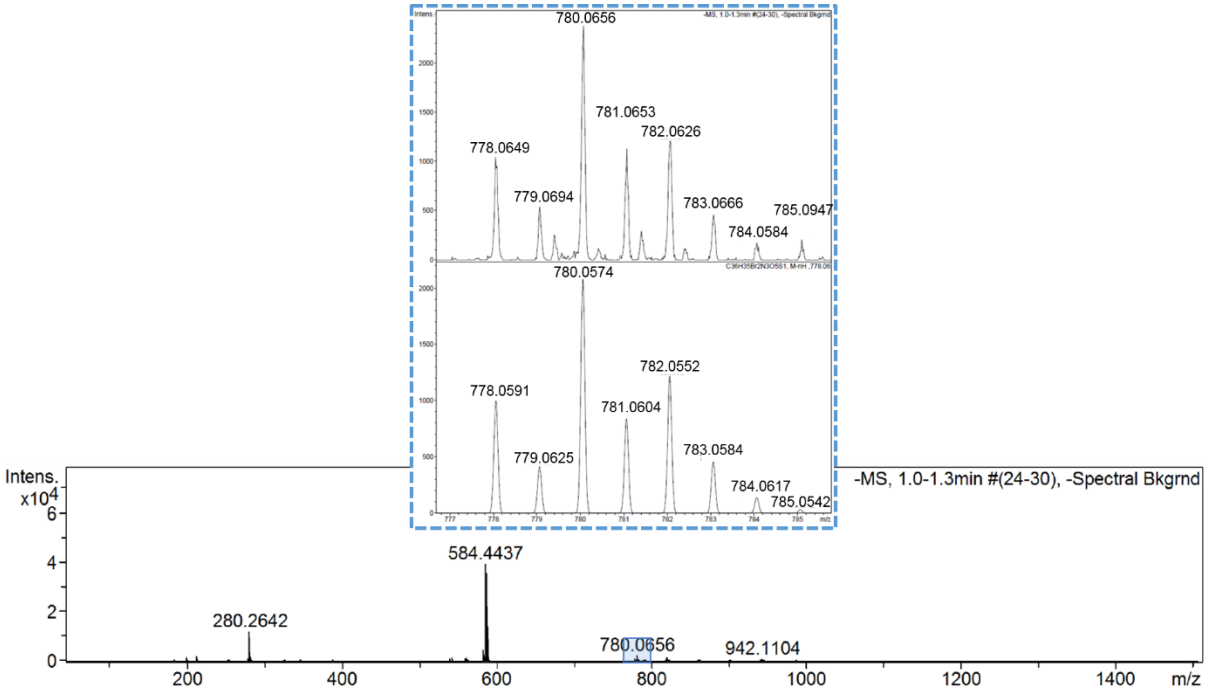

Figure 2.31. Mass spectrum of the product resulting from the reaction between compound **1** and fluorescein-5-thiosemicarbazide using ESI-, and amplification of the isotopic pattern.

Next, the most promising product formed between fluorescein-5-thiosemicarbazide and the tripodal ligand was reacted with Zn(ATSM/A) to try to couple this molecule to the system. The resulting product would be a potential bimodal molecule, incorporating a fluorophore and a radiochelator with potential selectivity for hypoxic tissue. The reaction was carried out with one equivalent of each compound dissolved in methanol and stirring at 80 ºC under reflux for 16 hours. After this time, the formed solid was filtered and the filtrate was dried under vacuum. Two different fractions, both as orange-yellow solids, emerged, and they were characterised by the common techniques but yielded no conclusive results: HPLC chromatograms showed multiple peaks, and NMR spectra were unclear, with peaks that could not be assigned to any of the proposed obtained molecules (*Figure 2.32*). This is not surprising given the solution equilibria likely to occur in wet solvents, and the possibility of protonation occurring during HPLC analysis (when using a mobile phase of acetonitrile and water both containing 0.1% TFA).

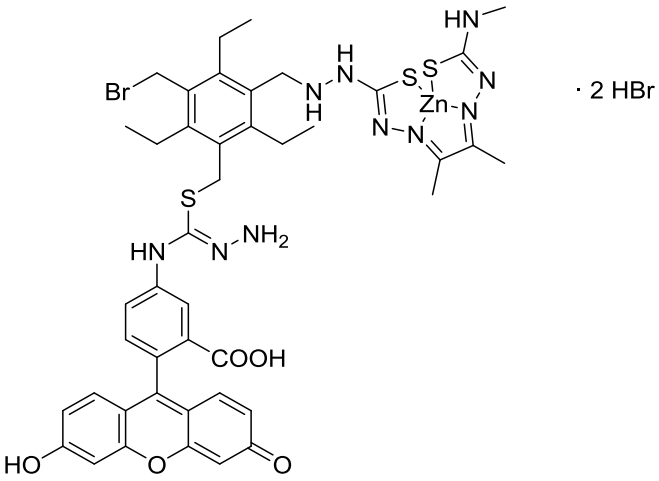

Figure 2.32. Desired product containing a fluorescent unit and a radiochelator.

Another attempted reaction was that between the fluorescein-tripodal derivative and a thiosemicarbazide compound, 4-methyl-3-thiosemicarbazide, as this type of products have potential anti-tumour activity (*Figure 2.33*).[27] For this purpose, one equivalent of the fluorescent tripodal derivative (shown in *Scheme 2.18*) and 2.2 equivalents of the thiosemicarbazide compound were dissolved in acetonitrile and stirred under reflux for 24 hours. The solvent was removed under reduced pressure and an orange solid was obtained, which was characterised by the common characterisation techniques but no clear conclusions could be deducted as it probably did not correspond to the expected product. By mass spectrometry, a peak due to the starting material, the fluorescein derivative, could be observed.

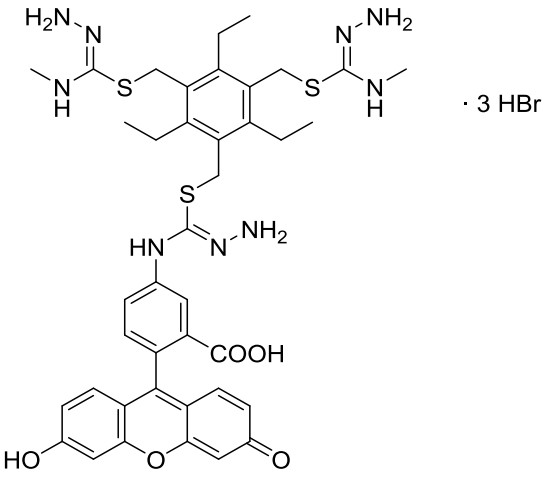

Figure 2.33. Proposed structure of the product from the reaction between the tripodal compound containing fluorescein-5-thiosemicarbazide and 4-methyl-3-thiosemicarbazide.

2.9. Radiolabelling experiments with zirconium-89

2.9.1. Cyclotron production of zirconium-89

In these experiments, the positron-emitting radiotracer zirconium-89 was prepared at the Wales Research and Diagnostic Positron Emission Tomography Imaging Centre (PETIC) via the $^{89}Y(p,n)^{89}Zr$ reaction using the cyclotron CYCLONE 18/9. The zirconium-89 radiolabelling experiments at PETIC were carried out under the supervision of Dr. Stephen Paisey.

2.9.2. Method development

The radioisotope zirconium-89 was obtained from the cyclotron in a 1 M oxalic acid solution and the pH was adjusted to 6.8 – 7.5 by addition of a few drops of a 1 M solution of sodium carbonate, in order to be suitable for radiolabelling the two DFO-based products (compounds **18** and **19**). The pH-adjusted $^{89}Zr^{4+}$ solution was then added to the product of interest in dimethylsulfoxide, and the reaction was stirred at room temperature for 1 hour. After this time, the two samples were analysed by radio-HPLC using a C18 column, with a solvent system of acetonitrile and water containing 0.1% of trifluoroacetic acid, but conclusive results were not obtained. Subsequently, the radiolabelling efficiency was determined by radio-TLC using an eluent of 50 mM diethylenetriaminepentaacetic acid (DTPA) (pH 5.5), in which the $^{89}Zr^{4+}$ bound to the compound appears at the origin of the plate (Rf < 0.1), and the free $^{89}Zr^{4+}$ cations are chelated by DTPA and elute with the solvent front (Rf > 0.9) (*Figure 2.34*). This procedure is based on a previously reported protocol.[28]

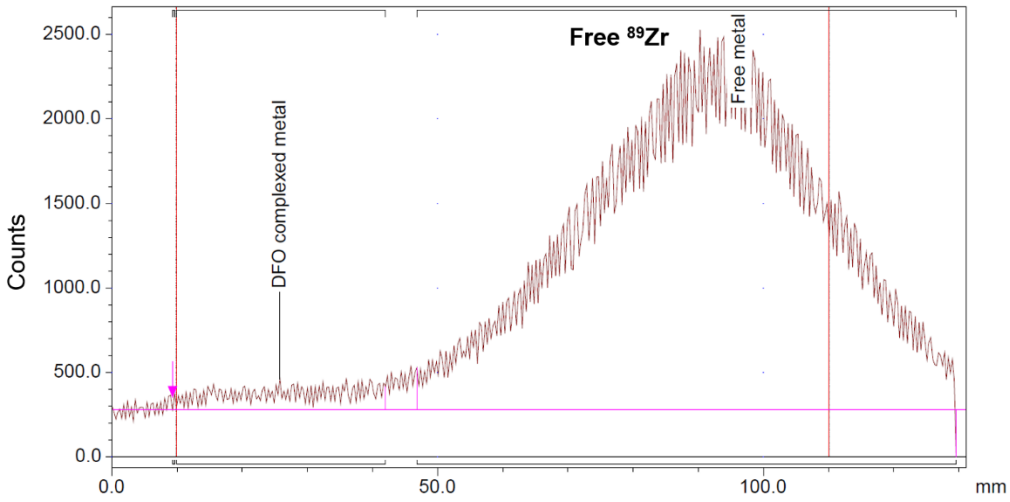

Figure 2.34. Radio-TLC chromatogram of free $^{89}Zr^{4+}$ ions. TLC was eluted using 50 mM DTPA as the mobile phase.

As the two used compounds (**18** and **19**) are based in deferoxamine, a well-known zirconium chelator, the coordination of the radioisotope to the ligands can be expected to be comparable

to that of DFO, on the hydroxamate groups of the ligand and with two water molecules in order to be octa-coordinated (*Scheme 2.19*).[29]

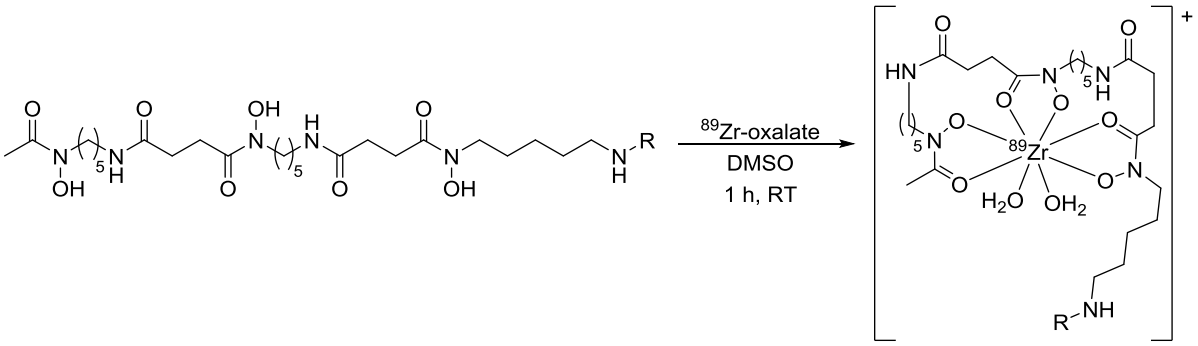

Scheme 2.19. Reaction between deferoxamine derivatives (compounds **18** and **19**) and zirconium-89 with proposed coordination.

The radiolabelling efficiency for compounds **18** and **19** showed to be of ≥ 99.9% (*Figure 2.35*).

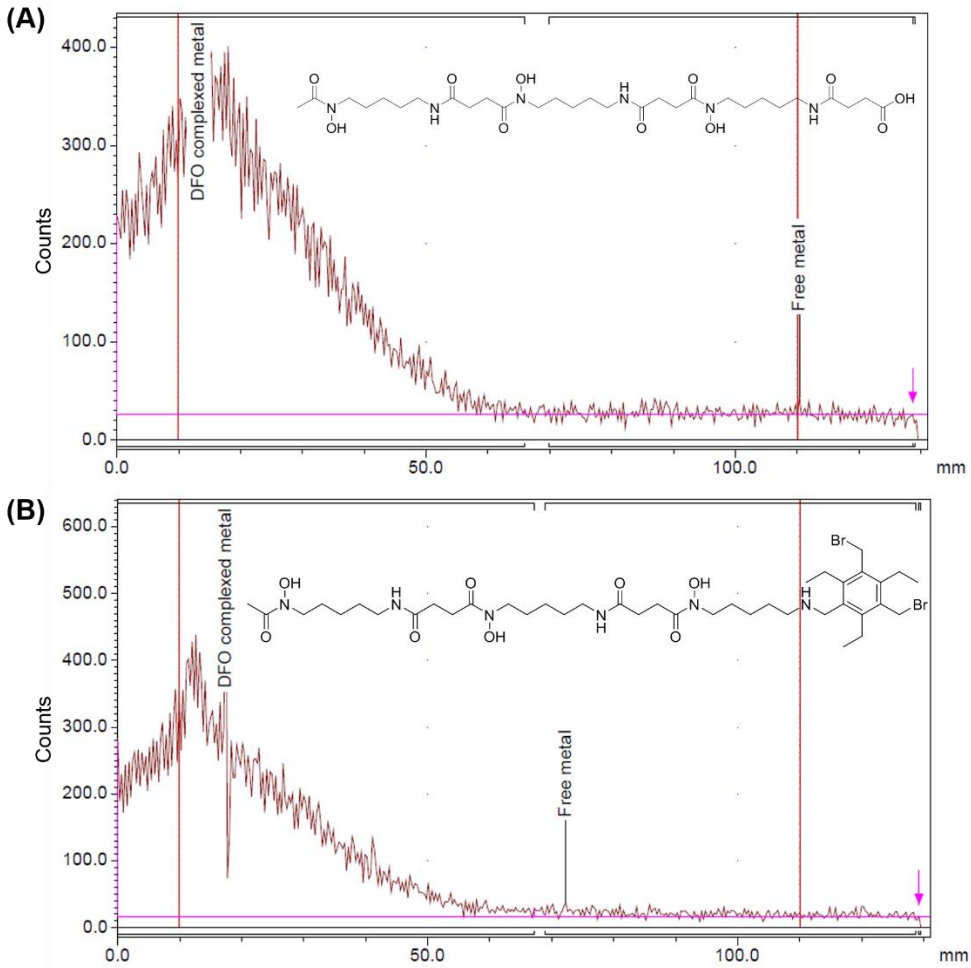

Figure 2.35. Radio-TLC chromatograms of compounds **18 (A)** and **19 (B)** with ^{89}Zr suggesting a RCY ≥ 99.9%. TLC was eluted using 50 mM DTPA as the mobile phase.

2.9.3. "Cold" chemistry reactions

The same method used to radiolabel the two DFO-based ligands was tried in "cold" chemistry, using $ZrCl_4$. The ligand and the zirconium salt were mixed in a 1.2:1 ratio under nitrogen in a Schlenk flask and stirred at room temperature overnight. Acetonitrile was used as a solvent, and a 1 M aqueous solution of K_2CO_3 was used to adjust the pH of the stock zirconium solution to approximately 7. Oils were obtained in both cases, which were analysed by mass spectrometry. The coordination of the ligands with the zirconium cation was expected (*Figure 2.36*), however in the mass spectra no evidence could be found for the formation of these complexes or for the incorporation of zirconium.

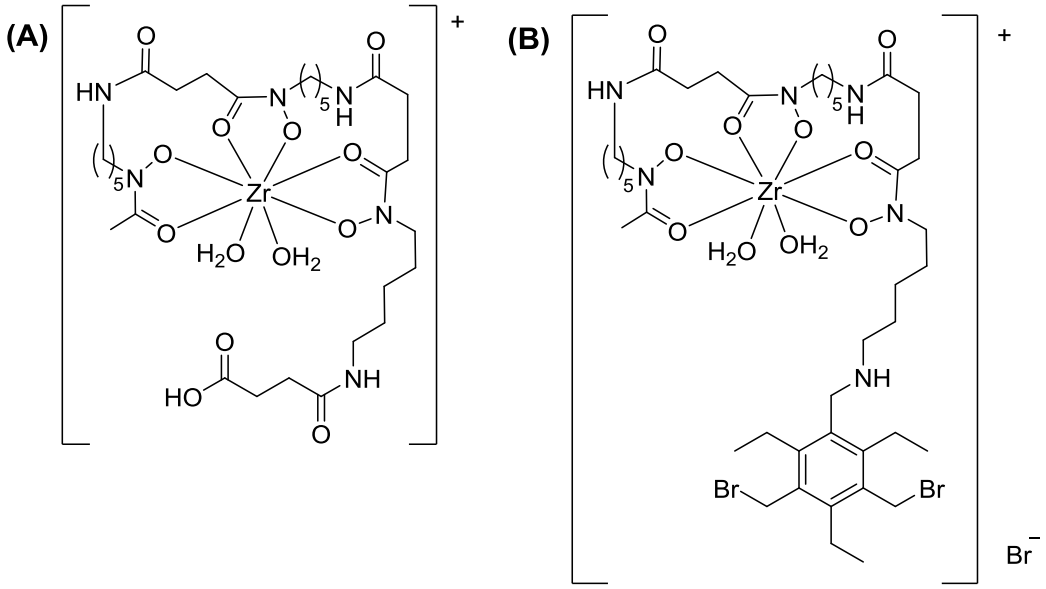

Figure 2.36. Expected products formed between Zr^{4+} and compounds **18 (A)**, and **19 (B)**.

2.10. Probing the functionality of new fluorophores: estimation of quantum yields

The quantum yield (QY) is an important physical property of a substance that gives an idea of the efficiency of a fluorescence process. The fluorescence quantum yield (Φ) expresses the ratio of the number of emitted photons to the number of absorbed photons per unit of time.[30] Accordingly, the Φ could be expressed as:

Φ = No. of emitted photons / No. of absorbed photons

The quantum yield is referred to as "relative" when it is measured according to a well-known standard and related to this by the following equation:

$$\phi s = \phi r * \frac{Ar}{As} * \frac{Es}{Er} * \frac{Ir}{Is} * \frac{n_{s^2}}{n_{r^2}}$$

Equation 2.1. Formula employed to calculate the quantum yield of the newly synthesised fluorescent compounds.

In this equation, the subscript *r* refers to the reference or standard ($Ru(bpy)_3^{2+}$ in this case), while *s* refers to the new compounds. ***Φr*** and ***Φs*** are the fluorescence QY of $Ru(bpy)_3^{2+}$ (0.042) and of the unknown sample, respectively. *A* is the absorbance of the solution, *E* is the corrected emission intensity, *I* is the relative intensity of the exciting light and *n* is the average refractive index of the solutions.[31, 32]

UV/visible and fluorescence spectra of solutions of known concentrations of the new fluorescent dyes in chloroform were acquired and the QY was measured at room temperature according to *Equation 2.1* (*Table 2.7*). A solution of $Ru(bpy)_3^{2+}$ in water with a concentration of 0.03 mg/mL was used as standard.

Table 2.7. Quantum yield calculations for the new BODIPY derivatives.

Compound	λ max_{abs} (nm)	λ max_{em} (nm)	Δλ (nm)	QY
2	504	511	7	0.12
5	504	515	11	0.11
6	504	515	11	0.13
13	505	515	10	0.07
16	504	509	5	0.57

By comparing the obtained results with different studies of BODIPY derivatives in chloroform as solvent, it can be seen that the values fall within the common range (0.01-0.82).[33] The synthesised BODIPY carboxylic acid derivative (compound **2**) and the mono- and disubstituted tripodal derivatives containing BODIPY (compounds **5** and **6**, respectively) present very similar quantum yield values, slightly higher than the one for the tripodal derivative containing a BODIPY molecule and a linker (compound **13**). Finally, the trisubstituted derivative containing one molecule of BODIPY and two different linkers (compound **16**) has a surprisingly higher quantum yield.

Normalised UV/visible spectra of compounds **2**, **5**, **6**, **13** and **16** in chloroform all showed the same absorption peak at around 504 nm (*Figure 2.37*).

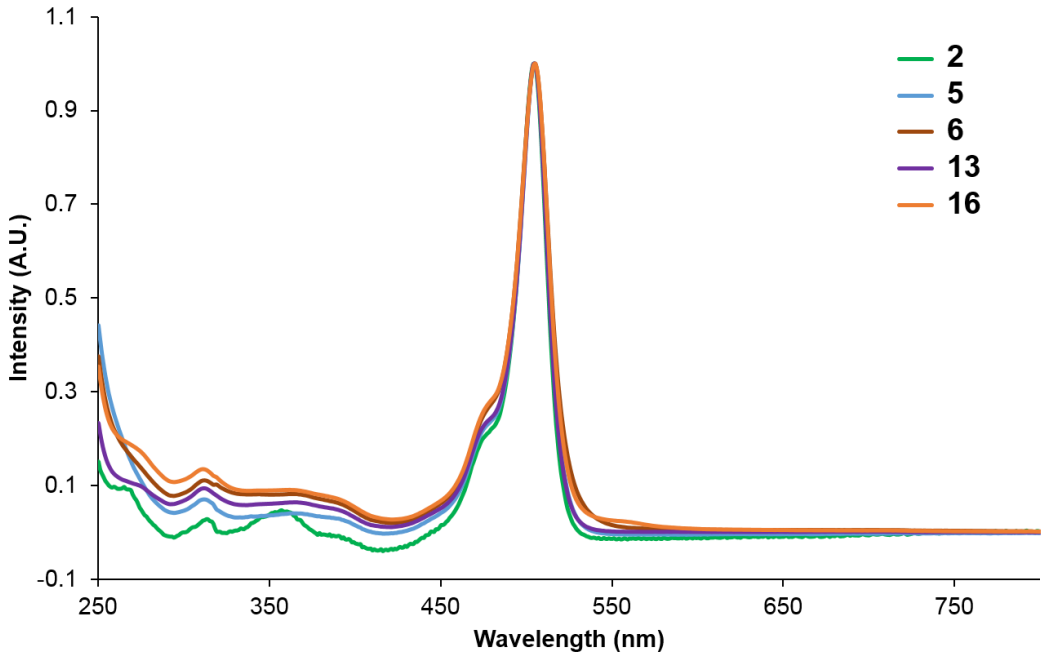

Figure 2.37. Normalised UV/visible spectra of compounds **2**, **5**, **6**, **13** and **16** in chloroform.

Fluorescence spectroscopy was also carried out to acquire the excitation and emission spectra of all the mentioned molecules and they all showed similar fluorescence profiles, with an excitation peak at 505 nm and an emission peak at 517 nm (*Figure 2.38*). The similarity in all the compounds fluorescent properties is due to the fact that they are all BODIPY derivatives based on compound **1**. Accordingly, the Stokes shift of these compounds is small, of around 12 nm (*Table 2.8*).

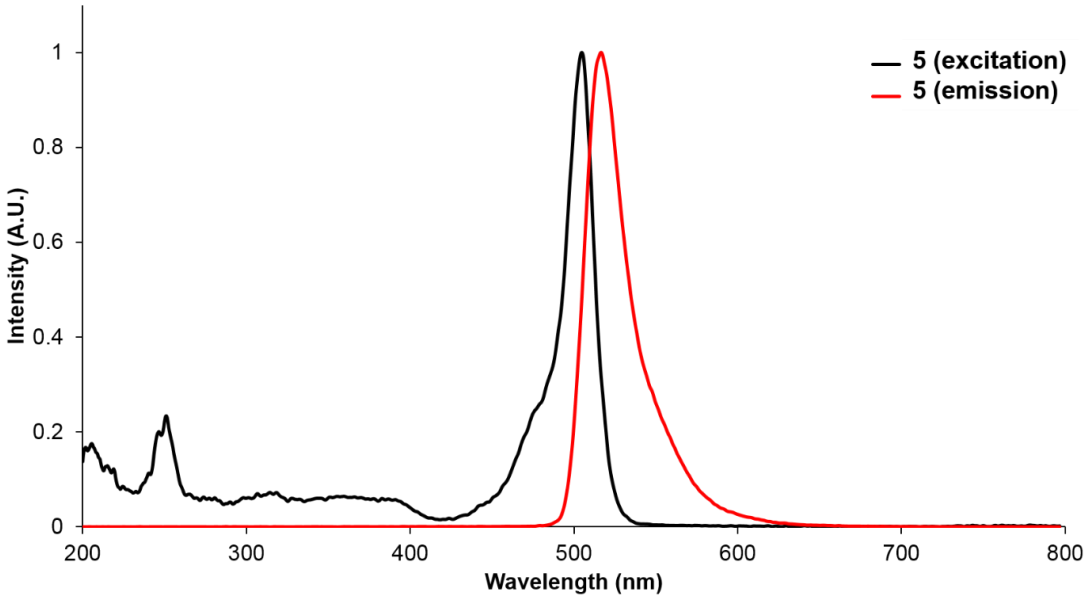

Figure 2.38. Normalised fluorescence spectrum of compound **5** in chloroform, showing excitation (black) and emission (red).

Table 2.8. Excitation and emission wavelengths for the UV/visible and fluorescence spectra of compound **5**, and its corresponding Stokes shift.

Compound	λ max_{ex} (nm)	λ max_{em} (nm)	Δλ (nm)
5	505	517	12

2.11. Epi-fluorescence and confocal fluorescence imaging investigations

PC-3 cells were incubated with a DMSO : serum-free medium (1:99) suspension of 100 μM concentration of some of the newly synthesised compounds containing a fluorophore. In order to study the uptake and distribution of these compounds in cells, single-photon laser scanning confocal microscopy was carried out. For this purpose, the prostate cancer (PC-3) cells were incubated for 15 minutes with each of the products at 37 ^{o}C and imaged. PC-3 cells were grown according to standard serial passage protocols, placed onto glass bottom dishes and allowed to grow to a suitable confluence.

The obtained images confirm the uptake by cells of compounds **2**, **5**, **6**, **13** and **17**, with the majority of their emission lying within the green and red channels. Furthermore, they do not seem to damage the cell morphology. The images show that for compounds **2**, **5** and **6** there is strong emission in the green and red channels of the spectra when the probe is excited at 488 nm, while only green emissions can be seen using 405 nm lasers (*Figure 2.39-2.40* and *Appendix A*).

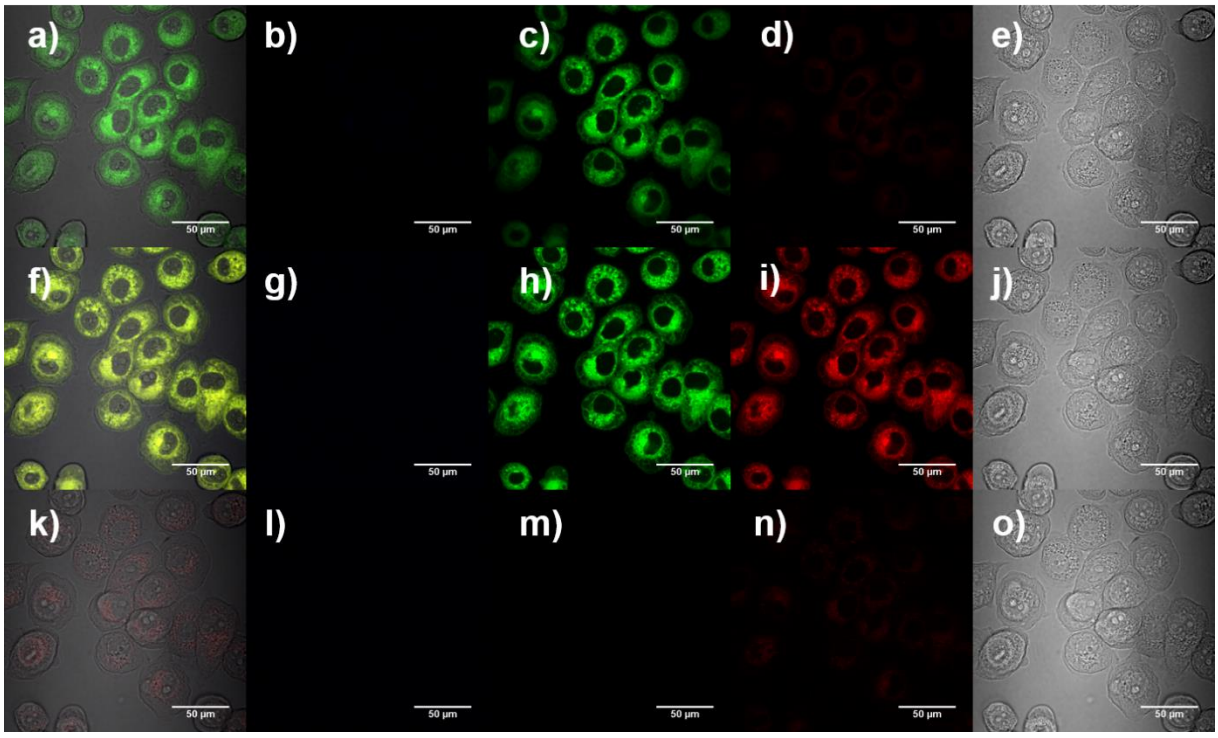

Figure 2.39. Single-photon laser scanning confocal microscopy of PC-3 cells incubated for 15 minutes at 37 ^{o}C with compound **2**. Final concentration: 100 μM in serum-free medium (1% DMSO). a-e) λ_{ex} = 405 nm; f-j) λ_{ex} = 488 nm; k-o) λ_{ex} = 561 nm. a, f, k) overlay of DIC-blue-green-red channels; b, g, l) blue channel (λ_{em} = 417-477 nm); c, h, m) green channel (λ_{em} = 500-550 nm); d, i, n) red channel (λ_{em} = 570-750 nm); e, j, o) DIC channel. Scale bar: 50 μm.

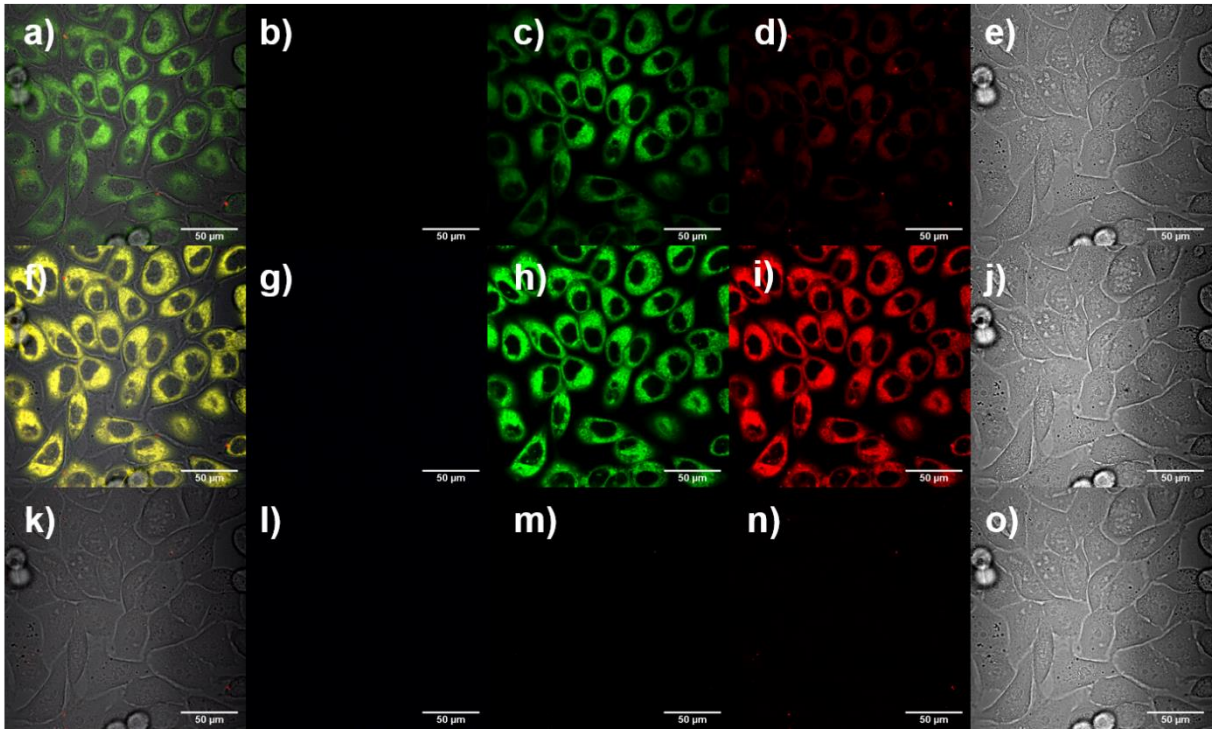

Figure 2.40. Single-photon laser scanning confocal microscopy of PC-3 cells incubated for 15 minutes at 37 ºC with compound **6**. Final concentration: 100 µM in serum-free medium (1% DMSO). a-e) λ_{ex} = 405 nm; f-j) λ_{ex} = 488 nm; k-o) λ_{ex} = 561 nm. a, f, k) overlay of DIC-blue-green-red channels; b, g, l) blue channel (λ_{em} = 417-477 nm); c, h, m) green channel (λ_{em} = 500-550 nm); d, i, n) red channel (λ_{em} = 570-750 nm); e, j, o) DIC channel. Scale bar: 50 µm.

Colocalisation studies with known, commercial dyes (Invitrogen) were carried out in order to understand how some of these compounds localise throughout the cell cytoplasm and organelles. For this purpose, trackers were used, in particular LysoTracker Red and Endoplasmic Reticulum (ER)-Tracker Red (*Figure 2.41*). In order to carry out these studies, prostate cancer cells were incubated for 30 minutes with the corresponding tracker at 37 ºC, after which they were washed and control images were taken of the cells with the tracker only. Following this, the compound of interest was added to the cells and these were incubated again for 20 minutes at 37 ºC. More images were acquired of the cells containing both the new product and the tracker (*Appendix A*).

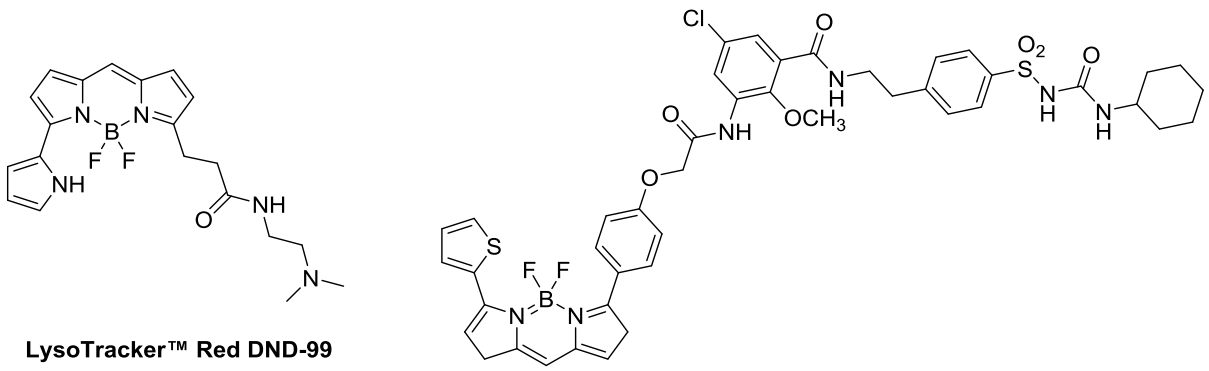

Figure 2.41. Structures of LysoTracker Red (left) and ER-Tracker Red (right) (Invitrogen).

When the LysoTracker Red (λ_{ex} = 577 nm, λ_{em} = 590 nm) was used, small emission in the blue channel could be observed when the probe was excited with a laser of 405 nm wavelength, apart from the emission in the green and red channels at 405 and 488 nm (*Figure 2.42*). When the ER-Tracker Red (λ_{ex} = 587 nm, λ_{em} = 615 nm) was used, emission in the red channel could be observed when the probe was excited with lasers of 405, 488 and 561 nm wavelength, apart from the normal emission due to the fluorophore in the green and red channels for lasers of 405 and 488 nm (*Figure 2.43*). From these studies, it can be concluded that the compounds **2**, **5** and **6** exhibit very strong fluorescence, they all enter the cells and distribute mainly in the cytoplasm, especially in the endoplasmic reticulum. There is no emission from the nuclei of the cells, and compounds **5** and **6** showed some precipitation during the incubation period, as can be seen from the confocal microscopy images.

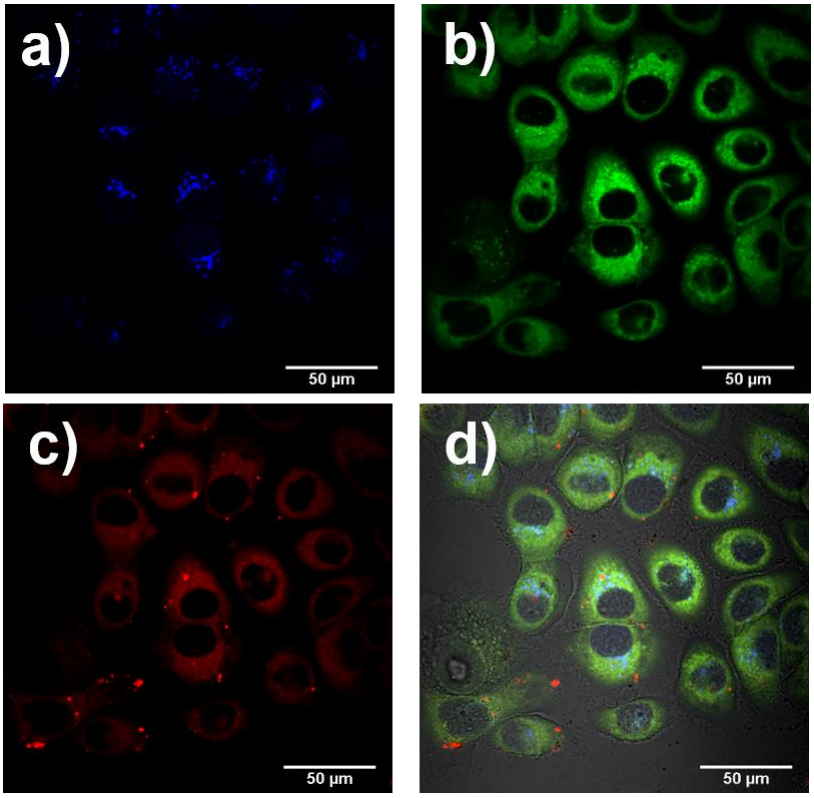

Figure 2.42. Single-photon laser scanning confocal microscopy of PC-3 cells incubated for 30 minutes at 37 ºC with LysoTracker Red, and 20 minutes with compound **5**. Final concentration: 100 µM in serum-free medium (1% DMSO) solution of compound **5**, with a 100 nM solution of LysoTracker Red. λ_{ex} = 488 nm. a) Blue channel (λ_{em} = 417-477 nm); b) green channel (500-550 nm); c) red channel (λ_{em} = 570-750 nm); d) overlay of DIC-blue-green-red channels. Scale bar: 50 µm.

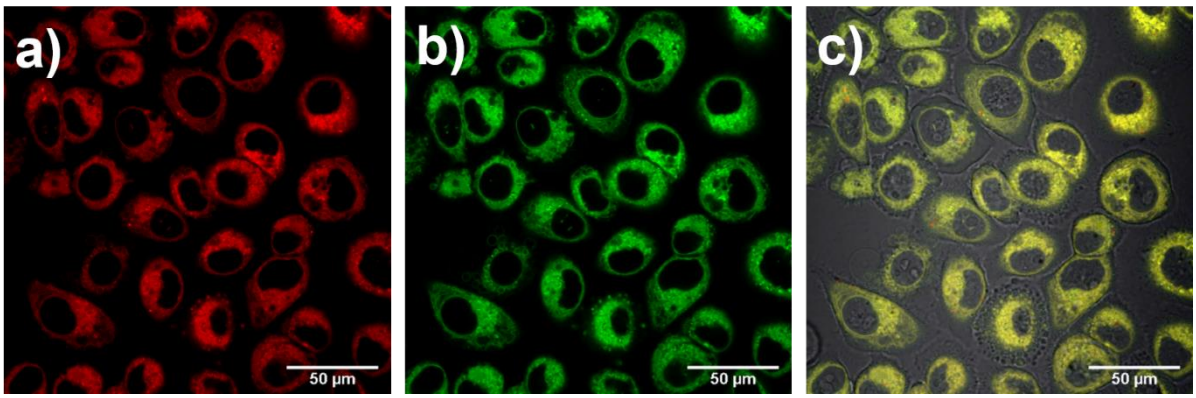

Figure 2.43. Single-photon laser scanning confocal microscopy of PC-3 cells incubated for 30 minutes at 37 ºC with ER-Tracker Red, and 20 minutes with compound **6**. Final concentration: 100 µM in serum-free medium (1% DMSO) solution of compound **6**, with a 1 µM solution of ER-Tracker Red. λ_{ex} = 488 nm. a) Red channel (λ_{em} = 570-750 nm); b) green channel (500-550 nm); c) overlay of DIC-blue-green-red channels. Scale bar: 50 µm.

Moreover, compounds **13** and **17** were also tested in prostate cancer cells by laser scanning confocal microscopy studies. The same incubation and imaging protocols previously described were followed. In the case of compound **13**, strong emission can be observed in the green channel when the probe is excited with lasers of 405 and 488 nm. There is some minor emission in the red channel for the three lasers used – 405, 488 and 561 nm wavelengths. This is probably due to precipitation of the compound, which was not completely soluble in the serum-free medium used for the microscopy studies (*Figure 2.44*).

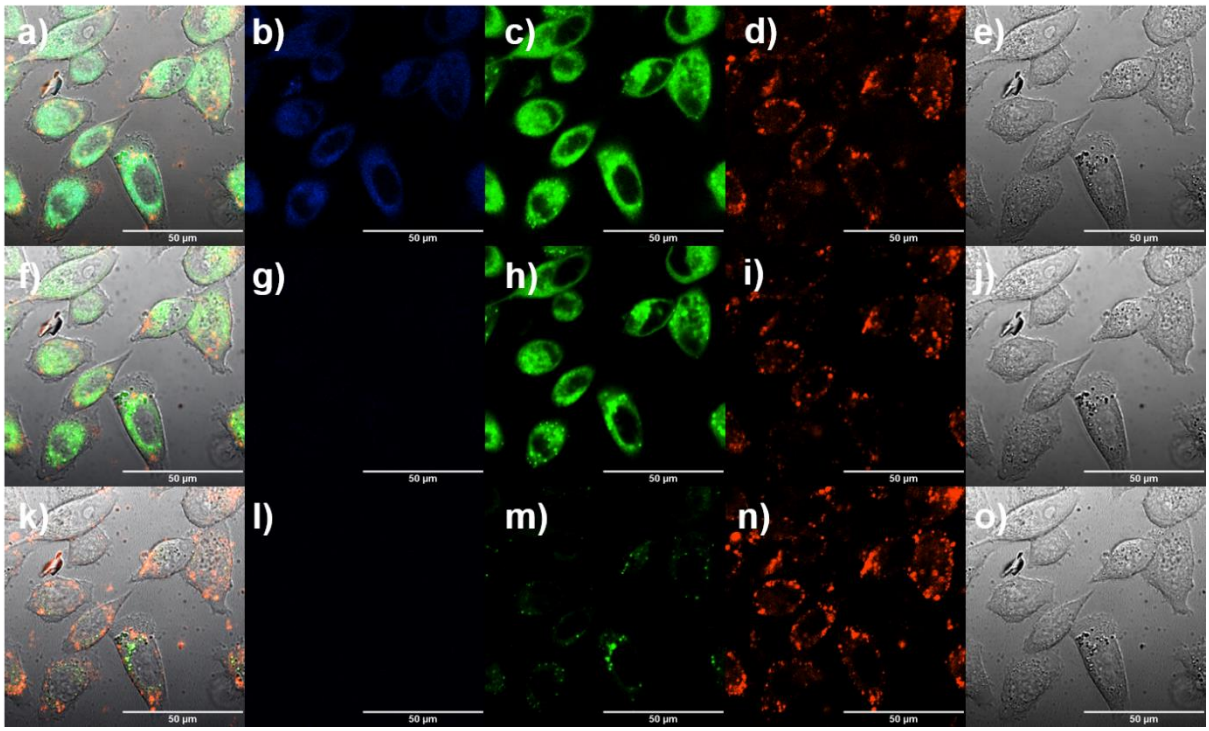

Figure 2.44. Single-photon laser scanning confocal microscopy of PC-3 cells incubated for 15 minutes at 37 ºC with compound **13**. Final concentration: 100 µM in serum-free medium (1% DMSO). a-e) λ_{ex} = 405 nm; f-j) λ_{ex} = 488 nm; k-o) λ_{ex} = 561 nm. a, f, k) overlay of DIC-blue-green-red channels; b, g, l) blue channel (λ_{em} = 417-477 nm); c, h, m) green channel (λ_{em} = 500-550 nm); d, i, n) red channel (λ_{em} = 570-750 nm); e, j, o) DIC channel. Scale bar: 50 µm.

Compound **17** showed to have strong emission in the green channel for lasers of 405 and 488 nm excitation wavelength, and some less strong emission for 561 nm (*Figure 2.45*). Weak emission in the blue channel when the probe is excited at 405 nm can also be observed. For this compound there is also some emission in the red channel, but this is probably due, as in the previous case, to precipitation of the compound in the cells, which is not completely soluble in the serum-free medium used for the analysis, and required extra phosphate buffered saline (PBS) washing to remove the excess of product.

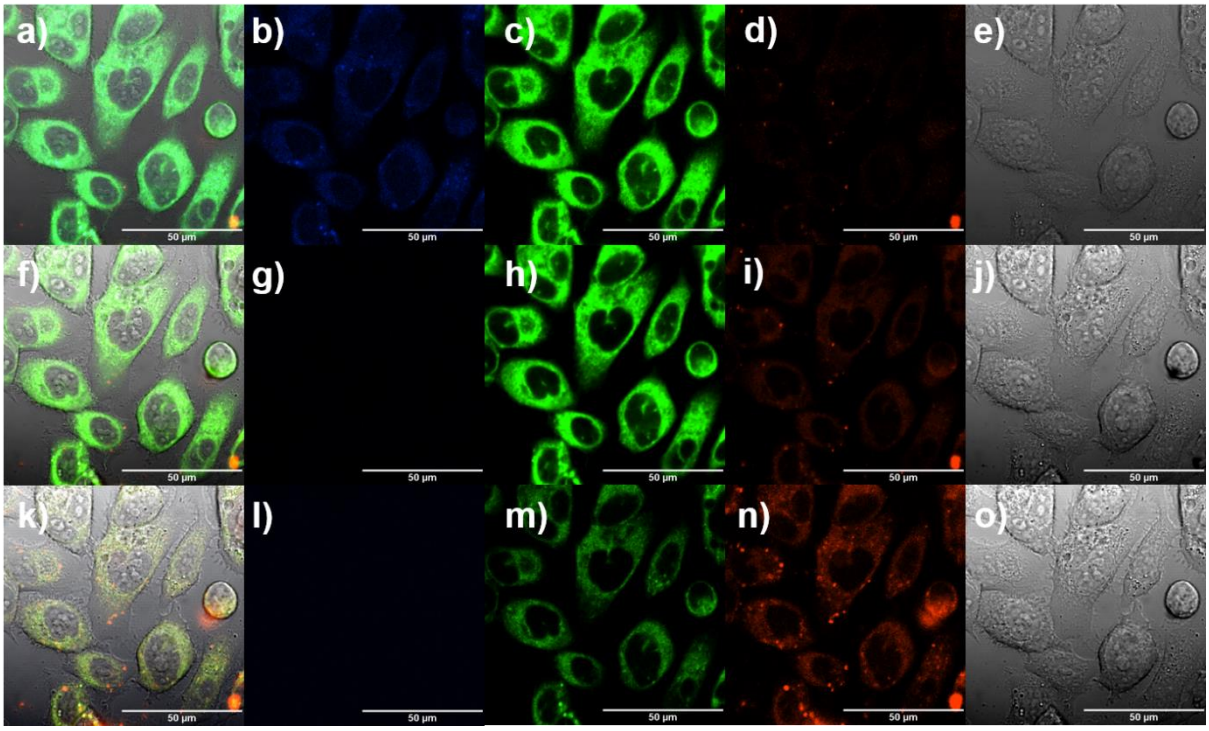

Figure 2.45. Single-photon laser scanning confocal microscopy of PC-3 cells incubated for 15 minutes at 37 ºC with compound **17**. Final concentration: 100 µM in serum-free medium (1% DMSO). a-e) λ_{ex} = 405 nm; f-j) λ_{ex} = 488 nm; k-o) λ_{ex} = 561 nm. a, f, k) overlay of DIC-blue-green-red channels; b, g, l) blue channel (λ_{em} = 417-477 nm); c, h, m) green channel (λ_{em} = 500-550 nm); d, i, n) red channel (λ_{em} = 570-750 nm); e, j, o) DIC channel. Scale bar: 50 µm.

The confocal microscopy studies showed that the compounds enter the cells and they do not modify the cell morphology. These findings constitute a promising result for using BODIPY-based derivatives as synthetic scaffolds for multimodality imaging applications, with the possibility of adding more functional molecules in further studies, such as a peptide or a radiochelator.

2.12. Investigations using two-photon fluorescence lifetime imaging microscopy

Fluorescence lifetime imaging microscopy (FLIM) was carried out with the most promising new fluorescent compounds to study their lifetime characteristics in both solution and in prostate cancer cells. The first experiments carried out were the testing of the lifetime of the new fluorophores in solution using DMSO as solvent. Time-correlated single-photon counting (TCSPC) was used for this purpose, followed by a FLIM study *in vitro* using PC-3 cells. All these experiments were carried out at the Rutherford Appleton Laboratory in the Central Laser Facilities (CLF) by Dr. Vincenzo Mirabello and Dr. Haobo Ge.

The products were tested by TCSPC (*Table 2.9*). Each photon detected and collected in TCSPC was plotted to calculate the fluorescence lifetime. The results obtained from TCSPC (*Figure 2.46*) consist of three components: χ^2, τ_n (ps) that is the lifetime, and τ_n (%) which is the lifetime percentage (*n* can be more than one if there is more than one component modelled). These last two components represent the duration within which the corresponding molecule exists in an excited state. Finally, τ_m is the overall lifetime. It can be observed that each compound can be detected in the solution and has a relatively high number of counts, especially compounds **2**, **13** and **17**.

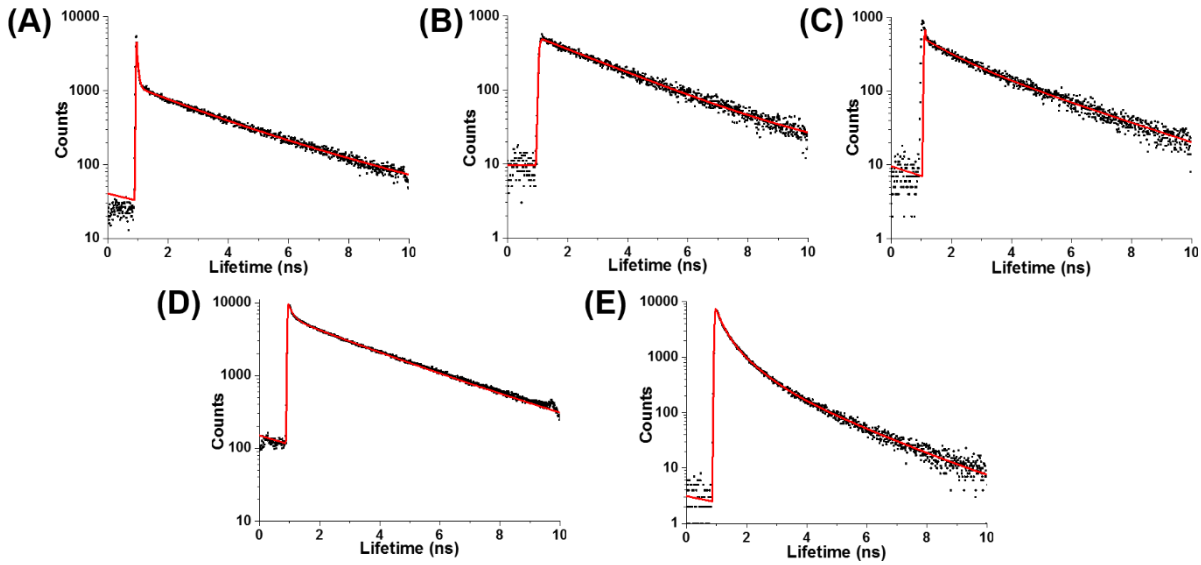

Figure 2.46. TCSPC decay and fitting curves for compounds **2 (A)**, **5 (B)**, **6 (C)**, **13 (D)**, and **17 (E)**, tested using (A), (D), (E) 10 mM and (B), (C) 100 μM solutions in DMSO excited at 810 nm with a laser power between 0.5 and 1.27 mW. Black dots are the measured counts at different times and the red lines are the fitting curves.

Table 2.9. Two-photon TCSPC data for compounds **2**, **5**, **6**, **13** and **17**. 10 mM solutions in DMSO were used for compounds **2**, **13** and **17**, and 100 μM solutions in DMSO for compounds **5** and **6**. They were excited at λ_{ex} = 810 nm with a laser power between 0.5 and 1.27 mW.

Compound	χ^2	τ_1 (ps)	a_1 (%)	τ_2 (ps)	a_2 (%)	τ_3 (ps)	a_3 (%)	τ_m (ps)
2	1.21	51	77.8	2238	15.0	4911	7.2	730
5	1.02	2655	100.0	-	-	-	-	2655
6	1.16	1133	43.2	3326	56.8	-	-	2379
13	1.50	155	39.4	2217	35.4	3834	25.3	1814
17	1.19	214	57.2	639	34.8	1930	7.9	1364

From all the compounds tested in solution, compound **5** has only one component for the fluorescence lifetime. Compound **6** has two components, and compounds **2**, **13** and **17** have three components in major or minor contribution. The τ_2 and τ_3 can be due to interactions of the compounds with the solvent (dimethylsulfoxide), or to the existence of isomers or pH-dependent protonated and non-protonated species.

There are three different ranges of values for χ^2: when it is 1.0, the fitting is optimal; values between 1.0 and 1.3 indicate incomplete single exponential fit; while if it is higher than 1.5, it suggests that there was significant noise within the TCSPC set-up or more than on the decay profile of the compound and the data cannot be considered completely reliable. According to this, all the results obtained for the tested molecules are reliable except for compound **13**, which has a χ^2 of 1.50. Data collected for compound **5** has the best fit, with a χ^2 of 1.02.

The two-photon excitation fluorescence spectra of solutions of the compounds in DMSO were collected in order to study the emission properties of these products when excited in a two-photon excitation regime. The curves for the five compounds tested (**2**, **5**, **6**, **7** and **13**) exhibited a sharp absorption peak at approximately 550 nm wavelength (*Figure 2.47*).

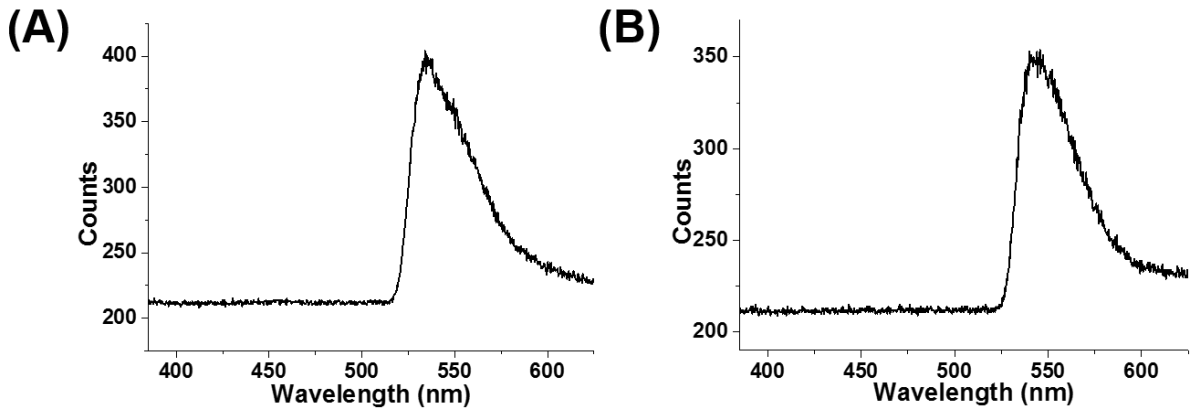

Figure 2.47. Two-photon excitation fluorescence spectra of solutions of **2 (A)**, and **13 (B)**, tested using 10 mM solutions in DMSO and excited at 810 nm with laser power between 0.5 and 1.27 mW.

The two-photon fluorescence spectra of these compounds in PC-3 cells were recorded at one or two different sites of the cells and at the background, which were imaged using single-photon laser scanning confocal microscopy (*Figure 2.48*). Compounds **2** and **13** were incubated in cells with LysoTracker Red and this can be seen in the curves, with a second peak emerging between 600 and 650 nm. Since all the tested products are BODIPY derivatives based on compound **1** they all have emission at the same region of the spectrum, between 500 and 550 nm.

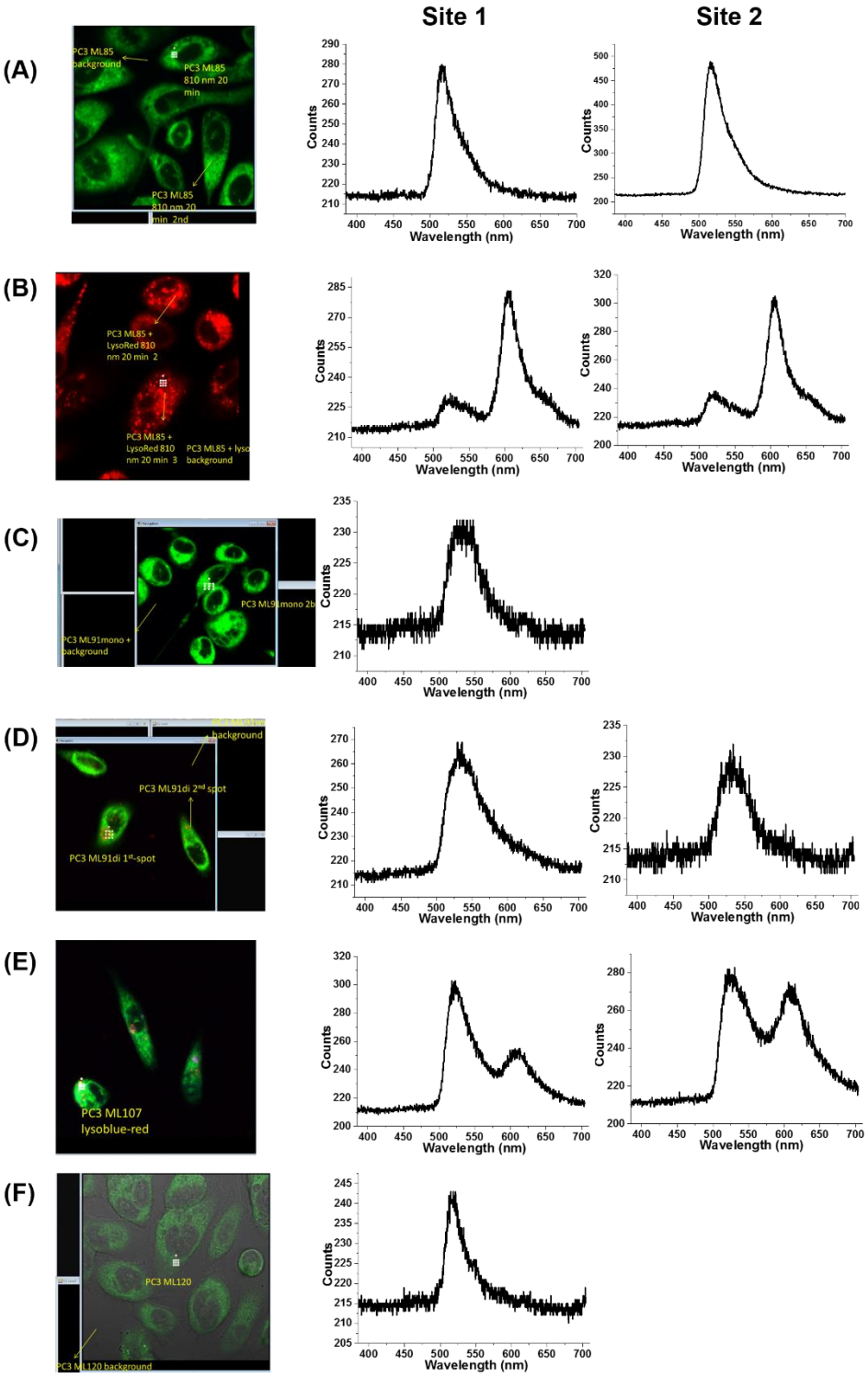

Figure 2.48. Single-photon laser scanning confocal fluorescence microscopy, and two-photon excitation fluorescence spectra of PC-3 cells treated with 10 mM solutions of each compound in 1% DMSO. λ_{ex} = 810 nm. Cells were incubated at 37 ºC for 20 minutes with **2 (A)**, **2 + LysoTracker Red (B)**, **5 (C)**, **6 (D)**, **13 + LysoTracker Red (E)**, and **17 (F)**.

The two-photon FLIM mapping and intensities in PC-3 cells were measured for compounds **2**, **5**, **6**, **13**, **17** and also **2** and **3** containing LysoTracker Red (*Figure 2.49*). It can be observed that these compounds enter the cells and accumulate mainly in the cytoplasm while emitting fluorescence. Fluorescence lifetime distribution curves are the overall fluorescence lifetime decays summarised from the fluorescence lifetime mapping in PC-3 cells. From these plots, it can be seen that the fluorescence lifetime distribution for compound **2** is between 2.5 and 3.5 ns, approximately. When it was added to the cells with a LysoTracker Red, which localises within the lysosomes, the fluorescence lifetime distribution of the same compound showed to be between approximately 1.5 and 2.5 ns. The maximum number of counts is at 2.0 ns, and the peak has a tail which is due to the tracker. Control studies of the commercial LysoTracker Red alone showed that it has a fluorescence lifetime distribution between 2.0 and 4.5 ns, with a maximum number of counts at 3.0 ns. For compound **5**, the fluorescence lifetime distribution is between 0.5 and 1.5 ns, approximately, with a tail that goes up to 3.0 ns but with a much lower number of counts. Compound **6** has a lifetime distribution between 1.6 and 2.8 ns, with a maximum number of counts at approximately 2.0 ns. Compound **13** alone and with a LysoTracker Red has a fluorescence lifetime distribution between approximately 0 and 2.0 ns, with a maximum number of counts at 0.5 ns. Finally, compound **17** has a fluorescence lifetime distribution between 2.0 and 3.5 ns, with a maximum number of counts around 2.5 ns. The number of counts is high for all the studied products, in particular for compounds **2**, **5** and **17**. All the compounds have two different components for the lifetime distribution in cells (*Table 2.10*), which can be seen in major or minor proportion in the fluorescence lifetime distribution curves. These are due to different interactions of the molecules with the solvent. In all the cases, τ_1 is the major component of the fluorescence lifetime, but for compound **6**, τ_1 and τ_2 exist in an almost 1:1 ratio. Moreover, the data collected are reliable, since all the values for χ^2 fall within the 1.0 – 1.3 range.

Table 2.10. Two-photon TCSPC data for compounds **2**, **2 + LysoTracker Red, 5**, **6**, **13**, **13 + LysoTracker Red** and **17**, tested using 10 mM solutions in DMSO in PC-3 cells excited at λ_{ex} = 810 nm with a laser power between 0.5 and 4.5 mW.

Compound	χ^2	τ_1 (ps)	a_1 (%)	τ_2 (ps)	a_2 (%)	τ_m (ps)
2	1.06	1384	71.4	6905	28.6	2963
2 + LysoTracker	1.02	1631	67.2	5693	32.8	2963
5	1.07	257	86.8	5077	13.2	895
6	1.05	384	50.9	2802	49.1	1570
13	1.13	116	90.2	1531	9.8	255
13 + LysoTracker	1.25	162	83.2	1662	16.8	414
17	1.10	1955	73.1	5340	26.9	2866

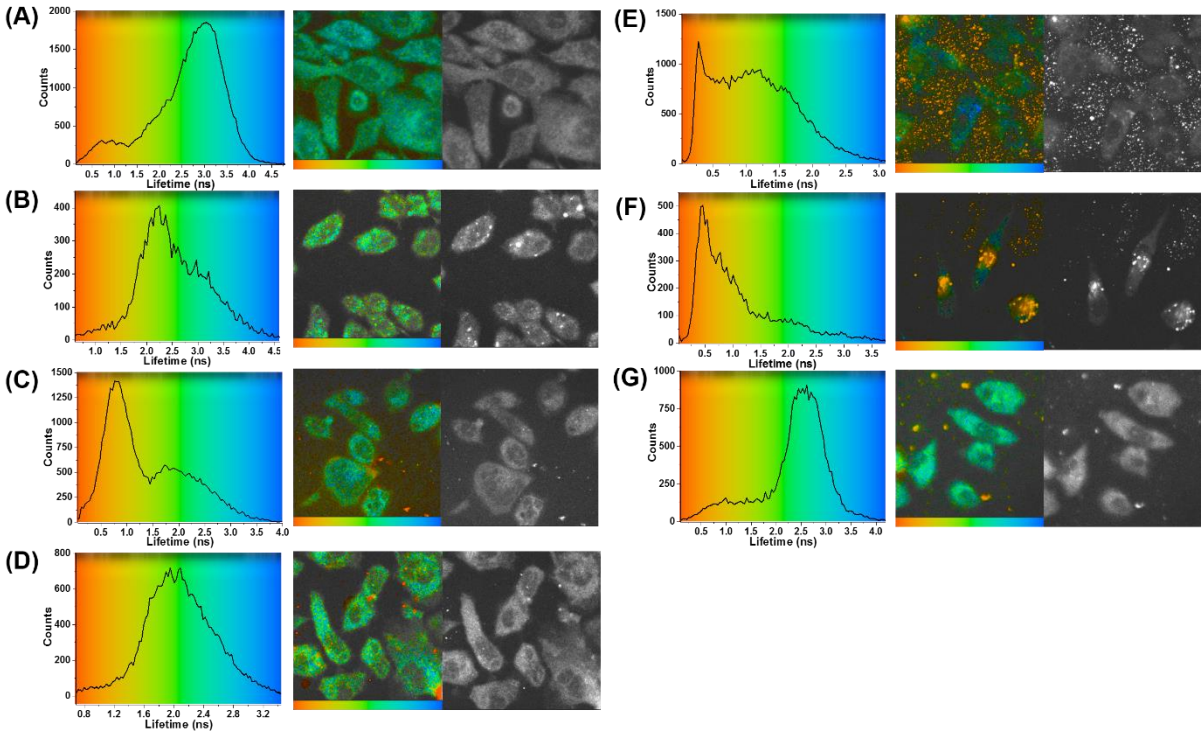

Figure 2.49. Fluorescence lifetime distribution curves, fluorescence lifetime mapping of τ_m, and two-photon fluorescence intensity diagram of PC-3 cells treated with 10 mM solutions of each compound in 1% DMSO. λ_{ex} = 810 nm. Cells were incubated at 37 ºC for 20 minutes with **2 (A)**, **2 + LysoTracker Red (B)**, **5 (C)**, **6 (D)**, **13 (E)**, **13 + LysoTracker Red (F)**, and **17 (G)**.

2.13. Cell viability by MTT assays

The use of tetrazolium salts is a commonly applied technique in cell biology to measure metabolic activity and cell viability and estimate the IC_{50} values of the drug candidates. The mechanism of action of MTT consists in the cellular uptake of the MTT dye, that is reduced by nicotinamide species (such as NAD(P)H) present in the mitochondria of the cells to form the formazan species, which are insoluble in the serum-free medium, and dimethylsulfoxide needs to be added in order to solubilise them and measure the absorbance (*Scheme 2.20*). The concentration can then be calculated from the absorbance, and the number of viable cells in the presence of a compound of interest can be calculated.[34-36]

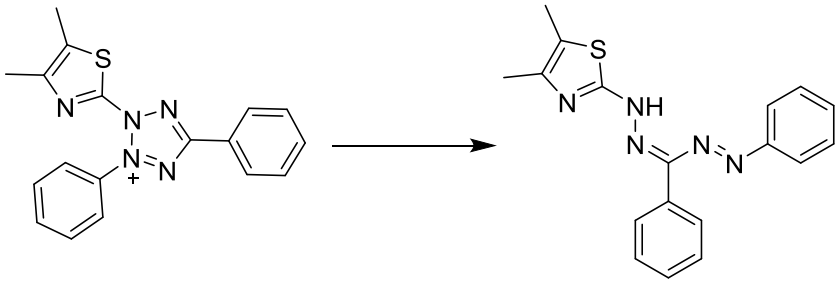

MTT **Formazan**

Scheme 2.20. Formation of the formazan dye detected in MTT assays by biological reduction of this molecule.

MTT (3-(4,5-dimethylthiazol-2-yl)-2,5-diphenyltetrazolium bromide) assays were carried out in order to estimate the IC_{50} value of the tripodal organic core used as starting material (compound **1**), the BODIPY carboxylic acid derivative (compound **2**), and the tripodal ligand with one and two of the bromomethyl arms substituted for a BODIPY derivative (compounds **5** and **6**, respectively) (*Figure 2.50*). The IC_{50} value corresponds to the half maximal inhibitory concentration, and it is a measure that indicates how effective a substance is to inhibit a specific biological process. In this case it refers to what concentration of compound is needed to kill half of the population of cells. MTT assays were carried out with the assistance of Dr. Haobo Ge.

In order to carry out these assays, PC-3 cells in 96 well plates were treated with each of the compounds in serum medium (1% DMSO) at different concentrations for 48 hours at 37 ^{o}C. Then, MTT was added to the cells and incubated for 2 hours. The insoluble formazan species was solubilised with 100 μL of DMSO. A spectrophotometer was used to quantify the absorbance of the solution by the cells (with an absorption wavelength of 570 nm) and a dose response curve was plotted to calculate the IC_{50} of each of the products (*Table 2.11*).

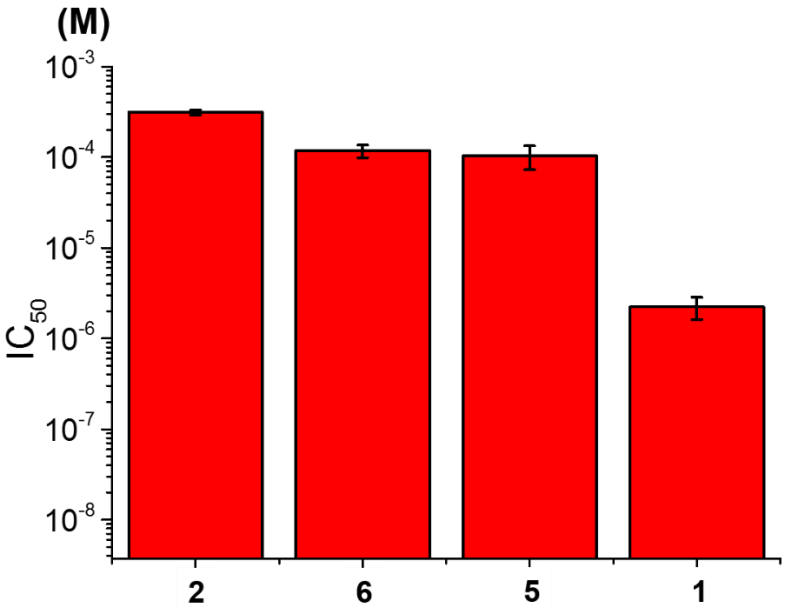

Figure 2.50. IC_{50} in PC-3 cells after 48 hours of treatment at 37 ºC with compounds **1**, **2**, **5** and **6**. (The data were collected from six repeated measurements on the same day; N = 1).

It can be seen that the tripodal ligand with the three bromomethyl arms (compound **1**) is the one with the lowest IC_{50}, meaning that it is the most toxic compound for the cells out of the four products tested here. The less cytotoxic product is the BODIPY derivative (compound **2**). When the bromomethyl arms of the starting tripodal ligand are substituted by one and two BODIPY derivatives, respectively (compounds **5** and **6**), the toxicity of the products decreases. It can be concluded that the three bromomethyl arms of compound **1** make it more toxic, and when these are substituted by the synthesised BODIPY derivative (compound **2**), which has very low cytotoxicity, the toxicity of the tripodal derivatives is also decreased.[37] Also, smaller molecules are usually more cytotoxic than larger molecules because they can be more easily up taken by cells.[38]

Table 2.11. Summary of compounds tested in MTT assays using PC-3 cells and IC_{50} values found for each of them.

Compound	IC_{50} / M
1	$(2.2 \pm 0.6)\cdot10^{-6}$
2	$(3.1 \pm 0.2)\cdot10^{-4}$
5	$(1.0 \pm 0.3)\cdot10^{-4}$
6	$(1.2 \pm 0.2)\cdot10^{-4}$

2.14. Summary of Chapter 2

Chapter 2 describes an investigation into the functionalisation of a symmetric tripodal organic core (compound **1**). After investigating several different reaction conditions and several types of precursor molecules, it was seen that the reaction between compound **1** and many carboxylic acid derivatives was successful. The mono-, di- and trisubstituted products were isolated in different yields and some of the unreacted tripodal starting material could be recovered. Reactions generally consisted in a nucleophilic substitution where the bromide group leaves the molecule. Moreover, the reaction conditions were optimised in order to make this reaction more compatible for the use of biomolecules, which can usually not stand high temperatures for prolonged periods of time. It was seen that using lower temperatures and a higher number of equivalents of compound **1**, the formation of the monosubstituted product was favoured. However, the step-wise functionalisation cannot be completely achieved and a mixture of products is obtained in all the cases.

A BODIPY derivative containing a carboxylic acid group was synthesised, characterised and incorporated as a tag. This was the fluorophore of choice due to its high fluorescence quantum yield and biocompatibility. The tripodal starting material containing three “arms” was successfully trisubstituted, forming three new ester bonds, with a succinate linker, an azido terminal linker and a BODIPY derivative. The azido terminal linker was attached with the idea of performing “click” chemistry using a DBCO-substituted deferoxamine derivative, but this was not successfully achieved. The succinate linker was attached with the idea of using it to include a peptide to the system, as will be described in *Chapter 3*. All the newly synthesised compounds were characterised by NMR spectroscopy, MS, FT-IR, HPLC, and UV/visible and fluorescence spectroscopy, when necessary.

Several other functionalisation reactions were attempted, including the functionalisation of the tripodal core with the fluorophore fluorescein-5-thiosemicarbazide. This reaction was tried using different conditions and in some cases a peak corresponding to the expected molecule could be observed in the mass spectrum, however in most cases the isolated solid could not be fully characterised.

The functionalisation of DFO probed to be feasible, and two deferoxamine derivatives were synthesised. Radiolabelling with zirconium-89 was carried out, yielding a radio-incorporation factor of ≥ 99.9% in both cases, which is promising in terms of new radiotracers design.

Imaging in PC-3 cell line was carried out using laser scanning confocal microscopy and FLIM, with single-photon and two-photon excitation regimes. The confocal microscopy results showed that the synthesised molecules are up taken by the living cells investigated, with good penetrability through the cell membrane, although they do not enter the nuclei. All of these compounds are retained in the cytoplasm and do not damage or alter the cell morphology. Colocalisation studies were performed using LysoTracker Red and ER-Tracker Red in PC-3 cells, and these showed how the tested molecules localise mainly in the endoplasmic reticulum.

FLIM experiments were carried out to determine the fluorescence lifetime, and the lifetime components distributions were measured for solutions of the fluorescent molecules in DMSO. In TCSPC, the fluorescence lifetime was observed, in all the cases with two or more components exponential fitting functions using standard protocols, consistent with previous investigations carried out by Prof. Stanley Botchway and his team at the Research Complex at Harwell.[39]

Toxicity assays were carried out on the tripodal starting material (compound **1**) and this substituted with one and two BODIPY derivatives (compounds **5** and **6**, respectively). They showed that by substituting the bromomethyl arms of the starting molecule with the fluorophore, the toxicity decreases significantly, making the materials more biocompatible and less toxic to the cancer cells investigated.

In summary, this new type of fluorophores show promising properties to be used as synthetic scaffolds for molecular imaging probes for *in vitro* studies, with relatively low toxicity levels and comparable with recently reported probes,[11] and opening up the possibility of further functionalisation.

2.15. References for Chapter 2

1. E. Oliveira, E. Bértolo, C. Núñez, V. Pilla, H. M. Santos, J. Fernández-Lodeiro, A. Fernández-Lodeiro, J. Djafari, J. L. Capelo and C. Lodeiro, *ChemistryOpen*, 2018, **7**, 9-52.
2. A. Wilson, G. Gasparini and S. Matile, *Chem. Soc. Rev.*, 2014, **43**, 1948-1962.
3. C. Pérez-Medina, D. Abdel-Atti, Y. Zhang, V. A. Longo, C. P. Irwin, T. Binderup, J. Ruiz-Cabello, Z. A. Fayad, J. S. Lewis, W. J. M. Mulder and T. Reiner, *J. Nucl. Med.*, 2014, **55**, 1706-1711.
4. K. J. Wallace, R. Hanes, E. Anslyn, J. Morey, K. V. Kilway and J. Siegel, *Synthesis*, 2005, 2080-2083.
5. C. Bernhard, C. Goze, Y. Rousselin and F. Denat, *Chem. Commun.*, 2010, **46**, 8267-8269.
6. A. Loudet and K. Burgess, *Chem. Rev.*, 2007, **107**, 4891-4932.
7. Y. Ni and J. Wu, *Org. Biomol. Chem.*, 2014, **12**, 3774-3791.
8. T. Kowada, H. Maeda and K. Kikuchi, *Chem. Soc. Rev.*, 2015, **44**, 4953-4972.
9. A. Cui, X. Peng, J. Fan, X. Chen, Y. Wu and B. Guo, *J. Photochem. Photobiol.*, 2007, **186**, 85-92.
10. P. A. Waghorn, M. W. Jones, A. McIntyre, A. Innocenti, D. Vullo, A. L. Harris, C. T. Supuran and J. R. Dilworth, *Eur. J. Inorg. Chem.*, 2012, **2012**, 2898-2907.
11. L. H. Davies, B. B. Kasten, P. D. Benny, R. L. Arrowsmith, H. Ge, S. I. Pascu, S. W. Botchway, W. Clegg, R. W. Harrington and L. J. Higham, *Chem. Commun.*, 2014, **50**, 15503-15505.
12. M. L. Bender, *Chem. Rev.*, 1960, **60**, 53-113.
13. J.-S. Lee, N.-y. Kang, Y. K. Kim, A. Samanta, S. Feng, H. K. Kim, M. Vendrell, J. H. Park and Y.-T. Chang, *J. Am. Chem. Soc.*, 2009, **131**, 10077-10082.
14. J. P. Holland, V. Divilov, N. H. Bander, P. M. Smith-Jones, S. M. Larson and J. S. Lewis, *J. Nucl. Med.*, 2010, **51**, 1293-1300.
15. X. Deng, C. Friedmann and J. Lahann, *Angew. Chem. Int. Ed.*, 2011, **50**, 6522-6526.
16. T. Friscic, *Chem. Soc. Rev.*, 2012, **41**, 3493-3510.
17. W. Rizvi, E. Khwaja, S. Siddiqui, N. V. S. D. K. Bhupathiraju and C. M. Drain, *J. Chem. Ed.*, 2018, **95**, 164-168.
18. S. K. Yang and M. Weck, *Soft Matter*, 2009, **5**, 582-585.
19. J. Clayden, N. Greeves and S. Warren, in *Organic Chemistry*, Oxford University Press, New York, 2nd edn., 2012, pp. 222-239.
20. A. J. Vernall, L. A. Stoddart, S. J. Briddon, S. J. Hill and B. Kellam, *J. Med. Chem.*, 2012, **55**, 1771-1782.
21. J. P. Holland, PhD Thesis, University of Oxford, 2008.
22. V. Becker, S. von Delius, M. Bajbouj, A. Karagianni, R. M. Schmid and A. Meining, *Gastrointest. Endosc.*, 2008, **68**, 319-323.
23. H. Komatsu, N. Iwasawa, D. Citterio, Y. Suzuki, T. Kubota, K. Tokuno, Y. Kitamura, K. Oka and K. Suzuki, *J. Am. Chem. Soc.*, 2004, **126**, 16353-16360.
24. W.-C. Sun, K. R. Gee, D. H. Klaubert and R. P. Haugland, *J. Org. Chem.*, 1997, **62**, 6469-6475.
25. N. O. McHedlov-Petrossyan, T. A. Cheipesh, S. V. Shekhovtsov, A. N. Redko, V. I. Rybachenko, I. V. Omelchenko and O. V. Shishkin, *Spectrochim. Acta A*, 2015, **150**, 151-161.
26. P. T. Corbett, J. Leclaire, L. Vial, K. R. West, J.-L. Wietor, J. K. M. Sanders and S. Otto, *Chem. Rev.*, 2006, **106**, 3652-3711.
27. J. Joseph, N. L. Mary and R. Sidambaram, *Synth. React. Inorg. M.*, 2010, **40**, 930-933.
28. M. J. W. D. Vosjan, L. R. Perk, G. W. M. Visser, M. Budde, P. Jurek, G. E. Kiefer and G. A. M. S. van Dongen, *Nat. Protocols*, 2010, **5**, 739-743.
29. J. P. Holland and N. Vasdev, *Dalton Trans.*, 2014, **43**, 9872-9884.
30. S. Fery-Forgues and D. Lavabre, *J. Chem. Ed.*, 1999, **76**, 1260.

31. M. A. Brouwer, *Pure Appl. Chem.*, 2011, **83**, 2213-2228.
32. A. T. R. Williams, S. A. Winfield and J. N. Miller, *Analyst*, 1983, **108**, 1067-1071.
33. R. Ziessel, G. Ulrich and A. Harriman, *New J. Chem.*, 2007, **31**, 496-501.
34. M. V. Berridge, P. M. Herst and A. S. Tan, *Biotechnol. Annu. Rev.*, 2005, **11**, 127-152.
35. T. Mosmann, *J. Immunol. Methods*, 1983, **65**, 55-63.
36. M. V. Berridge and A. S. Tan, *Arch. Biochem. Biophys.*, 1993, **303**, 474-482.
37. S. Zhang, T. Wu, J. Fan, Z. Li, N. Jiang, J. Wang, B. Dou, S. Sun, F. Song and X. Peng, *Org. Biomol. Chem.*, 2013, **11**, 555-558.
38. N. J. Yang and M. J. Hinner, *Methods Mol. Biol.*, 2015, **1266**, 29-53.
39. P. A. Waghorn, M. W. Jones, M. B. M. Theobald, R. L. Arrowsmith, S. I. Pascu, S. W. Botchway, S. Faulkner and J. R. Dilworth, *Chem. Sci.*, 2013, **4**, 1430-1441.

Chapter 3. Synthesis of imaging agents incorporating a bombesin derivative

3.1. Overview of Chapter 3

This Chapter describes the synthesis and spectroscopic characterisation of a rarely-explored peptide as a gastrin-releasing peptide (GRP) targeting analogue, the [7-13] fragment of bombesin, and its attempted incorporation into a fluorescent tripodal system with two BODIPY units described in the previous chapter (*Figure 3.1*). This fragment was chosen instead of the full length peptide due to the fact that it can be more easily synthesised and characterised, and it conserves the properties of the full length sequence. Moreover, a deferoxamine conjugate containing this shorter bombesin-based amino acid sequence has also been synthesised and characterised spectroscopically.

Bombesin is a peptide formed by 14 amino acids, and it is an amphibian homolog to the mammalian gastrin-releasing peptide, which has been studied as a targeting ligand for diagnosis and therapy of GRP positive tumours.[1]

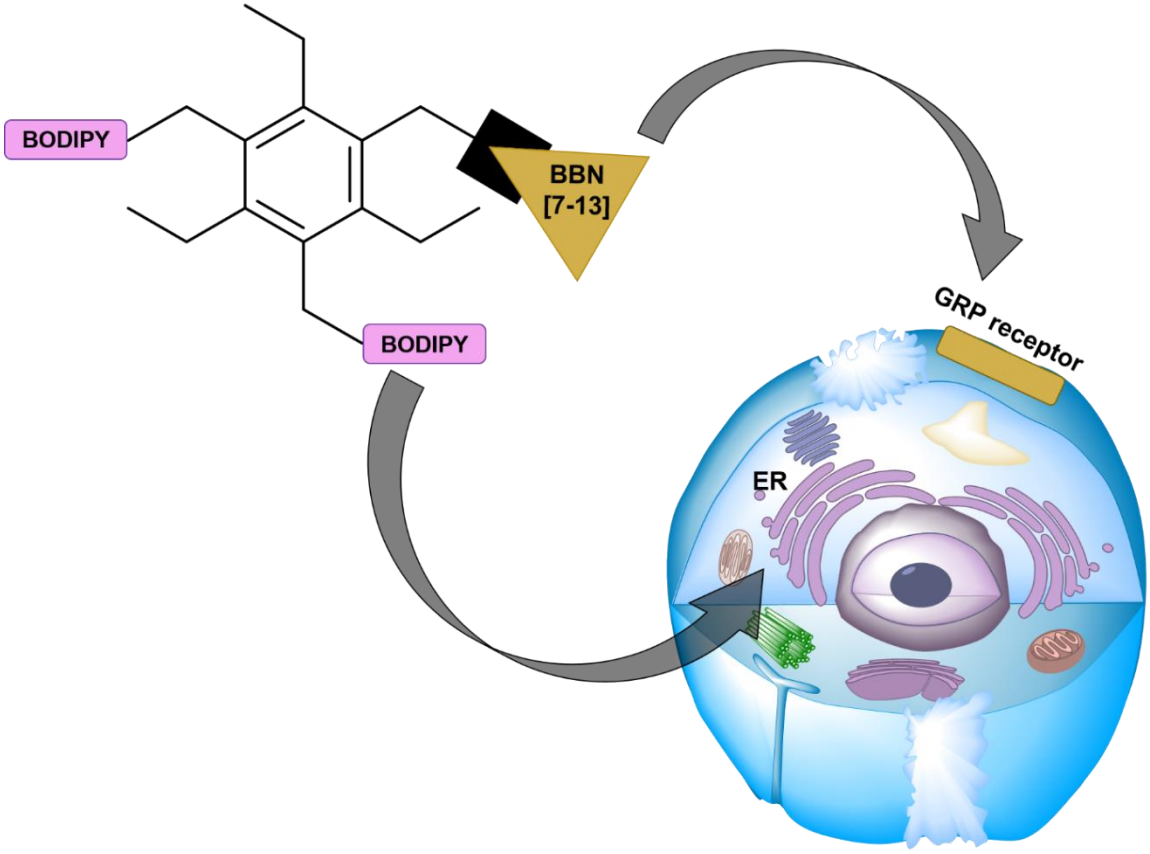

Figure 3.1. Schematic representation of a tripodal system incorporating the [7-13] bombesin fragment peptide and how this would get into a cell expressing the gastrin-releasing peptide (GRP) receptor.

Regulatory peptides are a type of peptide that take part in the information transfer process between cells in several different organs and tissues in the body, and can act locally or at a distance.[2] In general, regulatory peptides, such as the bombesin fragment used here, present many advantages: they are structurally small biomolecules, readily diffusible and they show a rapid clearance from the blood. For this reason, radiolabelled regulatory peptides are interesting potential agents for PET and SPECT imaging using radioisotopes for early diagnosis or treatment of human disease.[3, 4] Furthermore, high affinity receptors for these peptides are over-expressed in many cancer cells, and they can be used as new molecular targets for cancer diagnosis and therapy.[5] Peptides are efficient targeting elements suitable for the delivery of drugs to the tumour vessels, and many areas of research now focus on using the tumour-targeting potential of peptides to develop imaging agents and to direct drugs.[6, 7] Molecules containing fluorescent dyes and chelators for radioisotopes can be used to tag biomolecules such as peptides or antibodies using standard bioconjugation techniques, and the resulting new conjugates will constitute promising trimodal units for cell imaging and applications in PET and/or SPECT.[8]

Molecules containing targeting peptides can localise within the tumour receptors existing in cancer cells. In this context, peptide conjugates containing a bombesin fragment bind with strong affinity and selectivity to the gastrin-releasing peptide receptor (GRPr) and have been developed to target tumour cells overexpressing such receptors (*e. g.*, prostate, breast, ovarian and small cell lung cancer) using non-invasive imaging technologies.[9, 10] GRP receptors are located on the cellular membrane. Molecules incorporating targeting peptides represent relevant non-viral vectors for tumour targeting, imaging and therapy.[11] However, when a molecule contains two targeting units, the choice of targeting mode remains under debate.[12] In this case, the desired molecule would contain a BODIPY derivative, which is known to target the endoplasmic reticulum found in the cytoplasm of cells, and a bombesin sequence that binds to the GRPr positioned on the cellular membrane. It was unclear which targeting molecule would lead the distribution of the complex and whether the coexistence of both moieties could compromise the biological targeting capabilities of one of them.[13-15]

3.2. Synthesis and characterisation of the [7-13] bombesin fragment

The [7-13] bombesin fragment is a heptapeptide with affinity for a binding site on the bombesin/gastrin-releasing peptide receptor. It is the minimum sequence of the bombesin peptide that stimulates receptor activity.[16] It is formed by glutamine, tryptophan, alanine, valine, glycine, histidine and leucine (*Figure 3.2*).

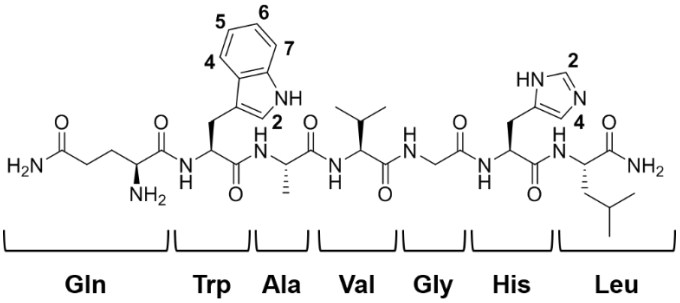

Figure 3.2. Structure of the [7-13] L-bombesin fragment synthesised hereby, showing the different amino acids that form the peptide: Gln-Trp-Ala-Val-Gly-His-Leu-NH_2.

The [7-13] bombesin sequence (compound **22**) was synthesised using solid-phase peptide synthesis (SPPS), with an automated peptide synthesiser (*Scheme 3.1*). The basic concept in solid-phase peptide synthesis is the step-wise construction of a peptide chain attached to an insoluble polymeric support (*e. g.*, a resin).[17] The amino acids used are protected by an Fmoc (9-fluorenylmethoxycarbonyl) group, which is attached to the N-terminal amino function of the molecule. Side-chain protection of other functional groups is provided by other protecting groups which are typically sensitive to acidic conditions. The Fmoc protecting group is base-labile, and it is usually removed with a base, in this case piperidine. The side-chain protecting groups are removed at the end by treatment of the peptide with trifluoroacetic acid (TFA), which also cleaves the bond that anchors the peptide to the resin support. The synthesis of this bombesin fragment has previously been carried out in the group and optimised throughout the years.[18]

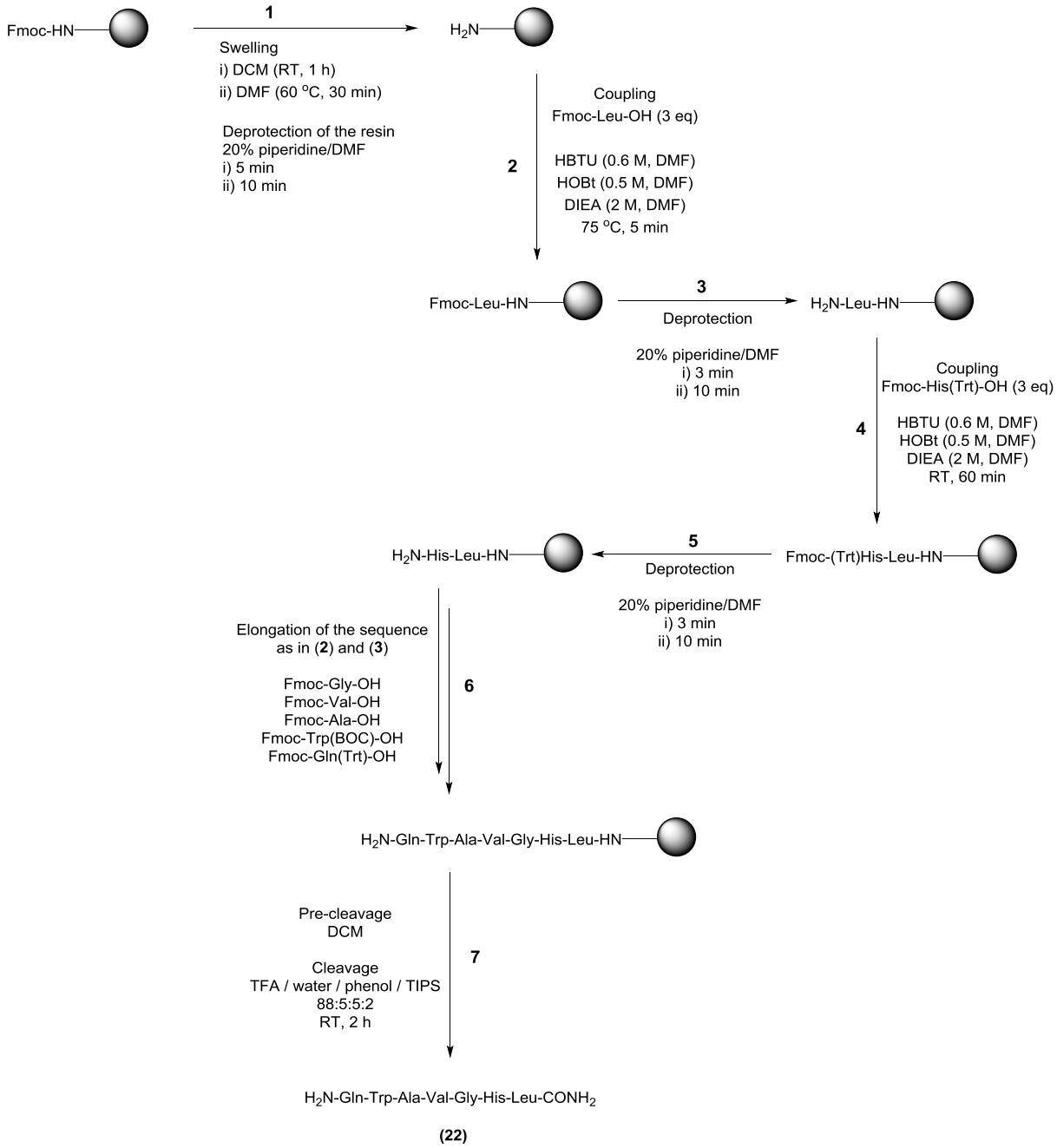

Scheme 3.1. Steps involved in the synthesis of the [7-13] bombesin fragment using solid-phase peptide synthesis.

To synthesise the [7-13] bombesin fragment, a Rink amide resin was used, with a loading capacity of 0.59 mmol/g. The resin was first swollen with dichloromethane and N,N'-dimethylformamide, followed by removal of the Fmoc group with a solution of 20% piperidine in N,N'-dimethylformamide. After deprotection, the coupling with the first amino acid was carried out. Three equivalents of each amino acid were used, all of them Fmoc protected. To carry out the coupling, solutions of *N,N,N′,N′*-tetramethyl-*O*-(1*H*-benzotriazol-1-yl)uronium

hexafluorophosphate (HBTU), 1-hydroxybenzotriazole (HOBt) and N,N-diisopropylethylamine (DIPEA) in N,N'-dimethylformamide were used. All the coupling reactions took place at 75 ºC, except the one for the second amino acid, Fmoc-His(Trt)-OH, which took place at room temperature and for a longer period of time. The different conditions for the coupling of Fmoc-His(Trt)-OH were chosen in order to avoid racemisation of this amino acid during the coupling step, which occurs at elevated temperatures.[19, 20] When the seven amino acids were coupled, the peptide was deprotected at the N-terminus and, finally, cleavage of the peptide from the resin was carried out for 2 hours with a cleavage "cocktail" of trifluoroacetic acid : water : phenol : triisopropylsilyl in a 88:5:5:2 (v/v/v/v) ratio. This particular cleavage "cocktail" composition was required due to the presence of Trp. Moreover, it has shown to yield good results in terms of cleavage yields and purity of the peptide for almost all types of peptides.[21, 22] The suspension of the resin in the cleavage "cocktail" was filtered and the peptide was precipitated by adding cold diethyl ether and collected by centrifugation. It was purified by semi-preparative HPLC using a C18 cartridge and water and acetonitrile as the solvent system, to yield a white solid. After purification, HPLC chromatography was carried out to test the purity of the product and it showed to be of 85%, with a major peak at 7.1 minutes and a much less intense peak at 2.8 minutes, corresponding to some side product of the reaction, possibly a truncated bombesin fragment.[23]

The compound obtained was characterised by NMR spectroscopy. The ^{1}H NMR spectrum of the bombesin fragment was acquired in deuterated methanol and the resonances were assigned with help of the two-dimensional ^{1}H-^{1}H COSY NMR spectrum. The chemical shifts of the resonances were in accordance with the values found in the literature.[24] The ^{1}H resonances for amino acid residues that contain aromatic groups (tryptophan and histidine) can be found between approximately 8.50 and 7.00 ppm (*Figure 3.*3). In this region, protons due to impurities occur and this makes it difficult for the resonances corresponding to the protons in the aromatic residues of Trp and His to be fully assigned. The region that goes from around 4.90 to 3.00 ppm contains the resonances due to the protons adjacent to the NH groups in the peptide backbone ($^{\alpha}$CH). Finally, the resonances of the protons in the side groups of the amino acids are observed in the region between approximately 3.20 to 0.85 ppm.

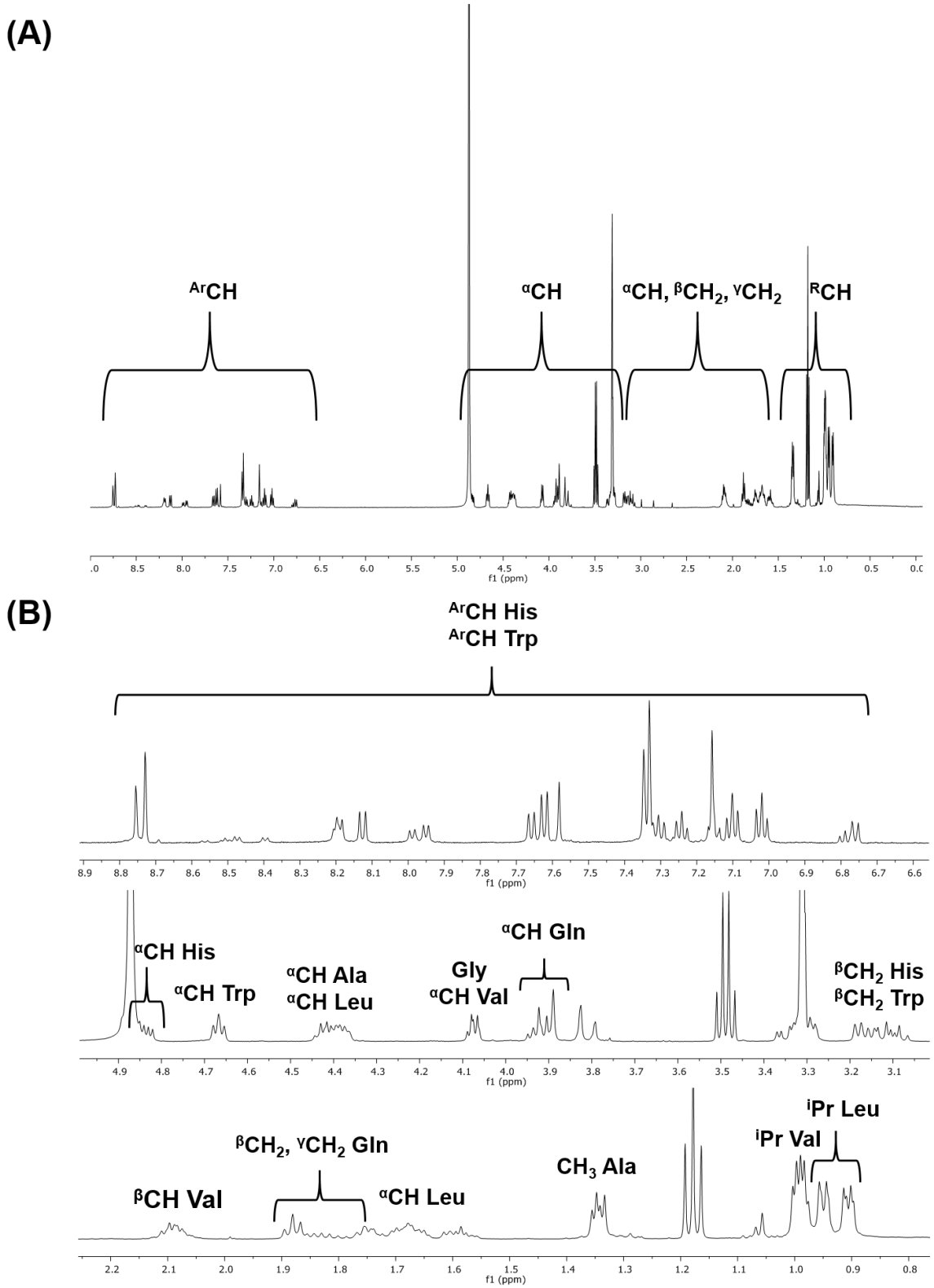

Figure 3.3. ^{1}H NMR (500 MHz, CD_3OD, 298 K) spectrum of the [7-13] bombesin fragment (compound **22**). **(A)** Whole spectrum, and **(B)** expansion of the different regions of the spectrum.

Furthermore, the solid was analysed by mass spectrometry using nanoelectrospray ionisation in positive mode, and from the spectrum, peaks due to the $[M+H]^+$ and $[M+Na]^+$ ions were observed at m/z = 809.4417 and 831.4227, respectively, as expected (*Figure 3.4*).

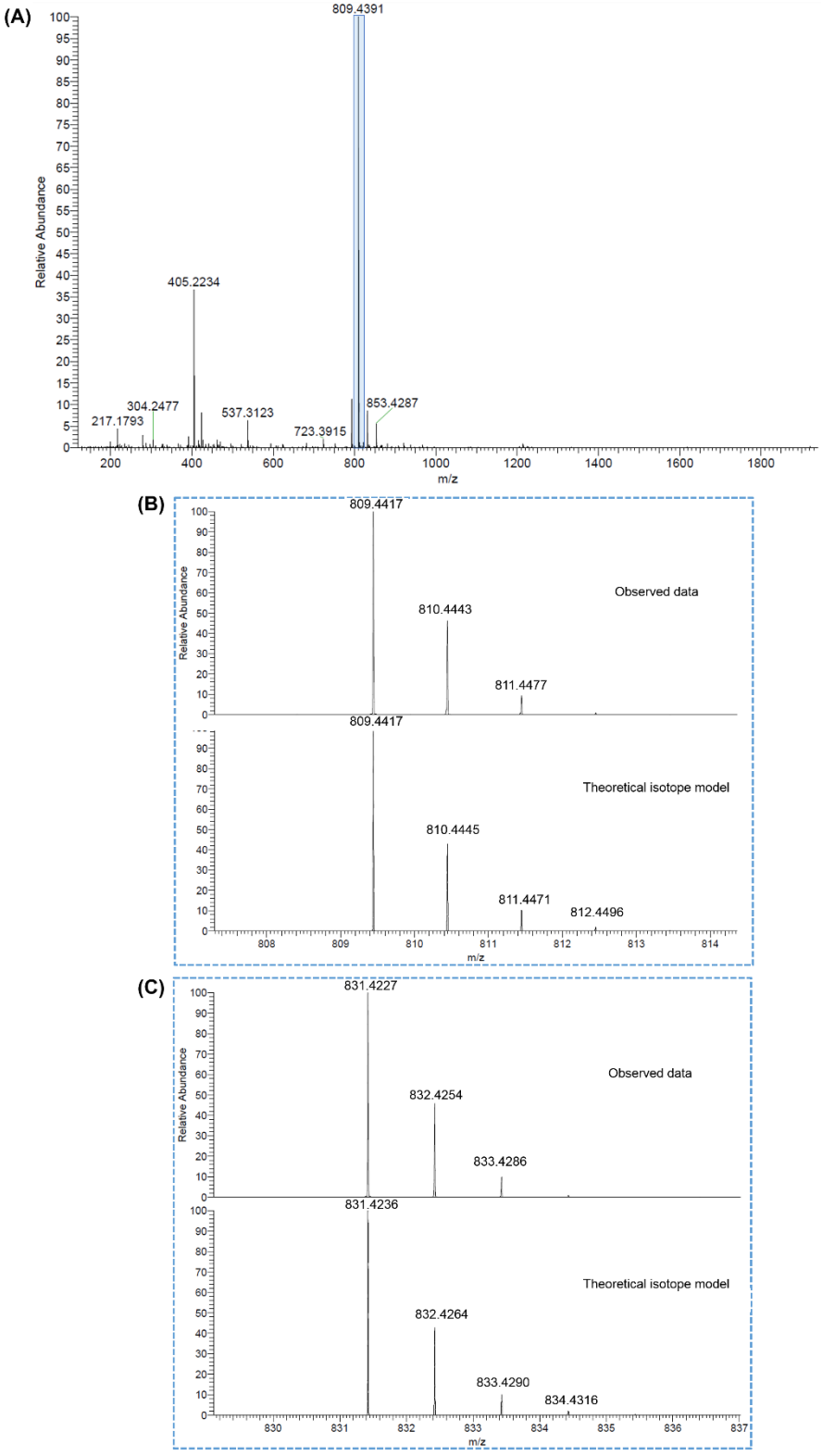

Figure 3.4. (A) Mass spectrum of compound **22** using nESI+, **(B)** isotopic pattern for $[M+H]^+$, and **(C)** isotopic pattern for $[M+Na]^+$.

Circular dichroism (CD) is a characterisation technique that uses the ability of chromophores to absorp differently left and right circularly polarised radiation. Such compounds either present chiral structures or are placed in chiral environments. Peptides can contain a number of chromophores that can generate CD signals: the peptide bond absorption is located in the far UV region (240 – 180 nm), and this area can provide information about the secondary structure of such molecules (α-helix and β-sheet). The UV region that goes from 320 to 260 nm is due to the aromatic amino acid side chains and can provide information about the tertiary structure of the peptide or protein.[25] Circular dichroism of the full length bombesin peptide has been reported in the literature for the investigation of the secondary structure of this peptide both in solid state and in solution. The results showed that the peptide can adopt different conformations depending on the concentration, consisting mainly in disordered structure and intermolecular β-sheet species.[26]

In this work, CD was used on the [7-13] L-bombesin fragment to study its chiral properties (*Figure 3.5*). 200 μM solutions of the compound in dimethylsulfoxide, water and acetonitrile were used. Maximum absorption peaks were obtained at 286 nm for the solution in dimethylsulfoxide, and 281 nm for the solutions in water and acetonitrile, as it can be seen from the UV/visible spectra. As expected, this peptide sequence does not show a defined secondary structure in solution. This is due to the fact that it is formed from only seven amino acids, and in order to have a secondary structure, peptides need to have at least ten amino acids. Accordingly, the structure of a disordered peptide can be expected for the [7-13] bombesin fragment synthesised hereby, with a random coil conformation. In all the cases, for the maximum absorption peak in the UV/visible spectrum, the CD spectra have a negative peak at around 285 nm (in the case of water, it looks like it is positive but this is due to the background noise). Therefore, it can be concluded that the molecule under study is chiral. This was expected as this compound is formed by chiral amino acid residues existing in the L- form.

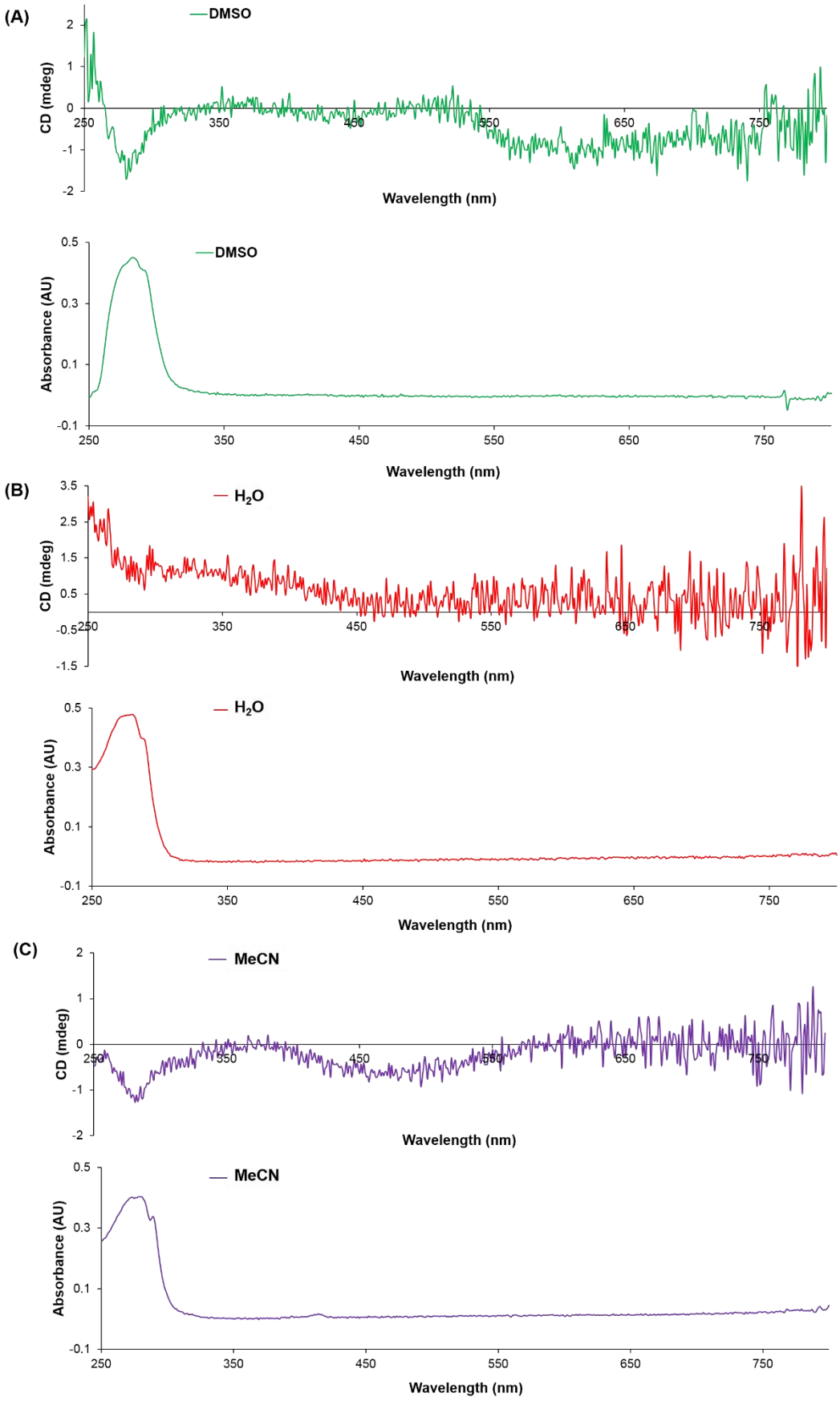

Figure 3.5. Circular dichroism spectra of the [7-13] L-bombesin fragment in **(A)** dimethylsulfoxide, **(B)** water, and **(C)** acetonitrile, together with their absorption spectra.

3.3. Synthetic strategies to incorporate the [7-13] bombesin fragment into a tripodal linker system

In order to attach the synthesised peptide fragment to the tripodal unit described in *Chapter 2*, a strategy using a succinate derivative linker was adapted from the literature and applied hereby.[27] The use of a molecule containing a BODIPY derivative to incorporate a peptide would allow a fluorescent system able to localise specifically within cancer cells with the corresponding receptor.

The first approach was the deprotection of the tripodal ligand containing a tert-butoxide protected acid linker using trifluoroacetic acid (TFA) and dichloromethane as solvent in a 1:1 ratio. This way, a free COOH group would be obtained for attachment to the peptide fragment (*Scheme 3.2*).

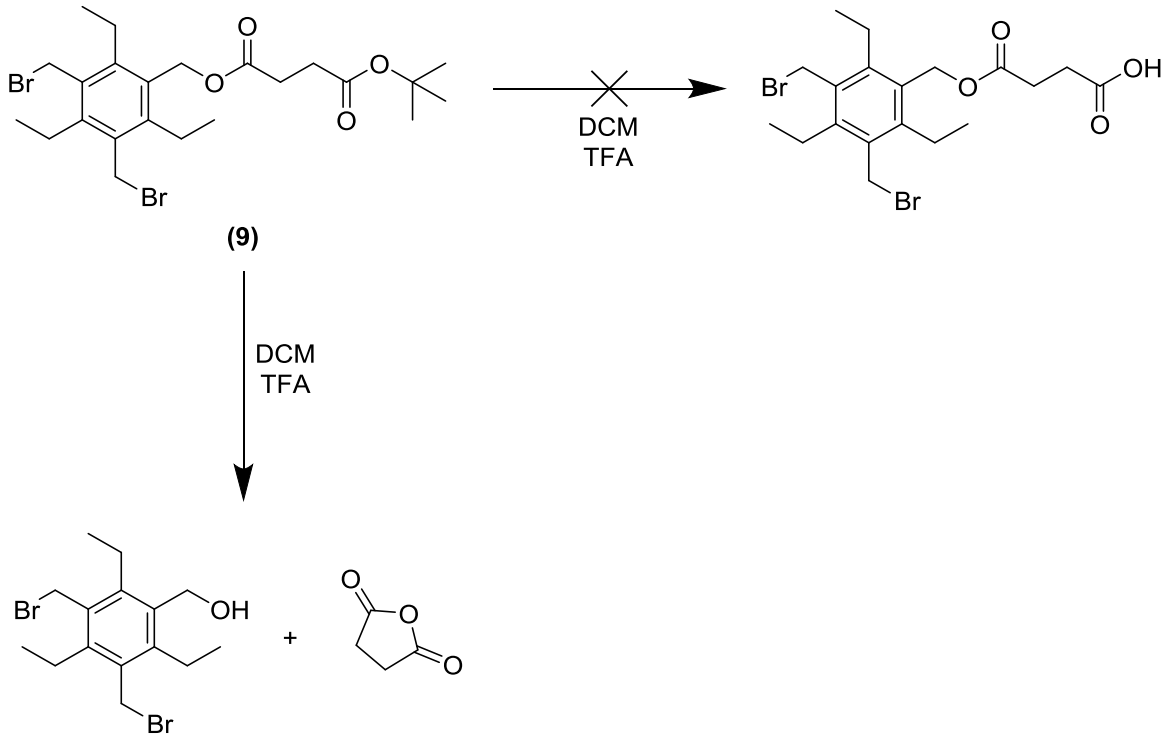

Scheme 3.2. Attempted deprotection reaction of compound **9** explored towards achieving a free carboxylic acid group.

This reaction was carried out overnight at room temperature and the solvent was removed under reduced pressure. The obtained solid was characterised by MS (using electrospray ionisation) and NMR spectroscopy, but the desired product of the reaction shown in the scheme above could not be isolated. ^{1}H NMR spectroscopy of the resulting mixture showed that the singlet peak due to the nine protons of the tert-butoxide group disappeared, but new resonances emerged. It can be concluded from the spectrum that the ester linkage existing

between the tripodal ligand and the linker breaks under the used conditions, and two products coexist in the final mixture: succinic anhydride and a tripodal molecule with a hydroxyl-methyl arm. This is consistent with the behaviour of various succinate prodrugs, where the ester linkage breaks under acidic conditions and the succinate derivative cycles to form succinic anhydride.[28, 29]

In order to test the suitability of the conditions applied for the removal of the tert-butoxide group and achieving the desired free carboxylic acid, the analogous reaction was carried out by using the succinate linker alone, and the product was characterised by NMR spectroscopy and MS (*Scheme 3.3*).

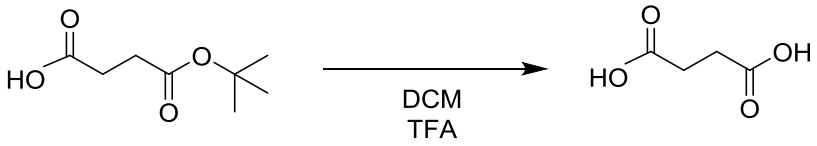

Scheme 3.3. Deprotection reaction of the succinate derivative linker to yield succinic acid.

The ^{1}H NMR spectrum of this product was consistent with that expected for this new molecule. The ^{1}H NMR spectrum of the starting material, 4-(tert-butoxy)-4-oxobutanoic acid, shows a singlet at 1.44 ppm due to the protons of the tert-butoxide group, H^1, and a multiplet between 2.63 and 2.52 ppm due to the four protons in the two CH_2 groups of the molecule, H^2 and H^3 (*Figure 3.6*). The spectrum of the new molecule, succinic acid, shows a singlet at 2.56 ppm that is due to the four protons in the two CH_2 groups of the product, H^2, which are now equivalent due to the symmetry of the molecule, and a broad singlet at around 5.10 ppm can be seen due to H^1, the acidic protons.

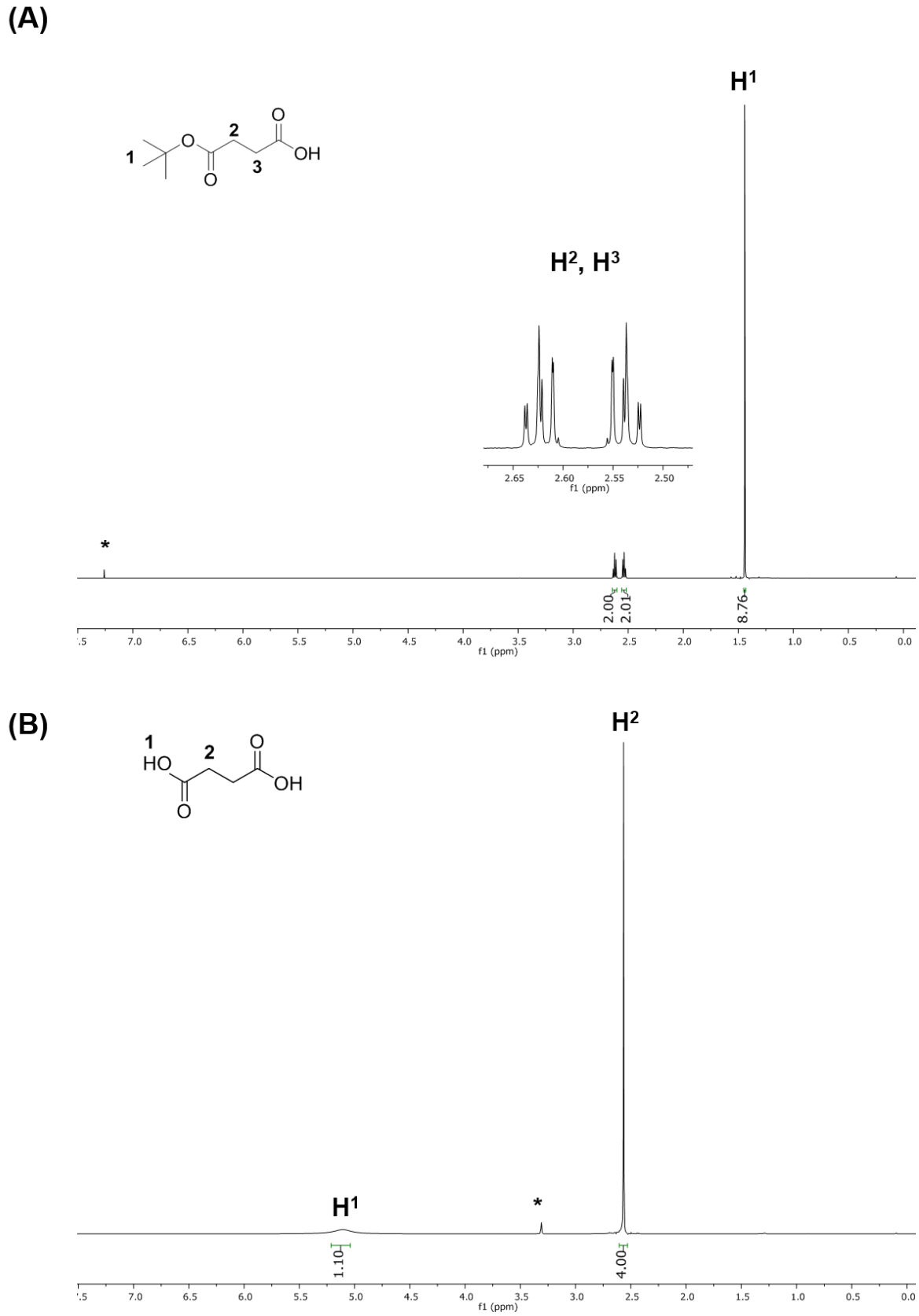

Figure 3.6. ^{1}H NMR (500 MHz, 298 K) spectra of **(A)** the starting material, 4-(tert-butoxy)-4-oxobutanoic acid ($CDCl_3$), and **(B)** succinic acid (CD_3OD).

Since the deprotection of the linker alone took place successfully under the conditions described above, the coupling between the [7-13] bombesin fragment and the protected succinate linker was carried out to try to identify the ideal reaction conditions (*Scheme 3.4*).

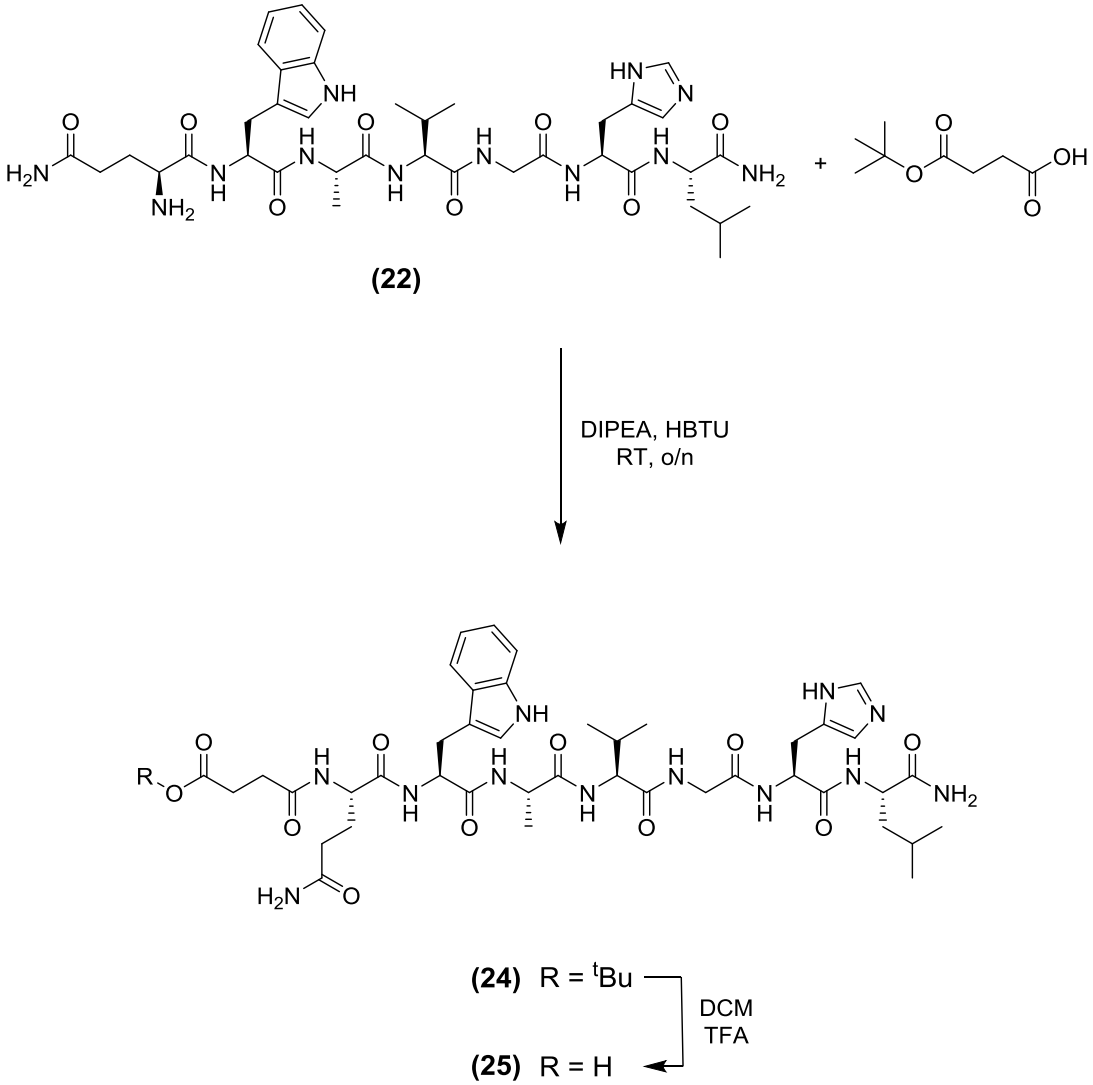

Scheme 3.4. Coupling of the [7-13] bombesin fragment to a succinate linker via a carboxylic acid-amine coupling reaction.

This coupling reaction between compound **22** and the succinate derivative was carried out mixing DIPEA and HBTU in a 2:1 ratio with the bombesin fragment and the linker containing a carboxylic acid group at room temperature under a flow of nitrogen. The reaction mixture was stirred overnight, and a pale white solid could be isolated, which corresponded to the expected product (compound **24**). It was analysed by mass spectrometry using positive mode electrospray ionisation, and from the spectrum peaks could be seen at m/z = 965.5235 and 987.5059, which correspond to the $[M+H]^+$ and $[M+Na]^+$ ions, respectively (*Figure 3.7*).

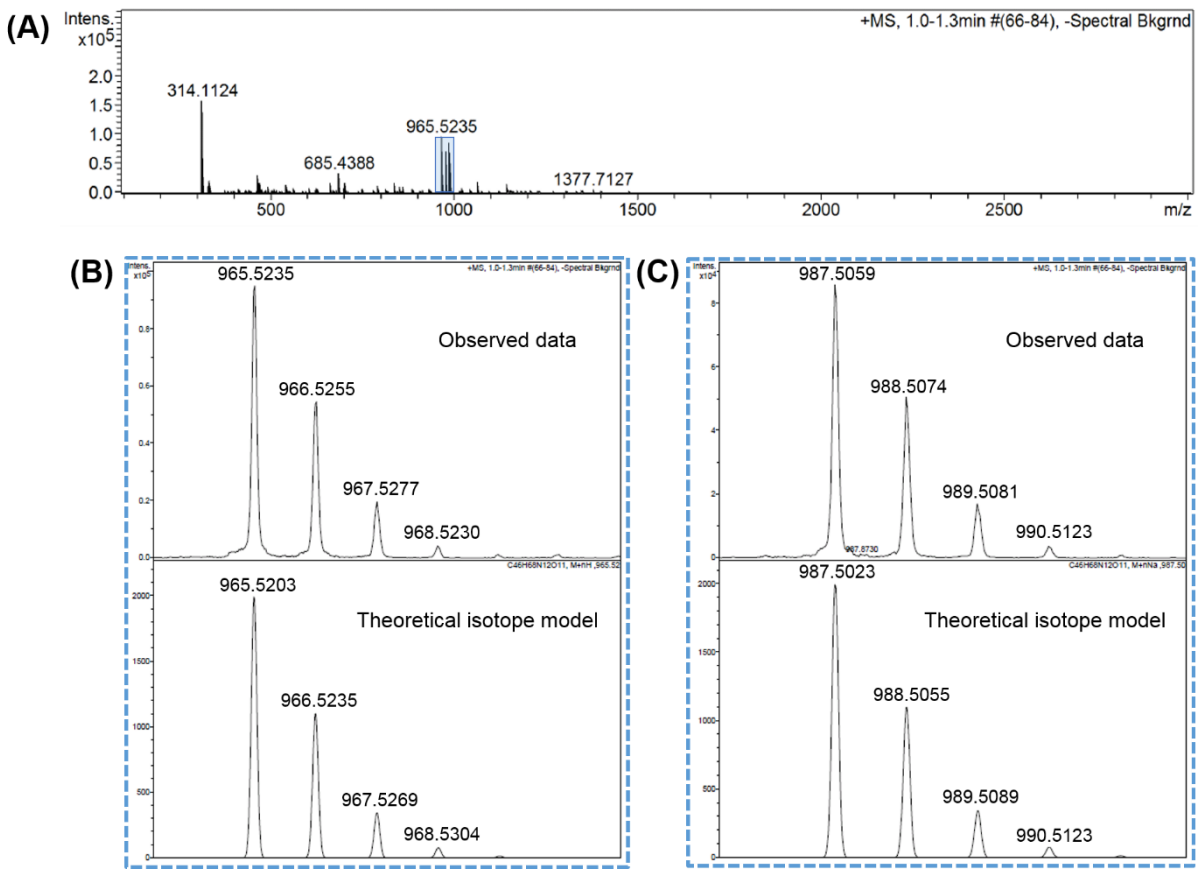

Figure 3.7. (A) Mass spectrum of compound **24** using ESI+, **(B)** isotopic pattern for $[M+H]^+$, and **(C)** isotopic pattern for $[M+Na]^+$.

The next step carried out was the deprotection of the conjugate formed between the bombesin fragment and the succinate linker, protected with a tert-butoxide group (compound **24**). This was achieved using the same conditions applied to 4-(tert-butoxy)-4-oxobutanoic acid, with dichloromethane and trifluoroacetic acid in a 1:1 ratio and stirring the contents overnight at room temperature (*Scheme 3.4*).

The desired product, the deprotected molecule (compound **25**), was isolated by removing the solvent under reduced pressure, and characterised by mass spectrometry using electrospray ionisation in positive mode (*Figure 3.8*).

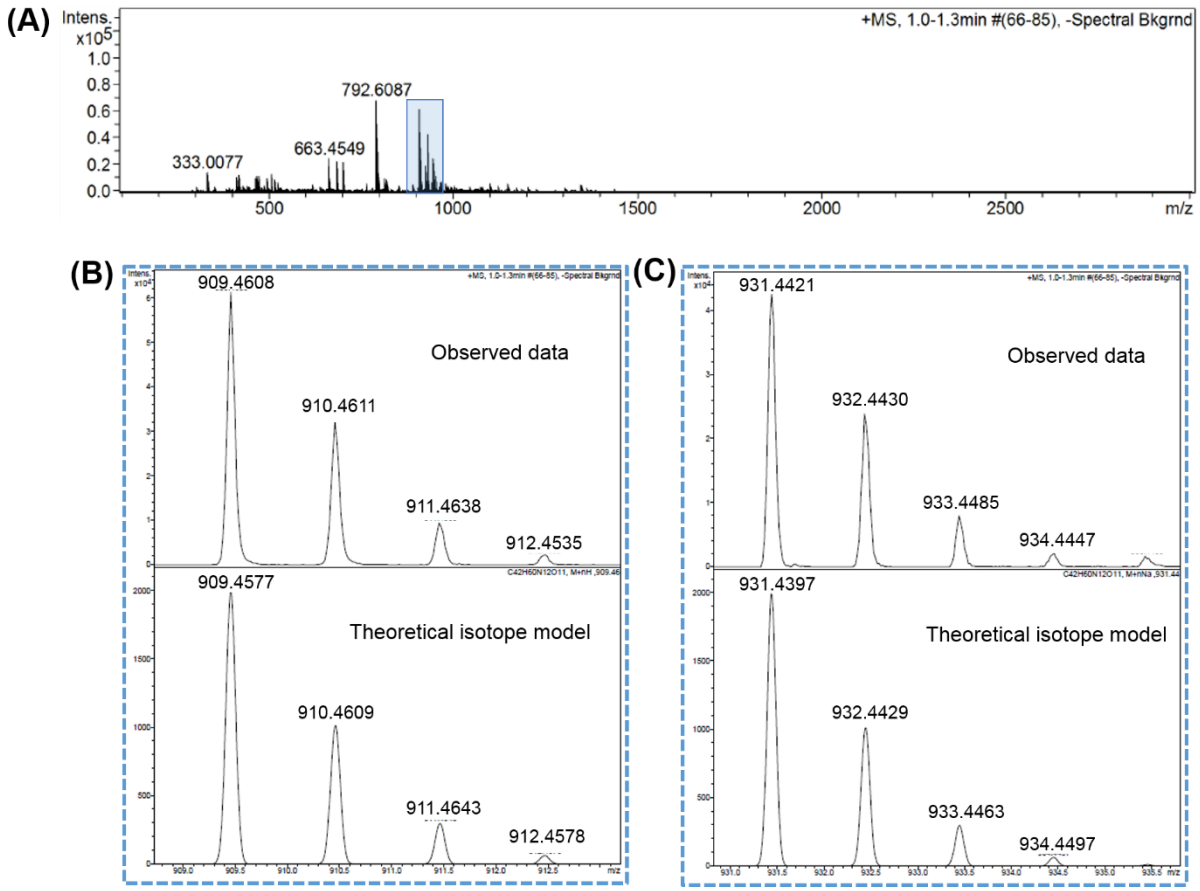

Figure 3.8. (A) Mass spectrum of compound **25** using ESI+, **(B)** isotopic pattern for $[M+H]^+$, and **(C)** isotopic pattern for $[M+Na]^+$.

The purity of compound **25** was analysed by HPLC using a solvent system of water and acetonitrile with 0.1% of TFA (*Figure 3.9*). A peak at 7.0 minutes in the 280 nm channel indicated that the product was obtained with a purity of approximately 93%, with an impurity corresponding to the 7% of the mixture that can be seen in the HPLC chromatogram at around 10.0 minutes, and could be due to some traces of the protected starting material remaining in the product.

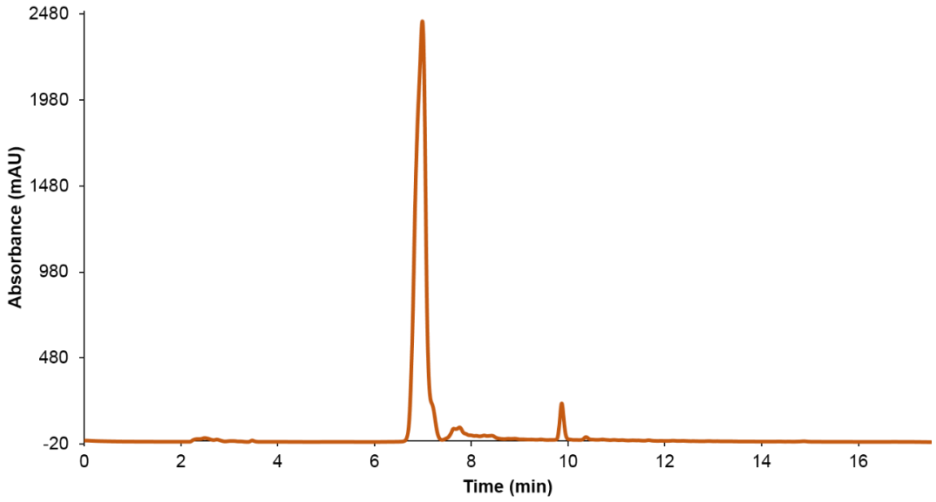

Figure 3.9. HPLC chromatogram of compound **25** in the 280 nm channel.

Once the coupling between the [7-13] bombesin fragment and the succinate linker was achieved, and the deprotection of the carboxylic acid group of the conjugate was successfully performed, the reaction between the bombesin-linker complex (compound **25**) and the tripodal ligand (compound **1**) was carried out.

The molecule resulting from this reaction was explored further, as a potential synthetic scaffold for a bimodal system with differing functionalities held together by the tripodal core, and containing a peptide fragment and two fluorescent moieties. In order to facilitate this reaction, the tripodal derivative chosen was compound **6**, which contains two BODIPY molecules and only a free bromomethyl arm (*Scheme 3.5*). This route was chosen as it would avoid the formation of di- and trisubstituted derivatives, given that only one arm would be available to undergo a nucleophilic substitution reaction. This would also likely make the isolation and characterisation of the final product simpler.

In order to carry out this reaction, the same conditions that proved successful as described in *Section 2.4* in *Chapter 2* for reactions involving these functional groups were used. The two reagents were dissolved with potassium carbonate in acetonitrile in a 1:1:1.5 ratio. These were stirred at room temperature overnight under a flow of nitrogen. After this time, the solvent was removed under reduced pressure and the orange oil that was obtained was isolated and analysed by NMR spectroscopy and MS. HPLC analysis was used to check the purity of the product. However, spectroscopic investigations did not yield conclusive results regarding the identity of the final product.

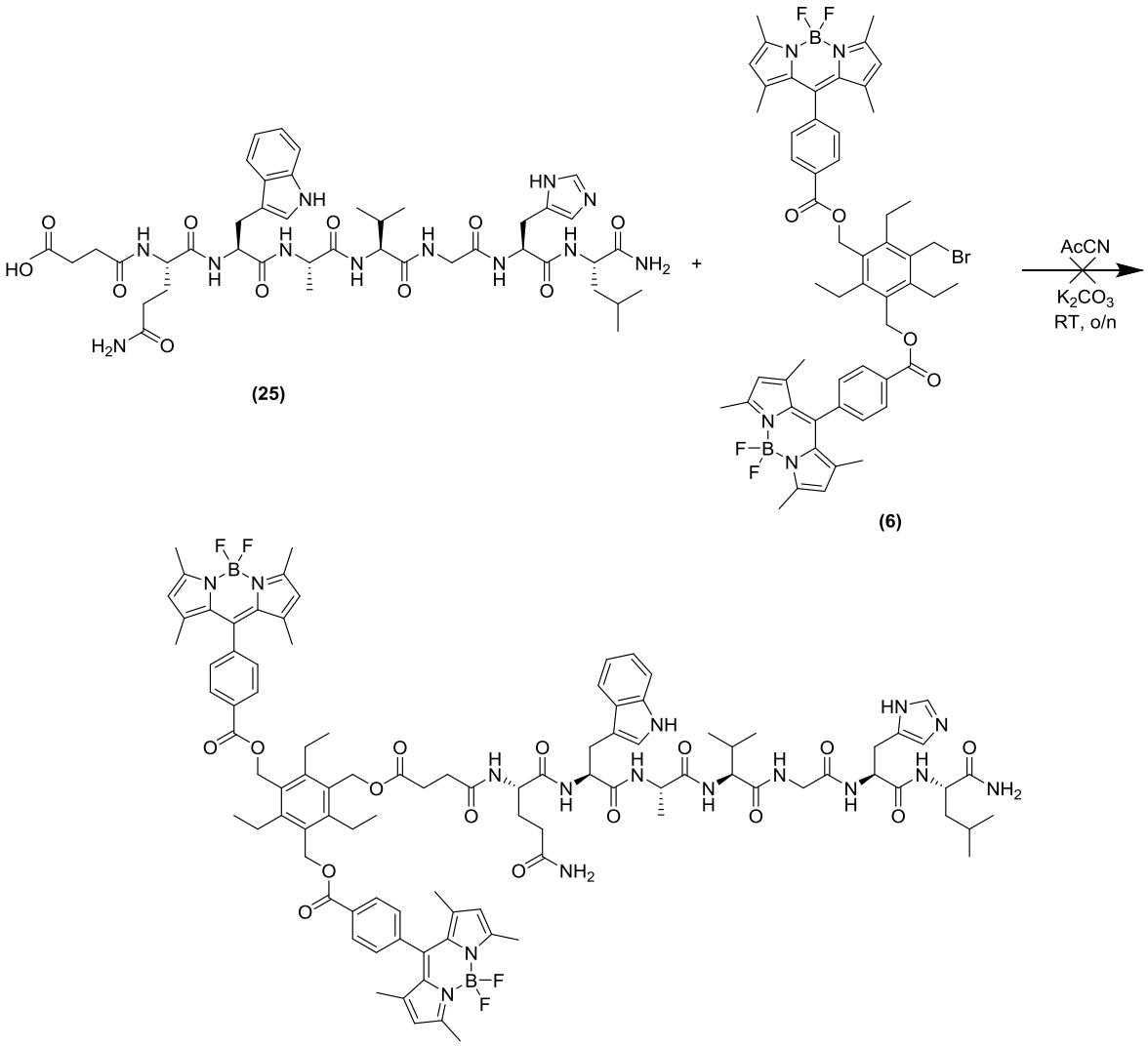

Scheme 3.5. Attempted reaction between compounds **25** and **6** to form a desired trisubstituted molecule, with fluorescent properties and a targeting peptide.

Mass spectrometry was carried out using a high definition electrospray ionisation method in positive (*Figure 3.10*) and negative modes coupled to an HPLC unit. The different peaks in the spectra were subtracted to calculate the m/z loss between each of them, and try to associate it to the loss of an amino acid, since using this method the fragmentation of the molecule into the individual amino acids or fragments could occur.[30] However, conclusive results could not be deducted, and it was not possible to find any peak at any charge that could be assigned to the desired molecule from the reaction or fragments of this.

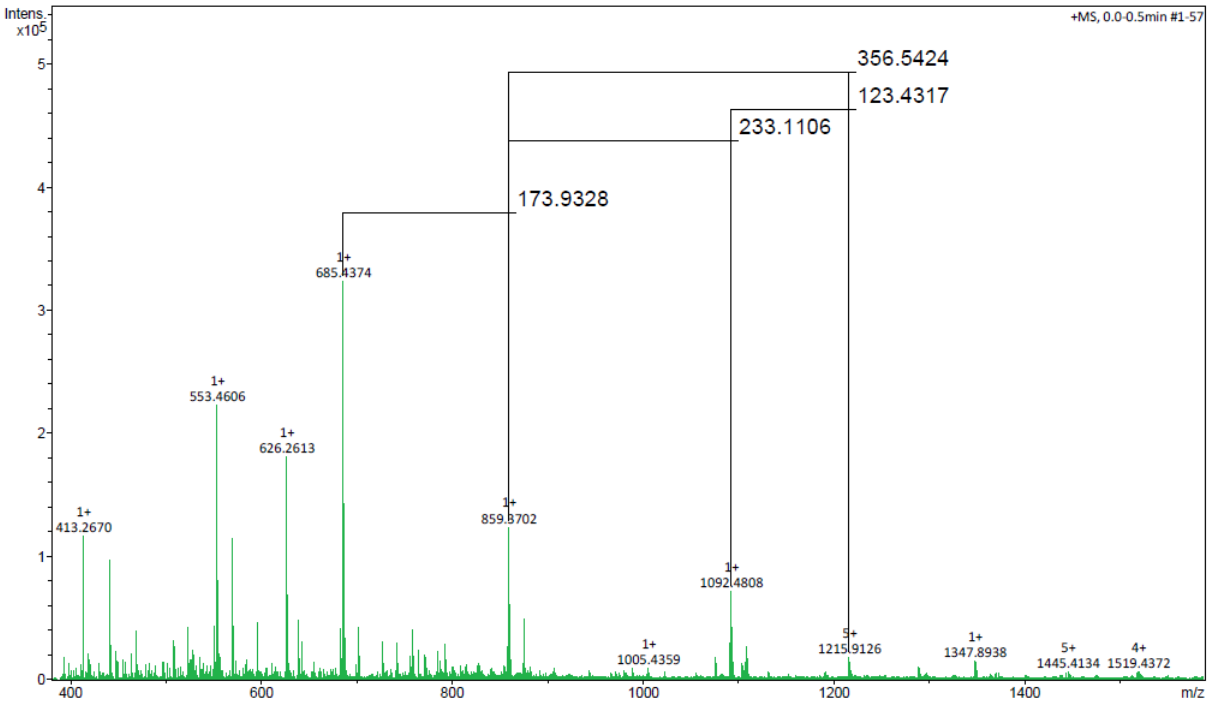

Figure 3.10. Mass spectrum of the product resulting from the reaction between compounds **25** and **6** using ESI+. Peaks corresponding to the expected molecule or fragments of this could not be identified.

The same reaction was carried out using the same reagents but at 80 ^{o}C and for a shorter period of time (three hours) to test its success at a higher temperature. From the mass spectrum of the product obtained by electrospray ionisation using both positive and negative modes, peaks corresponding to the molecular formula of the expected compound could not be observed. The reason why this reaction did not work as expected could be due to the large size of the two molecules and the steric hindrance for the two functional groups to react. Related chemistry has been used to link a variety of complex carboxylic acid derivatives to a similar scaffold. However, there are no examples of reactions with unprotected peptides.[27]

Due to time restrictions, it was not possible to repeat this reaction to find the right conditions to achieve the desired peptide-targeted final product. With more time and further investigations, this reaction should be achievable and this would constitute an interesting finding, as a peptide with these functionalities could be attached to the tripodal systems fully discussed in *Chapter 2*, and a potential multimodal molecule could be built. Potential further experiments would include carrying out the same reaction with simpler precursors, *i. e.*, using compound **1** and the peptide fragment, instead of the already disubstituted tripodal molecule. This would facilitate the reaction between the two functional groups of interest. If successful, the BODIPY tag could be incorporated to the system at a later stage.

3.4. Synthesis of a deferoxamine derivative targeted with the [7-13] bombesin fragment

Considering the challenges involved at incorporating fluorophores onto the bombesin fragment, a parallel approach was adopted. Compound **18** was used to attach the synthesised peptide fragment in order to create a molecule consisting of a potential radiochelator labelled with the [7-13] bombesin fragment (compound **23**) (*Scheme 3.6*). Radiolabelled bombesin-based peptides exhibit great potential as targeting vectors for imaging and radionuclide therapy of tumours expressing the GRPr.[31, 32] Maecke *et al*. reported a series of copper(II) radio-chelators targeted with bombesin.[33]

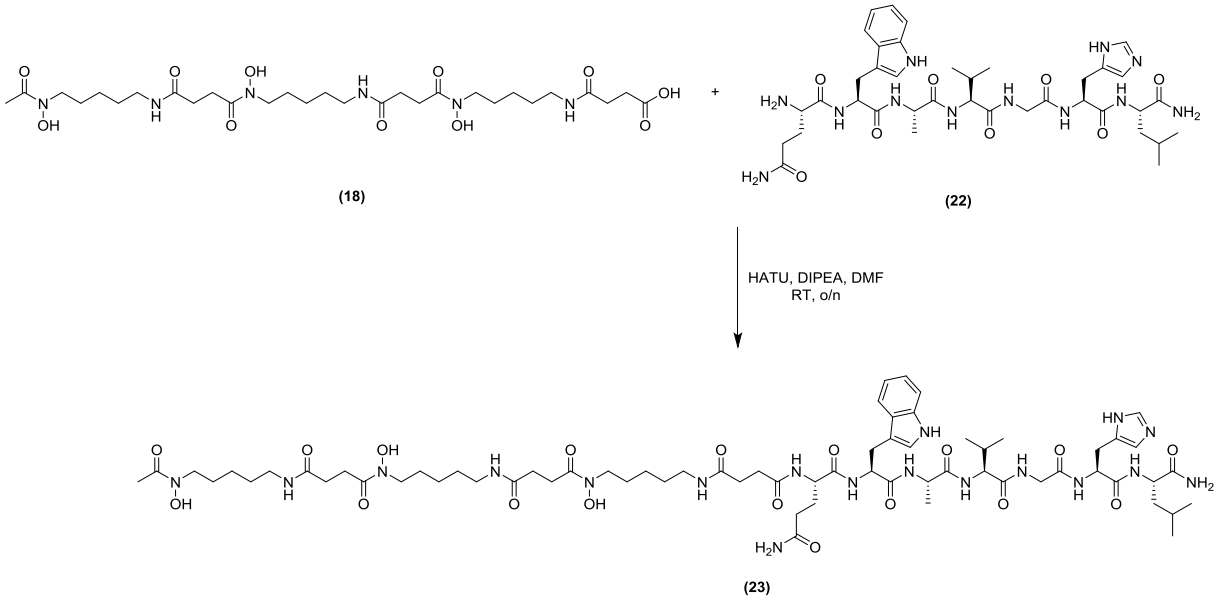

Scheme 3.6. Reaction between compounds **18** and **22** to yield compound **23**.

Several reaction conditions were investigated, and attempts to optimise these were made, as follows (*Table 3.1*). All the reactions were carried out at room temperature and using N,N'-dimethylformamide as solvent. The best conditions were found to be an overnight room temperature reaction, under nitrogen atmosphere and using all the reagents in a 1:1 ratio; the bombesin fragment, compound **18**, DIPEA and HBTU or 1-[bis(dimethylamino)methylene]-1*H*-1,2,3-triazolo[4,5-*b*]pyridinium 3-oxide hexafluorophosphate (HATU) (reactions 2 and 3, respectively). HBTU and HATU were used as activators of the carboxylic acid group, which was attacked by the N-terminal primary amino group of the [7-13] bombesin fragment to yield the new molecule as an orangish solid. The solvent of the reaction was removed under reduced pressure, and the crude reaction mixture was characterised by mass spectrometry using electrospray ionisation in positive mode (*Figure 3.11*). The peak at m/z = 1451.8096 corresponds to the molecular ion, $[M]^{+\cdot}$, and a peak of lower m/z ratio, at 809.4528, corresponds

to the free [7-13] bombesin fragment used as starting material, indicating that some unreacted compound still exists in the system, or fragmentation led to the appearance of this peak in mass spectrometry.

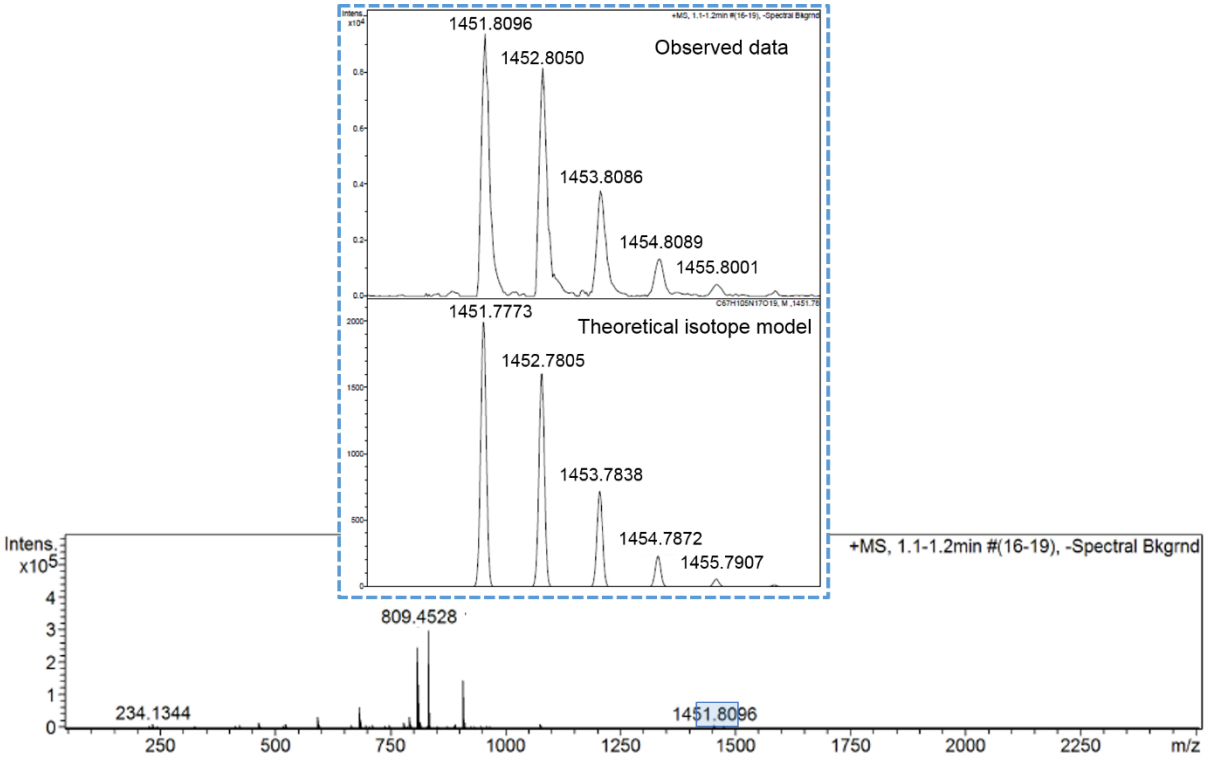

Figure 3.11. Mass spectrum of compound **23** using ESI+, and isotopic pattern for $[M]^+$.

Table 3.1. Reaction conditions used for the coupling between compounds **18** and **23**.

Entry	18 / eq	23 / eq	Activating reagent / eq	Base / eq	Time / h	Coupling
1	1	1	EDC, NHS / 1, 1	-	24	No
2	1	1	HBTU / 1	DIPEA / 1	16	Yes
3	1	1	HATU / 1	DIPEA / 1	16	Yes

Due to the broad diversity of peptides species available, there is not a general coupling reagent ideal for all the peptidyl bond formation reactions, and the most efficient coupling reagent for each type of reaction needs to be identified, which poses a challenge.[34] In general, HBTU and HATU are considered superior to carbodiimide-based reagents (*e. g.* EDC). HBTU and HATU are phosphonium and aminium salts, and these are considered the new generation of coupling reagents, which have become very popular in the last few years thanks to the advantages that they present: faster and more efficient couplings achievable with less epimerisation.[35] Moreover, it has been reported that HATU, a variant form of HBTU, is very efficient in difficult sterically hindered couplings and it usually produces a minimal level of racemisation. This is usually the reagent of choice when rapid and mild coupling reactions are required.[36]

Conditions using carbodiimide-based coupling reagents, specifically 1-ethyl-3-(3-dimethylaminopropyl)carbodiimide (EDC) were also applied, but the formation of the conjugate was not observed (*Scheme 3.7*). Carbodiimide reagents present some drawbacks, such as the rearrangement of the activated carboxylic acid into an unreactive urea derivative. For this reason, N-hydroxysuccinimide (NHS) was added as an additive with the aim of improving the efficiency of the reaction.[37] Furthermore, due to carbodiimides being condensing reagents, side reactions of unprotected amino acids side chains have been reported (such as the conversion of amides to nitriles). This creates the need for appropriate side-chain protecting groups to prevent such side reactions when these reagents are used.[38]

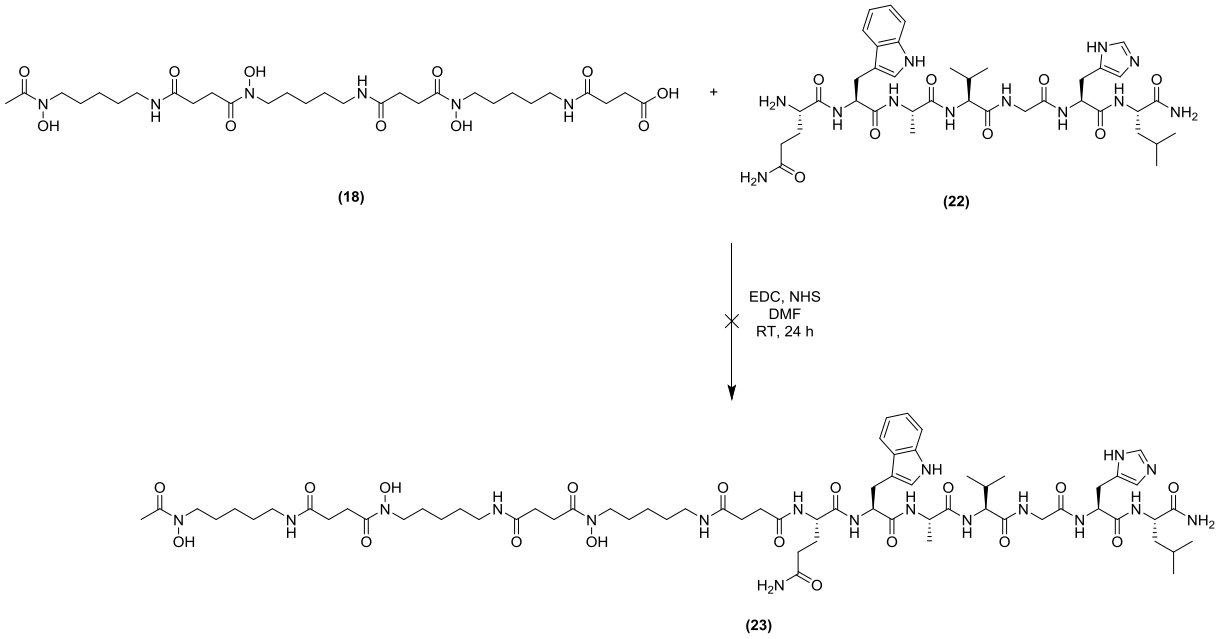

Scheme 3.7. Attempted reaction between compounds **18** and **22** to yield compound **23** using EDC and NHS.

The mechanism of the coupling reaction using HATU or HBTU, respectively, consists in the activation of the carboxylic acid group using such activating reagents.[39] The activated acid derivative, which is an ester, is then attacked by the amino function of the peptide. The reaction led to completion with the formation of the corresponding amide bond (*Scheme 3.8*).

In conclusion, a compromise of speed, purity and by-products produced needs to be achieved in order to choose the ideal coupling reagent for an amide bond formation reaction. In this case, it was found that HBTU and HATU, which constitute a new generation of coupling reagents, were useful to carry out a successful coupling reaction to achieve the desired product effectively.

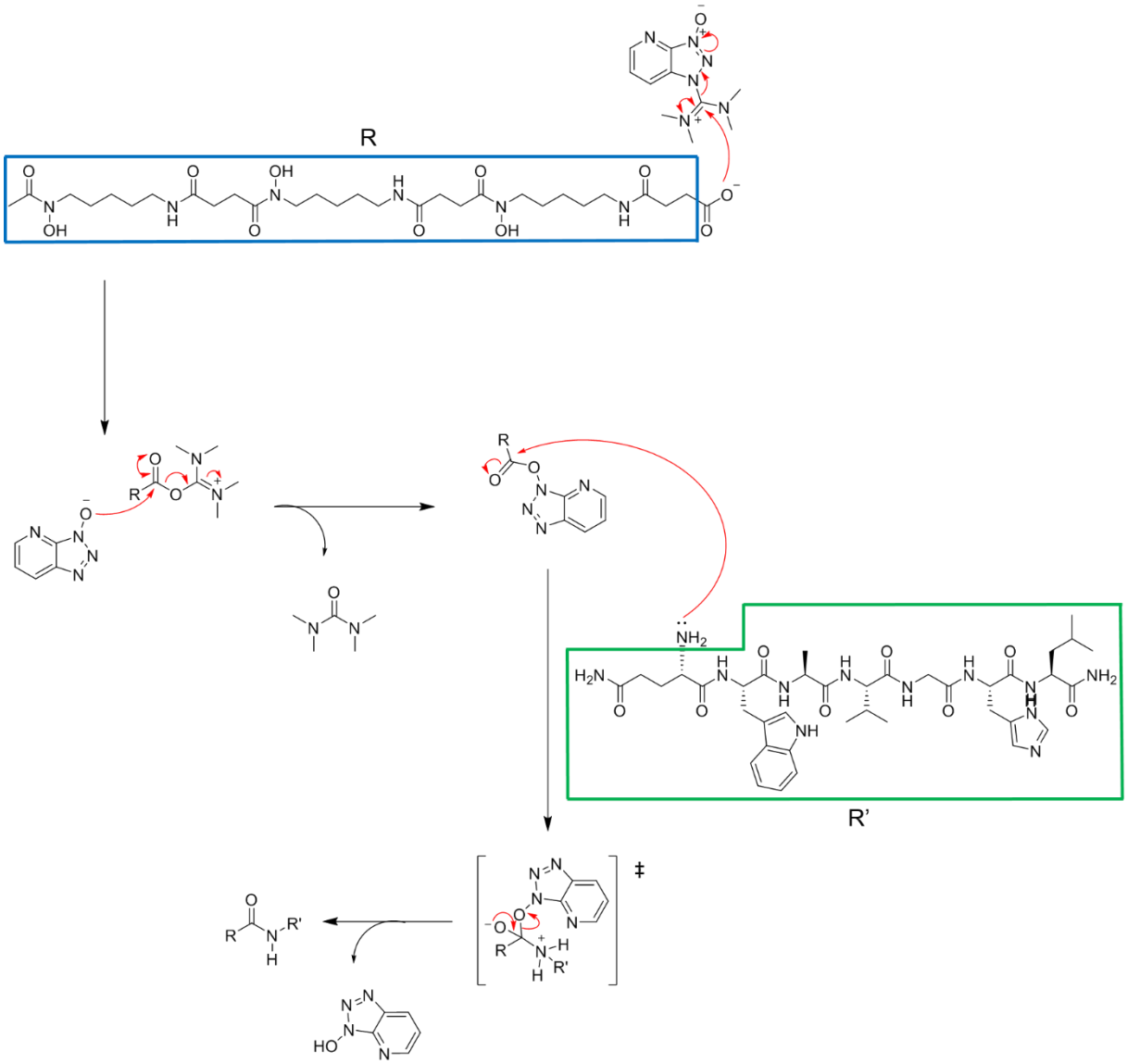

Scheme 3.8. Coupling reaction and mechanism between a carboxylic acid (DFO derivative) and a peptide ([7-13] bombesin fragment) using HATU.

3.5. Summary of Chapter 3

The [7-13] bombesin fragment was successfully synthesised via a solid-phase peptide synthesis strategy, and characterised using HPLC and MS, and also ^{1}H NMR spectroscopy was used to assign some of the proton resonances. A succinate linker derivative was attached to the peptide fragment via a carboxylic acid-amine coupling reaction, and the tert-butoxide group of the linker was later removed to provide a free N-terminal carboxylic acid group. This functional group was used to try to attach the peptide-linker fragment to the (already disubstituted) tripodal ligand precursor containing two BODIPY molecules (compound **6**). The same reaction conditions that proved to be successful in *Chapter 2* were used hereby, but at room temperature due to concerns regarding the stability of the peptide derivative. This reaction did not lead to the desired final product (consisting of the trisubstituted tripodal ligand) and the obtained mixture was explored by MS and NMR spectroscopy. Further studies need to be carried out in order to identify the correct reaction conditions to achieve the desired compound containing the bombesin fragment. Once this molecule was obtained, it would be interesting to perform cellular imaging investigations to observe the distribution of the compound in cells, given the importance of BODIPY derivatives in optical imaging applications.

Additionally, the as-synthesised [7-13] bombesin fragment was coupled to compound **18**, a deferoxamine derivative containing a carboxylic acid terminal group instead of an amino function. DFO is an important chelator recently used to bind radiometals (such as ^{68}Ga and ^{89}Zr) for PET and SPECT molecular imaging applications. This reaction was carried out using both HATU and HBTU as activating reagents. The deferoxamine-bombesin fragment conjugate was successfully characterised by MS, thus supporting the hypothesis that the new product (compound **23**) was isolated. This constitutes a promising scaffold for radiolabelling with the PET radioisotope zirconium-89, as it contains a DFO derivative, known to bind Zr(IV) in water, and it can potentially be used for PET imaging. Moreover, the incorporation of the [7-13] bombesin fragment facilitates the targeting of the molecule to cancer cells containing the gastrin-releasing peptide receptor.

Coordination reaction attempts to incorporate metal ions such as Ga(III) or Zr(IV) would prove the potential of this molecule to bind to radiometals, and further investigations into the radioimaging applications would be an important aspect of tracer development.

3.6. References for Chapter 3

1. C. A. Ferreira, L. L. Fuscaldi, D. M. Townsend, D. Rubello and A. L. B. Barros, *Biomed. Pharmacother.*, 2017, **87**, 58-72.
2. G. J. Dockray, *Sci. Prog.*, 1988, **72**, 21-35.
3. P. K. Nanda, S. R. Lane, L. B. Retzloff, U. S. Pandey and C. J. Smith, *Curr. Opin. Endocrinol. Diabetes Obes.*, 2010, **17**, 69-76.
4. H. Meisel, *J. Pept. Sci.*, 1997, **43**, 119-128.
5. M. Gotthardt, M. P. Béhé, H. Alfke and T. M. Behr, *Clin. Lung Cancer*, 2003, **5**, 119-124.
6. E. Garanger, D. Boturyn and P. Dumy, *Anticancer Agents Med. Chem.*, 2007, **7**, 552-558.
7. B. E. Rogers, M. E. Rosenfeld, M. B. Khazaeli, G. Mikheeva, M. A. Stackhouse, T. Liu, D. T. Curiel and D. J. Buchsbaum, *J. Nucl. Med.*, 1997, **38**, 1221-1229.
8. F. L. Thorp-Greenwood and M. P. Coogan, *Dalton Trans.*, 2011, **40**, 6129-6143.
9. R. Hueting, M. Christlieb, J. R. Dilworth, E. G. Garayoa, V. Gouverneur, M. W. Jones, V. Maes, R. Schibli, X. Sun and D. A. Tourwe, *Dalton Trans.*, 2010, **39**, 3620-3632.
10. R. Mansi, R. Minamimoto, H. Mäcke and A. H. Iagaru, *J. Nucl. Med.*, 2016, **57**, 67S-72S.
11. T. F. Massoud and S. S. Gambhir, *Genes Dev.*, 2003, **17**, 545-580.
12. P. A. Waghorn, *J. Labelled Comp. Radiopharm.*, 2014, **57**, 304-309.
13. P. A. Waghorn, M. W. Jones, M. B. M. Theobald, R. L. Arrowsmith, S. I. Pascu, S. W. Botchway, S. Faulkner and J. R. Dilworth, *Chem. Sci.*, 2013, **4**, 1430-1441.
14. J. R. Dilworth, S. I. Pascu, P. A. Waghorn, D. Vullo, S. R. Bayly, M. Christlieb, X. Sun and C. T. Supuran, *Dalton Trans.*, 2015, **44**, 4859-4873.
15. D. M. Schuster, C. Nanni and S. Fanti, *J. Nucl. Med.*, 2016, **57**, 61S-66S.
16. M. Knight, K. Takahashi, B. Chandrasekhar, A. Z. Geblaoui, R. T. Jensen, D. Strader and T. W. Moody, *Peptides*, 1995, **16**, 1109-1115.
17. R. H. Burdon and P. H. van Knippenberg, in *Laboratory Techniques in Biochemistry and Molecular Biology*, Elsevier, Amsterdam, 2nd edn., 1988, vol. 19, pp. 41-94.
18. F. Cortezon-Tamarit, PhD thesis, University of Bath, 2016.
19. R. Behrendt, P. White and J. Offer, *J. Pept. Sci.*, 2016, **22**, 4-27.
20. S. A. Palasek, Z. J. Cox and J. M. Collins, *J. Pept. Sci.*, 2007, **13**, 143-148.
21. J. Brask, F. Albericio and K. J. Jensen, *Org. Lett.*, 2003, **5**, 2951-2953.
22. N. A. Sole and G. Barany, *J. Org. Chem.*, 1992, **57**, 5399-5403.
23. K.-H. Hsieh, M. M. Demaine and S. Gurusidaiah, *Int. J. Pept. Protein Res.*, 1996, **48**, 292-298.
24. E. Gourni, P. Bouziotis, D. Benaki, G. Loudos, S. Xanthopoulos, M. Paravatou-Petsotas, M. Mavri-Vavagianni, M. Pelecanou, S. C. Archimandritis and A. D. Varvarigou, *J. Med. Chem.*, 2009, **52**, 4234-4246.
25. M. K. Sharon and C. P. Nicholas, *Curr. Protein Pept. Sci.*, 2000, **1**, 349-384.
26. P. Carmona, A. Lasagabaster and M. Molina, *Biochim. Biophys. Acta, Protein Struct. Mol. Enzymol.*, 1995, **1246**, 128-134.
27. G. K. Dewkar, P. B. Carneiro and M. C. T. Hartman, *Org. Lett.*, 2009, **11**, 4708-4711.
28. P. Gomes, N. Vale and R. Moreira, *Molecules*, 2007, **12**, 2484-2506.
29. R. Karaman, F. Beesan and D. Karaman, *J. Pharm. Res. Int.* , 2015, **4**, 361-390.
30. J. L. Jones, A. R. Dongre, A. Somogyi and V. H. Wysocki, *J. Am. Chem. Soc.*, 1994, **116**, 8368-8369.
31. S. Cheng, L. Lang, Z. Wang, O. Jacobson, B. Yung, G. Zhu, D. Gu, Y. Ma, X. Zhu, G. Niu and X. Chen, *Bioconjugate Chem.*, 2018, **29**, 410-419.
32. C. Liolios, B. Buchmuller, U. Bauder-Wüst, M. Schäfer, K. Leotta, U. Haberkorn, M. Eder and K. Kopka, *J. Med. Chem.*, 2018, DOI: 10.1021/acs.jmedchem.1027b01856.
33. H. Zhang, K. Abiraj, D. L. J. Thorek, B. Waser, P. M. Smith-Jones, M. Honer, J. C. Reubi and H. R. Maecke, *PLoS ONE*, 2012, **7**, e44046.

34. E. Valeur and M. Bradley, *Chem. Soc. Rev.*, 2009, **38**, 606-631.
35. T. I. Al-Warhi, H. M. A. Al-Hazimi and A. El-Faham, *J. Saudi Chem. Soc.*, 2012, **16**, 97-116.
36. C. A. G. N. Montalbetti and V. Falque, *Tetrahedron*, 2005, **61**, 10827-10852.
37. F. Albericio and L. A. Carpino, in *Methods in Enzymology*, Academic Press, London, 1st edn., 1997, vol. 289, pp. 104-126.
38. M. Bodanszky and J. Martinez, *Synthesis*, 1981, **1981**, 333-356.
39. D. A. Leas, J. Wu, E. L. Ezell, J. C. Garrison, J. L. Vennerstrom and Y. Dong, *ACS Omega*, 2018, **3**, 781-787.

Chapter 4. Synthesis and structural studies of tripodal thiosemicarbazide systems

4.1. Overview of Chapter 4

Self-assembly is a potent tool to assemble molecules and nanocomposites into ordered macroscopic structures. New functional materials can be obtained by self-assembly, such as photonic crystals and ordered DNA structures.[1] A variety of organic molecular building blocks for self-assembly in supramolecular chemistry are available (*Figure 4.1*).[2] Their intermolecular structures go from simply linear to bent or star-like, and contain different functional groups. Among them, tripod-shaped units have been commonly used to construct supramolecular structures. Some advantages for the use of these tripodal molecules are that they allow the formation of open networks with pores, which can be used for selective adsorption and immobilisation of guest molecular species.[3, 4] Intermolecular interactions (including hydrogen bonding, metal-ligand interactions or van der Waals interactions) between the different molecules or counter ions present in the structure can help to stabilise the porous networks.[5, 6] Such tripodal molecules usually consist of a flat core and peripheral arms including terminal functional groups of one type, and helping this way to create intermolecular interactions of the same strength and directionality.[7, 8]

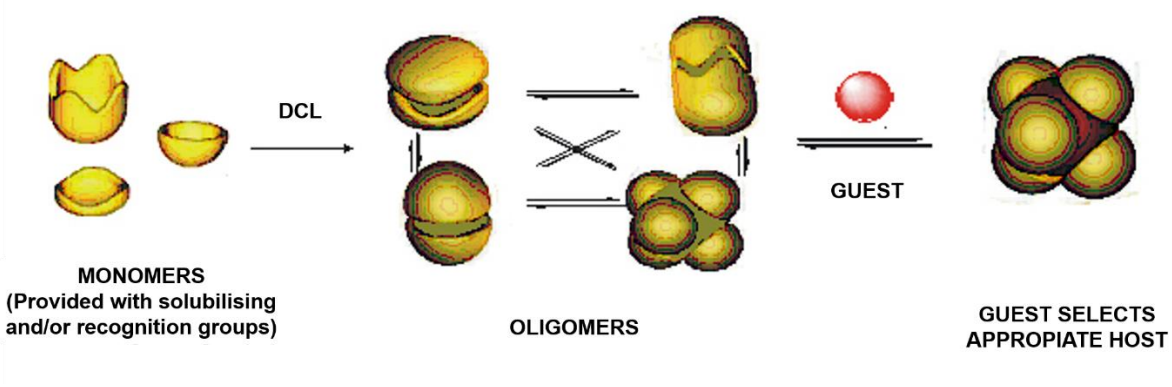

Figure 4.1. Schematic representation of the self-assembly of monomers to form oligomers and encapsulate guest species. Adapted from reference [9].

Tripodal ligands are tridentate molecules, and they constitute a type of versatile scaffolds to build mono- and polynuclear coordination compounds. They have the ability to potentially chelate metal ions and form stable complexes.[10] In many occasions, such tripodal organic compounds are built by coupling three binding strands with chelating moieties to an anchor unit *X* (*e.g.*, a single atom or a polyatomic platform, in this case a substituted benzene ring) with three functional groups for coupling with binding strands.

As it has already been described in *Chapter 1*, thiosemicarbazide derivatives and some of their transition metal ion complexes have several potential biological applications, including anti-fungal, anti-viral, anti-bacterial and anti-tumour activities.[11-13] Moreover, thiosemicarbazides are good scaffolds for self-assembly in supramolecular chemistry, due to the presence of multiple functional groups.[14]

This Chapter describes the synthesis of four tripodal ligands based on a benzene core substituted with three thiosemicarbazide arms. The difference between the ligands lies in the terminal group of the thiosemicarbazide arms (methyl, ethyl, phenyl and allyl groups). These ligands can also potentially be used to encapsulate metals, forming a cage-type structure. Initially, it was proposed that the reaction for the formation of the ligands went through an N-alkylation pathway on the terminal NH_2 group of the thiosemicarbazides. However, thanks to obtaining crystal structures for three of these four ligands, it was possible to see that what actually occurred was an S-alkylation. The structure and self-assembling properties of the ligands were studied by NMR spectroscopy, using conventional ^{1}H NMR and 2D NOESY, ROESY and DOSY NMR experiments. These types of compounds seem to self-assemble in solution at the concentrations used for the NMR experiments, as it can be seen from the obtained spectra, and has been previously reported for similar species.[15-18] The toxicity of the compounds was tested using crystal violet assays in prostate cancer (PC-3), mice breast cancer (EMT6) and epithelial fibroblast (FEK-4) cell lines.

Recently, there has been great interest in the investigation into the design and synthesis of molecules that are able to organise themselves into specific supramolecular arrangements that are stable in the solid state form. This is due to the fact that the incorporation of specific components into a crystal lattice can lead to the development of new materials with characteristic chemical and physical properties.[19, 20]

4.2. Synthesis of tripodal thiosemicarbazide derivatives

Ligands with a fully substituted benzene core containing three thiosemicarbazide arms were synthesised with the idea of using them as chelates for different metals. In order to achieve these compounds, the reagents 4-methyl-3-thiosemicarbazide, 4-ethyl-3-thiosemicarbazide, 4-phenyl-3-thiosemicarbazide and 4-allyl-3-thiosemicarbazide were used as starting materials, accordingly, together with compound **1**, which was described in *Chapter 2* (*Scheme 4.1*).

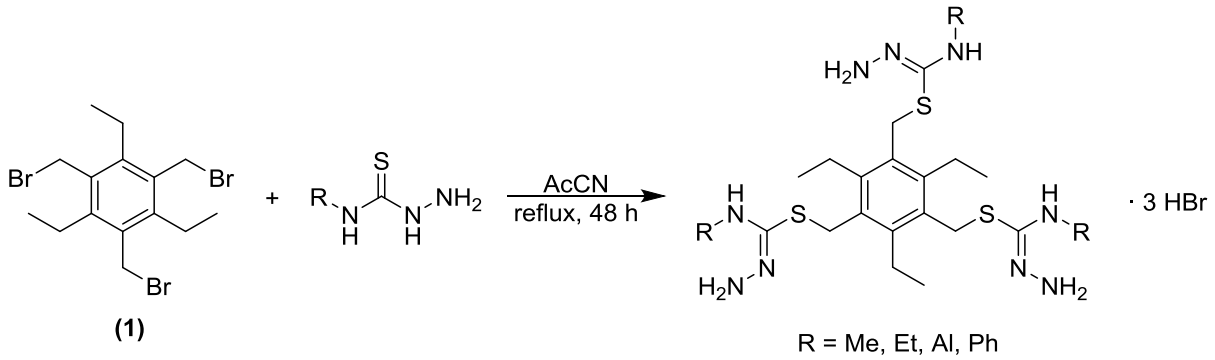

Scheme 4.1. Reaction to obtain compounds **26** (R = methyl), **27** (R = ethyl), **28** (R = phenyl) and **29** (R = allyl), as tri-HBr salts.

The starting materials were dissolved in acetonitrile in a 1:4 ratio for compound **1** and the corresponding thiosemicarbazide derivative, respectively, and the reaction mixture was heated under reflux for 48 hours. After this time, a solid could be isolated, characterised and used without further purification. Using four different thiosemicarbazide derivatives four compounds were obtained, which differed in the substituent of the trisubstituted arms (compounds **26**, **27**, **28** and **29**) (*Figure 4.2*).

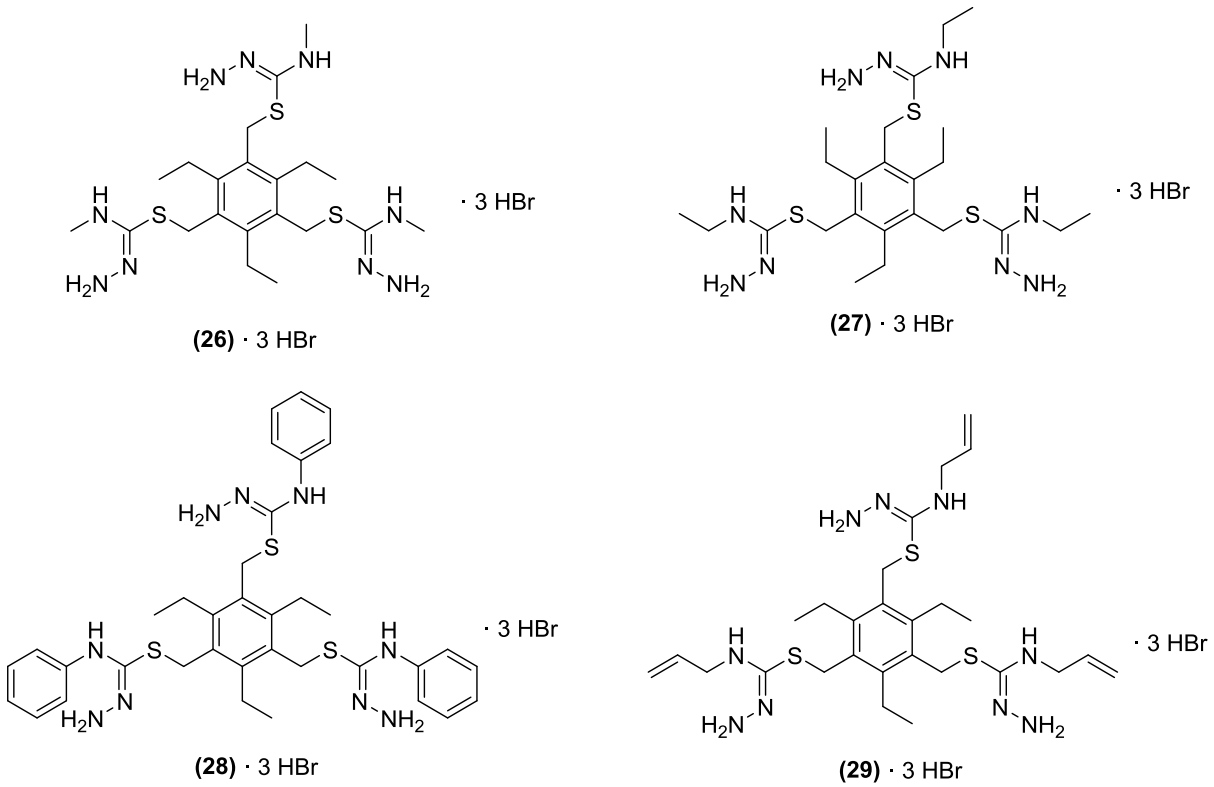

Figure 4.2. Compounds obtained from the reaction between compound **1** and four different thiosemicarbazide derivatives (*Scheme 4.1*).

The four compounds shown above were successfully characterised by mass spectrometry. The spectra showed peaks for the expected molecular formulae, as it can be seen for compound **29**; the spectrum obtained by positive mode nanoelectrospray ionisation shows a peak at m/z = 592.3010 that corresponds to the $[M+H]^+$ ion, and a peak at m/z = 296.6546 that corresponds to the doubly protonated species, $[M+2H]^{2+}$ (*Figure 4.3*).

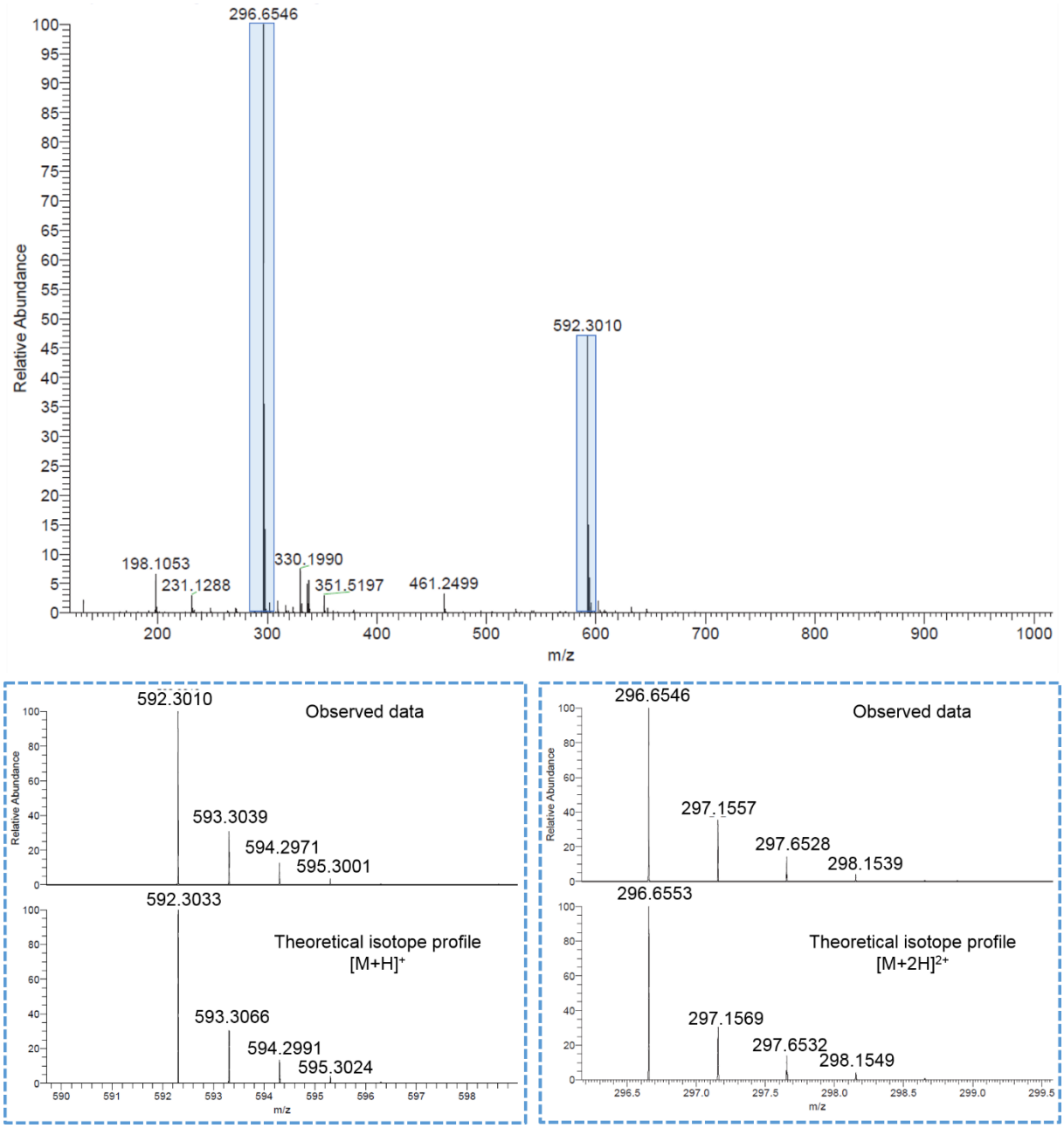

Figure 4.3. Mass spectrum of compound **29** using nESI+, and amplification of the isotopic patterns.

Compounds **26**, **27**, **28** and **29** were also characterised by infrared spectroscopy in the solid state. The FT-IR spectrum of compound **26** shows bands that can be assigned to stretching vibrations within the compound (*Figure 4.4* and *Table 4.1*). Accordingly, N-H stretching bands can be observed at 3161 cm^{-1}, and C-H stretching bands at around 2965 cm^{-1}. At 1650 cm^{-1} there are bands corresponding to C=N stretchings. Finally, at lower frequencies of approximately 739 and 664 cm^{-1}, there are bands that can be assigned to the stretching of C-S and C-Br groups, respectively. This type of vibrations in the FT-IR spectrum are characteristic for the four ligands synthesised hereby.

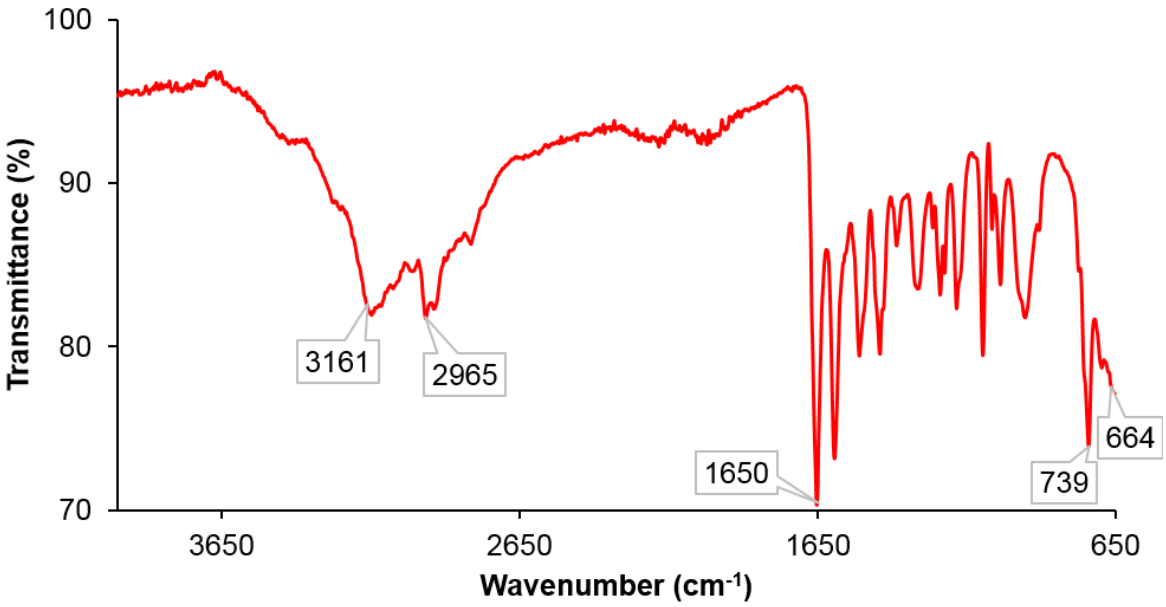

Figure 4.4. FT-IR spectrum of compound **26**.

Table 4.1. Band assignment for the FT-IR spectrum of compound **26** (*Figure 4.4*).

Wavenumber / cm^{-1}	Vibrational mode
3161	N-H st
2965	C-H st
1650	C=N st
739	C-S st
664	C-Br st

4.2.1. Synthesis of ligands under acidic and basic conditions

The efficiency of the previous synthesis under acidic and basic conditions was tested to see if the same product could still be obtained. Molecules that are pH-sensitive and change their structure and properties according to this parameter have been reported in the literature, and are known as molecular switches.[21-23] For the purpose of investigating if the synthesised thiosemicarbazide ligands can act as such, two reactions were performed using the same conditions as previously described (compound **1** and 4-ethyl-3-thiosemicarbazide in a 1:4 ratio, respectively), using acetonitrile as solvent and heating the reaction mixture under reflux for 48 hours. The initial pH of the mixture at room temperature was approximately 4. This is due to the slight acidity of the thiosemicarbazide derivatives.

In the case of the reaction carried out under acidic conditions, three drops of concentrated HCl were added to the reaction flask, and the pH of the mixture descended to 2. From the solution,

a white solid precipitated. After heating for 48 hours, the reaction mixture was yellow and contained a solid. The mixture was filtered and dried, and a light brown solid obtained. The filtrate was dried under reduced pressure and this yielded a purple oil. The two products were independently analysed by mass spectrometry, FT-IR and NMR spectroscopy. The ^{1}H NMR spectrum of the solid that was obtained by filtration from the final mixture showed the resonances for the expected molecule (compound **27**). The ^{1}H NMR spectrum of the solid that was obtained by drying the filtrate did not match with this structure, and instead it showed resonances corresponding to a mixture of the ligand and the starting material (compound **1**) (*Figure 4.5*).

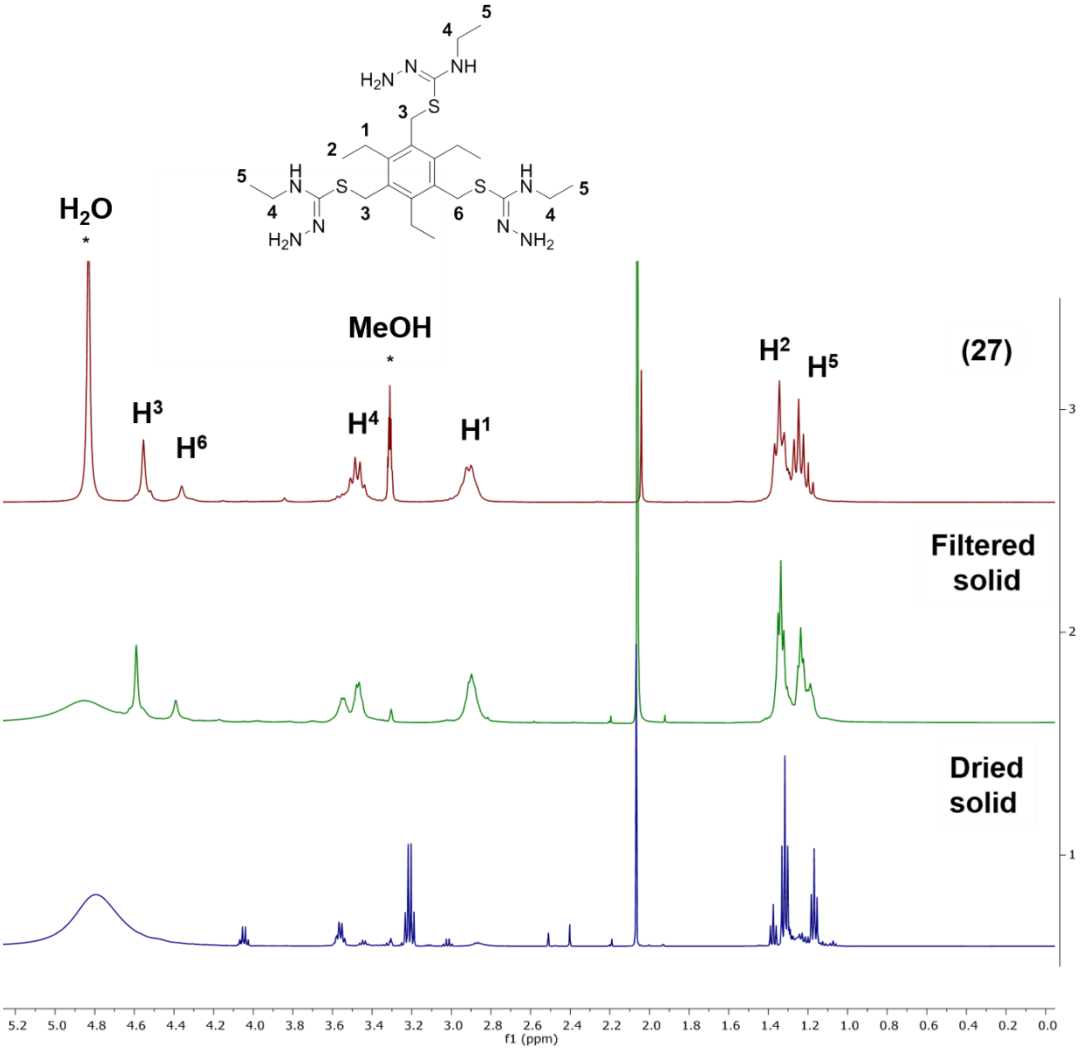

Figure 4.5. ^{1}H NMR (500 MHz, CD_3OD, 298 K) spectra of compound **27** (· 3 HBr), and of the filtered and dried solids from the reaction carried out using acidic conditions.

In the case of the reaction carried out under basic conditions, triethylamine was added to the starting mixture (initial pH = 4) at room temperature to adjust the pH to a value around 8-9. In this case, the formation of a white solid was also observed upon the addition of the base. After heating for 48 hours, the aspect of the mixture was an orange solution with a solid, which was

filtered and dried. A pink solid was isolated. The filtrate was dried under reduced pressure and yielded an orange solid. As for the previously described reaction, the two products were analysed by mass spectrometry, FT-IR and NMR spectroscopy. In this case, the ^{1}H NMR spectra of the solid obtained by filtration or by drying the filtrate did not show the resonances assignable to the expected product. Instead, they both showed similar resonances that are very close to the ones for the starting material (compound **1**) (*Figure 4.6*).

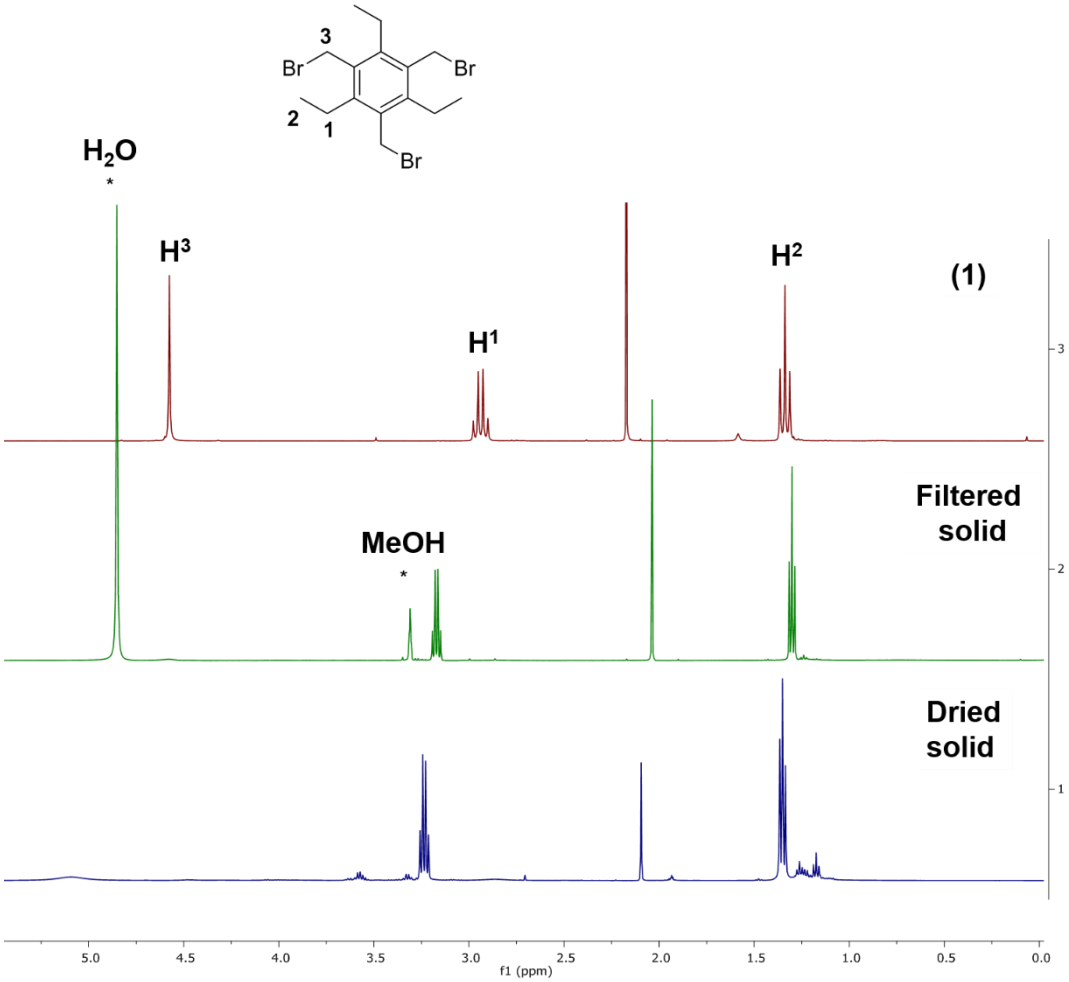

Figure 4.6. ^{1}H NMR (500 MHz, 298 K) spectra of compound **1** ($CDCl_3$), and of the filtered and dried solids from the reaction carried out using basic conditions (CD_3OD).

These results suggest that under acidic conditions the ligand of interest is formed, however this does not occur under basic conditions. This may be explained by the preferred formation of the –SH form of the thiosemicarbazide under acidic conditions. This favours the reaction between the –SH group and the CH_2Br arms of compound **1** to form the corresponding tripodal thiosemicarbazide compound.

4.3. Characterisation of the ligands and NMR study

Compounds **26**, **27**, **28** and **29**, isolated as their 3 HBr salts, were characterised by NMR spectroscopy. The proton resonances of such molecules are complex, since the structure of the compounds is not symmetric due to the different orientations of the arms with respect to the plane of the benzene ring. The ^{1}H NMR spectrum of compound **27** (recorded at 298 K) (*Figure 4.7*) shows a singlet at 4.55 ppm that integrates for 4 H and corresponds to the protons of the two methyl groups linked to the thiosemicarbazides, H^3. Another singlet at 4.36 ppm corresponds to the remaining methyl group of this kind, H^6. At around 3.47 ppm there is a peak with a multiplicity close to a quartet that integrates for 6 H and corresponds to the protons of the CH_2 groups in the three thiosemicarbazide arms, H^4. A multiplet at around 2.91 ppm integrating for 6 H corresponds to the protons of the CH_2 groups in the three ethyl arms of the complex, H^1. In the upfield region of the spectrum, there is a peak between 1.36 and 1.31 ppm that resembles a triplet and integrates for 9 H, which is due to H^2, the protons in the three CH_3 groups of the ethyl arms of the molecule. Finally, a multiplet between 1.27 and 1.17 ppm corresponds to 9 H and is due to H^5. It can be observed that the equivalent protons in the molecule appear as a multiplet instead of the multiplicity that would be expected. This is due to the chemical equivalence but magnetical inequivalence of these protons due to the different arms in the complex adopting different positions with respect to the plane of the benzene ring, which generates different surroundings for the protons. In summary, for compound **27** the equivalent protons of the three thiosemicarbazide arms appear at the same regions of the spectrum, except for H^3 and H^6, which are seen as two differentiated singlets.

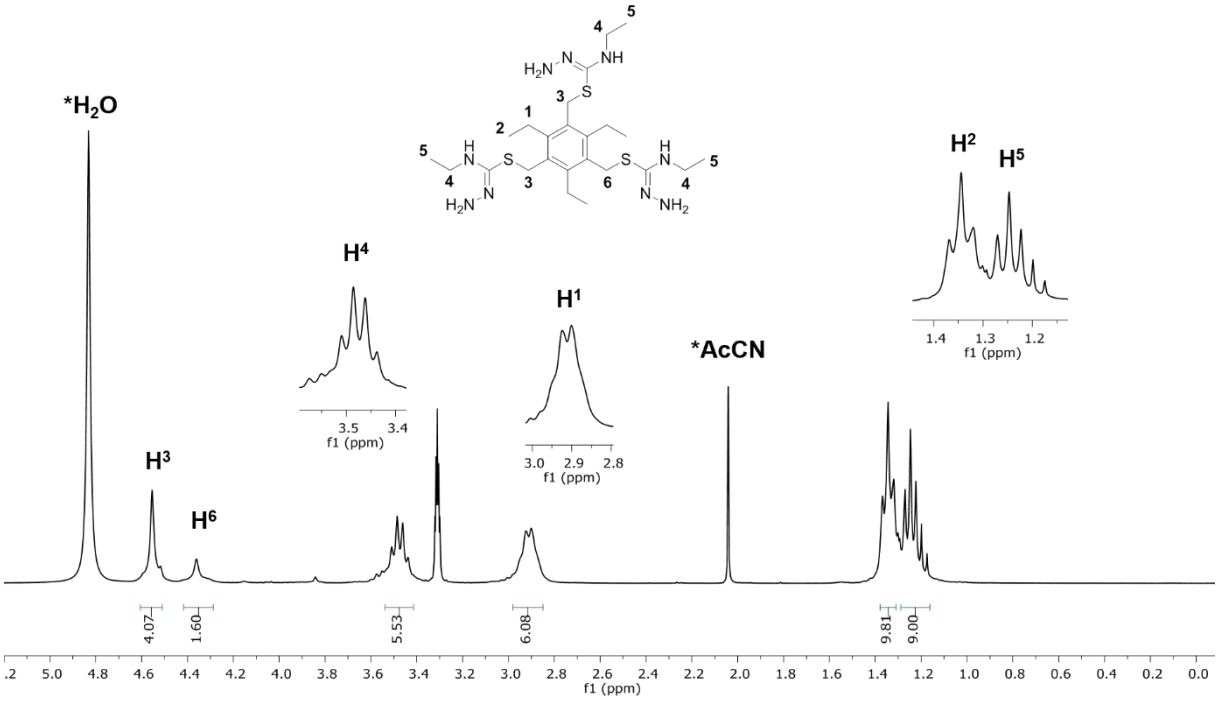

Figure 4.7. ^{1}H NMR (300 MHz, CD_3OD, 298 K) spectrum of compound **27** (· 3 HBr).

The ^{1}H NMR spectrum of compound **29** (recorded at 298 K) (*Figure 4.8*) shows a similar tendency to that observed in the spectrum of compound **27**. However, the main difference lies in the fact that for compound **29** all the protons in the three thiosemicarbazide arms appear divided in two: as if two of the arms were equivalent among them, and a third one was inequivalent and for this reason appears separately. Accordingly, the CH allyl protons appear as two multiplets between 6.02 – 5.92 ppm and 5.92 – 5.81 ppm and these integrate for 1 H (H^{9}) and 2 H (H^{5}), respectively. Other two multiplets between 5.41 – 5.31 ppm and 5.31 – 5.21 ppm that integrate for 2 H and 4 H, respectively, correspond to the CH_2 allyl protons, H^{10} and H^{6}. Two singlets at 4.54 ppm and 4.38 ppm correspond to H^{3} and H^{7}, respectively, the CH_2 groups that connect the thiosemicarbazide arms to the benzene ring. Between 4.10 and 4.06 ppm there is a multiplet with the shape of two peaks that correspond to 2 H and 4 H, respectively, and are due to H^{8} and H^{4}. In the upfield region of the spectrum there are two sets of peaks due to the protons from the CH_2CH_3 arms of the molecule. The 6 protons named as H^{1} appear as a multiplet between 2.90 and 2.86 ppm, and the 9 protons named as H^{2} are seen as a multiplet between 1.33 and 1.30 ppm.

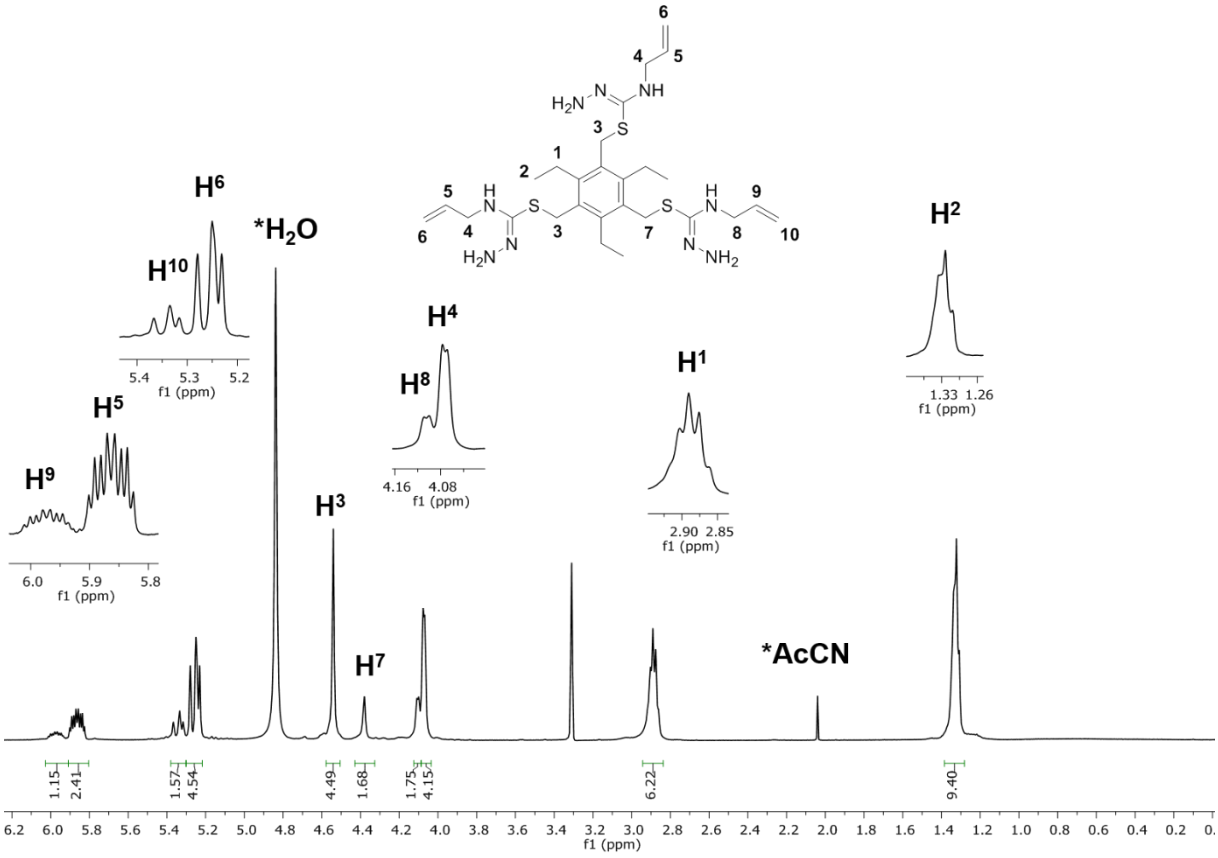

Figure 4.8. ^{1}H NMR (500 MHz, CD_3OD, 298 K) spectrum of compound **29** (· 3 HBr).

^{1}H-^{1}H nuclear Overhauser enhancement spectroscopy (NOESY) is an NMR experiment that can be useful to investigate the spatial relationships among proximal protons and study

structural details of their interaction. In this context, NOESY cross peaks indicate proximity between protons. NOESY uses the dipolar interaction between protons that are closer in space than around 5 Å. Such dipolar interactions depend also on how quickly the molecule tumbles in solution and on the molecular mass: a molecule of low molecular mass tumbles fast in solution, and a molecule of high molecular mass tumbles slowly compared to the previous, and for this reason it will have positive NOESY cross peaks.[24]

In this work, NOESY NMR was recorded using compounds **26**, **27**, **28** and **29** at 298 K. From the NOESY NMR spectrum of compound **26**, it can be observed that there are six correlations among the protons of this molecule (*Figure 4.9*). Correlations between the protons of the ethyl arms of the compound, H^1 and H^2, with the methyl groups of the thiosemicarbazide arms, H^3 and H^5, are observed. Also correlations between H^1 and H^2, and between H^3 and H^5. All these correlations are seen as positive peaks, which *a priori* would indicate that they are due to exchange. However, it is not possible to have exchange between these groups of protons (such as a CH_2 and a CH_3 of an ethyl group). Thus, it could be concluded that the molecule that is being studied has a higher molecular mass than expected, which would explain the existence of positive exchange peaks in the NOESY spectrum.[25] This would imply that this type of compounds self-assemble to form aggregates in the methanol solutions of the concentration used for these NMR experiments. It was found that methanol improved the formation of hydrogen bonding in the molecule, and this favoured self-aggregation into a polymeric network.

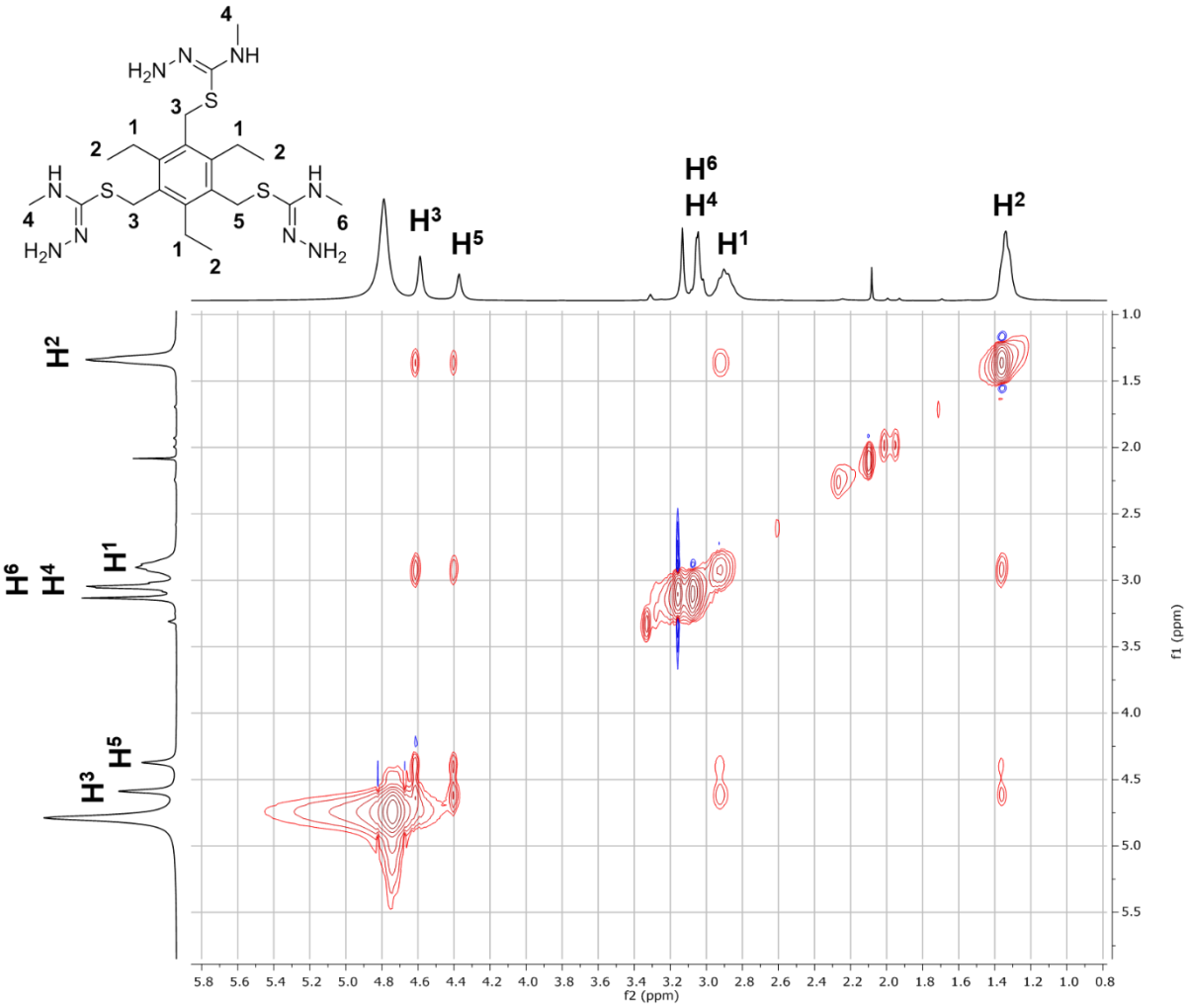

Figure 4.9. ^{1}H-^{1}H NOESY NMR (500 MHz, CD_3OD, 298 K) spectrum of compound **26** (· 3 HBr).

^{1}H-^{1}H rotating frame Overhauser enhancement spectroscopy (ROESY) is a 2D NMR technique useful to study possible intramolecular interactions within the different protons of a molecule. ROESY is seen as an alternative to NOESY in the study of molecules of intermediate or large size.[26, 27] NOESY experiments work for molecules of very low and very high molecular weight. However, for molecules of molecular weight between approximately 1000 and 2000 Da, NOESY does not work. In the case of molecules with a molecular mass within this interval, a ROESY experiment can help to obtain NOE information. Consequently, for high molecular weight molecules, NOESY and ROESY experiments will produce similar results, but the cross peaks will be in phase with the diagonal for a NOESY spectrum, and in the opposite phase for a ROESY.

The ROESY spectrum of compound **26** shows negative cross peaks that indicate spatial proximity between the protons in the ethyl arms of the molecule (H^1 and H^2) and the protons

from the thiosemicarbazide arms (H^3 and H^5), and between H^1-H^3, H^1-H^5, H^2-H^3 and H^2-H^5, respectively (*Figure 4.10*).

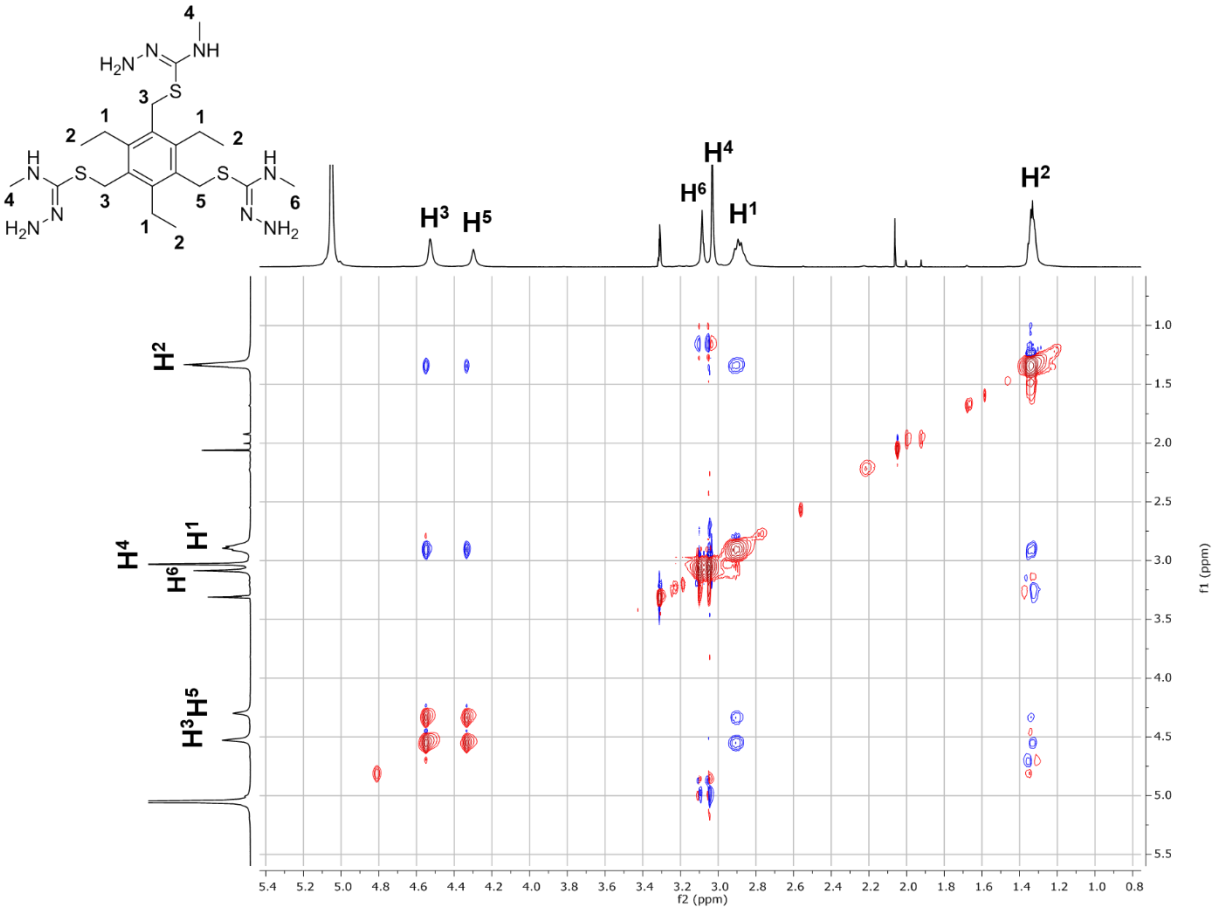

Figure 4.10. ^{1}H-^{1}H ROESY NMR (500 MHz, CD_3OD, 298 K) spectrum of compound **26** (· 3 HBr).

^{1}H diffusion-ordered spectroscopy (DOSY) is an NMR method discovered by Morris and Johnson,[28] that aims to identify the molecular components of a mixture sample and obtain information about their size. DOSY builds a two-dimensional spectrum: the first dimension (*x* axis) is a conventional ^{1}H NMR spectrum of the sample, and the second dimension (*y* axis) constitutes the diffusion coefficients of the different components present in it. It is possible to measure diffusion coefficients of different components of a mixture using DOSY NMR. These coefficients are important because they are sensitive to molecular size and shape, and can provide information about the molecular weight and molecule aggregation status.[29]

In this context, ^{1}H DOSY NMR was carried out on the four ligands (compounds **26**, **27**, **28** and **29**). All the 2D spectra showed the presence of only one compound in the sample and a signal for water (with a resonance at approximately 4.87 ppm), as it can be seen for compound **26** (*Figure 4.11*).

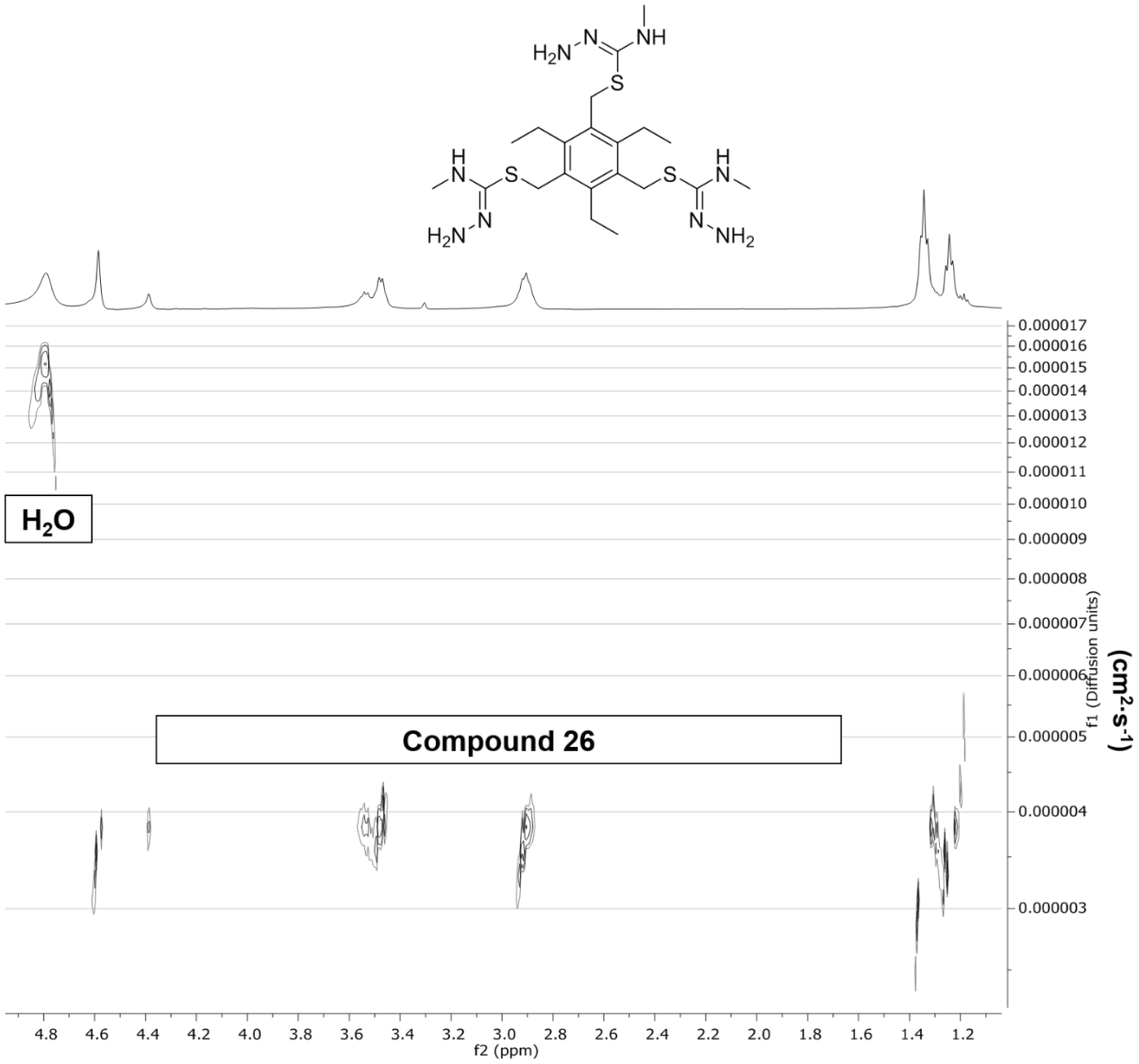

Figure 4.11. ^{1}H DOSY NMR (500 MHz, CD_3OD, 298 K) spectrum of compound **26** (· 3 HBr).

Moreover, the experimental diffusion coefficients (D_{exp}) for the four different compounds were calculated from the DOSY spectra in deuterated methanol using MestRenova (*Table 4.2*). The values for the D_{exp} of the four compounds tested were found to be between approximately $3.4 \cdot 10^{-10}$ m^2/s and $4.8 \cdot 10^{-10}$ m^2/s. These values are smaller than those expected for the corresponding single molecules, which presumably consist of just a substituted tripodal core.[30] Consequently, it can be concluded that these molecules self-aggregate in solution at the concentration needed to obtain an NMR spectrum using methanol as solvent, forming a larger product.[17, 31] Furthermore, the existence of hydrogen bonding making the molecules to self-assemble is also a possibility due to the elevate number of functional groups able to achieve such interactions.[32, 33] This matches with the information extracted from the NOESY experiments, which also suggested some degree of aggregation and the existence of bigger size structures in solution.

Table 4.2. Diffusion coefficient values found for compounds **26**, **27**, **28** and **29**, and for H_2O, calculated from the ^1H DOSY spectra using MestReNova.

Compound	Diffusion coefficient (· 10^{-10}) * / $m^2 \cdot s^{-1}$
26	3.83
27	3.42
28	4.76
29	4.15
H_2O	15.2

*The diffusion coefficient values were obtained in $cm^2 \cdot s^{-1}$ using MestRenova and converted to $m^2 \cdot s^{-1}$.

By using ^1H NMR spectroscopy on the ligands at room temperature (298 K), it was not possible to elucidate the resonances due to the protons in the different arms of the compounds with a well-defined multiplicity. For this purpose, NMR experiments at variable temperature were carried out, with the idea that at lower temperatures the molecule should decrease its motion and the different arms should stop rotating freely around the benzene ring plane. For compound **26**, ^1H NMR spectroscopy was performed at 213 K (-60 ^oC), 233 K (-40 ^oC), 253 K (-20 ^oC), 273 K (0 ^oC), 298 K (25 ^oC), 313 K (40 ^oC), and 323 K (50 ^oC) (*Figure 4.12*). It was observed that at lower temperatures the multiplicity of the resonances appear less defined, as it can be seen for the peak due to H^2 at around 1.30 ppm. This resonance appears as a well-defined triplet when the temperature is 40 ^oC or higher. Something similar occurs with the multiplet at around 2.85 ppm due to H^1: it has the shape of a multiplet at lower temperatures, and becomes more well-defined as the temperature increases, although it is not a clear quartet. The protons from the terminal methyl groups in the thiosemicarbazide arms (H^4 and H^6) appear at low temperatures as two independent peaks with the shape of multiplets between 3.15 and 2.95 ppm. When the temperature of the experiment reaches up to 50 ^oC, the two peaks initially separated merge in one multiplet. The resonances for H^3 and H^5 are two singlets at around 4.50 and 4.25 ppm, and their shape and position do not change considerably. However, due to the peak corresponding to water (present in the deuterated solvent) shifting from around 5.53 to 4.56 ppm as the temperature increases, when it reaches up to 50 ^oC the peak for H^3 cannot be observed as this is overlapped with the peak for water. This remarkable shift of the resonance due to H_2O presence may well be due to the hydrogen bonding interactions present in this molecule that change with the temperature.

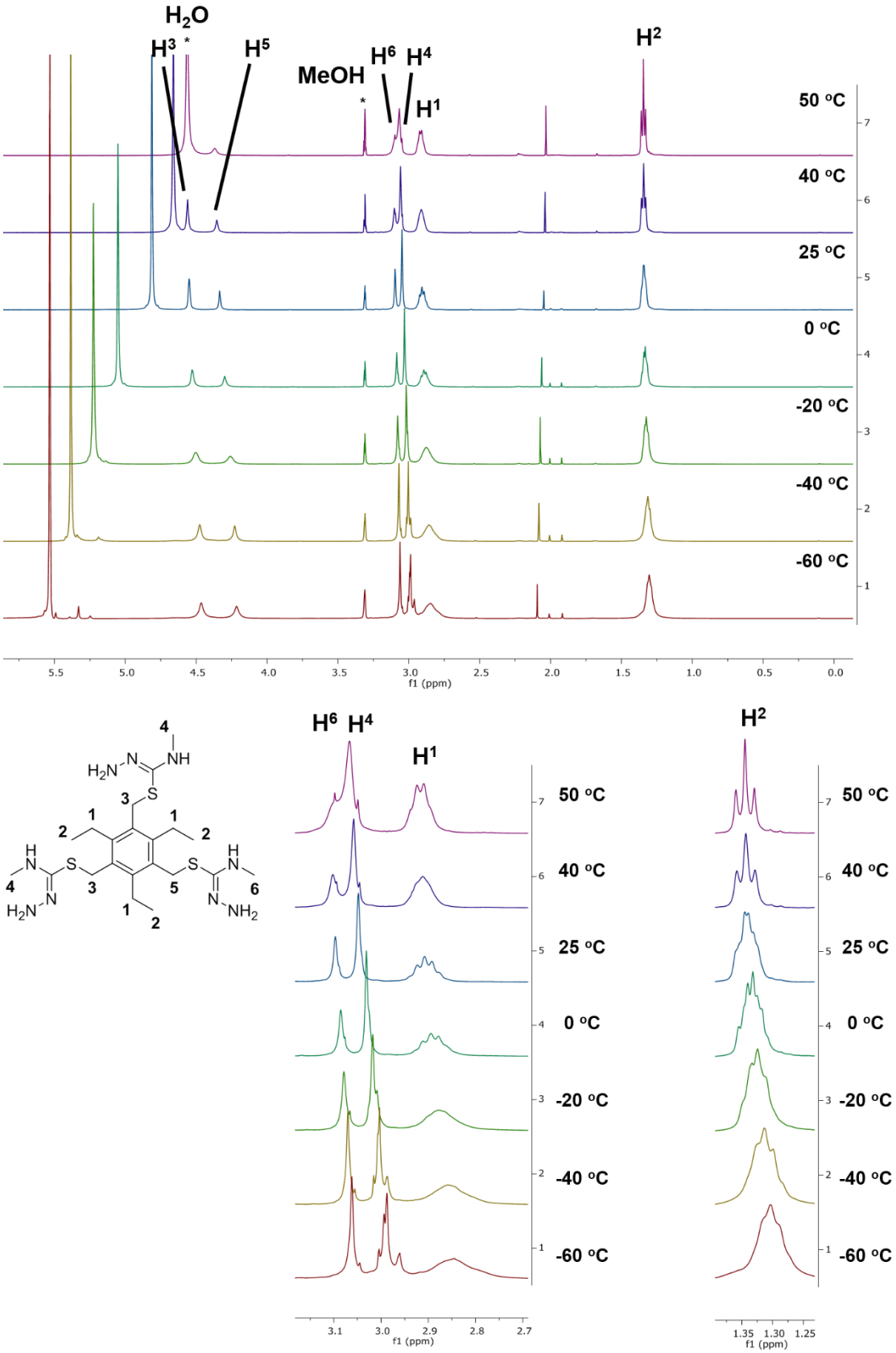

Figure 4.12. Variable temperature ^{1}H NMR (500 MHz, CD_3OD) spectra of compound **26** (· 3 HBr) at 213 K (-60 °C), 233 K (-40 °C), 253 K (-20 °C), 273 K (0 °C), 298 K (25 °C), 313 K (40 °C), and 323 K (50 °C).

Variable temperature ^{1}H NMR spectroscopy was also performed using compound **27**, at 233 K (-40 ºC), 298 K (25 ºC), and 313 K (40 ºC) (*Figure 4.13*). In this case, the same tendency is observed: the resonance due to H^2 becomes a triplet as the temperature increases. The resonance for H^1 also shows a more defined multiplicity when the temperature increases. However, the peaks due to H^4 and H^5 do not change significantly, and H^3 and H^6 appear as two different singlets at all the temperatures used for the experiments.

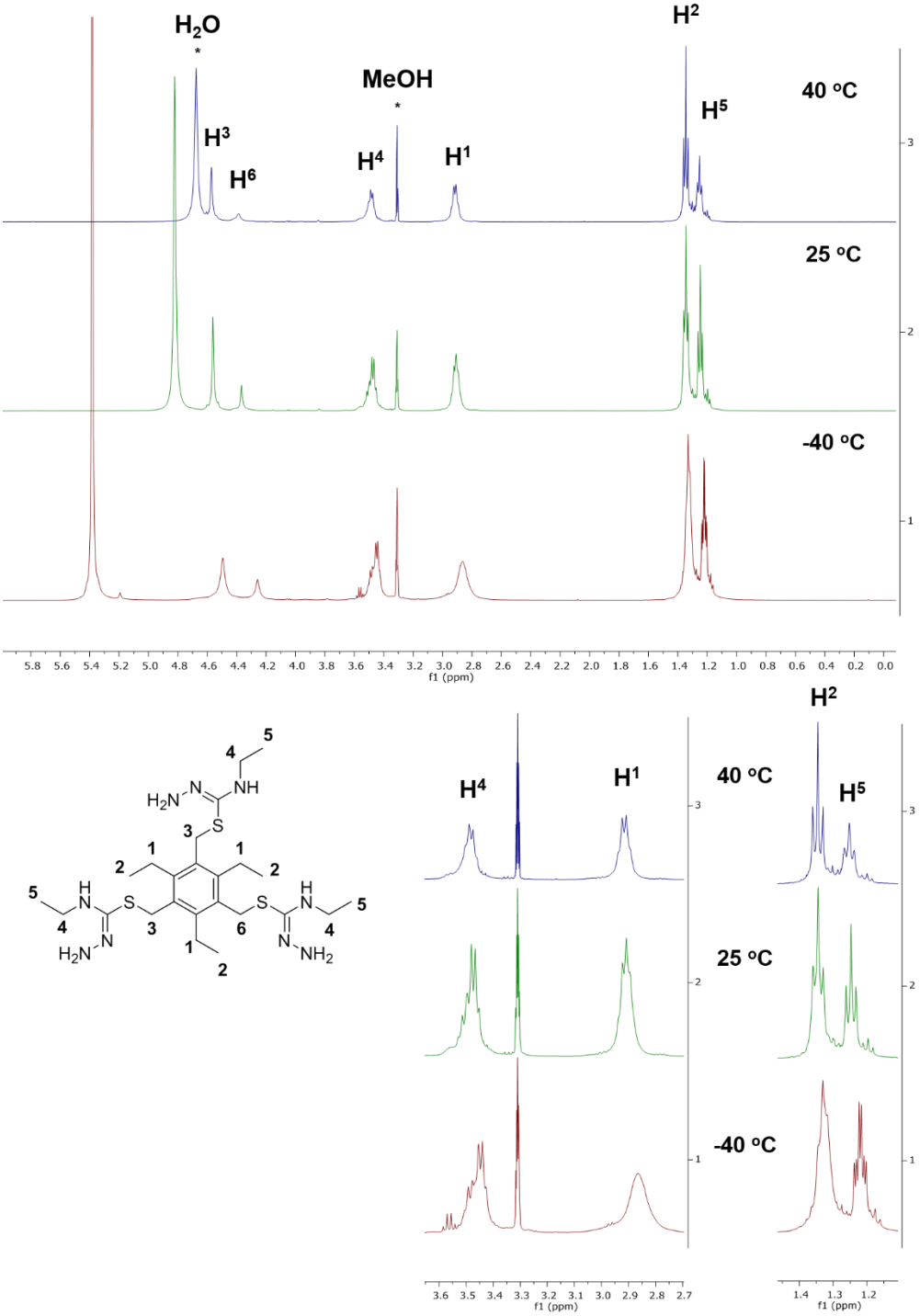

Figure 4.13. Variable temperature ^{1}H NMR (500 MHz, CD_3OD) spectra of compound **27** (· 3 HBr) at 233 K (-40 ºC), 298 K (25 ºC), and 313 K (40 ºC).

4.4. Single crystal X-ray diffraction: structural characterisation

It was initially thought that the reaction for the formation of the ligands with three thiosemicarbazide arms went through a mechanism in which the terminal amino group of the thiosemicarbazide acted as a nucleophile and removed the bromide atom from the arms of compound **1** (*Scheme 4.2*). In this case, the expected resulting compound would have been a trisubstituted tripodal core with each thiosemicarbazide derivative connected to the benzene core through the terminal N atom of the starting material molecule. This type of reactivity has been previously reported in the literature in many occasions.[34]

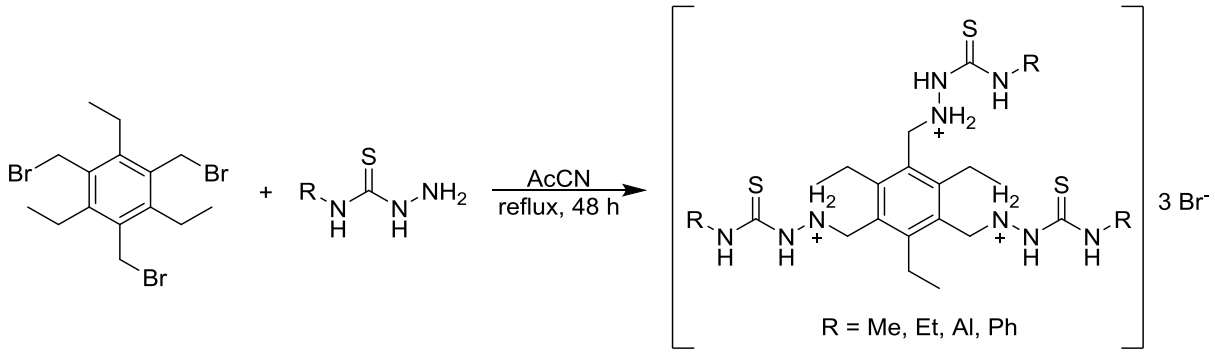

Scheme 4.2. Predicted reaction of compound **1** with thiosemicarbazide derivatives.

Therefore, it was not until a crystal suitable for single crystal X-ray diffraction was obtained and analysed that it was seen that this reaction actually occurs through the S atom of the thiosemicarbazide derivatives, and these are connected to the tripodal core by this atom. It is known that thiosemicarbazide derivatives present a tautomerism equilibrium between the keto and the enol forms of the molecule (thione/thiol equilibrium) (*Scheme 4.3*), and this finding reveals that, for the reaction treated in this chapter, the predominant reactive tautomer is that in the enol form. In some inorganic complexes, the enol form of thiosemicarbazides have been observed, rendering the thiosemicarbazide to act as a mono negatively charged ligand.[35, 36] The enol form is found in a number of metal complexes, though in these the SH group is often deprotonated. The S-alkylation of thiosemicarbazides was first reported by Yamazaki in 1975,[37] and it has been described on several occasions since then.[38-40]

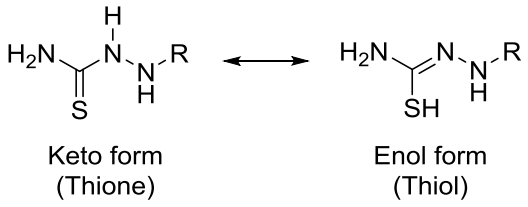

Scheme 4.3. Tautomerism equilibrium of a thiosemicarbazide.

In the case of compounds **26**, **27** and **29**, crystals suitable for single crystal X-ray diffraction were obtained by using liquid-liquid diffusion techniques. Each solid was dissolved in the minimum amount of methanol, and diethyl ether was the solvent of choice to form a second layer over the methanol one. The appearance of crystals was observed some weeks after the crystallisation experiment was set up. The single crystal X-ray diffraction data were collected and solved by Dr. Gabriele Kociok-Köhn.

The ORTEP representation of compound **29** shows a non-symmetrical structure, with the three ethyl arms pointing at the same direction, towards the upwards plane of the benzene ring (*Figure 4.14*). The three thiosemicarbazide arms are oriented in the same direction, downwards with respect to the benzene ring plane. The terminal allyl (NH-R) groups of the thiosemicarbazide arms are pointing upwards, the same direction as the ethyl arms of the molecule. Two of them are oriented on the left and the third one on the right. There are Br^- atoms that crystallise with the structure of the compound, and a methanol molecule from the solvent used to obtain the crystals.

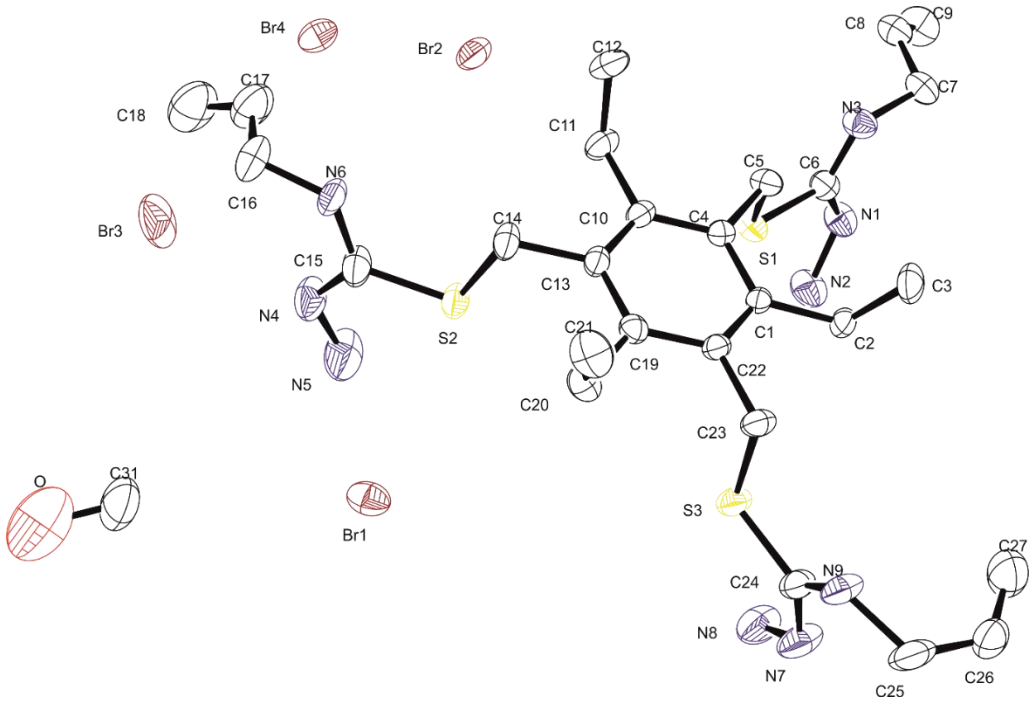

Figure 4.14. ORTEP diagram of the molecular structure of compound **29** (· 3 HBr).

The refinement of the crystal structure of the molecular formula for compound **29** showed that each unit cell contains two molecules of the product, each asymmetric unit with a molecular formula of $C_{27}H_{48}N_9S_3$. This implies that the molecule is triply protonated. Moreover, 6 Br^- atoms can be found in each unit cell in total, which play the role of counter ions (4 Br^- atoms can be seen in *Figure 4.14* because some of them are only partially occupied). A molecule of methanol (the solvent used to obtain the crystals) also localises in the unit cell. Accordingly,

the structure of compound **29** is a triply protonated molecule with three bromine atoms as counter ions and a delocalised double bond (it has been placed between two atoms in the representation for clarity) (*Figure 4.15*).

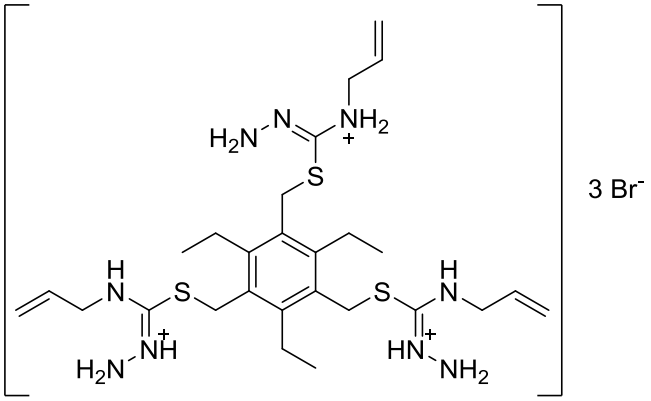

Figure 4.15. Compound **29** as shown in the crystal structure data, triply protonated and with three bromine atoms as counter ions.

The unit cell of compound **29**, with the disordered atoms being omitted for clarity, shows two molecules of the ligand that have intercalated arms: one of the molecules has the three ethyl arms upwards and the three thiosemicarbazide arms downwards, and the other one has them in opposite directions, downwards and upwards, respectively (*Figure 4.16*). Six Br^- atoms are disordered within the cell, distributing on the edges, faces, and inside the cell. Therefore, the two molecules of the same compound form a cage-like structure, and for this reason, these compounds have potential applicability as cages to encapsulate and bind ions and metals.[41]

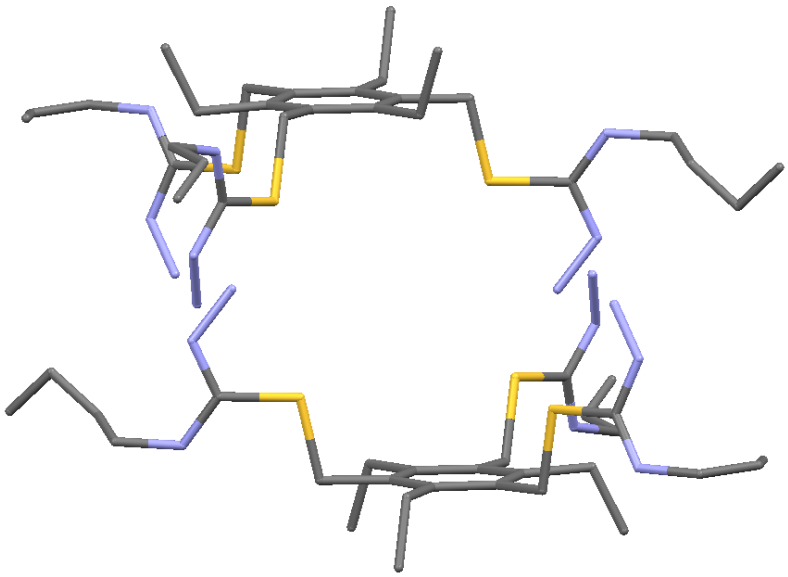

Figure 4.16. Molecular structure of compound **29** showing the two molecules found inside the unit cell.

The crystal structure of compound **29** showed to exhibit some degree of self-assembly through hydrogen bonding, from the N-H atoms of the molecules with the existing Br^- ions located in different places in the unit cell. The anion-assisted formation of discrete homodimeric and heterotetrameric assemblies by benzene-based protonated molecules has previously been described in the literature.[42] This promotes the creation of a polymer-type structure, with different layers of tripodal molecules ordered in the space (*Figure 4.17*).[43] The distance between two benzene rings located in two consecutive planes with the thiosemicarbazide arms pointing towards each other is about 8 Å, and the distance between two benzene rings in two consecutive planes with the ethyl arms pointing towards each other is about 5-6 Å. From this information, it cannot be considered that π-π stacking interactions exist among the molecules.[44, 45]

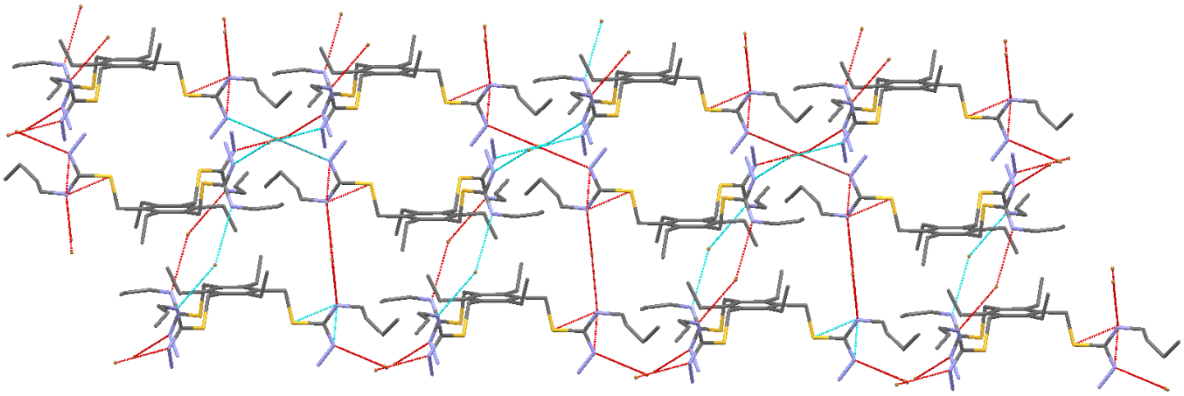

Figure 4.17. Different units of the molecular structure for compound **29** showing hydrogen bonding with the Br^- ions present in the crystal, and with the molecules being organised in different layers.

The existence of a self-assembled supramolecular structure was first revealed by NOESY NMR experiments, and confirmed using ^1H DOSY NMR when the calculated diffusion coefficients for these molecules were found to be smaller than expected for a single molecule of this size, suggesting that a bigger structure exists. This is also observed by single crystal X-ray diffraction, demonstrating that the self-assembly of this type of molecules also occurs in the solid state.

Two types of angles were measured in the molecule (*Figure 4.18*). On one side, the angle that form the ethyl arms with respect to the benzene ring, which is about 112° for the three of them. On the other side, the angle that the thiosemicarbazide arms form with respect to the benzene ring, calculated from the S atom to the C atom that forms the ring, has a value between 103 and 106°.

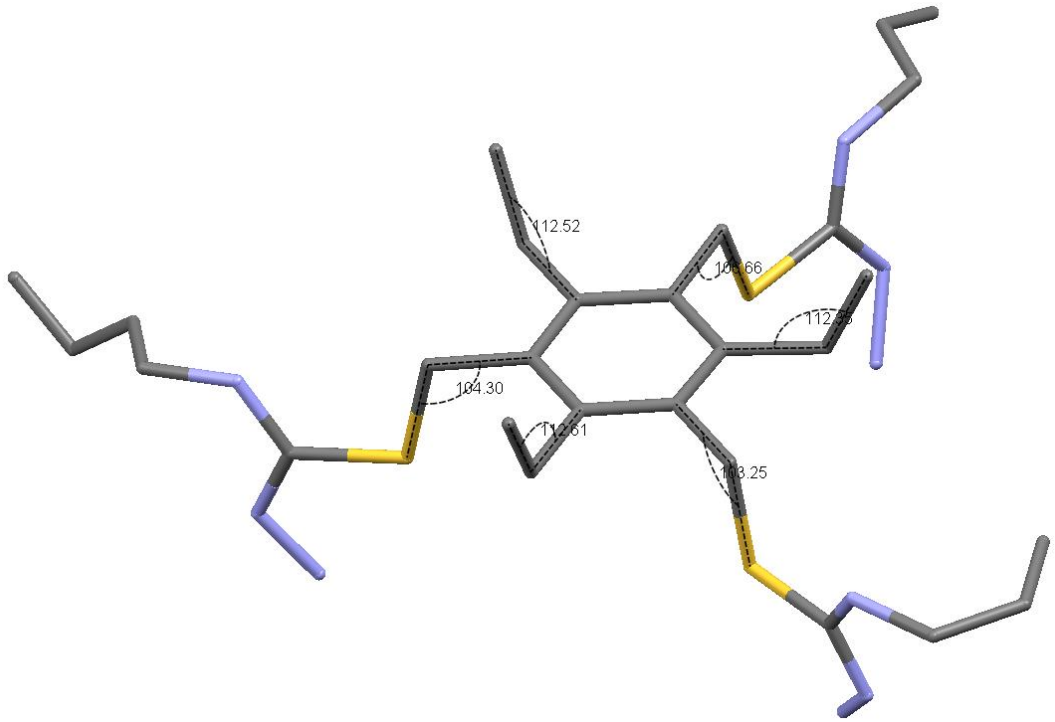

Figure 4.18. Molecular structure of compound **29** showing: (i) the angle formed between the plane benzene ring and the ethyl arms (112°), and (ii) the angle formed between the plane benzene ring and the thiosemicarbazide arms (103-106°).

The molecular structure of compound **26** was also elucidated. The unit cell of this molecule also showed to contain two units of the compound, with intercalated arms and forming a cage-like structure (*Figure 4.19*). Six Br^- atoms could also be found distributed within the unit cell, but these and the disordered parts were omitted in the representation for clarity. It can be seen that two of the terminal methyl substituents of the thiosemicarbazide arms are oriented in the same direction (downwards), while the third one is oriented towards the opposite direction (upwards). This is consistent with observations from NMR spectroscopy, whereby the resonances observed in the ^{1}H NMR spectrum of the molecule showed the three methyl groups as two independent singlets integrating for 6 H and 3 H, respectively.

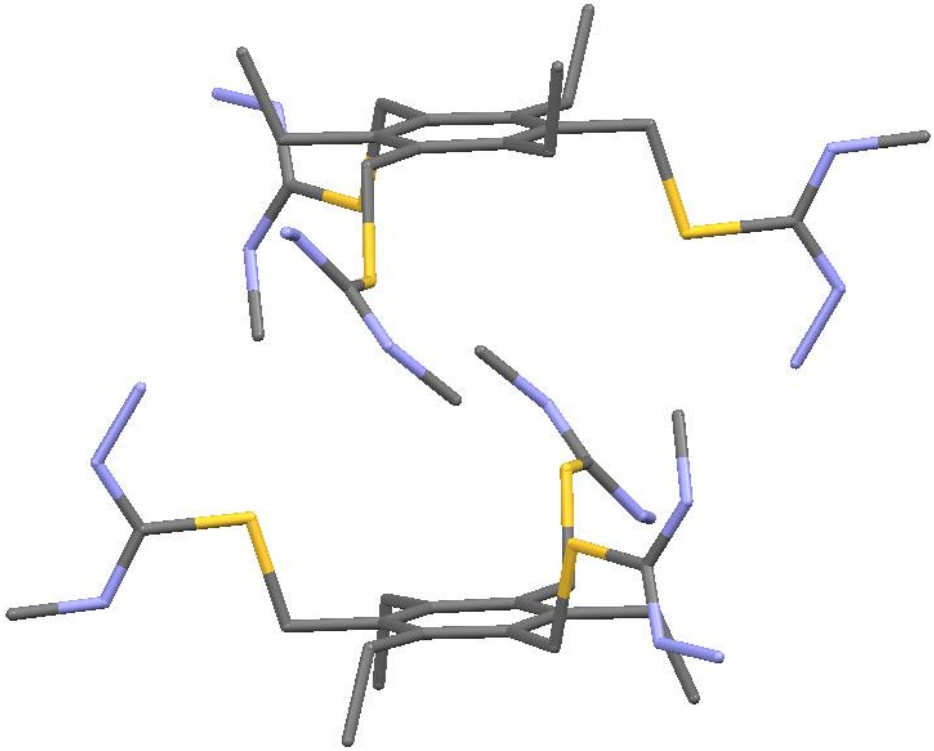

Figure 4.19. Molecular structure of compound **26** showing the two molecules that can be found inside the unit cell.

The last molecular structure that was found by single crystal X-ray diffraction was that of compound **27** (*Figure 4.20*). As for the previous cases, the disordered Br^- atoms found within the unit cell were omitted in the representation for clarity. In this structure, the three thiosemicarbazide arms of the two molecules located inside a unit cell point towards opposite directions, far from each other and with the ethyl arms of each compound that point towards each other, forming a cage-like structure. Regarding the terminal ethyl substituents in the three thiosemicarbazide arms, two of them are oriented in the same side of the plane, and the third one is oriented in the opposite side. This matches with the resonances observed in the ^1H NMR spectrum of this compound, that indicate that some of the groups of the thiosemicarbazide arms appear as two independent sets of protons.

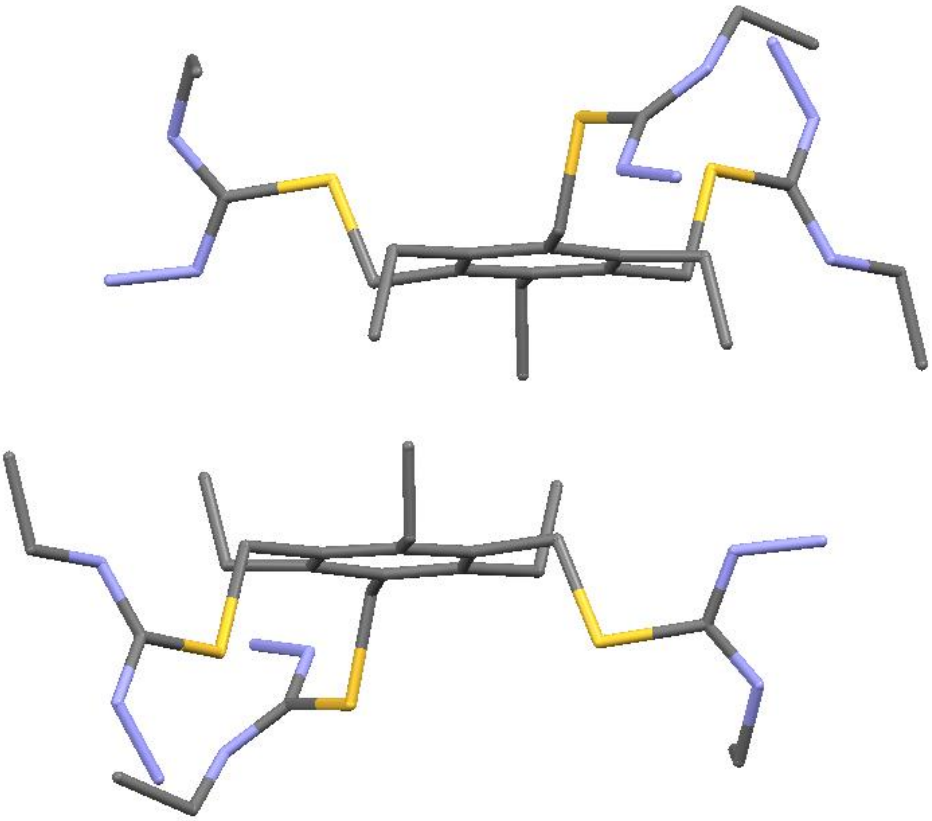

Figure 4.20. Molecular structure of compound **27** showing the two molecules found inside the unit cell.

By using the molecular structures obtained, the bond distances in the thiosemicarbazide arms were measured and compared to those in one of the starting materials, 4-methyl-3-thiosemicarbazide (CDCC No. 1205752) (*Figure 4.21*).[46] It can be seen that the bond distances do not change significantly with respect to those in the starting material (*Table 4.3*). The most notable change is that the S1-C1 distance seems to increase slightly, so that this bond loses some character of double bond. Conversely, the C1-N2 distance decreases, so that this bond retains some character of double bond. This can be explained by the existence of a delocalised double bond between the S1-C1, C1-N2 and C1-N3 system (*Scheme 4.4*). Both nitrogen atoms (N2 and N3) are bound to a hydrogen atom. Regarding the bond between the thiosemicarbazide arms and the benzene ring, this is evidently single.

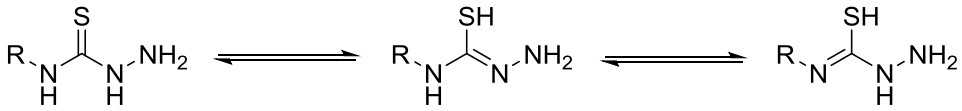

Scheme 4.4. Equilibrium existing in any thiosemicarbazide derivative, where the double bond is delocalised within three bonds.

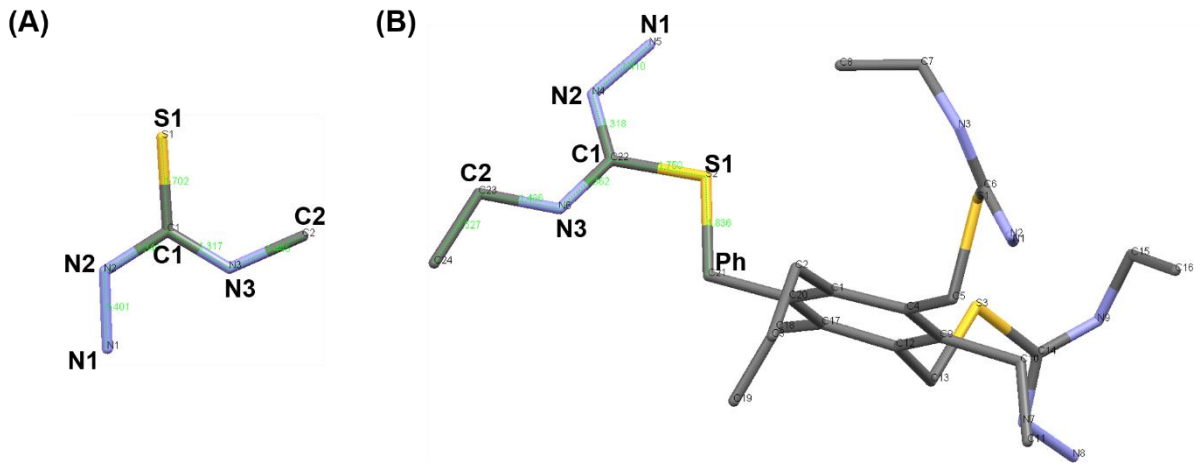

Figure 4.21. Molecular structures of 4-methyl-3-thiosemicarbazide **(A)**, and compound **27 (B)**, showing the labelled atoms used to calculate the bond distances.

Table 4.3. Distances (Å) of selected bonds in 4-methyl-3-thiosemicarbazide (TSC) and compounds **26**, **27** and **29** (these last three as 3 HBr salts) * (*Figure 4.21*).

Compound	S1-C1	C1-N2	C1-N3	N3-C2	N1-N2	S1-Ph
TSC	1.702(1)	1.346(2)	1.317(2)	1.445(2)	1.401(2)	-
26	1.751(3)	1.312(4)	1.313(4)	1.443(5)	1.406(4)	1.849(3)
27	1.757(4)	1.313(5)	1.306(5)	1.460(5)	1.410(4)	1.858(4)
29	1.742(3)	1.317(4)	1.321(4)	1.469(4)	1.419(4)	1.830(3)

***** To calculate the bond distances of the thiosemicarbazide arms in the synthesised compounds, one arm was taken as an example.

4.5. Attempted complexation to metals

Metal-based PET radiotracers have become a centre of attention in the past few years.[47-49] Zirconium, gallium and copper are elements with isotopes that can act as β^+-emitters and can therefore be used in positron emission tomography, such as zirconium-89, gallium-68 and copper-64.[50] The synthesis of new metal-based PET imaging agents requires a strong attention on the speciation of the metal ions in the presence of aqueous buffers and the environment.

Thiosemicarbazide compounds usually react with metallic cations, resulting in complexes where the thiosemicarbazides behave as chelating agents.[36] In this context, a broad number of reactions between the synthesised thiosemicarbazide derivatives (compounds **26**, **27**, **28** and **29**) and different metal salts were attempted (*Table 4.4*).

It was envisaged that these ligands could encapsulate a metal centre, similar to the cage structures synthesised by Willans *et al.,*[51] who created a rigid NHC cage ligand capable of binding metal ions, in particular Ag(I). The ligands used hereby were designed with possible anti-cancer functionality by incorporating thiosemicarbazide derivatives into their structure. Thiosemicarbazides have been reported to have enhanced anti-cancer properties when bound to a metal centre.[52]

The seventeen reactions carried out have been divided in three groups for discussion, according to the metal salt that was used as starting material, and are explained in detail in *Appendix B.2*. However, it was interesting to see the colour changes of every reaction while this was taking place and also the colour of the one or more solids that could be isolated at the end (*Table 4.5*).

Table 4.4. Reaction conditions tried between the tripodal thiosemicarbazide ligands and the different metal salts.

Entry	Metal salt / eq	Ligand / eq	Base / eq	Base (excess)	Solvent	T / ºC	Time / h
1	$ZrCl_4$ / 1	**26** / 1	LiOH / 3	$^tBuO^-$ K^+ (catalyst)	THF	90 (reflux)	24
2		**27** / 1	-	-	EtOH	25	24
3		**27** / 1	-	-	EtOH	60	5
4	$GaCl_3$ / 1	**26** / 1	LiOH / 3	$^tBuO^-$ K^+ (catalyst)	THF	90 (reflux)	24
5		**26** / 1	-	CH_3COONa (buffer)	MeOH	50 (reflux)	7
6		**26** / 1	-	-	MeOH	50 (reflux)	7
7		**27** / 1	-	-	EtOH	25	5
8	$InCl_3$ / 1	**26** / 1	-	CH_3COONa (buffer)	MeOH	50 (reflux)	7
9		**26** / 1	-	-	MeOH	50 (reflux)	7
10	$Cu(OAc)_2 \cdot H_2O$ / 1	**26** / 1	LiOH / 3	$^tBuO^-$ K^+ -	THF	90 (reflux)	24
11		**27** / 1	LiOH / 3	$^tBuO^-$ K^+ -	THF	90 (reflux)	24
12	$Cu(OAc)_2$ / 2	**29** / 1	-	-	MeOH	50 (reflux)	7
13	$Ni(OAc)_2 \cdot 4H_2O$ / 1	**27** / 1	LiOH / 3	$^tBuO^-$ K^+ -	THF	90 (reflux)	24
14		**27** / 1	K_2CO_3 / 3.5	-	MeOH	80 (reflux)	16
15	$Zn(OAc)_2$ / 1	**27** /1	K_2CO_3 / 3.5	-	MeOH	80 (reflux)	16
16	$Zn(OAc)_2$ / 2	**29** / 1	-	-	MeOH	50 (reflux)	7
17	$Zn(OAc)_2$ / 2 (added dropwise)	**29** / 1	-	-	MeOH	50 (reflux)	6

Table 4.5. Colours observed during the reactions carried out between the tripodal thiosemicarbazide ligands and the different metal salts, and of the resulting solid(s).

Entry	Metal salt	Colour of the reaction mixture (initial)	Colour of the reaction mixture (end of reaction)	Colour of the solid(s)
1	$ZrCl_4$	White suspension	Orange-brown suspension	Brown
2		Colourless transparent	-	Yellow-white
3		Colourless transparent	-	Pale yellow
4	$GaCl_3$	Yellowish transparent	Orange-brown suspension	Brown
5		Colourless transparent	-	White
6		Yellowish transparent	-	White
7		Colourless transparent	-	White
8	$InCl_3$	Colourless transparent	-	Pink-white
9		Colourless transparent	-	White
10	$Cu(OAc)_2 \cdot H_2O$	Light brown suspension	-	Green-brown
11		Dark brown suspension	-	Light brown
				Dark brown
12	$Cu(OAc)_2$	Dark blue suspension	Pale green suspension	Green-brown
				Dark brown
13	$Ni(OAc)_2 \cdot 4H_2O$	Greenish brown suspension	-	Light brown
14		Blue transparent	Green-brown suspension	Brown
15	$Zn(OAc)_2$	White suspension	-	White
16	$Zn(OAc)_2$	Yellowish transparent	-	Yellow
				Yellow
17	$Zn(OAc)_2$	White suspension	-	Yellow

4.6. Towards the bioconjugation of the tripodal system

In order to test the scope of reactions that allow the bioconjugation of the tripodal molecule, the synthesis of a trisubstituted tripodal molecule with three L-cysteine arms was explored. Amino acids are the basic building blocks that when combined can form proteins.[53] L-cysteine (a common and cheap amino acid) was chosen because, among all the possible amino acids, it is of great interest due to the multifunctional groups present in the molecule (-SH, -NH_2, -COOH).[54] These multiple functional groups can be used for the conjugation of metallic ions or other functional groups.[55] Moreover, cysteine is a non-essential amino acid that the body can synthesise, and it is responsible for the stabilisation of the secondary structure of proteins.[56]

This reaction was carried out using 4 equivalents of L-cysteine and 1 equivalent of compound **1**, applying the same conditions described for the thiosemicarbazide derivatives synthesis: acetonitrile as a solvent and stirring the contents for 48 hours under reflux (*Scheme 4.5*). A solid crashed out from the reaction (compound **30**), and it was filtered and washed with acetonitrile.

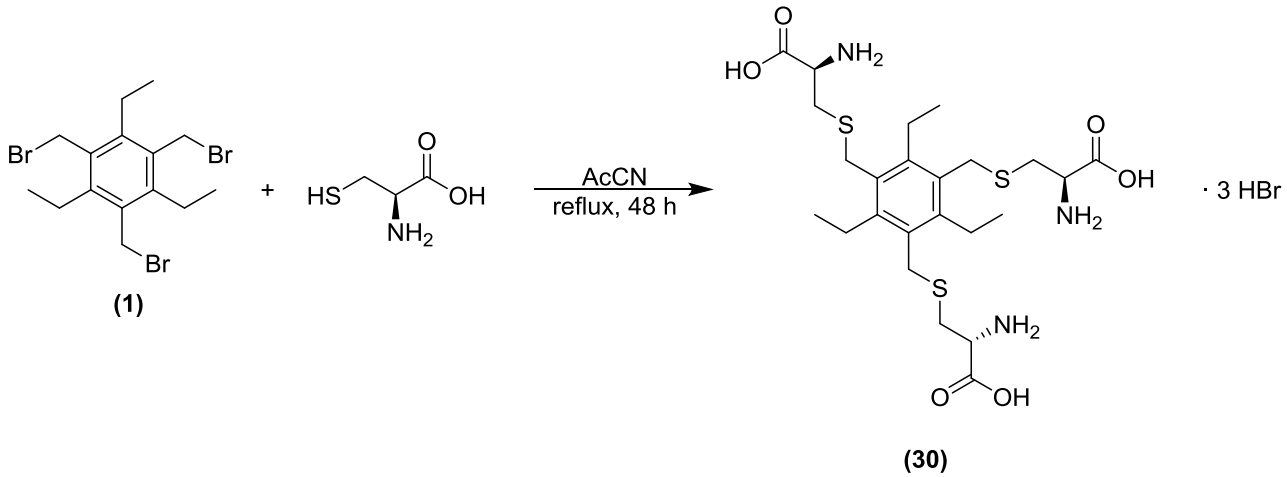

Scheme 4.5. Reaction between compound **1** and L-cysteine yielding compound **30** (· 3 HBr).

L-cysteine molecules present an isomerism equilibrium between the neutral and the zwitterion forms (*Scheme 4.6*). In this molecule, the nitrogen atoms from the primary amine groups act as donors in hydrogen bonds in which the carboxylate oxygen atoms that belong to adjacent molecules act as acceptors.[57] For this reason, strong hydrogen bonding can be expected in the obtained molecule, which contains three units of L-cysteine.

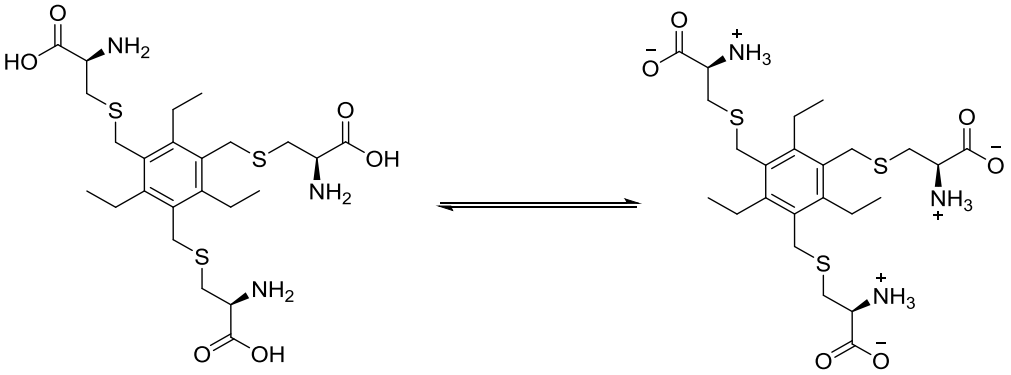

Scheme 4.6. Isomerism equilibrium between the neutral and zwitterion forms of L-cysteine in compound **30**.

The solid isolated from the reaction was characterised by NMR spectroscopy. Problems were found due to the insolubility of the compound in all the solvents tested, even when adding some drops of acid (trifluoroacetic acid) or base (triethylamine). However, the solid was slightly soluble in methanol and ^{1}H NMR spectroscopy was carried out (*Figure 4.22*). Some resonances could be identified and assigned to some of the protons of the molecule, such as the protons from the three CH_2CH_3 arms that, as for other derivatives, appeared as two multiplets between 3.00 – 2.78 ppm (H^1) and 1.32 – 1.12 ppm (H^2). Resonances assignable to protons from the cysteine arms were found as a triplet at 4.09 ppm (H^5) and a doublet at 3.08 ppm (H^4).

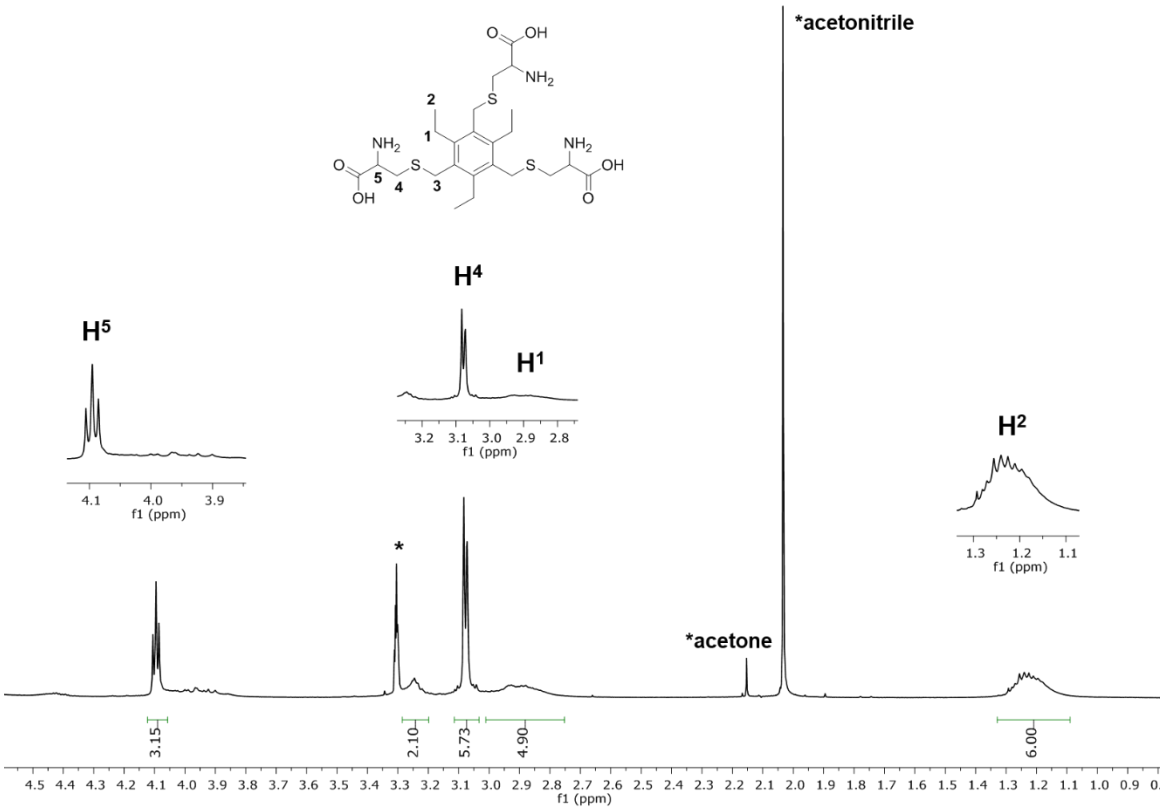

Figure 4.22. ^{1}H NMR (500 MHz, CD_3OD, 298 K) spectrum of compound **30** (· 3 HBr).

The solid from this reaction was also analysed by FT-IR spectroscopy and compared to the starting material, L-cysteine (*Figure 4.23*). It was observed from the spectrum of compound **30** that the characteristic band at around 2555 cm^{-1} corresponding to the S-H stretching in the cysteine molecule disappears when compared to the spectrum of L-cysteine. This suggests that the initial –SH group has reacted with the CH_2Br arms and it no longer exists in the final product.[58] Moreover, a band at around 3680 cm^{-1} that has a higher intensity in compound **30** than in the starting material indicates the existence of hydrogen bonding within the molecules.

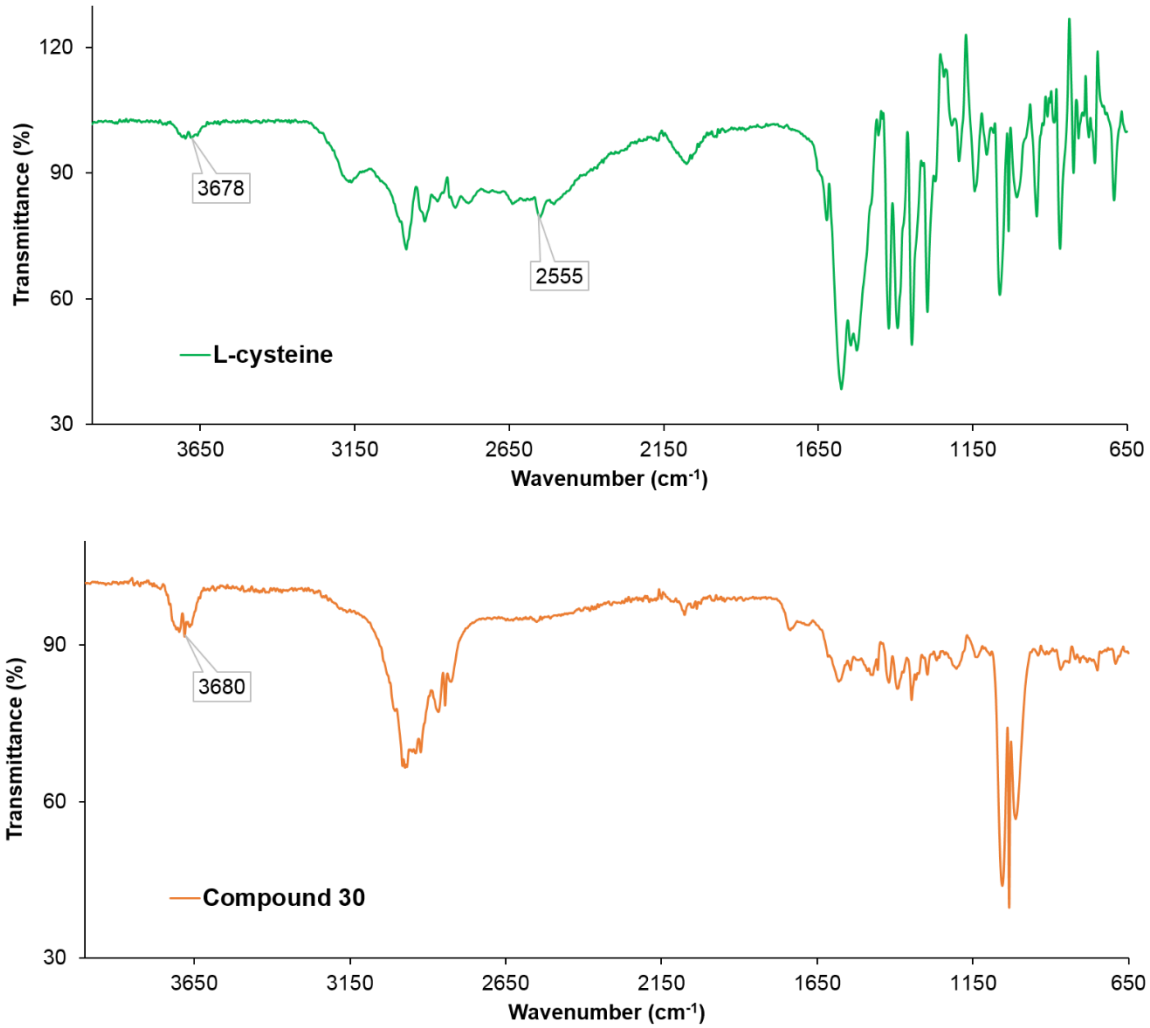

Figure 4.23. FT-IR spectra of compound **30** (· 3 HBr) (orange) and L-cysteine (green).

The mass spectrum of compound **30** when analysed using negative mode nanoelectrospray ionisation showed a peak at m/z = 560.1935, which corresponds to $[M-H]^-$ (*Figure 4.24*). This confirmed the formation of the desired molecule. This result constitutes a promising finding towards the functionalisation of biomolecules. Moreover, the resulting molecule is also a potential chelator for metal ions through the S, O and N atoms present in the molecular structure.

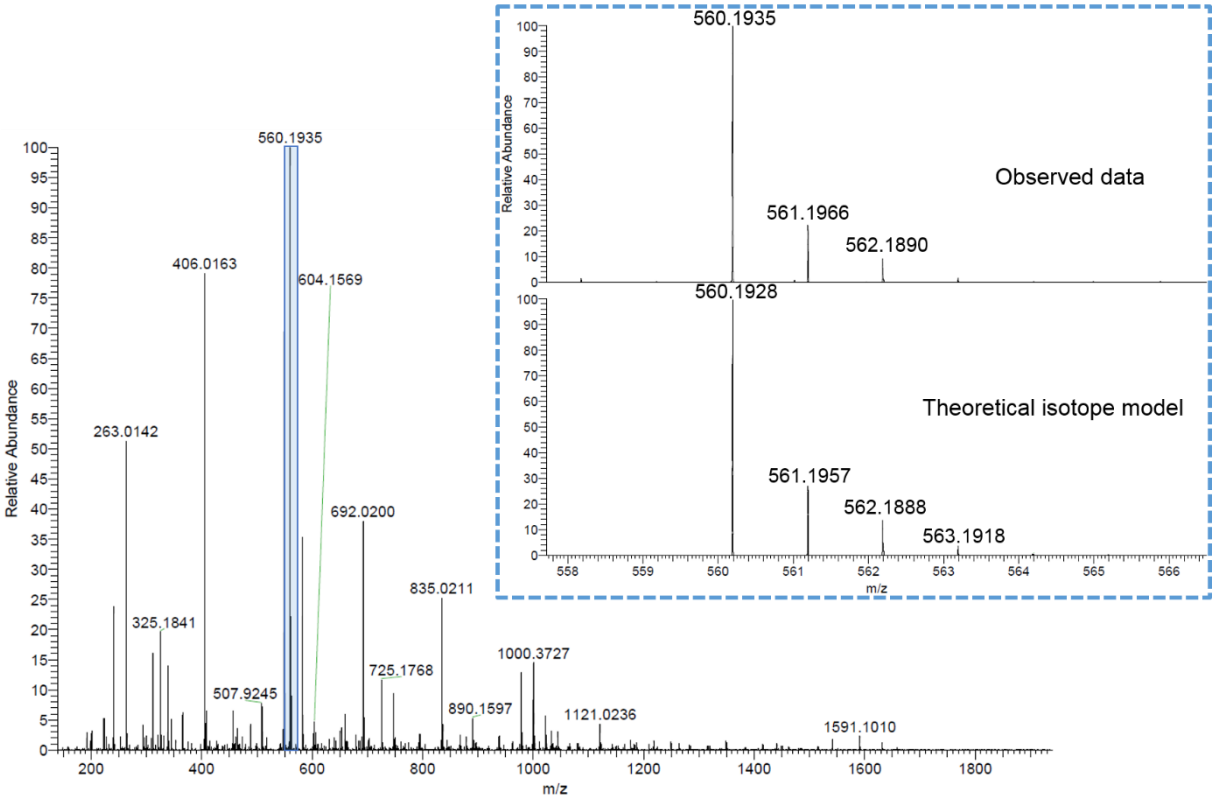

Figure 4.24. Mass spectrum of compound **30** using nESI-, and amplification of the isotopic pattern.

Moreover, to study if the toxicity of the thiosemicarbazide derivatives could be modified by replacing the Br^- counter ions by PF_6^-, an anion exchange reaction was carried out. For this purpose, 3 equivalents of $NH_4^+ PF_6^-$ and 1 equivalent of compound **26** were added to a flask and dissolved in methanol, then stirred for a few hours at room temperature (*Scheme 4.7*). Finally, the solvent was removed under reduced pressure and a white solid was obtained, that was tried to recrystallise by using several different techniques. This reaction was also attempted using dichloromethane as a solvent.

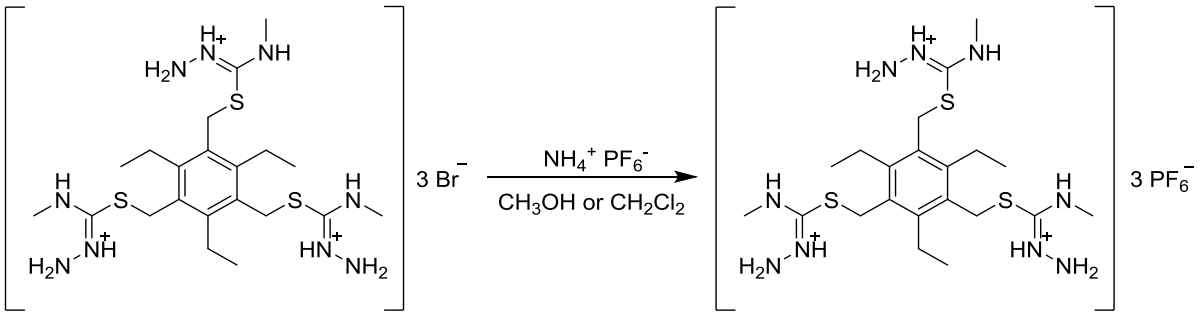

Scheme 4.7. Attempted anion exchange reaction to replace the Br^- ions by PF_6^- in compound **26**.

Crystals suitable for single crystal X-ray diffraction could not be obtained. Other techniques such as NMR spectroscopy and mass spectrometry were carried out but they did not confirm the success of this reaction.

4.7. Crystal violet assays

Crystal violet assays were carried out on compounds **26**, **27**, **28** and **29** (each considered as 3 HBr salts) using three different cell lines (PC-3, EMT6 and FEK-4), and the cell viability was measured after 24, 48 and 72 hours incubation times. To perform this type of assays, a crystal violet solution was added to the cells in order to stain them (*Figure 4.25*). The mechanism of action is different than that for MTT assays, since in this case the compound is not being reduced. When using a crystal violet solution after incubation of the cells with the compounds of interest, the cells are stained. Since the cells that are alive remain at the bottom of the plate, the well plates are carefully rinsed with water to remove all the dead cells. Subsequently, the alive cells are fixed with methanol and their absorbance is read with a plate reader (with an absorption wavelength of 570 nm), considering that only the alive cells are present in the plate and they will all emit light due to the staining with crystal violet. From the absorbance measure, the IC_{50} can be plotted and calculated (*Figure 4.26*). These assays were performed by Dr. Haobo Ge in the Department of Pharmacy and Pharmacology at the University of Bath.

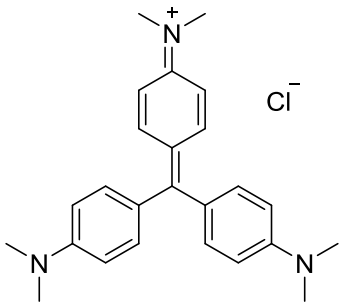

Figure 4.25. Structure of an organic chloride salt that is the monochloride salt of the crystal violet solution used to stain the cells.

In PC-3 cells, the least toxic molecule appears to be compound **26**, with a surprisingly high IC_{50} value when compared to the other compounds. However, it is noticeable that after 48 hours the compound is more toxic than after 72 hours. This was not expected, as it is thought that a compound becomes more toxic for cells after more hours have passed of its incubation. Compound **27** shows to be quite non-toxic in PC-3 cells as well, with IC_{50} values similar to the ones for compound **29**. Compound **28** is the most toxic one for PC-3 cells out of the four. Regarding the results obtained when carrying out the assays in an EMT6 cell line, compound **26** is still the least toxic one, although the same tendency where the molecule appears to be more toxic after 48 hours than after 72 hours is observed. The same anomaly happens with compound **28**, with a toxicity relatively higher than the one of compound **26**. Compounds **27**, **28** and **29** have IC_{50} values close to each other for the EMT6 cells type. The IC_{50} value for compound **27** decreases significantly from the 24 hours to the 48 hours measure, while the value for compound **29** decreases more gradually after each 24 hours interval. Finally, when

looking at the data obtained for the FEK-4 cell line, compound **26** still appears to be not very toxic in the micromolar range, however, the toxicity increases significantly after the 72 hours incubation period. Compound **27** is also quite non-toxic for this cell type, with IC_{50} values similar to the ones for compound **26** after the 24 and 72 hours period, but an increase in the IC_{50} value is observed after 48 hours of incubation, implying that this molecule is less toxic after 48 hours than after 24 or 72 hours. Compounds **28** and **29** are, therefore, the most toxic compounds out of the four in FEK-4 cells. For compound **28** there is a dramatic decrease of the IC_{50} value from the 24 hours to the 48 hours period. For compound **29**, the toxicity levels remain mostly unchanged during the three intervals of incubation periods, with the greater toxicity being after the 48 hours incubation time. In general, it can be concluded that compounds **28** and **29** are the most toxic out of the four in all the cell lines tested hereby (PC-3, EMT6 and FEK-4). The difference in the structure of these compounds lies in the terminal substituents of the thiosemicarbazide arms: a phenyl (compound **28**) and an allyl group (compound **29**). For the PC-3 and EMT6 cell lines, the toxicity levels of compounds **27**, **28** and **29** are close when compared to compound **26**. Furthermore, the overall toxicity of the four compounds is greater in EMT6 cells, followed by FEK-4 cells and finally they show less cytotoxicity when tested in PC-3 cells (*Table 4.6*).

Table 4.6. Summary of compounds tested using crystal violet assays in PC-3, EMT6 and FEK-4 cells and IC_{50} value found for each of them after 24, 48 and 72 hours incubation periods.

Compound	Cell line	IC_{50} (24 h) / μM	IC_{50} (48 h) / μM	IC_{50} (72 h) / μM
26	PC-3	1620 ± 37	115 ± 83	3170 ± 15
	EMT6	98 ± 4	84 ± 8	127 ± 38
	FEK-4	310 ± 69	273.9 ± 0.9	115 ± 10
27	PC-3	56 ± 4	51 ± 2	40 ± 2
	EMT6	58 ± 7	27 ± 2	23 ± 3
	FEK-4	326 ± 65	475 ± 38	104 ± 56
28	PC-3	11 ± 4	10 ± 6	10 ± 1
	EMT6	35 ± 3	19 ± 3	37 ± 2
	FEK-4	106 ± 21	21 ± 7	21 ± 6
29	PC-3	47 ± 2	41 ± 5	38 ± 2
	EMT6	50.0 ± 0.9	48 ± 5	38 ± 3
	FEK-4	91 ± 7	72 ± 6	100 ± 21

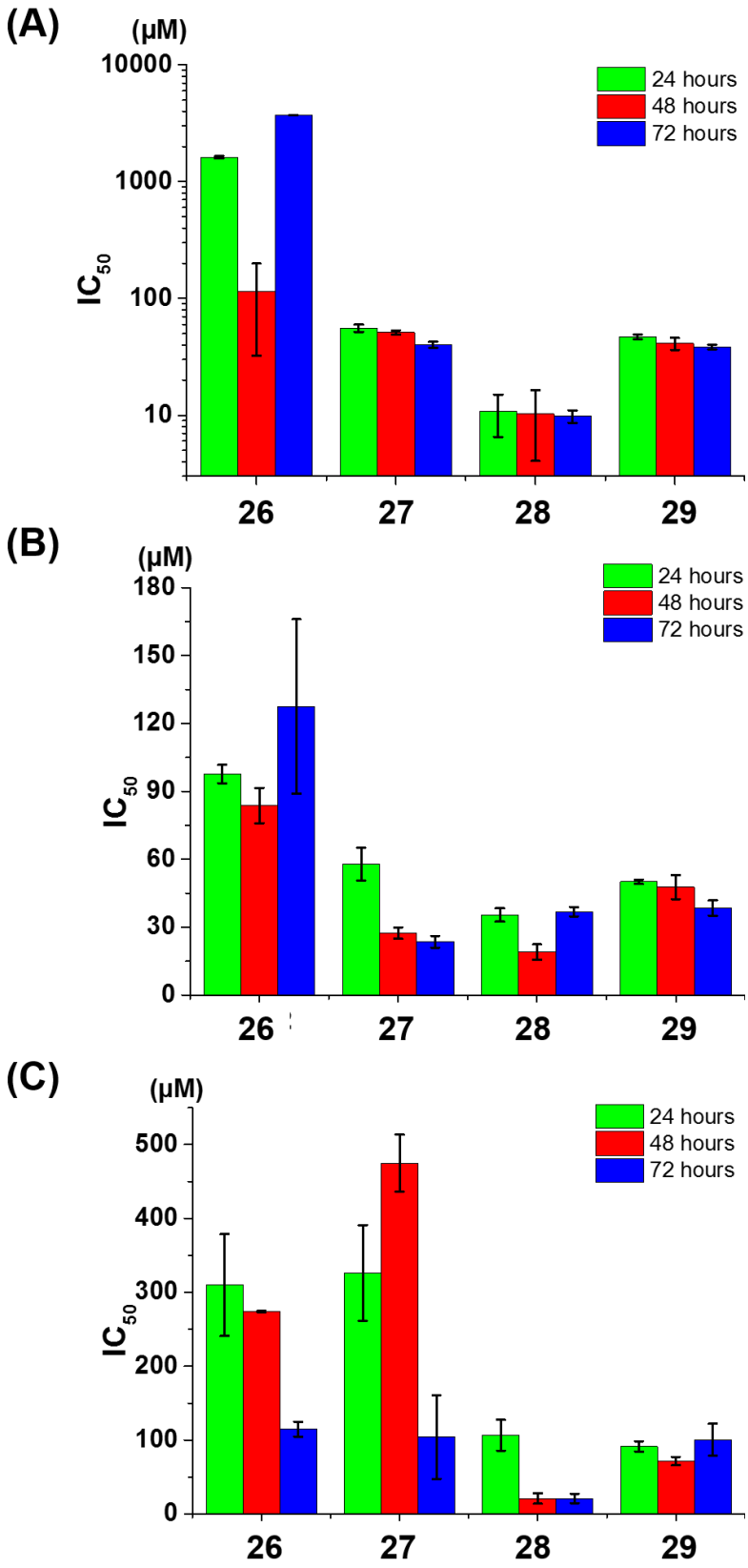

Figure 4.26. Crystal violet assays using **(A)** PC-3, **(B)** EMT6, and **(C)** FEK-4 cells incubated with compounds **26**, **27**, **28** and **29** (each as a 3 HBr salt) for 24, 48 and 72 hours.
(The data were collected from six repeated measurements on the same day; N = 1).

4.8. Summary of Chapter 4

Four ligands based on a benzene ring trisubstituted with thiosemicarbazide derivatives were synthesised and characterised (compounds **26**, **27**, **28** and **29**). Even though the initial thought was that an N-alkylation reaction was occurring on the thiosemicarbazide, after crystals suitable for single crystal X-ray diffraction were obtained for three of these ligands and their molecular structures elucidated, it was possible to see that what actually happened was an S-alkylation of the complexes. The molecular structures of these compounds showed that a unit cell contains two triply protonated molecules and six Br^- atoms that act as counter ions and are located at different places inside the cell, as well as a molecule of methanol (the solvent used to obtain the crystals). NOESY, ROESY and DOSY NMR experiments suggested the existence of a structure of higher molecular weight than a single molecule of the compound. Single crystal X-ray diffraction confirmed this by showing how several molecules in the solid state are interconnected by hydrogen bonding through the N-H and Br^- atoms of the structure. In addition, ^{1}H NMR spectroscopy did not show resonances with clear multiplicities, and for this reason variable temperature NMR experiments were performed to try to elucidate the expected multiplicity for each set of equivalent protons. It was seen that at higher temperatures the resonances showed better multiplicities, and this is likely due to the faster motion of the arms attached to the benzene ring when the temperature is higher, making the protons more equivalent between them due to having more similar environments.

The complexation of this type of thiosemicarbazide ligands with metals was attempted. Many reactions were carried out using zirconium(IV), gallium(III), indium(III), copper(II), nickel(II) and zinc(II) salts, and several conditions were used. The colour change of the reaction and the final obtained solid were reported, and all the solids were characterised using a broad range of techniques. NMR spectroscopy did not show any conclusive results, as sometimes peaks could not be observed and other times peaks were observed as for the free ligands used as starting material. By mass spectrometry the isotopic pattern of the expected complex, or any other form of the final molecule containing a metal, could not be identified. IR and Raman spectroscopy showed bands corresponding to the ligand used for the synthesis in each case. Moreover, UV/visible spectroscopy was performed and the spectra revealed the existence of metal species in the complexes when compared to the free ligands. In many cases, highly complex polymeric species could have formed.

A molecule with three L-cysteine arms was synthesised and characterised (compound **30**) following the same reaction conditions that proved to work for the thiosemicarbazide ligands.

This constitutes a promising finding towards the functionalisation of biomolecules with –SH functional groups.

Crystal violet assays were performed using the ligands (compounds **26**, **27**, **28** and **29**) in order to investigate their cell viability and cytotoxicity. It was seen that the ligand with the methyl substituent (compound **26**) was the least toxic out of the four in all the cell lines tested (PC-3, EMT6 and FEK-4). Instead, the ligands with phenyl and allyl substituents (compounds **28** and **29**, respectively) showed to be the most toxic ones in all the tested cell lines. In general, however, all the compounds showed relatively high IC_{50} values in the micromolar scale, which suggests that they are largely non-toxic molecules under these conditions.

4.9. References for Chapter 4

1. H. Shimoda, S. J. Oh, H. Z. Geng, R. J. Walker, X. B. Zhang, L. E. McNeil and O. Zhou, *Adv. Mater.*, 2002, **14**, 899-901.
2. D. K. Smith, A. R. Hirst, C. S. Love, J. G. Hardy, S. V. Brignell and B. Huang, *Prog. Polym. Sci.*, 2005, **30**, 220-293.
3. A. M. Castilla, W. J. Ramsay and J. R. Nitschke, *Acc. Chem. Res.*, 2014, **47**, 2063-2073.
4. H. Takahagi, S. Fujibe and N. Iwasawa, *Chem. Eur. J.*, 2009, **15**, 13327-13330.
5. P. Szabelski, D. Nieckarz and W. Rżysko, *J. Phys. Chem. C*, 2017, **121**, 25104-25117.
6. F. K.-C. Leung, F. Ishiwari, T. Kajitani, Y. Shoji, T. Hikima, M. Takata, A. Saeki, S. Seki, Y. M. A. Yamada and T. Fukushima, *J. Am. Chem. Soc.*, 2016, **138**, 11727-11733.
7. O. Kotova, R. Daly, C. M. G. dos Santos, M. Boese, P. E. Kruger, J. J. Boland and T. Gunnlaugsson, *Angew. Chem. Int. Ed.*, 2012, **51**, 7208-7212.
8. A. Ajayaghosh, P. Chithra and R. Varghese, *Angew. Chem. Int. Ed.*, 2007, **46**, 230-233.
9. Sofia Pascu's group website, http://people.bath.ac.uk/sp350/, (accessed March 2018).
10. J. Hamacek and A. Vuillamy, *Eur. J. Inorg. Chem.*, 2018, DOI: 10.1002/ejic.201800108.
11. A. E. Liberta and D. X. West, *Biometals*, 1992, **5**, 121-126.
12. I. Đilović, M. Rubčić, V. Vrdoljak, S. K. Pavelić, M. Kralj, I. Piantanida and M. Cindrić, *Bioorg. Med. Chem.*, 2008, **16**, 5189-5198.
13. M. J. M. Campbell, *Coord. Chem. Rev.*, 1975, **15**, 279-319.
14. S. Yokota, T. Kitaoka, J. Sugiyama and H. Wariishi, *Adv. Mater.*, 2007, **19**, 3368-3370.
15. D. Komáromy, M. C. A. Stuart, G. Monreal Santiago, M. Tezcan, V. V. Krasnikov and S. Otto, *J. Am. Chem. Soc.*, 2017, **139**, 6234-6241.
16. J. van Herrikhuyzen, P. Jonkheijm, A. P. H. J. Schenning and E. W. Meijer, *Org. Biomol. Chem.*, 2006, **4**, 1539-1545.
17. D. Fujita, Y. Ueda, S. Sato, N. Mizuno, T. Kumasaka and M. Fujita, *Nature*, 2016, **540**, 563.
18. T. Megyes, H. Jude, T. Grósz, I. Bakó, T. Radnai, G. Tárkányi, G. Pálinkás and P. J. Stang, *J. Am. Chem. Soc.*, 2005, **127**, 10731-10738.
19. A. S. Borovik, *Comments Inorg. Chem.*, 2002, **23**, 45-78.
20. J. H. van Esch and B. L. Feringa, *Angew. Chem. Int. Ed.*, 2000, **39**, 2263-2266.
21. S. Grunder, P. L. McGrier, A. C. Whalley, M. M. Boyle, C. Stern and J. F. Stoddart, *J. Am. Chem. Soc.*, 2013, **135**, 17691-17694.
22. Y. Shiraishi, Y. Tokitoh, G. Nishimura and T. Hirai, *Org. Lett.*, 2005, **7**, 2611-2614.
23. H. Ahn, J. Hong, S. Y. Kim, I. Choi and M. J. Park, *ACS Appl. Mater. Interfaces*, 2015, **7**, 704-712.
24. M. I. Gjerde, W. Nerdal and H. Høiland, *J. Colloid Interface Sci.*, 1996, **183**, 285-288.
25. A. Pastor and E. Martínez-Viviente, *Coord. Chem. Rev.*, 2008, **252**, 2314-2345.
26. J. M. Matsoukas, G. Bigam, N. Zhou and G. J. Moore, *Peptides*, 1990, **11**, 359-366.
27. R. A. Mantz, P. C. Trulove, R. T. Carlin and R. A. Osteryoung, *Inorg. Chem.*, 1995, **34**, 3846-3847.
28. K. F. Morris and C. S. Johnson, *J. Am. Chem. Soc.*, 1992, **114**, 3139-3141.
29. E. Durand, M. Clemancey, A.-A. Quoineaud, J. Verstraete, D. Espinat and J.-M. Lancelin, *Energy Fuels*, 2008, **22**, 2604-2610.
30. B. Mao, D. G. Calatayud, V. Mirabello, N. Kuganathan, H. Ge, R. M. J. Jacobs, A. M. Shepherd, J. A. Ribeiro Martins, J. Bernardino De La Serna, B. J. Hodges, S. W. Botchway and S. I. Pascu, *Chem. Eur. J.*, 2017, **23**, 9772-9789.
31. D. Šmejkalová and A. Piccolo, *Environ. Sci. Technol.*, 2008, **42**, 699-706.
32. G. S. Kapur, E. J. Cabrita and S. Berger, *Tetrahedron Lett.*, 2000, **41**, 7181-7185.
33. L. Avram and Y. Cohen, *Chem. Soc. Rev.*, 2015, **44**, 586-602.
34. N. Trotsko, M. Dobosz and E. Jagiełło-Wójtowicz, *Acta Pol. Pharm.*, 2007, **64**, 227-231.

35. A. G. Quiroga and C. Navarro Ranninger, *Coord. Chem. Rev.*, 2004, **248**, 119-133.
36. J. S. Casas, M. S. García-Tasende and J. Sordo, *Coord. Chem. Rev.*, 2000, **209**, 197-261.
37. C. Yamazaki, *Can. J. Chem.*, 1975, **53**, 610-615.
38. P. K. Srivastava, J. S. Upadhyaya and R. D. Sharma, *J. Chem. Eng. Data*, 1976, **21**, 388-389.
39. X. Ouyang, X. Chen, E. L. Piatnitski, A. S. Kiselyov, H.-Y. He, Y. Mao, V. Pattaropong, Y. Yu, K. H. Kim, J. Kincaid, L. Smith, W. C. Wong, S. P. Lee, D. L. Milligan, A. Malikzay, J. Fleming, J. Gerlak, D. Deevi, J. F. Doody, H.-H. Chiang, S. N. Patel, Y. Wang, R. L. Rolser, P. Kussie, M. Labelle and M. C. Tuma, *Bioorg. Med. Chem.*, 2005, **15**, 5154-5159.
40. L. Heinisch, M. Tonew and E. Tonew, *Pharmazie*, 1977, **32**, 752-756.
41. K. Pandurangan, J. A. Kitchen, S. Blasco, E. M. Boyle, B. Fitzpatrick, M. Feeney, P. E. Kruger and T. Gunnlaugsson, *Angew. Chem. Int. Ed.*, 2015, **54**, 4566-4570.
42. M. Arunachalam, S. Chakraborty, S. Marivel and P. Ghosh, *Cryst. Growth Des.*, 2012, **12**, 2097-2108.
43. T. Aytun, P. J. Santos, C. J. Bruns, D. Huang, A. R. Koltonow, M. Olvera de la Cruz and S. I. Stupp, *J. Phys. Chem. C*, 2016, **120**, 3602-3611.
44. C. R. Martinez and B. L. Iverson, *Chem. Sci.*, 2012, **3**, 2191-2201.
45. S. Alvarez, *Dalton Trans.*, 2013, **42**, 8617-8636.
46. C. C. Chambers, E. F. Archibong, S. M. Mazhari, A. Jabalameli, J. D. Zubkowski, R. H. Sullivan, E. J. Valente, C. J. Cramer and D. G. Truhlar, *J. Mol. Struct.*, 1996, **388**, 161-167.
47. M. D. Bartholomä, *Inorg. Chim. Acta*, 2012, **389**, 36-51.
48. T. J. Wadas, E. H. Wong, G. R. Weisman and C. J. Anderson, *Chem. Rev.*, 2010, **110**, 2858-2902.
49. J. Holub, M. Meckel, V. Kubíček, F. Rösch and P. Hermann, *Contrast Media Mol. Imaging*, 2015, **10**, 122-134.
50. L. E. McInnes, S. E. Rudd and P. S. Donnelly, *Coord. Chem. Rev.*, 2017, **352**, 499-516.
51. C. E. Willans, K. M. Anderson, P. C. Junk, L. J. Barbour and J. W. Steed, *Chem. Commun.*, 2007, 3634-3636.
52. J. Joseph, N. L. Mary and R. Sidambaram, *Synth. React. Inorg. M.*, 2010, **40**, 930-933.
53. G. Diaz Fleming, J. J. Finnerty, M. Campos-Vallette, F. Célis, A. E. Aliaga, C. Fredes and R. Koch, *J. Raman Spectrosc.*, 2009, **40**, 632-638.
54. J. Jiang, R. Yu, R. Yi, W. Qin, G. Qiu and X. Liu, *J. Alloys Compd.*, 2010, **493**, 529-534.
55. K. Chang and W. Chen, *ACS Nano*, 2011, **5**, 4720-4728.
56. J. C. Dobrowolski, J. E. Rode and J. Sadlej, *J. Mol. Struct.*, 2007, **810**, 129-134.
57. A. Pawlukojć, J. Leciejewicz, A. J. Ramirez-Cuesta and J. Nowicka-Scheibe, *Spectrochim. Acta A*, 2005, **61**, 2474-2481.
58. B. Zhang, X. Ye, W. Hou, Y. Zhao and Y. Xie, *J. Phys. Chem. B.*, 2006, **110**, 8978-8985.

Chapter 5. Nanoparticles-based systems for optical imaging

5.1. Overview of Chapter 5

In the past few decades, silica materials with magnetic cores have attracted the attention of many different areas of research due to the broad range of potential applications that they can offer (*Figure 5.1*).[1, 2] Iron oxide nanoparticles, in particular certain phases (*e.g.* γ-Fe_2O_3 maghemite or Fe_3O_4 magnetite), are magnetic and can be used as contrast agents in magnetic resonance imaging. The use of silica as an outer layer improves their biocompatibility and stability in aqueous media.[3] Among all the possible applications in life sciences, the attention of this chapter is focused on biomedical applications, both for therapy and diagnosis, thanks to the combined properties of all the agents involved in the nanocomposites.

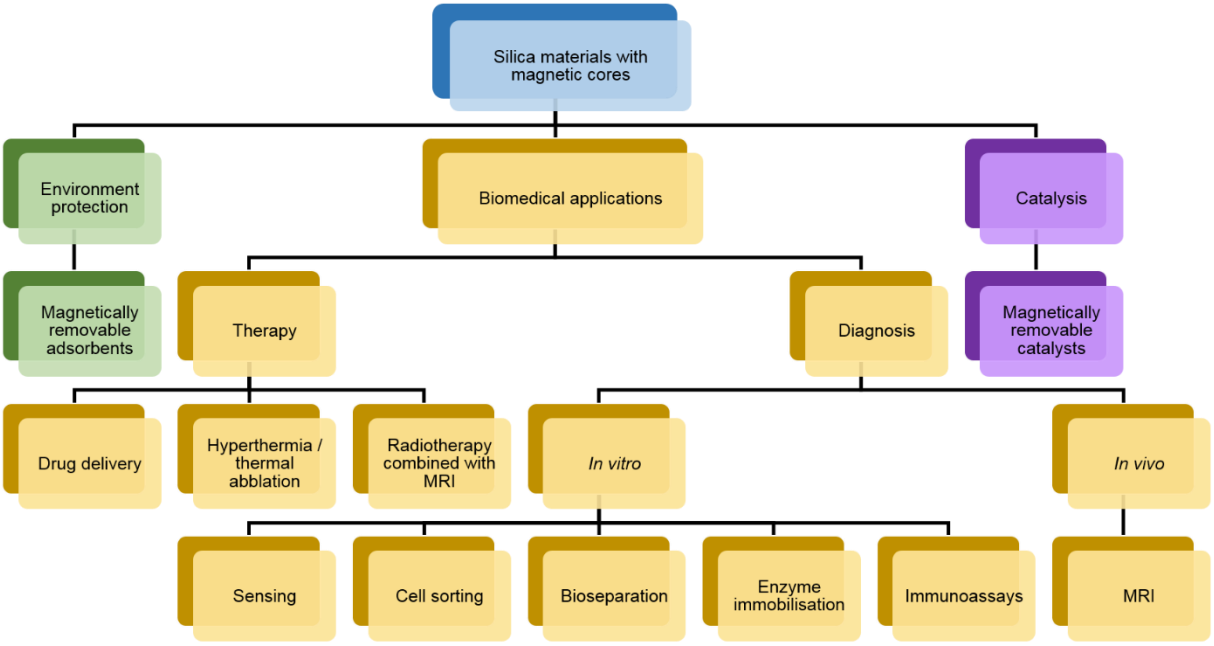

Figure 5.1. Most popular applications of silica nanomaterials with magnetic cores. Adapted from reference.[4]

This Chapter describes efficient methods of synthesis of iron oxide nanoparticles and effective encapsulation inside silica particles. Such encapsulation is believed to provide a protective layer around the nanoparticles, reducing oxygen molecule penetration in both air and aqueous media and making the particles more kinetically stable.[5] Furthermore, silica is resistant to swelling in organic or aqueous solvents, which means that the size of the silica particles remains unchanged in a wide range of solvents. Other advantages include the relatively easy functionalisation of the silica surface by a broad range of functional groups thanks to the readily available hydroxyl surface groups on the outer membrane of the silica, which provide intrinsic

hydrophilicity and allow surface attachment of many biomolecules such as antibody fragments and peptides by covalent binding.[5-8]

In this work, the iron oxide-silica core-shell nanoparticles were functionalised with two types of fluorophores. First, $Cd_{0.1}Zn_{0.9}Se$ quantum dots (QDs) were synthesised and encapsulated by silica together with the iron oxide core. Additionally, the fluorescent molecule Zn(ATSM/A) [diacetyl-2-(4-N-methyl-3-thiosemicarbazonato)-3-(4-N-amino-3-thiosemicarbazonato) zinc(II)] (compound **35c**) was synthesised and characterised and was attached to the surface of the silica nanoparticles.[9] Iron oxide nanoparticles were also coated with citric acid to prove the posterior functionalisation of the carboxylic acid groups with a BODIPY derivative described in *Section 2.3*. The as-synthesised nanocomposites (*Figure 5.2*) were subsequently tested in cells for imaging applications using one-photon and two-photon confocal microscopy and fluorescence lifetime techniques, and their toxicity was evaluated using different assays. Radiolabelling experiments were carried out with ^{68}Ga to test the potential applicability of such nanocomposites as synthetic scaffolds towards PET and SPECT imaging.

The nanocomposites were characterised by a host of different techniques such as Fourier transform infrared spectroscopy, powder X-ray diffraction, X-ray energy dispersive analysis, transmission electron microscopy, dynamic light scattering, Raman spectroscopy, thermogravimetric analysis and BET surface area measurements, and these findings will be discussed below.

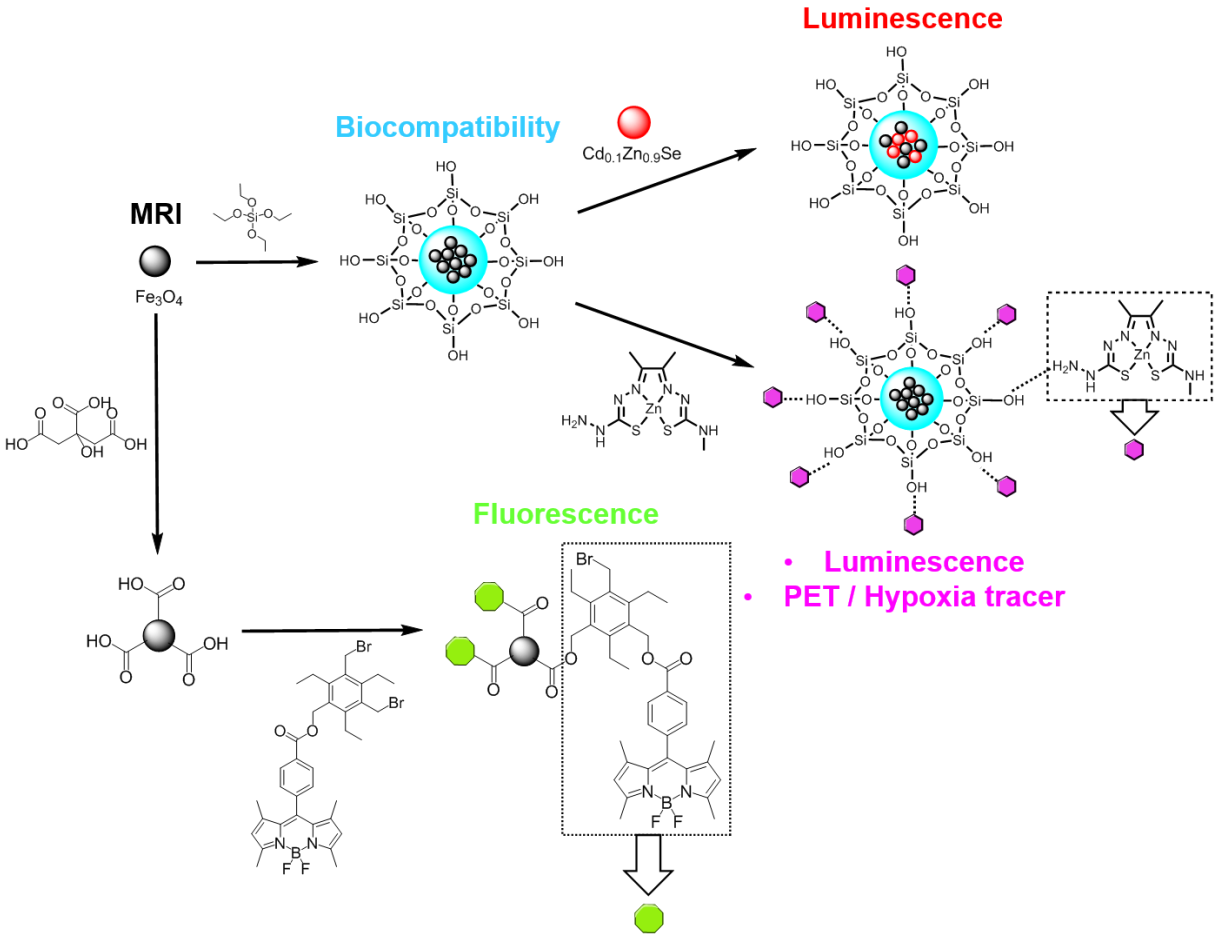

Figure 5.2. Summary of the different nanoparticles-based systems synthesised and the modality of imaging that each of them offers.

5.2. Synthesis and characterisation of iron oxide nanoparticles

Iron oxide nanoparticles have a diameter between 1 and 100 nanometres. The two main forms are magnetite (Fe_3O_4) and its oxidised form maghemite (γ-Fe_2O_3). They have attracted extensive interest due to their potential applications in many fields. As stated in *Section 5.1*, Fe_3O_4 nanoparticles are known contrast agents currently of interest for magnetic resonance imaging (MRI), and they also have superparamagnetic properties.[10-12] They are commonly used in a broad variety of therapeutic and diagnostic biomedical applications thanks to these properties, that enable tracking of theranostic nanomedicines by MRI. For *in vivo* applications, they can be administered intravenously into the body to detect and characterise lesions, tumours, and to visualise body tissues. When used for MRI *in vivo*, iron oxide nanoparticles cause a critical decrease in the relaxation rate of water protons due to their high magnetisation. This enhanced contrast allows MRI to differentiate between different organs in the body and also between several tissues. Furthermore, iron oxide nanoparticles benefit from high chemical stability, low toxicity and biocompatibility.[10, 13]

Because of these attributes, iron oxide nanoparticles were chosen as the foundation for this multimodal system design and synthesis. They were therefore synthesised in the magnetite phase via a co-precipitation method.[13] Among all the different methods of synthesis of iron oxide nanoparticles, this was chosen due to its simplicity and ease in controlling the particle size.[14] Solutions of iron (II) and iron (III) chlorides were prepared using deoxygenated water and 2 M HCl(aq). They were mixed, and subsequently added dropwise with mechanical stirring to a basic solution of potassium hydroxide. The formation of the black nanoparticles occurred instantly, according to *Equation 5.1*. The nanoparticles were then collected by magnetic decantation and washed with water.

$$Fe^{2+} + 2\ Fe^{3+} + 8\ OH^- \rightarrow Fe_3O_4 + 4\ H_2O$$

Equation 5.1. Co-precipitation method of synthesis of magnetite Fe_3O_4 nanoparticles applied hereby.

Transmission electron microscopy (TEM) was used to determine the size and morphology of the synthesised iron oxide nanoparticles core. In order to prepare the sample for analysis, a diluted solution of Fe_3O_4 in methanol was sonicated for 30 minutes. Then, a few drops of this solution were placed onto a copper grid and left to evaporate in air. The nanoparticles were shown to range between 5 and 10 nm in size with an almost spherical morphology. TEM observations reveal some degree of agglomeration (*Figure 5.3*). Nonetheless, the size and shape of this core was deemed promising for the next stage of the design strategy in core-shell magnetic nanoparticles.

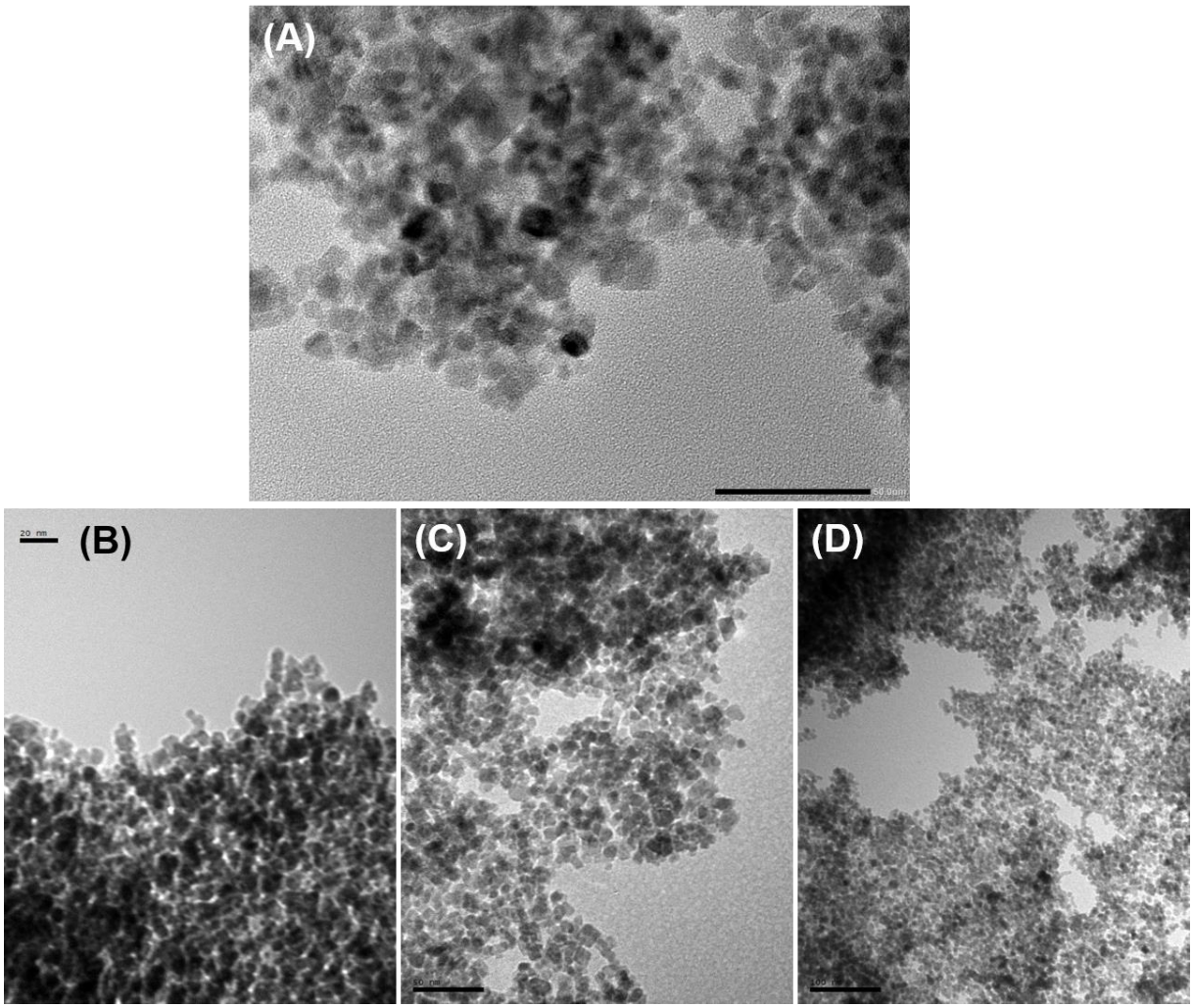

Figure 5.3. TEM micrographs of Fe_3O_4 nanoparticles. Scale bar: **(A)** 50 nm, **(B)** 20 nm, **(C)** 50 nm, and **(D)** 100 nm.

The elemental composition of the nanocomposites was analysed by energy dispersive X-ray spectroscopy (EDX), using EDX mapping assembled to the TEM instrument. As expected, both the EDX mapping (*Figure 5.4*) and the spectrum (*Figure 5.5*) showed that Fe and O were present in the sample, confirming the formation of iron oxide. In the EDX spectrum, peaks corresponding to Cu can be observed, which are due to the copper grid used as a support to analyse the sample.

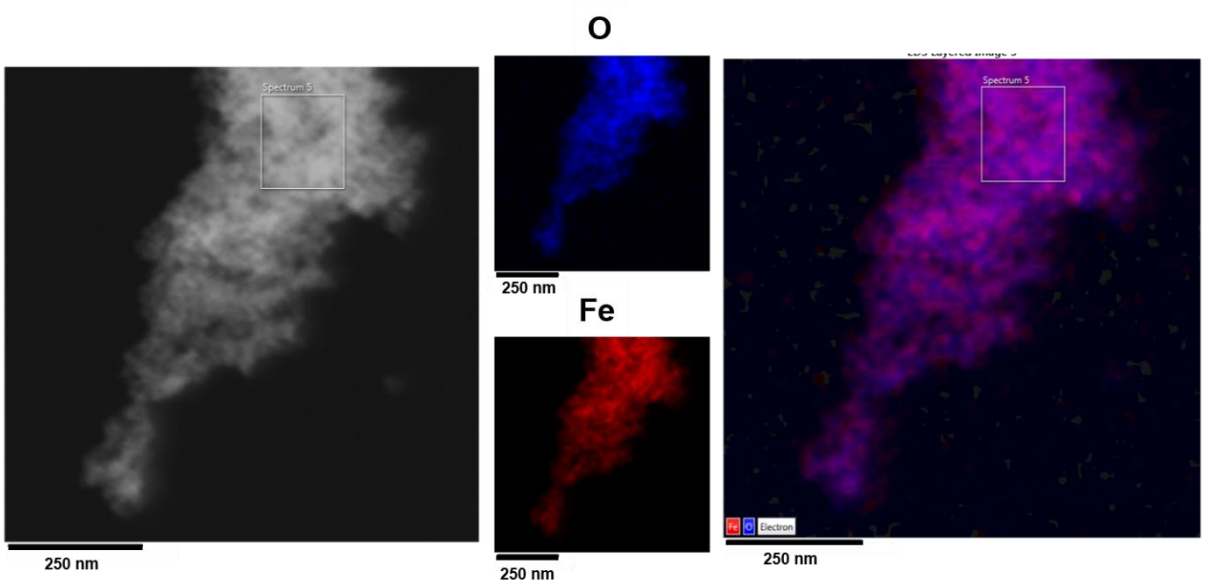

Figure 5.4. EDX mapping of Fe_3O_4 nanoparticles. TEM micrograph of the nanocomposite (left), colour code for each element (O: blue, Fe: red), and TEM micrograph with overlaid colours (right).

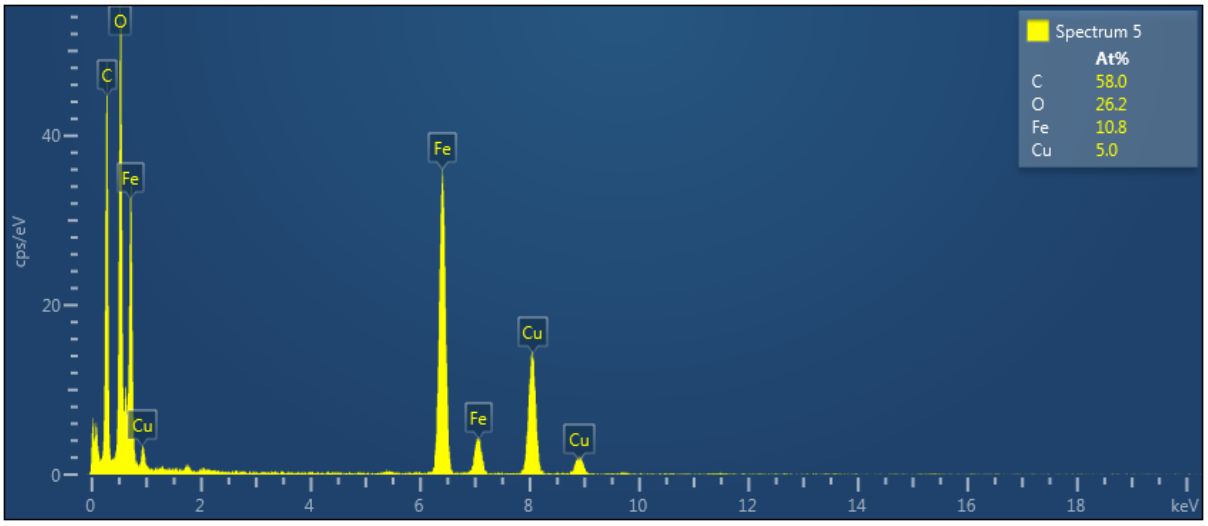

Figure 5.5. EDX spectrum and elemental composition of Fe_3O_4 nanoparticles.

5.3. Silica coating of iron oxide nanoparticles

Silica is one of the most suitable and common coating layers for superparamagnetic iron oxide nanoparticles (SPIONs) due to its chemical stability, biocompatibility and versatility for surface modification. The addition of a silica shell also leaves silanol functional groups available on the surface of the nanoparticles for the immobilisation of biomolecules, and protects the iron oxide from degradation or aggregation, while reducing the toxicity of the core.[15-18]

The previously synthesised magnetite Fe_3O_4 cores were coated with a silica shell via a microemulsion method of coating.[19] A water-in-oil (W/O) or reverse microemulsion was used, in which a surfactant was dissolved in an organic solvent (oil) to create spherical aggregates that are known as reverse micelles, where the polar head groups point towards the inside of the core.[20] In order to achieve this, the iron oxide nanoparticles were dispersed in oleic acid, added to a reaction vessel and dispersed in cyclohexane together with the surfactant polyoxyethylene(5)isooctylphenyl ether (IGEPAL CA-520), ammonium hydroxide and tetraethylorthosilicate, which was used as the silica precursor. The reaction mixture was mechanically stirred overnight, and after this time the Fe_3O_4@SiO_2 core-shell nanoparticles were collected by magnetic decantation and washed with methanol.

Achieving the desired transformation proved to be non-trivial, and many attempts of coating the nanoparticles ended unsuccessfully. In many cases, when the samples were analysed by TEM and the reaction was unsuccessful, it was noticed that the silica was present in the grid but it was not coating the nanoparticles (*Figure 5.6*).

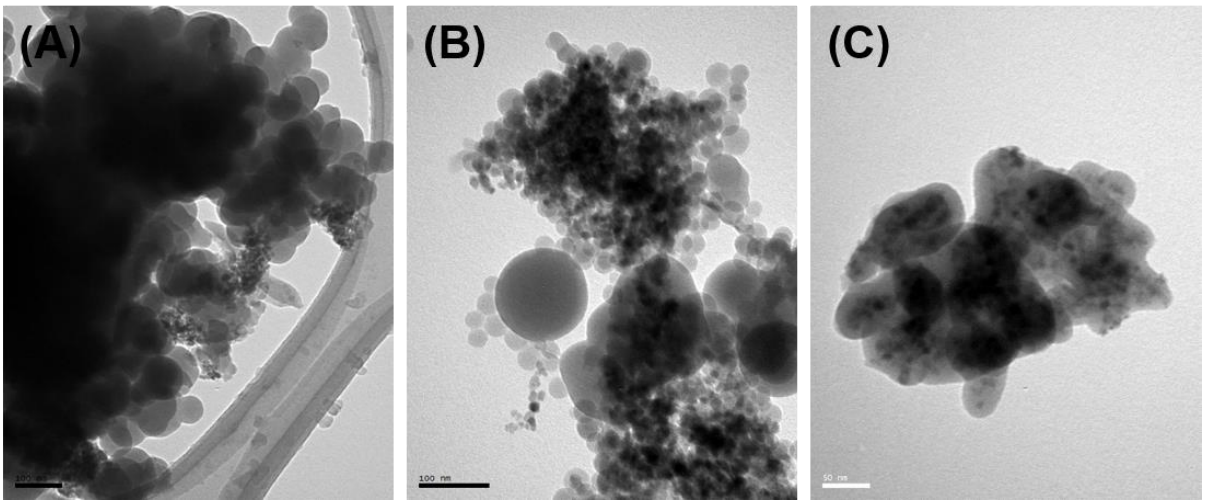

Figure 5.6. TEM micrographs of poorly coated Fe_3O_4@SiO_2 nanoparticles. Scale bar: **(A-B)** 100 nm, and **(C)** 50 nm.

After numerous attempts with varying reactant concentrations, the conditions that yielded the silica-coated nanoparticles with the desired morphology were found. 200 mg of Fe_3O_4 nanoparticles dispersed in 5 mL of cyclohexane were added, followed by 22 g of surfactant, and the mixture was dispersed in 350 mL of cyclohexane. Subsequently, 3.85 mL of tetraethylorthosilicate and 4.72 mL of ammonium hydroxide solution were added, and the mixture was mechanically stirred for 16 hours at room temperature. TEM was used to observe the nanocomposites, and the micrographs showed that they have a spherical shape, with a core-shell structure consisting of a dark contrast metal core and a light contrast silica shell. Silica-coated Fe_3O_4 nanoparticles of approximately 50 nm of diameter were hence obtained (*Figure 5.7*).

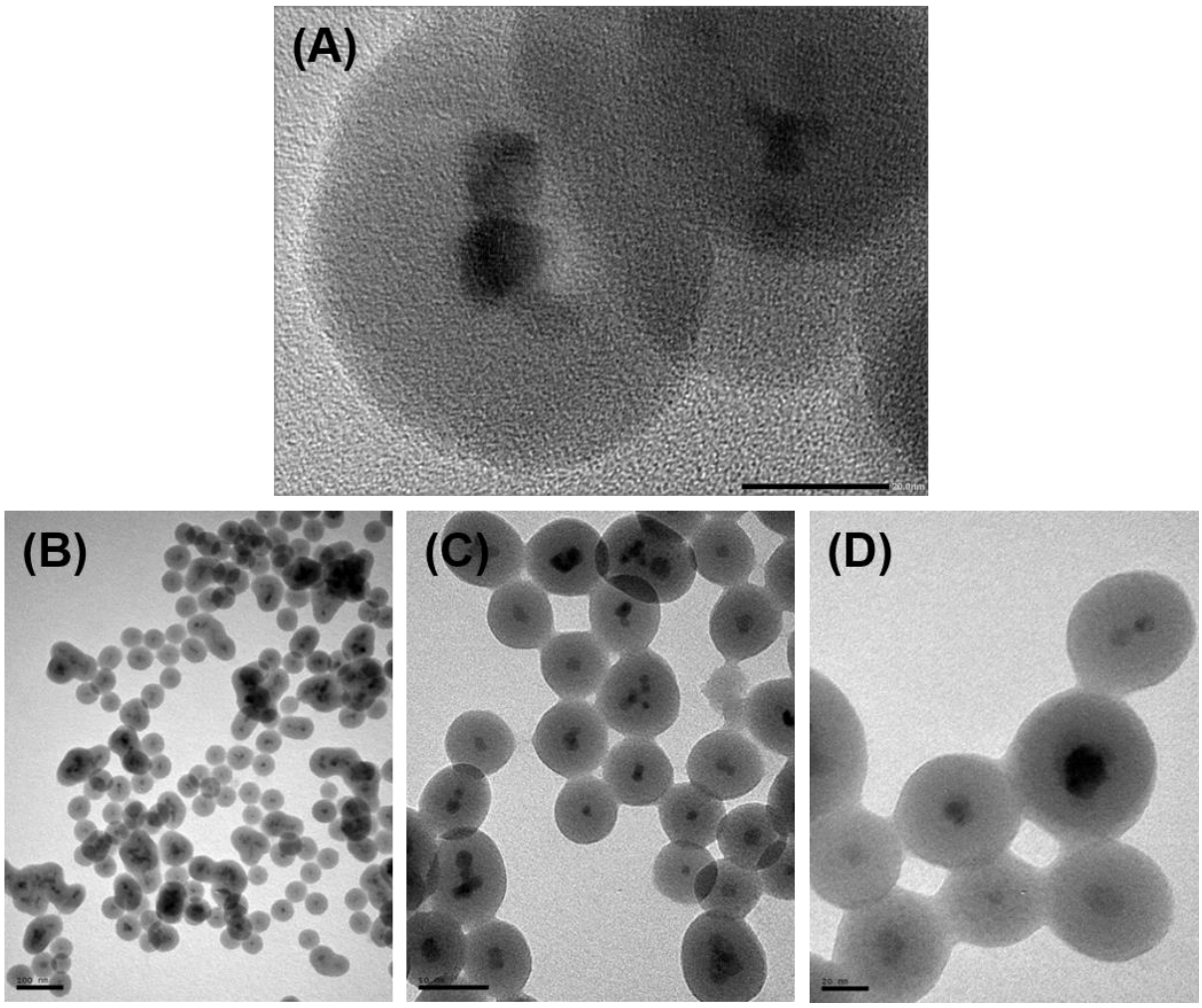

Figure 5.7. TEM micrographs of Fe_3O_4@SiO_2 core-shell nanoparticles. Scale bar: **(A)** 20 nm, **(B)** 100 nm, **(C)** 50 nm, and **(D)** 20 nm.

These TEM images also reveal that the coated nanoparticles are much better dispersed and display a lower degree of agglomeration than the non-coated nanoparticles. This is due to the role of the silica coating agent which prevents the agglomeration of the nanoparticles.[21]

EDX mapping was used to analyse the elemental composition of the nanocomposites (*Figure 5.8*). It can be seen that Fe, O and Si are the predominant elements in the maps. The EDX spectrum shows, apart from these three elements, the presence of C and Cu, which are present in the TEM grid used to visualise the sample (*Figure 5.9*).

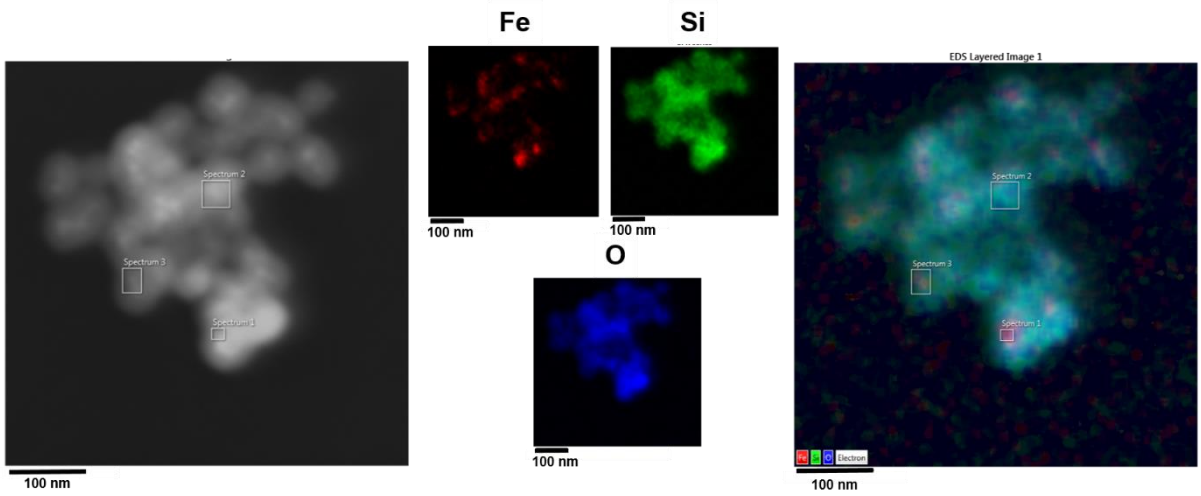

Figure 5.8. EDX mapping of Fe_3O_4@SiO_2 nanoparticles. TEM micrograph of the nanocomposite (left), colour code for each element (Fe: red, Si: green, O: blue), and TEM micrograph with overlaid colours (right).

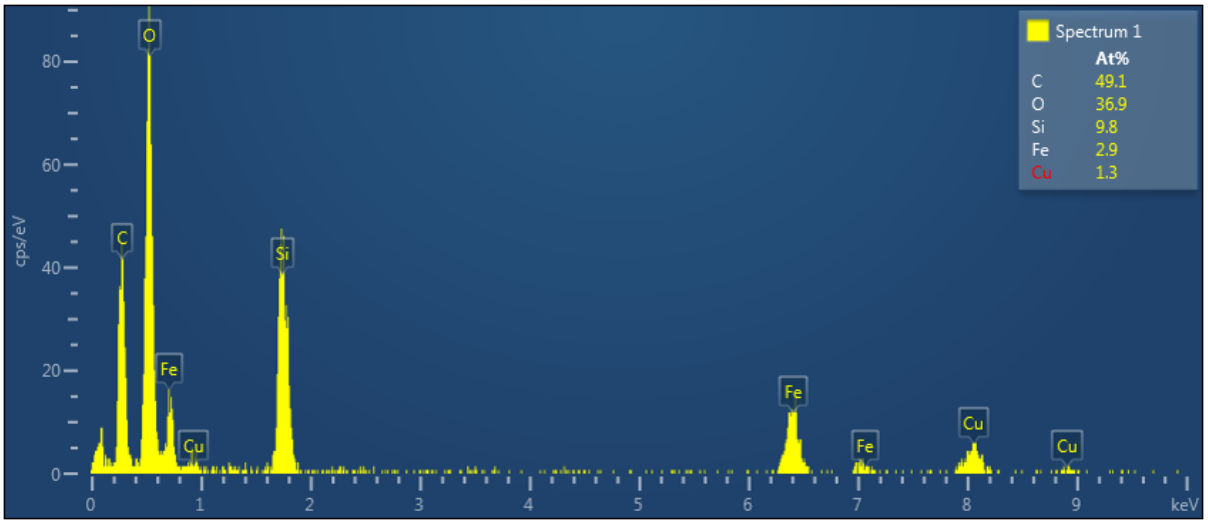

Figure 5.9. EDX spectrum and elemental composition of Fe_3O_4@SiO_2 nanoparticles.

The crystal phase and structure of the as-prepared nanoparticles with and without a silica shell were determined by powder X-ray diffraction (XRD) (*Figure 5.10*). The red curve, for the naked Fe_3O_4 nanoparticles, can be indexed to the face-centered cubic structure of magnetite according to its ICDD file No. 019-0629.[22] In this pattern, the peaks at 2θ = 30.2º, 35.5º, 43.2º, 53.5º, 57.1º and 62.9º correspond to the (220), (311), (400), (422), (511), and (440) crystalline planes of magnetite phase, respectively. In the blue curve, corresponding to the

nanocomposites after coating with silica, in addition to the diffraction peaks of Fe_3O_4 a new peak emerges at 2θ = 18.6º, most likely due to the holder used to analyse the sample. From this new pattern, it can be concluded that the obtained Fe_3O_4@SiO_2 nanospheres still have a face-centered cubic (fcc) phase. In this context, the addition of a silica shell via the microemulsion method did not affect the phase structure of the magnetic core.

From the X-ray spectra, it is noticeable that the synthesised nanoparticles do not show sharp and clear diffraction peaks corresponding to an extended crystalline structure. Instead, in both cases broad and poorly defined peaks appear in the spectra. This is typical for very small crystalline materials in which diffraction peaks cannot be well resolved.[16]

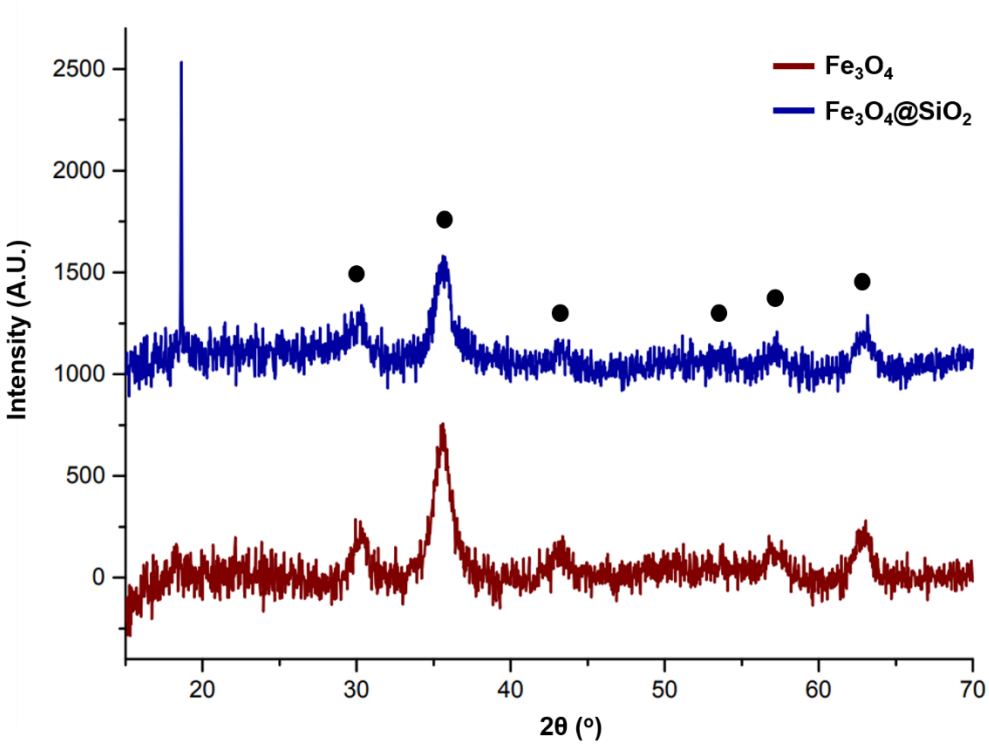

Figure 5.10. Powder X-ray diffraction patterns of the prepared Fe_3O_4 (red) and Fe_3O_4@SiO_2 (blue) nanoparticles. Black dots show diffractions of magnetite phase.

5.4. Synthesis of $Cd_{0.1}Zn_{0.9}Se$ quantum dots

Quantum dots (QDs) have characteristic optical properties that make them excellent probes for bioimaging applications.[23] Their narrow emission bands, continuous broad absorption band, high resistance to photo-bleaching, and higher extinction coefficients and quantum yields in comparison with organic dyes have attracted the attention of many researchers to use these nanocomposites as dyes for imaging applications.[24-26] It is known that QDs containing cadmium are toxic, which is mainly due to the presence of free Cd^{2+} ions released when non-coated QDs are exposed to an acidic microenvironment after cellular uptake.[27] Moreover, recent studies have shown that the toxicity of nanoparticles can be exploited as a novel form of therapy to kill cancer cells, as shown by Pompa *et al.,* who reported how ion-releasing nanoparticles can induce high levels of cytotoxicity due to the lysosome-enhanced Trojan horse effect.[28] Recent investigations have demonstrated that the surface coating of QDs can substantially influence the toxicity of the particles.[29, 30] In this context, Chu and collaborators demonstrated that the silica coating of CdSe quantum dots reduces the release of Cd^{2+} ions by up to 99.45%.[31] Therefore, there is a need for encapsulation techniques using benign materials with retention of efficient emission in biological media, and silica is an attractive alternative since, as already mentioned, is biocompatible and can be easily functionalised.[32]

Unlike the commercially available CdSe/ZnS quantum dots, in the $Cd_{0.1}Zn_{0.9}Se$ system, the Zn(II) and Se(0) are not part of the protective shell of CdSe. Instead, they are effective elements of the quantum dot core, capable of emitting simultaneously in the blue and red regions of the spectrum. It was envisaged that these QDs could be incorporated into the iron oxide-silica conglomerate so as to form multimodal systems with fluorescent properties.

In this context, $Cd_{0.1}Zn_{0.9}Se$ quantum dots were synthesised according to a previously reported procedure,[33] using stock solutions of Se and $ZnEt_2$ prepared in a glovebox, cadmium stearate and organic reagents, that were mixed at 330 ^oC according to the already described synthesis. The quantum dots were finally precipitated using a mixture of methanol:acetone and isolated by centrifugation and decantation. They were further washed with the methanol:acetone mixture to remove the excess of organic ligands and isolate pure $Cd_{0.1}Zn_{0.9}Se$, which were then dispersed in n-hexane.

The as-prepared $Cd_{0.1}Zn_{0.9}Se$ quantum dots were characterised by powder X-ray diffraction (*Figure 5.11*). Peaks marked with black dots corresponding to (111), (200), (220) and (311) of the cubic structural phase can be observed at 2θ = 23.7, 25.8^o, 42.2^o and 50.1^o, respectively.[34] When this spectrum is compared to those of pure CdSe and ZnSe, it can be observed that the

values of the peaks are closer to those of ZnSe, as the concentration of this species is higher in the ternary system.

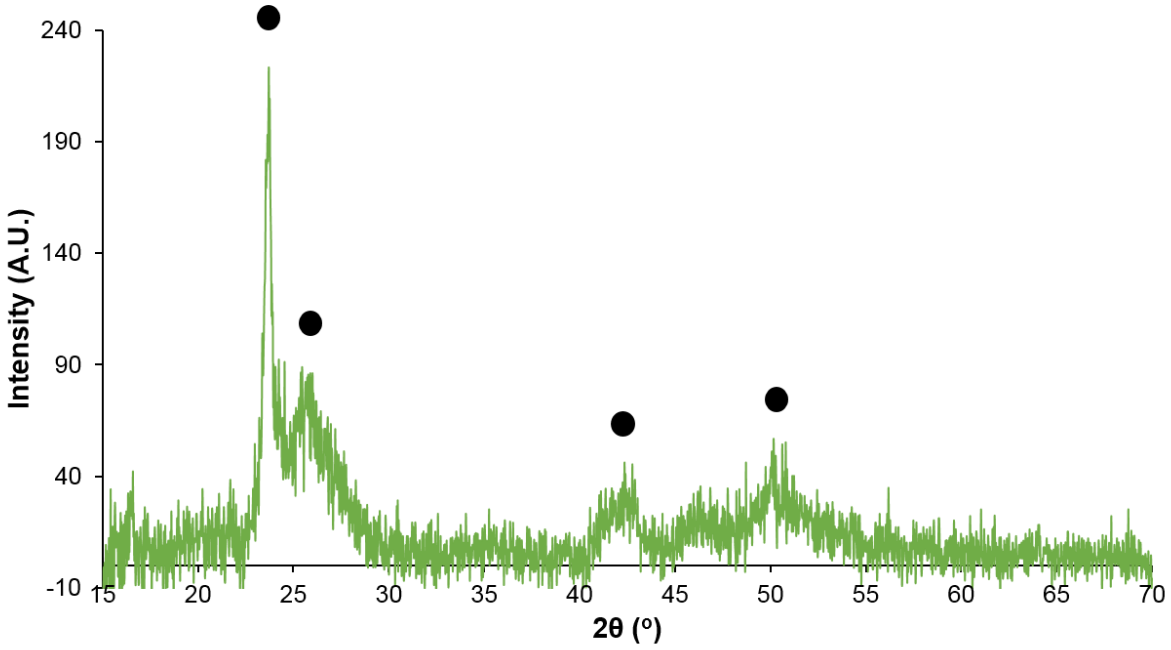

Figure 5.11. Powder X-ray diffraction pattern of $Cd_{0.1}Zn_{0.9}Se$ quantum dots. Black dots show peaks corresponding to a cubic phase structure.

5.5. Silica coating of iron oxide nanoparticles and $Cd_{0.1}Zn_{0.9}Se$ quantum dots

In order to create a fluorescent nanocomposite, the same microemulsion reaction described in *Section 5.3* was used (*Scheme 5.1*) to encapsulate simultaneously the $Cd_{0.1}Zn_{0.9}Se$ quantum dots and the iron oxide nanoparticles within a silica layer.[7, 32]

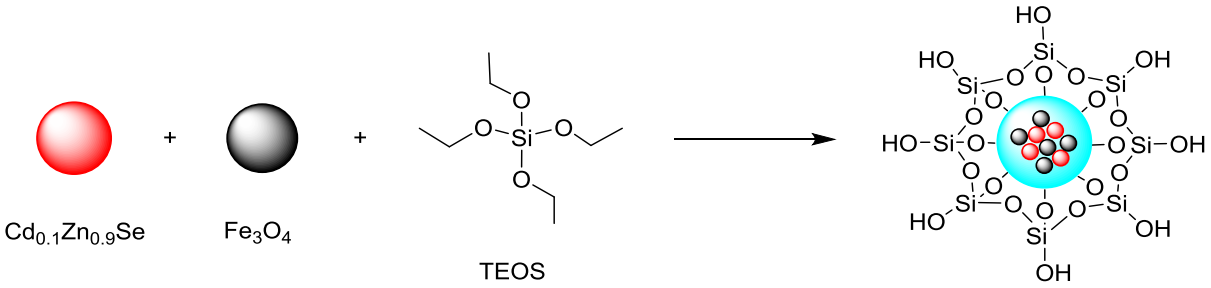

Scheme 5.1. Silica coating of Fe_3O_4 nanoparticles and $Cd_{0.1}Zn_{0.9}Se$ quantum dots.

IGEPAL CA-520 was used as the surfactant and dispersed in cyclohexane, together with the iron oxide nanoparticles and the quantum dots. Ammonium hydroxide was added and tetraethylorthosilicate was added next to act as the silica precursor. The reaction took place for 16 hours and, after this time, the nanocomposites were separated by centrifugation and washed with methanol.

Infrared spectroscopy was used to visualise the stretching bands due to this nanocomposite and compare them to the free coated and non-coated nanoparticles, and the free $Cd_{0.1}Zn_{0.9}Se$ quantum dots (*Figure 5.12*). Vibrational modes due to stretching bonds characteristics of every species could be identified (*Table 5.1*).

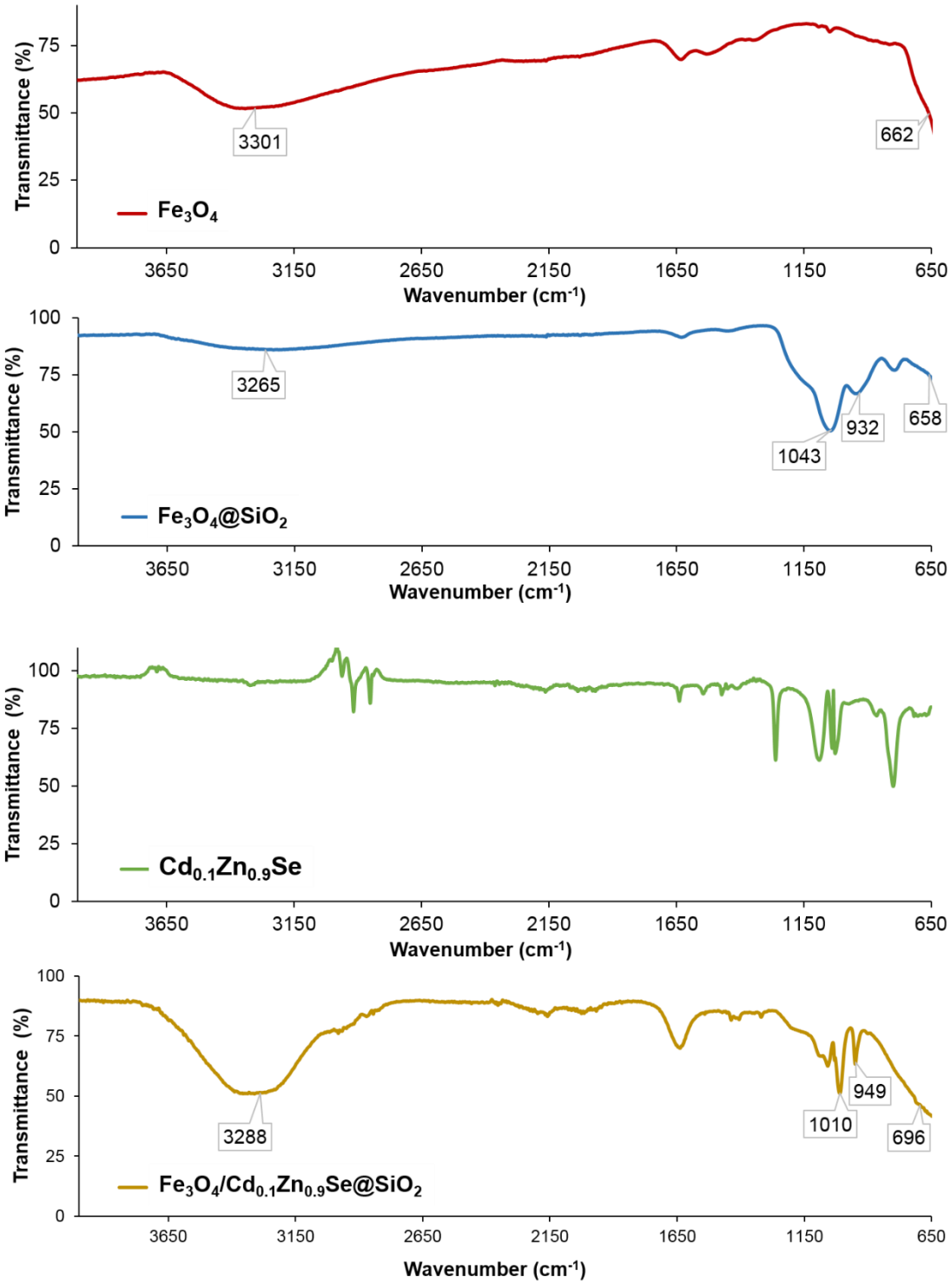

Figure 5.12. FT-IR spectra of Fe_3O_4 (red), $Fe_3O_4@SiO_2$ (blue), $Cd_{0.1}Zn_{0.9}Se$ (green) and $Fe_3O_4/Cd_{0.1}Zn_{0.9}Se@SiO_2$ (yellow).

Table 5.1. Band assignment for the FT-IR spectra of Fe_3O_4, $Fe_3O_4@SiO_2$, $Fe_3O_4/Cd_{0.1}Zn_{0.9}Se@SiO_2$ and $Cd_{0.1}Zn_{0.9}Se$ (*Figure 5.12*).

Nanoparticles	Wavenumber / cm^{-1}	Vibrational mode
Fe_3O_4	3301	O-H st
	662	Fe-O st
$Fe_3O_4@SiO_2$	3265	O-H st
	1043	Si-O-Si st
	932	Si-OH st
	658	Fe-O st
$Fe_3O_4/Cd_{0.1}Zn_{0.9}Se@SiO_2$	3288	O-H st
	1010	Si-O-Si st
	949	Si-OH st
	696	Fe-O st

The resulting $Fe_3O_4/Cd_{0.1}Zn_{0.9}Se@SiO_2$ nanoparticles were analysed by TEM (*Figure 5.13*). These nanocomposites have spherical morphology and sizes of approximately 50 nm, and they are homogeneously dispersed, with a dark contrast core and a light contrast silica shell. These characteristics are maintained from the $Fe_3O_4@SiO_2$ nanoparticles (*Section 5.3*).

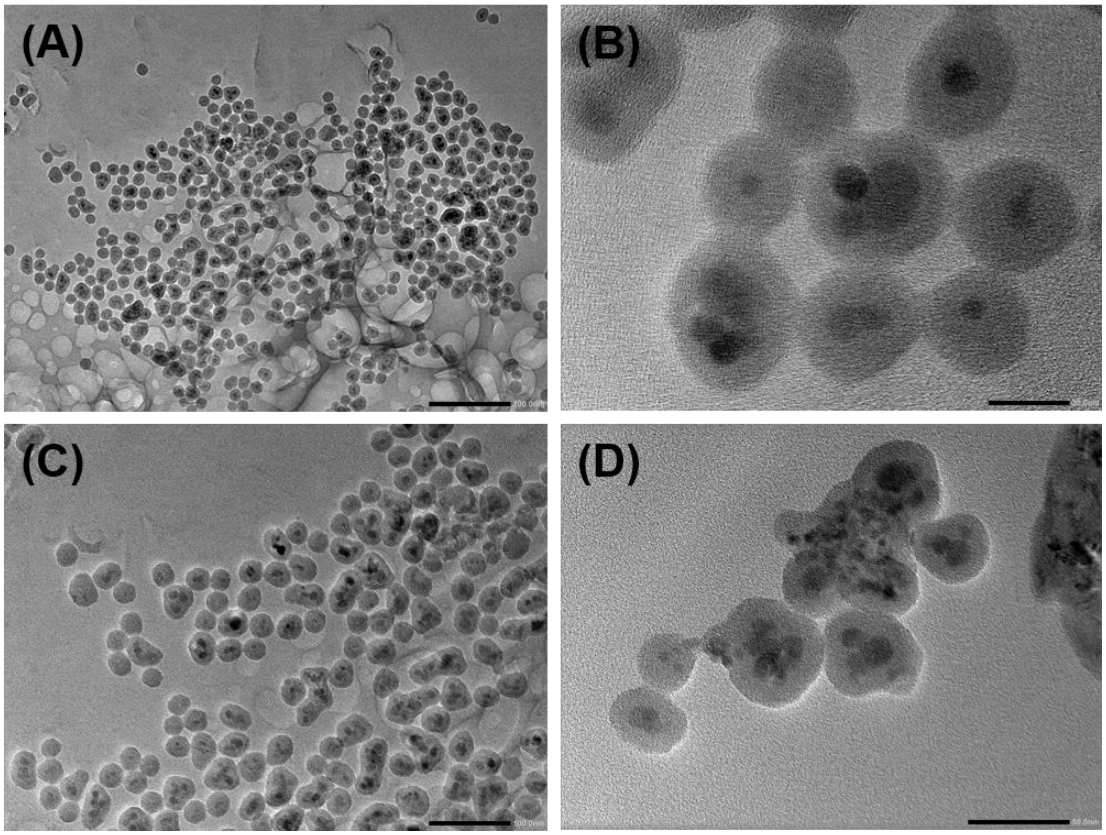

Figure 5.13. TEM micrographs of $Fe_3O_4/Cd_{0.1}Zn_{0.9}Se@SiO_2$ nanoparticles. Scale bar: **(A)** 200 nm, **(B)** 20 nm, **(C)** 100 nm, and **(D)** 50 nm.

EDX mapping shows the elemental composition of these nanoparticles. Cd, Zn, Se, Fe, O and Si are present in the EDX images and spectrum, with the last three being the predominant species (*Figure 5.14*). The EDX spectrum and percentage content of each element confirm the successful incorporation of Fe_3O_4 and $Cd_{0.1}Zn_{0.9}Se$ into silica shell nanoparticles (*Figure 5.15*). The atomic percentage of Fe and Se were found to be 5.98% and 1.01%, respectively, and by collecting a spectrum of the background it was possible to calculate that this corresponds to an approximately 2:1 ratio of Fe_3O_4:$Cd_{0.1}Zn_{0.9}Se$.

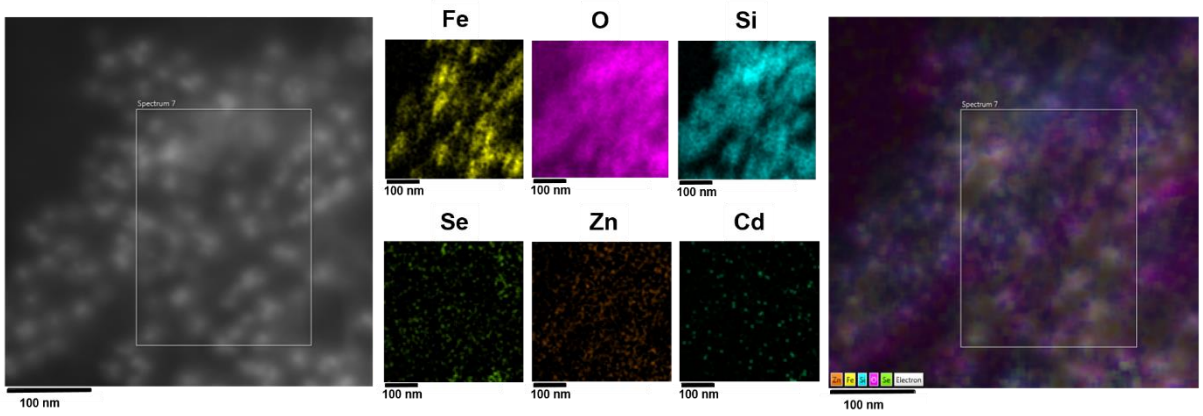

Figure 5.14. EDX mapping of $Fe_3O_4/Cd_{0.1}Zn_{0.9}Se@SiO_2$ nanoparticles. TEM micrograph of the nanocomposite (left), colour code for each element (Fe: yellow, O: pink, Si: blue, Se: green, Zn: orange, Cd: dark green), and TEM micrograph with overlaid colours (right).

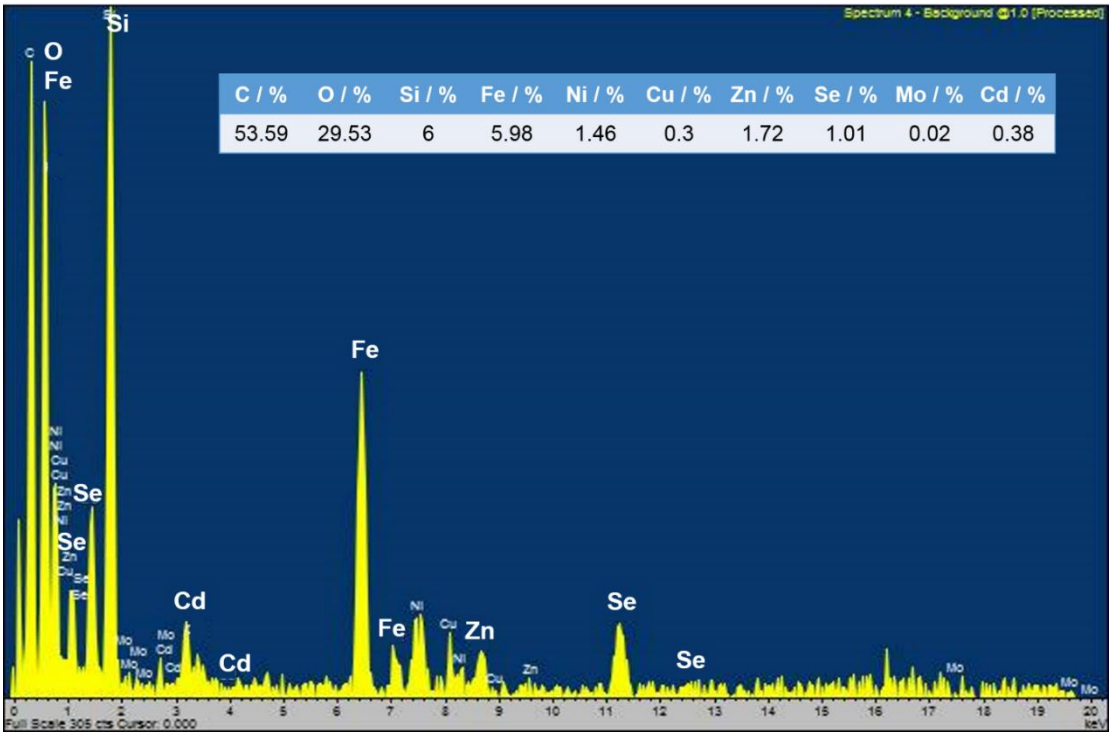

Figure 5.15. EDX spectrum and elemental composition of $Fe_3O_4/Cd_{0.1}Zn_{0.9}Se@SiO_2$ nanoparticles.

In order to determine the hydrodynamic diameter of the different nanoparticles prepared, dynamic light scattering (DLS) was used (Figure 5.16). Dispersions of 1 mg/mL of the corresponding nanocomposite in water were prepared and diluted as necessary to obtain the DLS spectra. The dispersions were first filtered with a filter of 0.45 μm in order to discard large particles of dust or large aggregations and obtain more reliable values.

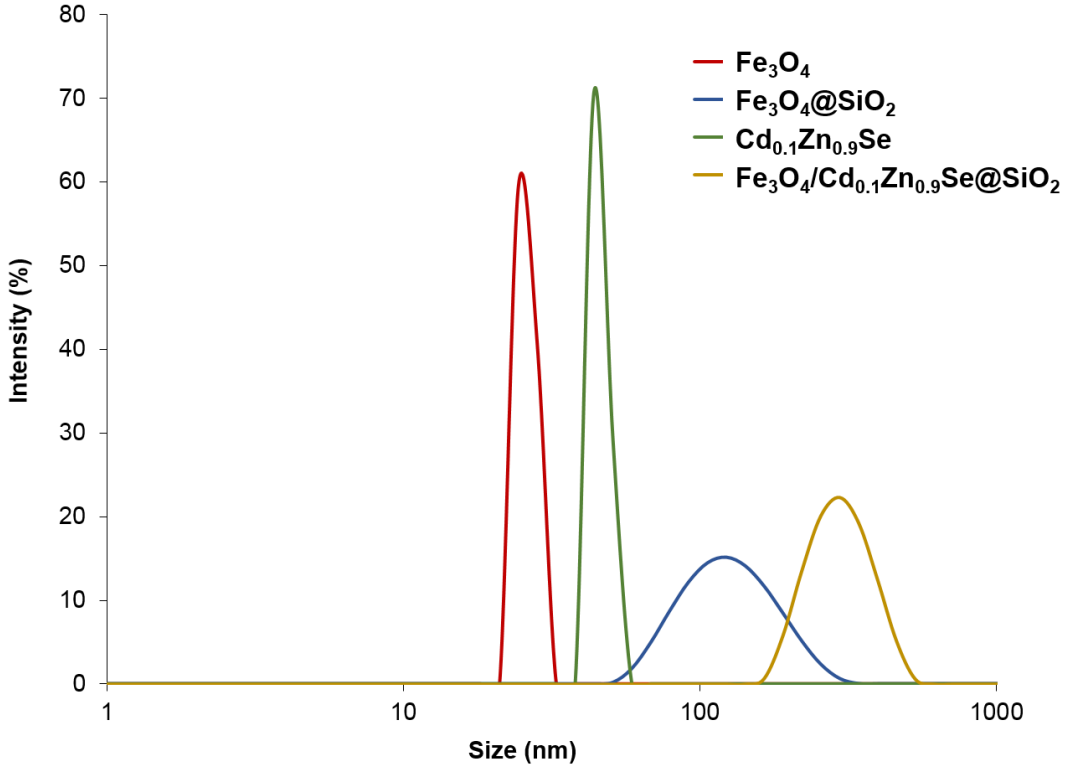

Figure 5.16. DLS spectra of Fe_3O_4, $Fe_3O_4@SiO_2$, $Cd_{0.1}Zn_{0.9}Se$ and $Fe_3O_4/Cd_{0.1}Zn_{0.9}Se@SiO_2$ nanoparticles, recorded using dispersions of the nanocomposites in water.

This technique is based on the idea that particles in suspension undergo random thermal motion (Brownian motion). This is modelled by the Stokes-Einstein equation (*Equation 5.2*), which relates the measured diffusion coefficient to particle size.

$$D_h = \frac{k_B T}{3\pi\eta D_t}$$

Equation 5.2. Stokes-Einstein equation.

From this equation, D_h is the hydrodynamic diameter (particle size), D_t is the translational diffusion coefficient (determined by dynamic light scattering), k_B is the Boltzmann's constant, T is the thermodynamic temperature and η is the dynamic viscosity.

As expected, the diameter values obtained by DLS are higher than those observed from the TEM micrographs of each sample.[35, 36] This is due to the fact that in DLS the hydrodynamic

diameter is measured, and this is defined as the size of a hypothetical hard sphere that diffuses in the same way as that of the particle being measured. However, in practice, particles in solution are not completely spherical, and they are dynamic and solvated, with solvent molecules surrounding them (hydration layer). Consequently, the calculated hydrodynamic diameter is only an indicative value of the apparent size of the dynamic hydrated/solvated particle.[37] Considering this, diameters of 28 nm were obtained for Fe_3O_4, 43 nm for $Cd_{0.1}Zn_{0.9}Se$ QDs, 122 nm for $Fe_3O_4@SiO_2$ and 295 nm for $Fe_3O_4/Cd_{0.1}Zn_{0.9}Se@SiO_2$, all of them higher than the ones observed by TEM (*Table 5.2*). This is due, as explained, to the solvation layer that surrounds the particles and the size of which is also included in the calculated diameter of these.

Table 5.2. Diameter values of the different nanocomposites observed by TEM and by DLS.

Nanoparticles	TEM diameter / nm	DLS diameter / nm
Fe_3O_4	5-10	28
$Fe_3O_4@SiO_2$	50	122
$Cd_{0.1}Zn_{0.9}Se$	-	43
$Fe_3O_4/Cd_{0.1}Zn_{0.9}Se@SiO_2$	50	295

The fluorescent properties of the $Fe_3O_4/Cd_{0.1}Zn_{0.9}Se@SiO_2$ nanocomposite were studied by fluorescence spectroscopy (*Figure 5.17*). Both the freshly synthesised $Cd_{0.1}Zn_{0.9}Se$ and the corresponding $Fe_3O_4/Cd_{0.1}Zn_{0.9}Se@SiO_2$ nanoparticles showed fluorescence emissions assignable to these QDs. The fluorescence spectra of $Cd_{0.1}Zn_{0.9}Se$ QDs and $Fe_3O_4/Cd_{0.1}Zn_{0.9}Se@SiO_2$ were recorded in 0.1 mg/mL hexane dispersions (λ_{ex} = 350 nm and λ_{ex} = 252 nm) and in 0.1 mg/mL methanol dispersions (λ_{ex} = 252 nm), respectively. Free, non-encapsulated quantum dots emit in wavelengths between 360 and 670 nm, with peaks of maximum emission at 395 and 607 nm, respectively. The fluorescence spectrum of $Fe_3O_4/Cd_{0.1}Zn_{0.9}Se@SiO_2$ nanoparticles shows the characteristic peaks in the red (552 – 687 nm) and blue (277 – 368 nm) regions of the spectrum, with maximum emission peaks at 593 and 301 nm, respectively. Moreover, a new emission peak appears at 500 nm in this spectrum, which is due to the quantum dots in the nanocomposite containing QDs and iron oxide nanoparticles encapsulated by silica.

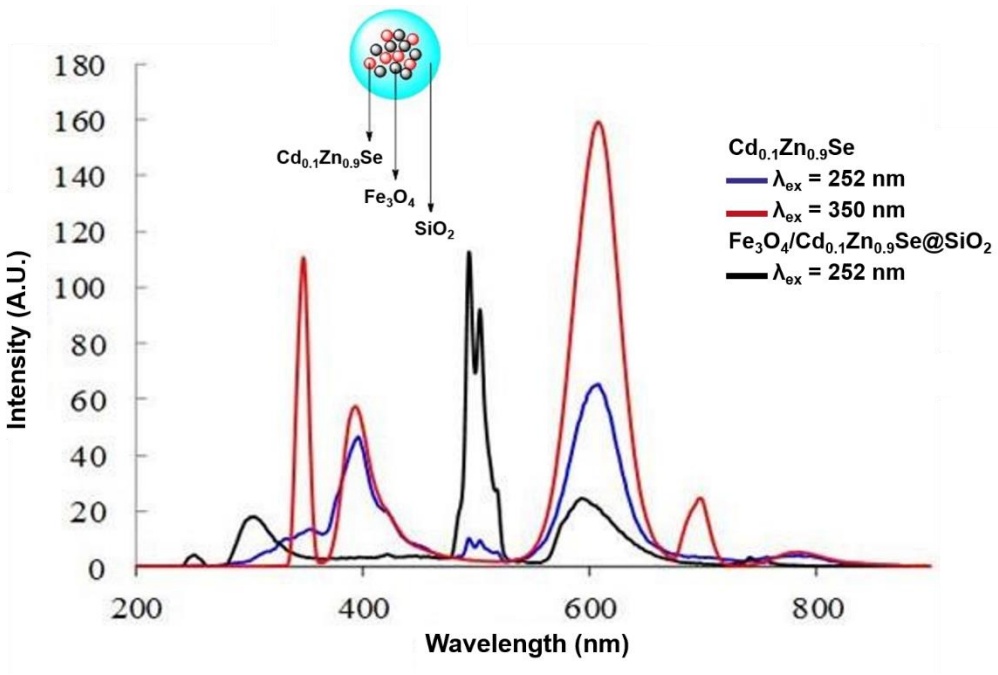

Figure 5.17. Fluorescence spectra of $Cd_{0.1}Zn_{0.9}Se$ (λ_{ex} = 350 nm, red line; λ_{ex} = 252 nm, blue line) and $Fe_3O_4/Cd_{0.1}Zn_{0.9}Se@SiO_2$ (λ_{ex} = 252 nm, black line).

The relative fluorescence quantum yield (QY) for the $Cd_{0.1}Zn_{0.9}Se$ QDs was calculated before and after encapsulation and was estimated with respect to anthracene in cyclohexane, which was used as a standard (*Table 5.3*).[38, 39] The QY for the $Fe_3O_4/Cd_{0.1}Zn_{0.9}Se@SiO_2$ nanoparticles was also measured, and it can be observed that this is reduced by a factor of 100 when the quantum dots are encapsulated within a silica shell. This is due to the fact that the Fe_3O_4 and the SiO_2 shell present simultaneously act as passivating agents for the $Cd_{0.1}Zn_{0.9}Se$ nanocrystals.[40, 41] Despite showing a significantly reduced fluorescence quantum yield, the $Fe_3O_4/Cd_{0.1}Zn_{0.9}Se@SiO_2$ nanoparticles were found to retain a luminescence emission profile which was traceable by confocal fluorescence microscopy.

Table 5.3. Calculated fluorescence QY for the free and silica encapsulated QDs synthesised species at different excitation wavelengths.

Sample	λ_{ex} / nm	QY
$Cd_{0.1}Zn_{0.9}Se$	350	0.15
	252	0.14
$Fe_3O_4/Cd_{0.1}Zn_{0.9}Se@SiO_2$	252	0.0014

5.6. Synthesis of the Zn(ATSM/A) molecular tag for hybrid magnetic nanoparticles

Diacetyl-2-(4-N-methyl-3-thiosemicarbazonato)-3-(4-N-amino-3-thiosemicarbazonato) zinc(II), also known as Zn(ATSM/A), can be converted to a complex with potential selectivity for hypoxic tissue *in vivo* and *in vitro* when the zinc is replaced by a copper radioisotope.[42-45]

Zn(ATSM/A) (compound **35c**) was synthesised with the aim of using it to functionalise the silica shell of the nanoparticles. The synthesis took place via a three steps reaction previously reported by Holland *et al.* (*Scheme 5.2*).[46]

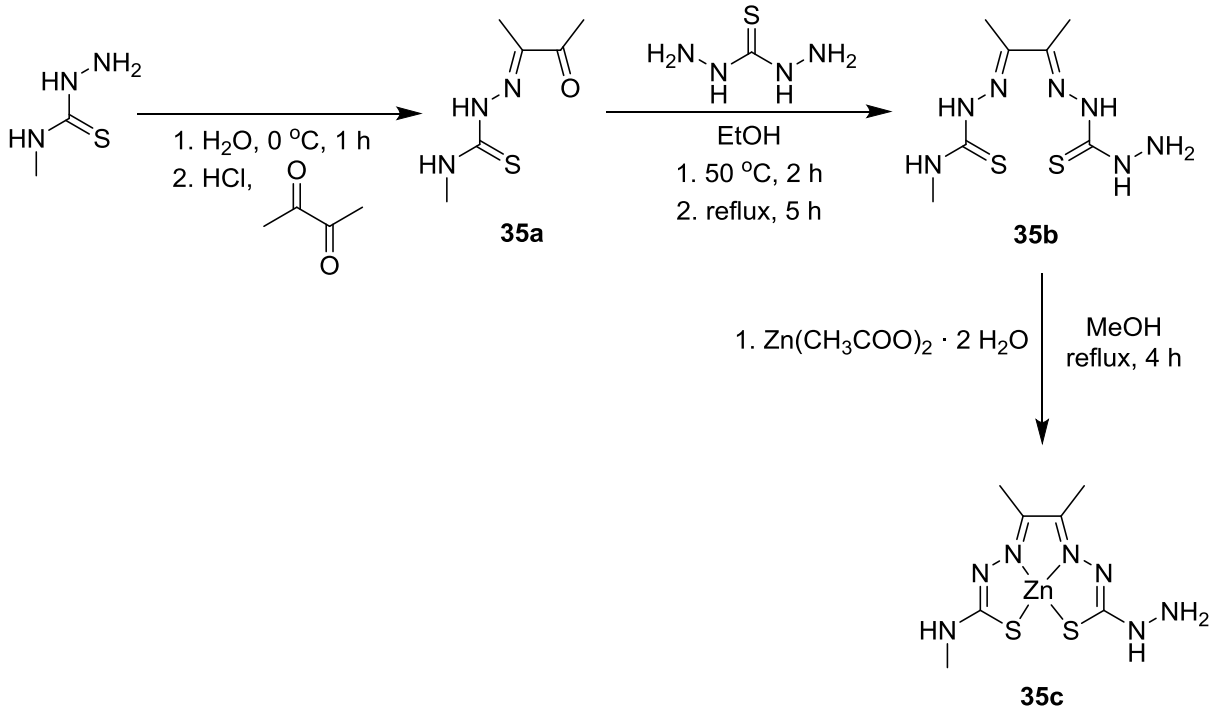

Scheme 5.2. Synthesis of Zn(ATSM/A) (compound **35c**).

Step 1 consisted of the reaction between 4-methyl-3-thiosemicarbazide and 2,3-butanedione in deionised water with HCl as catalyst at 0 °C during 1 hour to give compound **35a**. Step 2 was carried out by adding thiocarbohydrazide and compound **35a** to ethanol and stirring at 50 °C for 5 hours under reflux with HCl as catalyst. A solid was obtained, which was filtered and washed to yield H_2ATSM/A (compound **35b**), as a pale yellow solid. Finally, to obtain compound **35c**, H_2ATSM/A and zinc(II) acetate dihydrate were added to a flask and dissolved in methanol, then heated and stirred under reflux for 4 hours. The mixture was filtered and the precipitate was washed with methanol and diethyl ether. Zn(ATSM/A) was isolated as a yellow solid at the end of this reaction. The overall yield of this multi-step reaction was 29%.

Zn(ATSM/A) was analysed by ^{1}H NMR spectroscopy in deuterated dimethylsulfoxide (*Figure 5.18*). The two protons for the secondary amines can be found as two broad singlets at 8.24 and 7.24 ppm for the one next to the primary amine and the one next to a methyl group, respectively. The protons of the terminal primary amine appear as a singlet corresponding to 2 H at 4.76 ppm. The terminal methyl protons of the asymmetric arm appear as a singlet at 2.83 ppm integrating for 3 H. Finally, the two methyl groups on the back-bone of the molecule appear as two close singlets between 2.22 and 2.20 ppm due to the almost symmetry plane of the molecule, which is only disturbed by having a terminal methyl group and a terminal primary amine, one in each arm of the molecule.

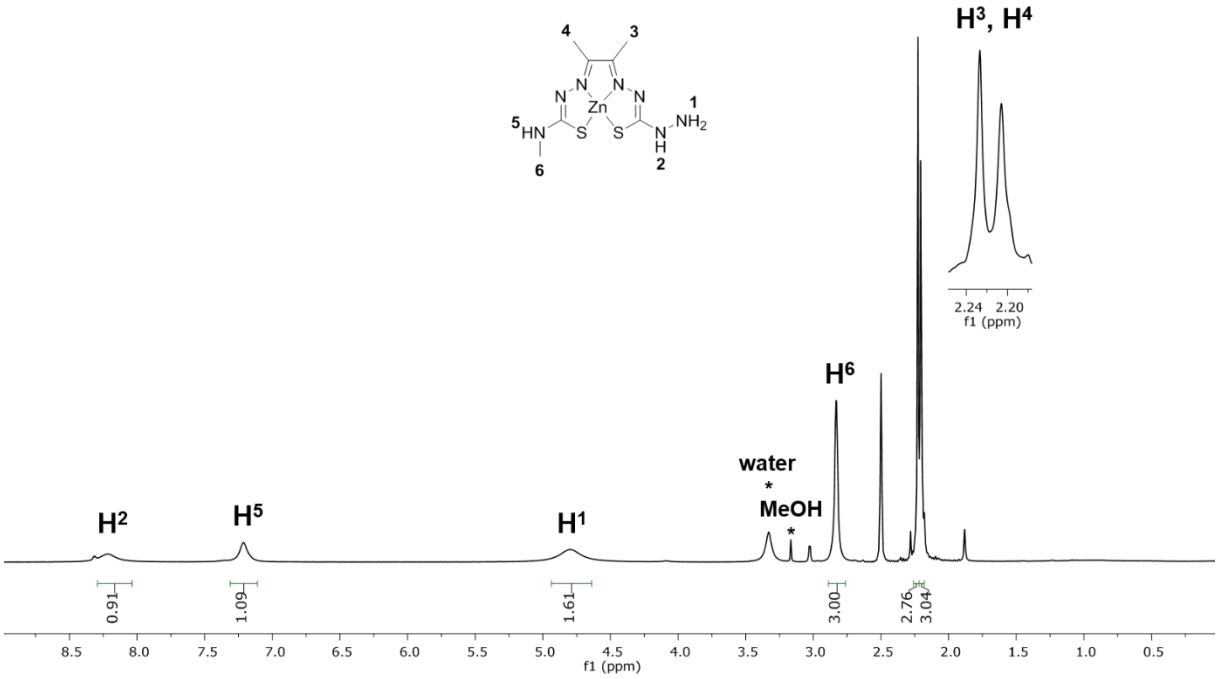

Figure 5.18. ^{1}H NMR (500 MHz, DMSO-d_6, 298 K) of Zn(ATSM/A).

The purity of this product was established by high-performance liquid chromatography (HPLC) with a solvent system of water and acetonitrile containing 0.1% of trifluoroacetic acid. When observing the absorbance at 280 nm, a unique peak can be seen at 8.8 minutes, and comparing it to the chromatograms of the starting materials it can be deduced that it corresponds to the compound of interest, proving that it does not contain any starting materials or other products as a mixture. However, peaks of very low intensity can be observed in the baseline between 2 and 12 minutes due to minor impurities, or to the possible protonation in the column due to the TFA present in the mobile phase.

5.7. Incorporation of Zn(ATSM/A) into the Fe_3O_4@SiO_2 core-shell nanoparticles

Zn(ATSM/A) was synthesised with the aim of having a fluorophore and potential PET chelator to functionalise the silica shell of the nanoparticles (*Scheme 5.3*), and to demonstrate that the outer surface of the core-shell nanocomposites can be functionalised with a pendant amino group. It is unclear if what occurs is a condensation reaction to form Si-N bonds at the surface of the nanoparticles or, more likely, the Zn(ATSM/A) molecule is bound to the surface by hydrogen bonding between the hydroxyl groups of the silica and the terminal amino groups of the metal-ligand complex.

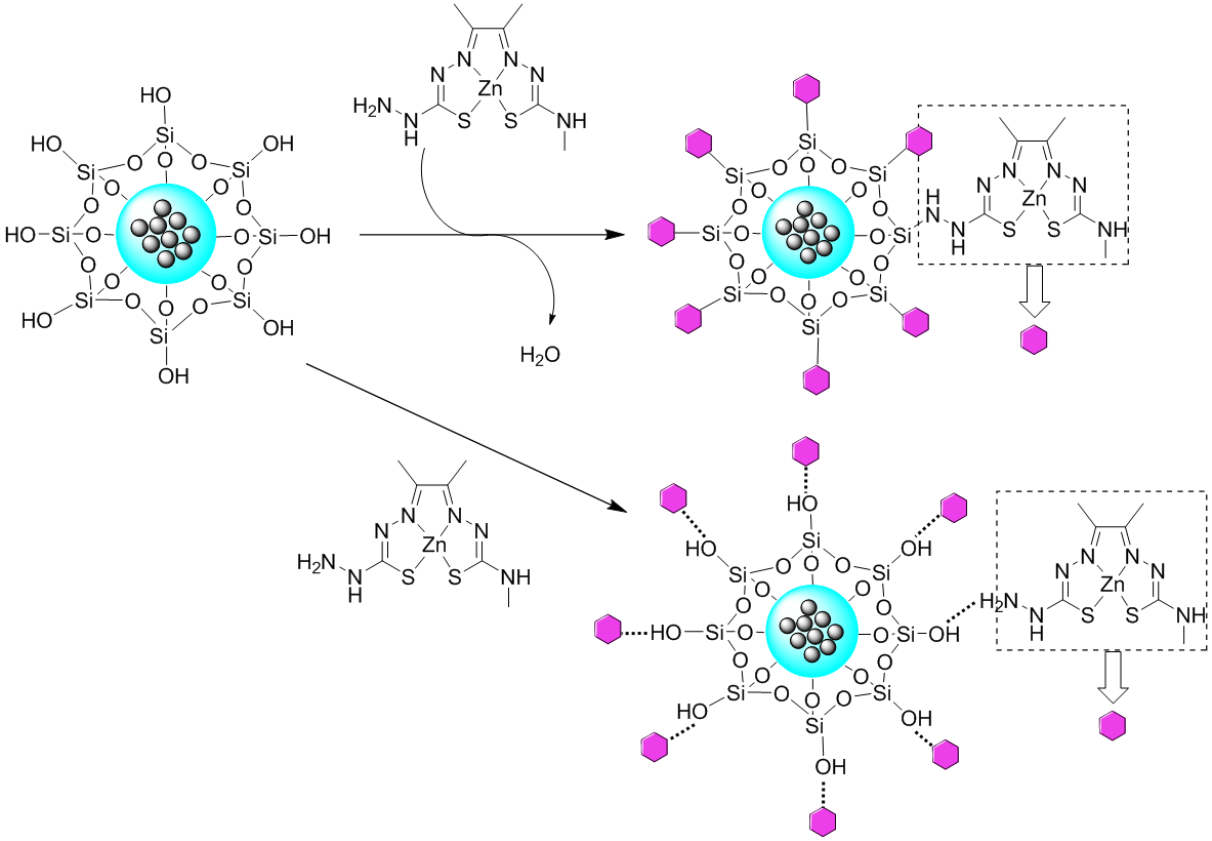

Scheme 5.3. Reaction of functionalisation of the silica shell of Fe_3O_4 nanoparticles with Zn(ATSM/A).

The reaction carried out to achieve this goal involved combining the Fe_3O_4@SiO_2 nanoparticles and Zn(ATSM/A) in methanol. The reaction mixture was heated to 80 ^oC under reflux and mechanically stirred overnight. The mixture was left to cool to room temperature and the obtained nanocomposite was separated by centrifugation and washed with methanol.

To confirm that the functionalisation of the silica shell with Zn(ATSM/A) had taken place, infrared spectroscopy analysis of the obtained nanocomposite and the starting materials was carried out in the solid state (*Figure 5.19*).

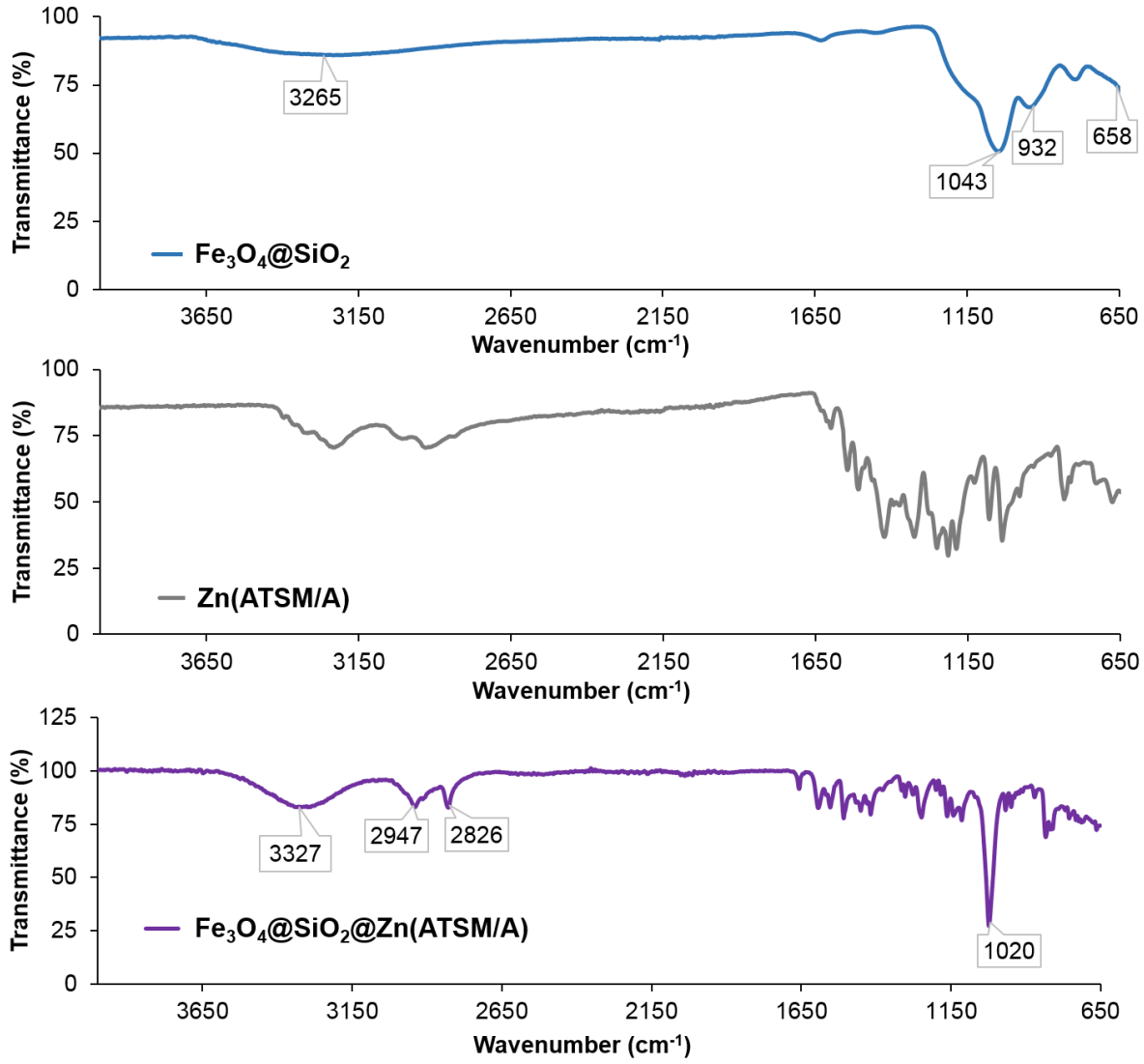

Figure 5.19. FT-IR spectra of Fe_3O_4@SiO_2 (blue), Zn(ATSM/A) (grey) and Fe_3O_4@SiO_2@Zn(ATSM/A) (purple).

The band at approximately 1020 cm^{-1} in the Fe_3O_4@SiO_2@Zn(ATSM/A) spectrum corresponds to the Si-O-Si stretching vibration. Bands between 1650 and 650 cm^{-1} can also be observed in the spectrum of the new nanocomposite, corresponding to expected vibrations emerging from the bonds within the Zn(ATSM/A) complex, and proving that the reaction took place (*Table 5.4*).

Table 5.4. Band assignment for the FT-IR spectra of $Fe_3O_4@SiO_2$ and $Fe_3O_4@SiO_2@Zn(ATSM/A)$ (*Figure 5.19*).

Nanoparticles	Wavenumber / cm^{-1}	Vibrational mode
$Fe_3O_4@SiO_2$	3265	O-H st
	1043	Si-O-Si st
	932	Si-OH st
	658	Fe-O st
$Fe_3O_4@SiO_2@Zn(ATSM/A)$	3327	O-H st
	2947	$C(sp^3)$-H st
	2826	$C(sp^2)$-H st
	1020	Si-O-Si st

Furthermore, TEM analysis and EDX mapping were carried out to study the morphology and composition of the new nanoparticles. TEM micrographs clearly show the addition of Zn(ATSM/A) onto the $Fe_3O_4@SiO_2$ system, with some excess of the complex in the grid (*Figure 5.20*).

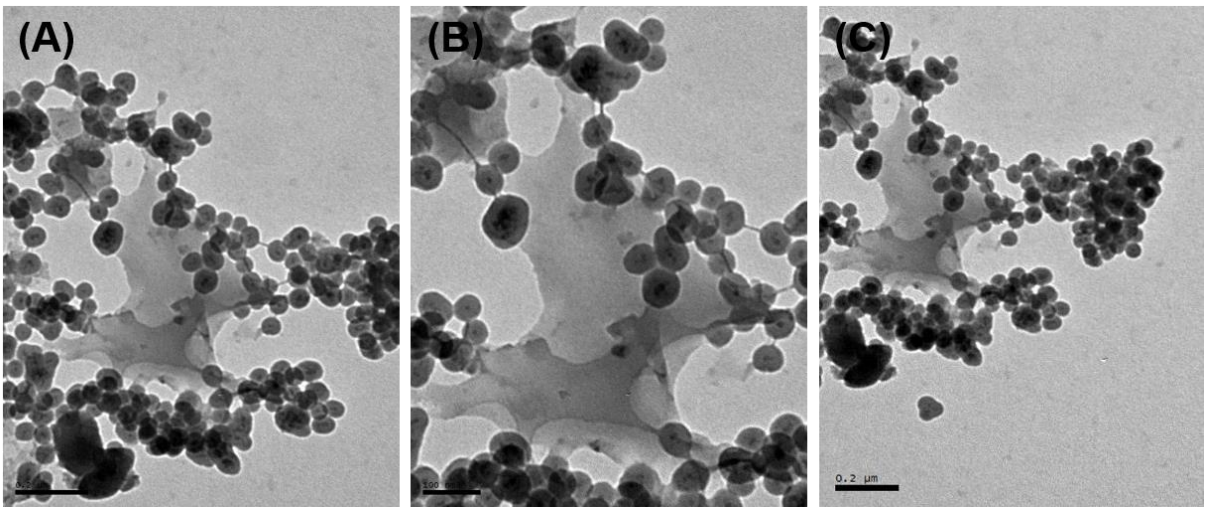

Figure 5.20. TEM micrographs of $Fe_3O_4@SiO_2@Zn(ATSM/A)$ nanoparticles. Scale bar: **(A)** 0.2 µm, **(B)** 100 nm, and **(C)** 0.2 µm.

In this case, scanning transmission electron microscopy (STEM) was used in dark field mode and this allowed the three-dimensional distribution of these nanoparticles in the grid to be seen. This showed how some iron oxide-silica core-shell nanocomposites are packed and slightly aggregated, while the metal-ligand complex, Zn(ATSM/A), is freely distributed in the sample located around the almost spherical nanoparticles (*Figure 5.21*).

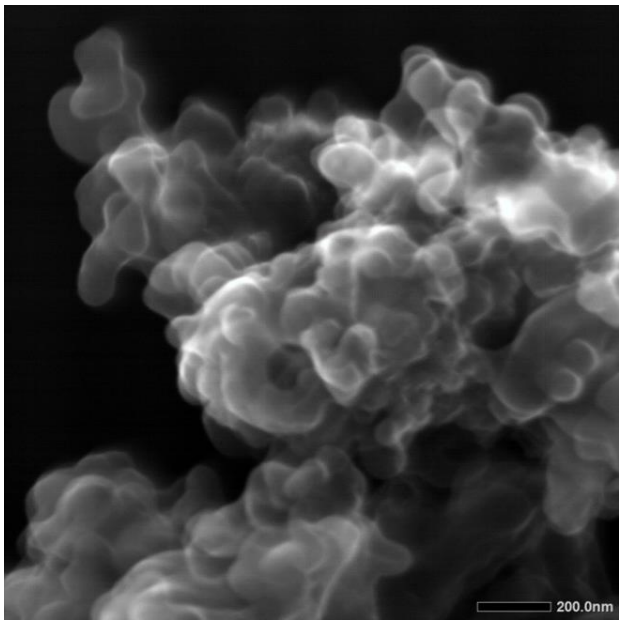

Figure 5.21. STEM image of Fe_3O_4@SiO_2@Zn(ATSM/A) nanoparticles using dark field mode.

EDX mapping images (*Figure 5.22*) and spectrum (*Figure 5.*23) of Fe_3O_4@SiO_2@Zn(ATSM/A) nanoparticles confirmed that the sample contains all the expected elements: Fe, Si, O, Zn, C, S and N (these last four pertaining to the Zn(ATSM/A) complex).

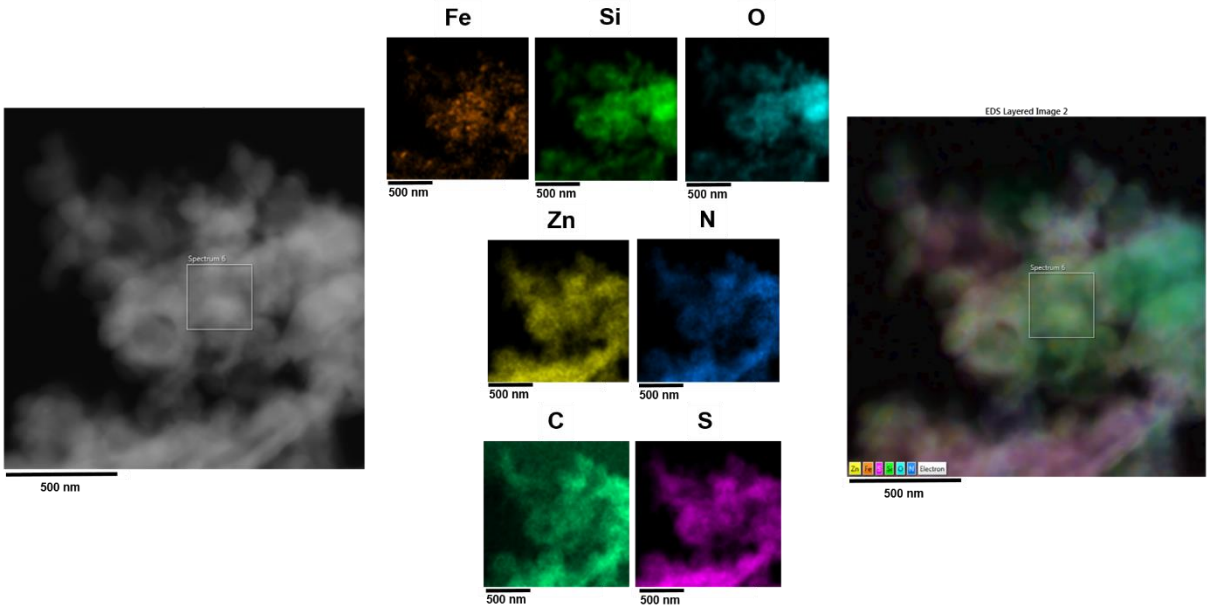

Figure 5.22. EDX mapping of Fe_3O_4@SiO_2@Zn(ATSM/A) nanoparticles**.** TEM micrograph of the nanocomposite (left), colour code for each element (Fe: orange, Si: green, O: light blue, Zn: yellow, N: blue, C: light green, S: pink), and TEM micrograph with overlaid colours (right).

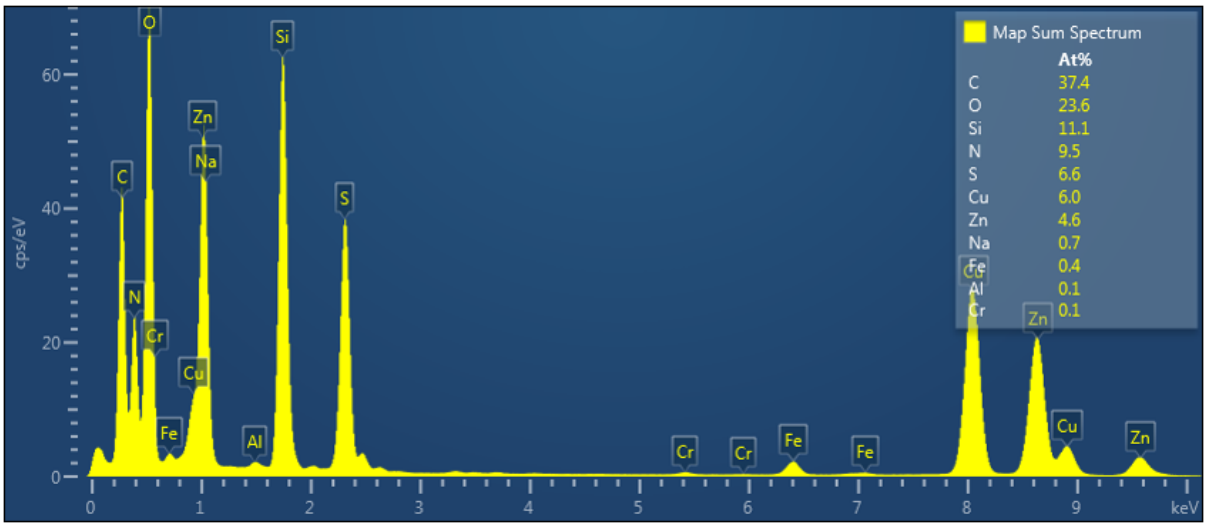

Figure 5.23. EDX spectrum and elemental composition of Fe_3O_4@SiO_2@Zn(ATSM/A) nanoparticles.

The hydrodynamic diameter was determined by DLS for the Fe_3O_4@SiO_2@Zn(ATSM/A) nanoparticles as well, using a 0.01 mg/mL dispersion of the nanocomposite in water (*Figure 5.24*). In this case, the molecule Zn(ATSM/A) is bound to the silica surface of the nanoparticles. For this reason, the obtained diameter size should include also the Zn(ATSM/A) that surrounds the nanoparticles, as this molecule is part of the system and moves with it. Consequently, an extended peak from 10 to 1000 nm can be observed.

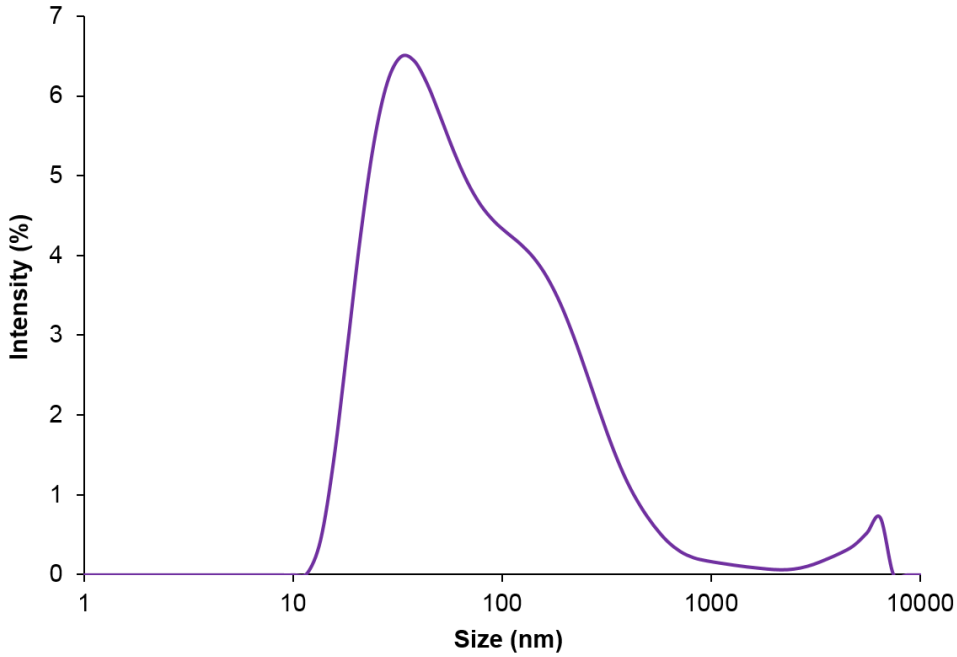

Figure 5.24. DLS spectrum of Fe_3O_4@SiO_2@Zn(ATSM/A) nanoparticles, recorded using a 0.01 mg/mL dispersion of the nanocomposite in water.

Raman spectroscopy of the Fe_3O_4@SiO_2@Zn(ATSM/A) nanoparticles and the starting materials, Fe_3O_4@SiO_2 and Zn(ATSM/A), was carried out in the solid state using a laser of 532 nm excitation wavelength in order to compare them to the new nanocomposite (*Figure 5.25*). Vibrations due to Si-O-Si bonds can usually be observed between 450 and 550 cm^{-1}. However, data was collected from 500 cm^{-1} and the Fe_3O_4@SiO_2 spectrum did not show any peaks. Peaks were expected for the other two materials because they contain many bonds that are active to Raman spectroscopy. In this context, peaks between 2800 and 3100 cm^{-1} can be assigned to vibrations of the C-H bonds, having sp^3 and sp^2 C atoms. The strong band at around 3200 cm^{-1} is due to the vibrations of the N-H functional group. Due to the small amount of sample that the specific Raman instrument analyses used, it was not possible to appreciate any sharp and well-defined peaks for any of the products and a baseline substraction needed to be carried out. Despite this, it is observable that the spectrum for Fe_3O_4@SiO_2 is a flat straight line, while the spectra for Zn(ATSM/A) and Fe_3O_4@SiO_2@Zn(ATSM/A) nanoparticles are not, showing some medium intensity peaks and presenting a similar aspect, which indicates that for the functionalised nanoparticles the Zn(ATSM/A) complex on the surface is being detected.

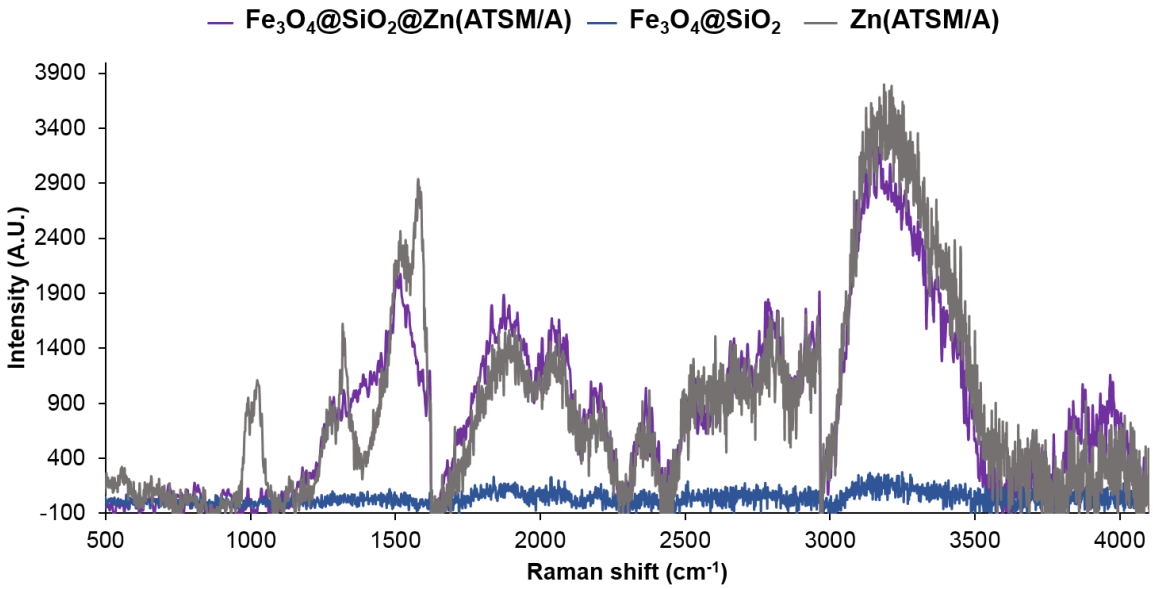

Figure 5.25. Raman spectra showing Fe_3O_4@SiO_2 (blue line), Zn(ATSM/A) (grey line), and Fe_3O_4@SiO_2@Zn(ATSM/A) (purple line).

5.8. Synthesis of citric acid-coated iron oxide nanoparticles and functionalisation with a BODIPY derivative

Superparamagnetic iron oxide nanoparticles used in these experiments were synthesised and characterised as described in *Section 5.2* and, in this case, citric acid was used to stabilise the magnetite particles. Citric acid was anchored onto the surface of freshly prepared nanoparticles by a direct addition method, with the carboxylic groups of this molecule making the nanoparticles more water-dispersible, and also providing sites for further functionalisation (*Scheme 5.4*).[47]

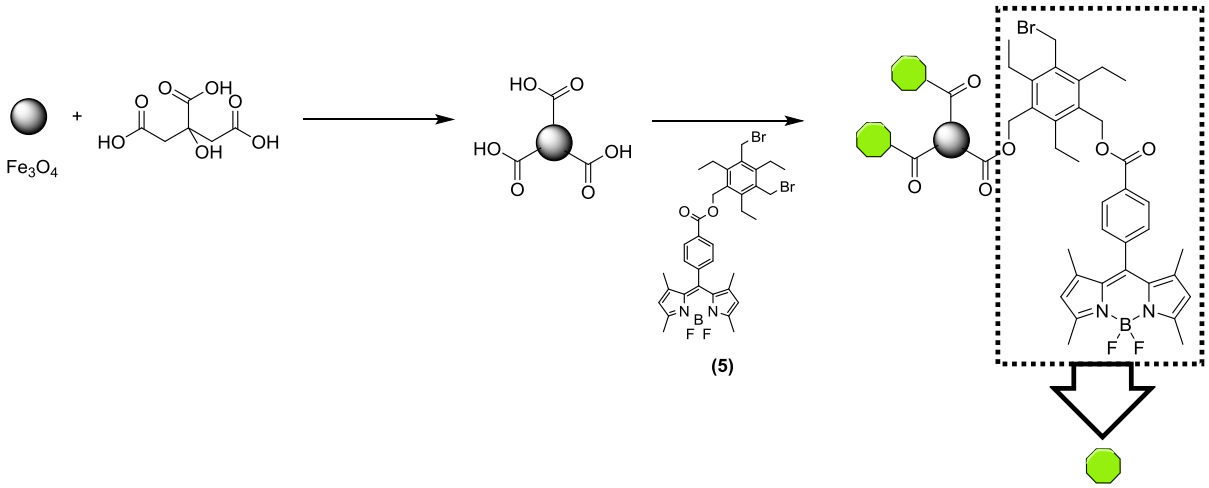

Scheme 5.4. Coating of Fe_3O_4 nanoparticles with citric acid and subsequent addition of a mono-functionalised BODIPY derivative (compound **5**).

Fe_3O_4 nanoparticles were dispersed in water and citric acid was dropwise added to the suspension until the pH was around 5 when measured with pH paper. The dark brown mixture was mechanically stirred for 3 hours at 85 ^oC, and after this time the resulting nanocomposite was isolated by centrifugation.

In order to synthesise compound **38**, the BODIPY derivative synthesised as described in *Section 2.4* (compound **5**) was used. A nucleophilic substitution reaction was carried out such that an ester bond was formed between the citric acid-coated nanoparticles and the tripodal core. Fe_3O_4 nanoparticles were added to a flask and dispersed in acetonitrile together with compound **5**, then the temperature was set to 100 ^oC and the mixture was mechanically stirred overnight. After this time, the nanocomposite was collected by centrifugation and washed with methanol.

Citric acid, citric acid-coated magnetic nanoparticles, and the coated nanoparticles incorporating the fluorophore were analysed by FT-IR (*Figure 5.26*).

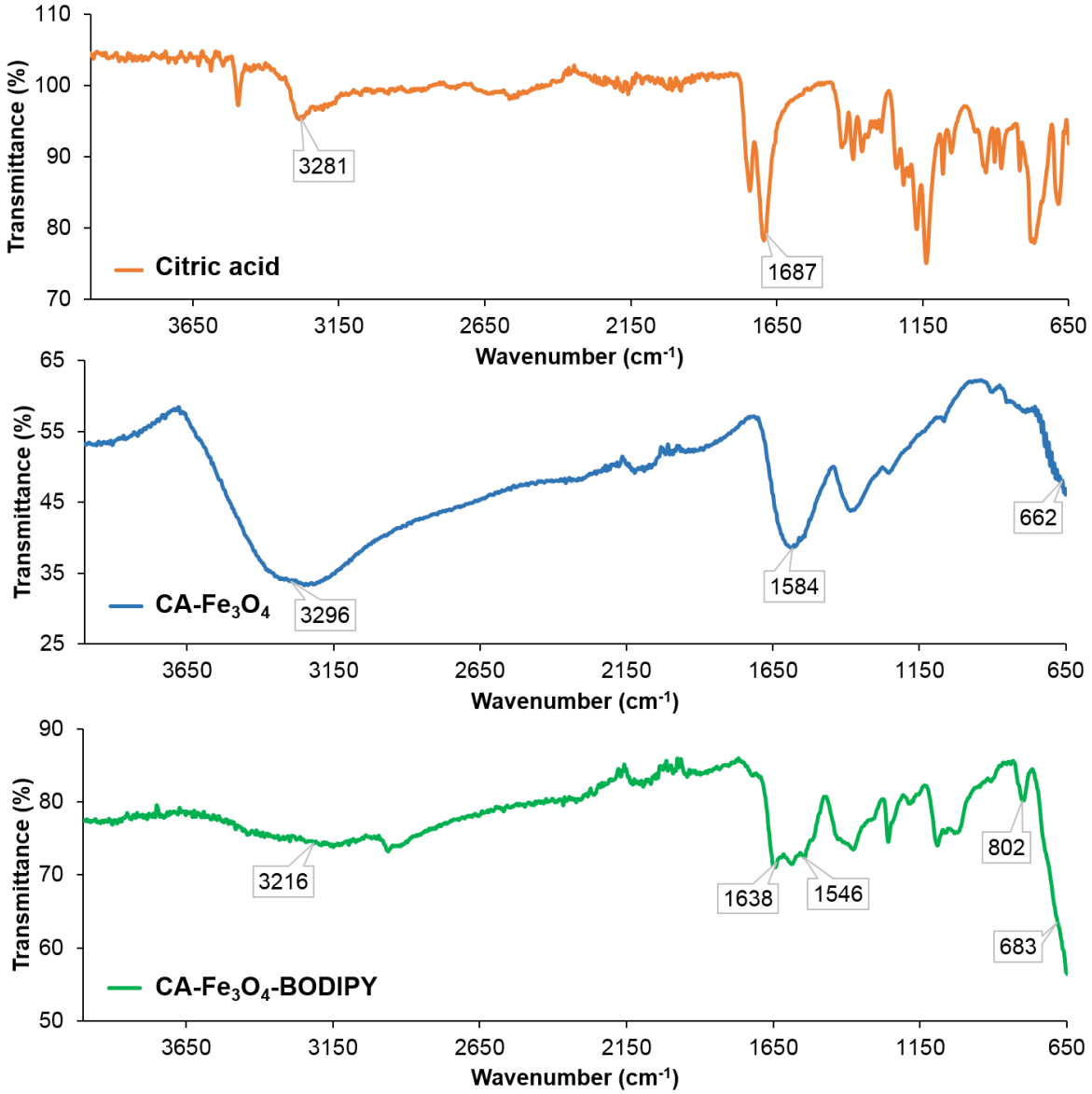

Figure 5.26. FT-IR spectra of citric acid (orange line), citric acid-coated Fe_3O_4 nanoparticles (blue line), and citric acid-coated nanoparticles functionalised with a BODIPY derivative (green line).

The FT-IR spectrum for citric acid shows clear bands, but the one for the citric acid-coated Fe_3O_4 nanoparticles shows only a few broad bands. Bands assignable to the stretching vibrations of the carbonyl group and C-Br stretching bands confirm the formation of the expected product (*Table 5.5*).

Table 5.5. Band assignment for the FT-IR spectra of citric acid, citric acid-coated Fe_3O_4 nanoparticles and citric acid-coated Fe_3O_4 nanoparticles containing a BODIPY derivative (*Figure 5.26*).

Compound	Wavenumber / cm^{-1}	Vibrational mode
Citric acid	3281	O-H st
	1687	C=O st
Citric acid-coated Fe_3O_4	3296	O-H st
	1584	C=O st
	662	Fe-O st
Citric acid-coated Fe_3O_4 with a BODIPY derivative	3216	O-H st
	1638	C=O st
	1546	B-F st
	802	C-Br st
	683	Fe-O st

DLS was used to measure the hydrodynamic diameter of the citric acid-coated Fe_3O_4 nanoparticles (*Figure 5.27*). For this purpose, a 0.01 mg/mL dispersion of the nanocomposite in water was used. As for the Fe_3O_4@SiO_2@Zn(ATSM/A) nanoparticles (*Section 5.7*), the citric acid molecules surrounding the nanoparticles are part of the same sphere, and for this reason the obtained value ranges from 10 to 1000 nm.

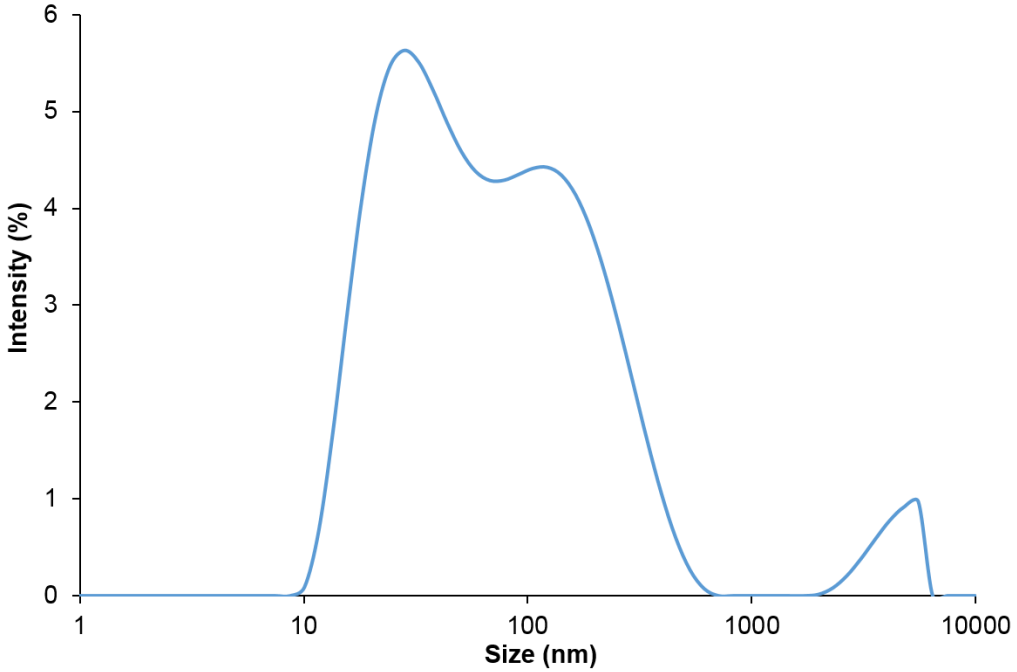

Figure 5.27. DLS spectrum of citric acid-coated iron oxide nanoparticles, recorded using a 0.01 mg/mL dispersion of the nanocomposite in water.

The porosity of this composite was checked by performing a detailed BET surface area analysis on magnetite Fe_3O_4 nanoparticles and citric acid-coated Fe_3O_4 nanoparticles. The specific surface area of these nanoparticles in the air-free powder state was measured by nitrogen physical adsorption, and calculated according to the Brunauer-Emmett-Teller (BET) equation. Prior to the measurements, the samples were degassed in vacuum at 90 ^oC for 4 hours. Adsorption isotherms were obtained which were converted to BET surface plots to calculate the surface area (*Table 5.6*). It is clear from the surface area values that the magnetite nanoparticles alone have a low surface area (116.47 m^2/g), whereas the surface area almost doubles after the coating with citric acid (206.58 m^2/g). This indicates the role of this compound in increasing the surface area, and indicates that the coated nanocomposite is more porous.[48]

Table 5.6. BET surface area and pore size obtained from BET measurements of citric acid-coated and uncoated Fe_3O_4 nanoparticles.

Nanoparticles	**BET surface area (m^2/g)**	**Pore size**	
		BJH Adsorption average pore diameter (4V/A)	**BJH Desorption average pore diameter (4V/A)**
Fe_3O_4	116.47	8.54 nm	7.87 nm
Citric acid-coated Fe_3O_4	206.58	5.09 nm	4.31 nm

The isotherm linear absolute plot and the isotherm pressure composition curves show that the citric acid-coated nanoparticles have the ability to adsorb (and later desorb) a higher amount of nitrogen gas than the free nanoparticles (*Figure 5.28*). This could be due to the fact that the coated nanoparticles have a higher surface area.[2]

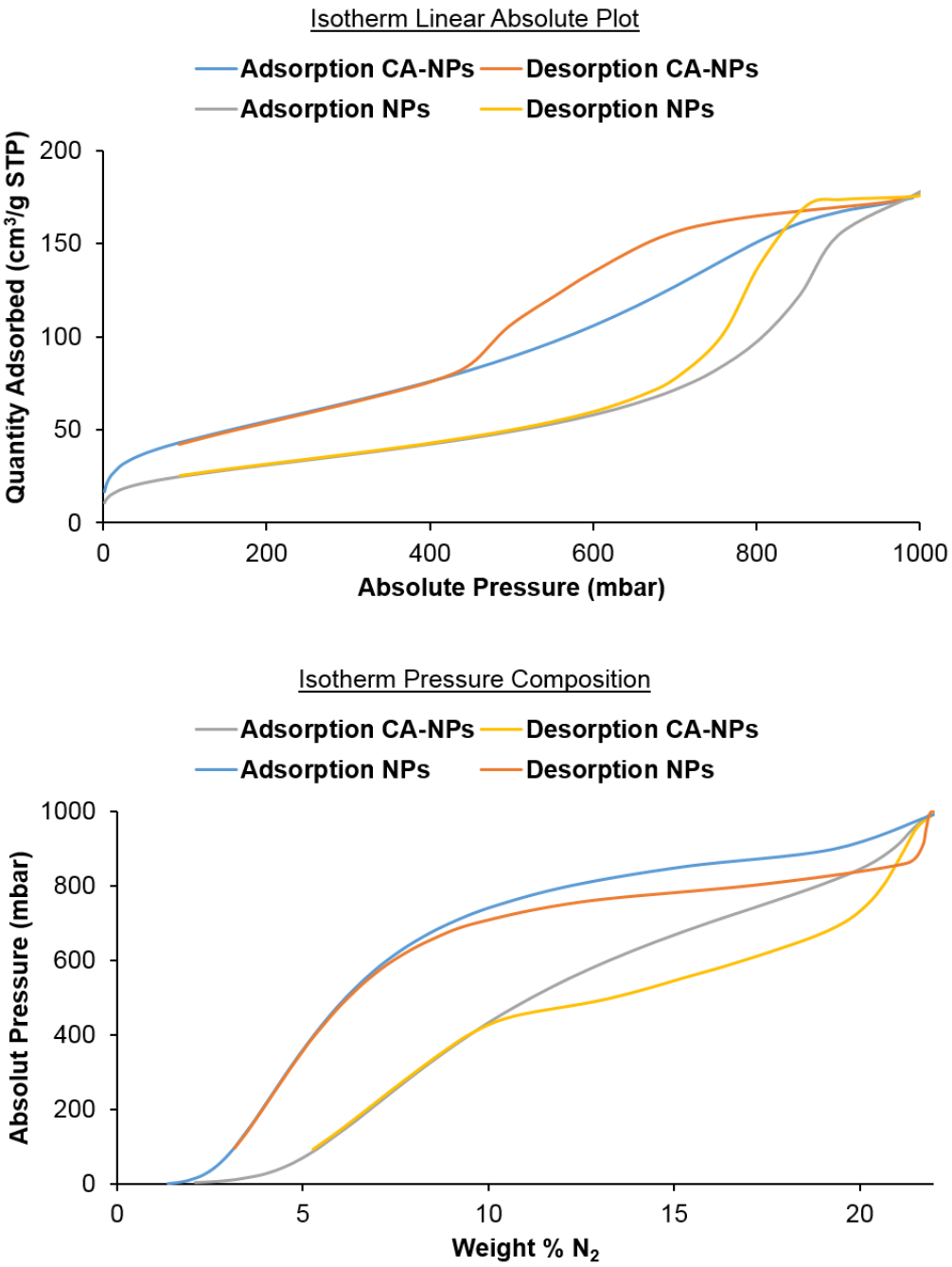

Figure 5.28. Adsorption and desorption curves for citric acid-coated nanoparticles (CA-NPs) and Fe_3O_4 nanoparticles (NPs).

The BET surface area plot and the BJH adsorption and desorption cumulative pore volume curves show that the free nanoparticles have larger volume pores (*Figure 5.29*).

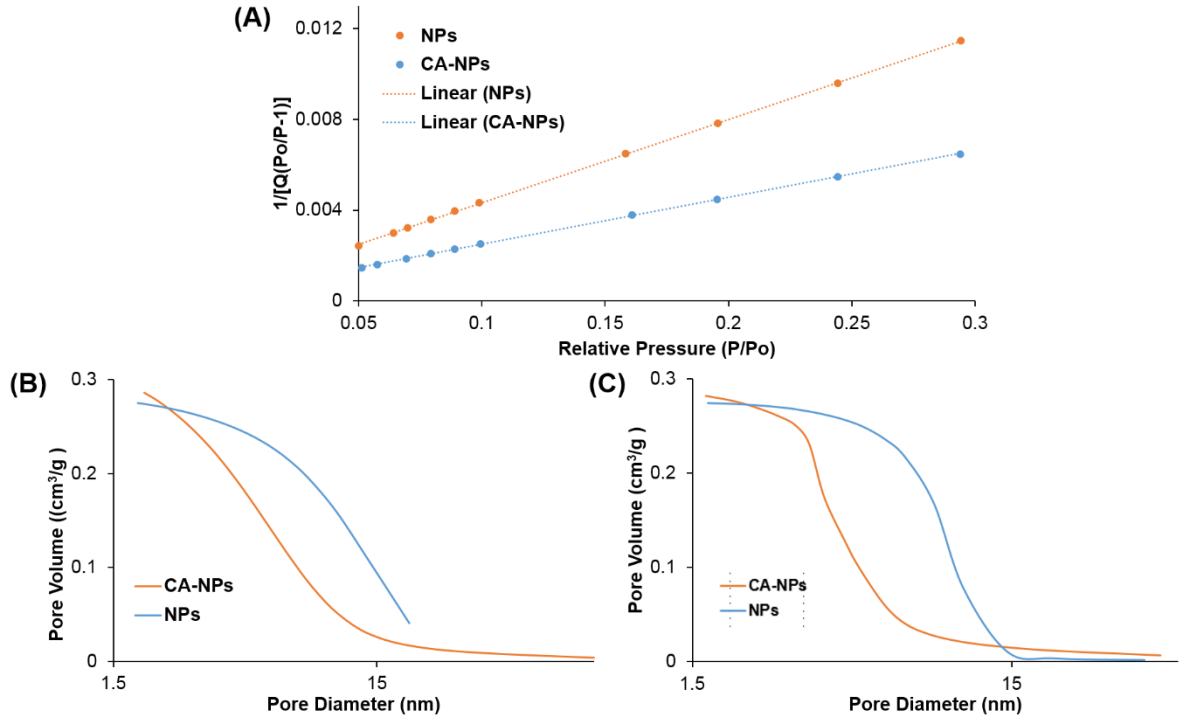

Figure 5.29. (A) BET surface area plot, **(B)** BJH adsorption cumulative pore volume curve, and **(C)** BJH desorption cumulative pore volume curve for citric acid-coated nanoparticles (CA-NPs) and Fe_3O_4 nanoparticles (NPs).

Thermogravimetric analysis (TGA) was used on all the previously described nanocomposites to determine the changes in their chemical and physical properties that they experience when the temperature is increased. In order to carry out these experiments, each sample was loaded into an alumina crucible and the temperature program was applied, consisting of a heating ramp at a rate of 10 K/min from 30 to 800 ºC. A cooling ramp started next, from 800 ºC and back to 30 ºC at a cooling rate of 20 K/min. Finally, the temperature was maintained at 30 ºC before ending the program. Phenomena such as vaporisation, sublimation, desorption/adsorption, desolvation and decomposition can usually be identified from TGA curves.[49] The TGA spectrum for Fe_3O_4 nanoparticles (red line) shows almost no loss of weight (less than 5%), indicating that this nanocomposite is stable up to 800 ºC (*Figure 5.30*). For $Fe_3O_4@SiO_2$ (blue line) and the citric acid-coated Fe_3O_4 nanoparticles (orange line) there is a weight loss of approximately 10%. This can be explained by the decomposition of the coating molecules in these two types of materials: the silica in one case, and the citric acid in the other case. For the $Fe_3O_4@SiO_2@Zn(ATSM/A)$ (purple line) and $Fe_3O_4/Cd_{0.1}Zn_{0.9}Se@SiO_2$ nanoparticles (yellow line) there is a significant decrease in the weight starting at approximately 200 ºC and going on until 500 ºC in both cases, to lose around 30% and 50% of their initial weight, respectively. As expected, loss of solvents cannot be observed for any of the tested

nanocomposites as these were previously dried, proving that there is no solvent adsorbed into the sample.

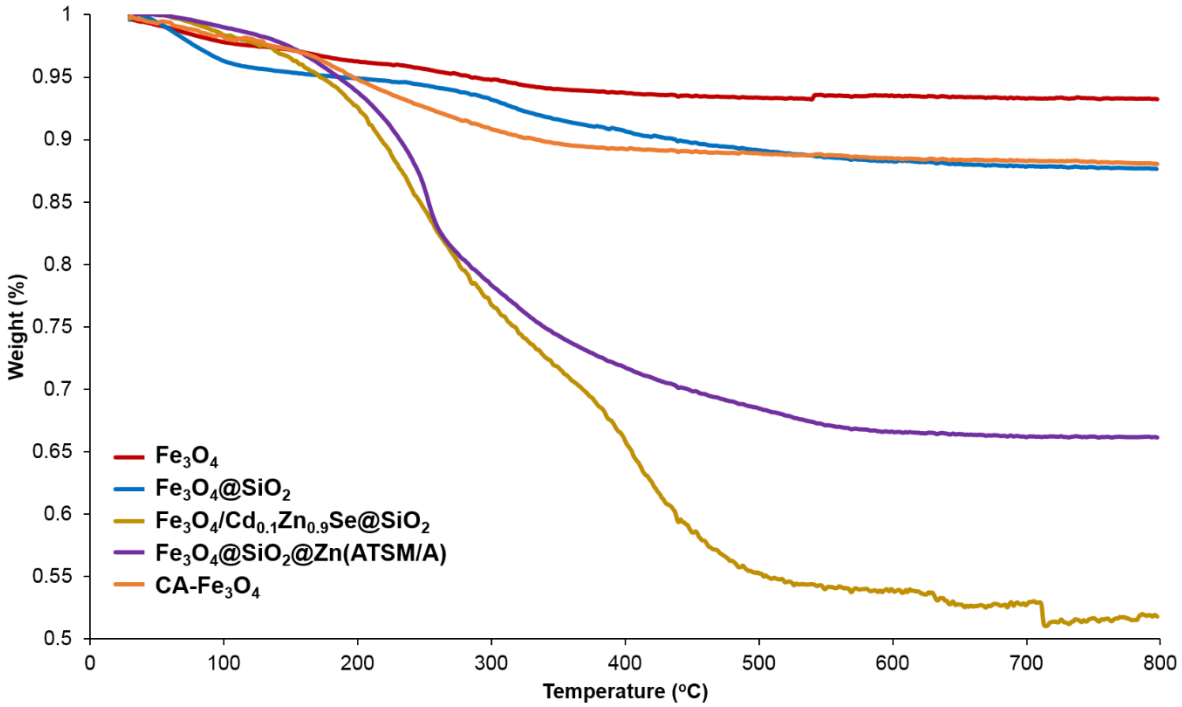

Figure 5.30 Thermogravimetric analysis spectra of Fe_3O_4 (red line), $Fe_3O_4@SiO_2$ (blue line), $Fe_3O_4/Cd_{0.1}Zn_{0.9}Se@SiO_2$ (yellow line), $Fe_3O_4@SiO_2@Zn(ATSM/A)$ (purple line), and citric acid-coated Fe_3O_4 nanoparticles (orange line).

5.9. Radiolabelling experiments with gallium-68

5.9.1. Generator production of gallium-68

In these experiments, the positron-emitting radiotracer [^{68}Ga]$GaCl_3$ was prepared at the Department of Surgery and Cancer of the Imperial College London using either a TiO_2 or a SnO_2-based column matrix ^{68}Ge/^{68}Ga generator via the (p,2n) reaction on gallium targets.

5.9.2. Radio-incorporation: method development

These radiolabelling experiments were carried out in order to confirm a general method established below (*Scheme 5.5*) for the incorporation of radioactive gallium into the silica shell of iron oxide nanoparticles. Taking into account the half-life of the ^{68}Ga radionuclide (67.7 min), the labelling incorporation was estimated for all the samples using either radio-TLC or measuring the final activity of the nanocomposite, and it is denoted here as “encapsulation factor“. The reaction times and the buffer solution used were adjusted accordingly to the properties of this radioisotope.[50]

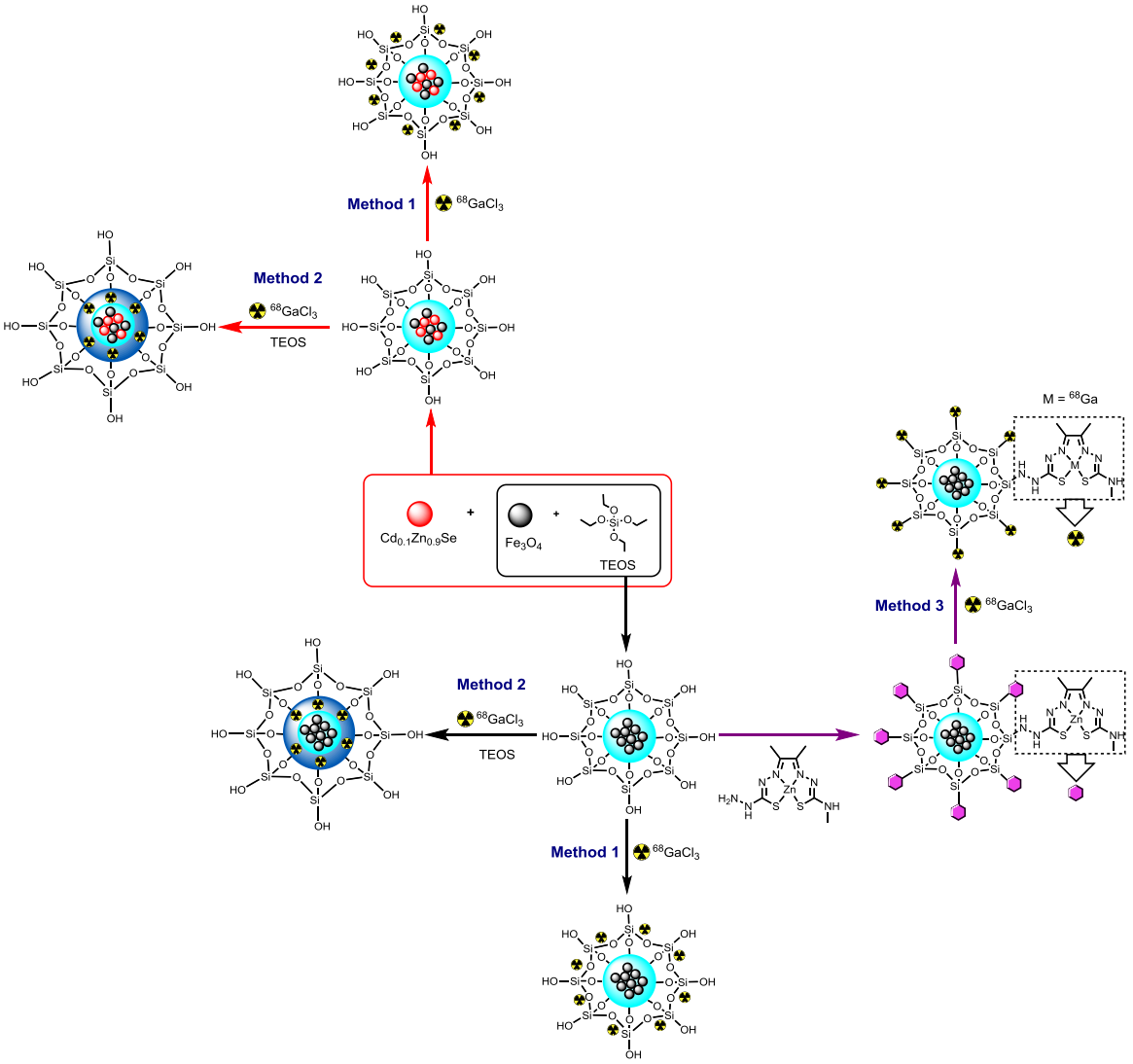

Scheme 5.5. Methods developed for the incorporation of ^{68}Ga into the nanoparticles-based systems previously described.

(a) Method 1: adsorption of ^{68}Ga within the silica matrix in $Fe_3O_4@SiO_2$ and $Fe_3O_4/Cd_{0.1}Zn_{0.9}Se@SiO_2$

Method 1 concerns the (non-covalent) adsorption of the radioisotope ^{68}Ga onto the surface of the silica network of $Fe_3O_4@SiO_2$ and $Fe_3O_4/Cd_{0.1}Zn_{0.9}Se@SiO_2$, following a chelator-free radiolabelling strategy. The general procedure used was the same for the two species: ^{68}Ga from a stock solution was added to a vial with ethanol, followed by the corresponding nanoparticles species and a sodium acetate buffer solution in order to adjust the pH to approximately 5, the optimum for this radioisotope. The reaction was carried out for 40 minutes at 90 ºC, using a vortex stirrer to mix the contents every few minutes. The radiolabelled nanocomposites were isolated by centrifugation and washed with methanol and water. In order to establish the labelling incorporation factor, radio-TLC was performed and compared to the

radio-TLC of the free ^{68}Ga ions (*Figure 5.31*). For both the Fe_3O_4@SiO_2 and Fe_3O_4/$Cd_{0.1}Zn_{0.9}Se$@SiO_2 nanoparticles, this factor was found to be ≥ 99.9%. This can be explained by the absence of a peak for the free ^{68}Ga ions in the radio-TLC chromatogram, which would appear around 63 mm in the *x* axis, and the presence of a sharp peak for the radiolabelled nanocomposite near 10 mm (*Figure 5.32*).

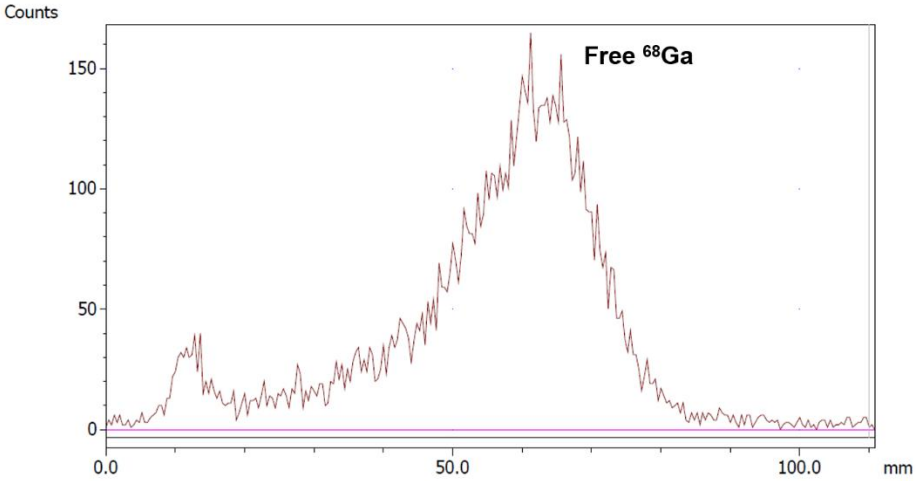

Figure 5.31. Radio-TLC chromatogram of aqueous ^{68}Ga ions used as starting material. TLC was eluted using 0.25 M ethylenediaminetetraacetic acid (EDTA) as the mobile phase.

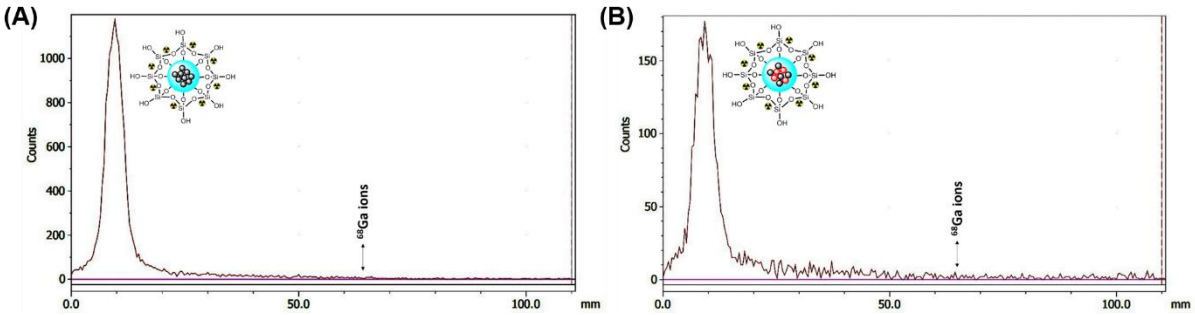

Figure 5.32. Radio-TLC chromatogram of **(A)** Fe_3O_4@SiO_2, and **(B)** Fe_3O_4/$Cd_{0.1}Zn_{0.9}Se$@SiO_2 with ^{68}Ga suggesting a RCY ≥ 99.9%. TLC was eluted using 0.25 M ethylenediaminetetraacetic acid (EDTA) as the mobile phase.

(b) Method 2: encapsulation of ^{68}Ga ions within a second silica shell in Fe_3O_4@SiO_2 and Fe_3O_4/$Cd_{0.1}Zn_{0.9}Se$@SiO_2

Method 2 involved the addition of a second silica shell in the Fe_3O_4@SiO_2 and Fe_3O_4/$Cd_{0.1}Zn_{0.9}Se$@SiO_2 nanoparticles used to encapsulate the ^{68}Ga radioisotope. The general procedure used was the same for the two species: IGEPAL CA-520 (the surfactant) was dispersed in cyclohexane in a vial, followed by the corresponding nanoparticles species, and the mixture was agitated with the help of a vortex stirrer. Next, an ammonium hydroxide

solution was added to form a reverse microemulsion, followed by tetraethylorthosilicate, the silica precursor which forms the second silica shell. Finally, ^{68}Ga was added from a stock solution together with a sodium acetate buffer and the reaction was carried out for 68 minutes at 90 ºC, to produce the formation of a silica shell that would encapsulate the radioisotope. The radiolabelled nanocomposites were isolated by centrifugation and washed with methanol and water, then separated by magnetic decantation. To estimate the radiolabelling factor in the final product of these reactions, radio-TLC was not available in the facilities, so the calculation was carried out manually by isolating each nanocomposite and measuring the final activity. The radio-incorporation factor (also denoted "encapsulation factor") was then calculated considering the initial and final activities of ^{68}Ga in each case, and it was found to be 70% and 66% for Fe_3O_4@SiO_2 and Fe_3O_4/$Cd_{0.1}Zn_{0.9}Se$@SiO_2 nanoparticles, respectively.

These lower radio-incorporation factors may be explained by the short time of the reaction. The coating reaction of the free nanoparticles takes place in 16 hours, so it would be expected that the formation of a second silica shell would need a similar amount of time to take place. However, due to the short half-life of the radioisotope ^{68}Ga, the maximum time that can be used to carry out this reaction is 68 minutes. Due to this limitation, it is possible that the second silica shell was not successfully formed around the Fe_3O_4@SiO_2 and Fe_3O_4/$Cd_{0.1}Zn_{0.9}Se$@SiO_2 nanoparticles to encapsulate the radioisotope, as desired. For this reason, free amounts of silica can be interacting with different amounts of ^{68}Ga and this might reduce the radio-incorporation factor once the final nanocomposite was separated by centrifugation and decantation. Both the reaction with the Fe_3O_4@SiO_2 and Fe_3O_4/$Cd_{0.1}Zn_{0.9}Se$@SiO_2 nanoparticles have a similar radiolabelling factor, as would be expected due to their similar sizes of approximately 50 nm, even though the core is constituted by iron oxide in one case and iron oxide and quantum dots in the other case.

(c) Method 3: reaction between ^{68}Ga and Fe_3O_4@SiO_2@Zn(ATSM/A)

Method 3 concerns the reaction between the radioisotope ^{68}Ga and the Fe_3O_4@SiO_2@Zn(ATSM/A) nanoparticles, which contain the metal-ligand complex Zn(ATSM/A) bond onto the silica surface. In this case, the Fe_3O_4@SiO_2@Zn(ATSM/A) nanoparticles dispersed in dimethylsulfoxide were added to a vial along with a solution containing ^{68}Ga, ethanol and a sodium acetate buffer to adjust the pH to 5. The mixture was heated at 90 ºC for 40 minutes and, after this time, the nanocomposite was collected by centrifugation and washed with water and methanol. The labelling incorporation factor was determined by radio-TLC (*Figure 5.33*), and it was found to be ≥ 99.9% as for Method **1**.

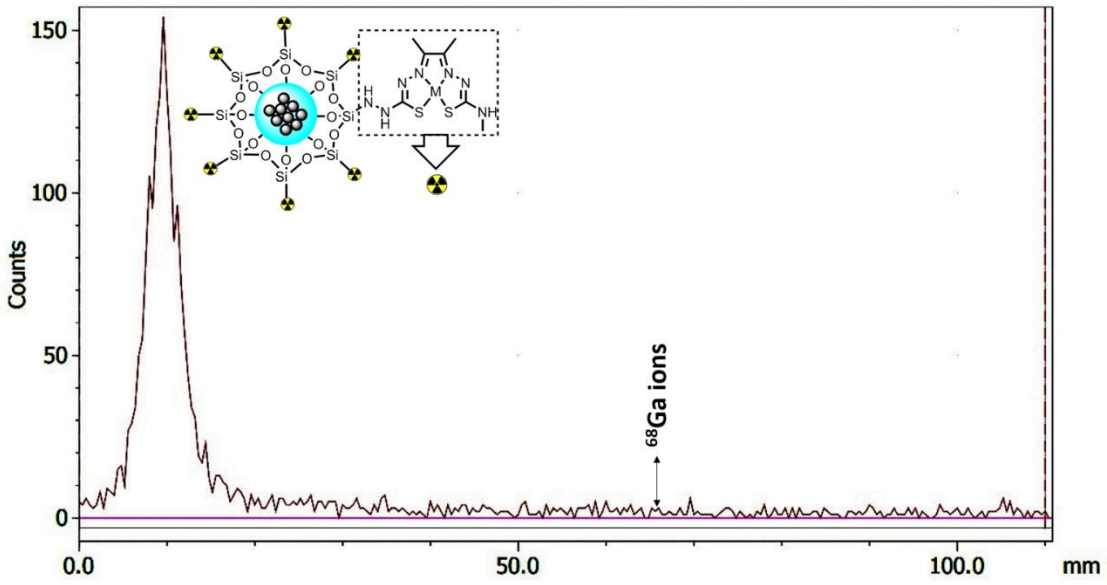

Figure 5.33. Radio-TLC chromatogram of Fe_3O_4@SiO_2@Zn(ATSM/A) with ^{68}Ga suggesting a RCY ≥ 99.9%. TLC was eluted using 0.25 M ethylenediaminetetraacetic acid (EDTA) as the mobile phase.

The mechanism of this reaction is not well understood. It has been reported that the complex Zn(ATSM/A) cannot be radiolabelled with ^{68}Ga via a transmetallation reaction when it is free in solution.[42] In order to confirm this, a reaction between Zn(ATSM/A) and ^{68}Ga was carried out, mixing these two products under the same conditions as described for the nanocomposite containing Zn(ATSM/A) (Method **3**). The final product was analysed by radio-HPLC (*Figure 5.34*). In the chromatogram, the only peak that can be seen is at approximately 2 minutes, corresponding to the free ^{68}Ga ions, and thus confirming that Zn(ATSM/A) does not contain any amount of this radioisotope and it was not radiolabelled.

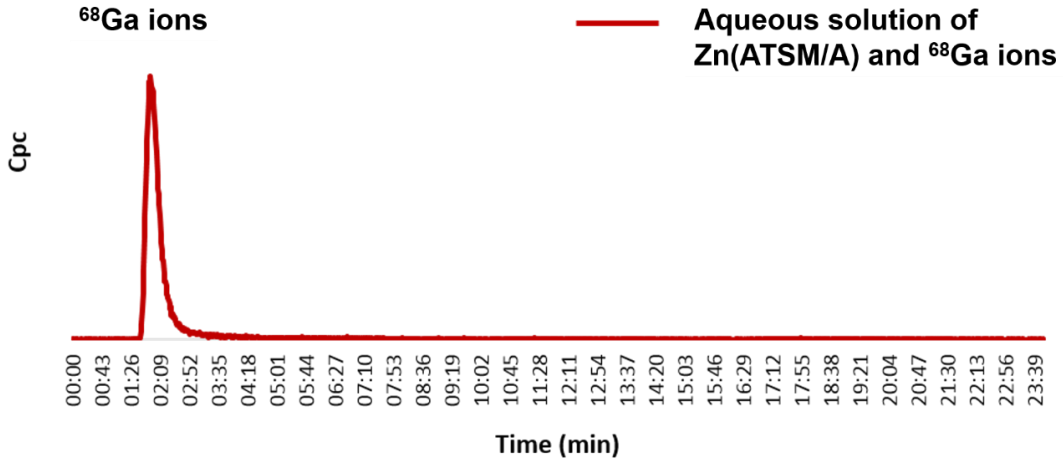

Figure 5.34. Radio-HPLC chromatogram of the aqueous solution obtained from the reaction between [^{68}Ga]$GaCl_3$ and Zn(ATSM/A). From this trace no radiolabelled product could be identified except from the free hydrated ^{68}Ga ions present at Rt = 2 minutes.

It could be thought that the transmetallation reaction takes place thanks to the $Fe_3O_4@SiO_2$ support to which the Zn(ATSM/A) complex is linked. But seeing as the reactions involving the adsorption of the radioisotope within the silica matrix of $Fe_3O_4@SiO_2$ and $Fe_3O_4/Cd_{0.1}Zn_{0.9}Se@SiO_2$ also yield a labelling incorporation of ≥ 99.9%, it cannot be concluded whether Zn(ATSM/A) plays a role in this reaction, and more studies are needed in order to confirm this. However, as it has been already mentioned, this molecule is fluorescent and is also a potential hypoxia tracer when transmetallated with copper(II), properties that add advantages to the incorporation of this compound into the nanoparticles systems.

(d) Summary of methods and results obtained in this section

The methods used were designed with a general approach in mind, and they could be easily adapted to other radioisotopes taking into consideration the half-life and optimum pH of the nucleus used. So, if a radioisotope with a longer half-life was used, *e.g.*, ^{64}Cu ($t_{1/2}$ = 12.7 hours), a similar radio-incorporation factor would be expected for Method **1**, while if carrying out Method **2**, this factor would be expected to be higher due to the longer half-life of the nucleus and the possibility of leaving the different components to react for a longer time. It is unclear if the radio-incorporation factor obtained in Method **3** would be affected as this would depend on whether it is the ATSM/A complex that is radiolabelled or whether adsorption onto the silica surface of the nanoparticles takes place. For other radioisotopes, considerations of changes in size and chemical properties would need to be taken into account in order to optimise the methods described in this section.[50]

Regarding the results obtained from each method, Methods **1** and **3** gave a radio-incorporation factor ≥ 99.9%, while in Method **2** it was reduced to 66-70% (*Table 5.7*).

Table 5.7. Summary of methods and nanoparticles systems used and their corresponding radio-incorporation factors (also denoted "encapsulation factors").

Method	Nanoparticles	Radio-incorporation factor / %
1	$Fe_3O_4@SiO_2$	≥ 99.9
	$Fe_3O_4/Cd_{0.1}Zn_{0.9}Se@SiO_2$	≥ 99.9
2	$Fe_3O_4@SiO_2$	70
	$Fe_3O_4/Cd_{0.1}Zn_{0.9}Se@SiO_2$	66
3	$Fe_3O_4@SiO_2$@Zn(ATSM/A)	≥ 99.9
	Zn(ATSM/A)	0

5.10. Epi-fluorescence and confocal fluorescence tests of the nanocomposites on a thin film

Single-photon laser scanning confocal microscopy imaging was carried out on thin films drying out on a glass bottom dish of $Cd_{0.1}Zn_{0.9}Se$, $Fe_3O_4/Cd_{0.1}Zn_{0.9}Se@SiO_2$ and $Fe_3O_4@SiO_2@Zn(ATSM/A)$ obtained from dispersions in methanol. The fluorescence response of the QDs and nanocomposite materials was tested using 405, 488 and 561 nm lasers and the images for the individual channel emissions and the emission overlay of the blue-green-red and DIC channels were recorded.

In the case of $Cd_{0.1}Zn_{0.9}Se$ quantum dots (*Figure 5.35*), it can be seen that the emission lies mainly in the red channel at all the excitation wavelengths, with some emission observed in the green channel as well after 405 and 488 nm laser excitation.

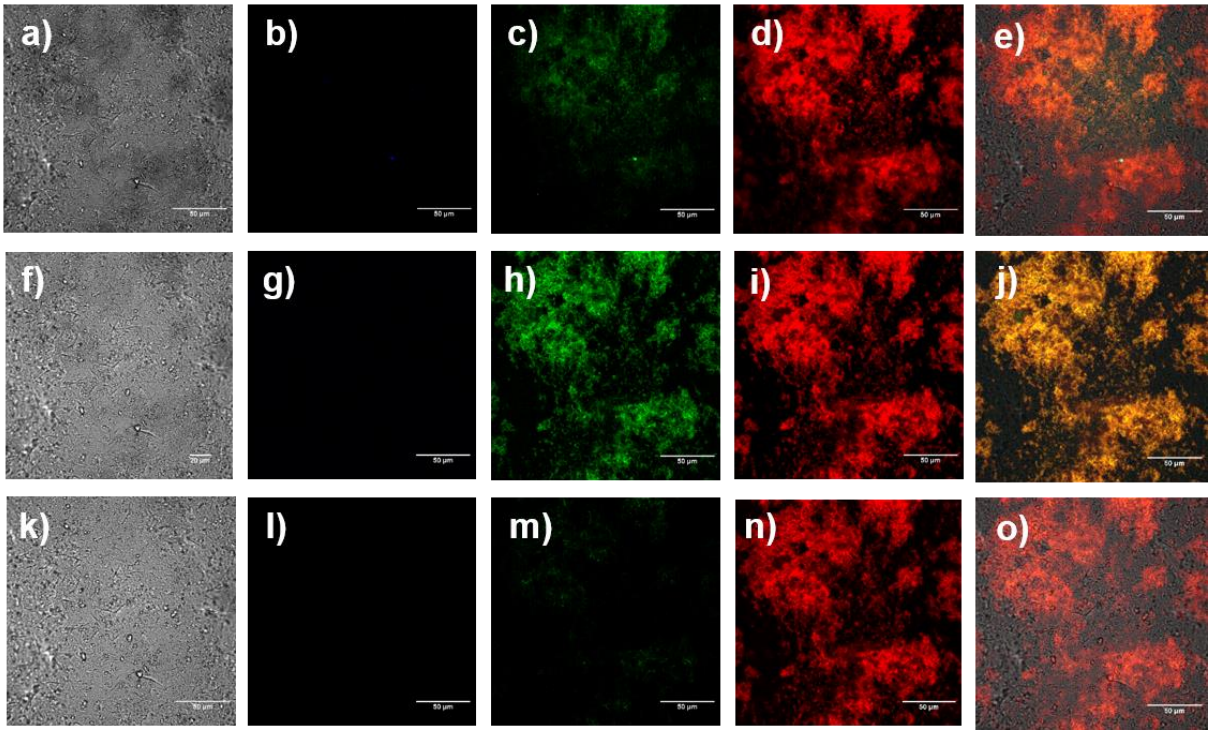

Figure 5.35. Single-photon laser scanning confocal microscopy of a $Cd_{0.1}Zn_{0.9}Se$ thin film of a methanol suspension. a-e) λ_{ex} = 405 nm; f-j) λ_{ex} = 488 nm; k-o) λ_{ex} = 561 nm. a, f, k) DIC channel; b, g, l) blue channel (λ_{em} = 417-477 nm); c, h, m) green channel (λ_{em} = 500-550 nm); d, i, n) red channel (λ_{em} = 570-750 nm); e, j, o) overlay of all the channels. Scale bar: 50 µm.

For the $Fe_3O_4/Cd_{0.1}Zn_{0.9}Se@SiO_2$ nanoparticles, the emission properties are the same as for the free $Cd_{0.1}Zn_{0.9}Se$ quantum dots (*Figure 5.36*).

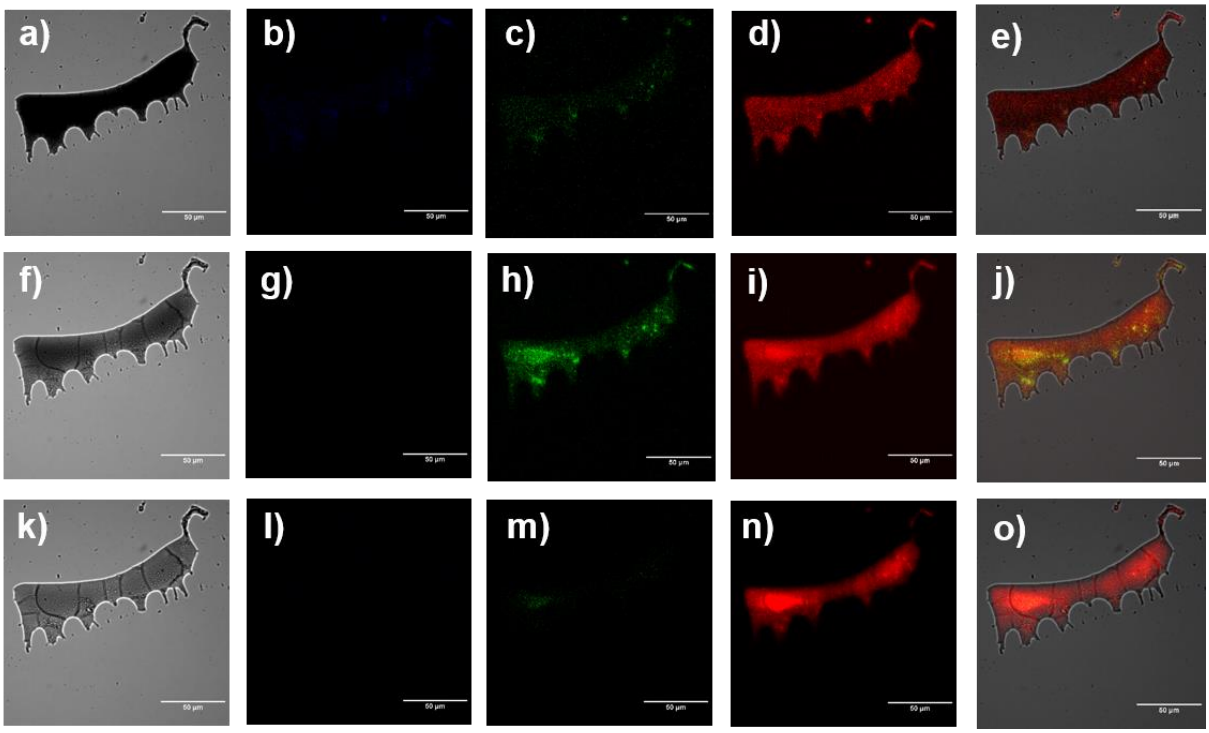

Figure 5.36. Single-photon laser scanning confocal microscopy of a $Fe_3O_4/Cd_{0.1}Zn_{0.9}Se@SiO_2$ thin film of a methanol suspension. a-e) λ_{ex} = 405 nm; f-j) λ_{ex} = 488 nm; k-o) λ_{ex} = 561 nm. a, f, k) DIC channel; b, g, l) blue channel (λ_{em} = 417-477 nm); c, h, m) green channel (λ_{em} = 500-550 nm); d, i, n) red channel (λ_{em} = 570-750 nm); e, j, o) overlay of all the channels. Scale bar: 50 µm.

$Fe_3O_4@SiO_2@Zn$(ATSM/A) nanoparticles emit in all the channels (blue, green and red) after excitation with a laser of 405 nm wavelength (*Figure 5.37*). When they are excited with lasers of 488 and 561 nm, the emission at the blue channel disappears, but they still show fluorescent properties in the green and red channels of the spectra. It can be noticed in the image that shows the overlay of all the channels that emission at 405 nm excitation wavelength does not colocalise (*Figure 5.37(e)*). This is probably due to the non-homogeneous distribution of the material in the thin film, caused by the drying method of the suspension used.

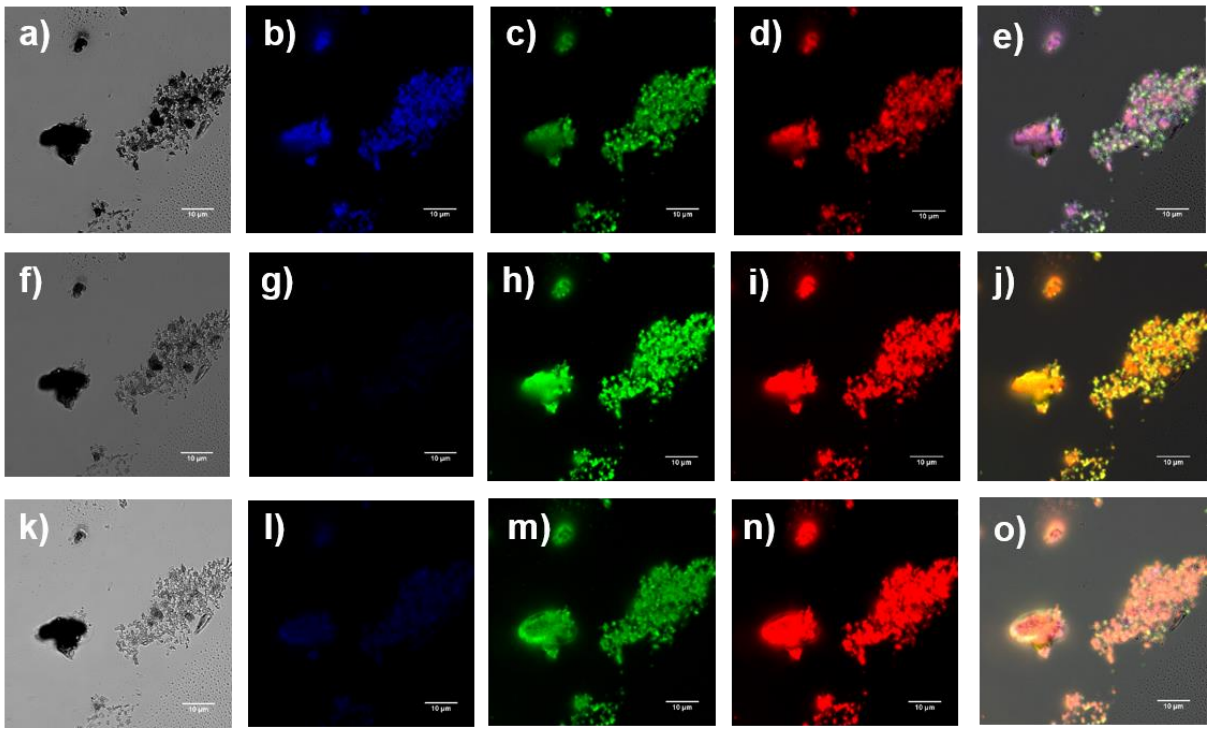

Figure 5.37. Single-photon laser scanning confocal microscopy of a Fe_3O_4@SiO_2@Zn(ATSM/A) thin film of a methanol suspension. a-e) λ_{ex} = 405 nm; f-j) λ_{ex} = 488 nm; k-o) λ_{ex} = 561 nm. a, f, k) DIC channel; b, g, l) blue channel (λ_{em} = 417-477 nm); c, h, m) green channel (λ_{em} = 500-550 nm); d, i, n) red channel (λ_{em} = 570-750 nm); e, j, o) overlay of the all the channels. Scale bar: 10 µm.

5.11. *In vitro* epi-fluorescence and confocal fluorescence investigations of the nanocomposites

In order to establish the potential of the nanocomposites as cancer imaging agents, PC-3 cells were incubated with a DMSO : serum-free medium (1:99) suspension of 10 µg/mL $Fe_3O_4/Cd_{0.1}Zn_{0.9}Se@SiO_2$ to carry out epi-fluorescence microscopy experiments (*Figure 5.38(a-e)*). Prostate cancer (PC-3) cells were grown according to standard serial passage protocols, placed onto glass bottom dishes and allowed to grow to a suitable confluence. $Fe_3O_4/Cd_{0.1}Zn_{0.9}Se@SiO_2$ nanoparticles were taken up by PC-3 cells, with the main emission lying within the blue and green channels and some minor emission in the red channel.

Further images were taken in order to gather more information regarding cellular internalisation and distribution of the compounds. PC-3 cells were incubated for 15 minutes with $Fe_3O_4/Cd_{0.1}Zn_{0.9}Se@SiO_2$ nanoparticles and imaged using single-photon laser scanning confocal microscopy (*Figure 5.38(f-t)*). These images show that there is broad emission across all the visible wavelengths when the probe is excited at 405 nm, while only green-red and red emissions are visible using 488 and 561 nm lasers, respectively. This is consistent with the fluorescence studies carried out, whereby the $Fe_3O_4/Cd_{0.1}Zn_{0.9}Se@SiO_2$ nanocomposite demonstrated emissive characteristics within the blue and red wavelength range of the visible spectrum. The confocal microscopy images show that $Fe_3O_4/Cd_{0.1}Zn_{0.9}Se@SiO_2$ localise throughout the cell cytoplasm and no emission comes from the nuclear region of the cells. Therefore, while the $Fe_3O_4/Cd_{0.1}Zn_{0.9}Se@SiO_2$ nanoparticles are effectively internalised within the cell, they do not penetrate the nuclear membrane. Furthermore, these nanocomposites do not seem to damage the morphology of the prostate cancer cells during the time of incubation and imaging studies.

Encapsulating the $Cd_{0.1}Zn_{0.9}Se$ nanocrystals in a thin silica matrix along with magnetic nanoparticles was performed to achieve a water-dispersible system, which retains the optical features of the free QDs as well as the magnetic properties of the iron oxide core. The fact that these nanoparticles are fully dispersible and kinetically stable in aqueous media, present fluorescent features, but they do not seem to penetrate the cellular membrane in short periods of time, constitutes a highly encouraging result for their use as synthetic scaffolds for bioimaging applications *in vitro* and makes these inorganic nanoparticles a unique and versatile device for such applications.

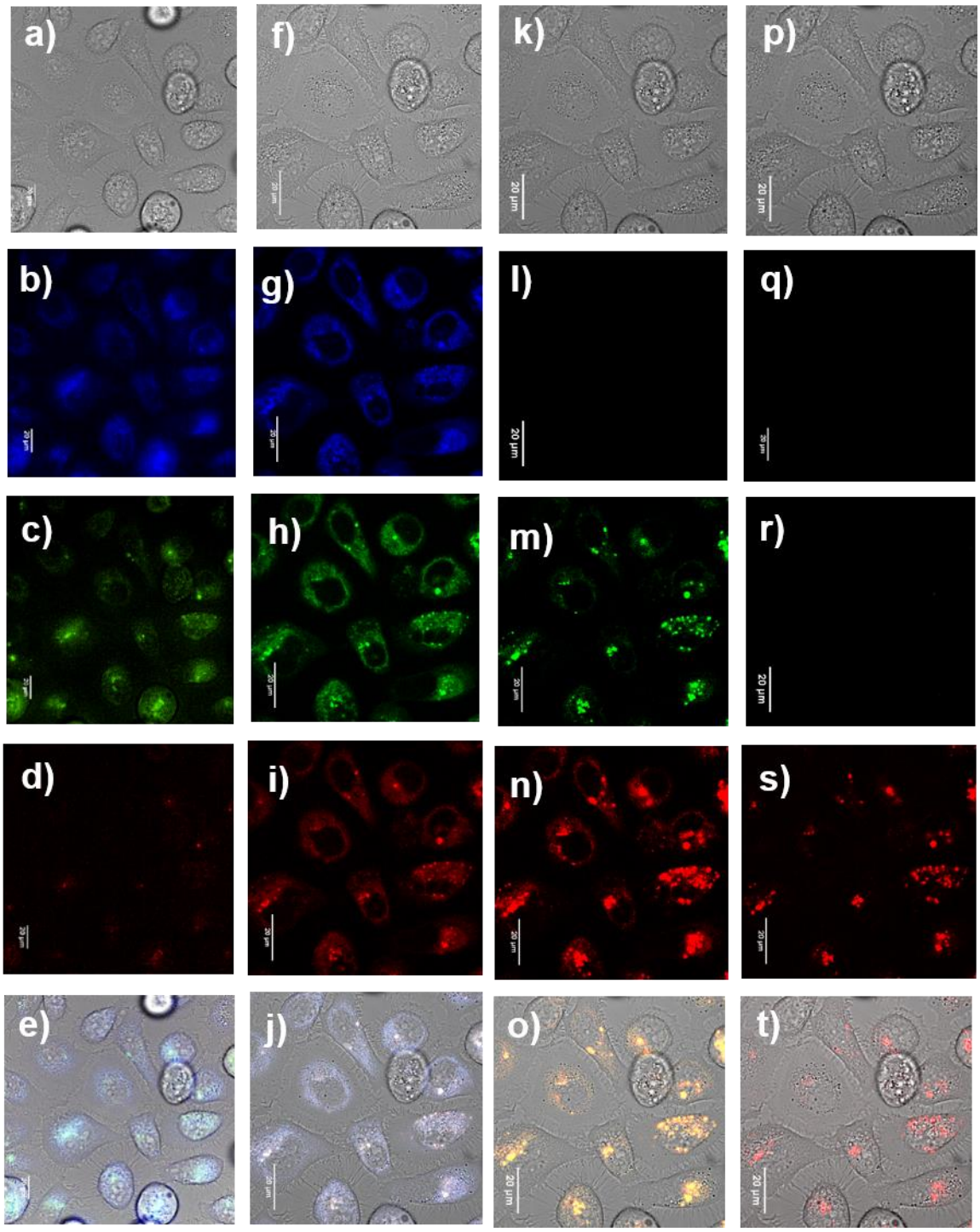

Figure 5.38. a-e) Epi-fluorescence and f-t) single-photon laser scanning confocal microscopy of PC-3 cells incubated for 15 minutes at 37 °C with $Fe_3O_4/Cd_{0.1}Zn_{0.9}Se@SiO_2$ NPs. Final concentration: 10 µg/mL in 1 : 99 DMSO : serum-free medium. . f-j) λ_{ex} = 405 nm; k-o) λ_{ex} = 488 nm; p-t) λ_{ex} = 561 nm. a, f, k, p) DIC channel; b, g, l, q) blue channel (λ_{em} = 417-477 nm); c, h, m, r) green channel (λ_{em} = 500-550 nm); d, i, n, s) red channel (λ_{em} = 570-750 nm); e, j, o, t) overlay of all the channels. Scale bar: 20 µm.

Epi-fluorescence microscopy (*Figure 5.39(a-e)*) and single-photon laser scanning confocal microscopy (*Figure 5.39(f-t)*) images of PC-3 cells incubated with a DMSO : serum-free medium (1:99) suspension of 10 µg/mL Fe_3O_4@SiO_2@Zn(ATSM/A) nanoparticles were gathered following the same protocol as for the nanoparticles and quantum dots. A homogeneous distribution of the particles is seen in the blue, green and red channels after 405 nm laser excitation, while it is visible only in the green and red channels and only in the red, respectively, after 488 and 561 nm laser excitation. Aggregates of the fluorescent probes are particularly visible in the green and red channels using lasers of 488 and 561 nm excitation. As for the previous fluorescent probe, Fe_3O_4@SiO_2@Zn(ATSM/A) nanoparticles are taken up by these types of cells, and they localise mainly in the cytoplasm without entering the nucleus and again they do not damage the cell morphology. This nanocomposite also presents fluorescent properties that make it a promising probe for bioimaging applications.

PC-3 cells were also incubated with the citric acid-coated Fe_3O_4 nanoparticles containing a BODIPY derivative covalently linked on their surface, and single-photon laser scanning confocal microscopy images were collected (*Figure 5.40*). The fluorophore emits light slightly in the blue channel, and more strongly in the green and red channels when excited with lasers of 405, 488 and 561 nm wavelengths, respectively. This type of nanoparticles are taken up by the PC-3 cells, and they localise mainly in the cytoplasm without entering the nucleus and do not alter the cell morphology.

Three dimensional confocal microscopy images can be used to show the distribution of a fluorophore within the cells. It can be observed in the case of the citric acid-coated Fe_3O_4 nanoparticles containing a BODIPY derivative that the NPs are evenly distributed throughout the cytoplasm. The maximum fluorescence intensity comes from inside the cytoplasm, with some degree of aggregation (*Figure 5.41*).[51]

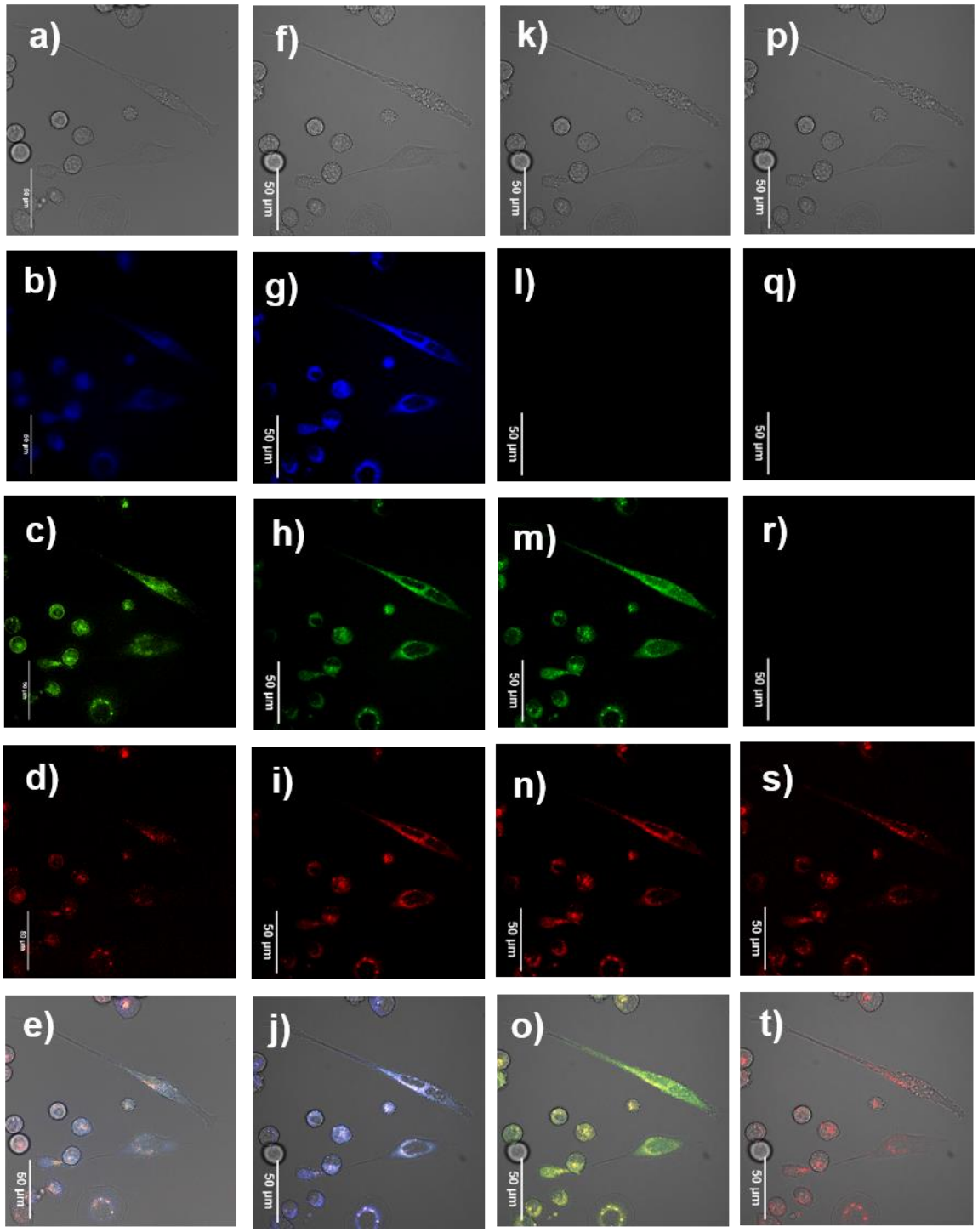

Figure 5.39. a-e) Epi-fluorescence and f-t) single-photon laser scanning confocal microscopy of PC-3 cells incubated for 15 minutes at 37 °C with Fe_3O_4@SiO_2@Zn(ATSM/A) NPs. Final concentration: 10 µg/mL in 1 : 99 DMSO : serum-free medium. . f-j) λ_{ex} = 405 nm; k-o) λ_{ex} = 488 nm; p-t) λ_{ex} = 561 nm. a, f, k, p) DIC channel; b, g, l, q) blue channel (λ_{em} = 417-477 nm); c, h, m, r) green channel (λ_{em} = 500-550 nm); d, i, n, s) red channel (λ_{em} = 570-750 nm); e, j, o, t) overlay of all the channels. Scale bar: 50 µm.

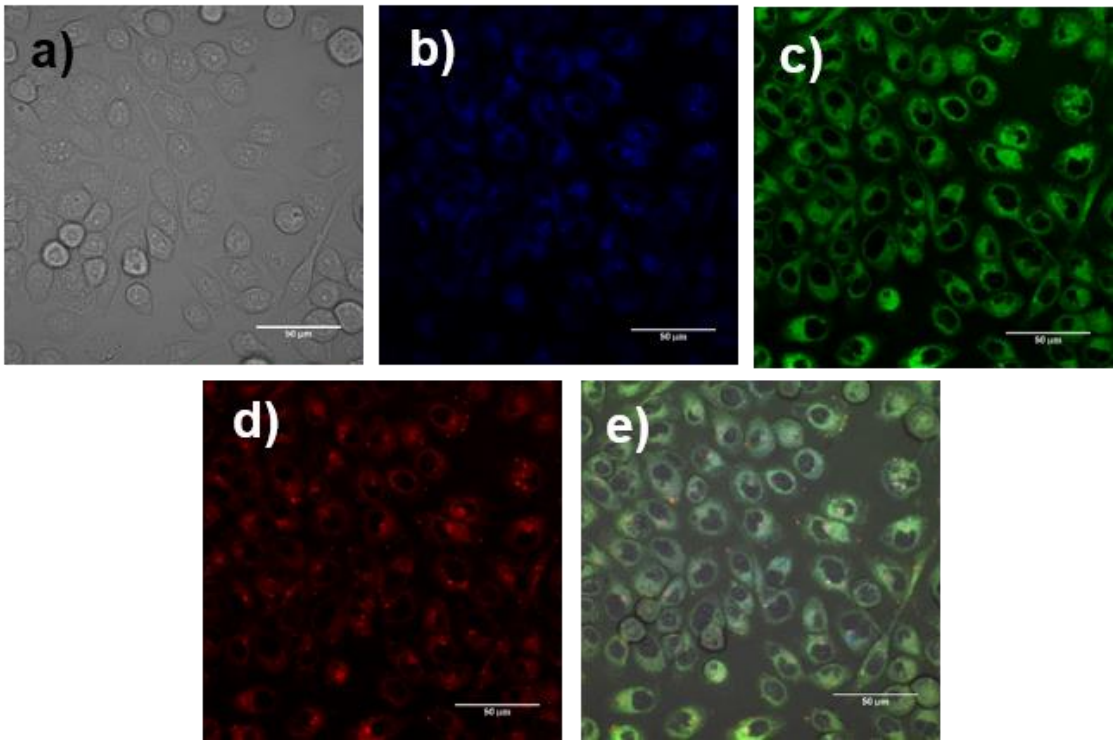

Figure 5.40 a-e) Single-photon laser scanning confocal microscopy of PC-3 cells incubated for 15 minutes at 37 ºC with citric acid-coated Fe_3O_4 NPs containing a BODIPY derivative covalently linked on their surface. Final concentration: 10 µg/mL in 1 : 99 DMSO : serum-free medium. a) DIC channel; b) blue channel (λ_{em} = 417-477 nm), λ_{ex} = 405 nm; c) green channel (λ_{em} = 500-550 nm), λ_{ex} = 488 nm; d) red channel (λ_{em} = 570-750 nm), λ_{ex} = 561 nm; e) overlay of all the channels. Scale bar: 50 µm.

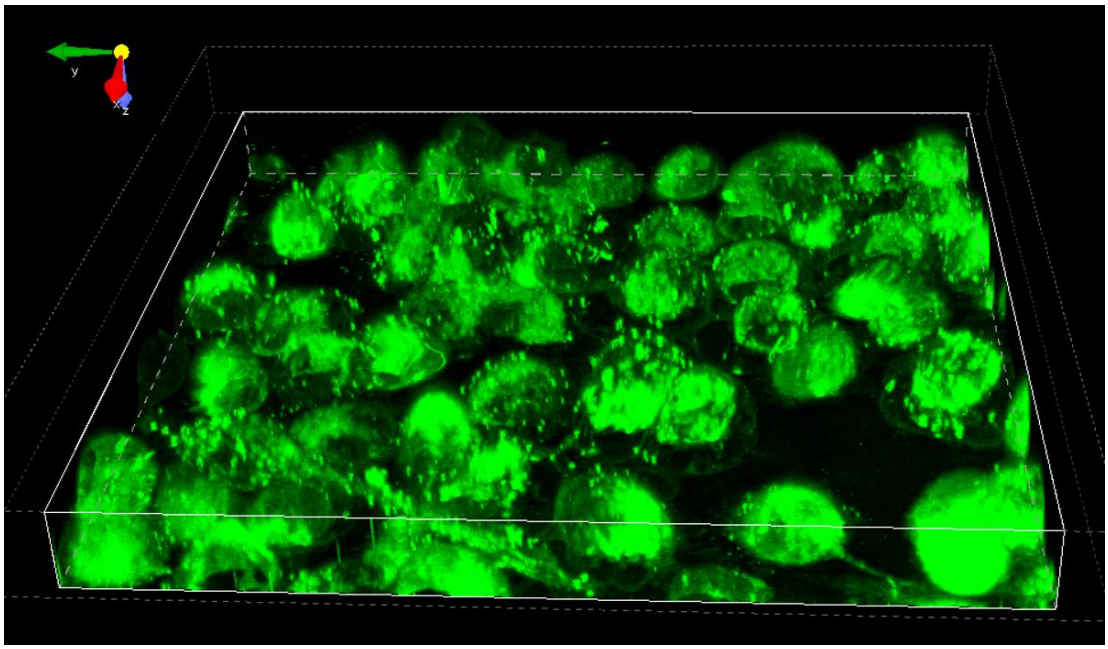

Figure 5.41. 3D representation of the confocal microscopy images of citric acid-coated Fe_3O_4 NPs containing a BODIPY derivative in fixed PC-3 cells incubated for 15 minutes at 37 ºC. The image shows the green channel, λ_{ex} = 488 nm (λ_{em} = 500-550 nm).

5.12. Two-photon fluorescence lifetime imaging microscopy

Fluorescence lifetime imaging microscopy (FLIM) methods were applied to investigate the lifetime of the synthesised nanocomposites containing fluorophores, which would give an indication of their kinetic stability in cells. Experiments started with testing the lifetime of the compounds in solution using DMSO as a solvent. Time-correlated single-photon counting (TCSPC) was used to measure lifetime decays, followed by an *in vitro* FLIM investigation. These experiments were carried out at the Rutherford Appleton Laboratory (RAL) in the Central Laser Facilities (CLF) with the assistance of Prof. Stanley W. Botchway and Dr. Vincenzo Mirabello. Fluorescence lifetime investigations were carried out and reported following a previously described protocol.[51, 52]

The fluorescence lifetimes of the free Zn(ATSM/A) tag, the as-synthesised $Cd_{0.1}Zn_{0.9}Se$ QDs, and the Fe_3O_4@SiO_2@Zn(ATSM/A) nanoparticles were investigated in solution by TCSPC using two-photon excitation techniques (*Table 5.8*).[53] Each photon detected and collected in TCSPC was plotted to calculate the fluorescence lifetime. The results obtained from TCSPC (*Figure 5.42*) consist of three components (χ^2, τ_n (ps), and τ_n (%)). τ_n represents the duration within which the corresponding nanocomposite exists in an excited state, and τ_m is the overall lifetime, which is the average between all the different individual lifetime components. For all the compounds tested except for the $Cd_{0.1}Zn_{0.9}Se$ quantum dots the number of counts for the lifetime is quite low, meaning that there is not much of each compound being detected in the solution. Therefore, only the data collected for the $Cd_{0.1}Zn_{0.9}Se$ QDs can be considered reliable and is reported here.

Table 5.8. Two-photon TCSPC data for $Cd_{0.1}Zn_{0.9}Se$ QDs, using a 1 mg/mL suspension in DMSO. The compound was excited at λ_{ex} = 810 nm, with a laser power of 12.4 mW.

Compound	χ^2	τ_1 (ps)	τ_1 (%)	τ_2 (ps)	τ_2 (%)	τ_m
$Cd_{0.1}Zn_{0.9}Se$	1.00	1243	54.1	6884	45.9	3831

The tested $Cd_{0.1}Zn_{0.9}Se$ quantum dots are shown to contain two lifetime components, with τ_1 being the main one but existing in an almost 1:1 ratio. This means that for this species there is more than one component that is fluorescent and the fluorescence lifetimes are individually different. The τ_2 can be due to several reasons, such as the existence of isomers, conformational changes in the solvent, or pH-dependent protonated and non-protonated forms of a molecule.[51]

As explained in *Chapter 2* (*Section 2.12*), if the value found for χ^2 falls within the 1.0 – 1.3 range, the data can be considered reliable.[54] According to this, the results shown for the tested nanocomposites are reliable.

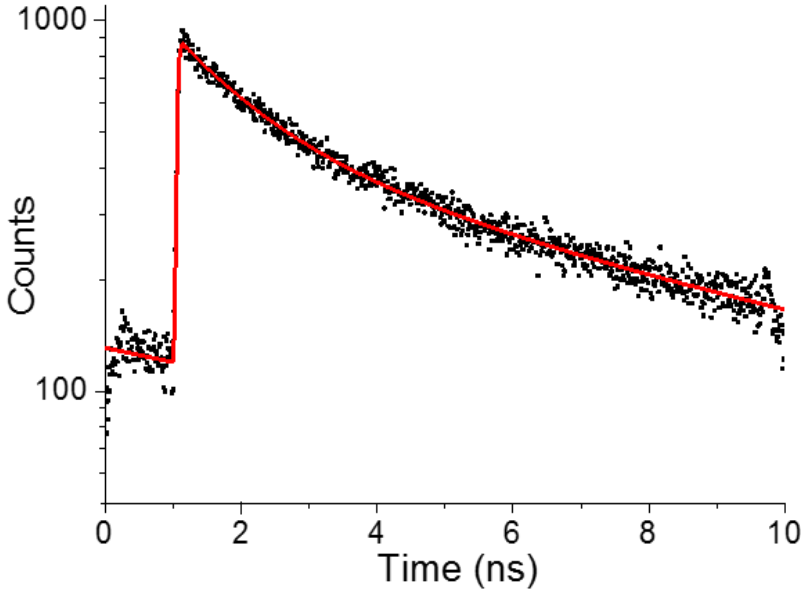

Figure 5.42. TCSPC decay and fitting curve for $Cd_{0.1}Zn_{0.9}Se$ QDs tested using a 1 mg/mL dispersion in DMSO excited at 810 nm with a laser power of 12.4 mW. Black dots are the measured counts at different times and the red line is the fitting curve.

The two-photon FLIM mapping and intensities in PC-3 cells were measured for Zn(ATSM/A) and the Fe_3O_4@SiO_2@Zn(ATSM/A) nanocomposite. It was observed that these compounds enter the cells and they seem to accumulate on the cell membrane. Fluorescence lifetime distribution curves are the overall fluorescence summarised from the fluorescence lifetime mapping in PC-3 cells (*Figure 5.43*). From the plot, it can be observed that the fluorescence lifetime distribution of Zn(ATSM/A) is between 1 and 1500 ps, and that of Fe_3O_4@SiO_2@Zn(ATSM/A) is between 1 and 2000 ps when they are both incubated in PC-3 cells. The distribution of lifetime in this curve is based on the corresponding components, that is, the proportion of individual lifetime. In both cases the lifetime distribution is broad, but in the case of Zn(ATSM/A) there is only an intense peak between 1 and 500 ps and a tail with less counts that follows until 1500 ps. The τ_m in cells when measured at the maximum number of counts (around 350 counts) for Zn(ATSM/A) is around 250 ps. Regarding the Fe_3O_4@SiO_2@Zn(ATSM/A) nanoparticles, the maximum number of counts reaches only up to 35, which means that this nanocomposite is less detected in cells, and corresponds to a τ_m in cells of approximately 750 ps.

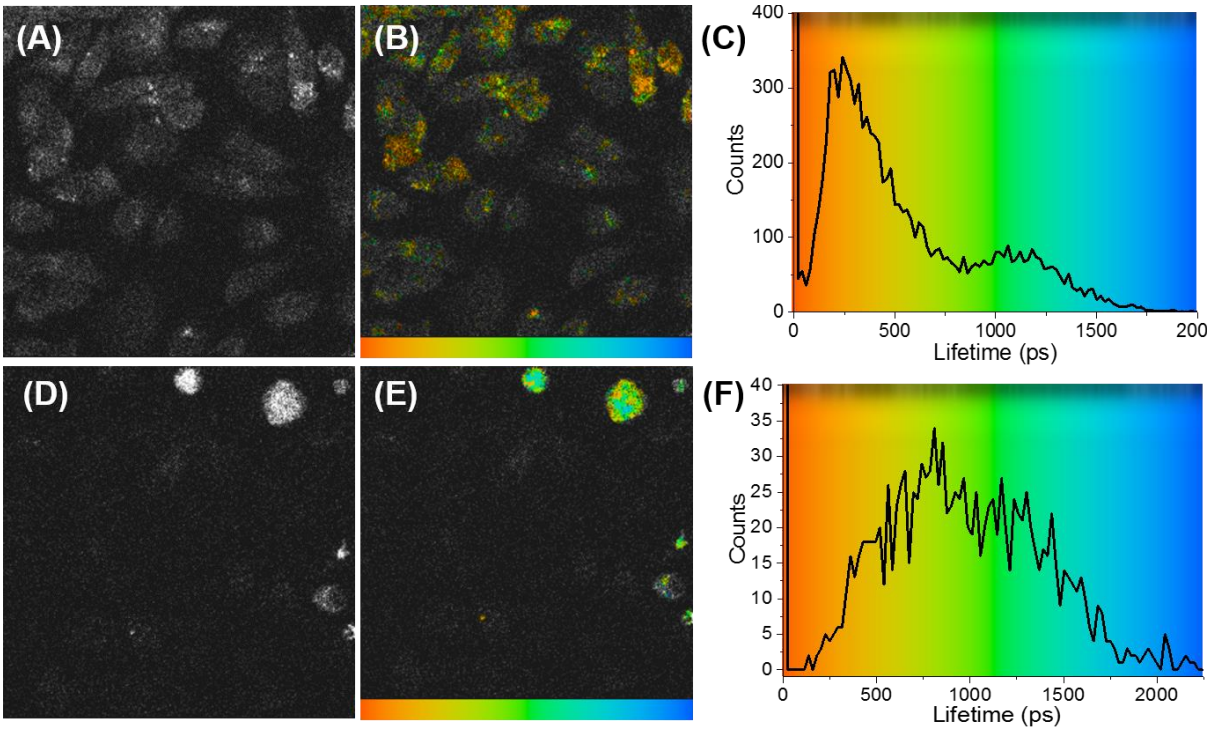

Figure 5.43. (A, D) Two-photon fluorescence intensity diagram; **(B, E)** fluorescence lifetime mapping of τ_m, and **(C, F)** fluorescence lifetime distribution curves of PC-3 cells treated with 1 mg/mL dispersions of each compound in 1% DMSO. λ_{ex} = 810 nm. Cells were incubated at 37 ºC for 15 minutes with **(A-C)** Zn(ATSM/A), and **(D-F)** Fe_3O_4@SiO_2@Zn(ATSM/A). Scale bar: 50 µm.

5.13. MTT assays with nanocomposites

MTT (3-(4,5-dimethylthiazol-2-yl)-2,5-diphenyltetrazolium bromide) assays were carried out with the assistance of Dr. Haobo Ge in order to determine the IC_{50} value for the functionalised iron oxide nanoparticles and starting materials and evaluate the toxicity of each of them in prostate cancer cells (*Figure 5.44*). The IC_{50} corresponds to the half maximal inhibitory concentration, and it is a measure that indicates how effectively a drug inhibits a specific biological process. In this case it refers to what concentration of compound is needed to kill half of the population of cells, *i.e.*, to reduce the cell viability to 50%.

In order to carry out these assays, 96 well plates containing PC-3 cells were treated with each of the nanocomposites at different concentrations for 48 hours at 37 ºC. Then, MTT was added to the cells and incubated for 2 hours. The insoluble formazan species was solubilised with DMSO. To quantify the absorbance of the solution by the cells, a spectrophotometer was used (with an absorption wavelength of 570 nm) and a dose response curve was plotted to calculate the IC_{50} of each of the products (*Table 5.9*).

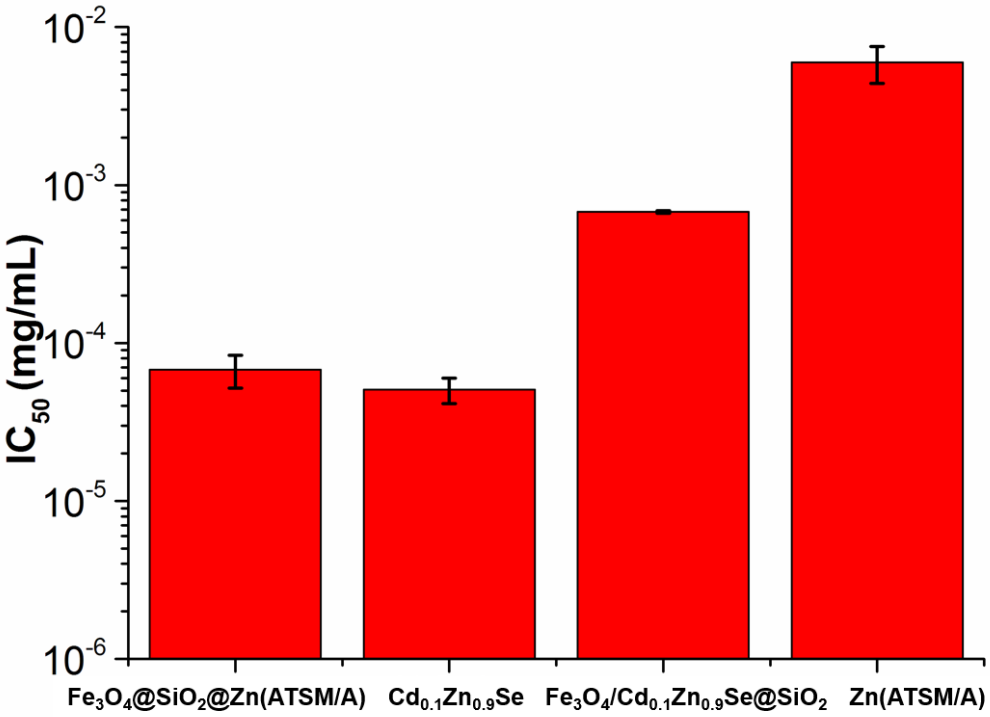

Figure 5.44. IC_{50} in PC-3 cells after 48 hours of treatment at 37 ºC with Fe_3O_4@SiO_2@Zn(ATSM/A), $Cd_{0.1}Zn_{0.9}Se$, Fe_3O_4/$Cd_{0.1}Zn_{0.9}Se$@SiO_2 nanoparticles and Zn(ATSM/A).
(The data was collected from six repeated measurements on the same day; N = 1).

Table 5.9. Summary of compounds tested in MTT assays using PC-3 cells and IC_{50} values found for each of them.

Compound	IC_{50} / mg/mL	IC_{50} / M
Fe_3O_4@SiO_2@Zn(ATSM/A)	$(6.8 \pm 1.6)\cdot10^{-5}$	-
$Cd_{0.1}Zn_{0.9}Se$	$(5.1 \pm 0.9)\cdot10^{-5}$	-
Fe_3O_4/$Cd_{0.1}Zn_{0.9}Se$@SiO_2	$(6.7 \pm 0.1)\cdot10^{-4}$	-
Zn(ATSM/A)	$(5.9 \pm 1.6)\cdot10^{-3}$	1.9 ± 0.5

Out of all the tested compounds, the one with the highest IC_{50} value and, consequently, the least toxic, is Zn(ATSM/A). This result was expected, as it is known that thiosemicarbazones are very biocompatible.[55] It is also confirmed that the encapsulation of the $Cd_{0.1}Zn_{0.9}Se$ quantum dots within a silica shell with iron oxide nanoparticles significantly decreases their toxicity. It is known that cadmium is a toxic metal, as it can be seen by the low IC_{50} value of the free quantum dots, but this study proves that thanks to the silica coating, which is a biocompatible material, the quantum dots can be safely encapsulated with no apparent leakage. It is unexpected to see such a low IC_{50} value for the Fe_3O_4@SiO_2@Zn(ATSM/A) nanoparticles, especially when compared to the one for the free Zn(ATSM/A).[56] In conclusion, MTT assays show that the biocompatibility of the system is improved when the fluorophores are encapsulated within a silica shell.

The same data collected from MTT assays performed in PC-3 cells were plotted as the normalised cell viability (%) as a function of the concentration (mg/mL) (*Figure 5.45*). Fe_3O_4 and Fe_3O_4@SiO_2 were included in this study also for comparison.

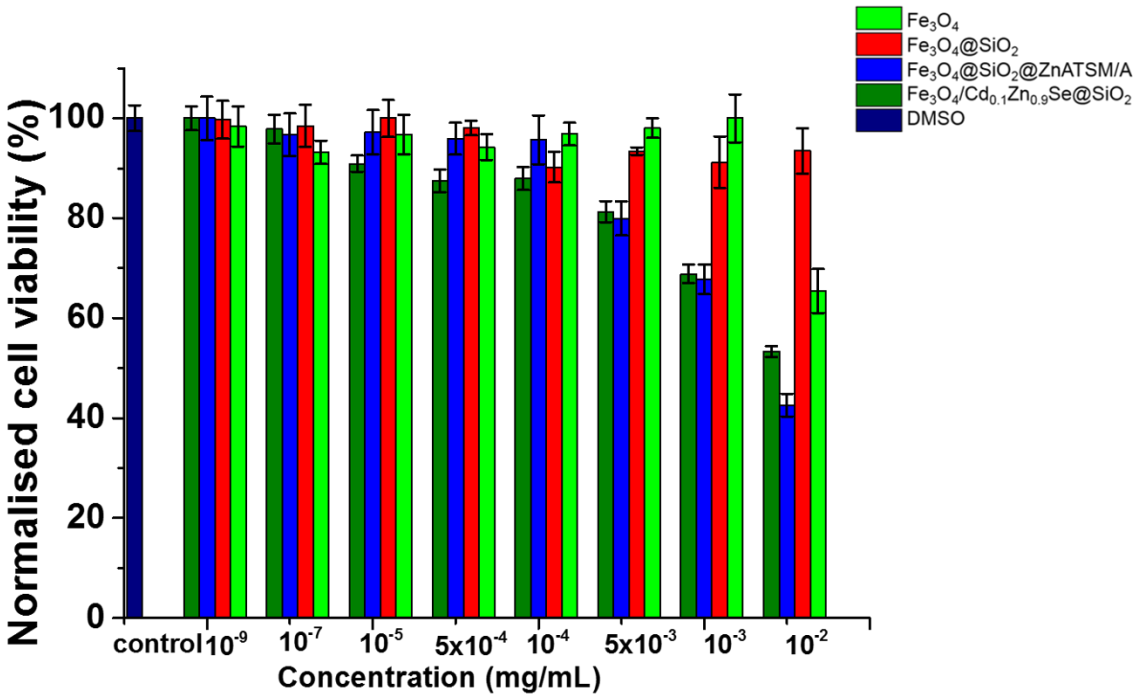

Figure 5.45. Normalised cell viability (%) of different nanocomposites depending on the concentration (mg/mL) and compared to dimethylsulfoxide (control).

At low concentrations (10^{-9} – 10^{-7} mg/mL) all the products show very low toxicity when compared to dimethylsulfoxide, which is used as a control and is given a normalised cell viability of 100%. When the concentration increases slightly to 10^{-5} – 10^{-3} mg/mL, the functionalised nanomaterials Fe_3O_4@SiO_2@Zn(ATSM/A) and $Fe_3O_4/Cd_{0.1}Zn_{0.9}Se$@$SiO_2$ prove to be more toxic than the coated and uncoated nanoparticles without any fluorophore attached. Finally, when the concentration is of the order of 10^{-2} mg/mL, the iron oxide-silica core-shell nanoparticles are the least toxic and still present a normalised cell viability of almost 100% on the timescale of the observation.

In conclusion, since imaging techniques use very low concentrations, of the order of 0.01 mg/mL, it appears that all the synthesised nanocomposites would be suitable and relatively non-toxic for this purpose.

5.14. Crystal violet assays for hypoxia testing

As described in the previous section, MTT assays were used to test the cytotoxicity of the synthesised nanoparticles in PC-3 cells. This type of assay uses mitochondrial activity to convert MTT into formazan, a purple dye.[57] Under hypoxia, mitochondrial activity is reduced, hence MTT assays are not suitable for determining the cell viability or cell survival rate under hypoxic conditions. For this reason, to test how the synthesised nanocomposites behave in cells under hypoxic conditions, another type of assay was carried out: crystal violet, which does not depend on mitochondrial activity.[58] These assays were carried out by Dr. Haobo Ge

In order to study whether some of the synthesised and functionalised nanoparticles (especially those containing Zn(ATSM/A)) have potential selectivity for hypoxic tissue *in vitro*, crystal violet assays were carried out in prostate cancer cells under normoxic and hypoxic conditions, using a crystal violet solution to stain the cells. After it was removed and the cells were left to dry, the well plates were read by a spectrophotometer reader at an absorption wavelength of 570 nm. In order to chemically induce hypoxia, a solution of cobalt (II) chloride hexahydrate in water was used in the regular cell media, which was later added to the cells and these were incubated overnight at 37 ^{o}C under an atmosphere of 5% carbon dioxide. $CoCl_2 \cdot 6H_2O$ works as a chemical inducer of the hypoxia-inducible factor-1 (HIF-1), which is the major transcription factor that is specifically activated during hypoxia.[59, 60] These assays were carried out using Fe_3O_4@SiO_2@Zn(ATSM/A) and Fe_3O_4/$Cd_{0.1}Zn_{0.9}Se$@SiO_2 dispersions, and Zn(ATSM/A) solutions under normoxic and hypoxic conditions (*Figure 5.46*), in order to compare the effects of the different nanocomposites in cells under different conditions.

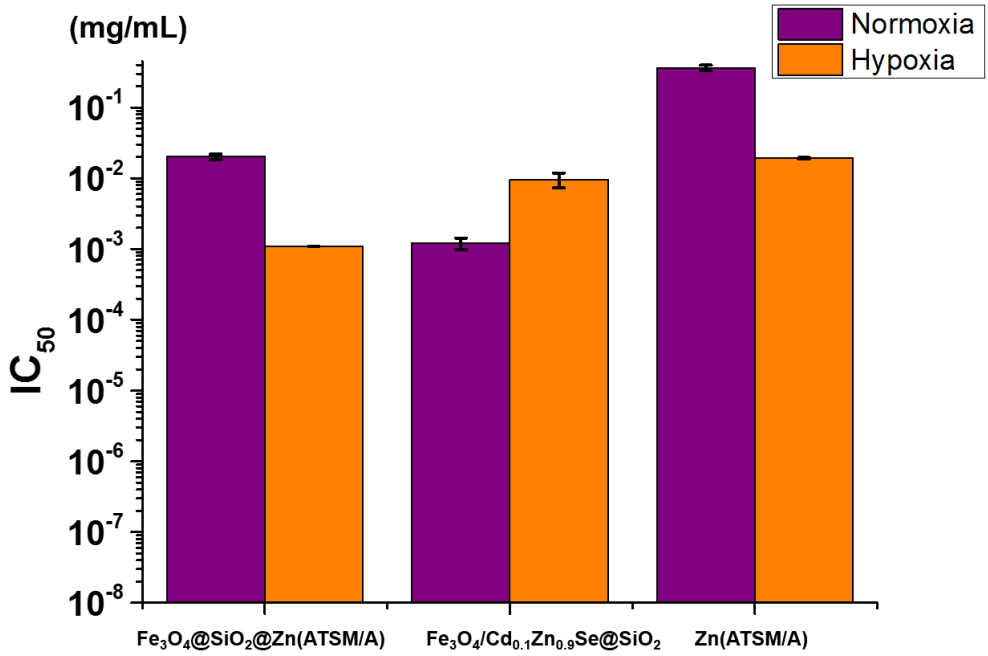

Figure 5.46. Crystal violet assays under normoxic (purple) and hypoxic (orange) conditions using PC-3 cells incubated with Fe_3O_4@SiO_2@Zn(ATSM/A) and $Fe_3O_4/Cd_{0.1}Zn_{0.9}Se$@$SiO_2$ nanoparticles, and Zn(ATSM/A). (The data was collected from six repeated measurements on the same day; N = 1).

Crystal violet assays show that under normoxic conditions, the $Fe_3O_4/Cd_{0.1}Zn_{0.9}Se$@$SiO_2$ nanoparticles have a lower IC_{50} value than the other two compounds, being more toxic (*Table 5.10*). However, when the assays were carried out under hypoxic conditions, the Fe_3O_4@SiO_2@Zn(ATSM/A) nanocomposite was found to be more toxic than the nanoparticles and quantum dots, and the IC_{50} value for the free Zn(ATSM/A) complex also diminishes. Under both normoxic and hypoxic conditions, Zn(ATSM/A) has a high IC_{50} value, which makes it very non-toxic.

Table 5.10. Summary of compounds tested with crystal violet assays using PC-3 cells under normoxic and hypoxic conditions and IC_{50} value found for each of them.

Compound	IC_{50} normoxia / mg/mL	IC_{50} hypoxia / mg/mL
Fe_3O_4@SiO_2@Zn(ATSM/A)	$(2.01 \pm 0.2)\cdot10^{-2}$	$(1.09 \pm 0.01)\cdot10^{-3}$
$Fe_3O_4/Cd_{0.1}Zn_{0.9}Se$@$SiO_2$	$(1.2 \pm 0.2)\cdot10^{-3}$	$(9 \pm 2)\cdot10^{-3}$
Zn(ATSM/A)	$(3.6 \pm 0.3)\cdot10^{-1}$	$(1.92 \pm 0.04)\cdot10^{-2}$

The same nanocomposites were tested in mice breast cancer (EMT6) cells using crystal violet assays under normoxic and hypoxic conditions to check their toxicity and IC_{50} values in this other cell line type (*Figure 5.47*). The same conditions and concentrations were used and hypoxia was chemically induced following the same protocol with $CoCl_2 \cdot 6H_2O$.

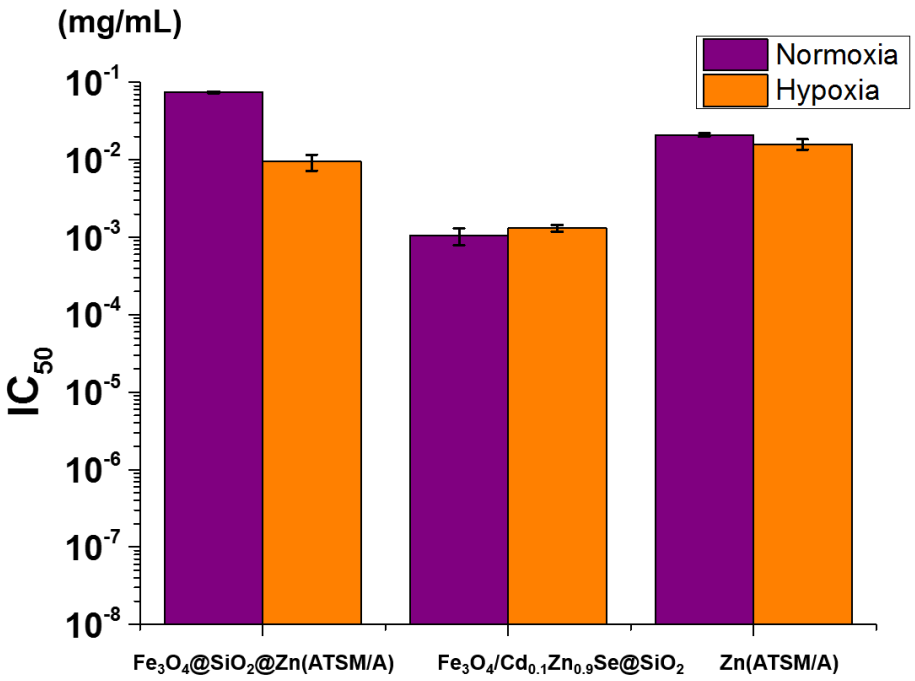

Figure 5.47. Crystal violet assays under normoxic (purple) and hypoxic (orange) conditions using EMT6 cells incubated with Fe_3O_4@SiO_2@Zn(ATSM/A) and $Fe_3O_4/Cd_{0.1}Zn_{0.9}Se$@$SiO_2$ nanoparticles, and Zn(ATSM/A). (The data was collected from six repeated measurements on the same day; N = 1).

Crystal violet assays carried out in EMT6 cells show that under normoxic conditions there is a similar trend as for PC-3 cells, with $Fe_3O_4/Cd_{0.1}Zn_{0.9}Se$@$SiO_2$ having a lower IC_{50} value than Fe_3O_4@SiO_2@Zn(ATSM/A) and Zn(ATSM/A). When the assays were carried out under hypoxic conditions, the trend in EMT6 cells is different to that in PC-3 cells: $Fe_3O_4/Cd_{0.1}Zn_{0.9}Se$@$SiO_2$ is the product with the lowest IC_{50} value and, for this reason, the most toxic one. The complex Zn(ATSM/A) keeps its high IC_{50} value in both cases, making it non-toxic for this type of cells as well. The main difference when compared to the studies carried out in PC-3 cells, is that for the Fe_3O_4@SiO_2@Zn(ATSM/A) nanoparticles and the Zn(ATSM/A) complex there is less of a difference between the IC_{50} values in hypoxic and normoxic conditions. (*Table 5.11*).

Table 5.11. Summary of compounds tested with crystal violet assays using EMT6 cells under normoxic and hypoxic conditions and IC_{50} value found for each of them.

Compound	IC_{50} normoxia / mg/mL	IC_{50} hypoxia / mg/mL
Fe_3O_4@SiO_2@Zn(ATSM/A)	$(7.4 \pm 0.2)\cdot10^{-2}$	$(9 \pm 2)\cdot10^{-3}$
$Fe_3O_4/Cd_{0.1}Zn_{0.9}Se$@$SiO_2$	$(1.0 \pm 0.2)\cdot10^{-3}$	$(1.3 \pm 0.1)\cdot10^{-3}$
Zn(ATSM/A)	$(2.1 \pm 0.1)\cdot10^{-2}$	$(1.6 \pm 0.2)\cdot10^{-2}$

5.15. Summary of Chapter 5

Chapter 5 describes an investigation into the synthesis and characterisation of iron oxide nanoparticles-based materials, including three types of fluorophores (*i. e.*, $Cd_{0.1}Zn_{0.9}Se$ QDs, Zn(ATSM/A) and a BODIPY derivative), which can be used as potential multimodal tools for magnetic resonance imaging, bioimaging applications and PET imaging.

Iron oxide nanoparticles were synthesised via a co-precipitation method and a silica layer was added by a reverse microemulsion method of coating. These nanocomposites were then functionalised using two different types of fluorophores. On one hand, $Cd_{0,1}Zn_{0.9}Se$ quantum dots, which have characteristics that make them good probes for imaging applications. On the other hand, the metal-ligand complex Zn(ATSM/A), which is a weak fluorophore and emits at some channels of the visible spectrum, with potential selectivity for hypoxic tissue when it is labelled with specific radioisotopes. For all the products, TEM was used to study their morphology and size, and EDX mapping was carried out to identify their elemental composition, among other techniques that were used to confirm the formation of such nanocomposites and study their properties (powder X-ray diffraction, IR spectroscopy, DLS, Raman spectroscopy, TGA, BET surface area analysis and epi-fluorescence and confocal microscopy). Consequently, water-dispersible, biocompatible and luminescent nanocomposites with dimensions of around 50 nm were obtained, which retained the magnetic properties of the iron oxide nanoparticles core. These were found to also retain some of the emissive characteristics of the encapsulated quantum dots.

Radiolabelling experiments using the radioisotope ^{68}Ga were carried out following three different methods: (i) adsorption of the radionucleus into the silica shell of the nanoparticles, (ii) encapsulation of ^{68}Ga within a second silica shell that coats the nanoparticles, and (iii) reaction between nanoparticles containing Zn(ATSM/A) bound onto their surface and ^{68}Ga. The first and last method used gave radio-incorporation factors of ≥ 99.9% when measured by radio-TLC, while the formation of a second silica shell to encapsulate the radioisotope gave a lower yield, probably due to the short time allowed for the reaction to take place due to the short half-life of ^{68}Ga (67.7 min). Overall, it was demonstrated that it is possible to radiolabel the magnetic and fluorescent nanocomposites with ^{68}Ga via the general methods developed, in some cases using chelator-free strategies.

Cellular imaging experiments in a PC-3 cell line were carried out using laser scanning confocal microscopy and FLIM, with single-photon and two-photon excitation techniques. The confocal microscopy results show that the functionalised nanoparticles are taken up by cells, with good

penetrability through the cell membrane, although they do not enter the nuclear membrane of the cells and therefore do not enter the nucleus. All of these compounds are retained in the cytoplasm and they do not damage or alter the cell morphology.

Regarding the FLIM experiments, the fluorescence lifetime and components distribution were measured for dispersions of the fluorescent nanocomposites in DMSO. Using TCSPC, the fluorescence lifetime was observed for the $Cd_{0.1}Zn_{0.9}Se$ quantum dots, with two components exponential fitting functions. The measured χ^2 value was within the acceptable range (< 1.5), making the values obtained reliable.

Toxicity assays were also carried out on these nanocomposites, and they showed that by adding a silica shell and encapsulating the different components inside of this, the toxicity decreases significantly, making the materials more *in vitro* biocompatible and non-toxic. Consequently, the materials were shown to be safe-to-handle and benign hybrid nanoparticles of potential utility as trimodal medical imaging probes that allow simultaneous PET, MRI and fluorescence imaging. MTT and crystal violet assays were carried out using prostate cancer cells and mice breast cancer cells. For the crystal violet studies, hypoxia was chemically induced in some cells and these were cultivated with the corresponding nanocomposites. Those compounds containing Zn(ATSM/A) tags seemed to show more toxicity for prostate cancer cells grown under hypoxia, with a lower IC_{50} value under these type of conditions, making them interesting agents for hypoxic therapy.

Another nanoparticles system, based on a citric acid layer coating the nanoparticles was also synthesised and characterised. This nanomaterial was functionalised with a BODIPY derivative based on a monofunctionalised tripodal ligand with two free arms, making the whole system highly fluorescent most likely due to the properties of this dye to act as a bio-orthogonal unit, and further investigations are necessary.

5.16. References for Chapter 5

1. M. Mahmoudi, S. Sant, B. Wang, S. Laurent and T. Sen, *Adv. Drug Deliv. Rev.*, 2011, **63**, 24-46.
2. A. S. Teja and P.-Y. Koh, *Prog. Cryst. Growth Charact. Mater.*, 2009, **55**, 22-45.
3. M. A. Malvindi, V. De Matteis, A. Galeone, V. Brunetti, G. C. Anyfantis, A. Athanassiou, R. Cingolani and P. P. Pompa, *PLoS ONE*, 2014, **9**, e85835.
4. K. Gdula, E. Skwarek, A. Dąbrowski and I. V. Melnyk, *Adsorpt. Sci. Technol.*, 2017, **35**, 432-438.
5. W. Wu, Q. He and C. Jiang, *Nanoscale Res. Lett.*, 2008, **3**, 397.
6. K. Gdula, E. Skwarek and A. Dąbrowski, in *Nanophysics, Nanophotonics, Surface Studies, and Applications*, Springer International Publishing, Cham, 2016, pp. 529-542.
7. P. Sun, H. Zhang, C. Liu, J. Fang, M. Wang, J. Chen, J. Zhang, C. Mao and S. Xu, *Langmuir*, 2010, **26**, 1278-1284.
8. R. Yi, G. Ye, D. Pan, F. Wu, M. Wen and J. Chen, *J. Mater. Chem. A*, 2014, **2**, 6840-6846.
9. S. I. Pascu, P. A. Waghorn, T. D. Conry, B. Lin, H. M. Betts, J. R. Dilworth, R. B. Sim, G. C. Churchill, F. I. Aigbirhio and J. E. Warren, *Dalton Trans.*, 2008, 2107-2110.
10. X. Zhou, W. Xu, Y. Wang, Q. Kuang, Y. Shi, L. Zhong and Q. Zhang, *J. Phys. Chem. C*, 2010, **114**, 19607-19613.
11. D. P. Joshi, G. Pant, N. Arora and S. Nainwal, *Heliyon*, 2017, **3**, e00253.
12. Wahajuddin and S. Arora, *Int. J. Nanomedicine*, 2012, **7**, 3445-3471.
13. A. P. Philipse, M. P. B. Vanbruggen and C. Pathmamanoharan, *Langmuir*, 1994, **10**, 92-99.
14. A. Sood, V. Arora, J. Shah, R. K. Kotnala and T. K. Jain, *Mater. Sci. Eng. C*, 2017, **80**, 274-281.
15. Z.-C. Xing, Y. Chang and I.-K. Kang, *Sci. Technol. Adv. Mater.*, 2010, **11**, 014101.
16. S. Santra, R. Tapec, N. Theodoropoulou, J. Dobson, A. Hebard and W. Tan, *Langmuir*, 2001, **17**, 2900-2906.
17. Z. Li, J. C. Barnes, A. Bosoy, J. F. Stoddart and J. I. Zink, *Chem. Soc. Rev.*, 2012, **41**, 2590-2605.
18. M. Rosso-Vasic, E. Spruijt, Z. Popovic, K. Overgaag, B. van Lagen, B. Grandidier, D. Vanmaekelbergh, D. Dominguez-Gutierrez, L. De Cola and H. Zuilhof, *J. Mater. Chem.*, 2009, **19**, 5926-5933.
19. M. J. Jacinto, P. K. Kiyohara, S. H. Masunaga, R. F. Jardim and L. M. Rossi, *Appl. Catal. A*, 2008, **338**, 52-57.
20. M. A. Malik, M. Y. Wani and M. A. Hashim, *Arabian J. Chem.*, 2012, **5**, 397-417.
21. M. Aghazadeh, I. Karimzadeh, T. Doroudi, M. R. Ganjali, P. H. Kolivand and D. Gharailou, *Appl. Phys. A*, 2017, **123**, 529.
22. R. K. Sharma, H. Kumar and A. Kumar, *RSC Adv.*, 2015, **5**, 43371-43380.
23. I. V. Martynenko, A. P. Litvin, F. Purcell-Milton, A. V. Baranov, A. V. Fedorov and Y. K. Gun'ko, *J. Mater. Chem. B*, 2017, **5**, 6701-6727.
24. H. D. Dhaygude, S. K. Shinde, D. P. Dubal, N. B. Velhal, D.-Y. Kim and V. J. Fulari, *Ionics*, 2017, **23**, 223-231.
25. X. Michalet, F. F. Pinaud, L. A. Bentolila, J. M. Tsay, S. Doose, J. J. Li, G. Sundaresan, A. M. Wu, S. S. Gambhir and S. Weiss, *Science*, 2005, **307**, 538-544.
26. S. S. Boxi and S. Paria, *Dalton Trans.*, 2016, **45**, 811-819.
27. N. Huang, S. Cheng, X. Zhang, Q. Tian, J. Pi, J. Tang, Q. Huang, F. Wang, J. Chen, Z. Xie, Z. Xu, W. Chen, H. Zheng and Y. Cheng, *Nanomedicine: NBM*, 2017, **13**, 83-93.
28. S. Sabella, R. P. Carney, V. Brunetti, M. A. Malvindi, N. Al-Juffali, G. Vecchio, S. M. Janes, O. M. Bakr, R. Cingolani, F. Stellacci and P. P. Pompa, *Nanoscale*, 2014, **6**, 7052-7061.

29. K. Peynshaert, S. J. Soenen, B. B. Manshian, S. H. Doak, K. Braeckmans, S. C. De Smedt and K. Remaut, *Acta Biomater.*, 2017, **48**, 195-205.
30. L. Ye, K.-T. Yong, L. Liu, I. Roy, R. Hu, J. Zhu, H. Cai, W.-C. Law, J. Liu, K. Wang, J. Liu, Y. Liu, Y. Hu, X. Zhang, M. T. Swihart and P. N. Prasad, *Nat. Nanotechnol.*, 2012, **7**, 453.
31. M. Chu, Y. Sun and S. Xu, *J. Nanopart. Res.*, 2008, **10**, 613-624.
32. N. Insin, J. B. Tracy, H. Lee, J. P. Zimmer, R. M. Westervelt and M. G. Bawendi, *ACS Nano*, 2008, **2**, 197-202.
33. X. Zhong, M. Han, Z. Dong, T. J. White and W. Knoll, *J. Am. Chem. Soc.*, 2003, **125**, 8589-8594.
34. M. Xia, C. Liu, Z. Zhao, J. Wang, C. Lin, Y. Xu, J. Heo, S. Dai, J. Han and X. Zhao, *Sci. Rep.*, 2017, **7**, 42359.
35. F. Boulmedais, P. Bauchat, M. J. Brienne, I. Arnal, F. Artzner, T. Gacoin, M. Dahan and V. Marchi-Artzner, *Langmuir*, 2006, **22**, 9797-9803.
36. J. Lim, S. P. Yeap, H. X. Che and S. C. Low, *Nanoscale Res. Lett.*, 2013, **8**, 1-14.
37. W. I. Goldburg, *Am. J. Phys.*, 1999, **67**, 1152-1160.
38. A. T. R. Williams, S. A. Winfield and J. N. Miller, *Analyst*, 1983, **108**, 1067-1071.
39. I. B. Berlman, in *Handbook of Fluorescence Spectra of Aromatic Molecules*, Academic Press, New York, 2nd edn., 1971, pp. 96-106.
40. D. A. R. Barkhouse, A. G. Pattantyus-Abraham, L. Levina and E. H. Sargent, *ACS Nano*, 2008, **2**, 2356-2362.
41. C. Bullen and P. Mulvaney, *Langmuir*, 2006, **22**, 3007-3013.
42. R. Hueting, *J. Labelled Comp. Radiopharm.*, 2014, **57**, 231-238.
43. I. S. Alam, R. L. Arrowsmith, F. Cortezon-Tamarit, F. Twyman, G. Kociok-Kohn, S. W. Botchway, J. R. Dilworth, L. Carroll, E. O. Aboagye and S. I. Pascu, *Dalton Trans.*, 2016, **45**, 144-155.
44. P. D. Bonnitcha, S. R. Bayly, M. B. M. Theobald, H. M. Betts, J. S. Lewis and J. R. Dilworth, *J. Inorg. Biochem.*, 2010, **104**, 126-135.
45. A. L. Vavere and J. S. Lewis, *Dalton Trans.*, 2007, **35**, 4893-4902.
46. J. P. Holland, F. I. Aigbirhio, H. M. Betts, P. D. Bonnitcha, P. Burke, M. Christlieb, G. C. Churchill, A. R. Cowley, J. R. Dilworth, P. S. Donnelly, J. C. Green, J. M. Peach, S. R. Vasudevan and J. E. Warren, *Inorg. Chem.*, 2007, **46**, 465-485.
47. P. Padwal, R. Bandyopadhyaya and S. Mehra, *J. Chem. Technol. Biotechnol.*, 2015, **90**, 1773-1781.
48. S. Laurent, D. Forge, M. Port, A. Roch, C. Robic, L. Vander Elst and R. N. Muller, *Chem. Rev.*, 2008, **108**, 2064-2110.
49. M. E. de Sousa, M. B. Fernández van Raap, P. C. Rivas, P. Mendoza Zélis, P. Girardin, G. A. Pasquevich, J. L. Alessandrini, D. Muraca and F. H. Sánchez, *J. Phys. Chem. C*, 2013, **117**, 5436-5445.
50. J. R. Lamb and J. P. Holland, *J. Nucl. Med.*, 2017, **59**, 382-389.
51. B. Mao, D. G. Calatayud, V. Mirabello, N. Kuganathan, H. Ge, R. M. J. Jacobs, A. M. Shepherd, J. A. Ribeiro Martins, J. Bernardino De La Serna, B. J. Hodges, S. W. Botchway and S. I. Pascu, *Chem. Eur. J.*, 2017, **23**, 9772-9789.
52. Z. Hu, R. L. Arrowsmith, J. A. Tyson, V. Mirabello, H. Ge, I. M. Eggleston, S. W. Botchway, G. Dan Pantos and S. I. Pascu, *Chem. Commun.*, 2015, **51**, 6901-6904.
53. W. Becker, A. Bergmann, M. A. Hink, K. König, K. Benndorf and C. Biskup, *Microsc. Res. Tech.*, 2004, **63**, 58-66.
54. J. A. Tyson, V. Mirabello, D. G. Calatayud, H. Ge, G. Kociok-Köhn, S. W. Botchway, G. Dan Pantoş and S. I. Pascu, *Adv. Funct. Mater.*, 2016, **26**, 5641-5657.
55. D. Dayal, D. Palanimuthu, S. V. Shinde, K. Somasundaram and A. G. Samuelson, *J. Biol. Inorg. Chem.*, 2011, **16**, 621-632.
56. J. R. Dilworth and R. Hueting, *Inorg. Chim. Acta*, 2012, **389**, 3-15.
57. M. Feoktistova, P. Geserick and M. Leverkus, *Cold Spring Harb. Protoc.*, 2016, **2016**, pdb.prot087379.

58. K. Lirdprapamongkol, H. Sakurai, S. Abdelhamed, S. Yokoyama, T. Maruyama, S. Athikomkulchai, A. Viriyaroj, S. Awale, H. Yagita, S. Ruchirawat, J. Svasti and I. Saiki, *Oncol. Rep.*, 2013, **30 5**, 2357-2364.
59. J.-P. Piret, D. Mottet, M. Raes and C. Michiels, *Ann. N. Y. Acad. Sci.*, 2002, **973**, 443-447.
60. D. Wu and P. Yotnda, *J. Vis. Exp.*, 2011, e2899.

Chapter 6. Conclusions and future work

Medical imaging includes a broad variety of techniques such as PET, SPECT and MRI, and is a potent tool for the diagnosis, follow-up and treatment of many diseases and tumours. The development of new multimodal systems to apply in these different techniques has been studied in this thesis, as described below chapter by chapter.

Chapter 2 describes the synthesis of potential multimodal systems based on a tripodal organic core: a benzene ring with three alternated CH_2Br arms that can be functionalised. BODIPY was the fluorophore of choice to give fluorescent properties to the system due to its many advantages (*e.g.*, high quantum yields and low cytotoxicity). Accordingly, a BODIPY derivative with a carboxylic acid pendant group was synthesised and characterised. The conditions to functionalise the tripodal starting material via a nucleophilic substitution reaction were found after several attempts, and also for the posterior purification to separate the potential mono-, di- and trisubstituted products present in the final mixture. First, the reaction was attempted with benzoic acid due to the simplicity of the molecule and its ready availability, and mono- and disubstituted products were isolated from the final mixture. Accordingly, a mono- and disubstituted BODIPY derivatives were synthesised and characterised. Two different linkers were also attached to the tripodal core: one of them, with a terminal protected carboxylic acid group will later be used to attach a peptide, and the other one, with an azido terminal group, was attached with the aim of performing “click” chemistry using a dibenzocyclooctyne (DBCO) acid derivative. For this purpose, a reaction to try to couple a deferoxamine (DFO) molecule to a DBCO acid was attempted, although unsuccessfully, and this would have later been used to attach on the azido terminal linker via a strain-promoted alkyne-azide cycloaddition (SPAAC) (copper-free) reaction. More efforts should be made in the future to carry out this reaction, finding the right conditions and following its progress at each step. The optimisation of the reaction conditions for the functionalisation of the tripodal core was carried out, to investigate the effects that changing a parameter would have in the mono- : disubstituted ratio in the final mixture, and also to make the reaction more accessible to biomolecules, which often cannot react at high temperatures for long periods of time. Therefore, three parameters were investigated: time, temperature and the stoichiometry of the starting materials. Regarding time, it was found that the distribution of the products is achieved after a short period of time, and the ratio obtained after one hour does not change significantly when compared to the final one, after 26 hours. Regarding the temperature at which the reaction takes place, it was found that a lower temperature favours the formation of the monosubstituted product in the final mixture and there is a minor amount of unreacted tripodal ligand. When the stoichiometry of the starting

materials is modified so that the number of equivalents of the tripodal ligand is bigger than for the carboxylic acid used, it was seen that the amount of monosubstituted product in the final mixture is higher in comparison to the amount of disubstituted product, which decreases considerably. MTT assays were performed to study the cell viability of the BODIPY derivatives and the starting tripodal ligand, and it was seen that the cytotoxicity of the latter decreases dramatically when the terminal bromide atoms are substituted by one and two BODIPY molecules, respectively. Moreover, colocalisation studies were carried out using single-photon laser scanning confocal microscopy with LysoTracker Red and ER-Tracker Red. It was concluded that BODIPY derivatives localise mainly in the cytoplasm, especially in the endoplasmic reticulum. Moreover, two-photon fluorescence lifetime imaging microscopy investigations were carried out to study the lifetime properties of the BODIPY derivatives both in solution and in PC-3 cells. All the compounds showed to exhibit one or more components for the fluorescence lifetime. Less successfully, functionalisation reactions of the tripodal core with fluorescein-5-thiosemicarbazide and Zn(ATSM/A) were attempted, unsuccessfully due to the complexity of these compounds. Two deferoxamine derivatives were synthesised and they were radiolabelled with zirconium-89 ($t_{1/2}$ = 78.4 h) following an established protocol in use at PETIC, leading to a nearly quantitative radiochemical yield.

Chapter 3 describes the synthesis of the [7-13] bombesin fragment using solid-state phase peptide synthesis with a Rink amide resin and Fmoc-protected amino acids, and its subsequent purification using a semi-preparative HPLC. The deprotection of the tripodal-linker compound synthesised in *Chapter* 2 was carried out to achieve the free carboxylic acid group, although unsuccessfully, due to the breakage of the ester linkage that binds the linker to the tripodal core, consistent with the behaviour of various succinate prodrugs. Another strategy was followed, attaching the peptide sequence to the same linker and performing its deprotection, which was achieved without major difficulties. The coupling of the bombesin-deprotected linker compound to the tripodal ligand containing two BODIPY units synthesised in *Chapter* 2 was carried out, but the desired trisubstituted product could not be isolated from the final reaction mixture. More attempts should be carried out in the future to identify the successful conditions to accomplish this reaction. Moreover, if this compound could be synthesised, it would be interesting to perform confocal fluorescence studies to investigate where it localises within the cells, as it is known that BODIPY is a targeting molecule for the endoplasmic reticulum, while the bombesin peptide tends to bind with strong affinity to the gastrin-releasing peptide receptor existing in the cellular membrane. Additionally, a molecule consisting of the [7-13] bombesin fragment attached to a deferoxamine derivative was synthesised. The coupling was performed using both HATU/DIPEA and HBTU/DIPEA, and both sets of conditions proved to work. In the future, it would be promising to perform radiolabelling experiments using this molecule and

zirconium-89, as it should have a high radiochemical yield due to the presence of DFO, a strong chelator for such radioisotope. Moreover, MTT assays should be carried out to investigate the cell viability of this conjugate.

Chapter 4 describes the synthesis and structural characterisation of ligands based on thiosemicarbazides. In this context, four ligands were synthesised using the symmetric tripodal core and creating systems with three thiosemicarbazide derivatives arms. Compounds with methyl, ethyl, phenyl and allyl terminal groups were synthesised. NMR spectroscopy was performed in order to characterise these ligands and study their orientation in space. For this purpose, ^{1}H NMR spectra were recorded and the resonances were assigned, showing the thiosemicarbazide arms as two groups, one set of resonances integrating for two of them and the other set integrating for the third arm. NOESY NMR spectroscopy was also carried out and a surprise raised to see positive peaks that indicate chemical exchange between different groups in the molecule, such as CH_2 and CH_3 in the ethyl arms of the compound. Next, a ROESY NMR experiment was performed to try to understand whether the positive peaks in the NOESY spectrum actually corresponded to exchange. Instead, the ROESY spectrum showed negative peaks, which indicate spatial proximity between protons. This suggested for the first time that such molecules have a size bigger than expected, so that they cannot be properly analysed by NOESY NMR. Moreover, ^{1}H DOSY NMR experiments were carried out, and the molecules showed to be pure. The diffusion coefficients were calculated for the four ligands, and their values were smaller than expected, suggesting that a bigger size molecule than it was originally thought happens in the solutions used for the NMR experiments. Variable temperature NMR was carried out at higher and lower temperatures than room temperature to try to elucidate the multiplicity of the peaks, and it was seen that at higher temperatures the resulting spectra were more good looking than at lower temperatures, due to the higher speed and motion of the arms at higher temperatures, which make the different protons more magnetically and chemically equivalent. Crystals suitable for single crystal X-ray diffraction were obtained for three of the four ligands as HBr salts. They were analysed, and the molecular structures showed how a unit cell contained two molecules of the ligand, each triply protonated, and forming a cage-like structure. Six Br^- counter ions in total, as well as a molecule of methanol, the solvent used to achieve the crystals, were localised within the unit cell. Hydrogen bonding was observed through the N-H atoms of the molecules and the Br^- ions located around the unit cell. Moreover, the distance of the bonds between the atoms that form the thiosemicarbazide were measured and compared to those in one of the starting materials, 4-methyl-3-thiosemicarbazide. They did not show to change significantly, suggesting that the delocalised double bond existing in the starting material is conserved, in the S-C, C-N and C-N system. Attempted complexation reactions of the ligands with metals were attempted using

Zr(IV), Ga(III), In(III), Cu(II), Ni(II) and Zn(II) salts. In all the cases, solids of different colours were obtained, which were characterised by MS, NMR, Raman and IR spectroscopy, elemental analysis and UV/visible spectroscopy. The presence of a metal in most of the compounds is evidenced through these techniques, although the final structure cannot be elucidated. Furthermore, the formation of a complex with three L-cysteine arms was accomplished, showing promising results for the functionalisation of biomolecules. Anion exchange reactions were carried out without clear results. Finally, crystal violet assays were performed using the four ligands in PC-3, EMT6 and FEK-4 cells after 24, 48 and 72 hours of incubation, evidencing the low toxicity of the products in the micromolar concentration range.

Chapter 5 describes the synthesis and characterisation of imaging agents based on magnetite phase iron oxide nanoparticles. This type of nanoparticles were chosen due to their magnetic properties, which allow them to be used as contrast agents for magnetic resonance imaging, and their low toxicity levels. The nanoparticles were coated with a silica shell and two types of fluorophores were used: on one side, inorganic $Cd_{0.1}Zn_{0.9}Se$ quantum dots nanocrystals, and on the other side, a slightly fluorescent and potential hypoxia targeting molecule, Zn(ATSM/A). The nanocomposites were characterised by TEM, EDX, powder X-ray diffraction, IR and Raman spectroscopy, DLS, fluorescence spectroscopy, BET surface area analysis and TGA, accordingly. Moreover, a nanocomposite consisting of the iron oxide nanoparticles with a citric acid coating and a monofunctionalised BODIPY derivative was synthesised. Radiolabelling experiments using the radioisotope gallium-68 ($t_{1/2}$ = 67.7 min) were carried out and three different methods were developed: (i) the adsorption of the radioisotope onto the silica matrix, (ii) the encapsulation of the radioisotope within a second silica shell, and (iii) the possible transmetallation of the Zn(ATSM/A) complex attached onto the surface of the nanoparticles. The radiochemical incorporation factors were found to be: (i) ≥ 99.9%, (ii) 66-70%, and (iii) ≥ 99.9%, respectively. One-photon and two-photon confocal fluorescence investigations were carried out on thin films and *in vitro* using PC-3 cells, and the nanocomposites containing quantum dots and Zn(ATSM/A) showed to emit light in the green and red channels of the spectrum. FLIM studies were performed as well. MTT cell viability assays were carried out and they showed that when the nanoparticles are coated with a silica matrix their cytotoxicity decreases dramatically. Crystal violet assays were performed under normoxic and hypoxic conditions on PC-3 and EMT6 cells with the compounds containing Zn(ATSM/A) and quantum dots. The results showed that the compounds incorporating Zn(ATSM/A) are more toxic for hypoxic cells in PC-3 cells, but the trend is not conserved in EMT6 cells.

Overall, the work presented herein constitutes promising results towards the synthesis of new potential multimodal tools for *in vitro* and *in vivo* imaging, including fluorescent materials both

based in single molecules and nanocomposites, with the potential of being radiolabelled with high radiochemical yields.

Chapter 7. Experimental Section

7.1. Materials and Methods

All solvents and reagents for the synthesis and characterisation of the compounds described in this section were purchased from commercial sources (Sigma Aldrich, Alfa Aesar, Acros Organics, Merck Chemicals, Fluorochem or Fisher Scientific) and used without further purification unless otherwise stated. Commercial solvents were reagent or HPLC grade obtained from Sigma Aldrich or VWR. The water used was from a Millipore milli-Q purification system. Anhydrous solvents were obtained from a PS-400-7 Innovative technologies Solvent Purification System. Reactions executed under nitrogen atmosphere using Schlenk line techniques are indicated.

Nuclear Magnetic Resonance Spectroscopy

Nuclear magnetic resonance (NMR) spectra were recorded at 298 K on either a 300 MHz (^{1}H) Bruker Avance or a 500 MHz (^{1}H) Agilent ProPulse spectrometers, using the solvent indicated in each case. ^{1}H and ^{13}C{^{1}H} chemical shifts are referenced to tetramethylsilane (TMS). Chemical shifts are given in ppm and multiplicities are described as singlet (s), doublet (d), triplet (t), quartet (q) or multiplet (m). Broad peaks are described as (br). Coupling values, *J*, are given in Hz. NOESY, ROESY and variable temperature NMR experiments were carried out using a 500 MHz Bruker Avance II+ NMR instrument. Variable temperature NMR spectra were recorded with the assistance of Dr. John Lowe.

Mass Spectrometry

Mass spectra were recorded either at the University of Bath or at the EPSRC UK National Mass Spectrometry Facility in Swansea. When carried out at the university, the mass spectra were conducted on either an ESI-TOF or a LC-QTOF mass spectrometer and solutions of 1 ng/mL were prepared using methanol or acetonitrile as a solvent. When recorded at the NMSF in Swansea, the method used is indicated in each case.

Fourier Transform Infrared Spectroscopy

FT-IR spectra in the 4000 – 650 cm^{-1} range were recorded on a Perkin Elmer Frontier FT-IR instrument. Wavenumbers are given in cm^{-1}, and vibrational modes are described as asymmetrical (as) or symmetrical (sy) stretching (st) and bending (δ).

Raman Spectroscopy

Raman spectroscopy measurements were carried out in the solid state on a Renishaw inVia system using a laser of 532 nm excitation wavelength.

High-Performance Liquid Chromatography

HPLC analyses were performed on an analytical reverse-phase Dionex UltiMate 3000 HPLC system, using a Dionex C18 Acclaim column. The solvent system was formed by water and acetonitrile, each containing 0.1% of trifluoroacetic acid.

Method **A**: Gradient; t = 0 min, AcCN = 5%; t = 1 min, AcCN = 5%; t = 6 min, AcCN = 95%, t = 13 min, AcCN = 95%; t = 16 min, AcCN = 95%; t = 20 min, AcCN = 5%. Flow rate = 0.8 mL/min.

Method **B**: Gradient; t = 0 min, AcCN = 5%; t = 7.5 min, AcCN = 95%; t = 15 min, AcCN = 95%, t = 18 min, AcCN = 95%. Flow rate = 0.8 mL/min.

Flash Chromatography

Where products required purification by flash chromatography, a Biotage Isolera automatic purification system was used, with the solvent system indicated in each case, using 10, 25 or 50 g Biotage SNAP silica cartridges.

Powder X-ray diffraction

Analyses of crystalline structure and phase identification of materials were performed by X-ray diffraction on a XRD Bruker AXS D8-Advance with a monochromatised source of Cu-$K\alpha_1$ radiation (λ = 1.54018 Å) at 1.6 kW (40 kV, 40 mA). A 2theta/omega scan was performed with a step width of 0.033^o (2θ) and step time of 1345.1 s. Samples were prepared by placing a drop of a methanol dispersion of particles onto a single crystal silicon plate. Powder X-ray diffraction analyses were carried out with the assistance of Dr. Gabrielle Kociok-Köhn.

Transmission Electron Microscopy

TEM images were obtained mostly on a JEOL JEM1200EXII operating at 120 kV at the Microscopy and Analysis Suite at the University of Bath. A high resolution JEOL JEM-2100Plus operating at 200 kV in the same facility was also used to acquire some images. Samples were prepared by placing a drop of a diluted dispersion of the nanocomposite in an appropriate solvent onto a 400-mesh carbon-coated copper grid and left to dry on air overnight.

Energy Dispersive X-ray Spectroscopy

EDX data was collected from a JEOL JEM-2100Plus transmission electron microscope coupled with energy dispersive X-ray spectroscopy at the Microscopy and Analysis Suite at the University of Bath, using the same grids as for TEM.

Dynamic Light Scattering

DLS data was acquired on a Malvern Zetasizer Nano ZS instrument in the Department of Chemistry at the University of Bath, using disposable polystyrene cuvettes.

Circular Dichroism

CD data was acquired from a Chirascan (Applied Photophysics) instrument connected to a nitrogen gas unit (Claino Brezza) in the Department of Chemistry at the University of Bath.

Brunauer, Emmet and Teller (BET) Surface Area Analysis and Barrett-Joyner-Halenda (BJH) Pore Size and Volume Analysis

In order to carry out BET measurements, approximately 300 mg of sample were inserted into a glass tube and degassed at 90 ^{o}C for 4 hours to remove any solvent, moisture or contaminant molecules that might be adsorbed and prevent the surface of the nanocomposite from being fully accessible to the nitrogen molecules. Nitrogen adsorption was performed on a 3Flex unit from Micromeritics. All the calculations (BET, DFT, BJH, etc.) were done using the program MicroActive. BET measurements were carried out with the assistance of Dr. Rémi Castaing.

Thermogravimetry with Evolving Gas Analysis

Thermogravimetric analysis was carried out on a Setsys Evolution TGA 16/18 from Setaram. The program Calisto was employed to collect and process the data. The sample was loaded into a 170 µL alumina crucible. The temperature program consisted of a succession of isothermal steps and heating and cooling ramps. The temperature was set at 30 ^{o}C initially and maintained for 120 seconds. Following this, a heating ramp took place at a rate of 10 K/min until 800 ^{o}C were reached, which lasted for 4620 seconds. Next, a cooling ramp started at a rate of 20 K/min until the temperature was again 30 ^{o}C, after 2310 seconds. This final temperature was maintained for 900 seconds. All the mentioned steps were performed under an air flow, which was then stopped and the sample was left at 30 ^{o}C for 15 more seconds. TGA was carried out with the assistance of Dr. Rémi Castaing.

Single Crystal X-Ray Diffraction

X-ray crystallography data were collected at 150(2) K on an Agilent SuperNova Dual diffractometer, using monochromated Cu-Kα radiation (λ = 1.54184 Å). All structures were solved with SHELXT and refined by a full-matrix least-squares procedure based on F^2. Single crystal X-ray diffraction and structure refinement were carried out by Dr. Gabrielle Kociok-Köhn.

Elemental Analysis

CHN analyses were carried out at London Metropolitan University.

Peptide Synthesiser

Peptides were synthesised on a Biotage Initiator+ Alstra automated microwave peptide synthesiser, using the resin type and method indicated in each case.

UV/visible Spectroscopy

UV/visible spectra were acquired from a Perkin Elmer Lambda 35 Spectrometer or from a Perkin Elmer Lambda 650 Spectrometer using two 1 cm quartz cuvettes.

Fluorescence Spectroscopy

Fluorescence spectra were acquired on a Perkin Elmer LS55 Luminescence Spectrometer using a 1 cm quartz cuvette.

Cell culturing and cell plate preparation

Cell lines used in this project included prostate cancer cells (PC-3), epithelial fibroblast cells (FEK-4) and mice breast cancer cells (EMT6). Cells were normally frozen at -196 ^{o}C under liquid nitrogen until they were required to use, then cells were thawed quickly and incubated at 37 °C under a 5% carbon dioxide environment. Different cell lines required different solvent systems to grow: FEK-4 cells were incubated in an Eagle's Minimum Essential Medium (EMEM), whilst both PC-3 and EMT6 cells were cultured in Roswell Park Memorial Institute (RPMI) medium. All media contained activated foetal calf serum (FCS) (10% for PC-3 and EMT6, and 15% for FEK-4), 0.5% penicillin/streptomycin (10,000 IU·mL^{-1}/10,000 mg·mL^{-1}) and 1% L-glutamine. Cell culturing was carried out with the assistance of Dr. Haobo Ge.

MTT Assays

After splitting the cells, cells (3 x 10^3 cells per well) were seeded on a sterile 96 well plate and incubated for 48 hours in order to let the cells adhere to the plates. The compound of interest was then subsequently loaded at different concentrations into the wells and incubated for 48 hours more. The concentrations used ranged between 250 μM or 0.01 mg/mL and 1 nM or 1 ng/mL (1% DMSO with compound, 99% RPMI (10% FCS) for PC-3 and EMT6 cells). Subsequently, cells were washed three times with PBS, and 3-(4,5-dimethylthiazol-2-yl)-2,5-diphenyltetrazolium bromide (MTT) was added (0.5 mg/mL in serum-free medium (SFM)), followed by a two hours incubation. After aspiration to remove the serum-free medium, 100 μL of DMSO was added to solubilise the precipitated formazan species, and 96 well plates were read by an ELISA plate reader, Molecular Devices Versa Max (BN02877). The absorption

wavelength was 570 nm, and 690 nm wavelength was used as a reference. Cell viability studies were carried out with the assistance of Dr. Haobo Ge.

Crystal Violet Assays

After splitting the cells, cells (3×10^3 cells per well) were seeded on a sterile 96 well plate and incubated for 48 hours in order to let the cells adhere to the plates. The compound of interest was then subsequently loaded at different concentrations into the wells and incubated for 48 hours more. The concentrations used ranged between 250 μM or 0.01 mg/mL and 1 nM or 1 ng/mL (1% DMSO with compound, 99% RPMI (10% FCS) for PC-3 and EMT6 cells, and 1% DMSO with compound, 99% EMEM (15% FCS) for FEK-4 cells). Subsequently, the medium from the plates was carefully aspirated so as not to disturb the colonies, and the plates were gently washed with PBS. Next, a mixture of methanol:PBS (1:1) was added in a sufficient volume to cover the colonies, and it was left for 15 minutes. After this time, it was removed and 100% methanol was added for a further 15 minutes. The methanol was then removed and 0.5% crystal violet solution (in 20% methanol and 80% water) was added and left to allow sufficient staining. The crystal violet solution was removed by carefully rinsing the cell plates with an indirect flow of tap water. The plates were inverted and left on the bench at room temperature to dry the water. Methanol (200 μL) was added to each well, and the plate was incubated with its lid on for 20 minutes at room temperature on a bench rocker with a frequency of 20 oscillations per minute. The 96 well plates were then read by an ELISA plate reader, Molecular Devices Versa Max (BN02877). The absorption wavelength was 570 nm, and 690 nm wavelength was used as a reference. This was carried out by Dr. Haobo Ge.

Chemically Induced Hypoxia

A 25 mM stock solution of cobalt (II) chloride hexahydrate ($CoCl_2 \cdot 6H_2O$) in water was prepared immediately before use. $CoCl_2$ at a final concentration of 100 μM was used in the regular cell culture media to induce hypoxia in cells. The $CoCl_2$-containing media was then added to the cells and these were incubated for 24 hours at 37 ^oC under a 5% carbon dioxide environment. This step was carried out before adding the compounds of interest to the cells, as a pre-incubation of the cells with a hypoxia inducing agent. This was carried out by Dr. Haobo Ge.

Laser Scanning Confocal Microscopy

Laser scanning confocal microscopy was performed using a Nikon A1Rsi Laser Scanning Confocal Microscope System fitted with 60X oil objective lens, and equipped with three lasers of 405, 488 and 561 nm. The microscope was also fitted with a motorised piezo z-stage, halogen lamp and mercury lamp for epi-fluorescence microscopy. All the images were processed using functions within the NIS elements software package.

Two-Photon Fluorescence Lifetime Imaging Microscopy

Two-photon excitation experiments were performed at the Rutherford Appleton Laboratory (Central Lasers Facility, Research Complex at Harwell) by Dr. Vincenzo Mirabello and Dr. Haobo Ge. A mode-locked Mira titanium sapphire laser (Coherent Lasers Ltd, USA), generating 180-fs pulses at 75 MHz and emitting light at a wavelength of 710 – 970 nm was used for the two-photon excitation experiments. The laser was pumped by a solid state continuous wave 532 nm laser (Verdi V18, Coherent Laser Ltd), with the oscillator fundamental output of 915 ± 2 nm or 810 ± 2 nm. The laser beam was focused to a diffraction limited spot through a water immersion ultraviolet corrected objective (Nikon VC x60, NA1.2) and specimens were illuminated at the microscope stage of a modified Nikon TE2000-U with UV transmitting optics. The focused laser spot was raster scanned using an XY galvanometer (GSI Lumonics). Fluorescence emission was collected and passed through a coloured glass filter (BG39) and detected by fast microchannel plate photomultiplier tube used as the detector (R3809-U, Hamamatsu, Japan). These were linked via a TCSPC PC module SPC830. Lifetime calculations were obtained using SPCImage analysis software.

Quantum Yield calculation

Room temperature fluorescence QY was calculated according to the following equation:

$$\phi s = \phi r * \frac{Ar}{As} * \frac{Es}{Er} * \frac{Ir}{Is} * \frac{n_{s^2}}{n_{r^2}}$$

Equation 7.1. Formula employed to calculate the quantum yield of the new fluorescent compounds.

In this equation, the subscript *r* refers to the reference ($Ru(bpy)_3^{2+}$), while *s* refers to the other compounds. Φr and Φs are the fluorescence QY of $Ru(bpy)_3^{2+}$ (0.042) and unknown, respectively. *A* is the absorbance of the solution, *E* is the corrected emission intensity, *I* is the relative intensity of the exciting light and *n* is the average refractive index of the solutions.

Radiolabelling experiments

Experiments involving ^{68}Ga were performed at the Department of Surgery and Cancer of the Imperial College London with the assistance of Sophia Sarpaki, and those involving ^{89}Zr were carried out at the Wales Research and Diagnostic Positron Emission Tomography Imaging Centre (PETIC) with the assistance of Dr. Stephen Paisey.

7.2. Experimental procedures

7.2.1. Synthesis of compounds from Chapter 2

1,3,5-tris(bromomethyl)-2,4,6-triethylbenzene (1)

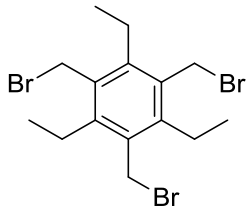

This synthesis was carried out following a previously reported procedure with some modifications,[1] as described below.

Zinc powder (3.36 g, 51.30 mmol) was dissolved in 33 mL of acetic acid in a three-neck round-bottom flask under nitrogen and stirring. When the zinc was dissolved, HBr in acetic acid (33% wt) (34.5 mL) was added slowly through an addition funnel. Triethylbenzene (8.0 mL, 42.40 mmol), paraformaldehyde (13.80 g) and HBr in acetic acid (33% wt) (103 mL) were then added to the solution. The mixture was heated to 90 ^{o}C under reflux and stirred for 48 hours. After this time, heat was stopped and the solution was left to cool for 2 hours. When it had cooled, the precipitate was filtered and washed three times with water, then the solid was left on the freeze-drier overnight. The red-brown filtrate was heated again to 90 ^{o}C and stirred for 24 more hours. The new precipitate was then filtered and again the filtrate was left to react for 24 more hours at 90 ^{o}C. Finally, a white powder was obtained, which was left on the freeze-drier overnight to dry.

Yield: 49% (9.11 g).

^{1}H NMR (300 MHz, $CDCl_3$, 298 K): δ (ppm) 4.58 (s, 6H, CH_2Br), 2.94 (q, J = 7.6 Hz, 6H, CH_2CH$_3$), 1.34 (t, J = 7.6 Hz, 9H, CH$_2$CH_3).

^{13}C{^{1}H} NMR (75 MHz, $CDCl_3$, 298 K): δ (ppm) 145.1, 132.8, 28.7, 22.9, 15.8.

nESI-MS^{+}: m/z calculated for $C_{15}H_{21}Br_3$: 457.9511, found 457.9507 $[M+NH_4]^+$ (for $C_{15}H_{21}{}^{79}Br^{79}Br^{81}Br$).

IR: $\tilde{\nu}$ (cm^{-1}): 2966, 2872, 2300-1900, 1570, 957, 901, 703.

HPLC (Method A): Rt (min): 12.4.

4-(5,5-difluoro-1,3,7,9-tetramethyl-5*H*-4λ^4,5λ^4-dipyrrolo[1,2-*c*:2',1'-*f*][1,3,2]diazaborinin-10-yl)benzoic acid (2)

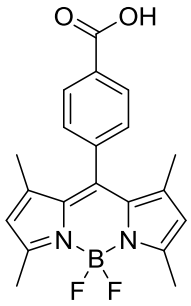

This synthesis was carried out following a previously reported procedure with some modifications,[2, 3] as described below.

2,4-dimethylpyrrole (1.99 mL, 19.40 mmol, 2.25 eq) and 4-formylbenzoic acid (1.30 g, 8.63 mmol, 1 eq) were dissolved in 1 L of dichloromethane under a nitrogen in a round-bottom flask. Two drops of trifluoroacetic acid were added, and the solution was stirred at room temperature for 1 hour. After this time, 2,3-dichloro-5,6-dicyano-1,4-benzoquinone (DDQ; 1.96 g, 8.63 mmol, 1 eq) was added dissolved in 20 mL of dichloromethane and the purple reaction mixture was stirred for another hour. Next, triethylamine (20 mL) and boron trifluoride diethyl etherate (20 mL) were added and the reaction mixture was stirred for 3 hours, after which it was quenched by the addition of water (500 mL) and extracted with dichloromethane (3 x 200 mL). The combined organic extracts were dried with anhydrous $MgSO_4$, filtered and concentrated under reduced pressure. The purple crude slurry was purified by silica gel chromatography (0-8% methanol in dichloromethane), and the different fractions were collected and analysed. The desired fractions were recrystallised from THF/hexane to give a red solid.

Yield: 19% (0.60 g).

^{1}H NMR (500 MHz, DMSO-d_6, 298 K): δ (ppm) 8.10 (d, J = 8.3 Hz, 2H, o-Ar*H*), 7.53 (d, J = 8.2 Hz, 2H, m-Ar*H*), 6.19 (s, 2H, NC(CH_3)C*H*C(CH_3)), 2.46 (s, 6H, NC(C*H*$_3$)CHC(CH_3)), 1.33 (s, 6H, NC(CH_3)CHC(C*H*$_3$)).

^{19}F NMR (470 MHz, DMSO-d_6, 298 K): δ (ppm) -143.7 (q, J = 32.0 Hz, 2F, B*F*$_2$).

^{13}C{^{1}H} NMR (126 MHz, DMSO-d_6, 298 K): δ (ppm) 166.8, 155.2, 150.2, 142.6, 138.4, 135.5, 131.5, 130.1, 128.4, 121.6, 14.2, 14.0.

ESI-MS$^-$: m/z calculated for $C_{20}H_{19}BF_2N_2O_2$: 367.1438, found 367.1455 [M-H]$^-$.

IR: $\tilde{\nu}$ (cm^{-1}): 3109, 2922, 1878, 1681, 1191.

HPLC (Method B): Rt (min): 9.9.

General procedure (A) for the synthesis of monosubstituted compounds

1,3,5-tris(bromomethyl)-2,4,6-triethylbenzene, a carboxylic acid derivative and potassium carbonate were added to a round-bottom flask, followed by acetonitrile. The reaction mixture was stirred and heated to 100 ºC, then connected to a reflux condenser. The reaction was monitored by TLC, and after 16 hours heating was stopped. The mixture was left to cool to room temperature, and the solvent was removed under reduced pressure. The product was dissolved in dichloromethane and washed three times with NaOH(aq) 1 M. The organic layers were collected and dried with anhydrous $MgSO_4$, then the solvent was removed under reduced pressure to yield a powder. In all the cases, TLC showed three spots. The final product was purified by silica gel column chromatography with a solvent system of ethyl acetate in hexane in different ratios as specified in each case. In some occasions it was possible to isolate the disubstituted product as well as the monosubstituted material.

3,5-bis(bromomethyl)-2,4,6-triethylbenzyl benzoate (3)

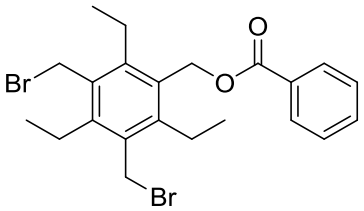

1,3,5-tris(bromomethyl)-2,4,6-triethylbenzene (compound **1**) (0.25 g, 0.56 mmol, 1 eq), benzoic acid (0.07 g, 0.56 mmol, 1 eq) and potassium carbonate (0.12 g, 0.85 mmol, 1.5 eq) were dissolved in 20 mL of acetonitrile and were reacted as per **General procedure (A)**. The final product was purified by silica gel column chromatography with a solvent system of 4% ethyl acetate in hexane.

Yield: 38% (0.10 g).

^{1}H NMR (500 MHz, $CDCl_3$, 298 K): δ (ppm) 8.06 – 8.03 (m, 2H, o-Ar*H*), 7.58 – 7.53 (m, 1H, p-Ar*H*), 7.44 – 7.40 (m, 2H, m-Ar*H*), 5.44 (s, 2H, C*H*$_2$O), 4.64 (s, 4H, C*H*$_2$Br), 3.00 (q, *J* = 7.6 Hz, 2H, p-C*H*$_2$CH$_3$), 2.93 (q, *J* = 7.6 Hz, 4H, o-C*H*$_2$CH$_3$), 1.39 (t, *J* = 7.6 Hz, 3H, p-CH$_2$C*H*$_3$), 1.29 (t, *J* = 7.6 Hz, 6H, o-CH$_2$C*H*$_3$).

^{13}C{^{1}H} NMR (126 MHz, $CDCl_3$, 298 K): δ (ppm) 166.8, 146.2, 145.2, 145.1, 133.2, 132.4, 130.9, 129.8, 128.5, 61.2, 28.9, 22.9, 22.9, 16.1, 15.8.

APCI-MS^{+}: m/z calculated for $C_{22}H_{26}Br_2O_2$: 505.0178, found 505.0185 $[M+Na]^+$ (for $C_{22}H_{26}{}^{79}Br^{81}BrO_2$).

IR: ν̃ (cm^{-1}): 2961, 2870, 2300-1900, 1717, 1450, 1266, 1024, 953, 904, 706.

HPLC (Method B): Rt (min): 7.9.

(5-(bromomethyl)-2,4,6-triethyl-1,3-phenylene)bis(methylene) dibenzoate (4)

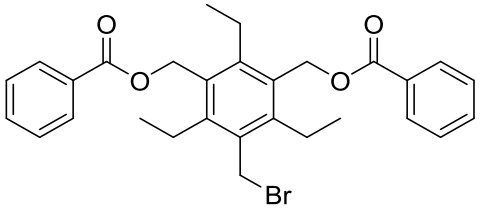

This product was obtained from the synthesis and purification of compound **3**.

Yield: 21% (0.06 g).

^{1}H NMR (500 MHz, $CDCl_3$, 298 K): δ (ppm) 8.05 (d, *J* = 7.8 Hz, 4H, o-Ar*H*), 7.58 – 7.51 (p, 2H, p-Ar*H*), 7.42 (t, *J* = 7.7 Hz, 4H, m-Ar*H*), 5.48 (s, 4H, C*H*$_2$O), 4.68 (s, 2H, C*H*$_2$Br), 2.97 (q, *J* = 7.6 Hz, 4H, C*H*$_2$CH$_3$), 2.89 (q, *J* = 7.5 Hz, 2H, C*H*$_2$CH$_3$), 1.32 (t, *J* = 7.6 Hz, 6H, CH$_2$C*H*$_3$), 1.24 (t, *J* = 7.5 Hz, 3H, CH$_2$C*H*$_3$).

^{13}C{^{1}H} NMR (126 MHz, $CDCl_3$, 298 K): δ (ppm) 166.8, 147.3, 146.3, 133.2, 132.1, 130.6, 130.1, 129.9, 128.5, 61.4, 29.3, 23.1, 23.0, 16.5, 16.2.

APCI-MS^{+}: m/z calculated for $C_{29}H_{31}BrO_4$: 542.1734, found 542.1732 $[M+NH_4]^+$; 547.1288, found 547.1289 $[M+Na]^+$.

IR: ṽ (cm^{-1}): 2961, 2870, 2300-1900, 1717, 1450, 1266, 1024, 953, 904, 706.

HPLC (Method B): Rt (min): 6.5.

3,5-bis(bromomethyl)-2,4,6-triethylbenzyl 4-(5,5-difluoro-1,3,7,9-tetramethyl-5*H*-4λ^4,5λ^4-dipyrrolo[1,2-*c*:2',1'-*f*][1,3,2]diazaborinin-10-yl)benzoate (5)

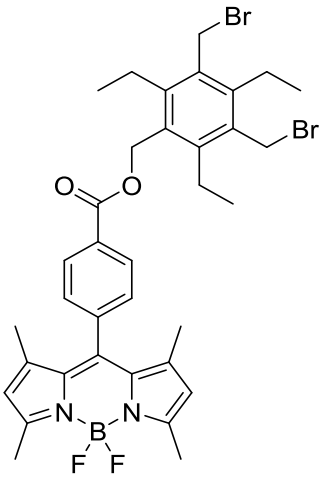

1,3,5-tris(bromomethyl)-2,4,6-triethylbenzene (compound **1**) (0.25 g, 0.56 mmol, 1 eq), 4-(5,5-difluoro-1,3,7,9-tetramethyl-5*H*-4λ^4,5λ^4-dipyrrolo[1,2-*c*:2',1'-*f*][1,3,2]diazaborinin-10-yl)benzoic acid (compound **2**) (0.21 g, 0.56 mmol, 1 eq) and potassium carbonate (0.12 g, 0.85 mmol, 1.5 eq) were dissolved in 20 mL of acetonitrile and were reacted as per **General procedure (A)**. The final product was purified by silica gel column chromatography with a solvent system of 10-20% ethyl acetate in hexane.

Yield: 20% (0.08 g).

^{1}H NMR (500 MHz, $CDCl_3$, 298 K): *δ* (ppm) 8.16 (d, J = 8.3 Hz, 2H, o-Ar*H*), 7.38 (d, J = 8.3 Hz, 2H, m-Ar*H*), 5.98 (s, 2H, NC(CH_3)C*H*C(CH_3)), 5.48 (s, 2H, CH_2O), 4.63 (s, 4H, CH_2Br), 2.99 (q, J = 7.6 Hz, 2H, C$H_2$$CH_3$), 2.94 (q, J = 7.7 Hz, 4H, C$H_2$$CH_3$), 2.54 (s, 6H, NC(C$H_3$)CHC($CH_3$)), 1.38 (t, J = 7.6 Hz, 2H, CH_2CH_3), 1.35 (s, 6H, NC(CH_3)CHC(CH_3)), 1.30 (t, J = 7.5 Hz, 4H, CH_2CH_3).

^{13}C{^{1}H} NMR (126 MHz, $CDCl_3$, 298 K): *δ* (ppm) 166.2, 156.1, 146.2, 145.4, 142.9, 140.2, 140.1, 132.5, 131.0, 130.7, 130.6, 128.6, 121.6, 61.5, 53.5, 28.9, 23.0, 22.9, 16.2, 15.8, 14.6, 14.3.

nESI-MS$^+$: m/z calculated for $C_{35}H_{39}BBr_2F_2N_2O_2$: 729.1501, found 729.1490 $[M+H]^+$ (for $C_{35}H_{39}B^{79}Br^{81}BrF_2N_2O_2$).

IR: ṽ (cm^{-1}): 2965, 1726, 1541, 1189, 737.

HPLC (Method B): Rt (min): 13.9.

3-(bromomethyl)-5-(((4-(5,5-difluoro-1,3,7,9-tetramethyl-5*H*-4λ^4,5λ^4-dipyrrolo[1,2-*c*:2',1'-*f*][1,3,2]diazaborinin-10-yl)benzoyl)oxy)methyl)-2,4,6-triethylbenzyl 4-(5,5-difluoro-1,3,7,9-tetramethyl-5*H*-4λ^4,5λ^4-dipyrrolo[1,2-*c*:2',1'-*f*][1,3,2]diazaborinin-10-yl)benzoate (6)

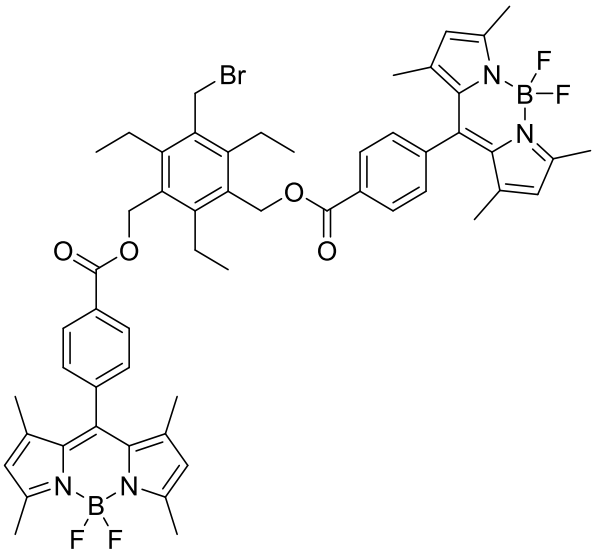

This product was obtained from the synthesis and purification of compound **5**.

Yield: 13% (0.08 g).

^{1}H NMR (500 MHz, $CDCl_3$, 298 K): *δ* (ppm) 8.16 (d, J = 8.3 Hz, 4H, o-Ar*H*), 7.38 (d, J = 8.2 Hz, 4H, m-Ar*H*), 5.96 (s, 4H, NC(CH_3)C*H*C(CH_3)), 5.53 (s, 4H, CH_2O), 4.68 (s, 2H, CH_2Br), 3.00 (d, J = 7.6 Hz, 4H, C$H_2$$CH_3$), 2.95 (d, J = 7.4 Hz, 2H, C$H_2$$CH_3$), 2.54 (s, 12H, NC(C$H_3$)CHC($CH_3$)), 1.43 – 1.23 (m, 21H, CH_2CH_3, NC(CH_3)CHC(CH_3), CH_2CH_3).

^{13}C{^{1}H} NMR (126 MHz, $CDCl_3$, 298 K): *δ* (ppm) 171.2, 166.1, 156.1, 147.2, 146.5, 142.9, 140.2, 140.2, 132.3, 130.6, 128.6, 121.6, 61.6, 60.5, 53.5, 29.8, 23.1, 21.1, 16.5, 16.2, 14.6, 14.3.

nESI-MS$^+$: m/z calculated for $C_{55}H_{57}B_2BrF_4N_4O_4$: 1033.4072, found 1033.4051 $[M+NH_4]^+$ (for $C_{55}H_{57}B_2{}^{79}BrF_4N_4O_4$).

IR: ṽ (cm^{-1}): 2926, 1714, 1543, 1189, 735.

HPLC (Method A): Rt (min): 7.5.

6-azidohexanoic acid (7)

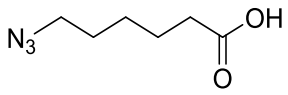

Bromohexanoic acid (0.25 g, 1.28 mmol, 1 eq) was added to a round-bottom flask and dissolved in 20 mL of dimethylsulfoxide. Next, sodium azide (0.12 g, 1.92 mmol, 1.5 eq) was added to the flask, and the reaction mixture was stirred at room temperature for 16 hours. After this time, 50 mL of water was added to the flask and it was extracted with diethyl ether (3 x 150 mL). The organic phases were collected and dried over $MgSO_4$, then filtered and concentrated under reduced pressure to yield a yellow oil.

Yield: 66% (0.13 g).

^{1}H NMR (500 MHz, $CDCl_3$, 298 K): δ 10.62 (s, 1H, COO*H*), 3.24 (t, *J* = 6.9 Hz, 2H, C*H*$_2$N$_3$), 2.33 (t, *J* = 7.4 Hz, 2H, C*H*$_2$COOH), 1.66 – 1.60 (m, 2H, C*H*$_2$CH$_2$N$_3$), 1.60 – 1.54 (m, 2H, C*H*$_2$CH$_2$COOH), 1.47 – 1.34 (m, 2H, N$_3$CH$_2$CH$_2$C*H*$_2$).

^{13}C{^{1}H} NMR (126 MHz, $CDCl_3$, 298 K): δ 179.9, 51.2, 33.8, 28.5, 26.1, 24.1.

nESI-MS^{-}: m/z calculated for $C_6H_{11}N_3O_3$: 156.0781, found 156.0778 $[M-H]^-$.

IR: ṽ (cm^{-1}): 2942, 2091, 1705, 1250.

HPLC (Method B): Rt (min): 8.4.

3,5-bis(bromomethyl)-2,4,6-triethylbenzyl 6-azidohexanoate (8)

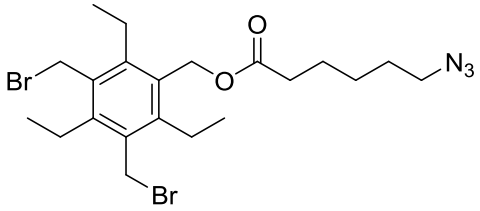

1,3,5-tris(bromomethyl)-2,4,6-triethylbenzene (compound **1**) (0.23 g, 0.53 mmol, 1 eq), 6-azidohexanoic acid (compound **7**) (0.08 g, 0.53 mmol, 1 eq) and potassium carbonate (0.11 g, 0.79 mmol, 1.5 eq) were dissolved in 20 mL of acetonitrile and were reacted as per **General procedure (A)**. The final product was purified by silica gel column chromatography with a solvent system of 2-20% ethyl acetate in hexane.

Yield: 29% (0.08 g).

^{1}H NMR (500 MHz, $CDCl_3$, 298 K): δ (ppm) 5.18 (s, 2H, CH_2O), 4.60 (s, 4H, CH_2Br), 3.26 (t, *J* = 6.9 Hz, 2H, C$H_2$$N_3$), 2.96 (q, *J* = 7.6 Hz, 2H, p-C$H_2$$CH_3$), 2.84 (q, *J* = 7.6 Hz, 4H, o-C$H_2$$CH_3$), 2.35 (t, *J* = 7.5 Hz, 2H, COCH_2), 1.71 – 1.64 (m, 2H, $COCH_2$CH_2), 1.64 – 1.56 (m, 2H, C$H_2$$CH_2$$N_3$), 1.44 – 1.39 (m, 2H, C$H_2$$CH_2$$CH_2$$N_3$), 1.35 (t, *J* = 7.6 Hz, 3H, p-CH_2CH_3), 1.25 (t, *J* = 7.7 Hz, 6H, o-CH_2CH_3).

^{13}C{^{1}H} NMR (126 MHz, $CDCl_3$, 298 K): *δ* (ppm) 173.6, 145.9, 145.1, 132.4, 130.9, 60.6, 51.3, 34.2, 28.9, 28.6, 26.3, 24.6, 22.9, 22.7, 16.1, 15.7.

nESI-MS^{+}: m/z calculated for $C_{21}H_{31}Br_2N_3O_2$: 535.1102, found 535.1085 $[M+NH_4]^+$ (for $C_{21}H_{31}{}^{79}Br^{81}BrN_3O_2$).

IR: ṽ (cm^{-1}): 2969, 2095, 1732, 1243.

HPLC (Method A): Rt (min): 7.2.

3,5-bis(bromomethyl)-2,4,6-triethylbenzyl tert-butyl succinate (9)

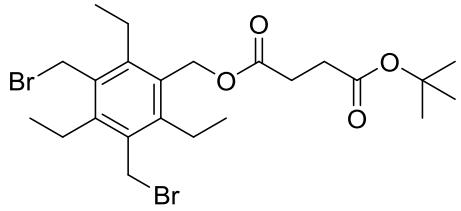

1,3,5-tris(bromomethyl)-2,4,6-triethylbenzene (compound **1**) (0.25 g, 0.56 mmol, 1 eq), 4-(tert-butoxy)-4-oxobutanoic acid (0.10 g, 0.56 mmol, 1 eq) and potassium carbonate (0.12 g, 0.85 mmol, 1.5 eq) were dissolved in 20 mL of acetonitrile and were reacted as per **General procedure (A)**. The final product was purified by silica gel column chromatography with a solvent system of 10% ethyl acetate in hexane.

Yield: 30% (0.09 g).

^{1}H NMR (500 MHz, $CDCl_3$, 298 K): *δ* (ppm) 5.20 (s, 2H, C*H*$_2$O), 4.59 (s, 4H, C*H*$_2$Br), 2.95 (q, J = 7.7 Hz, 2H, p-C*H*$_2$CH$_3$), 2.84 (q, J = 7.6 Hz, 4H, o-C*H*$_2$CH$_3$), 2.60 (s, 2H, COC*H*$_2$), 2.54 (s, 2H, C*H*$_2$CO), 1.42 (s, 9H, C(C*H*$_3$)$_3$), 1.35 (t, J = 7.6 Hz, 3H, p-CH$_2$C*H*$_3$), 1.25 (t, J = 7.6 Hz, 6H, o-CH$_2$C*H*$_3$).

^{13}C{^{1}H} NMR (126 MHz, $CDCl_3$, 298 K): δ (ppm) 172.7, 171.5, 146.0, 145.2, 132.4, 130.8, 80.9, 60.9, 30.4, 29.6, 28.9, 28.2, 22.9, 22.9, 16.1, 15.8.

nESI-MS^{+}: m/z calculated for $C_{23}H_{34}Br_2O_4$: 552.1143, found 552.1132 $[M+NH_4]^+$ (for $C_{23}H_{34}{}^{79}Br^{81}BrO_4$).

IR: ν̃ (cm^{-1}): 2965, 1718, 1260, 997, 796.

HPLC (Method B): Rt (min): 12.3.

3,5-bis(bromomethyl)-2,4,6-trimethylbenzyl benzoate (10)

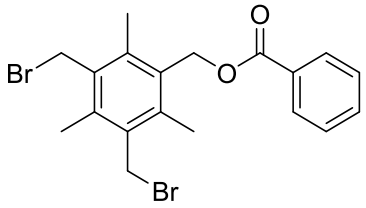

1,3,5-tris(bromomethyl)-2,4,6-trimethylbenzene (0.20 g, 0.50 mmol, 1 eq), benzoic acid (0.06 g, 0.50 mmol, 1 eq) and potassium carbonate (0.10 g, 0.75 mmol, 1.5 eq) were dissolved in 20 mL of acetonitrile and were reacted as per **General procedure (A)**. The final product was purified by silica gel column chromatography with a solvent system of 10% ethyl acetate in hexane.

^{1}H NMR (500 MHz, $CDCl_3$, 298 K): *δ* (ppm) 8.07 – 7.98 (m, 2H, o-Ar*H*), 7.60 – 7.52 (m, 1H, p-Ar*H*), 7.48 – 7.37 (m, 2H, m-Ar*H*), 5.48 (s, 2H, C*H*$_2$O), 4.61 (s, 4H, C*H*$_2$Br), 2.51 (s, 6H, o-C*H*$_3$), 2.50 (s, 3H, p-C*H*$_3$).

^{13}C{^{1}H} NMR (126 MHz, $CDCl_3$, 298 K): δ (ppm) 166.6, 139.0, 138.2, 133.2, 131.6, 130.0, 129.8, 128.5, 61.9, 31.0, 30.3, 15.9, 15.5.

nESI-MS^{+}: m/z calculated for $C_{19}H_{20}Br_2O_2$: 458.0148, found 458.0143 $[M+NH_4]^+$ (for $C_{19}H_{20}{}^{79}Br^{81}BrO_2$).

IR: ṽ (cm^{-1}): 2922, 1713, 1451, 1259, 1024, 936, 711.

HPLC (Method B): Rt (min): 14.9.

(5-(bromomethyl)-2,4,6-trimethyl-1,3-phenylene)bis(methylene) dibenzoate (11)

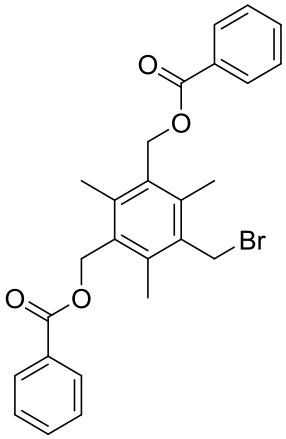

This product was obtained from the synthesis and purification of compound **10**.

^{1}H NMR (500 MHz, $CDCl_3$, 298 K): *δ* (ppm) 8.07 – 8.02 (m, 4H, o-Ar*H*), 7.60 – 7.52 (m, 2H, p-Ar*H*), 7.46 – 7.39 (m, 4H, m-Ar*H*), 5.51 (s, 4H, C*H*$_2$O), 4.65 (s, 2H, C*H*$_2$Br), 2.56 (s, 3H, C*H*$_3$), 2.55 (s, 6H, C*H*$_3$).

^{13}C{^{1}H} NMR (126 MHz, $CDCl_3$, 298 K): δ (ppm) 166.7, 140.0, 139.2, 133.2, 133.0, 131.4, 130.1, 129.8, 128.5, 62.1, 30.5, 16.4, 15.9.

nESI-MS^{+}: m/z calculated for $C_{26}H_{25}BrO_4$: 500.1255, found 500.1250 $[M+NH_4]^+$ (for $C_{26}H_{25}{}^{79}BrO_4$).

IR: ν̃ (cm^{-1}): 2922, 1715, 1269, 1106, 932, 703.

HPLC (Method B): Rt (min): 16.5.

3,5-bis(bromomethyl)-2,4,6-trimethylbenzyl tert-butyl succinate (12)

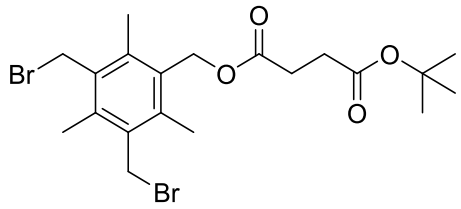

1,3,5-tris(bromomethyl)-2,4,6-triethylbenzene (0.25 g, 0.62 mmol, 1 eq), 4-(tert-butoxy)-4-oxobutanoic acid (0.11 g, 0.62 mmol, 1 eq) and potassium carbonate (0.13 g, 0.93 mmol, 1.5 eq) were dissolved in 20 mL of acetonitrile and were reacted as per **General procedure (A)**. The final product was purified by silica gel column chromatography with a solvent system of 10% ethyl acetate in hexane.

Yield: 22% (0.07 g).

^{1}H NMR (500 MHz, $CDCl_3$, 298 K): δ (ppm) 5.23 (s, 2H, CH_2O), 4.58 (s, 4H, CH_2Br), 2.61 – 2.56 (m, 2H, COCH_2), 2.56 – 2.49 (m, 2H, CH_2CO), 2.46 (s, 3H, p-CH_3), 2.42 (s, 6H, o-CH_3), 1.41 (s, 9H, C(CH_3)$_3$).

^{13}C{^{1}H} NMR (126 MHz, $CDCl_3$, 298 K): δ (ppm) 172.5, 171.4, 138.9, 138.1, 133.1, 131.4, 80.8, 61.5, 30.4, 30.2, 29.4, 28.1, 15.8, 15.4.

nESI-MS^{+}: m/z calculated for $C_{20}H_{28}Br_2O_4$: 510.0673, found 510.0655 $[M+NH_4]^+$ (for $C_{20}H_{28}{}^{79}Br^{81}BrO_4$).

IR: $\tilde{\nu}$ (cm^{-1}): 2931, 1727, 1148, 962, 731.

HPLC (Method B): Rt (min): 16.9.

General procedure (B) for the synthesis of disubstituted compounds

The monosubstituted tripodal ester derivative, the new carboxylic acid derivative and potassium carbonate were added to a round-bottom flask, followed by acetonitrile. The reaction mixture was stirred and heated to 100 ºC, then connected to a reflux condenser. The reaction was monitored by TLC, and after 16 hours heating was stopped. The mixture was left to cool to room temperature, and the solvent was removed under reduced pressure. The product was dissolved in dichloromethane and washed three times with NaOH(aq) 1 M. The organic layers were collected and dried with anhydrous $MgSO_4$, then the solvent was removed under reduced pressure to yield a powder. The final product was purified by silica gel column chromatography with a solvent system of ethyl acetate in hexane in different ratios as specified in each case. In some cases it was possible to isolate the trisubstituted product as well as the disubstituted material.

3-(bromomethyl)-5-(((4-(5,5-difluoro-1,3,7,9-tetramethyl-5*H*-4λ^4,5λ^4-dipyrrolo[1,2-*c*:2',1'-*f*][1,3,2]diazaborinin-10-yl)benzoyl)oxy)methyl)-2,4,6-triethylbenzyl tert-butyl succinate (13)

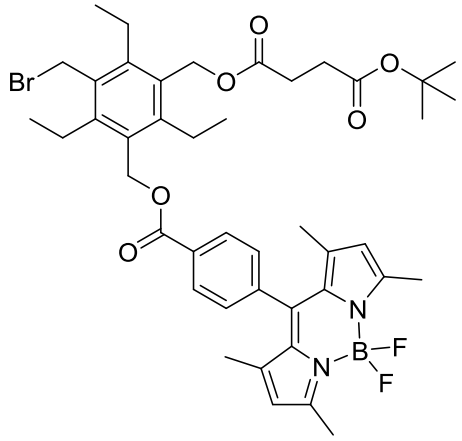

3,5-bis(bromomethyl)-2,4,6-triethylbenzyl 4-(5,5-difluoro-1,3,7,9-tetramethyl-5*H*-4λ^4,5λ^4-dipyrrolo[1,2-*c*:2',1'-*f*][1,3,2]diazaborinin-10-yl)benzoate (compound **5**) (25 mg, 30 µmol, 1 eq), 4-(tert-butoxy)-4-oxobutanoic acid (6 mg, 30 µmol, 1 eq) and potassium carbonate (7 mg, 50 µmol, 1.5 eq) were dissolved in 10 mL of acetonitrile and were reacted as per **General procedure (B)**. The final product was purified by silica gel column chromatography with a solvent system of 15-45% ethyl acetate in hexane.

Yield: 18% (5 mg).

^{1}H NMR (500 MHz, $CDCl_3$, 298 K): *δ* (ppm) 8.16 (d, J = 8.3 Hz, 2H, o-Ar*H*), 7.38 (d, J = 8.5 Hz, 2H, m-Ar*H*), 5.98 (s, 2H, NC(CH_3)C*H*C(CH_3)), 5.51 (s, 2H, CH_2Br), 5.26 (s, 4H, CH_2O), 2.86 (q, J = 7.6 Hz, 4H, C$H_2$$CH_3$), 2.78 (q, J = 7.5 Hz, 2H, C$H_2$$CH_3$), 2.61 – 2.56 (m, 4H, COCH_2CH_2CO), 2.55 (s, 6H, NC(CH_3)CHC(CH_3)), 1.42 (s, 9H, C(CH_3)$_3$), 1.34 (s, 6H, NC(CH_3)CHC(CH_3)), 1.25 – 1.18 (m, 9H, CH_2CH_3).

^{13}C{^{1}H} NMR (126 MHz, $CDCl_3$, 298 K): *δ* (ppm) 207.0, 172.7, 171.5, 166.2, 156.2, 147.2, 147.1, 142.8, 140.2, 131.1, 130.8, 130.6, 130.2, 130.0, 128.6, 121.6, 80.9, 61.7, 61.1, 31.1, 30.4, 29.5, 28.2, 23.1, 23.1, 16.6, 16.5, 14.8, 14.7.

EI-MS$^+$: m/z calculated for $C_{43}H_{52}BBrF_2N_2O_6$: 820.3, found 820.4 $[M]^{+\cdot}$ (for $C_{43}H_{52}B^{79}BrF_2N_2O_6$).

IR: ṽ (cm^{-1}): 2923, 1731, 1546, 1148, 739.

HPLC (Method B): Rt (min): 7.1.

3-(((6-azidohexanoyl)oxy)methyl)-5-(bromomethyl)-2,4,6-triethylbenzyl tert-butyl succinate (14)

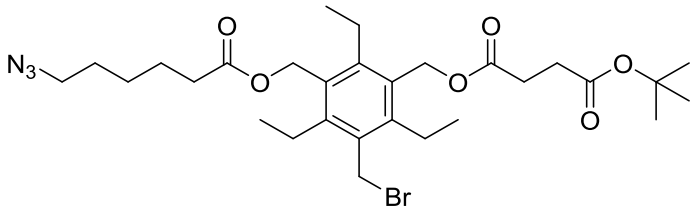

3,5-bis(bromomethyl)-2,4,6-triethylbenzyl tert-butyl succinate (compound **9**) (0.24 g, 0.45 mmol, 1 eq), 6-azidohexanoic acid (compound **7**) (0.07 g, 0.45 mmol, 1 eq) and potassium carbonate (0.09 g, 0.67 mmol, 1.5 eq) were dissolved in 25 mL of acetonitrile and were reacted as per **General procedure (B)**. The final product was purified by silica gel column chromatography with a solvent system of 5-20% ethyl acetate in hexane.

Yield: 30% (0.08 g).

^{1}H NMR (500 MHz, $CDCl_3$, 298 K): δ (ppm) 5.19 (d, J = 10.1 Hz, 4H, CH_2O), 4.61 (s, 2H, CH_2Br), 3.25 (t, J = 6.9 Hz, 2H, COCH_2CH$_2$CH$_2$CH$_2$CH$_2$N$_3$), 2.85 (q, J = 6.1 Hz, 4H, CH_2CH$_3$), 2.73 (q, J = 7.6 Hz, 2H, CH_2CH$_3$), 2.58 (d, J = 7.0 Hz, 2H, COCH_2CH$_2$CO), 2.54 (d, J = 5.8 Hz, 2H, COCH$_2$CH_2CO), 2.34 (t, J = 7.5 Hz, 2H, CH_2N$_3$), 1.67 (p, J = 7.5 Hz, 2H, CH_2CH$_2$N$_3$), 1.59 (p, J = 7.1 Hz, 2H, COCH$_2$CH_2CH$_2$CH$_2$CH$_2$N$_3$), 1.44 – 1.37 (m, 11H, CH_2CH$_2$CH$_2$N$_3$, C(CH_3)$_3$), 1.29 – 1.21 (m, 6H, CH$_2$CH_3), 1.16 (t, J = 7.5 Hz, 3H, CH$_2$CH_3).

^{13}C{^{1}H} NMR (126 MHz, $CDCl_3$, 298 K): δ (ppm) 173.5, 172.6, 171.4, 146.7, 145.9, 145.9, 132.0, 130.5, 130.4, 80.8, 60.9, 60.7, 51.2, 34.1, 30.3, 29.5, 29.1, 28.6, 28.1, 26.3, 24.5, 22.9, 16.3, 16.1.

nESI-MS^{+}: m/z calculated for $C_{29}H_{44}BrN_3O_6$: 627.2752, found 627.2740 $[M+NH_4]^+$ (for $C_{29}H_{44}{}^{79}BrN_3O_6$).

IR: $\tilde{\nu}$ (cm^{-1}): 2974, 2095, 1728, 1143.

HPLC (Method B): Rt (min): 12.3.

3,5-bis(((6-azidohexanoyl)oxy)methyl)-2,4,6-triethylbenzyl tert-butyl succinate (15)

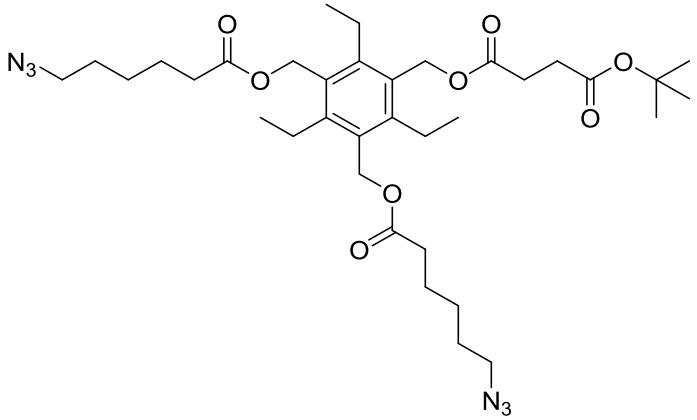

This product was obtained from the synthesis and purification of compound **14**.

Yield: 35% (0.11 g).

^{1}H NMR (500 MHz, $CDCl_3$, 298 K): δ (ppm) 5.22 (s, 2H, CH_2O), 5.20 (s, 4H, CH_2O), 3.24 (t, J = 6.9 Hz, 4H, COCH_2CH$_2$CH$_2$CH$_2$CH$_2$N$_3$), 2.74 (q, J = 7.5 Hz, 6H, CH_2CH$_3$), 2.60 – 2.51 (m, 4H, COCH_2CH_2CO), 2.33 (t, J = 7.5 Hz, 4H, CH_2N$_3$), 1.66 (p, J = 7.6 Hz, 4H, CH_2CH$_2$N$_3$), 1.59 (p, J = 7.6 Hz, 4H, COCH$_2$CH_2CH$_2$CH$_2$CH$_2$N$_3$), 1.43 – 1.37 (m, 13H, CH_2CH$_2$CH$_2$N$_3$, C(CH_3)$_3$), 1.17 (t, J = 7.5 Hz, 9H, CH$_2$CH_3).

^{13}C{^{1}H} NMR (126 MHz, $CDCl_3$, 298 K): δ (ppm) 173.5, 172.5, 171.3, 146.7, 146.7, 130.1, 80.7, 77.4, 77.1, 76.9, 60.9, 60.7, 51.2, 34.1, 30.3, 29.4, 28.6, 28.0, 26.3, 24.5, 22.9, 16.3.

APCI-MS^{+}: m/z calculated for $C_{35}H_{54}N_6O_8$: 704.4347, found 704.4345 $[M+NH_4]^+$, 709.3901, found 709.3901 $[M+Na]^+$.

IR: $\tilde{\nu}$ (cm^{-1}): 2935, 2095, 1728, 1144.

HPLC (Method B): Rt (min): 12.3.

General procedure (C) for the synthesis of trisubstituted compounds

The disubstituted tripodal ester derivative, the new carboxylic acid derivative and potassium carbonate were added to a round-bottom flask, followed by acetonitrile. The reaction mixture was stirred and heated to 100 ºC, then connected to a reflux condenser. The reaction was monitored by TLC, and after 16 hours heating was stopped. The mixture was left to cool to room temperature, and the solvent was removed under reduced pressure. The product was dissolved in dichloromethane and washed three times with NaOH(aq) 1 M. The organic layers were collected and dried with anhydrous $MgSO_4$, then the solvent was removed under reduced pressure to yield a powder. The final product was purified by silica gel column chromatography with a solvent system of ethyl acetate in hexane in different ratios as specified in each case.

3-(((6-azidohexanoyl)oxy)methyl)-5-(((4-(5,5-difluoro-1,3,7,9-tetramethyl-5*H*-4λ^4,5λ^4-dipyrrolo[1,2-*c*:2',1'-*f*][1,3,2]diazaborinin-10-yl)benzoyl)oxy)methyl)-2,4,6-triethylbenzyl tert-butyl succinate (16)

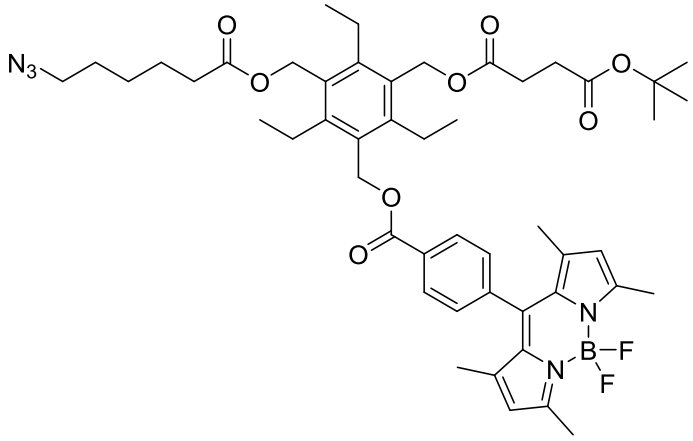

3-(((6-azidohexanoyl)oxy)methyl)-5-(bromomethyl)-2,4,6-triethylbenzyl tert-butyl succinate (compound **14**) (39 mg, 60 µmol, 1 eq), 4-(5,5-difluoro-1,3,7,9-tetramethyl-5*H*-4λ^4,5λ^4-dipyrrolo[1,2-*c*:2',1'-*f*][1,3,2]diazaborinin-10-yl)benzoic acid (compound **2**) (24 mg, 60 µmol, 1 eq) and potassium carbonate (13 mg, 90 µmol, 1.5 eq) were dissolved in 10 mL of acetonitrile and were reacted as per **General procedure (C)**. The final product was purified by silica gel column chromatography with a solvent system of 15-35% ethyl acetate in hexane.

Yield: 6% (3 mg).

^{1}H NMR (500 MHz, $CDCl_3$, 298 K): *δ* (ppm) 8.15 (d, J = 8.0 Hz, 2H, o-Ar*H*), 7.38 (d, J = 8.3 Hz, 2H, m-Ar*H*), 5.98 (s, 2H, NC(CH_3)C*H*C(CH_3)), 5.51 (s, 2H, C*H*$_2$O-BODIPY), 5.23 (s, 2H, C*H*$_2$O), 5.21 (s, 2H, C*H*$_2$O), 3.26 (t, J = 6.9 Hz, 2H, COC*H*$_2$$CH_2CH_2CH_2CH_2N_3$), 2.90 – 2.82 (m, 2H, C*H*$_2$$CH_3$), 2.75 (q, J = 7.5 Hz, 4H, C*H*$_2$$CH_3$), 2.62 – 2.57 (m, 4H, COC*H*$_2$C*H*$_2$CO), 2.55 (s, 6H, NC(C*H*$_3$)CHC(CH_3)), 2.34 (t, J = 7.5 Hz, 2H, C*H*$_2$$N_3$), 1.68 (p, J = 7.6 Hz, 2H, C*H*$_2$$CH_2N_3$), 1.60 (p, J = 7.1 Hz, 2H, $COCH_2$C*H*$_2$$CH_2CH_2N_3$), 1.42 (s, 9H, C(C*H*$_3$)$_3$), 1.40 – 1.13 (m, 17H, C*H*$_2$$CH_2CH_2N_3$, CH_2C*H*$_3$, NC(CH_3)CHC(C*H*$_3$), CH_2C*H*$_3$).

^{13}C{^{1}H} NMR (126 MHz, $CDCl_3$, 298 K): *δ* (ppm) 173.7, 172.7, 171.5, 146.9, 146.8, 130.6, 130.2, 130.2, 128.6, 80.9, 61.0, 60.9, 51.3, 34.2, 31.6, 31.1, 30.4, 30.3, 29.8, 29.5, 28.7, 28.2, 26.4, 24.6, 23.0, 16.5, 14.7.

IR: ṽ (cm^{-1}): 2935, 2095, 1727, 1145, 949.

HPLC (Method B): Rt (min): 14.6.

(Z)-3-(((4-(5,5-difluoro-1,3,7,9-tetramethyl-5*H*-4λ^4,5λ^4-dipyrrolo[1,2-*c*:2',1'-*f*][1,3,2]diazaborinin-10-yl)benzoyl)oxy)methyl)-2,4,6-triethyl-5-(((N-methylcarbamohydrazonoyl)thio)methyl)benzyl 4-(5,5-difluoro-1,3,7,9-tetramethyl-5*H*-4λ^4,5λ^4-dipyrrolo[1,2-*c*:2',1'-*f*][1,3,2]diazaborinin-10-yl)benzoate (17)

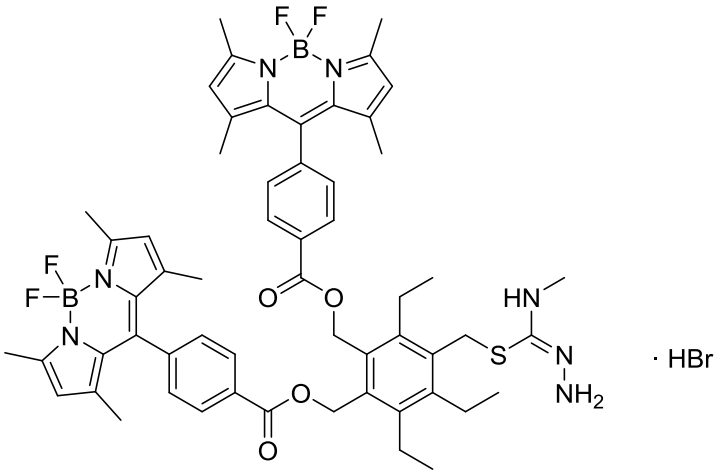

3-(bromomethyl)-5-(((4-(5,5-difluoro-1,3,7,9-tetramethyl-5*H*-4λ^4,5λ^4-dipyrrolo[1,2-*c*:2',1'-*f*][1,3,2]diazaborinin-10-yl)benzoyl)oxy)methyl)-2,4,6-triethylbenzyl 4-(5,5-difluoro-1,3,7,9-tetramethyl-5*H*-4λ^4,5λ^4-dipyrrolo[1,2-*c*:2',1'-*f*][1,3,2]diazaborinin-10-yl)benzoate (compound **6**) (46 mg, 40 µmol, 1 eq) and 4-methyl-3-thiosemicarbazide (5 mg, 40 µmol, 1 eq) were added to a flask and dissolved in 10 mL of acetonitrile. The solution was heated to 100 ^{o}C under reflux and stirred for 16 hours. After this time, heating was stopped and the reaction mixture was left to cool down. The solvent was removed under reduced pressure and the resulting solid was dissolved in chloroform and washed with water (3 x 30 mL). Chloroform was removed under reduced pressure and a brown-red solid was obtained, which was dried under vacuum.

Yield: 95% (44 mg).

^{1}H NMR (500 MHz, $CDCl_3$, 298 K): *δ* (ppm) 8.22 – 8.10 (m, 4H, o-Ar*H*), 7.36 (d, *J* = 8.2 Hz, 4H, m-Ar*H*), 5.96 (s, 4H, NC(CH_3)C*H*C(CH_3)), 5.53 (s, 4H,), 4.67 (s, 2H, C*H*$_2$O-S), 2.98 – 2.91 (m, 6H, C*H*$_2$CH3), 2.89 – 2.82 (m, 3H, SCNHC*H*$_3$), 2.53 (s, 12H, NC(C*H*$_3$)CHC(CH_3)), 1.32 (s, 12H, NC(CH_3)CHC(C*H*$_3$)), 1.28 – 1.20 (m, 9H, CH_2C*H*$_3$).

^{13}C{^{1}H} NMR (126 MHz, $CDCl_3$, 298 K): *δ* (ppm) 166.2, 156.1, 146.7, 142.9, 140.1, 131.0, 130.6,128.5, 121.6, 61.8, 32.0, 31.5, 31.1, 30.8, 30.3, 29.8, 25.2, 23.4, 23.2, 22.8, 21.5, 17.9, 16.6, 14.6.

LC-MS$^+$: m/z calculated for $C_{57}H_{63}B_2F_4N_7O_4S$: 1040.4874, found 1040.4874 $[M+H]^+$.

IR: ṽ (cm^{-1}): 2981, 1628, 1521, 1158, 731.

HPLC (Method B): Rt (min): 11.1.

Reaction conditions optimisation

General Procedure

1,3,5-tris(bromomethyl)-2,4,6-trimethylbenzene or 1,3,5-tris(bromomethyl)-2,4,6-triethylbenzene (compound **1**) (in the case of the reaction time study), benzoic acid and potassium carbonate were added to a round-bottom flask, followed by acetonitrile. The reaction mixture was stirred at the temperature and for the time specified in each case. The ratio of the different products in the final mixture was measured in different ways according to each factor screen.

Temperature screen

In this case, after cooling to room temperature, the solvent was removed under reduced pressure. The product was dissolved in dichloromethane and washed three times with NaOH(aq) 1 M. The organic phase was evaporated to dryness and the products were isolated by silica gel column chromatography (10% ethyl acetate in hexane).

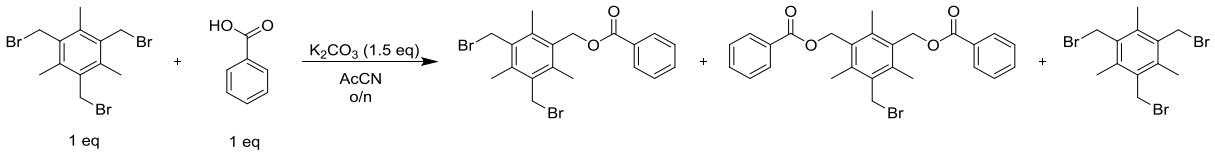

Temperature (ºC)	Non-reacted starting material (%)	Monosubstituted product (%)	Disubstituted product (%)
RT (25)	12	60	28
40	27	42	31
60	42	26	32

1,3,5-tris(bromomethyl)-2,4,6-triethylbenzene stoichiometry

As for the temperature screen, after cooling to room temperature, the solvent was removed under reduced pressure. The product was dissolved in dichloromethane and washed three times with NaOH(aq) 1 M. The organic phase was evaporated to dryness and the products were isolated by silica gel column chromatography (10% ethyl acetate in hexane).

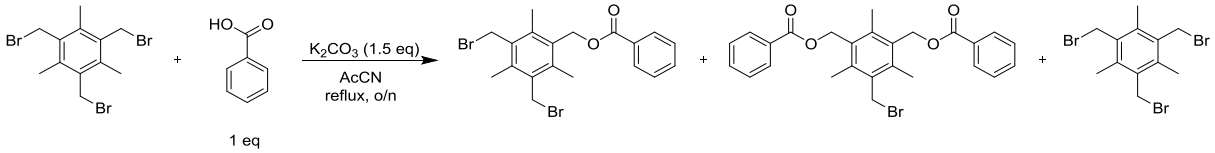

Starting material equivalents	Non-reacted starting material (%)	Monosubstituted product (%)	Disubstituted product (%)
2	9	77	14
5	34	66	-

Reaction time

To obtain the ratio of products at each time of interest, an aliquot of the reaction mixture at such time was taken. It was filtered through cotton wool, and dried. ^{1}H NMR spectroscopy was then carried out, and from the integration of three peaks corresponding to the starting material, the mono- and the disubstituted products, respectively, the ratio of each product in the mixture was calculated.

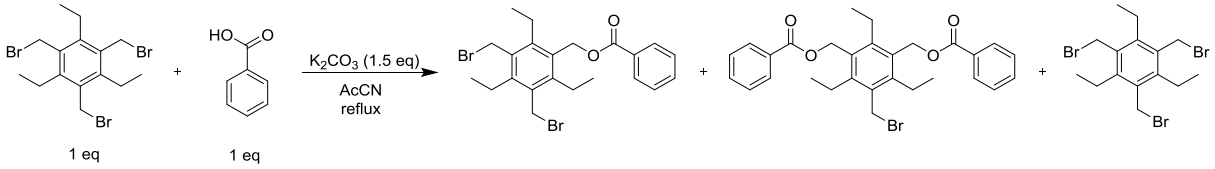

Time (h)	Non-reacted starting material (%)	Monosubstituted product (%)	Disubstituted product (%)
0	49	40	11
1	41.5	44	14.5
2	42	45	13
3	43	43	14
4	42	45	13
6	42	45	13
8	43	44	13
24	40	46	14
26	40	46	14

Radiolabelling experiments involving zirconium-89

3,14,25-trihydroxy-2,10,13,21,24,32-hexaoxo-3,9,14,20,25,31-hexaazapentatriacontan-35-oic acid (18)

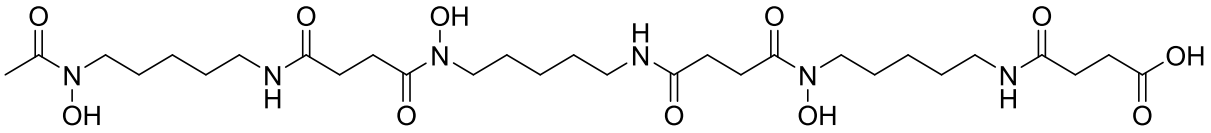

Deferoxamine mesylate salt (100 mg, 150 μmol, 1 eq) was added to a Schlenk flask and dissolved in 20 mL of N,N'-dimethylformamide under a flow of nitrogen. Next, succinic anhydride (18 mg, 180 μmol, 1.2 eq) dissolved in 10 drops of dimethylsulfoxide was dropwise added, followed by triethylamine (20 μL, 143 μmol). The reaction mixture was stirred at room temperature for 48 hours. After this time, the solvent was removed under vacuum and the oil obtained was washed with petroleum ether a few times until it yielded a light brown powder.

Yield: 79% (79 mg).

ESI-MS: m/z calculated for $C_{29}H_{52}N_6O_{11}$: 659.3621, found 659.3631 $[M-H]^-$; 661.3767, found 661.3763 $[M+H]^+$; 683.3586, found 683.3625 $[M+Na]^+$.

HPLC (Method A): Rt (min): 6.9.

***N*^{1}-(5-((3,5-bis(bromomethyl)-2,4,6-triethylbenzyl)amino)pentyl)-*N*^{1}-hydroxy-*N*^{4}-(5-(*N*-hydroxy-4-((5-(N-hydroxyacetamido)pentyl)amino)-4-oxobutanamido)pentyl)succinamide (19)**

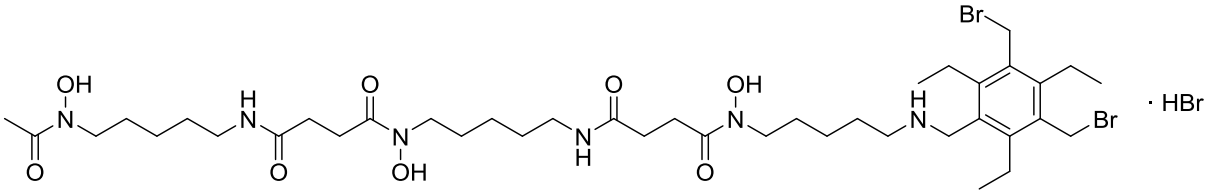

Deferoxamine mesylate salt (30 mg, 54 μmol, 1 eq) was added to a Schlenk flask and dissolved in 10 mL of N,N'-dimethylformamide under a flow of nitrogen. While stirring at 25 ºC, 1,3,5-tris(bromomethyl)-2,4,6-triethylbenzene (compound **1**) (24 mg, 55 μmol, 1.2 eq) was added, followed by triethylamine (6 μL, 43 μmol). After 48 hours stirring at this temperature, the reaction was stopped and the solvent was removed under vacuum. The oil obtained was washed with diethyl ether a few times until it yielded a pale brown powder.

ESI-MS$^-$: m/z calculated for $C_{40}H_{68}Br_2N_6O_8$: 919.3377, found 919.3429 $[M-H]^-$ (for $C_{40}H_{68}{}^{79}Br^{81}BrN_6O_8$).

HPLC (Method A): Rt (min): 7.4.

Synthesis of zirconium-89

The positron-emitting radiotracer ^{89}Zr was prepared at the Wales Research and Diagnostic Positron Emission Tomography Imaging Centre via the $^{89}Y(p,n)^{89}Zr$ reaction using the cyclotron CYCLONE 18/9.

General procedure for the radiolabelling of DFO-based compounds (20 and 21)

The radioisotope zirconium-89 was obtained in 1 M (aq) oxalic acid, and in order to be suitable for radiolabelling the compounds of interest, the pH was adjusted to 6.8 - 7.5 by the addiction of a 1 M solution of sodium carbonate. Next, the pH-adjusted $^{89}Zr^{4+}$ solution was added to each of the two compounds (compounds **18** and **19**) separately in dimethylsulfoxide, and the two reaction mixtures were stirred at room temperature for 1 hour. After this time, the radiolabelling efficiency was determined by radio-TLC using an eluent of 50 mM DTPA (pH 5.5). The radiolabelling efficiency for both compounds was shown to be 100%.

7.2.2. Synthesis of compounds from Chapter 3

[7-13] Bombesin fragment [Leu-His-Gly-Val-Ala-Trp-Gln] (22)

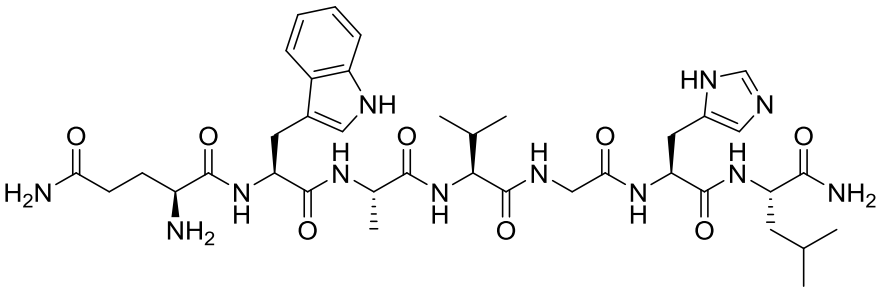

First, the Rink amide resin (1.00 g, loading: 0.59 mmol/g) was swelled for 1 hour in dichloromethane at room temperature, followed by 30 minutes in N,N'-dimethylformamide at 60 ºC. After swelling, the resin was deprotected with a solution of 20% piperidine in N,N'-dimethylformamide for 5 and 10 minutes, and then the coupling with the first amino acid, Fmoc-Leu-OH (3 eq) was carried out with solutions of HBTU (0.6 M in DMF), HOBt (0.5 M in DMF) and DIPEA (2 M in DMF), for 5 minutes at 75 ºC. After the coupling, the amino acid was deprotected with a solution of 20% piperidine in N,N'-dimethylformamide for 3 and 10 minutes, and then the coupling with the second amino acid, Fmoc-His(Trt)-OH (3 eq), was performed using HBTU (0.6 M in DMF), HOBt (0.5 M in DMF) and DIPEA (2 M in DMF) for 60 minutes at room temperature. The following amino acids (Fmoc-Gly-OH, Fmoc-Val-OH, Fmoc-Ala-OH, Fmoc-Trp(Boc)-OH, Fmoc-Gln(Trt)-OH, each 3 eq) were coupled to the peptide following the same conditions as for Fmoc-Leu-OH, for 5 minutes at 75 ºC. Finally, the peptide was deprotected and a pre-cleavage wash with dichloromethane was performed. Cleavage of the peptide from the resin was achieved by treatment with TFA / water / phenol / TIPS (5 mL, 88:5:5:2, v/v/v/v) for 2 hours. After this time, the suspension of the resin in the cleavage "cocktail" was filtered and the peptide was precipitated by adding cold diethyl ether. The peptide was collected by centrifugation and washed further with diethyl ether to yield a white solid.

Yield: 76% (0.36 g).

nESI-MS$^+$: m/z calculated for $C_{38}H_{56}N_{12}O_8$**:** 809.4417, found 809.4417 $[M+H]^+$, 831.4236, found 831.4227 $[M+Na]^+$.

HPLC (Method A): Rt (min): 7.1.

(S)-N1-((2S,5S,8S,14S,17S)-14-((1*H*-imidazol-5-yl)methyl)-17-carbamoyl-1-(1*H*-indol-3-yl)-8-isopropyl-5,19-dimethyl-3,6,9,12,15-pentaoxo-4,7,10,13,16-pentaazaicosan-2-yl)-2-(3,14,25-trihydroxy-2,10,13,21,24,32-hexaoxo-3,9,14,20,25,31-hexaazapentatriacontan-35-amido)pentanediamide (23)

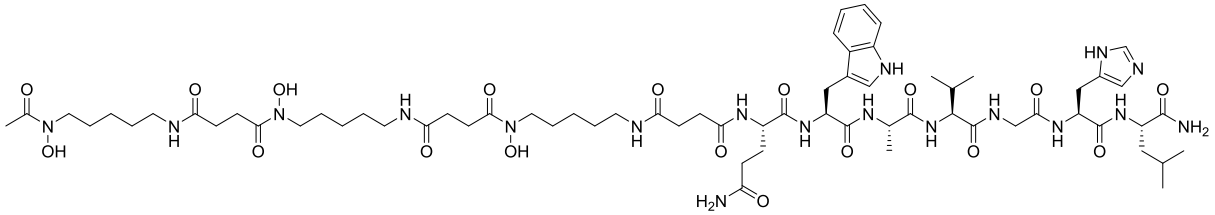

3,14,25-trihydroxy-2,10,13,21,24,32-hexaoxo-3,9,14,20,25,31-hexaazapentatriacontan-35-oic acid (compound **18**) (16 mg, 25 µmol, 1 eq) was added to a Schlenk flask and dissolved in 1 mL of N,N'-dimethylformamide. HATU (9 mg, 25 µmol, 1 eq) was added to the flask and the mixture was stirred at 25 ºC for 10 minutes under a nitrogen atmosphere. Next, the [7-13] bombesin fragment (compound **22**) (20 mg, 25 µmol, 1 eq) was added and the solution was stirred under the same conditions for 20 minutes. After this time, N,N'-diisopropylethylamine (4 µL, 25 µmol, 1 eq) was added and the reaction mixture was stirred for 16 hours. Finally, the solvent was removed under reduced pressure and a pale pink solid was obtained.

ESI-MS$^+$: m/z calculated for $C_{67}H_{105}N_{17}O_{19}$**:** 1451.7773, found 1451.8061 $[M]^{+\cdot}$, 1474.7665, found 1474.7894 $[M+Na]^+$.

Tert-butyl (6S,9S,12S,15S,21S,24S)-21-((1*H*-imidazol-5-yl)methyl)-9-((1*H*-indol-3-yl)methyl)-6-(3-amino-3-oxopropyl)-24-carbamoyl-15-isopropyl-12,26-dimethyl-4,7,10,13,16,19,22-heptaoxo-5,8,11,14,17,20,23-heptaazaheptacosanoate (24)

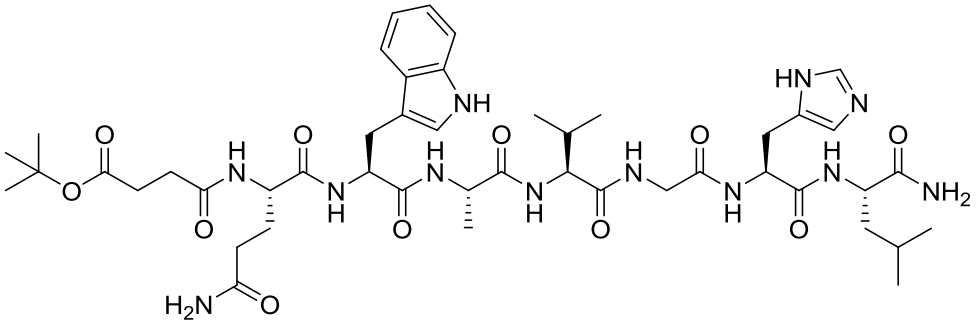

The [7-13] bombesin fragment (compound **22**) (20 mg, 25 µmol, 1.1 eq) and 4-(tert-butoxy)-4-oxobutanoic acid (4 mg, 23 µmol, 1 eq) were added to a Schlenk flask and dissolved in 1 mL of N,N'-dimethylformamide under a flow of nitrogen. Next, N,N'-diisopropylethylamine (12 µl, 68 µmol, 3 eq) and HBTU (13 mg, 34 µmol, 1.5 eq) were added to the flask and the reaction mixture was stirred for 16 hours at 25 ºC. After this time, 2 mL of water was added and extractions with ethyl acetate were carried out (3 x 10 mL). The organic phase was finally washed with 10 mL of water, before removing the solvent under reduced pressure. A pale pink solid was obtained.

nESI-MS$^+$: m/z calculated for $C_{46}H_{68}N_{12}O_{11}$**:** 965.5209, found 965.5193 $[M+H]^+$.

(6S,9S,12S,15S,21S,24S)-21-((1*H*-imidazol-5-yl)methyl)-9-((1*H*-indol-3-yl)methyl)-6-(3-amino-3-oxopropyl)-24-carbamoyl-15-isopropyl-12,26-dimethyl-4,7,10,13,16,19,22-heptaoxo-5,8,11,14,17,20,23-heptaazaheptacosanoic acid (25)

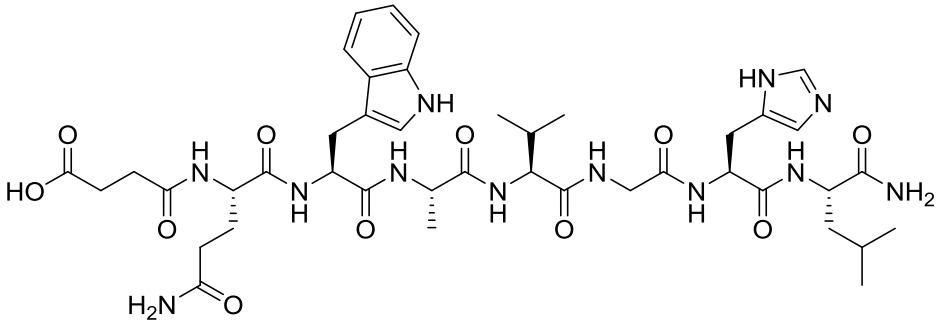

Tert-butyl (6S,9S,12S,15S,21S,24S)-21-((1*H*-imidazol-5-yl)methyl)-9-((1*H*-indol-3-yl)methyl)-6-(3-amino-3-oxopropyl)-24-carbamoyl-15-isopropyl-12,26-dimethyl-4,7,10,13,16,19,22-heptaoxo-5,8,11,14,17,20,23-heptaazaheptacosanoate (compound **24**) (11 mg, 11 µmol) was added to a flask and dissolved in 2 mL of dichloromethane. Next, 2 mL of trifluoroacetic acid was added and the reaction mixture was stirred for 16 hours at 25 ºC. After this time, the solvent was removed under reduced pressure to yield a yellowish solid.

Yield: 85% (9 mg).

ESI-MS$^+$: m/z calculated for $C_{42}H_{60}N_{12}O_{11}$**:** 909.4577, found 909.4608 $[M+H]^+$, 931.4397, found 931.4421 $[M+Na]^+$.

HPLC (Method B): Rt (min): 6.9.

7.2.3. Synthesis of compounds from Chapter 4

(2,4,6-triethyl-5-((((Z)-N-methylcarbamohydrazonoyl)thio)methyl)-1,3-phenylene)bis(methylene) (1*E*,1'*E*)-bis(methylcarbamohydrazonothioate) (26)

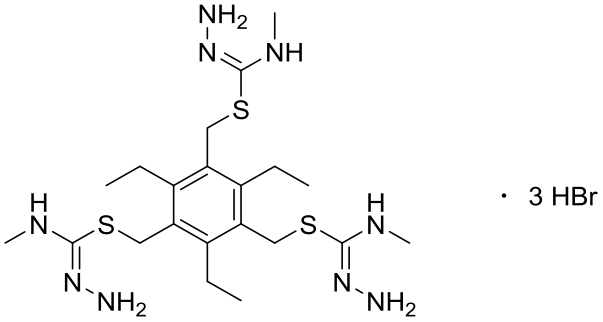

· 3 HBr

1,3,5-tris(bromomethyl)-2,4,6-triethylbenzene (compound **1**) (2.13 g, 4.80 mmol, 1 eq) and 4-methyl-3-thiosemicarbazide (2.03 g, 19.30 mmol, 4 eq) were added to a Schlenk flask and dissolved in 50 mL of acetonitrile under a nitrogen atmosphere. The flask was connected to a reflux condenser and the solution was heated to 70 ^{o}C and stirred for 48 hours. After this time, the precipitate was filtered and washed with acetonitrile (6 x 10 mL), and it was left on the freeze-drier for 16 hours. A white powder was obtained.

Yield: 69% (2.50 g).

^{1}H NMR (300 MHz, CD_3OD, 298 K): δ (ppm) 4.59 (s, 4H, CH_2S), 4.37 (s, 2H, CH_2S), 3.13 (s, 3H, NHCH_3), 3.08 – 2.99 (m, 6H, NHCH_3), 2.94 – 2.83 (m, 6H, CH_2CH$_3$), 1.41 – 1.28 (m, 9H, CH$_2$CH_3).

^{13}C{^{1}H} NMR (75 MHz, CD_3OD, 298 K): δ (ppm) 172.2, 169.1, 147.6, 147.4, 146.9, 129.1, 129.0, 128.9, 31.8, 31.1, 30.6, 24.2, 16.9, 16.8.

nESI-MS^{+}: m/z calculated for $C_{21}H_{39}N_9S_3$**:** 514.2563, found 514.2533 $[M+H]^{+}$.

IR: $\tilde{\nu}$ (cm^{-1}): 3161, 2965, 1650, 739, 664.

HPLC (Method A): Rt (min): 7.6.

E.A. ($C_{21}H_{39}N_9S_3 \cdot 3$ HBr): Calculated: C, 33.34%; H, 5.60%; N, 16.66%. Found: C, 31.69%; H, 5.77%; N, 15.67%.

(2,4,6-triethyl-5-((((*Z*)-N-ethylcarbamohydrazonoyl)thio)methyl)-1,3-phenylene)bis(methylene) (1*E*,1'*E*)-bis(ethylcarbamohydrazonothioate) (27)

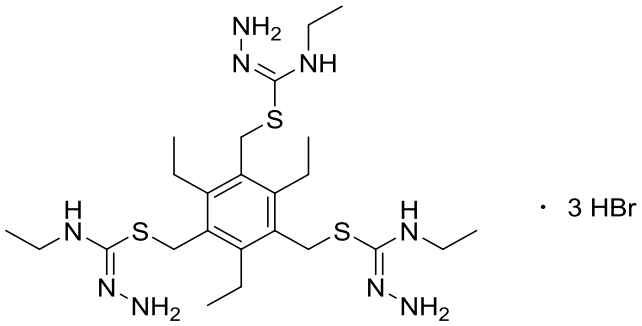

1,3,5-tris(bromomethyl)-2,4,6-triethylbenzene (compound **1**) (1.00 g, 2.26 mmol, 1 eq) and 4-ethyl-3-thiosemicarbazide (1.18 g, 9.07 mmol, 4 eq) were added to a Schlenk flask and dissolved in 25 mL of acetonitrile under a nitrogen atmosphere. The flask was connected to a reflux condenser and the solution was heated to 70 ^{o}C and stirred for 48 hours. After this time, the precipitate was filtered and washed with acetonitrile (6 x 10 mL), and it was left on the freeze-drier for 16 hours. A white powder was obtained.

Yield: 85% (1.54 g).

^{1}H NMR (300 MHz, CD_3OD, 298 K): δ (ppm) 4.55 (s, 6H, CH_2S), 3.47 (q, J = 7.2 Hz, 6H, NHCH_2CH$_3$), 2.91 (q, J = 8.0 Hz, 6H, CCH_2CH$_3$), 1.39 – 1.30 (m, 9H, CCH$_2$CH_3), 1.30 – 1.16 (m, 9H, NHCH$_2$CH_3).

^{13}C{^{1}H} NMR (75 MHz, CD_3OD, 298 K): δ (ppm) 168.3, 147.7, 129.3, 40.3, 31.9, 24.3, 16.8, 15.1.

nESI-MS^{+}: m/z calculated for $C_{24}H_{45}N_9S_3$**:** 556.3033, found 556.3023 $[M+H]^{+}$.

IR: $\tilde{\nu}$ (cm^{-1}): 3144, 2965, 1652, 723.

HPLC (Method A): Rt (min): 6.6.

E.A. ($C_{24}H_{45}N_9S_3 \cdot 3$ HBr): Calculated: C, 36.10%; H, 6.06%; N, 15.79%. Found: C, 34.08%; H, 5.87%; N, 14.33%.

(2,4,6-triethyl-5-((((*Z*)-N-phenylcarbamohydrazonoyl)thio)methyl)-1,3-phenylene)bis(methylene) (1*E*,1'*E*)-bis(phenylcarbamohydrazonothioate) (28)

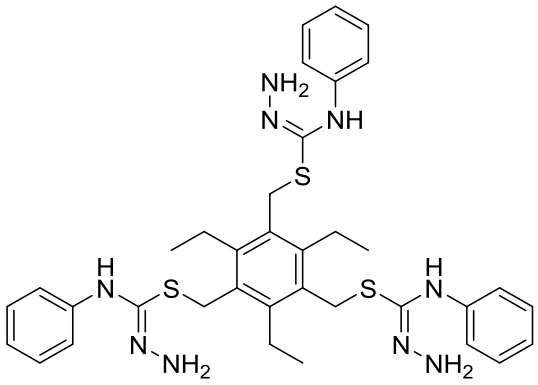

· 3 HBr

1,3,5-tris(bromomethyl)-2,4,6-triethylbenzene (compound **1**) (0.50 g, 1.13 mmol, 1 eq) and 4-phenyl-3-thiosemicarbazide (0.76 g, 4.53 mmol, 4 eq) were added to a Schlenk flask and dissolved in 20 mL of acetonitrile under a nitrogen atmosphere. The flask was connected to a reflux condenser and the solution was heated to 70 ºC and stirred for 48 hours. After this time, the precipitate was filtered and washed with acetonitrile (6 x 10 mL), and it was left on the freeze-drier for 16 hours. A clear brown powder was obtained.

Yield: 48% (0.52 g).

^{1}H NMR (500 MHz, CD_3OD, 298 K): *δ* (ppm) 7.74 – 7.03 (m, 15H, Ar-*H*), 4.55 – 4.20 (m, 4H, C*H*$_2$S), 3.85 – 3.68 (m, 2H, C*H*$_2$S), 2.98 – 2.55 (m, 6H, C*H*$_2$CH$_3$), 1.33 – 1.01 (m, 9H, CH$_2$C*H*$_3$).

^{13}C{^{1}H} NMR (126 MHz, CD_3OD, 298 K): *δ* (ppm) 131.9, 131.3, 131.1, 130.7, 130.6, 130.2, 130.0, 127.9, 124.1, 121.1, 119.2, 32.3, 23.8, 23.0, 16.6.

nESI-MS^{+}: m/z calculated for $C_{36}H_{45}N_9S_3$**:** 700.3033, found 700.3017 $[M+H]^+$.

IR: ṽ (cm^{-1}): 2928, 1494, 736.

HPLC (Method B): Rt (min): 3.3.

E.A. ($C_{36}H_{45}N_9S_3$ · 3 HBr): Calculated: C, 45.87%; H, 5.13%; N, 13.37%. Found: C, 40.87%; H, 5.15%; N, 13.32%.

(5-((((Z)-N-allylcarbamohydrazonoyl)thio)methyl)-2,4,6-triethyl-1,3-phenylene)bis(methylene) (1*E*,1'*E*)-bis(allylcarbamohydrazonothioate) (29)

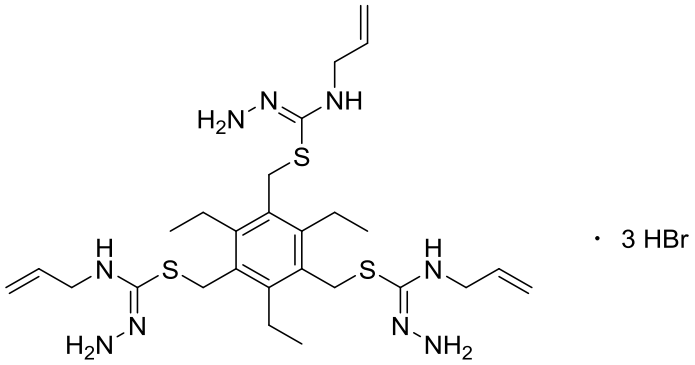

1,3,5-tris(bromomethyl)-2,4,6-triethylbenzene (compound **1**) (0.50 g, 1.13 mmol, 1 eq) and 4-allyl-3-thiosemicarbazide (0.48 g, 4.53 mmol, 4 eq) were added to a Schlenk flask and dissolved in 20 mL of acetonitrile under a nitrogen atmosphere. The flask was connected to a reflux condenser and the solution was heated to 70 ºC and stirred for 48 hours. After this time, the precipitate was filtered and washed with acetonitrile (6 x 10 mL), and it was left on the freeze-drier for 16 hours. A pale pink powder was obtained.

Yield: 89% (0.84 g).

^{1}H NMR (500 MHz, CD_3OD, 298 K): *δ* (ppm) 6.03 – 5.93 (m, 1H, C*H*=CH_2), 5.91 – 5.81 (m, 2H, C*H*=CH_2), 5.39 – 5.30 (m, 2H, CH=C*H*$_2$), 5.30 – 5.21 (m, 4H, CH=C*H*$_2$), 4.54 (s, 4H, C*H*$_2$S), 4.10 (d, J = 5.5 Hz, 2H, NHC*H*$_2$CH), 4.07 (d, J = 5.0 Hz, 4H, NHC*H*$_2$CH), 3.31 (s, 2H, C*H*$_2$S), 2.95 – 2.83 (m, 6H, C*H*$_2$$CH_3$), 1.43 – 1.27 (m, 9H, CH_2C*H*$_3$).

^{13}C{^{1}H} NMR (126 MHz, CD_3OD, 298 K): *δ* (ppm) 167.8, 146.3, 132.0, 130.9, 128.0, 116.7, 116.6, 46.0, 45.7, 30.7, 23.0, 15.4.

nESI-MS^{+}: m/z calculated for $C_{27}H_{45}N_9S_3$**:** 592.3033, found 592.3010 $[M+H]^+$.

IR: ṽ (cm^{-1}): 3137, 2968, 1656, 737.

HPLC (Method B): Rt (min): 6.6.

E.A. ($C_{27}H_{45}N_9S_3$ · 3 HBr): Calculated: C, 38.85%; H, 5.80%; N, 15.10%. Found: C, 37.70%; H, 5.72%; N, 14.10%.

3,3',3''-(((2,4,6-triethylbenzene-1,3,5-triyl)tris(methylene))tris(sulfanediyl))tris(2-aminopropanoic acid) (30)

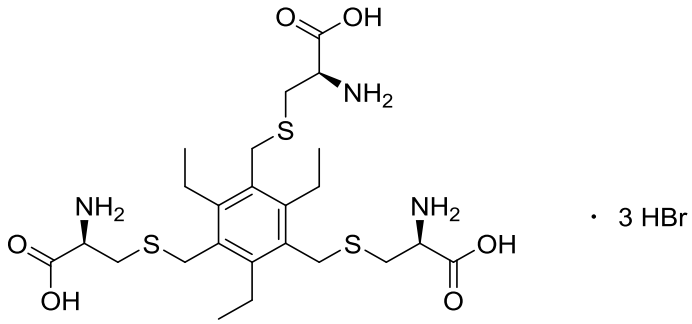

1,3,5-tris(bromomethyl)-2,4,6-triethylbenzene (compound **1**) (0.25 g, 0.56 mmol, 1 eq) and L-cysteine (0.27 g, 2.26 mmol, 4 eq) were added to a Schlenk flask and dissolved in 20 mL of acetonitrile under a nitrogen atmosphere. The flask was connected to a reflux condenser and the solution was heated to 70 ^{o}C and stirred for 48 hours. After this time, the precipitate was filtered and washed with acetonitrile (6 x 10 mL), and it was left on the freeze-drier for 16 hours. A white powder was obtained.

nESI-MS^{-}: m/z calculated for $C_{24}H_{39}N_3O_6S_3$**:** 560.1935, found 560.1928 $[M-H]^{-}$.

7.2.4. Synthesis of compounds from Chapter 5

Iron oxide nanoparticles – Fe_3O_4 (31)

Fe_3O_4

This synthesis was carried out following a previously reported procedure with some modifications,[4] as described below.

In one flask, 10 mL of an aqueous acid solution of $FeCl_3 \cdot 6H_2O$ 1 M (2.73 g, 10.00 mmol) was prepared with deoxygenated water under a nitrogen atmosphere. In another flask, 2.5 mL of an aqueous acid solution of $FeCl_2 \cdot 4H_2O$ 2 M (0.99 g, 5.00 mmol) was prepared with deoxygenated water under a nitrogen atmosphere and using a glovebox to avoid the oxidation of Fe^{2+}. Both compounds were dissolved in HCl 2 M. Then, 10 mL of the $FeCl_3$ solution were added to the 2.5 mL of the $FeCl_2$ solution in a Schlenk flask, under a nitrogen atmosphere and stirring. Immediately after mixing, the solution containing the iron chlorides was added dropwise to 125 mL of potassium hydroxide solution (0.7 M) prepared with deoxygenated water. The flask was mechanically stirred during the addition and for the next 30 minutes. After this time, the black precipitate formed was separated with a magnet and washed with water (3 x 250 mL). The obtained nanoparticles were further washed with water and centrifuged. Finally, oleic acid (1 mL, 3.16 mmol) dissolved in 5 mL of acetone was added dropwise.

IR: $\tilde{\nu}$ (cm^{-1}): 3239, 601.
XRD: 2θ = 30.2º, 35.5º, 43.2º, 53.5º, 57.1º and 62.9º, corresponding to the (220), (311), (400), (422), (511), and (440) crystalline planes of magnetite phase, respectively.

Coating of IONPs with a silica shell using a microemulsion method – Fe_3O_4@SiO_2 (32)

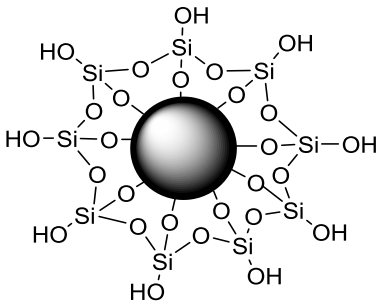

This synthesis was carried out following a previously reported procedure with some modifications,[5] as described below.

Polyoxyethylene(5)isooctylphenyl ether (IGEPAL CA-520) (44.60 g) was dispersed in 700 mL of cyclohexane. Then, 200 mg of Fe_3O_4 nanoparticles dispersed in cyclohexane (20 mg·mL^{-1}) was added. The mixture was stirred until it became transparent. After this step, 9.4 mL of ammonium hydroxide (29% aqueous solution) was added to form a reverse microemulsion. Finally, 7.7 mL of tetraethylorthosilicate (TEOS) was added as a silica precursor. The solution was mechanically stirred for 16 h. After this time, the nanocomposite was precipitated with methanol and separated by magnetic decantation.

IR: $\tilde{\nu}$ (cm^{-1}): 3239, 1045, 950, 601.
XRD: 2θ = 30.2º, 35.5º, 43.2º, 53.5º, 57.1º and 62.9º, corresponding to the (220), (311), (400), (422), (511), and (440) crystalline planes of magnetite phase, respectively. New peak emerges at 2θ = 18.6º, corresponding to the (111) crystalline plane.

Synthesis of $Cd_{0.1}Zn_{0.9}Se$ quantum dots (33)

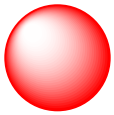

$Cd_{0.1}Zn_{0.9}Se$

This synthesis was carried out following a previously reported procedure with some modifications,[6] as described below.

Stock solutions of Se and $ZnEt_2$ were prepared in a glovebox under argon. Cadmium stearate (0.20 g, 0.30 mmol), stearic acid (0.17 g, 0.60 mmol), TOPO (5.00 g), and ODA (5.00 g) were added to a flask, and the mixture was heated to 330 ^oC while stirring under a flow of argon until a clear solution formed. At this temperature, a solution containing Se (0.12 g, 1.50 mmol) dissolved in TOP was injected into the reaction flask and the temperature was set to 290 °C. After 5-10 minutes under stirring, the heating was removed to stop the reaction and allow the flask to cool to room temperature. After 1 hour, the mixture of CdSe and organic ligands was heated up to 300 °C again. An aliquot (3 mL) of the as-prepared crude CdSe reaction mixture, containing 0.10 mmol of CdSe, was transferred into a three-neck round-bottom flask and heated to 300 °C. At this temperature, 450 µL of $ZnEt_2$ (TOP solution, 0.2 M) and 450 µL of Se (TOP solution, 0.2 M) were injected. After the addition, the reaction mixture was heated for 6 minutes, and then heating was removed to stop the reaction. Once the mixture reached room temperature, 9 mL of chloroform was added under stirring. Quantum dots were precipitated using a mixture of 1:1 methanol : acetone and isolated by centrifugation and decantation. The same mixture of 1:1 methanol : acetone (5 x 25 mL) was used to wash the QDs from the excess of organic ligands. Finally, $Cd_{0.1}Zn_{0.9}Se$ nanocrystals were dispersed in 9 mL of n-hexane.

XRD: 2θ = 23.7^o, 25.8^o, 42.2^o, 50.1^o, corresponding to the (111), (200), (220) and (311) crystalline planes.

Synthesis of $Cd_{0.1}Zn_{0.9}Se$ QDs modified silica-coated magnetic IONPs (34)

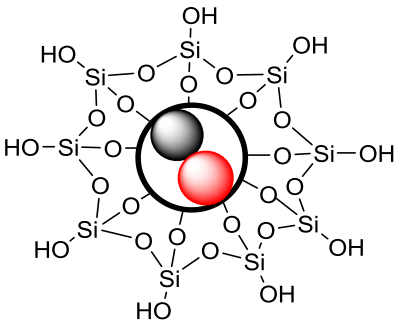

IGEPAL CA-520 (2.23 g) was dispersed in 35 mL of cyclohexane. Then, 5 mg of Fe_3O_4 nanoparticles dispersed in cyclohexane (20 mg·mL^{-1}) was added, followed by 1 mL of $Cd_{0.1}Zn_{0.9}Se$ QDs. The mixture was mechanically stirred until it became transparent. After this step, 485 µL of ammonium hydroxide (29% aqueous solution) was added to form a reverse microemulsion. Finally, 385 µL of TEOS was added as the silica precursor. The solution was mechanically stirred for 16 h. After this time, the nanocomposite was separated and washed with methanol by centrifugation and magnetic decantation.

IR: ṽ (cm^{-1}): 3318, 1633, 1013, 651.

Synthesis of diacetyl-2-(4-N-methyl-3-thiosemicarbazonato)-3-(4-N-amino-3-thiosemi carbazonato) zinc(II), Zn(ATSM/A) (35)

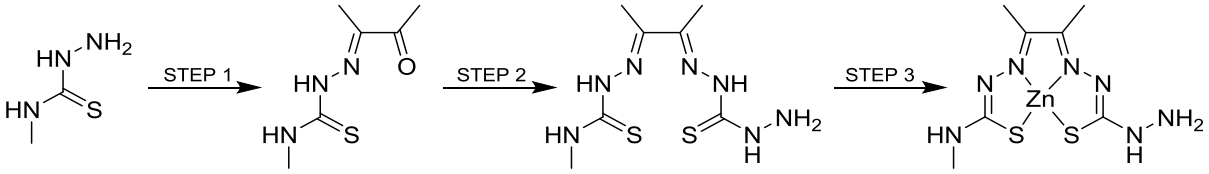

This synthesis was carried out following a previously reported procedure with some modifications,[7] as described below.

- Step 1: Synthesis of diacetyl-2-(4-N-methyl-3-thiosemicarbazone) **(35a)**

4-methyl-3-thiosemicarbazide (3.45 g, 32.80 mmol, 1 eq) was added to 100 mL of deionised water and vigorously stirred at strictly 0 °C. Next, 5 drops of concentrated HCl was added followed by the rapid addition of 2,3-butanedione (3.5 mL, 39.90 mmol, 1.2 eq) from a syringe. The yellow solution quickly became opaque as a white precipitate formed. After 1 hour of stirring at 0 °C, the precipitate was collected by filtration, washed thoroughly with cold water (5 x 30 mL) and dried on air over filter paper overnight. The compound was recrystallised from hot aqueous ethanol and a fluffy white solid was obtained.

Yield: 56% (3.18 g).

^{1}H NMR (300 MHz, DMSO-d_6, 298 K): δ (ppm) 10.59 (s, 1 H, CSN*H*N), 8.59 (s, 1 H, CH_3N*H*CS), 3.04 (s, 3 H, CH_3N*H*), 2.40 (s, 3 H, CH_3CO), 1.94 (s, 3 H, CH_3CN).

^{13}C{^{1}H} NMR (75 MHz, DMSO-d_6, 298 K): δ (ppm) 197.8, 179.3, 145.8, 31.7, 25.1, 10.3.

nESI-MS^{+}: m/z calculated for $C_6H_{11}N_3OS$: 196.0515, found 196.0513 $[M+Na]^{+}$.

- Step 2: Synthesis of diacetyl-2-(4-N-methyl-3-thiosemicarbazone)-3-(4-N-amino-3-thiosemicarbazone), H_2ATSM/A **(35b)**

Thiocarbohydrazide (1.96 g, 18.51 mmol, 1 eq) was added to 105 mL of ethanol in a 3-neck round-bottom flask and the suspension was stirred at 50 °C. 4-N-substituted monoketothiosemicarbazone (compound **35a**) (3.21 g, 18.51 mmol, 1 eq) was added in small portions over 2 hours. After the final addition, 5 drops of 10% HCl(aq) was added and the reaction mixture was heated under reflux for 5 hours. During this time a cream/white suspension formed. The mixture was allowed to cool to room temperature, and then the precipitate was collected by filtration, washed with ethanol (2 x 30 mL) and diethyl ether (5 x 30 mL), and dried under vacuum. The product was recrystallised from warm DMSO/water, and a pale yellow powder was obtained.

Yield: 80% (3.89 g).

^{1}H NMR (300 MHz, DMSO-d_6, 298 K): δ (ppm) 10.23 (s, 2 H, NHCSN*H*N), 9.70 (s, 1 H, N*H*NH_2), 8.36 (s, 1 H, CH_3N*H*CS), 4.96 (s, 2 H, NHN*H_2*), 3.00 (d, 3 H, *J* = 4.43 Hz, NHC*H_3*), 2.18 (s, 3 H, C*H_3*CN), 2.18 (s, 3 H, C*H_3*CN).

^{13}C{^{1}H} NMR (75 MHz, DMSO-d_6, 298 K): δ (ppm) 178.7, 176.2, 148.4, 148.4, 31.5, 11.9, 11.9.

EI-MS^{+}: m/z calculated for $C_7H_{15}N_7S_2$: 261.1, found 261.0 $[M]^{+\cdot}$.

- Step 3: Synthesis of diacetyl-2-(4-N-methyl-3-thiosemicarbazonato)-3-(4-N-amino-3-thiosemicarbazonato) zinc(II), Zn(ATSM/A) **(35c)**

H_2ATSM/A (compound **35b**) (3.50 g, 13.39 mmol, 1 eq) was added to 74 mL of methanol in a round-bottom flask and the suspension was stirred. Zinc(II) acetate dihydrate (3.53 g, 16.07 mmol, 1.2 eq) was added to the flask, and the mixture was heated under reflux for 4 hours. After this time, the suspension was left to cool down and the precipitate was then filtered and washed with methanol (3 x 30 mL) and diethyl ether (7 x 30 mL). The yellow-green precipitate was left to dry on the freeze-drier overnight.

Yield: 65% (2.18 g).

^{1}H NMR (500 MHz, DMSO-d_6, 298 K): δ (ppm) 8.22 (br s, 1 H, N*H*NH_2), 7.21 (s, 1 H, CH_3N*H*), 4.80 (s, 2 H, NHN*H_2*), 2.83 (d, 3 H, *J* = 3.98 Hz, C*H_3*NH), 2.23 (s, 3 H, C*H_3*CN), 2.21 (s, 3 H, C*H_3*CN).

^{13}C{^{1}H} NMR (126 MHz, DMSO-d_6, 298 K): δ (ppm) 178.3, 177.2, 145.8, 145.8, 29.2, 13.9, 13.9.

APCI-MS^{+}: m/z calculated for $C_7H_{13}N_7S_2Zn$: 324.0038, found 324.0037 $[M+H]^{+}$.

IR: $\tilde{\nu}$ (cm^{-1}): 3236, 2925, 1426, 1039.

HPLC (Method A): Rt (min): 8.1.

Zn(ATSM/A) modified silica-coated magnetic IONPs (36)

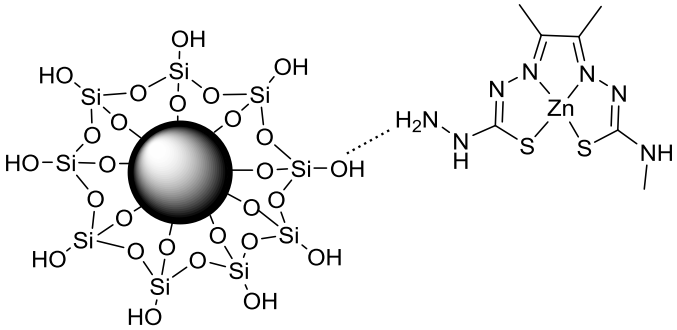

Fe_3O_4@SiO_2 nanoparticles (0.10 g) were added to a round-bottom flask and dispersed in 200 mL of methanol. Next, Zn(ATSM/A) (compound **35c**) (0.10 g, 0.31 mmol) was added to the flask and the mixture was mechanically stirred and heated to 80 ºC under reflux. After 16 hours, the mixture was left to cool to room temperature, then the nanocomposite was separated by magnetic decantation and centrifugation and it was further washed with methanol.

IR: ṽ (cm^{-1}): 3327, 2947, 2826.

Citric acid-coated magnetic IONPs (37)

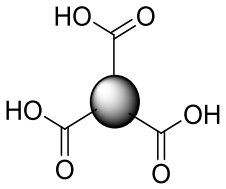

This synthesis was carried out following a previously reported procedure with some modifications,[8] as described below.

Dry Fe_3O_4 nanoparticles (1.20 g, 5.20 mmol) were dispersed in 85 mL of milli-Q water. Then, a 0.1 g/mL citric acid aqueous solution was added to the nanoparticles dispersion while this was mechanically stirred, until pH 5 was achieved. The mixture was heated to 85 °C and stirred for 3 hours. After this time, it was left to cool to room temperature and the nanocomposites were isolated by centrifugation.

IR: ṽ (cm^{-1}): 3359, 2955, 2939, 1462, 1130, 1032, 663.

3,5-bis(bromomethyl)-2,4,6-triethylbenzyl 4-(5,5-difluoro-1,3,7,9-tetramethyl-5*H*-4λ^4,5λ^4-dipyrrolo[1,2-*c*:2',1'-*f*][1,3,2]diazaborinin-10-yl)benzoate functionalised citric acid-coated magnetic IONPs (38)

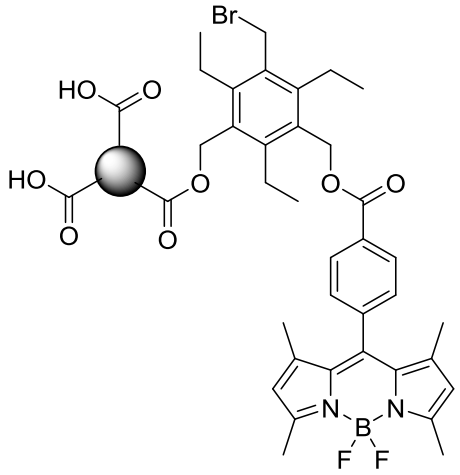

3,5-bis(bromomethyl)-2,4,6-triethylbenzyl 4-(5,5-difluoro-1,3,7,9-tetramethyl-5*H*-4λ^4,5λ^4-dipyrrolo[1,2-*c*:2',1'-*f*][1,3,2]diazaborinin-10-yl)benzoate (compound **5**) (50 mg, 70 μmol) and citric acid-coated Fe_3O_4 nanoparticles (100 mg) were mixed in a round-bottom flask and dispersed in 25 mL of acetonitrile. The reaction mixture was heated to 100 ^oC under reflux and it was mechanically stirred for 16 hours. After this time, the mixture was left to cool to room temperature and it was centrifuged. The obtained nanocomposite was washed with methanol twice and isolated by centrifugation.

IR: ṽ (cm^{-1}): 2972, 2138, 1654, 1601, 1569, 1388, 1263, 1098, 806, 656.

Radiolabelling experiments involving gallium-68

Synthesis of gallium-68

The positron-emitting radiotracer [^{68}Ga]$GaCl_3$ was prepared at the Department of Surgery and Cancer of the Imperial College London using either a TiO_2 or a SnO_2-based column matrix ^{68}Ge/^{68}Ga generator via the (p,2n) reaction on gallium targets.

General procedure for Method 1: Fe_3O_4@SiO_2@^{68}Ga (39) and Fe_3O_4/$Cd_{0.1}Zn_{0.9}Se$@SiO_2@^{68}Ga (40)

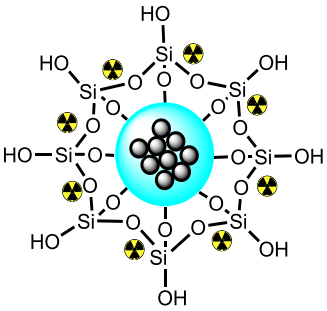

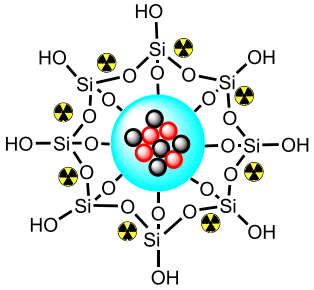

The nanoparticles system (Fe_3O_4/$Cd_{0.1}Zn_{0.9}Se$@SiO_2 or Fe_3O_4@SiO_2) (1 mg) dispersed in dimethylsulfoxide (1 mg/mL) was centrifuged and 30 µL of the precipitated nanocomposite was added to a Wheaton vial along with 0.2 mL of ethanol, 50 µL of [^{68}Ga]$GaCl_3$ solution (from a 133 MBq stock solution) and 0.1 mL of a sodium acetate buffer solution in order to adjust the pH to approximately 5. The reaction was carried out for 40 minutes at 90 ºC, using a vortex stirrer to mix the contents every 10 minutes. After this time, the radiolabelled nanocomposites were isolated by centrifugation and washed with methanol and water. Then, the radiolabelling efficiency was determined by radio-TLC.

RCY (Fe_3O_4@SiO_2@^{68}Ga) ≥ 99.9 %

RCY (Fe_3O_4/$Cd_{0.1}Zn_{0.9}Se$@SiO_2@^{68}Ga) ≥ 99.9 %

General procedure for Method 2: Fe_3O_4@SiO_2@^{68}Ga@SiO_2 (41) and Fe_3O_4/$Cd_{0.1}Zn_{0.9}Se$@SiO_2@^{68}Ga@SiO_2 (42)

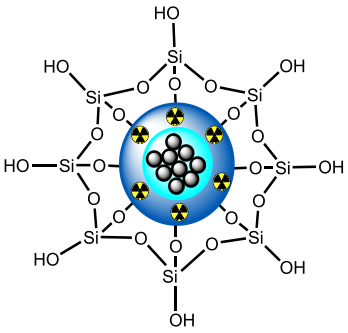

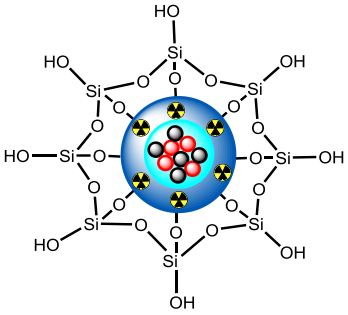

The nanoparticles system (Fe_3O_4/$Cd_{0.1}Zn_{0.9}Se$@SiO_2 or Fe_3O_4@SiO_2) (1 mg) dispersed in dimethylsulfoxide (1 mg/mL) was centrifuged and 30 µL of the precipitated nanocomposite was added to a Wheaton vial along with 3.5 mL of cyclohexane, 50 µL of [^{68}Ga]$GaCl_3$ solution (from a 133 MBq stock solution) and 24 µL of tetraethylorthosilicate. The reaction mixture was heated to 90 °C and reacted for 68 minutes, using a vortex stirrer to mix the contents every 10 minutes. The resulting nanocomposite was transferred to centrifuge vials and washed once with methanol and three more times with water, then separated by magnetic decantation.

RCY (Fe_3O_4@SiO_2@^{68}Ga@SiO_2) = 70 %

RCY (Fe_3O_4/$Cd_{0.1}Zn_{0.9}Se$@SiO_2@^{68}Ga@SiO_2) = 66 %

General procedure for Method 3: Fe_3O_4@SiO_2@Zn(ATSM/A)@^{68}Ga (43)

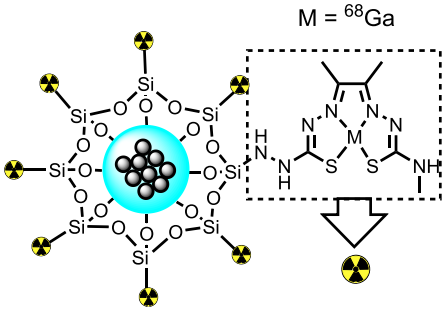

Fe_3O_4@SiO_2@Zn(ATSM/A) nanoparticles (1 mg) dispersed in dimethylsulfoxide (1 mg/mL) were centrifuged and 50 µL of the precipitated nanocomposite was added to a Wheaton vial along with 0.1 mL of [^{68}Ga]$GaCl_3$ solution (from a 133 MBq stock solution), 0.2 mL of ethanol and 0.1 mL of a sodium acetate buffer solution in order to adjust the pH to approximately 5. The reaction was carried out for 40 minutes at 90 °C, using a vortex stirrer to mix the contents every 10 minutes. The resulting nanocomposite was transferred to centrifuge vials and washed once with methanol and three more times with water, then separated by magnetic decantation. After this time, the radiolabelling efficiency was determined by radio-TLC.

RCY (Fe_3O_4@SiO_2@Zn(ATSM/A)@^{68}Ga) ≥ 99.9 %

Reaction between Zn(ATSM/A) and [^{68}Ga]$GaCl_3$: Zn(ATSM/A)@^{68}Ga (44)

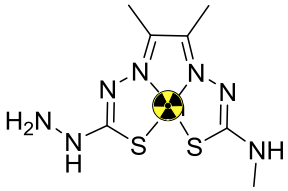

Zn(ATSM/A) (1 mg) dispersed in dimethylsulfoxide (1 mg/mL) was centrifuged and 50 µL of the precipitate was added to a Wheaton vial along with 0.1 mL of [^{68}Ga]$GaCl_3$ solution (from a 133 MBq stock solution), 0.2 mL of ethanol and 0.1 mL of a sodium acetate buffer solution in order to adjust the pH to approximately 5. The reaction was carried out for 40 minutes at 90 °C, using a vortex stirrer to mix the contents every 10 minutes. The resulting product was transferred to centrifuge vials and washed once with methanol and three more times with water, then separated by centrifugation. After this time, the radiolabelling efficiency was determined by radio-HPLC.

RCY (Zn(ATSM/A)@^{68}Ga) = 0 %

7.3. References for Chapter 7

1. K. J. Wallace, R. Hanes, E. Anslyn, J. Morey, K. V. Kilway and J. Siegel, *Synthesis*, 2005, 2080-2083.
2. A. Cui, X. Peng, J. Fan, X. Chen, Y. Wu and B. Guo, *J. Photochem. Photobiol.*, 2007, **186**, 85-92.
3. P. A. Waghorn, M. W. Jones, A. McIntyre, A. Innocenti, D. Vullo, A. L. Harris, C. T. Supuran and J. R. Dilworth, *Eur. J. Inorg. Chem.*, 2012, 2898-2907.
4. A. P. Philipse, M. P. B. van Bruggen and C. Pathmamanoharan, *Langmuir*, 1994, **10**, 92-99.
5. M. J. Jacinto, P. K. Kiyohara, S. H. Masunaga, R. F. Jardim and L. M. Rossi, *Appl. Catal., A*, 2008, **338**, 52-57.
6. X. Zhong, M. Han, Z. Dong, T. J. White and W. Knoll, *J. Am. Chem. Soc.*, 2003, **125**, 8589-8594.
7. J. P. Holland, F. I. Aigbirhio, H. M. Betts, P. D. Bonnitcha, P. Burke, M. Christlieb, G. C. Churchill, A. R. Cowley, J. R. Dilworth, P. S. Donnelly, J. C. Green, J. M. Peach, S. R. Vasudevan and J. E. Warren, *Inorg. Chem.*, 2007, **46**, 465-485.
8. E. Cheraghipour, S. Javadpour and A. R. Mehdizadeh, *J. Biomed. Sci. Eng.*, 2012, **5**, 5.

Appendix A (*Chapter 2*)

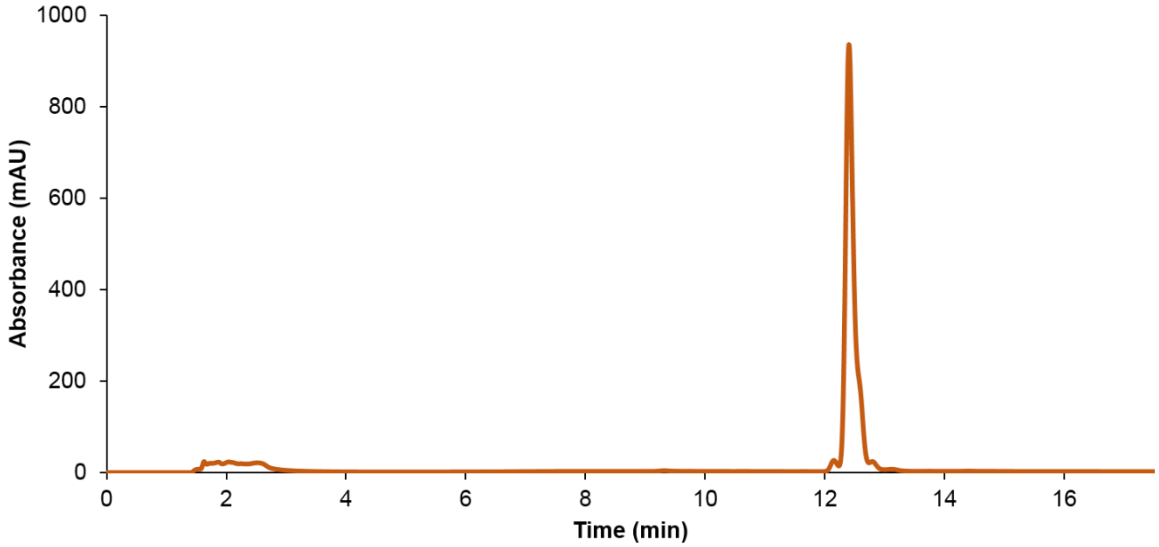

Figure A.1. HPLC chromatogram of compound **1** in the 280 nm channel.

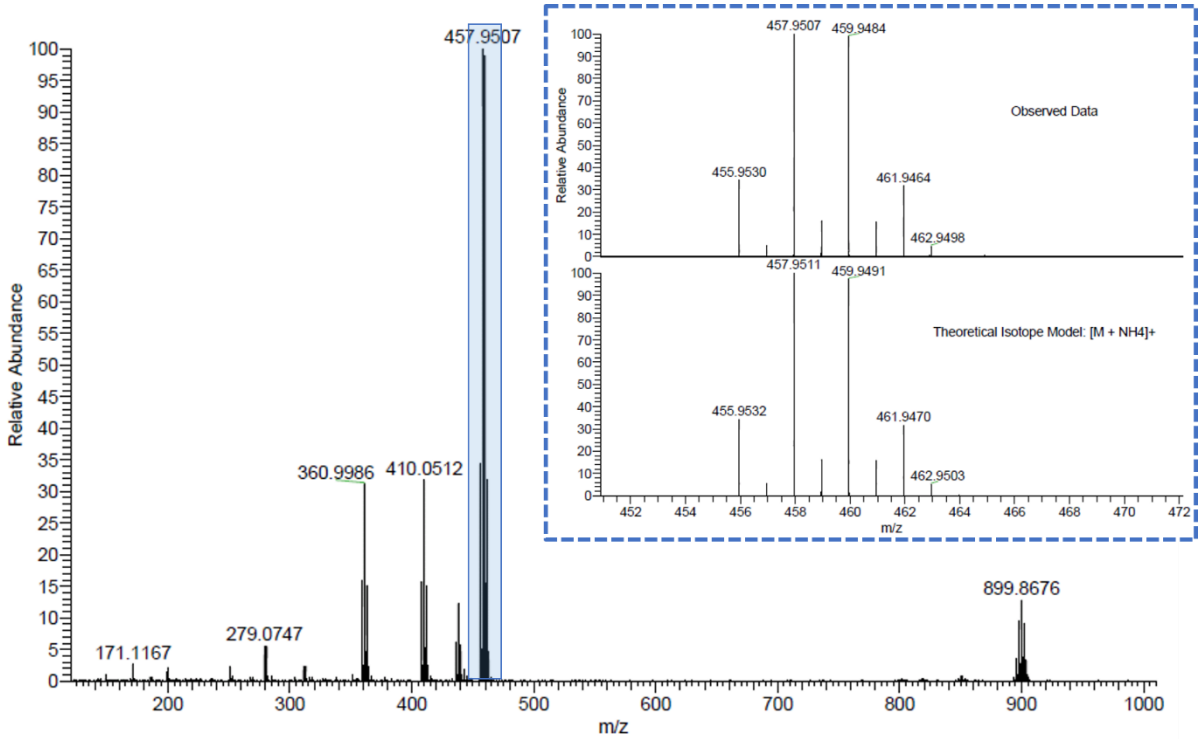

Figure A.2. Mass spectrum of compound **1** using nESI+, and amplification of the isotopic pattern.

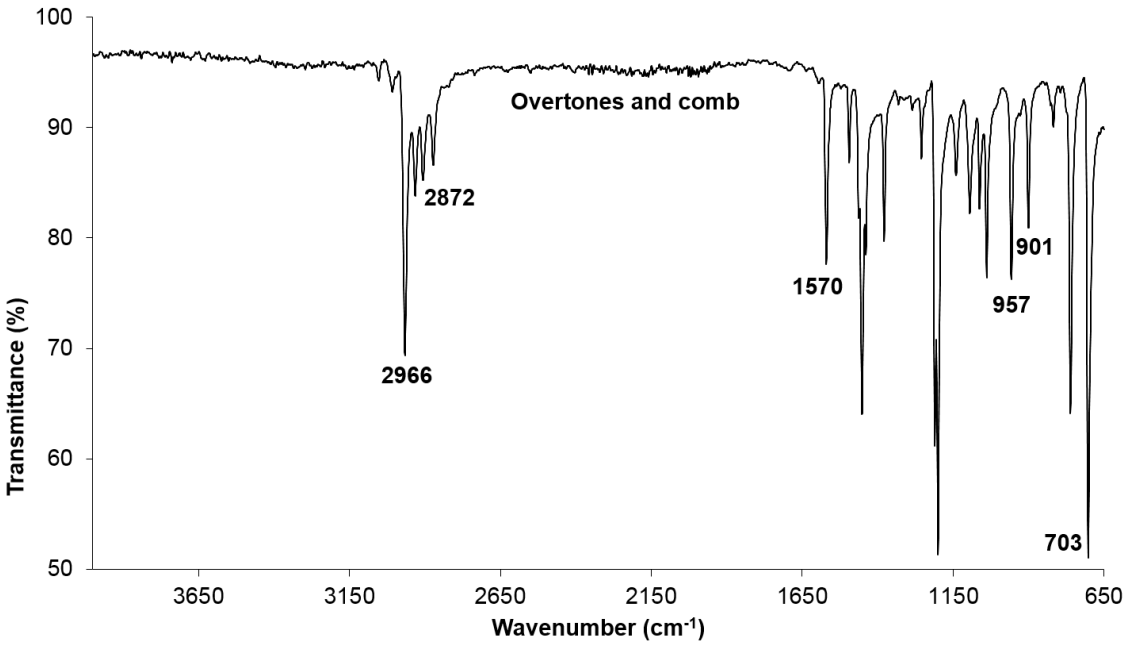

Figure A.3. FT-IR spectrum of compound **1**.

Table A.1. Band assignment for the FT-IR spectrum of compound **1** (*Figure A.3*).

Wavenumber (cm^{-1})	Peak intensity	Vibrational mode
2966	Multiplet, strong	ar. C – H st
2872	Multiplet, medium	C – H st (alkyl)
2300 – 1900	Very weak	Overtones and comb
1570	Medium	ar. C – C st
957	Medium	ar. C – H δ oop
901	Weak	C = C δ
703	Strong	C – Br st

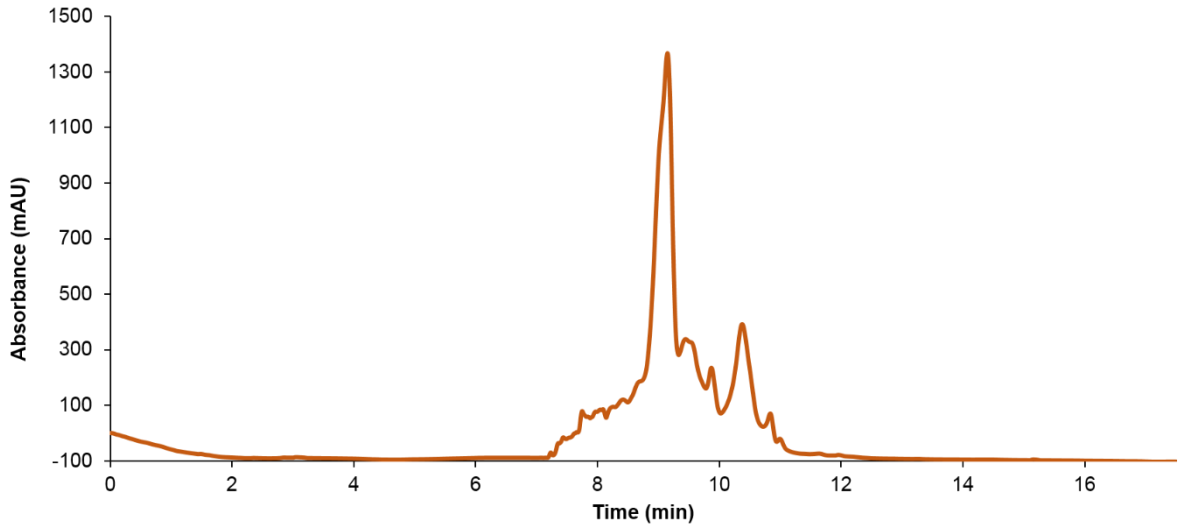

Figure A.4. HPLC chromatogram of compound **2** in the 500 nm channel.

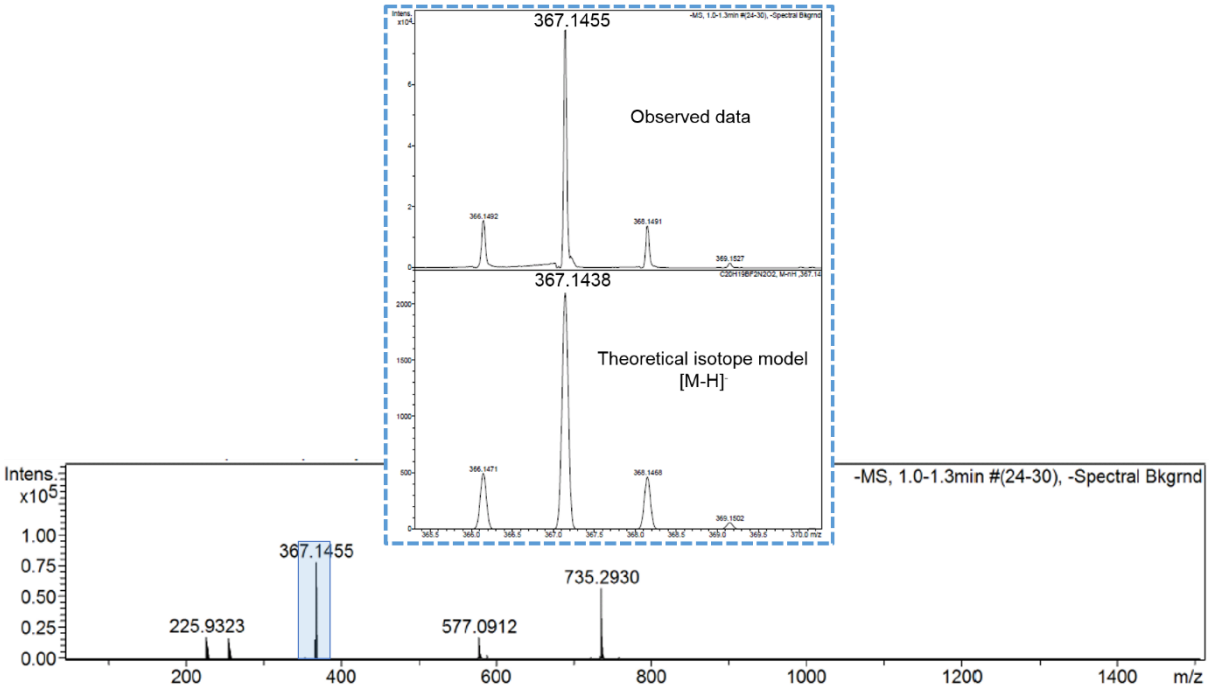

Figure A.5. Mass spectrum of compound **2** using ESI-, and amplification of the isotopic pattern.

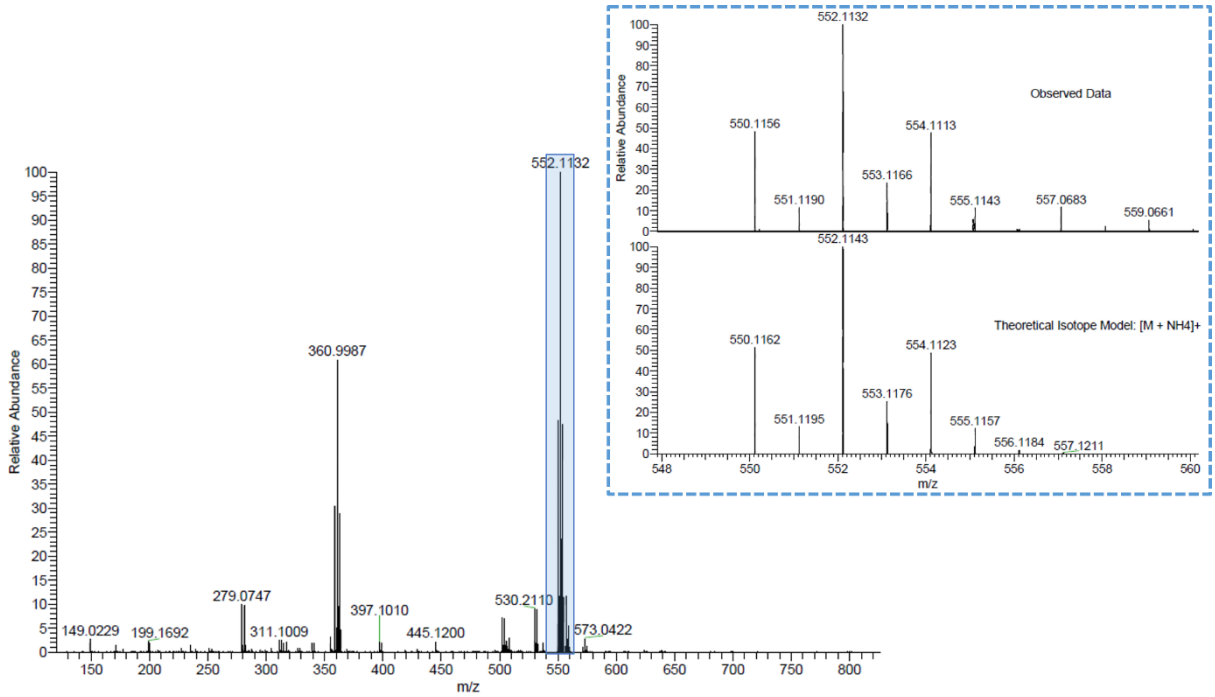

Figure A.6. Mass spectrum of compound **9** using nESI+, and amplification of the isotopic pattern.

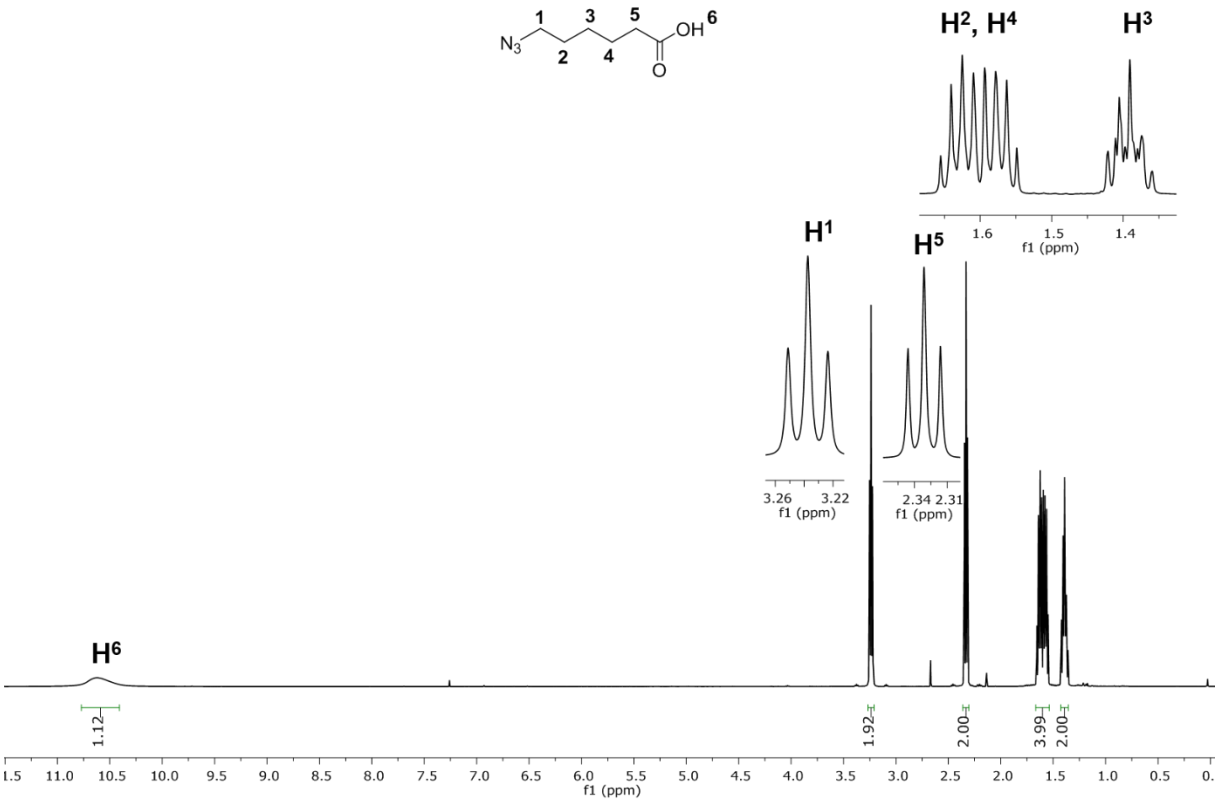

Figure A.7. ^{1}H NMR (500 MHz, $CDCl_3$, 298 K) spectrum of compound **7**.

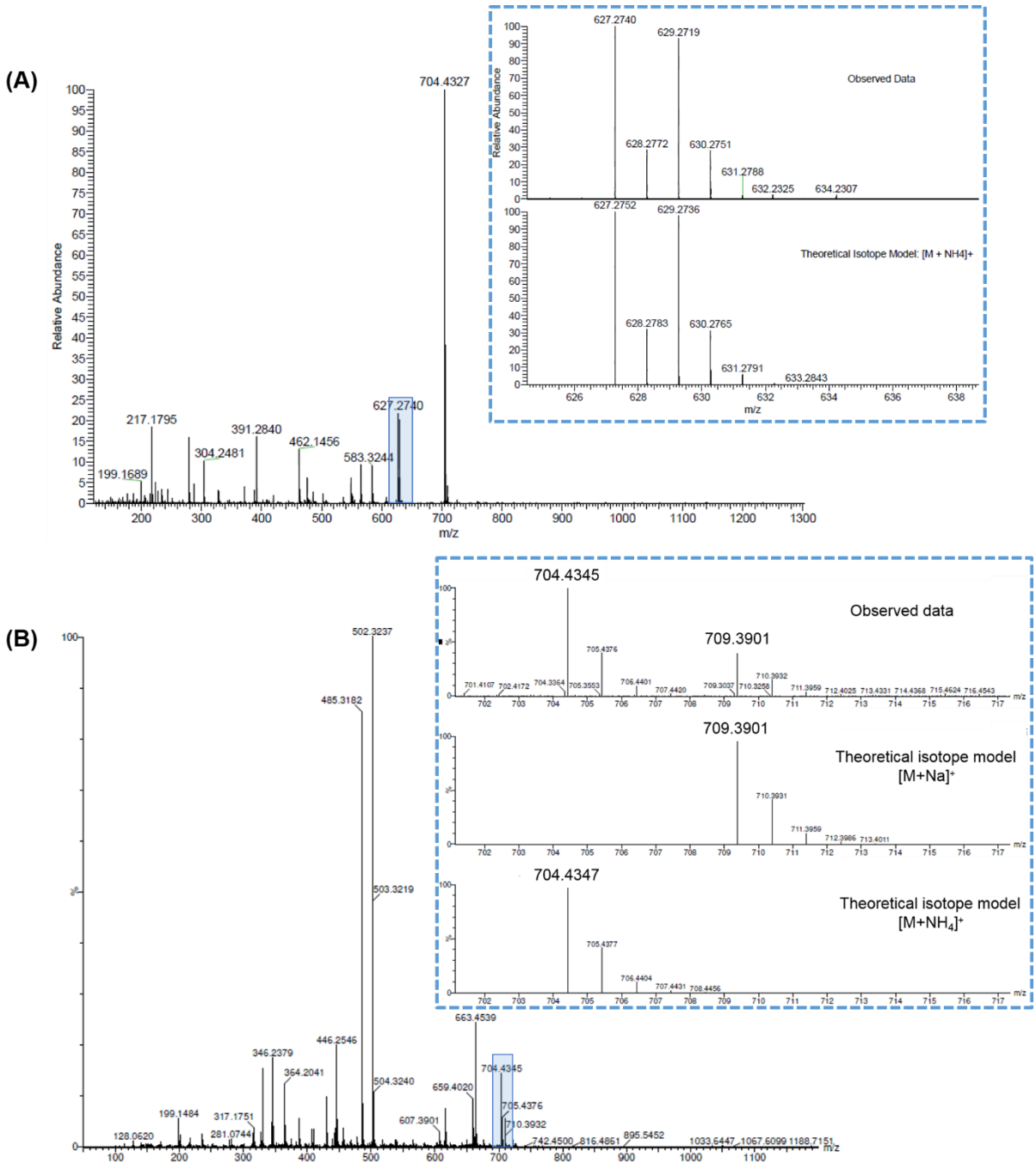

Figure A.8. (A) Mass spectrum of compound **14** using nESI+, and **(B)** mass spectrum of compound **15** using APCI+, and amplification of the respective isotopic patterns.

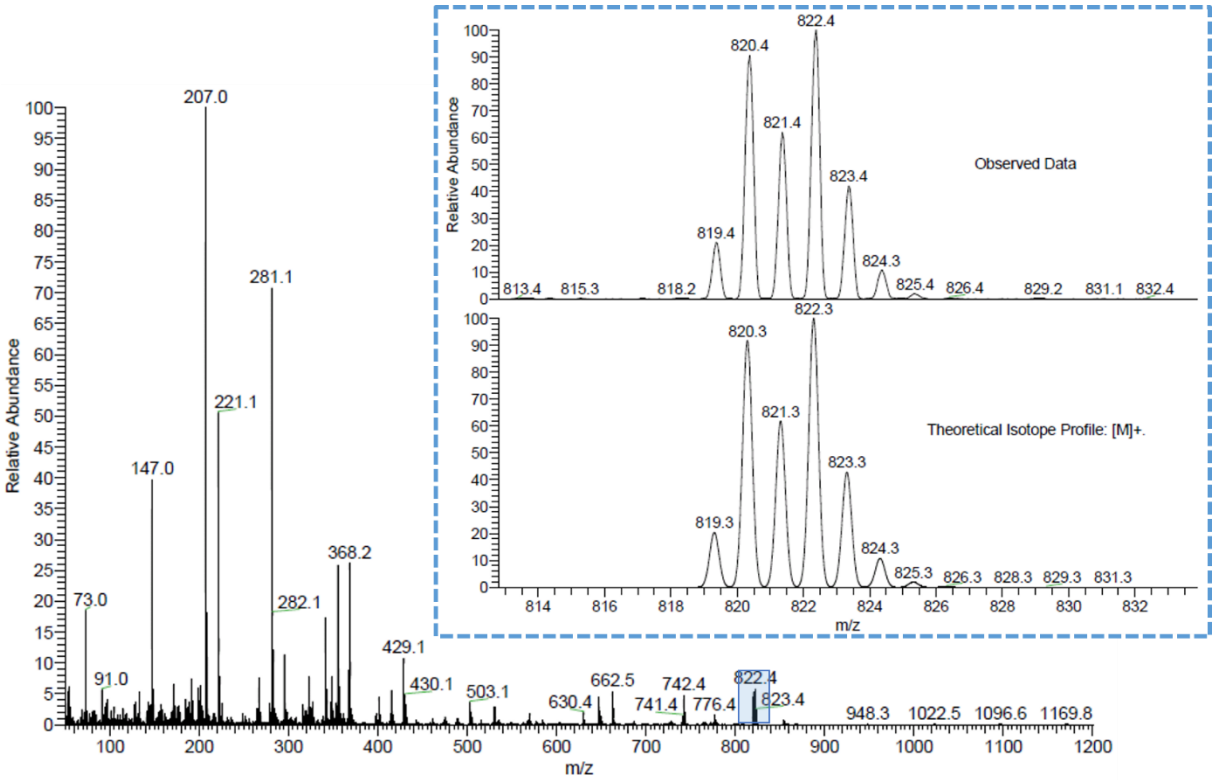

Figure A.9. Mass spectrum of compound **13** using EI+, and amplification of the isotopic pattern.

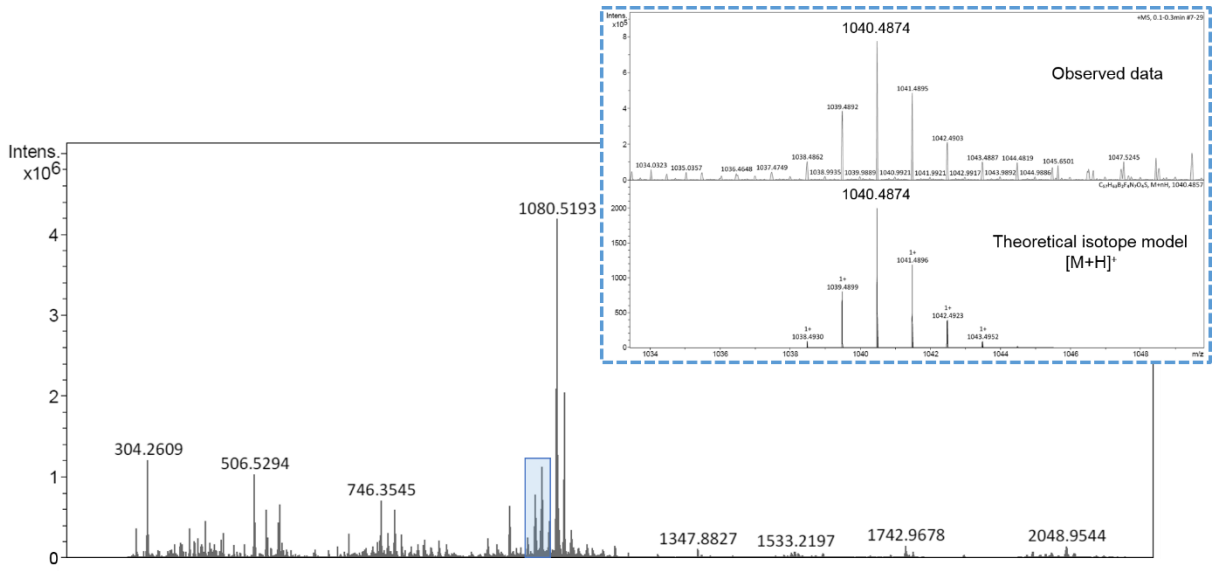

Figure A.10. Mass spectrum of compound **17** using ESI+, and amplification of the isotopic pattern.

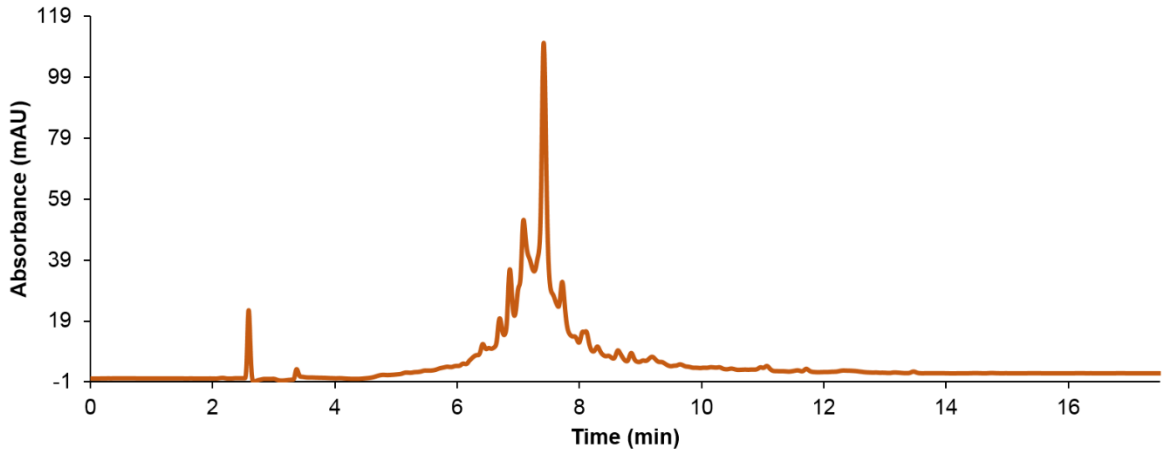

Figure A.11. HPLC chromatogram of compound **19** in the 280 nm channel.

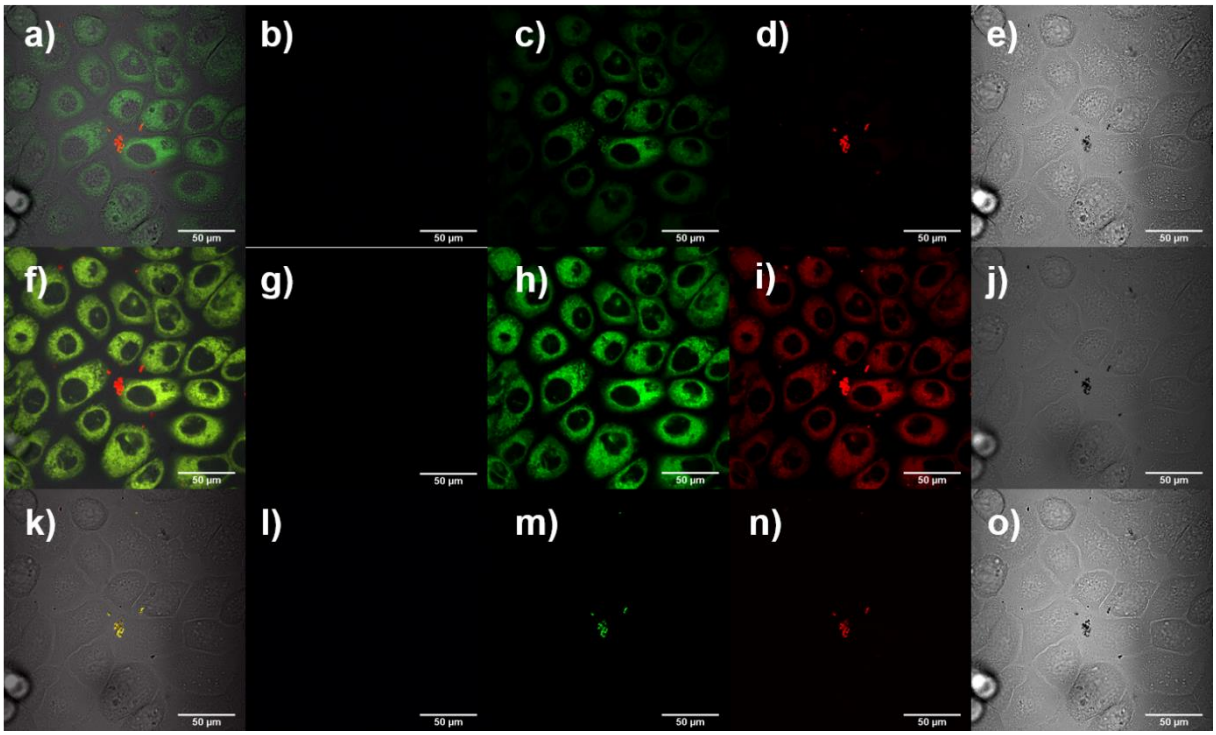

Figure A.12. Single-photon laser scanning confocal microscopy of PC-3 cells incubated for 15 minutes at 37 ºC with compound **5**. Final concentration: 100 µM in serum-free medium (1% DMSO). a-e) λ_{ex} = 405 nm; f-j) λ_{ex} = 488 nm; k-o) λ_{ex} = 561 nm. a, f, k) overlay of DIC-blue-green-red channels; b, g, l) blue channel (λ_{em} = 417-477 nm); c, h, m) green channel (λ_{em} = 500-550 nm); d, i, n) red channel (λ_{em} = 570-750 nm); e, j, o) DIC channel. Scale bar: 50 µm.

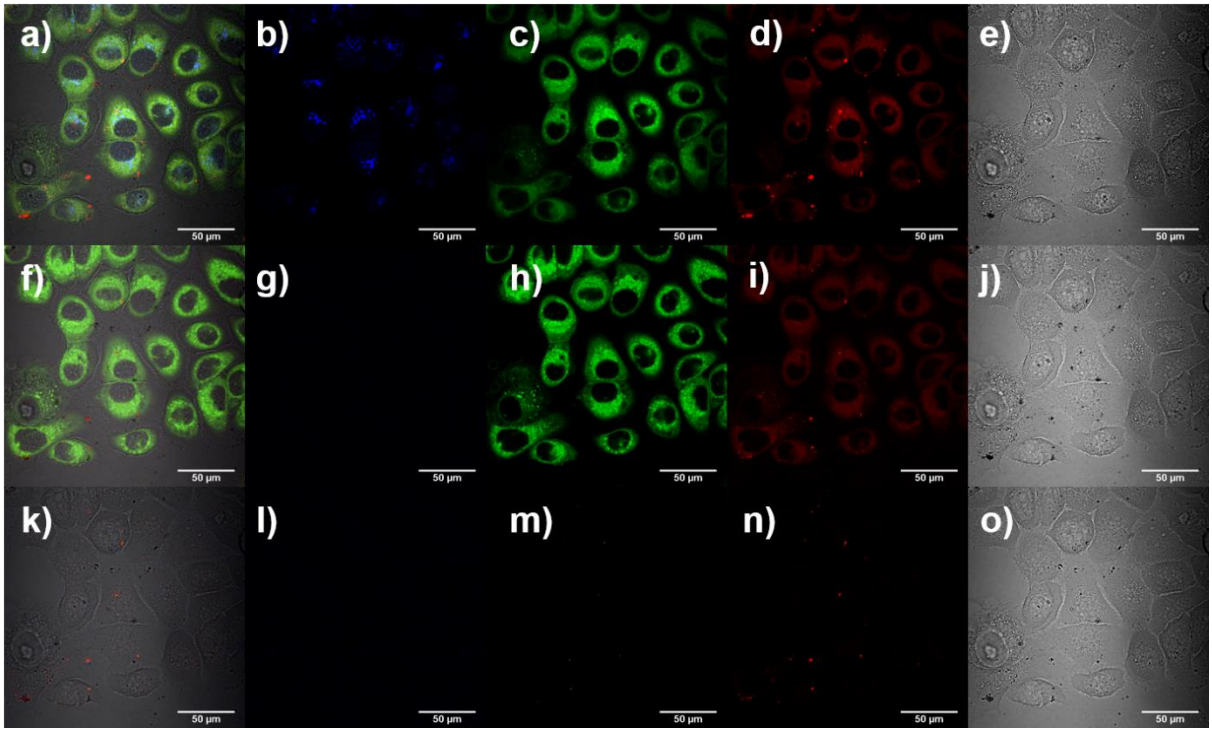

Figure A.13. Single-photon laser scanning confocal microscopy of PC-3 cells incubated for 30 minutes at 37 ºC with LysoTracker Red, and 20 minutes with compound **5**. Final concentration: 100 µM in serum-free medium (1% DMSO) solution of compound **5**, with a 100 nM concentration solution of LysoTracker Red. a-e) λ_{ex} = 405 nm; f-j) λ_{ex} = 488 nm; k-o) λ_{ex} = 561 nm. a, f, k) overlay of DIC-blue-green-red channels; b, g, l) blue channel (λ_{em} = 417-477 nm); c, h, m) green channel (λ_{em} = 500-550 nm); d, i, n) red channel (λ_{em} = 570-750 nm); e, j, o) DIC channel. Scale bar: 50 µm.

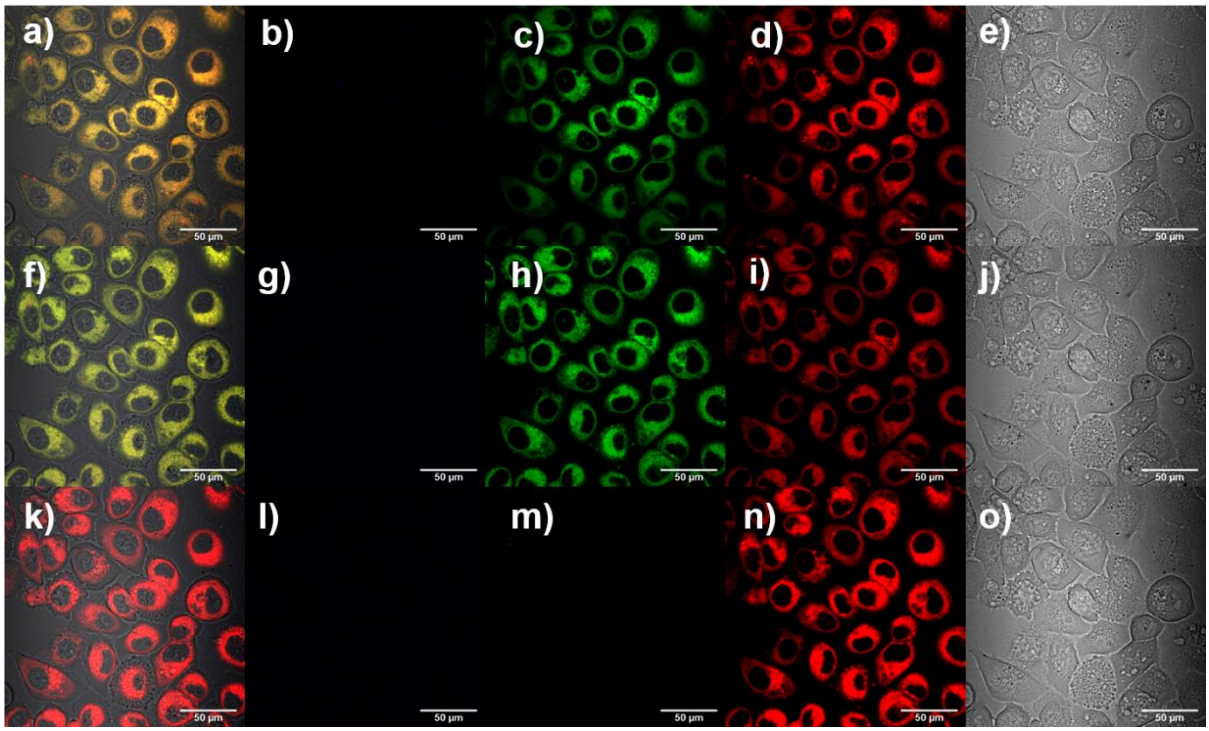

Figure A.14. Single-photon laser scanning confocal microscopy of PC-3 cells incubated for 30 minutes at 37 ºC with ER-Tracker Red, and 20 minutes with compound **5**. Final concentration: 100 µM in serum-free medium (1% DMSO) solution of compound **6**, with a 100 nM concentration solution of ER-Tracker Red. a-e) λ_{ex} = 405 nm; f-j) λ_{ex} = 488 nm; k-o) λ_{ex} = 561 nm. a, f, k) overlay of DIC-blue-green-red channels; b, g, l) blue channel (λ_{em} = 417-477 nm); c, h, m) green channel (λ_{em} = 500-550 nm); d, i, n) red channel (λ_{em} = 570-750 nm); e, j, o) DIC channel. Scale bar: 50 µm.

Appendix B.1 (*Chapter 4*)

Crystallographic data for Compound 26

Table B.1. Crystal data and structure refinement for compound **26**.

Identification code	s17sip9	
Empirical formula *	C12.20 H25.98 Br1.30 N4.50 O1.08 S1.50	
Formula weight	404.76	
Temperature	150(2) K	
Wavelength	1.54184 Å	
Crystal system	Triclinic	
Space group	P-1	
Unit cell dimensions	a = 12.0106(3) Å	a = 114.815(2)°
	b = 13.7028(3) Å	b= 94.995(2)°
	c = 13.9941(3) Å	g = 111.719(2)°
Volume	1860.12(8) $Å^3$	
Z	1	
Density (calculated)	1.445 Mg/m^3	
Absorption coefficient	5.371 mm^{-1}	
F(000)	835	
Crystal size	0.200 x 0.080 x 0.080 mm^3	
Theta range for data collection	3.633 to 73.133°.	
Index ranges	-14<=h<=14, -16<=k<=16, -17<=l<=17	
Reflections collected	33227	
Independent reflections	7397 [R(int) = 0.0425]	
Completeness to theta = 67.684°	100.0 %	
Refinement method	Full-matrix least-squares on F^2	
Data / restraints / parameters	7397 / 78 / 522	
Goodness-of-fit on F^2	1.062	
Final R indices [I>2sigma(I)]	R1 = 0.0443, wR2 = 0.1276	
R indices (all data)	R1 = 0.0481, wR2 = 0.1320	
Extinction coefficient	n/a	
Largest diff. peak and hole	1.121 and -0.509 $e.Å^{-3}$	

*** Moiety formula** (estimated from “checkcif”): 2 (C21 H40 N9 S3), 2 (C2 H6 O), 0.5 (C2 H3 O), C H4 O, 0.812 (C H3).

Crystallographic data for Compound 27

Table B.2. Crystal data and structure refinement for compound **27**.

Identification code	s17sip8	
Empirical formula *	C51 H108 Br5 N18 O4 S8	
Formula weight	1693.58	
Temperature	150(2) K	
Wavelength	1.54184 Å	
Crystal system	Triclinic	
Space group	P-1	
Unit cell dimensions	a = 12.5296(5) Å	a = 112.797(3)°
	b = 13.5000(5) Å	b = 98.550(3)°
	c = 13.9378(4) Å	g = 109.516(4).
Volume	1940.77(13) $Å^3$	
Z	1	
Density (calculated)	1.449 Mg/m^3	
Absorption coefficient	5.552 mm^{-1}	
F(000)	875	
Crystal size	0.180 x 0.060 x 0.040 mm^3	
Theta range for data collection	3.631 to 73.066°.	
Index ranges	-15<=h<=15, -16<=k<=15, -17<=l<=16	
Reflections collected	13739	
Independent reflections	7543 [R(int) = 0.0333]	
Completeness to theta = 67.684°	99.0 %	
Refinement method	Full-matrix least-squares on F^2	
Data / restraints / parameters	7543 / 13 / 544	
Goodness-of-fit on F^2	1.033	
Final R indices [I>2sigma(I)]	R1 = 0.0476, wR2 = 0.1332	
R indices (all data)	R1 = 0.0553, wR2 = 0.1401	
Extinction coefficient	n/a	
Largest diff. peak and hole	1.144 and -1.154 $e.Å^{-3}$	

*** Moiety formula** (estimated from “checkcif”): 2 (C24 H48 N9 S3), O S2, C H4 O2, C H4 O, C H3 O, 5 (Br), H.

Crystallographic data for Compound 29

Table B.3. Crystal data and structure refinement for compound **29**.

Identification code	s17sip11	
Empirical formula *	C55 H100 Br6 N18 O S6	
Formula weight	1701.34	
Temperature	150.00(10) K	
Wavelength	1.54184 Å	
Crystal system	Triclinic	
Space group	P-1	
Unit cell dimensions	a = 12.0882(4) Å	a = 96.535(3)°
	b = 13.7029(4) Å	b = 112.376(3)°
	c = 14.4245(4) Å	g = 114.554(3)°
Volume	1901.63(11) $Å^3$	
Z	1	
Density (calculated)	1.486 Mg/m^3	
Absorption coefficient	5.734 mm^{-1}	
F(000)	870	
Crystal size	0.100 x 0.100 x 0.050 mm^3	
Theta range for data collection	3.502 to 73.158°.	
Index ranges	-13<=h<=14, -16<=k<=16, -17<=l<=16	
Reflections collected	16908	
Independent reflections	7539 [R(int) = 0.0310]	
Completeness to theta = 67.684°	100.0 %	
Absorption correction	Semi-empirical from equivalents	
Max. and min. transmission	1.00000 and 0.83398	
Refinement method	Full-matrix least-squares on F^2	
Data / restraints / parameters	7539 / 14 / 531	
Goodness-of-fit on F^2	1.071	
Final R indices [I>2sigma(I)]	R1 = 0.0429, wR2 = 0.1105	
R indices (all data)	R1 = 0.0494, wR2 = 0.1158	
Extinction coefficient	n/a	
Largest diff. peak and hole	1.515 and -0.807 $e.Å^{-3}$	

*** Moiety formula** (estimated from “checkcif”): 2 (C27 H48 N9 S3), C H4 O, 6 (Br).

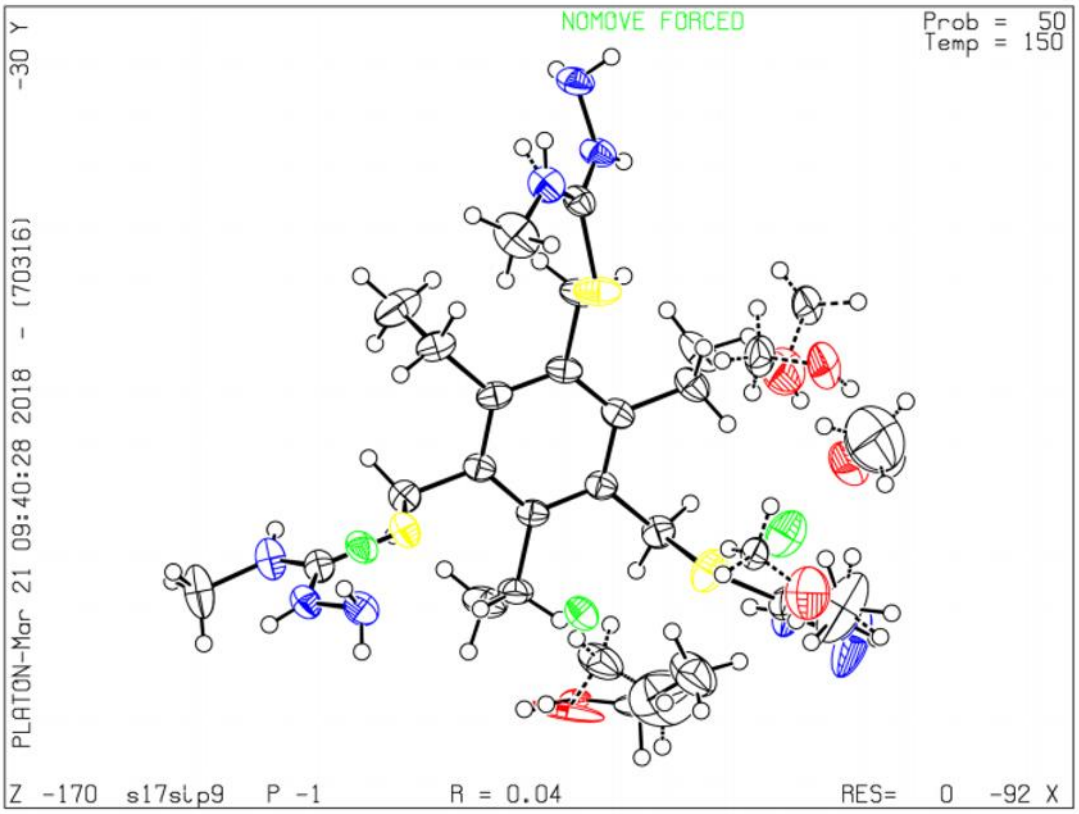

Figure B.1. Crystal structure for compound **26** (generated from "checkcif").

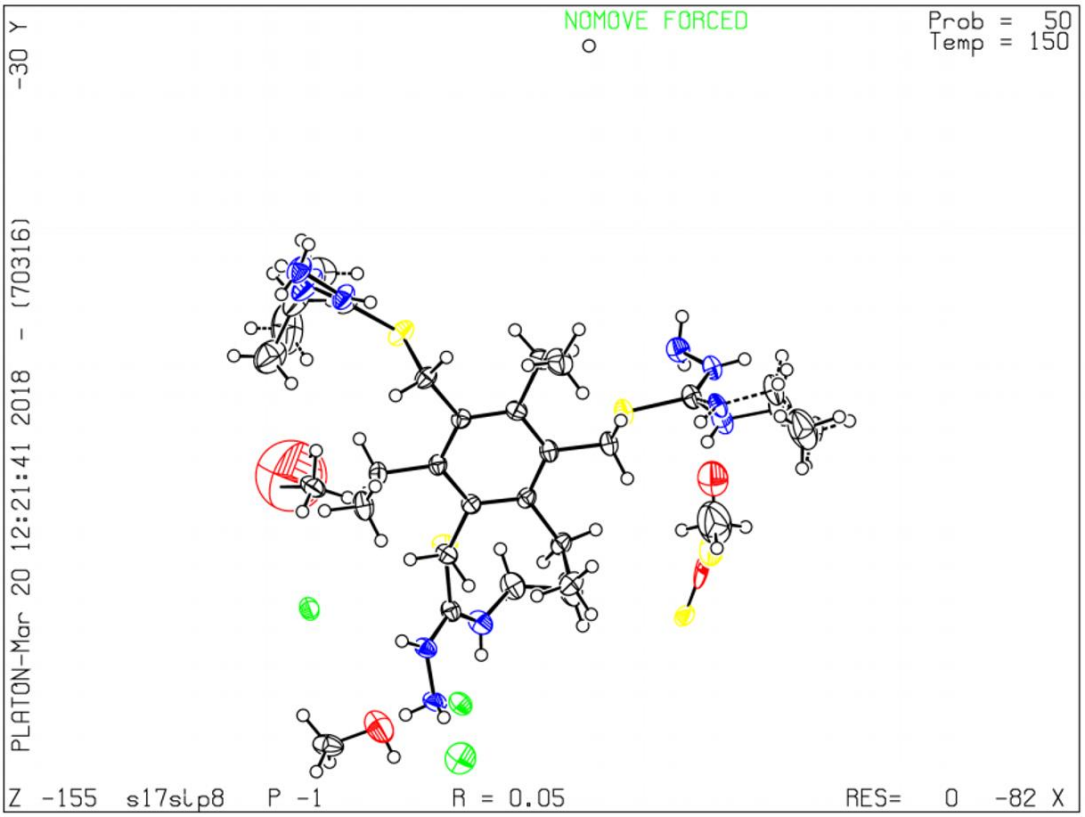

Figure B.2. Crystal structure for compound **27** (generated from "checkcif").

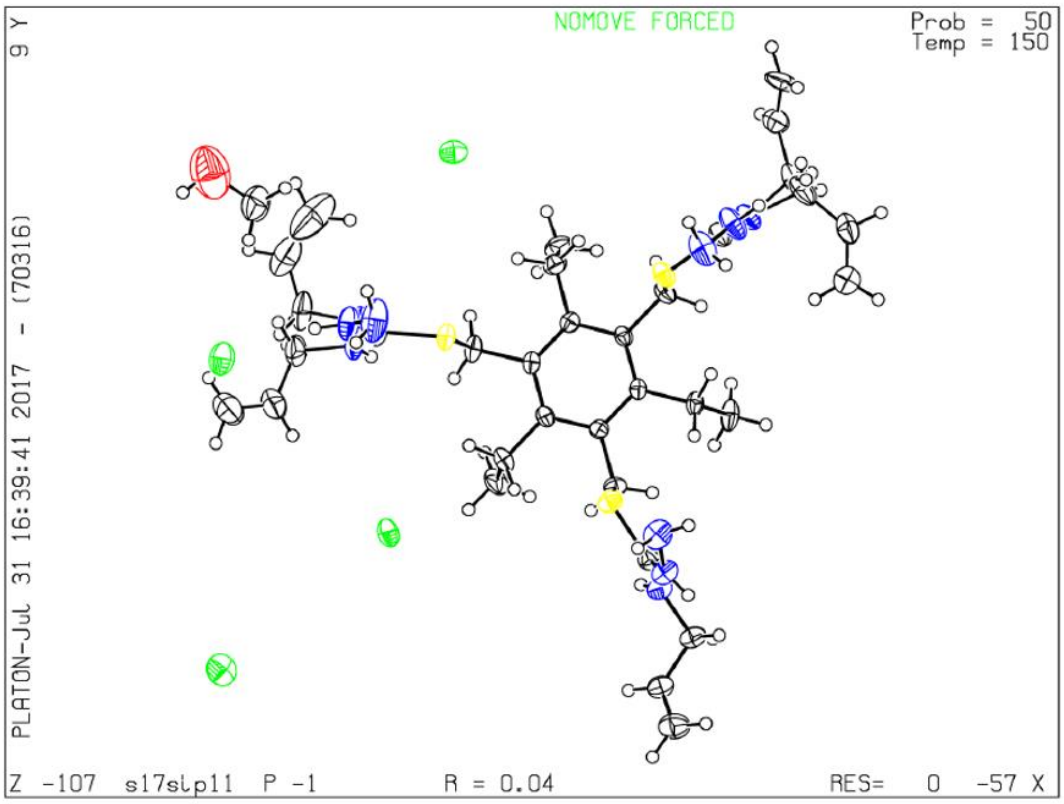

Figure B.3. Crystal structure for compound **29** (generated from "checkcif").

Appendix B.2 (*Chapter 4*)

Attempted complexation to metals

- **Attempted complexation with zirconium(IV)**

Zirconium exists in aqueous solutions mainly as Zr(IV), with an oxidation state of +4. This cation is a hard (Lewis) acid and has an ionic radius of 0.74-0.84 Å.[1] The tetravalent cation Zr^{4+} usually forms 6- and 8-coordinate complexes.[2, 3] Zirconium is an early transition metal and, for this reason, its ion presents relatively low effective nuclear charge. Zr has high oxidation states and the electron configuration for Zr(IV) consists in the loss of all the valence d-electrons, $4d^0$. The large charge density of Zr(IV) is strongly polarising, and this leads to a dramatic increase in acidity of the coordinated aqua ligands, with a strong tendency of forming oxides and hydroxides, which quickly undergo hydrolysis to form highly insoluble polymeric and colloidal species.[4]

For the purpose of coordinating Zr^{4+} to the thiosemicarbazide derivatives, $ZrCl_4$ was used to try to form a coordination complex with the tripodal thiosemicarbazide ligands synthesised in this chapter. The stoichiometry and geometry of the obtained compounds are difficult to predict as these will depend on a number of things: reaction kinetics, synthesis, analysis, etc. Accordingly, and considering that Zr(IV) is oxophilic, a couple of structures were considered. Among other possibilities, a complex consisting in a Zr^{4+} ion surrounded by one molecule of the ligand, with the metal coordinated on the N atoms of the latter, and with two extra water molecules attached to Zr(IV) to complete the octa-coordination would be possible, as would be a complex containing one Zr^{4+} ion and two molecules of the ligand, encapsulating the metal while forming a cage (*Figure B.4*).

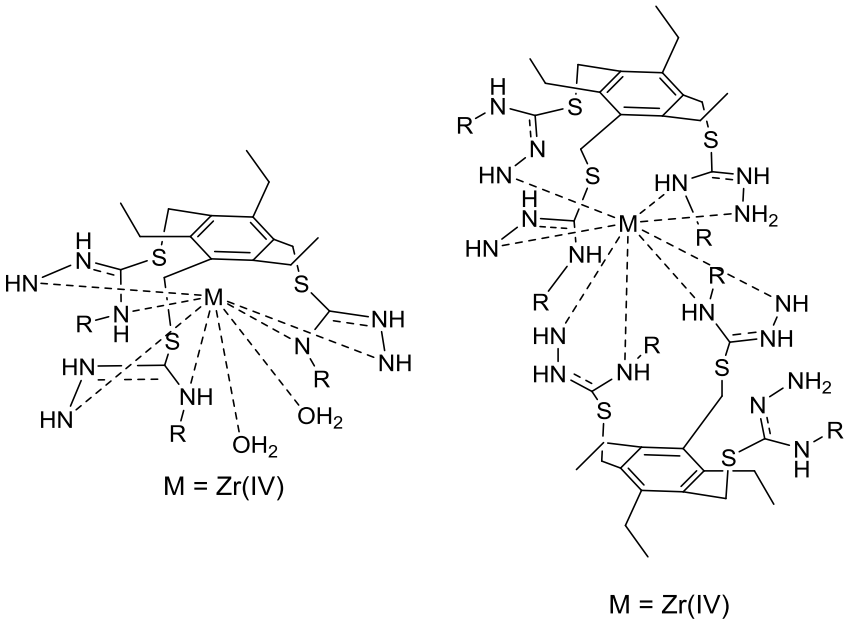

Figure B.4. Proposed structures of two complexes between Zr(IV) and a tripodal thiosemicarbazide ligand, one involving one unit of the latter (left), and the other one involving two units of the ligand forming a cage (right).

Three different reaction conditions were tried to coordinate Zr(IV) using compounds **26** and **27**, respectively. In all the cases, a yellow/brown solid was obtained. It was characterised by mass spectrometry using different methods: electrospray and nanoelectrospray ionisation, matrix-assisted laser desorption/ionisation (MALDI), and atmospheric-pressure chemical ionisation (APCI) with an atmospheric solids analysis probe (ASAP) in case the products were sensitive to water. No evidence of the target materials could be found in the APCI and MALDI analyses of these samples, the latter one being performed with two different matrices. Therefore, none of the data gave any indication of the target compounds, or the presence of the metal used for these reactions, Zr(IV). Using ESI+ and nESI+ on the products obtained from the reactions 2 and 3 (*Table 4.4*), a high intensity peak at m/z = 556.3019 could be identified in the spectra, which corresponds to the ligand used as starting material (compound **27**) with an extra proton, $[M+H]^+$ (*Figure B.5*).

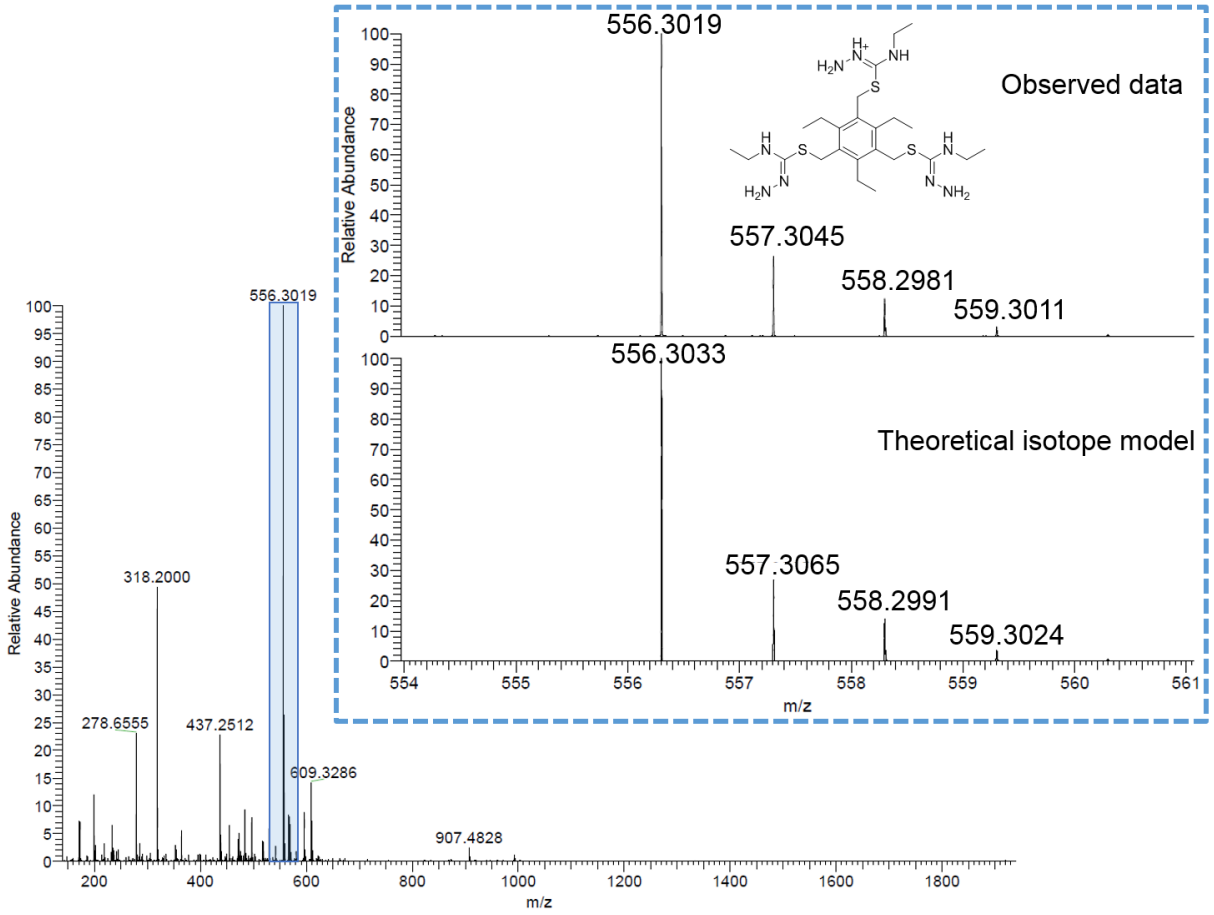

Figure B.5. Mass spectrum of the product from reaction 2 using nESI+, and amplification of the isotopic pattern found for the starting material (compound **27**).

- **Attempted complexation with gallium(III) and indium(III)**

Elements in the Group 13 of the Periodic Table, especially gallium and indium, have atoms with similar properties. The most common ions for these elements, Ga^{3+} and In^{3+}, have valence electrons with the configuration nd^{10}. Both elements have radioisotopes that can be used in PET and SPECT imaging: gallium-68 and indium-111, respectively. The coordination chemistry of gallium and indium is dominated by the +3 oxidation state. They are both hard Lewis acids and tend to form six-coordinate complexes, producing thermodynamically stable complexes with ligands that are hard Lewis bases. Such ligands should contain oxygen and nitrogen donor atoms.[5-7] Gallium can form, in some occasions, four- and five-coordinate complexes, while indium can only form six-coordinated species due to the larger ionic radii.[6]

In aqueous solutions, the only stable oxidation state of gallium is +3, and the free hydrated Ga^{3+} ion is stable only under acidic conditions. It can easily form the insoluble complex $Ga(OH)_3$ in an aqueous environment, while at the physiological pH the solubility is high due to the formation of almost only $[Ga(OH)_4]^-$ ions. The formation of $Ga(OH)_3$ can be mostly avoided

by adding stabilising weak ligands such as acetate or citrate in the preparation of the complexes.[8] It has already been mentioned that thiosemicarbazide derivatives have many advantages, including their anti-microbial properties. Thanks to this, gallium complexes with this type of compounds can present anti-microbial effects and the activities of the metal and the ligand are enhanced.[9]

The ion Ga^{3+} has similar properties to the high spin Fe^{3+} with respect to their coordination chemistry and the majority of chelators being hexadentate. They have similar ionic radii: 62 pm for Ga^{3+} and 65 pm for Fe^{3+}, and the same preferred coordination number of six, although gallium complexes can also be four- or five-coordinated, but they are not so common.[2, 8] When using a Ga^{3+} chelate for radiopharmaceutical purposes in a physiological environment, it is important for the complex to be thermodynamically stable towards hydrolysis and be kinetically inert during the period of clinical use, in a way such that ligand exchange with the blood serum protein transferrin can be avoided. Transferrin has a high affinity for Fe^{3+}, and also for Ga^{3+} at the physiological environment. For this reason, in order to use a gallium complex for clinical purposes, the Ga^{3+}-ligand complexes should be more stable than the Ga^{3+}-transferrin complex or be kinetically inert so that they do not exchange with this protein.[8]

$GaCl_3$ and $InCl_3$ were used as sources of Ga(III) and In(III), respectively, to coordinate them to a tripodal thiosemicarbazide ligand under a variety of conditions, both anhydrous and in aqueous solvents. Gallium and indium compounds usually form complexes with thiosemicarbazide derivatives being coordinated by the S and N donor atoms of the ligand, with a remaining Cl^- atom coordinated to the metal centre that still remains from the metal salt used as starting material (*Figure B.6*).

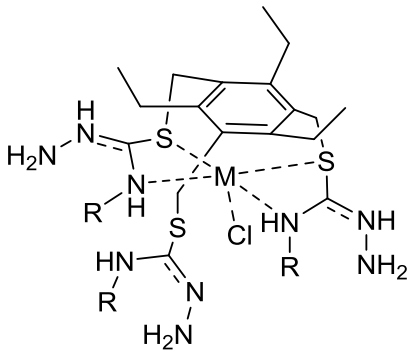

M = Ga(III), In(III)

Figure B.6. Proposed structure of a complex between a M(III), which can be Ga^{3+} or In^{3+}, and a tripodal thiosemicarbazide ligand.

Four different reaction conditions using $GaCl_3$ were tested, and other two using $InCl_3$. When the conditions shown in the entry 4 of the table were used, a brown solid was isolated, while a white solid was obtained using the reaction conditions shown in the entries [5-9]. All the products were characterised by mass spectrometry using the same methods as before (ESI, nESI, MALDI and APCI). Ions correlating with the proposed molecular structure or variations of this were not observed, neither ions that correspond to two ligands encapsulating one metal atom or other more complex structures of the kind. Moreover, there was no evidence of Ga-containing species. However, for reactions [5-9] a peak could be observed in the mass spectrum due to the protonated ligand used as starting material, $[M+H]^+$, which are compounds **26** and **27**, accordingly (*Figure B.7*).

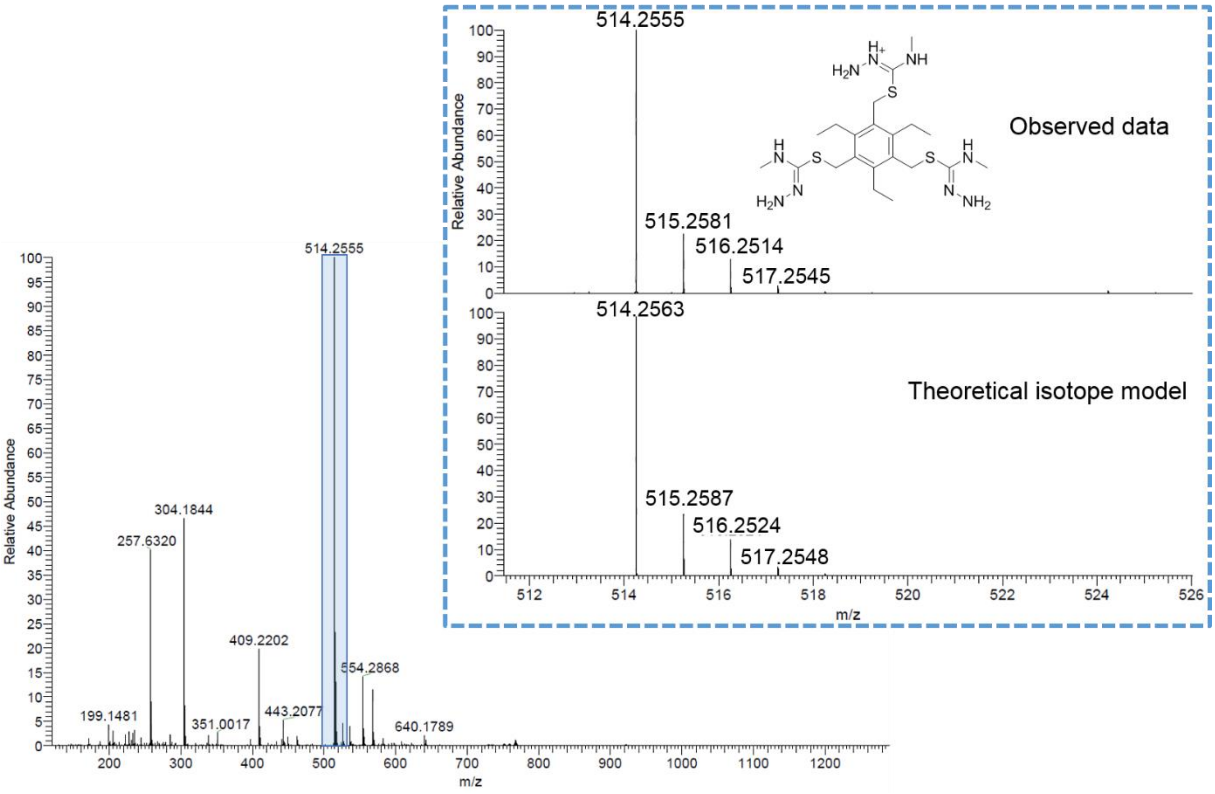

Figure B.7. Mass spectrum of the product from reaction 5 using nESI+, and amplification of the isotopic pattern found for the starting material (compound **26**).

Reactions 5 and 8 were carried out adding a sodium acetate buffer solution to control the pH of the reaction mixture and adjust it to approximately 4, the optimum pH for these two different metal ions to react and be chelated to form a metal-ligand complex.

Metal ions from the Group 13 of the Periodic Table (Al, Ga, In and Tl) do not have a main biological role. However, they are all NMR active nuclides, and as such they can be used in nuclear magnetic resonance spectroscopy of biologically relevant systems. Except thallium, all these metal ions are quadrupolar, which means that they are particularly sensitive to ligand

type and coordination geometry.[10] In the case of gallium, there are two quadrupolar NMR active nuclei of this element: ^{69}Ga and ^{71}Ga. Even though ^{71}Ga is less naturally abundant, it is generally the isotope of choice to perform NMR spectroscopy due to its sensitivity and lower quadrupolar moment.

In this work, ^{71}Ga NMR spectroscopy was performed at the University of Oxford by Dr. Nick Rees to try to identify the presence of this metal in the product from reaction 4 (*Figure B.8*). Gallium seems to be present in the molecule, as the spectrum is not a flat line. However, as ^{71}Ga NMR spectra can only be obtained when the Ga(III) ions are in a highly symmetrical local environment (*e.g.*, in octahedral $[Ga(H_2O)_6]^{3+}$ or in tetrahedral $[Ga(OH)_4]^-$), it is not possible to identify any peak in the spectrum for this molecule.[11, 12]

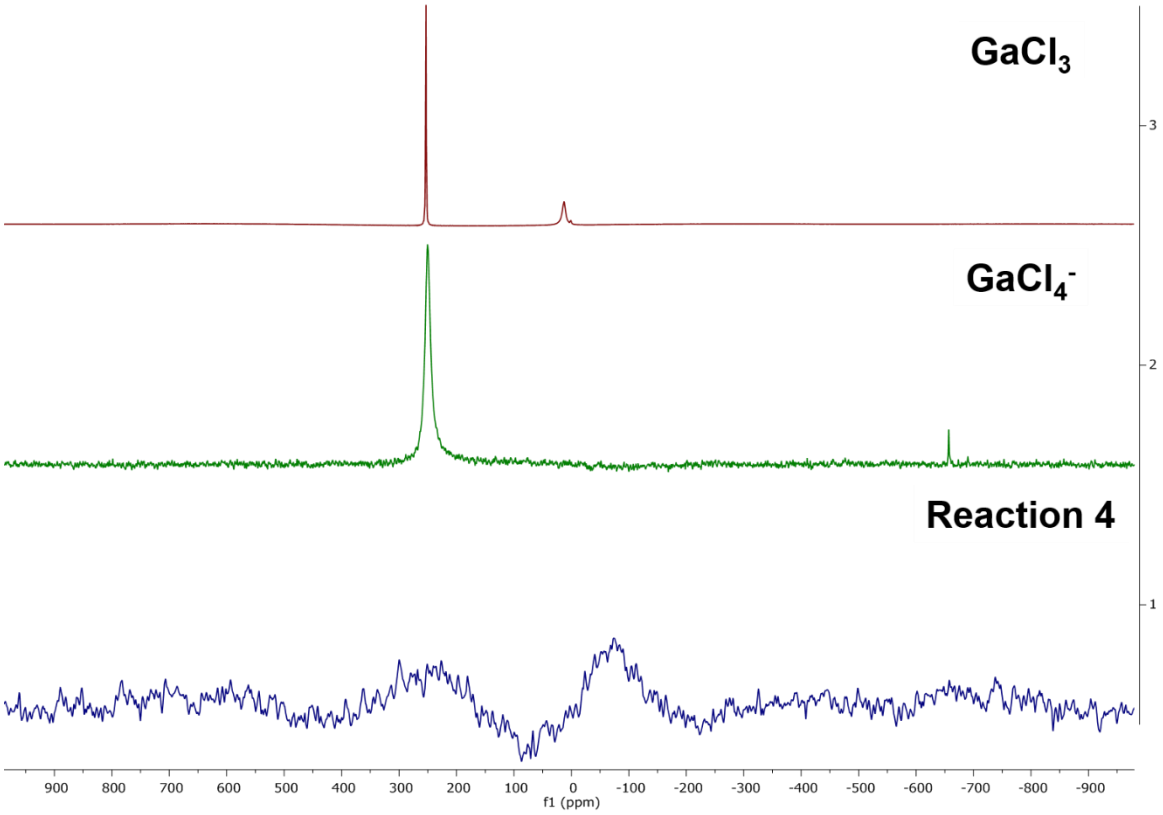

Figure B.18. ^{71}Ga NMR (152 MHz, 298 K) spectra of $GaCl_3$ (DMSO-d_6) (red line), $GaCl_4^-$ (CD_2Cl_2) (green line), and the product from reaction 4 (DMSO-d_6) (blue line).

- **Attempted complexation with copper(II), nickel(II) and zinc(II)**

Copper is a biologically active and essential ion, whose chelating ability and its positive redox potential allow the participation of this species in biological transport reactions.[13] The most important oxidation state of copper to form complexes is the divalent Cu(II), as it has a greater stability than Cu(I).[2] Cu(II)-thiosemicarbazide complexes can be difficult to characterise by

techniques such as NMR spectroscopy due to copper(II) complexes being paramagnetic. For this reason, reactions with nickel(II) and zinc(II) were also performed as the resulting compounds should be, *a priori*, easier to characterise as both elements are diamagnetic in these oxidation states.[14]

Accordingly, three different reaction conditions were tested using $Cu(OAc)_2$ and $Zn(OAc)_2$, and two different ones using $Ni(OAc)_2 \cdot 4H_2O$. Solids of different brownish tones were obtained for Cu(II) and Ni(II), while the solids resulting from the reactions with Zn(II) were all yellow or white. The proposed structure resulting from the complexation of the tripodal thiosemicarbazide ligands with these metal salts is a tetra-coordinated system where the metal is bound to the chelator by the two N and the two S atoms of the latter (*Figure B.9*).

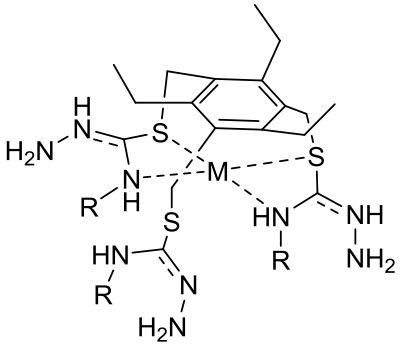

M = Cu(II), Ni(II), Zn(II)

Figure B.9. Proposed structure of a complex between a M(II), which can be Cu^{2+}, Ni^{2+} or Zn^{2+}, and a tripodal thiosemicarbazide ligand.

All the solids obtained were characterised by mass spectrometry using ESI, nESI, MALDI and APCI methods. No evidence of ions that correspond to the proposed molecule or ions with isotope profiles that show the incorporation of the metal ions were observed. In this case, it was not possible to find either peaks corresponding to the tripodal thiosemicarbazide ligand used as starting material. Since none of the starting materials could be identified through the characterisation techniques, there is the possibility that a complex polymeric structure was formed.

- **Further characterisation of the compounds and discussion**

Elemental analysis was carried out on the ligands (compounds **26**, **27**, **28** and **29**), considering that they are tri-HBr salts, and the products resulting from reactions 14 and 15 (*Table B.4*). The percentages found for C, H and N for the ligands are close to the expected percentages, although there is a difference of between 1 and 5% for C, and up to 1% for N. The expected

percentages were calculated adding to the system 3 HBr molecules, which can be found in the crystal structures of the products and remain from the triply brominated starting material.

Table B.4. Elemental analysis results and expected values for the tripodal thiosemicarbazide ligands and two complexes with Ni(II) and Cu(II).

	Found (%) / Expected (%)					
Compound	**C**		**H**		**N**	
26 · 3 HBr	31.69	33.34	5.77	5.60	15.67	16.66
27 · 3 HBr	34.08	36.10	5.87	6.06	14.33	15.79
28 · 3 HBr	40.87	45.87	5.15	5.13	13.32	13.37
29 · 3 HBr	37.70	38.85	5.72	5.80	14.10	15.10
Reaction 14	47.13	46.75	7.15	7.68	8.94	20.45
Reaction 15	46.07	46.25	6.62	7.60	6.44	20.23

The ligands (compounds **26**, **27**, **28** and **29**) and the products from the complexation reactions were characterised by Raman spectroscopy (*Figure B.10*). The spectra of compounds **26** and **27** are alike, with similar peaks and intensities. This is due to the similarity in the structure of these two compounds, which only differ in three extra methyl groups at the end of each thiosemicarbazide arm for compound **27**. However, the spectra of compounds **28** and **29** are different among them and in comparison to the previous two ligands, as these two molecules have a phenyl and an allyl group, respectively, at the end of each of the three thiosemicarbazide arms. Regarding the products obtained from some of the reactions, those of reactions 5 and 6 have similar Raman spectra, as they are both solids coming from a reaction between compound **26** and $GaCl_3$. The solids from reactions 8 and 9 are both potentially $InCl_3$ derivatives with compound **26**, and their spectra also present many similarities in peaks and intensities. The solid from reaction 12 is a Cu(II) derivative with compound **29**, and the one from reaction 16 is a Zn(II) derivative with the same compound. These two solids have different Raman spectra. The solid from reaction 12 has a high intensity peak at around 650 cm^{-1}, while the solid from reaction 16 does not have it. All the products have a very high intensity peak at around 100 cm^{-1} (*Table B.5*).

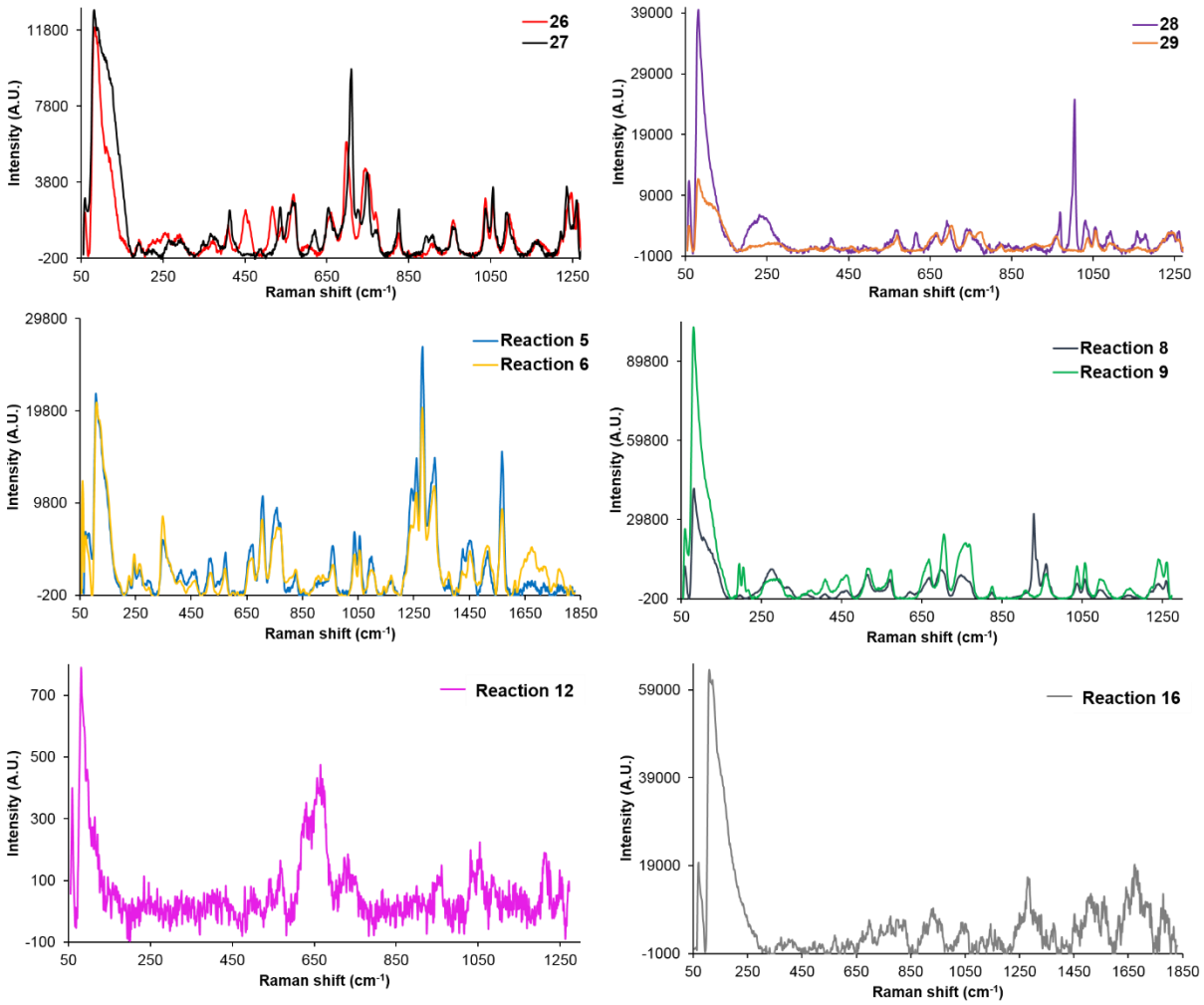

Figure B.10. Raman spectra of compounds **26** (red), **27** (black), **28** (purple), **29** (orange), and products from reactions 5 (blue), 6 (yellow), 8 (dark grey), 9 (green), 12 (pink) and 16 (grey).

Table B.5. Band assignment for the Raman spectra of compounds **26**, **27**, **28**, and **29**, and products from reactions 5, 6, 8, 9, 12 and 16 (*Figure B.10*).[15, 16]

Wavenumber / cm^{-1}	Vibrational mode
~ 1650	ν(NC)
1600 - 1400	ν(CC), δ(HCC), δ(HCH), δ(CCC)
1315 - 1200	ν(NC), δ(HNC)
~ 1100	ν(NN)
1000 - 990	δ(CCC)
~ 720	ν(SC)
~ 430	δ(CCN)
270 – 240	ω(CNNC)
~ 155	δ(NCC), δ(NNC), δ(CNN)
~ 85	ω(CNCS), τ(C-NH_2)

Infrared spectroscopy was also carried out in the solid state (*Figure B.11*) and, although the vibrations in the spectra of the expected metal-ligand complexes when compared to the ligand used as starting material are similar, they appear at slightly different wavenumbers (*Table B.6*).[17] Accordingly, it can be observed that the band corresponding to v(C=N) is shifted in the metal-ligand complexes to a lower frequency. However, the coordination positions of the ligands with the metals cannot be elucidated using FT-IR, as the lowest recorded frequency is 650 cm^{-1}, and these would appear at smaller wavenumbers.

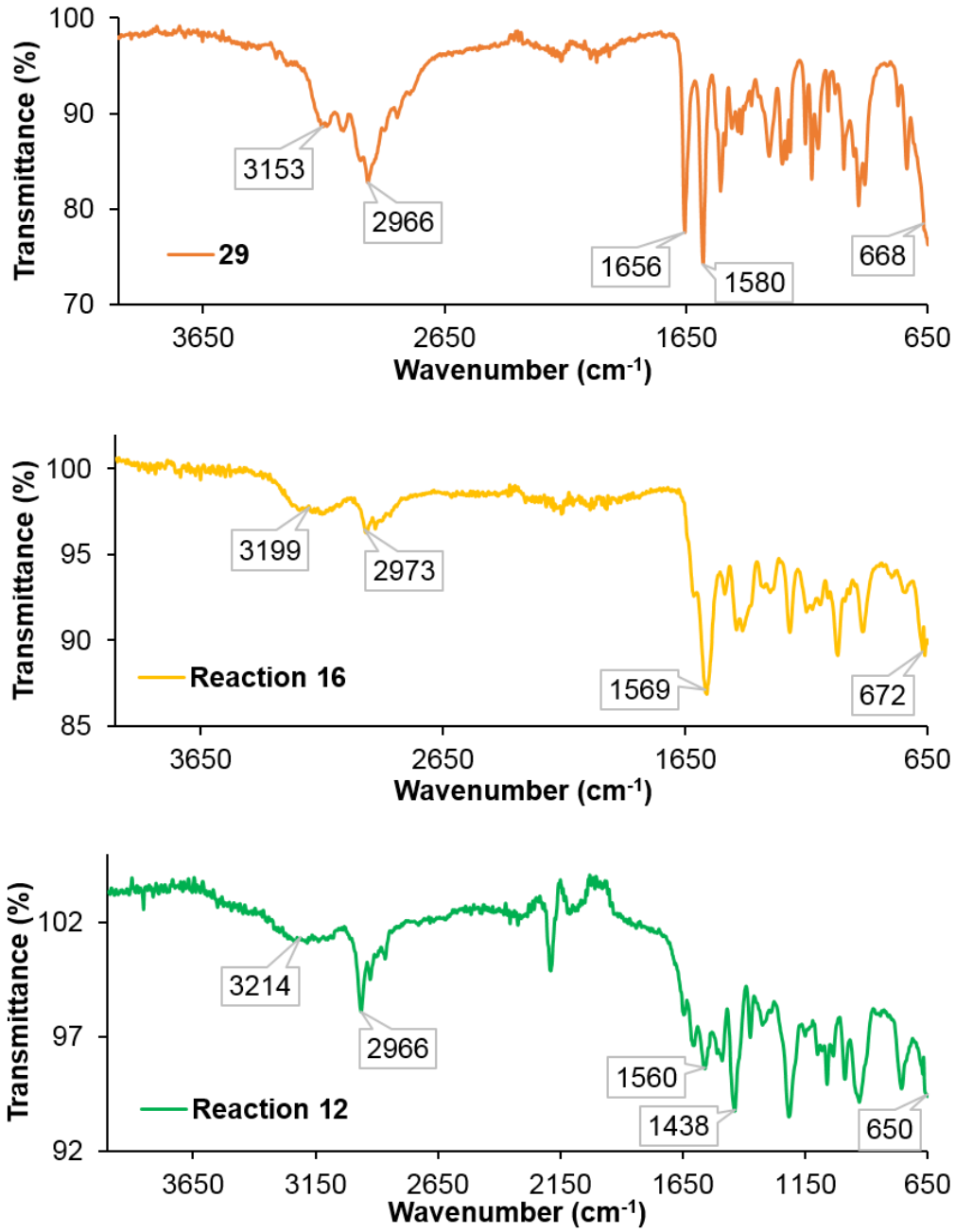

Figure B.11. FT-IR spectra of compound **29** (orange), and products from reactions 16 (yellow) and 12 (green).

Table B.6. Band assignment for the FT-IR spectra of compound **29** and products from reactions 16 and 12 (*Figure B.11*).

Compound	Wavenumber / cm^{-1}	Vibrational mode
29	3153	N-H st
	2966	C-H st
	1656	C=N st
	1580	
	668	C-S st
Reaction 16	3199	N-H st
	2973	C-H st
	1569	C=N st
	672	C-S st
Reaction 12	3214	N-H st
	2966	C-H st
	1560	C=N st
	1438	
	650	C-S st

UV/visible spectroscopy was carried out in order to compare the properties of the tripodal thiosemicarbazide ligands with those of the products from the reactions with metals (*Figure B.12*). The spectrum of compound **26** shows a sharp peak at 262 nm. The spectra of the solids from some reactions carried out using this compound (1, 4, 9 and 10) are overlaid with the spectrum of compound **26**. The products from reactions 4 and 10 have maximum intensity peaks at 261 nm, and the one from reaction 9 has its maximum at 270 nm. The three solids have a peak followed by a tail, which is likely due to the charge transfer band in the metal-ligand complex. Solid 1 has relative maximums at 261 nm and 381 nm, and an absolute maximum at 359 nm. The shape of the spectrum for this product is peculiar and different to the other three, with two curves and three peaks. The spectrum of compound **27** shows a maximum intensity peak at 268 nm. The close wavelength might be due to the similar structures of compounds **26** and **27**. When compared to the spectra of the products from reactions 14 and 15, which were carried out using this ligand as starting material, they have similar maxima, the latter two being at 270 nm. However, the shape of the peak is different in each case; the spectra of the two solids have a tail, likely due again to the charge transfer band in the complex. In general, there are wider peaks in the spectra of the potential synthesised complexes than in those of the ligands. Fluorescence spectroscopy was carried out but the compounds showed not to be fluorescent.

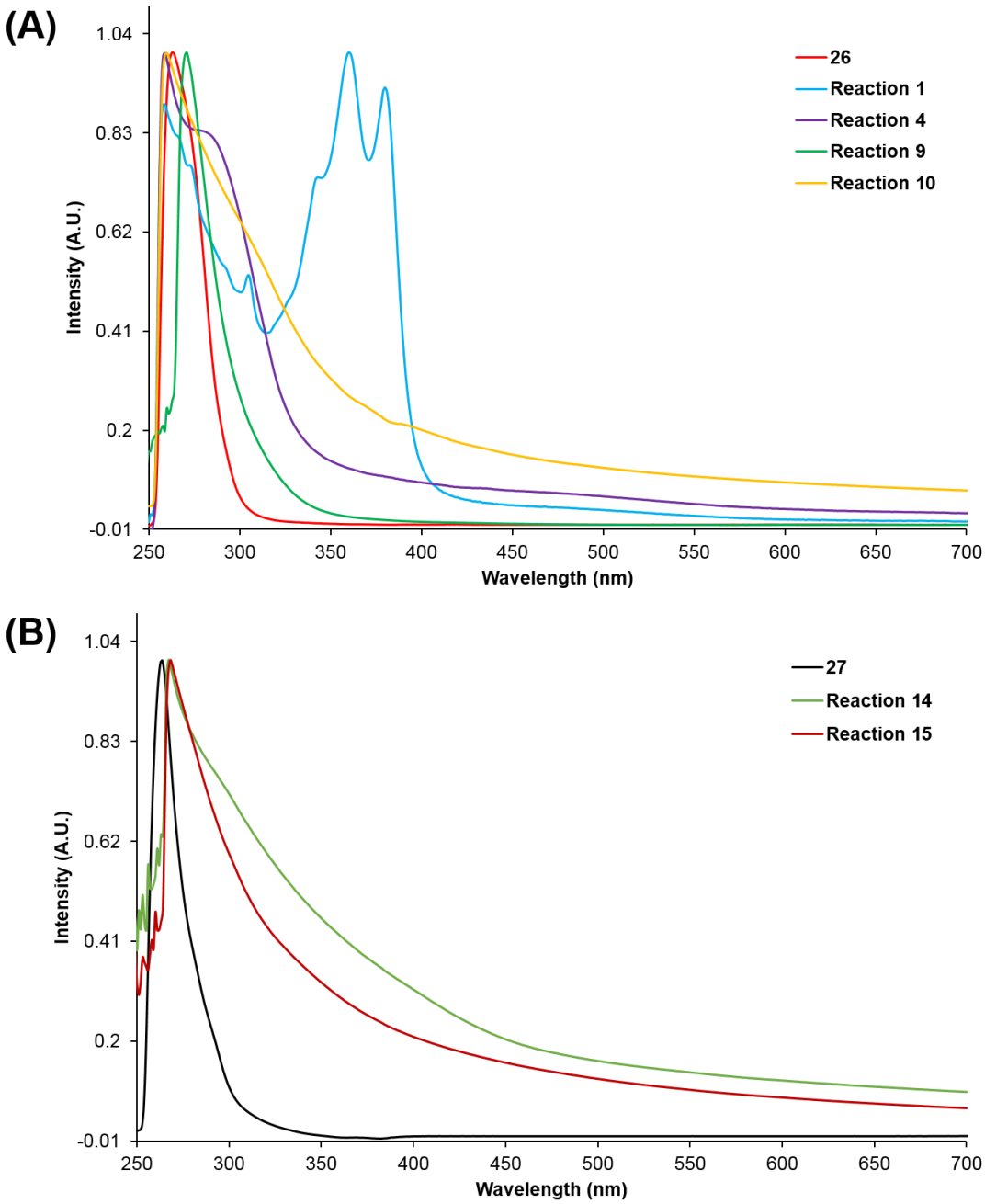

Figure B.12. Normalised UV/visible spectra of compounds **26** (red) and **27** (black), and products from reactions 1 (blue), 4 (purple), 9 (green), 10 (yellow), 14 (light green) and 15 (dark red).

NMR spectroscopy analyses were carried out on these solids but the results were not conclusive: in some cases, only peaks due to solvents and water could be observed, while in other cases the spectra presented similar resonances to those in the spectra of compounds **26**, **27**, **28** and **29**. For some products, new resonances appeared in the spectra of the resulting solids, but it was not possible to assign them.

Numerous attempts to grow crystals of these molecules for single crystal X-ray diffraction analysis were carried out, all of them unsuccessfully.

Looking at all the data collected to analyse these potential metal-ligand complexes, conclusions can be made. While mass spectrometry does not show evidence of the formation of the complexes, other analysis such as UV/visible spectroscopy show peaks that indicate that a metal is present in the product and coordinated to a ligand. Moreover, IR spectroscopy shows signals corresponding to the ligand used as starting material for each reaction, which is coherent as the organic part is the one that can be seen in the IR spectra and this remains unchanged from the ligand. Raman spectroscopy suggests the same, with some visible peaks assignable to the stretching of bonds in the ligand. In summary, the formation of complexes with metals possibly worked, but the structure of the final products could not be identified. When complexes could be synthesised, even without having the desired analytical information, they could potentially be air and water sensitive. This is not desired for an *in vivo* imaging agent. Moreover, all the solids resulting from the reactions with the metals were highly insoluble in aqueous and organic solvents, therefore not suitable for *in vivo* or *in vitro* studies. Finally, the formation of polymer-like structures, with many units of the ligand and metal ion used, should also be considered, as it has been seen to happen in the crystal structures through hydrogen bonding. This would hinder even more the characterisation of the products.

References for Appendix B.2

1. R. Shannon, *Acta Crystallogr. A*, 1976, **32**, 751-767.
2. L. E. McInnes, S. E. Rudd and P. S. Donnelly, *Coord. Chem. Rev.*, 2017, **352**, 499-516.
3. A. S. Solovkin and Z. N. Tsvetkova, *Russ. Chem. Rev.*, 1962, **31**, 655.
4. T. E. Macdermott, *Coord. Chem. Rev.*, 1973, **11**, 1-20.
5. R. G. Pearson, *J. Am. Chem. Soc.*, 1963, **85**, 3533-3539.
6. K. George, M. Jura, W. Levason, M. E. Light, L. P. Ollivere and G. Reid, *Inorg. Chem.*, 2012, **51**, 2231-2240.
7. A. Evers, R. D. Hancock, A. E. Martell and R. J. Motekaitis, *Inorg. Chem.*, 1989, **28**, 2189-2195.
8. M. Fani, J. P. André and H. R. Maecke, *Contrast Media Mol. Imaging*, 2008, **3**, 53-63.
9. J. A. Lessa, G. L. Parrilha and H. Beraldo, *Inorg. Chim. Acta*, 2012, **393**, 53-63.
10. J. P. André and H. R. Mäcke, *J. Inorg. Biochem.*, 2003, **97**, 315-323.
11. Q. Zhou, C. Henoumont, L. Vander Elst, S. Laurent and R. N. Muller, *Contrast Media Mol. Imaging*, 2011, **6**, 165-167.
12. J. D. Glickson, T. P. Pitner, J. Webb and R. A. Gams, *J. Am. Chem. Soc.*, 1975, **97**, 1679-1683.
13. D. X. West, A. E. Liberta, S. B. Padhye, R. C. Chikate, P. B. Sonawane, A. S. Kumbhar and R. G. Yerande, *Coord. Chem. Rev.*, 1993, **123**, 49-71.
14. D. Palanimuthu, S. V. Shinde, K. Somasundaram and A. G. Samuelson, *J. Med. Chem.*, 2013, **56**, 722-734.
15. Y. Sert, B. Miroslaw, Ç. Çırak, H. Doğan, D. Szulczyk and M. Struga, *Spectrochim. Acta A*, 2014, **128**, 91-99.
16. S. Muthu, E. Elamurugu Porchelvi, M. Karabacak, A. M. Asiri and S. S. Swathi, *J. Mol. Struct.*, 2015, **1081**, 400-412.
17. R. M. El-Shazly, G. A. A. Al-Hazmi, S. E. Ghazy, M. S. El-Shahawi and A. A. El-Asmy, *Spectrochim. Acta A*, 2005, **61**, 243-252.